

# Optimization in Geometric Materials

Combining Algebraic and Riemannian Geometry to Optimize  
Geometric Constraint Systems in Materials Science

---

**Matthias Himmelmann**

## Dissertation

to obtain the academic degree  
“doctor rerum naturalium”  
(Dr. rer. nat.)  
in the scientific discipline “Geometry”



submitted to the  
Institute of Mathematics  
Faculty of Science  
University of Potsdam

Disputation held in Potsdam, Germany, on January 06, 2025

Unless otherwise indicated, this work is licensed under a Creative Commons License Attribution – NonCommercial – NoDerivatives 4.0 International. This does not apply to quoted content and works based on other permissions.

To view a copy of this licence visit:

<https://creativecommons.org/licenses/by-nc-nd/4.0/legalcode.en>

First supervisor: Prof. Dr. Myfanwy Evans  
Second supervisor: Ass. Prof. Dr. Alexander Heaton

Reviewers: Prof. Dr. Timo de Wolff  
Prof. Dr. Frank Sottile

Published online on the  
Publication Server of the University of Potsdam:  
<https://doi.org/10.25932/publishup-66927>  
<https://nbn-resolving.org/urn:nbn:de:kobv:517-opus4-669274>



---

# Abstract

---

This thesis aims to investigate particular geometric materials with algebro-geometric constraints by combining physically meaningful geometric models with coarse discretizations and robust optimization routines. Ultimately, this makes the investigation of previously inaccessible, increasingly complex structures feasible. It is a promising endeavor to explore robust numerical optimization techniques in conjunction with geometric models since the main objective in many physical systems is the minimization of energy. Energies occur in various real-world scenarios, be it facet tension in soap film, intermolecular pair potentials, entropy, and the elastic energy occurring in a material's deformation. All these different types of energy are discussed in some form in this thesis.

With primary applications in civil engineering and architecture, framework materials are used to investigate both a structure's rigidity and flexibility. A large class of geometric constraint systems can be modeled by framework materials. These structures are given by embedded graphs with their edges equipped with physical distance constraints. Via the Euclidean distance between points, their deformations provide a compelling connection between materials science and algebraic geometry. When adding elastic elements carrying intrinsic energy to the framework, a tensegrity framework is created, paradoxically stabilizing an otherwise flexible structure.

This work considers two distinct applications of rigidity theory. Firstly, we generate random point processes in the square to experimentally verify asymptotic bounds for the local and global rigidity of the corresponding Gilbert frameworks. This leads to an enhanced understanding of what typically prevents a graph's unique realizability in  $\mathbb{R}^2$ . Secondly, the regular dodecahedron with edge length and coplanarity constraints is examined. This polytope is rigid and we can locally describe the deformation space induced by edge-contractions.

To study material deformations effectively, a reliable and robust method for traversing the configuration space is essential. For this reason, the metric projection onto the constraint set is considered, matching geodesics up to second order. By using homotopy continuation to solve the implicit closest point problem, we can prove theoretical convergence guarantees. This method relies on a predictor-corrector scheme based on Newton's method with adaptive step sizes. As such, it prevents the jumping between connected components. The retraction map is applied in Riemannian optimization routines after constructing appropriate step sizes and directions of descent. These algorithms provide an invaluable tool for the optimization over smooth constraint sets, which has led to successful applications in dynamical systems, robotics, and computer vision. Analyzing the algorithm's performance on multiple examples, Newton's method is more efficient than the predictor-corrector scheme. Still, the theoretical guarantees justify the computational overhead of the predictor step in many cases.

Lipid bilayers minimize surface tension, suggesting that they can be modeled as minimal surfaces using Riemannian geometry. These membranes occur in many organic settings. For ordered phases with crystalline symmetry, periodic bicontinuous minimal surfaces provide

established models. Conversely, a minimal surface model for amorphous phases does not exist. To sample the space of minimal surfaces, we propose two models for generating disordered interfaces in combination with a topology-stabilized curvature optimization routine. We provide experimental evidence for why disordered surfaces can form by investigating two homogeneity measures on all generated surfaces. In addition, our work demonstrates the degree to which the curvature homogeneity of the cubic Gyroid surface is superior to its entropy-favored amorphous counterparts. It thereby contributes a general geometric result of relevance to bicontinuous structure formation in soft matter and biology across all lengthscales, relevant to both ordered and amorphous phases.

Triply periodic cylinder packings constitute another geometric system that we investigate in this thesis. Some of these packings exhibit a cooperative unwinding mechanism, reminiscent of auxeticity. This property describes an expansive lateral response upon stretching a material in a fixed direction, making such structures a prime target for the design of metamaterials with targeted functionality, such as impact protection and filtration. We create a robust geometric model based on tensegrity frameworks for the configuration space of two filaments in tight, orthogonal contact. The corresponding elastic elements are constructed by assuming that the incompressible cylinders want to minimize their length. It is used to compute the deformation paths of two particular cylinder packings via Riemannian optimization and homotopy-based path-tracking. As a result, we show that both structures are auxetic by multiple definitions.

Finally, we generalize the theory of weavings to surfaces. Constructing a robust model based on tensegrity frameworks to study weavings in curved space results in a nonlinear optimization problem. This tensegrity model is suitable for analyzing tangled weaves and complex contact geometries. Our model is most robust on surfaces where all points are geometrically identical. It accurately simulates the behavior of weavings on the sphere and the flat torus. In order to find the weave that energetically prefers the sphere the most, we deform the underlying surface into a spheroid. The energy landscape resulting from this deformation reveals that the more regular the weave, the more it prefers the sphere.

---

## Deutsche Zusammenfassung

---

Die vorliegende Dissertation hat das Ziel, bestimmte Materialien zu untersuchen, die algebro-geometrischen Nebenbedingungen genügen, indem physikalisch motivierte geometrische Modelle mit groben Diskretisierungen und robusten Optimierungsroutinen kombiniert werden. Dies ermöglicht die Betrachtung zuvor unzugänglicher, zunehmend komplexer Strukturen. Da viele physikalische Systeme als Hauptziel die Minimierung ihrer Energie haben, stellt die Kombination von robusten, numerischen Optimierungsmethoden und geometrischen Modellen einen vielversprechenden Ansatz dar. Energien treten in verschiedenen Szenarien auf, sei es als Oberflächenspannung in Seifenhäuten, intermolekulare Wechselwirkungen, Entropie oder als elastische Energie, die bei der Deformation eines Materials auftritt. Alle diese verschiedenen Energieformen werden in dieser Arbeit in der einen oder anderen Form behandelt.

Fachwerke sind eingebettete Graphen, deren Kanten mit physikalischen Abstandsbedingungen ausgestattet sind. Mit primären Anwendungen im Bauingenieurwesen und in der Architektur werden sie verwendet, um sowohl die Starrheit als auch die Flexibilität einer Struktur zu untersuchen. Eine große Klasse von geometrischen Systemen kann durch Fachwerke modelliert werden. Mittels des Euklidischen Abstand zwischen Knoten bieten ihre Deformierungen eine überzeugende Verbindung zwischen Materialwissenschaft und algebraischer Geometrie. Durch das Hinzufügen von elastischen Elementen, die intrinsische Energie tragen, entsteht ein Tensegrity-Fachwerk, welches paradoxeise eine ansonsten flexible Struktur stabilisiert.

Diese Arbeit betrachtet zwei unterschiedliche Anwendungen der Starrheitstheorie. Erstens erzeugen wir zufällige Punktprozesse in einem Quadrat, um asymptotische Schranken für die lokale und globale Starrheit der entsprechenden Gilbert-Fachwerke experimentell zu überprüfen. Dies führt zu einem verbesserten Verständnis dafür, was typischerweise die eindeutige Realisierbarkeit eines Graphen in  $\mathbb{R}^2$  verhindert. Zweitens werden konvexe Polytope mit Kantenlängen- und Koplanaritätsbedingungen untersucht. Wir zeigen dass der reguläre Dodekaeder starr ist und liefern eine lokale Beschreibung des zugehörigen, durch Kantenkontraktionen induzierten Deformationsraum.

Um Materialverformungen effektiv zu untersuchen, ist eine zuverlässige und robuste Methode zur Durchquerung des Konfigurationsraums unerlässlich. Aus diesem Grund wird die metrische Projektion auf die Nebenbedingungen betrachtet, welche Geodäten bis zur zweiten Ordnung annähert. Durch die Verwendung einer Homotopie-Fortsetzung zur Lösung des impliziten Problems des nächstgelegenen Punkts können wir theoretische Konvergenzgarantien nachweisen. Die Homotopy-Fortsetzung basiert auf einem Prädiktor-Korrektor-Verfahren, welches seinerseits auf dem Newtonverfahren mit adaptiven Schrittweiten fußt. Dadurch wird das Springen zwischen Zusammenhangskomponenten verhindert. Durch die Berechnung von geeigneten Schrittweiten kann die Retraktionsabbildung in Riemannschen Optimierungsalgorithmen angewendet werden. Diese Algorithmen sind ein nützliches Werkzeug für die Optimierung unter glatten Nebenbedingungen, was bereits zur erfolgreichen Anwendungen in dynamischen

Systemen, Robotik und Computer Vision geführt hat. Bei der Leistungsanalyse des Algorithmus anhand von mehreren Beispielen ist das Newtonverfahren effizienter als das Prädiktor-Korrektor-Verfahren. Dennoch rechtfertigen theoretische Garantien in vielen Fällen den rechnerischen Mehraufwand des Prädiktorschritts.

Doppellipidschichten minimieren die Oberflächenspannung, was darauf hindeutet, dass sie als Minimalflächen mit Hilfe der Riemannschen Geometrie modelliert werden können. Diese Membranen kommen in vielen organischen Umgebungen vor. Für geordnete Phasen mit kristalliner Symmetrie bieten periodische bikontinuierliche Minimalflächen etablierte Modelle. Im Gegensatz dazu existiert ein Minimalflächenmodell für amorphe Phasen nicht. Wir schlagen in dieser Arbeit zwei Modelle zur Erzeugung ungeordneter Minimalflächen in Kombination mit einer topologiestabilisierten Krümmungsoptimierungsroutine vor. Experimenten belegen wir, dass ungeordnete Flächen entstehen können, indem wir zwei Homogenitätsmaße auf allen erzeugten Flächen untersuchen. Darüber hinaus zeigt diese Arbeit, inwieweit die Krümmungshomogenität der kubischen Gyroid- und Diamantflächen ihren entropisch günstigeren amorphen Gegenstücken überlegen ist. Damit trägt sie zu einem allgemeinen geometrischen Verständnis sowohl für geordnete als auch für amorphe Phasen bei, was für die strukturelle Selbstassemblierung in weicher Materie und in organischen Systemen auf allen Längenskalen relevant ist.

Dreifach periodische Zylinderpackungen stellen ein weiteres geometrisches System dar, das in dieser Arbeit untersucht wird. Einige dieser Packungen zeigen einen kooperativen Mechanismus, der an auxetische Materialien erinnert. Diese Materialeigenschaft beschreibt eine expansive laterale Reaktion beim Dehnen eines Materials in eine feste Richtung. Damit sind solche Strukturen besonders für das Design von Metamaterialien mit gezielter Funktionalität geeignet, wie z.B. Aufprallschutz und Filtration. Hierzu erstellen wir ein robustes geometrisches Modell basierend auf Tensegrity-Fachwerken für den Konfigurationsraum von zwei Filamenten inorthogonalem Kontakt. Die entsprechenden elastischen Elemente werden konstruiert, indem angenommen wird, dass die unelastischen Zylinder ihre Länge minimieren wollen. Dieses Modell wird verwendet, um die Deformationen von zwei bestimmten Zylinderpackungen über Riemannsche Optimierung und ein homotopie-basiertes Prädiktor-Korrektor-Verfahren zu approximieren. Als Ergebnis zeigen wir, dass beide Strukturen nach mehreren Definitionen auxetisch sind.

Schließlich verallgemeinern wir die Theorie von Verflechtungen in der Ebene auf Flächen im  $\mathbb{R}^3$ . Die Konstruktion eines robusten Modells basierend auf Tensegrity-Fachwerken zur Untersuchung von Verflechtungen im gekrümmten Raum führt zu einem nichtlinearen Optimierungsproblem. Dieses Tensegrity-Modell eignet sich zur Analyse von verzweigten Verflechtungen mit komplexen Kontaktgeometrien. Unser Modell ist auf der Sphäre und dem flachen Torus am robustesten, da dort alle Punkte geometrisch identisch sind. Um die Verflechtung zu finden, welche energetisch die Sphäre bevorzugen, deformieren wir die zugrunde liegende Fläche zu einem Sphäroid. Die dieser Deformation zugehörige Potentialhyperfläche zeigt, dass die Verflechtung die Sphäre umso mehr bevorzugt, je regelmäßiger sie ist.

---

## Acknowledgements

---

First and foremost, I would like to express my deepest gratitude to my supervisor, *Myfanwy Evans*, who helped me through this thesis with her continuous support, valuable advice and constant availability for discussions. She introduced me to the fascinating world of geometric materials, promoted an exceptionally positive group dynamic, and encouraged the open exchange of ideas. By granting me the freedom to independently explore topics and by supporting my participation in various workshops, she significantly facilitated my research. Without a doubt, she has been the ideal mentor for my Ph.D. project.

Moreover, I want to express my appreciation to my second supervisor, *Alex Heaton*, who was available for various late-night discussions about numerical algebraic geometry and Riemannian optimization. Bouncing ideas back and forth and solving problems related to rigidity and tensegrity frameworks was not only productive but also immensely enjoyable.

*Gerd Schröder-Turk* deserves my sincere gratitude as well. He proposed an exciting problem about disordered minimal surfaces that challenged me to learn many new skills and go well beyond my mathematical comfort zone. During countless hours of exchanges of ideas about how to approach the problem best, I learned invaluable lessons about interdisciplinary research. I have particularly enjoyed our incredibly productive joint problem-solving sessions.

Special thanks go to *Bernd Sturmfels* who connected me with this intriguing field of research that I might not have otherwise encountered.

In addition, I had the pleasure of collaborating with *May Cai, Katie Clinch, Martin Cramer Pedersen, Sean Dewar, Matteo Gallet, Georg Grasegger, Michael Klatt, Jan Legerský, Birte Ostermann, Philipp Schönhöfer, Bernd Schulze, Martin Winter* and *Albert Zhang*. Many useful discussions occurred both at various workshops and online. I am grateful for the input, creative solutions, and perspectives that these collaborations provided. It is truly remarkable to realize how many people contributed, directly or indirectly, to the development of this dissertation.

The research community at conferences and workshops was extraordinarily welcoming, allowing me to engage in numerous valuable discussions on topics ranging from rigidity theory, real algebraic geometry, and metric geometry to computational problems, implementation details, and material properties. In particular, I want to thank *Paul Breiding, Timo de Wolff, Elisenda Feliu, Stephen Hyde, Alison La Porta, Tony Nixon, Signe Lundqvist, Vira Raichenko, Henrik Schumacher* and *Meera Sitharam*, as well as many others I met during my Ph.D. journey.

This endeavor would not have been possible without my parents, who nurtured my scientific curiosity from a young age and supported me in various ways through my studies and my life.

Emphatically and wholeheartedly, I want to thank my partner, *Isa*, for her unwavering support. She always listened to my worries and problems and played a crucial role in enhancing the thesis, both in terms of syntax and language. I could not have asked for a better partner during this stressful time.

Finally, I would like to acknowledge the financial support from the project “Discretization in

Geometry and Dynamics” (SFB 109) in the Deutsche Forschungsgemeinschaft (DFG), without which this work would not have been possible. I also appreciate the educational software license provided by SideFX Houdini, which was instrumental in my research.

---

# Table of Contents

---

|   |           |
|---|-----------|
| Abstract . . . . .  | iv        |
| Deutsche Zusammenfassung . . . . .  | vi        |
| Acknowledgements . . . . .  | viii      |
| <b>1 Introduction</b>   | <b>12</b> |
| 1.1 Context of this Work . . . . .  | 13        |
| 1.2 Structure and Significance . . . . .                                    | 18        |
| <b>2 Geometric Theory of Framework Materials</b>                            | <b>24</b> |
| 2.1 Literature Review . . . . .   | 27        |
| 2.1.1 Background in Algebraic Geometry . . . . .                            | 27        |
| 2.1.2 Bar-and-Joint Frameworks and Rigidity Theory . . . . .                | 31        |
| 2.1.2.1 Periodic Frameworks . . . . .                                       | 35        |
| 2.1.2.2 Auxeticity . . . . .  | 38        |
| 2.1.3 Tensegrity Frameworks . . . . .                                       | 43        |
| 2.1.3.1 Multistability . . . . .  | 45        |
| 2.2 Asymptotic Global Rigidity of Geometric Random Graphs . . . . .         | 49        |
| 2.3 Flexing the Regular Dodecahedron . . . . .                              | 56        |
| <b>3 Riemannian Optimization by Homotopy Continuation</b>                   | <b>63</b> |
| 3.1 Riemannian Manifolds . . . . .  | 65        |
| 3.2 Background: Riemannian Optimization and Homotopy Continuation . . . . . | 73        |
| 3.2.1 Riemannian Optimization . . . . .                                     | 74        |
| 3.2.2 Homotopy Continuation . . . . .                                       | 77        |
| 3.3 Algorithms and Theoretical Results . . . . .                            | 79        |
| 3.3.1 Newton's Method . . . . .   | 80        |
| 3.3.2 Homotopy Continuation by Newton's Method . . . . .                    | 81        |
| 3.3.3 Predictor-Corrector Approach . . . . .                                | 86        |
| 3.4 Backtracking Line Search . . . . .                                      | 89        |
| 3.5 Algebraic Varieties and Singularities . . . . .                         | 95        |
| 3.6 Guaranteeing the Existence of Minima with Projectivization . . . . .    | 98        |
| 3.7 Statistics: Maximum Likelihood Retraction . . . . .                     | 101       |
| 3.8 Rigidity and Flexibility: Approximation of Deformation Paths . . . . .  | 108       |
| 3.9 HomotopyOpt.jl . . . . .  | 112       |
| 3.10 Performance Analysis of the Euclidean Distance Retraction . . . . .    | 113       |
| 3.10.1 Examples . . . . .   | 115       |
| 3.10.2 Conclusion . . . . .   | 121       |

|  |            |
|--|------------|
| <b>4 Homogeneity of Disordered Minimal Surfaces</b>                            | <b>123</b> |
| 4.1 Curvature and Minimal Surfaces . . . . .                                   | 127        |
| 4.1.1 Hilbert’s Embedding Theorem . . . . .                                    | 137        |
| 4.1.2 Families of Triply Periodic Minimal Surfaces . . . . .                   | 138        |
| 4.2 Homogeneity Measures for Minimal Surfaces . . . . .                        | 142        |
| 4.2.1 Curvature Fluctuation . . . . .  | 142        |
| 4.2.2 Isotropy Index . . . . .   | 145        |
| 4.2.3 Examples of Triply Periodic Minimal Surfaces . . . . .                   | 147        |
| 4.3 Results: Construction Methods for Disordered Minimal Surfaces . . . . .    | 150        |
| 4.3.1 Topology-Stabilized Generation of Minimal Surfaces . . . . .             | 151        |
| 4.3.2 Construction of Amorphous Diamond Minimal Surfaces . . . . .             | 156        |
| 4.3.2.1 Skeletal Graphs of Bicontinuous Minimal Surfaces . . . . .             | 156        |
| 4.3.2.2 Homogeneity of the Amorphous Diamond Minimal Surface . . . . .         | 158        |
| 4.3.3 Construction of Minimal Surfaces by Repulsive Catenoidal Necks . . . . . | 163        |
| 4.3.3.1 Distance Functions on the Flat Torus . . . . .                         | 164        |
| 4.3.3.2 Minimally Energetic Point Clouds on the Torus . . . . .                | 166        |
| 4.3.3.3 Voronoi-Based Polyhedral Interface Between Two Networks . . . . .      | 169        |
| 4.3.4 Relaxation Algorithm to Enhance Isotropy . . . . .                       | 171        |
| 4.3.5 Superior Uniformity of Bicontinuous Cubic Phases . . . . .               | 173        |
| 4.4 Concluding Remarks . . . . .   | 175        |
| 4.4.1 Future Experiments and Mathematical Analyses . . . . .                   | 177        |
| <b>5 Deformations of Curved Cylinder Packings</b>                              | <b>179</b> |
| 5.1 Cylinder Packings on the Gyroid Minimal Surface . . . . .                  | 181        |
| 5.2 Negative Poisson’s Ratio . . . . .   | 183        |
| 5.3 The Configuration Space of Two Filaments in Tight Contact . . . . .        | 187        |
| 5.4 Constructing a Stable Periodic Tensegrity . . . . .                        | 189        |
| 5.5 Computing Deformation Paths Algorithmically . . . . .                      | 195        |
| 5.6 Deformation Results for the Tensegrity Structures . . . . .                | 197        |
| 5.7 Conclusion . . . . .   | 202        |
| <b>6 Weaving Models on Manifolds</b>   | <b>204</b> |
| 6.1 Frameworks on Surfaces . . . . .   | 206        |
| 6.1.1 Coning . . . . .   | 209        |
| 6.1.2 Concentric Spheres . . . . .   | 210        |
| 6.2 Weavings on Surfaces . . . . .   | 210        |
| 6.2.1 A Tensegrity Model for Weavings . . . . .                                | 213        |
| 6.2.2 Examples of Entangled Weavings . . . . .                                 | 219        |
| 6.3 Weavings on Deforming Spheres . . . . .                                    | 226        |
| <b>7 Conclusion</b>  | <b>232</b> |
| 7.1 Reflection on the Research Process of this Thesis . . . . .                | 232        |
| 7.2 Contributions to the Field and Future Research . . . . .                   | 233        |

---

## Introduction

---

Geometry is a decisive factor in the selection of evolutionarily advantageous traits in flora and fauna. This concept extends to the attainment of energetically favorable states in physical systems. The term “geometry” originates from ancient Greek, where it literally means “earth measurement”. This word figuratively conveys the pursuit of humanity to accurately describe and understand their surroundings. Ranging from micro- to macroscale and from animate to inanimate structures, principles of geometry appear in numerous materials. Geometric concepts can be observed in the arrangement of flower petals [18], plant physiology [277], the formation of photonic chitin nanostructures [329], and viral self-assemblies [249]. It extends to inanimate processes such as crystallization [219], curved space-time in general relativity [182] and packings of filaments [112] and soap bubbles, such as foam [113]. Associated principles are used in the design of metamaterials with prescribed microstructures and targeted functionality. These include metal-organic frameworks [264], the creation of photonic effects [333], shape-morphing origami and kirigami [180] as well as the design of 3D structures of a specific shape [9, 209]. In many of these scenarios, the geometry emerges through the minimization of energy functionals. For instance, the free energy of solvation is known to impact many self-assembly processes [246, 249]; curvature energies describe the facet tension and bending energy of membranes [89, 277] and distance energies play a role in the organization of molecules in space [115, 158]. Since the minimization of objective functions is the goal of mathematical optimization, this highlights a clear connection between geometric materials and optimization.

In this work, we concentrate on a particular class of geometric materials, namely geometric constraint systems described by algebraic equations. As one of the oldest mathematical concepts, polynomials can be found in a myriad of real-world scenarios. Traditionally, the geometric properties of multivariate polynomials and their roots are studied in the research field of algebraic geometry. The collection of the zeros of a polynomial system is called an *algebraic variety*. Modern algebraic geometry builds on these ideas by exploring several generalizations: The nonnegativity of real polynomials [171], the development of computational and numerical methods to examine explicit systems of equations [35, 54] and the investigation of partial differential equations [228, 304] are all active fields of research. Strategies associated with algebraic geometry are applied in numerous scenarios relating to materials science. As an example, embedded graphs whose edges come with Euclidean distance constraints are called *bar-and-joint frameworks*. While their primary applications are in structural engineering and architecture, frameworks are also utilized in soft matter physics, biochemistry, and kinematics. Computational algebraic geometry can be used to parametrize deformation paths and to investigate the rigidity of frameworks [133, 134]. Since the problem of determining a structure’s rigidity is coNP-hard [1], nonlinear approaches can make use of the nonnegativity of polynomials to prove a framework’s rigidity [82]. Numerical algebraic geometry strategies are essential for

computer vision and robotics [56, 299] and find applications in the design of dilatant mechanisms [44]. The study of nonnegative polynomials can be combined with differential equations to study chemical reaction networks. In doing so, we can predict the concentration of reacting organic species in a solution [228]. In the spirit of this thesis, polynomial nonnegativity serves as a powerful tool for solving optimization problems with polynomial constraints [102].

Algebraic varieties are smooth almost everywhere, so it is unlikely that an optimization routine with polynomial constraints runs into singularities. Provided that we have a method to escape singularities, we can thus treat polynomial constraint sets analogous to smooth manifolds. This prompts the research question: Can we combine smooth optimization techniques with robust geometric models to analyze and design materials?

## 1.1 Context of this Work

We propose a three-stage program for geometric design. It consists of developing an understanding of the underlying physical structure (stage 1), applying geometric constraint systems for modeling (stage 2), and the utilization of smooth optimization schemes (stage 3). Indeed, geometric materials are present in many physical systems. As an introductory example, the hexagonal tiling of the Euclidean plane is considered. This tesselation occurs in honeycombs of beehives and is depicted in Figure 1.1.1. The honeycombs take the shape of hexagons due to surface tension. This way, bees optimize their resources: Hexagons require the least amount of wax

while having the capacity to store the most honey. In mathematical terms, the hexagonal tiling is a regular tessellation of the Euclidean plane such that each tile has the same area and minimal total perimeter. The associated problem is known as the honeycomb conjecture [147]. The cell packing problem gives a second reason for the formation of hexagonal honeycombs, as individual bees glue the honeycombs they create to form a beehive [313]. Both of these intricate results are intuitive for the worker bees that construct honeycombs without a proper mathematical education.



**Figure 1.1.1:** Bees use the hexagonal tesselation to generate honeycombs.  
(image source: Pixabay)

Hexagonal tilings also appear in the graphene nanostructure. This material attracts commercial interest due to its electronic properties [338]. In addition, graphene has an extraordinarily high stiffness [66]. The corresponding scientific background document for the Nobel Prize award in Physics from 2010 impressively states that “[a] hypothetical hammock measuring  $1m^2$  made from graphene [...] could hold a cat without breaking [...] and would weigh less than [...] one of the cat’s whiskers” [292]. In other words, it is an exceptionally strong structure whose properties far exceed comparable materials.

The previous two applications of the hexagonal tiling in beehives and graphene focus on rigid structures that do not deform. However, the hexagonal tiling can be transformed into a flexible structure with intriguing deformative properties. By interpreting the tiling as a periodic

bar-and-joint framework in a deformable torus, fixing the edge lengths, and ignoring the facets, we obtain a flexible structure. We later show that the resulting honeycomb framework exhibits a dilatant property known as *auxeticity* (cf. [43]). Auxetic materials can be characterized as structures that exhibit a perpendicular expansion upon stretching the material in a chosen direction, a somewhat counterintuitive property. This is quantified by a negative Poisson's ratio [195]. Auxetic materials can occur naturally, for instance as polyurethane foam [203], skin cells [112], arteries, and tendons [263]. They are also a prime target in the geometric design of metamaterials with prescribed microstructures and targeted functionality, such as impact protection and filtration [26, 189].

Energetically favorable geometric materials emerge in various settings, which is particularly relevant in the self-assembly of copolymers and lipid mesophases. Diblock copolymers have an extraordinary phase transition diagram, dependent on the concentration of individual polymers [208]. Most notably, so-called minimal surfaces emerge in this setting. A minimal surface is a 2-dimensional Riemannian manifold embedded in  $\mathbb{R}^3$  that locally minimizes its area. Physical models are typically constructed by submerging a wireframe scaffold into a soap solution, forming a soap film [100]. Minimal surfaces find application in design and architecture by minimizing the necessary amount of material. For example, the design of the Munich Olympic Stadium is inspired by soap membranes [318]. Due to the favorable mechanical properties of minimal surfaces, they are the target of medicinal research in bone reconstruction [272]. Among the class of minimal surfaces, membranes that are periodic in 3 orthogonal directions are most common in nature because a crystalline structure allows the tiling of large volumes. These surfaces can occur as self-assembled bicontinuous cubic phases in copolymers and lipid mesophases [246, 337] and as biological intracellular membranes [17]. The Gyroid as depicted in Figure 1.1.2 is particularly common. This minimal surface occurs in butterfly wing scales to create photonic effects [329]. The chitin nanostructure in the butterfly wings forms a photonic crystal on a length scale close to the wavelength of visible light. This creates iridescence caused by wave interference.

Mathematically, minimal surfaces can be described using the language of Riemannian geometry. To characterize the local changes in a manifold's geometry, the metric tensor [68, p.92f.] and the shape operator [197, p.235f.] are two important invariants of Riemannian manifolds. They describe the curvedness of an embedded surface  $\mathcal{M}$ . In particular, both invariants combined enable the computation of the mean curvature  $H$  and Gaussian curvature  $K$  in each point of the surface [255, Cor. 8.1.3]. Assume now that  $\mathcal{M}$  is oriented and compact. As a prime example of geometric functionals, the Canham-Helfrich energy [89, p.44f.] describes

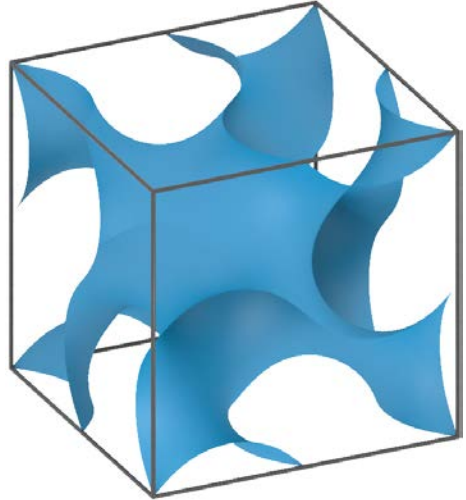


**Figure 1.1.2:** The Gyroid is a triply periodic minimal surface that was first described by Alan Schoen [280].

the elastic free energy of lipid bilayers under fixed volume of  $\text{int}(\mathcal{M})$  [156]. It has the form

$$\int_{\mathcal{M}} (k_H \cdot (H - H_0)^2 - k_G \cdot K) dA$$

for the bending rigidities  $k_H, k_G \geq 0$  and target mean curvature  $H_0$ . Therefore, the shape of membranes highly depends on the curvature. As a special case of the Canham-Helfrich functional, the Willmore energy [328] is obtained with the constants  $k_G = H_0 = 0$  and  $k_H = 1$ . All minimal surfaces ( $H = 0$ ) are global minima of the Willmore functional. Consequently, the Willmore energy can be used as an objective function to find minimal surfaces.

There are many known examples of ordered triply periodic minimal surfaces, such as the Primitive, Diamond and Gyroid that exist in positive-dimensional deformation families [215, 325]. In addition to these highly symmetric phases, nature displays a vast array of other minimal surfaces such as amorphous phases. For instance, sponge phases appear as a membrane between two solvents [267] and the sea urchin endoskeleton possesses a disordered component connecting the ordered Primitive and Diamond phases [178].

Still, the bicontinuous, ordered cubic phases are more prominent in nature. Currently, the Primitive, Diamond and Gyroid surfaces are the triply periodic minimal surfaces with the lowest known variance in their Gaussian curvature [283]. As a result, one may wonder if the Gyroid is the most homogeneous triply periodic minimal surface or whether other membranes have a lower fluctuation of Gaussian curvature.

Cylinder packings are useful in the analysis of crystalline structures [20] and have been successfully applied in the construction and design of metal-organic frameworks [242, 264]. These structures combine high porosity, good mechanical properties, and a substantial surface area [340]. Some chiral cylinder packings possess a special dilatant property. For instance, the  $\Sigma^+$  cylinder packing depicted in Figure 1.1.3(l.) is proposed as a model for the swelling of corneocytes when soaked in water and its expansion is reminiscent of auxeticity [112].

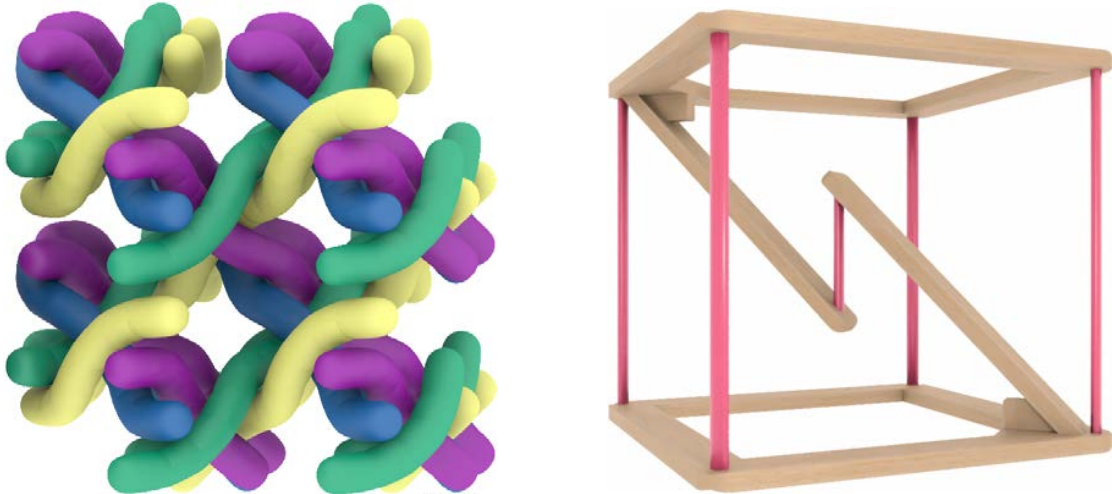


**Figure 1.1.3:** The curvilinear cylinder packing  $\Sigma^+$  is used in modeling the packing of skin cells (l.). Its deformative behavior can be approximated using tensegrities. Therefore, we visualize a reinforced tensegrity sculpture which can be built out of wood, glue, and rubber bands (r.).

To model cylinder packings, *tensegrity frameworks* prove to be a practical tool in discretizing

an otherwise infeasibly complicated configuration space. The term “tensegrity” was coined by the architect Buckminster Fuller [59]. Tensegrity frameworks differ from traditional bar-and-joint frameworks by incorporating elastic elements under tension in addition to rigid bars. Such a tensegrity framework is depicted in Figure 1.1.3(r.). As no rigid bars connect the top and bottom square, this construct is purely stabilized by its elastic elements. Tensegrities are used in architecture and civil engineering [224, 306], robotics [63], art [298], molecular biology [103, 173, 320] and anatomy [200]. Apart from their application on earth, their resilience and lightweight design have made tensegrities attractive for aerospace engineers [8, 315, 344]. Due to their flexibility, there is no limit to the structures’ shape, size, and deformability.

A tensegrity model for cylinder packings can be constructed by placing cables along the central axes of the cylinders and bars whenever two cylinders touch [242]. However, under deformation that model exhibits a chaotic behavior and breaks symmetry. The formulation of a robust and discretized geometric model for cylinder packings and the implementation of a robust algorithm to compute deformation pathways is an open problem that is addressed in this work.

More generally, framework materials are part of the larger class of geometric constraint systems that use geometrically motivated constraints to describe physical systems. Computer-aided design software is often used in geometric modeling, modern manufacturing processes, and engineering projects [343]. Granular materials, i.e. packings of spherical particles, are included in this broader context, just as kinetics, formation control, kirigami, and origami are.

Many geometric constraint systems including tensegrity frameworks require prior equilibration. In silico, this is achieved using optimization techniques. Mathematical optimization is a broad field that is only marginally narrowed by considering approaches specifically designed for constraint programming. When given constraints describing a set  $\mathcal{C} \subset \mathbb{R}^n$ , the goal is to find a point  $x^* \in \mathcal{C}$  minimizing a function  $f : \mathcal{C} \rightarrow \mathbb{R}$ . Integer linear programming restricts this problem to finding integral solutions  $x^* \in \mathbb{Z}^n$  with linear inequality constraints and a linear objective function  $f$ . In other words,  $\mathcal{C}$  consists of the integral points inside a polyhedron. This approach is applied in logistical scheduling, territorial partitioning, and energy system optimization. Since many NP-complete problems, such as the famous traveling salesman problem, can be reduced to solving an integer linear program, solving a generic integer linear program is also NP-complete. Therefore, successful solution approaches typically involve elaborate heuristics and more recently, machine learning [29].

Linear programming relaxes integer linear programming by allowing non-integral points and falls into the broader field of convex optimization. Here, the objective function is convex, and the constraints  $\mathcal{C}$  form a convex set. The most important property associated with convex optimization is that each local minimum is a global minimum [49, p.138f.]. Not only statistical estimation and data analysis, but also signal processing, and optimal control profit from solving these optimization problems.

A different approach is offered by constrained polynomial optimization. In this setting, the objective function is a polynomial and the constraint set  $\mathcal{C}$  is a semialgebraic set described by polynomial inequalities and equalities. Polynomial optimization can equivalently be viewed as the maximization of a real  $\lambda$  such that  $f(x) - \lambda$  is nonnegative over  $\mathcal{C}$ . This fact relates the nonnegativity of polynomials to polynomial optimization. Generally, we cannot expect that there

is a unique minimizer or that there exists a minimum at all. A common relaxation is to consider the sums of squares (SOS) approach [294]. However, the collection of SOS polynomials is usually a proper subset of the nonnegative polynomials [160]. For this reason, weaker relaxations are typically considered [171, 227]. Polynomial optimization is a powerful tool since polynomials appear in a plethora of real-world applications, such as motion planning, geometric modeling, resource control, and chemical reaction networks.

The most general form of constraint optimization is nonlinear optimization, where the constraint set  $\mathcal{C}$  is described by real-valued inequalities and equalities and the objective function  $f$  is a real-valued function. In this unrestrictive setting, Lagrange multipliers are a common solution strategy to transform the problem into the search for zeros of a system of equations [234, p.320f.]. Due to the optimization problem's generality, it is applicable to all constraint optimization scenarios, though a more tailored approach typically yields better results.

Nevertheless, it is not sensible to apply an arbitrary optimization scheme to geometric constraint systems. In all previously discussed applications, a robust nonlinear optimization algorithm respecting the underlying geometry and topology of the constraint set is necessary. Otherwise, the model for a material may undergo non-physical, discontinuous shape changes. Riemannian optimization provides a suitable framework for this setting, as it allows to smoothly traverse the constraint set [47]. In this context, smooth objective functions  $f$  are considered on a smooth, embedded manifold  $\mathcal{C}$ .

The basic idea of Riemannian optimization is simple: To find the minimum, start somewhere on the manifold and move along a descent direction in the tangent space. Eventually, you hope to find a point locally minimizing the objective function. Using the exponential map we can smoothly move on the constraint set. Taking a point and a vector as input reminds us of the unconstrained gradient descent algorithm; this provides an intuitive justification for its application in optimization. Yet, for many manifolds, the exponential map does not have an explicitly known form, and solving the associated differential equations is generally difficult. For these reasons, the exponential map is typically approximated by a retraction [166].

Robust techniques and theoretical results accompany a well-chosen Riemannian metric and retraction map [47, 259]. Such methods require prior knowledge of a suitable retraction, ideally with an explicit formula. These are available for many common matrix manifolds whose elements have a natural matrix representation [4]. While Riemannian optimization is a powerful tool in many applications, for less common, implicitly defined manifolds or algebraic varieties, there are no readily available formulas for retractions. Therefore, retraction maps applicable to an arbitrary manifold are desirable. The closest point problem on an embedded submanifold of  $\mathbb{R}^n$  is a second-order approximation of the corresponding exponential map [5]. Extending this result to ambient manifolds with more general Riemannian metrics and creating a robust algorithmic framework to solve the local implicit closest point problem remain open problems that are addressed in this thesis.

The previous paragraphs have constructed a narrative of how geometric constraint systems can be used to model and simulate real-world systems. By combining the three stages of geometric modeling, it becomes possible to invent new geometric designs. In this context, the interplay of all three stages of geometric modeling can be used as an exploratory ground

for developing new techniques. This tenet in combination with the onset of 3D printing has led to the creation of many new structures. For instance, the design of auxetic materials enables the production of structures with high toughness combined with variable permeability. These materials have ramifications in biomedicine and textiles [6, 12, 44, 263]. Intelligent fabrics represent another innovation. Currently, adjusting to environmental changes requires frequently changing clothes. Instead, intelligent fabrics offer a controlled heat transfer and local actuation in fabrics to adapt to environmental conditions [271]. Lastly, the inverse construction of curved surfaces is a relevant application of geometric design. For instance, the selective heating and cooling of parts in a material make it possible to create arbitrary shapes through the manipulation of curvature [9, 139]. In alternative approaches, knitted fabrics have been modeled in a yarn-level simulation [300] and wood has been used as a material to create bending-active curves [261] and smooth surfaces with targeted mechanical properties [210]. In addition, a design algorithm has been proposed for weaving the Kagome lattice with topological defects into surfaces out of ribbons [258]. Even though topological defects have long been conjectured to weaken the mechanical properties of a material, recent experiments demonstrate that the introduction of small pores in gold strengthens the metal while improving its elasticity [75]. All of these settings provide inspiring challenges for applying the principles of geometric design.

## 1.2 Structure and Significance

In this thesis, we make use of these geometric design principles to investigate several geometric constraint systems. In the literature review, key concepts regarding the rigidity and flexibility of bar-and-joint frameworks are explored.

### Geometric Theory of Framework Materials

Framework materials composed of rigid bars and joints provide the foundation to model many materials. Chapter 2 presents the necessary preliminaries about frameworks and rigidity theory. Defined as embedded graphs with edge length constraints, frameworks are inherently algebraic objects characterized by quadratic polynomials. This makes techniques from algebraic geometry applicable, which is why we introduce relevant algebraic concepts in Section 2.1.1. With these tools the configuration space of frameworks is defined in algebraic terms in Section 2.1.2. We distinguish between rigid and flexible frameworks. The former term describes real isolated solutions of the system of edge length constraints, whereas flexibility describes the ability of a framework to deform while maintaining the edge length distance. Rigid frameworks do not admit such deformations. In Section 2.1.2.1, a framework's rigidity is discussed in the context of finite and periodic frameworks. Even though for structural engineers the rigidity of a framework is relevant, in this thesis we focus on their flexibility. This attribute can generate models for materials under deformation. A particularly interesting deformative property is auxeticity, describing an expansive response in lateral directions upon stretching a material. This concept is introduced in Section 2.1.2.2.

As framework materials do not have to consist solely of rigid elements, they can include flexible components such as cables and struts. By additionally possessing energy terms, they give rise to nonlinear optimization problems and are called tensegrity frameworks. In Section 2.1.3 we

show that simple tensegrities can have complicated and discontinuous behavior, creating novel possibilities in materials design.

As an initial application of this theoretical foundation, geometric random graphs are considered in Section 2.2. First, samples are drawn from a Poisson point process with mean  $n$  to place points in the square with area  $n$ . Then, disks centered in the points are uniformly expanded to create a geometric random graph  $G$ : Whenever two points lie in the same disk, an edge is added between the points. This process stops when the framework is rigid. According to Asimow and Roth [24], the rigidity of  $G$  can be checked via a simple combinatorial criterion. Following Takabe and Wadayama [309], there are asymptotic bounds for the  $k$ -connectivity of the geometric random graph. In an ongoing project with Katie Clinch and Sean Dewar, we conjecture and experimentally verify that similar bounds hold for the rigidity and unique realizability of planar frameworks obtained from such Poisson point processes. A necessary condition for global rigidity is that each of the underlying graph's vertices has degree 3. However, this criterion is not sufficient. We denote the maximal subgraph where each vertex has at least degree 3 by  $H_3$ . Still, there exists a sufficient criterion, requiring that the graph is 3-connected and redundantly rigid [176, Thm. 7.1]. When determining which of these two properties typically prevents  $H_3$  from achieving global rigidity, we find that it is usually its 3-connectivity.

Next, we consider the rigidity of polytopes with coplanarity and edge length constraints in Section 2.3. Among the platonic solids, the regular tetrahedron, octahedron, and icosahedron are rigid under these constraints. This is a consequence of the Cauchy-Dehn Theorem [14, p.421]. Conversely, the cube is flexible, admitting a 3-dimensional deformation space. In an ongoing project with Bernd Schulze, Martin Winter, and Albert Zhang, we prove that the regular dodecahedron is rigid in Theorem 2.3.9. Despite the dodecahedron's rigidity, we can investigate what happens when some of the edge lengths change. We find that altering the length of a single edge results in 3 curves through the regular dodecahedron that can be obtained by smoothly gluing the deformation paths corresponding to 8 unique configurations nearby. One of these deformation paths loops back to the regular dodecahedron, forming a nodal singularity.

## Riemannian Optimization by Homotopy Continuation

On any smooth manifold  $\mathcal{M}$ , there exists an exponential map  $\text{Exp} : T\mathcal{M} \rightarrow \mathcal{M}$ . Taking a point  $p$  and tangent vector  $v$  as arguments, we can draw a parallel to local optimization techniques such as gradient descent. Instead of taking a linear step, the exponential map allows us to follow smooth curves on the manifold. Riemannian optimization is a technique to solve nonlinear optimization problems, whose constraint set defines an embedded smooth manifold. To traverse the vanishing locus of geometric constraint systems, Chapter 3 thus focuses on Riemannian optimization. It contains results and material from the publication by Heaton and Himmelmann [153].

The ingredients for any Riemannian optimization scheme comprise a way to move on the manifold, a choice of step sizes, and descent directions. Since the exponential map is not explicitly available for all manifolds, we approximate it by a retraction obtained from orthogonal projection (cf. Section 3.2.1). In Euclidean ambient space, it is known that orthogonally projecting to an embedded submanifold's tangent space is a second-order approximation of

the exponential map [5]. By considering the Fisher metric on the open probability simplex  $\Delta_{n-1} = \{x \in \mathbb{R}_{>0}^n : \sum_{i=1}^n x_i = 1\}$ , we can construct a similar retraction to Euclidean space and prove that it is second-order in Section 3.7. The closest point problem is another nonlinear optimization problem, raising the question of how this approach helps in solving the initial problem. By using homotopy continuation (cf. Section 3.2.2), we can track the solution curve on the manifold resulting from parametrizing the line  $p + tv$ . Knowing the initial solution  $p$  to the closest point problem, this approach becomes feasible. For tracking the solution path, a combination of predictor (e.g. Euler’s method) and corrector (e.g. Newton’s method) is employed. Since homotopy continuation extensively focuses on robustness, there are theoretical guarantees in place ensuring that the paths are smooth [299, Thm. 7.1.1] and there are heuristics to avoid jumping between paths [312, 316]. These facts make the computation of retractions based on homotopy continuation particularly robust.

In Section 3.3, we prove that for  $p \in \mathcal{M}$  and  $v \in T_p \mathcal{M}$  with sufficiently small norm  $|v|$ , there exists a discretization of the line segment  $\overline{p, p+v}$  such that continuation methods converge to the correct point. We explicitly provide bounds on what “sufficiently small” means. Theorem 3.3.7 is independent of whether an Euler predictor step is performed or not. In this scenario, the Euler step does not provide any additional computational or theoretical benefits and higher-order predictor schemes are preferable.

Backtracking line search with Wolfe conditions is a popular tool for discerning suitable step sizes in iterative optimization algorithms (cf. [234, p.33f.]). By slightly generalizing existing results in Section 3.4, we can generate sequences of step sizes that ensure that Riemannian optimization schemes converge to a critical point. Since critical points can be saddle points and local optimization can get stuck in singularities, a heuristic for escaping such situations is devised in Section 3.5. This lets us extend the Riemannian optimization algorithm to algebraic sets. Moreover, it is not necessary that a minimum even exists. We investigate scenarios where we can guarantee the existence of minima in Section 3.6.

In applications requiring the iterative optimization algorithm to stay on the same connected component, using a retraction is exceptionally suitable. In particular, geometric constraint systems fall in this category. They are a focal point in this chapter. For this reason, Section 3.8 outlines how retractions can be used to compute deformation paths.

Even though there is a multitude of Riemannian optimization packages (e.g. [33, 48, 222, 331]), typically they either ask the user to provide a retraction for the given manifold or merely provide explicit retractions for common matrix manifolds. In contrast, we implement the general-purpose Riemannian optimization package `HomotopyOpt.jl` based on homotopy continuation and explain its usage in Section 3.9. While the numerical experiments in Section 3.10 show that it may lack efficiency, it can produce results on arbitrary implicitly defined polynomial constraint systems. While directly applying Newton’s method to the Lagrange multiplier system is efficient, it is easy to find examples where it either diverges or converges to an incorrect solution. This highlights the robustness of the retraction based on homotopy continuation and justifies its development.

## Homogeneity of Disordered Minimal Surfaces

Staying within the context of Riemannian manifolds, the mean and Gaussian curvature of surfaces are important invariants. These terms are known to be of high relevance in the energy minimization of surface tension. Thus, curvature terms can be found in many physical models. Triply periodic minimal surfaces, having zero mean curvature at every point, provide a particularly compelling surface family in this context. Cubic, bicontinuous minimal surfaces appear abundantly in nature. In more recent times, the scientific community has shown an increased interest in disordered and amorphous phases [178, 267]. In Chapter 4, we construct two models to sample the space of cubic triply periodic minimal surfaces to reliably generate disordered structures.

After reviewing the classical mathematical background for minimal surfaces in Section 4.1, Hilbert’s Embedding Theorem is discussed. It states that there is no complete regular surface in  $\mathbb{R}^3$  with constant negative Gaussian curvature. Consequently, curvature heterogeneities are expected in minimal surfaces, since they are negatively curved by construction. Many classical examples of triply periodic minimal surfaces have already been known in the late 19th century. When allowing their cubic unit cell to vary, these surfaces exist in deformation families (cf. Section 4.1.2).

To study the homogeneity of triply periodic minimal surfaces, we introduce two surface invariants in Section 4.2: The curvature fluctuation and the isotropy. While the former is a dimensionless variance measure for surfaces, the latter describes the distribution of a surface’s unit normal field via the Gauss map, determining if there are preferred directions. We compare these measures across several classical triply periodic minimal surfaces in Section 4.2.3. Among these structures, the Gyroid is conjectured to be the most homogeneous, which may explain its abundance in nature.

As a first approach to create disordered minimal surfaces, the 4-regular amorphous diamond net is tubified to generate an initial configuration for curvature optimization routines, as detailed in Section 4.3.2. This popular technique creates high-quality continuous random networks by limiting the potential topologies. By taking a closer look at what makes the Gyroid so homogeneous, we discover that its curvature distribution concentrates around a single value, allowing this minimal surface to have a narrower distribution. The curvature distribution of the amorphous diamond looks smoother than the Gyroid’s, requiring more surface area at the surface’s flat points and slower decline for large absolute values of Gaussian curvature.

As a second approach, repulsive point clouds placed on parallel layers in the periodic unit cell are considered in Section 4.3.3. Each point represents a catenoidal neck connecting two non-adjacent voids separated by the parallel planes. This way, the points lie in two disconnected volumes that can be used to create a separating surface by computing generalized Voronoi cells. In Section 4.3.1, a topology-stabilized curvature optimization routine is developed in the Surface Evolver [50] to obtain a minimal surface from either initial configuration. The algorithm avoids pinch-offs, meaning that the surfaces’ catenoidal necks do not collapse during the optimization runtime.

We thoroughly compare the aforementioned homogeneity measures by using both of these approaches to generate several disordered minimal surfaces. Since the unit cell is fixed in

our experiments, the inherent randomness means that disordered structures are typically not isotropic. In many cases, the cubic unit cell is unlikely to be the optimal choice. Inspired by the foam relaxation algorithm from Evans et al. [113], an algorithm for enforcing isotropy based on the Householder transform is developed in Section 4.3.4. It cannot reduce the anisotropy of all minimal surfaces, suggesting that some triply periodic minimal surfaces arise as isolated solutions. In these cases, small perturbations of the unit cell cause the surface to be a nonzero local minimum of the squared mean curvature integral instead. Finally, in Section 4.4 the results from the experiments are compared to the classical minimal surfaces from earlier sections to put our models into perspective. While disordered structures are often less isotropic, this investigation highlights that their curvature fluctuation is comparable to many classical examples.

## Deformations of Curved Cylinder Packings

In Chapter 5, we concentrate on triply-periodic cylinder packings described by tightly-wound curvilinear cylinders in space. Building on the previous chapter, we show that these packings emerge from tubified line arrangements on the Gyroid minimal surface in Section 5.1. We are particularly interested in the chiral  $\Pi^+$  and  $\Sigma^+$  packings, as they have exhibited auxetic behavior in previous experiments when deformed [112, 242]. Auxeticity is introduced in Section 5.2. This property can be described in terms of a negative Poisson's ratio, which is the negative proportion of transverse strain divided by axial strain of a deforming material. In other words, the counterintuitive auxeticity measures that a material which is stretched in one direction expands in the orthogonal directions. Containing results from the publication by Himmelmann and Evans [161], the goal of this chapter is then to find an auxetic deformation path for both, the  $\Pi^+$  and  $\Sigma^+$  packings.

The curvilinearity of the cylinders makes the configuration space complicated. To build a discretized model, we begin with investigating the configuration space of two filaments in tight, orthogonal contact in Section 5.3. Inspired by related mathematical and experimental results, we derive a tetrahedral tensegrity model for cylinder packings in Section 5.4. This model takes into account that two cylinders can have many idealized contact geometries, ranging from a single point to a diamond-shaped curve [65, §9]. In a previous study by Oster et al. [242], they observed symmetry-breaking and an initial phase of chaotic behavior. Conversely, this new model produces a smooth and symmetric response, confirming its robustness. We show that it is possible to find a feasible point of the optimization problem by an explicit construction in Proposition 5.4.8. When considering the nets **bmn** and **sgn** naturally associated with the cylinder packings  $\Pi^+$  and  $\Sigma^+$ , we can extend that proposition to find feasible points of the nonlinear optimization problems associated to the cylinder packings in Corollary 5.4.10. Taking this point as an initial configuration, we can use the Riemannian optimization algorithm introduced in Chapter 3 to find an equilibrium. Approximating deformation paths starting from this equilibrium is possible by applying the path-tracking algorithm described in Section 5.5.

The expansion of both, the  $\Pi^+$  and  $\Sigma^+$  cylinder packings, is reminiscent of auxeticity [112, 242]. We relate the geometric definition of Borcea and Streinu [43] with the engineer's perspective of a negative Poisson's ratio in Propositions 5.2.2 and 5.2.4. This enables us to

experimentally show that the tensegrity models of the  $\Pi^+$  and  $\Sigma^+$  cylinder packings are auxetic by both definitions in Section 5.6. The  $\Sigma^+$  packing even possesses a small region where its Poisson’s ratio is below  $(-1)$ , signifying that the expansion in lateral directions is faster than the stretching itself. All stable isotropic materials have a Poisson’s ratio above  $(-1)$  [137]. Therefore, the “hyper-auxetic” behavior we observe in the  $\Sigma^+$  packing is highly interesting from a material-scientific perspective [230].

## Weaving Models on Manifolds

Weaving is a technique of creating textiles by interlacing two distinct sets of threads or filaments. Examples include denim and linen, but also cotton fabric. Along with knitted and chemically-bonded fabrics, weavings constitute one of the most popular forms of textile. The omnipresence of woven fabrics in fashion thus suggests that an improved understanding of the underlying geometry is beneficial.

The inverse problem for surfaces describes the task of explicitly describing moves to construct a target surface from an initial material. It is generally hard to solve [9]. In Chapter 6, we constrain weavings to already curved surfaces to obtain an intuition for how to generate curvature in weavings. In previous work, weavings have been defined in the Euclidean plane (cf. [121]). We generalize that construction to oriented Riemannian 2-manifolds in Section 6.2. By using available results and constructions from the literature on frameworks on algebraic surfaces laid out in Section 6.1, we develop a tensegrity model for weavings on surfaces in Section 6.2.1. Analogous to the previous chapter, this tensegrity model is constructed by placing cables along the central axes of the threads. To model the interlacing of yarn, offset surfaces can be used to track the relevant over-under information. There are two choices of unit normal fields for oriented surfaces, so equally distributing the vertices in both normal directions provides a well-defined notion of “over” and “under”. For smooth surfaces and sufficiently small  $\varepsilon > 0$ , the  $\pm\varepsilon$ -surface is smooth as well. We show that the  $\pm\varepsilon$ -offset surfaces can be described by an implicit equation, leading to a nonlinear optimization problem that can be solved using the Riemannian optimization algorithm developed in Chapter 3. As shown in Proposition 6.2.14, it is possible to explicitly construct a feasible point of this optimization problem. This enables techniques from Riemannian optimization, as this construction allows us to produce a reasonable initial configuration. In Section 6.2.2, we follow Evans and Hyde [273] to construct multiple examples of entangled weavings on surfaces, with a particular focus on the sphere. We find that our proposed model is robust and leads to symmetric weavings. For more general surfaces other than the sphere and the flat torus, it is not yet clear how to meaningfully construct weavings. For visualization purposes, a polynomial interpolation scheme is devised to turn the discrete tensegrity model into a smooth weaving.

In Section 6.3, the quasistatic behavior of weavings on deforming spheres is examined. For this purpose, the sphere is deformed into prolate and oblate spheroids. Not all previously introduced weaves are stable under perturbations and deform into degenerate configurations. More robust weaves typically favor the sphere over oblate and prolate spheroids. The flatter the threads of the weaves lie on the surface, the more the sphere is energetically favorable, as is highlighted in the hysteresis loops in Figures 6.3.3 and 6.3.5.

---

## Geometric Theory of Framework Materials

---

**Chapter Synopsis:** Framework materials can be described by embedded graphs with edge length constraints. These constructs are commonly used to investigate both a structure's rigidity and flexibility. Their deformations provide a compelling connection between materials science and algebraic geometry. When adding elastic elements carrying intrinsic energy to the framework, a tensegrity framework is created, paradoxically stabilizing an otherwise flexible structure. Even simple tensegrities can exhibit complicated, discontinuous behavior and possess multiple stable equilibria.

In this chapter, we consider two distinct applications of framework materials. First, we generate random point processes in the square to experimentally verify asymptotic bounds for the local and global rigidity of Gilbert frameworks. This leads to an enhanced understanding of what typically prevents the unique realizability of a graph in  $\mathbb{R}^2$ . Secondly, the convex polytopes with edge length and coplanarity constraints are examined as a generalization of frameworks. We prove that the regular dodecahedron is rigid and we locally describe the deformation space induced by edge-contractions.

Combining an embedded graph with physical distance constraints on its edges, bar-and-joint frameworks provide a simple model for many different applications. Such embedded graphs can either be flexible or rigid. Frameworks are called rigid when the edge length constraints do not allow them to move beyond the ambient Euclidean isometries. Otherwise, they are flexible, signifying the existence of a continuous motion deforming the structure. A framework's rigidity depends on the dimension it is embedded in. On the real line, two edges with length 1 joined in a single vertex cannot move. In  $\mathbb{R}^2$ , one of the edges can freely rotate around the mutual joint, while the other edge is fixed. The dual concepts of rigidity and flexibility are two sides of the same coin. Determining whether a framework is rigid in  $\mathbb{R}^d$  is a coNP-hard problem for  $d \geq 2$  [1], so deciding its flexibility is NP-hard. For that reason, stronger assumptions are historically employed to prove a structure's rigidity.

The origins of rigidity theory date back as far as 1813, when Cauchy proved that every 3-dimensional, simplicial, convex polytope is rigid [70]. In 1864, Maxwell established a condition for infinitesimal rigidity [213] that was used by Dehn to extend Cauchy's Theorem to polytopes with infinitesimally rigid faces [94]. The main motivation for scientists to study framework rigidity came from structural engineering and was allegedly reignited by the revelation of the Eiffel Tower in Paris at the World Fair of 1889. However, not all triangulated polytopes are rigid and Bricard showed in 1897 that there are flexible, non-convex polyhedra with infinitesimally rigid faces [57]. A realization of "Bricard's octahedron" is depicted in Figure 2.1.1(1.).

Pollaczek-Geiringer introduced the first combinatorial characterization of rigidity for frameworks with generic coordinates in 1927, defined solely in terms of the underlying graph

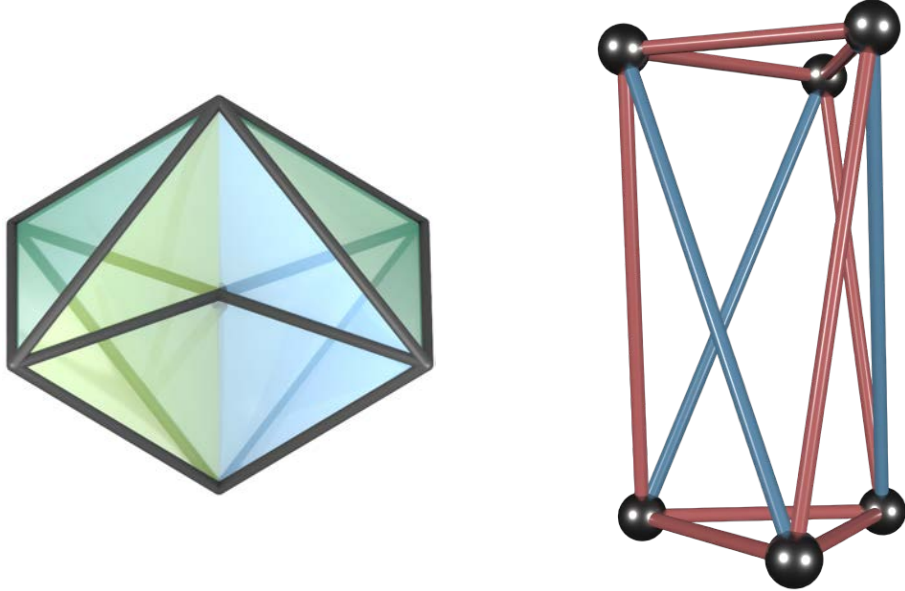


**Figure 2.1.1:** We depict a flexible realization of the generically rigid Bricard’s octahedron (l.) and a stable tensegrity framework (r.) consisting of rigid bars (blue) and flexible cables (red).

[253]. The theorem was lost to time and rediscovered in 1970 by Laman [196] who is now commonly used as a namesake. Connelly was able to extend the linear notion of infinitesimal rigidity to the weaker concept of higher-order rigidity in 1980 by using equilibrium stresses [79]. Stresses describe linear relations between the constraint system’s generating equations in a given realization, providing a powerful tool for investigating a framework’s rigidity. In 1962, Buckminster Fuller introduced the term “tensegrity frameworks” after incorporating tensile and compressive energy components [59]. These structures were mathematically formalized and connected to bar-and-joint frameworks around 1980 through the extensive use of equilibrium stresses by Connelly [79], and Roth and Whiteley [266]. The T3-prism tensegrity framework is depicted as an example in Figure 2.1.1(r.).

Today, rigidity theory is evolving in multiple new directions. In addition to considering ambient metrics different from the Euclidean metric [190] and applying matroids to rigidity theory [176], tropical geometry has produced intriguing results [38, 67], for example about counting realization. Moreover, frameworks are constrained to surfaces [232, 270], applied in matrix completion problems [177] and underlying symmetries are exploited [42, 265, 288].

The applications of framework rigidity are diverse. Civil engineers use “trusses” synonymously with frameworks [34, p.287f.] to analyze the stiffness and robustness of structures [136, 179]. In granular materials and packing problems, the rigidity of the corresponding contact graph indicates in how far a packing is jammed [99, 211]. Finally, associated techniques can be used to determine molecular conformations in space [158, 327] and to investigate the rigidity of proteins and other biomolecules [145, 159].

On the other end of the spectrum, flexible frameworks have recently garnered increased attention. Kempe’s Universality Theorem [274] shows that any bounded subset of an algebraic curve in  $\mathbb{R}^2$  can be traced by an appropriate planar framework. The inverse design of a structure with only rigid bars that follows a prescribed mechanism makes frameworks a particularly

compelling model. Accordingly, flexible configurations of frameworks are studied by artists [324], have applications to quasicrystalline structures [339], are used in the design of robots [308] and have the ability to generate interesting quasistatic properties [43].

Throughout this thesis, frameworks are a recurring and crucial concept. The Riemannian optimization algorithm that is developed in Chapter 3 provides a robust way to approximate deformation paths and equilibrate geometric constraint systems. In Chapter 5, we construct a robust geometric model for triply periodic cylinder packings based on tensegrity frameworks. Similarly, in Chapter 6 we create a geometric model for weaves on surfaces. In all cases, there is a particular focus on the involved frameworks' flexibility. This is emphasized by the investigation of several deformative attributes, such as a framework's dilatancy and energy landscape.

The first part of this chapter (cf. Section 2.1) provides a literature review on rigidity theory and considers several insightful examples. As framework materials are inherently algebraic objects, they can be described by a system of polynomial constraints. For that reason, Section 2.1.1 introduces several related key aspects from algebraic geometry.

In Section 2.1.2, fundamental concepts from rigidity theory are established, ranging from a framework's infinitesimal to its second-order rigidity. In preparation for later chapters, periodicity is discussed in Section 2.1.2.1. Periodic frameworks require an alternative definition to the rigidity of embedded graphs in  $\mathbb{R}^d$ . The group of isometries is different and for two adjacent vertex orbits there can be multiple incident edge orbits. When periodic frameworks are deformed, some exhibit a dilatant property known as auxeticity, specified by an expansive lateral response when the material is stretched. Such materials are characterized by a negative Poisson's ratio [297]. In Section 2.1.2.2, a complementary geometric theory is developed.

Next, we shift our view to tensegrity frameworks. These structures differ from traditional bar-and-joint frameworks by incorporating cables and struts in addition to bars. Respectively, Section 2.1.3 explains how these new types of edges exert tensile and compressive forces on the framework. Even simple tensegrities can have complicated dynamical behavior and may exert discontinuous jumps upon deformation. This property, known as "multistability," is associated with the presence of multiple energetically favorable configurations. Section 2.1.3.1 offers an algebraic description of this discontinuous behavior.

Two novel contributions are subsequently utilized as a vehicle for transporting several other concepts from rigidity theory, such as the unique realizability of graphs and coplanarity constraints. In Section 2.2, a Poisson process with expected value  $n$  is used to place points in the square of area  $n$ . On these points, a geometric random graph is constructed by growing disks around the points and adding edges whenever two points lie in the same disk, stopping with a rigid framework. We experimentally verify asymptotic bounds on the associated radii necessary for rigidity.

Finally, in Section 2.3, the Platonic solids with edge length and coplanarity constraints are considered. Except for the dodecahedron, the rigidity and flexibility of the Platonic solids have already been determined. After generalizing the theory of rigid frameworks to these new constraints, we outline a proof for the regular dodecahedron's second-order rigidity and describe deformations induced by edge-contractions.

## 2.1 Literature Review

In the literature review portion of this dissertation, we introduce essential concepts in frameworks and rigidity theory. We begin by providing the necessary background information in algebraic geometry that is used to study bar-and-joint frameworks later on.

### 2.1.1 Background in Algebraic Geometry

Traditionally, “algebraic geometry” comprises the study of multivariate polynomials and their roots, with algebraic structures such as *rings*  $R$  playing an important role. These objects are defined by binary operations  $+$  and  $\cdot$ , such that  $(R, +)$  forms an abelian group.  $(R, \cdot)$  forms a semi-group and is distributive over the  $+$  operation. As a related concept, *ideals* are given by subgroups of  $(R, +)$  that are closed under multiplication with elements of  $R$ . We call an ideal  $I$  a *prime ideal* if  $I \subsetneq R$  and for  $ab \in I$  with  $a, b \in R$  it holds that  $a \in I$  or  $b \in I$ . For additional information on commutative algebra, Cox et al. [86, App. A] provide a thorough introduction. Following Michałek and Sturmfels [218, p.19], we start with the definition of algebraic varieties.

**Definition 2.1.2.** Let  $k$  be a field and let  $k[x_1, \dots, x_d] = \bigoplus_{i \in \mathbb{N}_0} x_d^i \cdot k[x_1, \dots, x_{d-1}]$  be the polynomial ring over  $k$  in  $d$  variables. Take any family of polynomials  $S \subset k[x_1, \dots, x_d]$ . The *algebraic variety* or *vanishing locus* corresponding to  $S$  is defined by

$$\mathcal{V}(S) = \{p = (p_1, \dots, p_d) \in k^d : f(p) = 0 \ \forall f \in S\}.$$

In contrast, given any subset  $W \subset k^d$ , we can define the *vanishing ideal* of  $W$  by

$$\mathcal{I}(W) = \{f \in k[x_1, \dots, x_d] : f(w) = 0 \ \forall w \in W\}.$$

Many textbooks assume that an algebraic variety is *irreducible*, meaning it cannot be written as the union of proper non-trivial subvarieties (c.f. [149, p.3]). To differentiate these concepts,  $\mathcal{V}(S)$  from Definition 2.1.2 is called an *algebraic set*. Any algebraic set can be decomposed into the union of algebraic varieties and irreducible algebraic sets correspond to prime vanishing ideals [218, Prop. 2.3]. As the term algebraic variety introduced in Definition 2.1.2 is more prevalent in the applied literature, we will stick to this notation and permit reducible sets as algebraic varieties as well.

It is easy to verify that  $\mathcal{I}(W)$  defines an ideal: If two polynomials  $f_1$  and  $f_2$  vanish on  $W$ , so does their sum and their respective product with arbitrary elements of  $k[x_1, \dots, x_d]$ . Additionally,  $\mathcal{I}(W)$  is a radical ideal, meaning that if a polynomial power  $f^m$  lies in  $\mathcal{I}(W)$ , then  $\mathcal{I}(W)$  also contains the polynomial  $f$  itself. This can be realized as follows: Take any  $w \in W$ . If  $f(w)^m = 0$ , one of the factors must vanish, as  $k$  is a field, so  $f(w) = 0$ . Finally, in an algebraically closed field such as  $\mathbb{C}$ , Hilbert’s Nullstellensatz [218, Thm. 6.5] provides a one-to-one correspondence between radical ideals and algebraic varieties: Any radical ideal  $I \subset k[x_1, \dots, x_d]$  satisfies  $\mathcal{I}(\mathcal{V}(I)) = I$  and for any variety  $V \subset k^d$ , concatenating the operators  $\mathcal{V}$  and  $\mathcal{I}$  returns  $\mathcal{V}(\mathcal{I}(V)) = V$ . Let us now prove a property of algebraic varieties which is a direct result of Definition 2.1.2.

**Proposition 2.1.3.** *If  $I_1, I_2 \subset k[x_1, \dots, x_d]$  are ideals, then*

$$\mathcal{V}(I_1) \cup \mathcal{V}(I_2) = \mathcal{V}(I_1 \cdot I_2).$$

*Given a family of ideals  $(I_j)_{j \in J}$  in  $k[x_1, \dots, x_d]$ , it holds that*

$$\bigcap_{j \in J} \mathcal{V}(I_j) = \mathcal{V}\left(\sum_{j \in J} I_j\right).$$

*Proof.* For the first claim, assume that  $p \in \mathcal{V}(I_1) \cup \mathcal{V}(I_2)$  is given. Then,  $p$  needs to lie in one of the two arguments. Without loss of generality, assume that  $p \in \mathcal{V}(I_1)$ . Per Definition 2.1.2, all  $f \in I_1$  vanish on  $p$ , including  $f(p) \cdot g(p) = 0$  for an arbitrary  $g \in k[x_1, \dots, x_d]$ . Consequently,  $p \in \mathcal{V}(I_1 \cdot I_2)$ .

Conversely, assume that  $p \notin \mathcal{V}(I_1) \cup \mathcal{V}(I_2)$ . By definition, there are polynomials  $f \in I_1$  and  $g \in I_2$  such that  $f(p) \neq 0$  and  $g(p) \neq 0$ . Since  $k$  is a field, it also holds that  $f(p) \cdot g(p) \neq 0$ , implying that  $p \notin \mathcal{V}(I_1 \cdot I_2)$ .

For the second claim, first take any  $p \in \bigcap_{j \in J} \mathcal{V}(I_j)$ , translating to  $p \in \mathcal{V}(I_j)$  for each  $j \in J$ . An arbitrary sum of 0's is still 0, so  $p \in \mathcal{V}(\sum_{j \in J} I_j)$ .

The other inclusion can be realized by taking any  $p \notin \bigcap_{j \in J} \mathcal{V}(I_j)$ . Therefore,  $p \notin \mathcal{V}(I_j)$  for at least one  $j$ , meaning that  $f_j(p) \neq 0$  for some  $f_j \in I_j$ . Then,  $f_j \in \sum_{j \in J} I_j$ , so  $p \notin \mathcal{V}(\sum_{j \in J} I_j)$ .  $\square$

With the properties from Proposition 2.1.3, algebraic varieties satisfy most properties for closed sets in a topological space [226, p.76]. What remains to be shown is that the ambient space and the empty set are closed. Proving this is trivial, as  $\mathcal{V}(\{0\}) = k^d$  and  $\mathcal{V}(k[x_1, \dots, x_d]) = \emptyset$ .

**Definition 2.1.4.** The collection of algebraic varieties in  $k^d$  forms a basis of closed sets for the *Zariski topology*. Given a set  $W \subset k^d$ , its *Zariski closure* is the smallest algebraic variety  $V \supset W$ , so  $V = \mathcal{V}(\mathcal{I}(W))$ .

By the Hilbert Basis Theorem [86, p.77], the polynomial ring  $k[x_1, \dots, x_d]$  is Noetherian, so every ideal is finitely generated. Hence, any  $I \subset k[x_1, \dots, x_d]$  can be represented as

$$I = \langle f_1, \dots, f_s \rangle = \left\{ \sum_{j=1}^s g_j \cdot f_j : g_j \in k[x_1, \dots, x_d] \right\}$$

for some  $f_j \in I$ , which we will call *generators* of  $\mathcal{I}$ . In particular, this finiteness allows us to discuss geometric properties such as orthogonality, tangency and singularity in algebraic varieties. This requires the notion of the partial derivative operator  $\partial/\partial x_j$  and gradient  $\nabla f = (\partial f / \partial x_j)_{j \in [d]}$  [268, p.215f.]

**Definition 2.1.5.** Let  $V$  denote a variety with corresponding vanishing ideal

$$\mathcal{I}(V) = \langle f_1, \dots, f_s \rangle \subset k[x_1, \dots, x_d].$$

The *dimension* of  $V$  is given by the maximum length  $h$  of chains  $V_0 \subsetneq \dots \subsetneq V_h \subset V$  containing irreducible, non-empty subvarieties. If  $V$  is irreducible, a point  $p \in V$  is called a *singularity* if

the Jacobian  $df(p) = \left( \frac{\partial f_i}{\partial x_j}(p) \right)_{i \in [s], j \in [d]}$  has smaller rank than the codimension  $d - h$ . If  $V$  is reducible, a singularity in  $p$  additionally occurs when  $p$  belongs to more than one irreducible component of  $V$ . Finally, the collection of singularities of  $V$  is called the *singular locus*  $\text{Sing}(V)$ .

Another common way to conceptualize a variety  $V$ 's dimension is to calculate the Jacobian's rank  $r = \text{rank } df(p)$  for a generic point  $p$  in the algebraic closure  $\bar{k}^d$ . In that case,  $\dim(V) = d - r$  [299, p.239f.]. Furthermore, the notion of singularity in Definition 2.1.2 does not depend on the choice of generators:

**Proposition 2.1.6.** *Let an ideal  $I \subset k[x_1, \dots, x_d]$  be given by two different sets of generators, namely  $I = \langle f_1, \dots, f_s \rangle = \langle g_1, \dots, g_m \rangle$ . Then, the ranks of the Jacobians  $df(p)$  and  $dg(p)$  agree for any  $p \in \mathcal{V}(I)$ .*

*Proof.* We proceed to prove the statement by contradiction. Without loss of generality, assume that  $\text{rank}(dg(p)) > \text{rank}(df(p))$ . Thus, there exists  $\nabla g_n(p) \notin \text{span}(\nabla f_i(p))_{i \in [s]}$ . Nevertheless, any element of  $\langle f_1, \dots, f_s \rangle$  can be expressed as a  $k[x_1, \dots, x_d]$ -linear combination in the generators. In particular,  $g_n \in I$ , so  $g_n = \sum_{i=1}^s c_i f_i$ , implying that

$$\frac{\partial}{\partial x_j} g_n(p) = \frac{\partial}{\partial x_j} \left( \sum_{i=1}^s c_i f_i \right)(p) = \sum_{i=1}^s \left( \frac{\partial c_i}{\partial x_j} f_i + \frac{\partial f_i}{\partial x_j} c_i \right)(p) = \sum_{i=1}^s \frac{\partial f_i}{\partial x_j}(p) \cdot c_i(p)$$

for any  $p \in \mathcal{V}(I)$  and  $j \in \{1, \dots, d\}$ , as  $f_i(p) = 0$ . Consequently  $\nabla g_n(p) \in \text{span}(\nabla f_i(p))_{i \in [s]}$ , contradicting the assumption and thereby proving the claim.  $\square$

Our objective now shifts to deriving conditions for tangency and orthogonality to a given variety.

**Definition 2.1.7.** Let a variety  $V = \mathcal{V}(f_1, \dots, f_s)$  and a point  $p \in V$  be given. If  $p$  is not a singularity, we call  $p$  *regular*. Assuming  $p$  is regular, we can define the *tangent space*  $T_p V$  of  $V$  at  $p$  as the kernel of the Jacobian  $df(p)$ . The *normal space*  $N_p V$  of  $V$  at  $p$  is given by the row space of  $df(p)$ .

Algebraic varieties exhibit a rich diversity of structures, capable of approximating smooth, compact manifolds with arbitrary precision [10]. Their versatility finds application in diverse fields such as the kinematic analysis of robots [335], biochemical reaction networks [96], and image reconstruction [56]. Their capacity to contain singularities distinguishes them from manifolds. The collection of a variety's regular points forms a smooth manifold [22, Thm. 2.5.15], whereas the set of singular points defines a proper subvariety [149, Thm. 5.3]. All of these arguments indicate that investigating the local behavior around singularities is a reasonable pursuit.

**Remark 2.1.8.** While in regular points a variety's tangent space is defined, it seems natural to extend this concept to any point on  $V$ . To do so, we can define the *tangent cone* for hypersurfaces  $V = \mathcal{V}(f)$  by  $\widehat{T}_p V = \mathcal{V}(f_{p,\min})$ . To understand what  $f_{p,\min}$  means, assume that for  $p \in k^n$  we decompose the polynomial  $f$  as

$$f = f_{p,0} + f_{p,1} + \dots + f_{p,d}$$

where  $f_{p,j}$  is the  $k$ -linear combination of terms of the form  $(x_1 - p_1)^{\alpha_1} \cdots (x_d - p_d)^{\alpha_d}$  for  $p \in k^n$ ,  $\alpha_i \in \mathbb{Z}_{\geq 0}$  and  $\sum_{i=1}^d \alpha_i = j$ . In this notation,  $f_{p,0} = f(p)$  and  $f_{p,1}(x) = \sum_{j=1}^d \frac{\partial f}{\partial x_j}(p) \cdot (x_j - p_j)$  by Taylor's Theorem [311, p.52f.]. The condition that  $f_{p,1} = 0$  thus exactly characterizes the tangent space in regular points  $p \in V$  (cf. Definition 2.1.7). Finally,  $f_{p,\min}$  denotes the lowest degree term  $f_{p,j}$  in  $f$  that is not identically zero [86, p.527]. This procedure generalizes to arbitrary algebraic varieties via  $\hat{T}_p V = \mathcal{V}(\langle f_{p,\min} : f \in \mathcal{I}(V) \rangle)$ . Conveniently, in nonsingular points  $p$  both definitions agree  $\hat{T}_p V = T_p V$ , while in singular points the tangent space is the linear hull of the tangent cone [225, p.167].

We now intend to provide an intuition for notions introduced in several definitions from this chapter by considering their behavior in two examples.

**Example 2.1.9.** To illustrate the geometric concepts from Definitions 2.1.5 and 2.1.7, a curve on the saddle manifold  $V_1 = \{(x, y, z) \in \mathbb{R}^3 : z = x^2 - y^2 \text{ and } x^2 + y^2 + z^2 = 0.5\}$  and the double cone  $V_2 = \{(x, y, z) \in \mathbb{R}^3 : z^2 = x^2 + y^2\}$  are investigated. Both varieties are depicted in Figure 2.1.10.

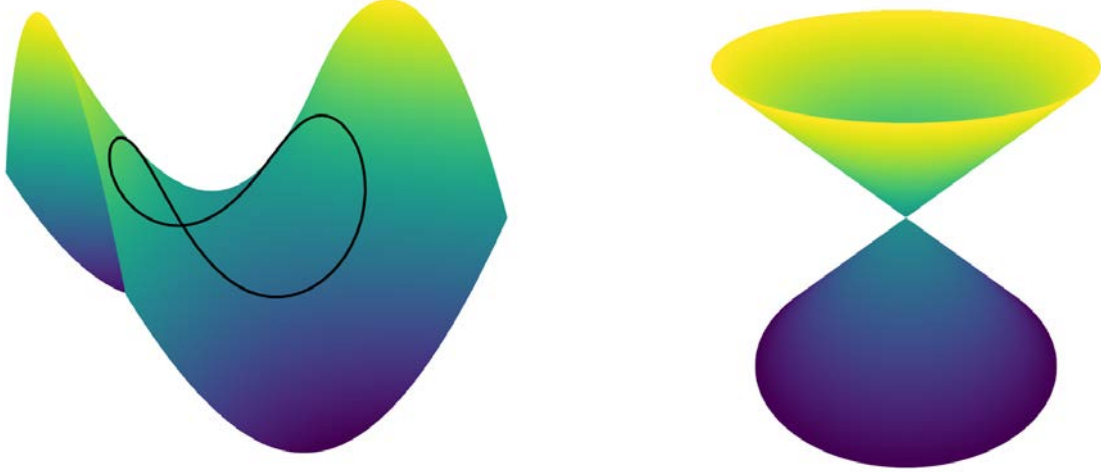


**Figure 2.1.10:** A curve on the hyperbolic paraboloid  $V_1$  (l.) and the double cone  $V_2$  with a singularity in 0 (r.). Both surfaces are algebraic varieties and are colored with respect to their  $z$ -value, ascending from blue to yellow.

Starting out with  $V_1$ , the corresponding Jacobian is given by

$$df_1(x, y, z) = \begin{pmatrix} -2x & 2y & 1 \\ 2x & 2y & 2z \end{pmatrix}.$$

As its rank does not drop except in the  $z$ -axis which does not lie on  $V_1$ , this variety contains no singularities, is irreducible, and has dimension 1. The tangent space at  $p \in V_1$  is given by

$$T_p V_1 = \begin{pmatrix} -2p_1 \\ 2p_2 \\ 1 \end{pmatrix} \times \begin{pmatrix} p_1 \\ p_2 \\ p_3 \end{pmatrix} \cdot \mathbb{R} = \begin{pmatrix} 2p_2 \cdot p_3 - p_2 \\ p_1 + 2p_1 \cdot p_3 \\ -4p_1 \cdot p_2 \end{pmatrix} \cdot \mathbb{R},$$

since the normal space at  $p$  is orthogonal to the tangent space and is equal to the Jacobian's row space by Definition 2.1.7.

Analogously,  $V_2$  is irreducible, since it cannot be decomposed into affine linear spaces. Its Jacobian is given by  $(-2x, -2y, 2z)$ , which is zero only at the origin, so  $V_2$  has a singularity at 0. Consequently,  $V_2$ 's dimension is 2 as well. The tangent space at  $p \in V_2 \setminus \{0\}$  is

$$T_p V_2 = \{(x, y, z) \in \mathbb{R}^3 : z = 1 + \frac{1}{p_3}(p_1(x - p_1) + p_2(y - p_2))\}.$$

Since the polynomial generating  $V_2$  is homogeneous of degree 2, its tangent cone (see Remark 2.1.8) reproduces the variety  $\widehat{T}_0 V_2 = V_2$ , motivating the name “cone”.

### 2.1.2 Bar-and-Joint Frameworks and Rigidity Theory

This section summarizes the basic geometric and algebraic definitions of rigidity theory, which studies stiff structures devoid of mechanisms. We begin by considering embedded graphs, known as frameworks.

**Definition 2.1.11.** Given a graph  $G = (V, E)$  and a map  $p : V \rightarrow \mathbb{R}^d$ , a *d-dimensional framework*  $\mathcal{F}$  is a tuple  $(G, p)$ . We call  $p$  a *realization of  $G$  in  $\mathbb{R}^d$* . The edges of  $G$  are called the *bars* of  $\mathcal{F}$ .

The idea behind framework rigidity is that an embedded graph with edge length constraints increasingly loses its flexibility as more edges are added. Each additional edge  $ij \in E$  comes with a bar length constraint of the form  $\|p(i) - p(j)\| = \ell_{ij} \in \mathbb{R}_{>0}$  with fixed bar lengths  $\ell_{ij}$ . Note that we slightly abuse notation by writing  $ij$  for the unordered edge  $\{i, j\}$ . The bars are connected in universal joints, enabling them to freely rotate. Therefore, investigating a framework's rigidity is the same as checking whether the realization  $p : V \rightarrow \mathbb{R}^d$  is a real-isolated solution of the polynomial system resulting from combining all edge length equations. In other words, there is no continuous curve through  $p(v_1) \times p(v_2) \times \cdots \times p(v_n)$  in  $\mathbb{R}^{d|V|}$  for the vertices  $V = \{v_1, v_2, \dots, v_n\}$  that does not correspond to an isometry of  $\mathbb{R}^d$ . On the one hand, this definition is perfectly viable and characterizes framework rigidity. On the other hand, proving that a solution is real-isolated generally is complicated. For this reason, textbooks usually take a different approach to framework rigidity, making use of the fact that the underlying polynomial system solely consists of quadrics. Consequently, the notion of congruent realizations is introduced in the following.

**Definition 2.1.12.** Consider two realizations  $p, q : V \rightarrow \mathbb{R}^d$  of the same finite graph  $G = (V, E)$  in  $\mathbb{R}^d$ . They are called *congruent*, if all their edges  $ij \in E$  have the same length:

$$\|p(i) - p(j)\| = \|q(i) - q(j)\|.$$

In  $\mathbb{R}^d$ , there are infinitely many congruent realizations and the collection of all these configurations is called the *realization space* of the framework. Many are given by Euclidean isometries composed of rotations and translations; so they are often called *trivial* and disregarded. Factoring out the Euclidean motions from the framework's realization space, one obtains its *configuration space*. This notion paves the way for the definition of infinitesimal rigidity appearing in Schulze and Whiteley [287], a property that is most interesting to structural engineers.

**Definition 2.1.13.** Given a bar-and-joint framework  $(G, p)$  in  $\mathbb{R}^d$  on a finite graph  $G = (V, E)$ , consider the polynomial system

$$b_{ij} = \sum_{k=1}^d (p_{ik} - p_{jk})^2 - \ell_{ij}^2 \quad \text{for } ij \in E$$

with variables  $(p_{mn} : m \in \{1, \dots, |V|\}, n \in \{1, \dots, d\})$  representing the realization  $p : V \rightarrow \mathbb{R}^d$  and fixed edge-lengths  $\ell_{ij} > 0$ . The corresponding *rigidity matrix* with  $|E|$  rows and  $d|V|$  columns can be described in terms of the system's Jacobian:

$$R_G(p) = \frac{1}{2} \left( \frac{\partial b_{ij}}{\partial p_{mn}}(p) \right)_{ij \in E, (m,n) \in [|V|] \times [d]} \in \mathbb{R}^{|E| \times d|V|}.$$

Then, an *infinitesimal motion*  $u$  is an element of  $\ker R_G(p)$ . We call an infinitesimal motion *trivial* if it extends to an ambient isometry. In the case of  $\mathbb{R}^d$ , this means that for all vertices  $i \in V$  we have  $u_i = p_i S + t$  for a skew-symmetric matrix  $S$  (a rotation) and a vector  $t$  (a translation). If each infinitesimal motion is trivial, we call the framework *infinitesimally rigid*, else *infinitesimally flexible*.

The fact that the constraint system describing a framework's deformation space purely consists of polynomials puts this problem in the realm of algebraic geometry, making related techniques applicable (cf. Section 2.1.1). This is further highlighted by the fact that the framework's rigidity matrix is nothing but a scaled version of the polynomial system's Jacobian. By Definition 2.1.7, this means that the infinitesimal motions lie in the tangent space at the framework's realization in  $\mathbb{R}^{d|V|}$ . Assuming that the framework's underlying graph contains at least  $d+1$  vertices, the Euclidean motions can be factored out by constraining the matrix whose rows are given by the first  $d+1$  points of the framework to be lower-triangular with zeros on the diagonal. This operation effectively reduces the framework's degrees of freedom by  $d(d+1)/2$ . The following theorem applies this construction to the infinitesimal rigidity of frameworks in  $\mathbb{R}^d$ .

**Theorem 2.1.14** (cf. [80, Prop. 2.2]). *A framework  $(G, p)$  is infinitesimally rigid in  $\mathbb{R}^d$  if and only if either the rank of  $R_G(p)$  is  $d|V| - d(d+1)/2$  or  $(G, p)$  is a simplex.*

Every infinitesimally rigid framework is locally rigid [80, Thm. 2.1], meaning that it is a real-isolated solution of the polynomial system  $b$  modulo ambient isometries. However, infinitesimal flexibility does not necessarily mean that a framework is not locally rigid. When we find non-trivial motions but still want to insist that the structure is rigid, we need to look at higher-order information than the system's linearization. To understand this, we follow the definitions from Connelly and Gortler [81]:

**Definition 2.1.15.** Given a bar-and-joint framework  $(G, p)$ , we call an element  $\omega \in \text{coker } R_G(p)$  of the rigidity matrix' cokernel an *equilibrium stress*. If there is an equilibrium stress  $\omega$  for  $(G, p)$  such that

$$\sum_{ij \in E} \omega_{ij} \|u(i) - u(j)\|^2 > 0$$

for each non-trivial infinitesimal motion  $u$ , then we call the framework *prestress stable*.

We define a *second-order motion*  $p''$  by the equality

$$R_G(p) p'' + R_G(u) u = 0$$

for an infinitesimal motion  $u$ . If there is no second-order motion, we call the framework *second-order rigid*.

Definition 2.1.15 distinguishes the concepts of prestress stability and second-order rigidity. The notion of equilibrium stresses connects these ideas, as highlighted in Proposition 2.1.16. Comparing this result to the definition of prestress stability reveals that these concepts are related by a change in the existing and universal quantifiers' order.

**Proposition 2.1.16** (cf. [81, Prop. 2.5]). *A framework  $(G, p)$  is second-order rigid in  $\mathbb{R}^d$  if and only if for every non-trivial infinitesimal motion  $u \in \mathbb{R}^{d|V|}$ , there is an equilibrium stress  $\omega$  such that*

$$\sum_{ij \in E} \omega_{ij} \|u(i) - u(j)\|^2 > 0.$$

While the algebraic distinction between an infinitesimal motion and an equilibrium stress is subtle, the geometric difference is rather intuitive. Motions are directions on the vertices in which the framework wants to move. Stresses are weights on edges indicating whether the bar wants to expand or compress when interpreting the framework as a tensegrity. Hence, we can think of stresses as an energy on the framework that can potentially balance infinitesimal motions.

**Theorem 2.1.17** (cf. [81, Thm. 2.6]). *For any given framework  $(G, p)$  in  $\mathbb{R}^d$  the following implications  $(1) \Rightarrow (2) \Rightarrow (3) \Rightarrow (4)$  hold:*

(1)  $(G, p)$  is infinitesimally rigid.

(2)  $(G, p)$  is prestress stable.

(3)  $(G, p)$  is second-order rigid.

(4)  $(G, p)$  is (locally) rigid.

*None of these implications are reversible.*

A large class of natural objects, such as most polyhedra [81], will fall into one of the first three categories pointed out in Theorem 2.1.17. Identifying an object that doesn't fit the criteria of second-order rigidity, yet doesn't exhibit flexibility, demands considerable effort [82]. For these reasons, we will refrain from defining higher-order rigidity in this thesis. To familiarize ourselves with these concepts, we will begin by examining an example for each of these categories.

**Example 2.1.18.** To illustrate rigidity, let us consider three examples: The first one is the Moser spindle and can be seen in Figure 2.1.19(1.). To factor out the rigid motions, we pin the bottom horizontal line. As a pointed pseudo-triangulated polygon, it is infinitesimally rigid [303, Thm. 3.6].

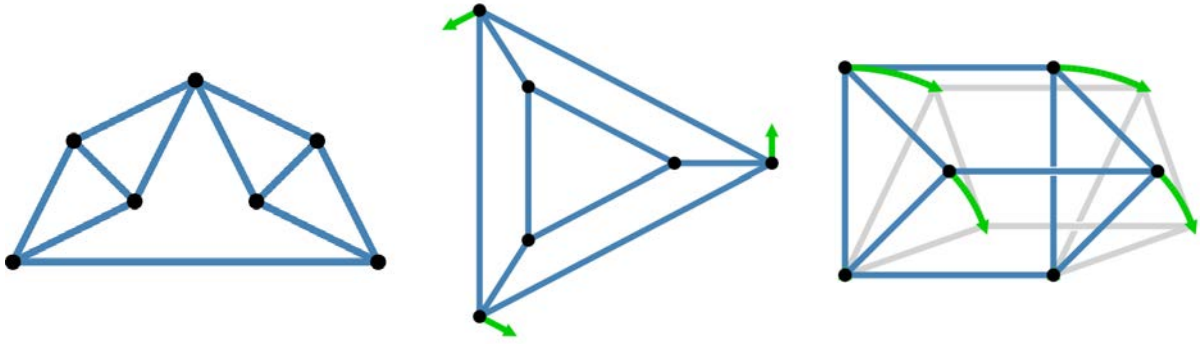


**Figure 2.1.19:** An infinitesimally rigid framework (l.), a locally rigid framework that is not infinitesimally rigid (c.) and a flexible framework (r.). The green arrows indicate an infinitesimal motion and the gray shadow depicts a different configuration in the framework's configuration space.

The second framework is the projection of a tetrahedral frustum. To factor out the Euclidean motions, we fix the inner triangle's vertices on the vertical line. Any triangle is infinitesimally rigid, implying that the entire inner triangle is pinned. The framework has a non-trivial infinitesimal motion given by the counter-clockwise rotation of the outer triangle, parametrized by a rotation that is only applied to the outside vertices. The infinitesimal motion and the framework itself are depicted in Figure 2.1.19(c.). We plan to show that this framework is prestress stable. Since its only equilibrium stress  $\omega$  is given by 2 on the inner triangle's edges,  $-1$  on the outer triangle's bars, and 6 on the intermediate edges, we can deduce that for an arbitrary  $\varphi \in [0, 2\pi)$  and for the motion  $u : V \rightarrow \mathbb{R}^2$ :

$$\begin{aligned}
\sum_{ij \in E} \omega_{ij} \cdot \|u(i) - u(j)\|^2 &= 6 \cdot 3 \cdot \underbrace{(\sin(\varphi)^2 + \cos(\varphi)^2)}_{=1} \\
&\quad - 1 \cdot \left( \sum_{j=1}^3 \left( \sin\left(\frac{j \cdot 2\pi}{3}\right) - \sin\left(\frac{(j-1) \cdot 2\pi}{3}\right) \right)^2 \right. \\
&\quad \left. + \left( \cos\left(\frac{j \cdot 2\pi}{3}\right) - \cos\left(\frac{(j-1) \cdot 2\pi}{3}\right) \right)^2 \right) + 2 \cdot 0 \\
&= 18 - \left( 6 - 2 \cdot \sum_{j=1}^3 \sin\left(\frac{j \cdot 2\pi}{3}\right) \cdot \sin\left(\frac{(j-1) \cdot 2\pi}{3}\right) \right. \\
&\quad \left. - 2 \cdot \sum_{j=1}^3 \cos\left(\frac{j \cdot 2\pi}{3}\right) \cdot \cos\left(\frac{(j-1) \cdot 2\pi}{3}\right) \right) \\
&= 18 - \underbrace{\left( 6 - 2 \cdot \sum_{i=1}^3 \cos\left(\frac{2\pi}{3}\right) \right)}_{=-3/2} > 0,
\end{aligned}$$

using trigonometric identities. In fact, the absolute values of sin and cos are bounded above by 1. Therefore, the tetrahedral frustum is prestress stable and consequently rigid by Theorem 2.1.17, even though it has an infinitesimal motion.

Finally, consider the 3-prism in Figure 2.1.19(r.). The framework is flexible, even though the edge count works out: There are 9 degrees of freedom and 9 edges, so Theorem 2.1.14 seems applicable. The framework's high degree of symmetry makes it non-generic, so shearing it simultaneously maintains all bar-length constraints. An exemplary deformation path can be parametrized with the use of a computer algebra system such as **Singular** [93].

### 2.1.2.1 Periodic Frameworks

While the previous section deals with finite frameworks, in the real world materials often admit symmetries that can be exploited. Periodic frameworks naturally occur for example in crystals, and help to significantly reduce the complexity of the investigation of an infinite framework's rigidity. For that, we define an analogous notion to Definition 2.1.11, introducing periodic frameworks in a  $d$ -torus  $\mathbb{R}^d/\Lambda$  for a full-dimensional lattice  $\Lambda \subset \mathbb{R}^d$ .

**Definition 2.1.20** (cf. [45]). A  *$d$ -periodic graph*  $(G, \Gamma)$  is a simple, connected, infinite graph  $G = (V, E)$  with finite degree at every vertex together with a free abelian periodicity group  $\Gamma \subset \text{Aut}(G)$  of rank  $d$ , with finitely many vertex orbits  $V/\Gamma$  and edge orbits  $E/\Gamma$ .

We define a  *$d$ -periodic framework*  $\mathcal{F} = (G, \Gamma, p, \pi)$  by a placement  $p : V \rightarrow \mathbb{R}^d$  of the  $d$ -periodic graph  $G$ 's vertices and an injective group representation  $\pi : \Gamma \rightarrow \mathcal{T}(\mathbb{R}^d)$  in the translation group of  $\mathbb{R}^d$ , whose image  $\pi(\Gamma)$  has maximal rank  $d$ . In addition, we require the compatibility condition of  $p$  and  $\pi$  for each  $\gamma \in \Gamma$  and  $v \in V$ :

$$p(\gamma v) = \pi(\gamma)p(v).$$

Assume we are given the representation of the configuration  $p : V/\Gamma \rightarrow \mathbb{R}^d$  inside  $\mathbb{R}^d/\Lambda$  for the vertex orbits  $V/\Gamma$ . Then, any edge can be equipped with information about the translational unit cells that it connects, making the representation of the periodic graph well-defined. Say for example that  $ij \in E$  connects  $p_i$  with  $p_j + \lambda_{ij}$  for some  $\lambda_{ij} \in \Lambda$ . This lets us express  $\lambda_{ij}$  in terms of the lattice's minimal generating set  $(\lambda_1, \dots, \lambda_d)$  as  $\lambda_{ij} = \sum_{k=1}^d (m_{ij})_k \lambda_k$  with  $m_{ij} \in \mathbb{Z}^d$ . Rewriting the edge  $ij \in E$  as its orbit via  $\{i, j; m_{ij}\}$  makes  $\langle G, m \rangle$  a *gain graph* and  $(\langle G, m \rangle, p)$  a  *$d$ -periodic orbit framework* on  $\mathbb{R}^d/\Lambda$  [265]. A  $d$ -periodic framework's data is thus described by the vertex orbits  $V_m = \{v_1, \dots, v_n\}$ , the edge orbits of the form  $E_m = \{\{i, j; m_{ij}\} : ij \in E\}$  for the *gain*  $m : E \rightarrow \mathbb{Z}^d$  and a placement  $p : V_m \rightarrow \mathbb{R}^d/\Lambda$ .

To study a periodic framework's rigidity, we need to extend the notions that are discussed in Section 2.1.2. Crucially, isometries on the  $d$ -Torus  $\mathbb{R}^d/\Lambda$  differ from the ones on  $\mathbb{R}^d$ , as an isometry must preserve all distances between points. In other words,  $\|p_i - (p_j + \lambda)\|$  must be preserved for all  $\lambda \in \Lambda$ , leaving only translations as rigid motions in the torus [265]. Distances are invariant under the choice of unit cell, since

$$\|(p_i + z) - (p_j + \lambda + z)\| = \|p_i - (p_j + \lambda)\|.$$

This notion is well-defined because by construction all edge orbits can be represented as  $\{i, j; m_{ij}\}$ . Following Ross [265], we formulate rigidity in the periodic setting.

**Definition 2.1.21.** Let  $(\langle G, m \rangle, p)$  be a  $d$ -periodic orbit framework on  $\mathbb{R}^d/\Lambda$  with the lattice  $\Lambda$  given by a minimal generating set  $(\lambda_1, \dots, \lambda_d)$ . A *motion* of  $(\langle G, m \rangle, p)$  is an assignment of continuous functions  $P_i : [0, 1] \rightarrow \mathbb{R}^d$  to each vertex such that

1.  $P_i(0) = p(v_i)$  for  $i = 1, \dots, n$  and
2. for all edge orbits  $\{i, j; m_{ij}\}$  in  $E_m$  with  $t \in [0, 1]$  the edge-distances are preserved:

$$\|P_i(t) - (P_j(t) + \lambda_{ij})\| = \|p(v_i) - (p(v_j) + \lambda_{ij})\|$$

$$\text{for } \lambda_{ij} = \sum_{k=1}^d (m_{ij})_k \lambda_k.$$

If a motion  $(P_i)_{i=1}^d$  preserves all distances  $\|p_i - (p_j + \lambda)\|$  for arbitrary  $i, j \in \{1, \dots, n\}$  and  $\lambda \in \Lambda$ , we call it a *rigid motion*. A periodic orbit framework is called *rigid on a fixed torus*  $\mathbb{R}^d/\Lambda$  if all of its motions are rigid motions.

The notion of infinitesimal rigidity (cf. Definition 2.1.13) extends to the periodic setting, as laid out in Ross [265]:

**Definition 2.1.22.** Let  $(\langle G, m \rangle, p)$  be a  $d$ -periodic orbit framework on  $\mathbb{R}^d/\Lambda$  with a minimal generating set of  $\Lambda$  given by  $(\lambda_1, \dots, \lambda_d)$ . Then, an *infinitesimal motion* is an assignment of velocities  $u : V_m \rightarrow \mathbb{R}^d$  to each of the vertices  $\{v_1, \dots, v_n\}$  with  $u(v_i) = u_i$  such that

$$(u_i - u_j) \cdot (p_i - (p_j + \lambda_{ij})) = 0$$

for each edge orbit  $\{i, j; m_{ij}\}$  in  $E_m$  and  $\lambda_{ij} = \sum_{k=1}^d (m_{ij})_k \lambda_k$ . A *trivial infinitesimal motion* is an infinitesimal motion that preserves all distances between pairs of vertices:

$$(u_i - u_j) \cdot (p_i - (p_j + \lambda)) = 0$$

for arbitrary  $i, j \in \{1, \dots, n\}$  and  $\lambda \in \Lambda$ . We call the periodic orbit framework *infinitesimally rigid* if all infinitesimal motions are trivial.

It can be shown that the trivial infinitesimal motions on  $\mathbb{R}^d/\Lambda$  are completely characterized by translations [265, Prop. 4.2]. To describe infinitesimal rigidity, an edge-count theorem can be formulated, similar to Section 2.1.2. To accomplish this, we require the periodic counterpart of the rigidity matrix, as described in Ross [265, p.23].

**Definition 2.1.23.** The *periodic rigidity matrix*  $R_{\langle G, m \rangle}(p)$  of a periodic orbit framework  $(\langle G, m \rangle, p)$  on  $\mathbb{R}^d/\Lambda$  with a minimal generating set  $(\lambda_1, \dots, \lambda_d)$  of the lattice  $\Lambda$  is a  $|E_m| \times d|V_m|$  matrix that records equations in the space of possible infinitesimal motions. The row of the periodic rigidity matrix  $R_{\langle G, m \rangle}(p)$  corresponding to the edge orbit  $\{i, j; m_{ij}\}$  can be expressed as

$$\{i, j; m_{ij}\} \begin{pmatrix} & i & & j & \\ & \vdots & & \vdots & \\ \cdots 0 & p_i - (p_j + \lambda_{ij}) & 0 \cdots 0 & (p_j + \lambda_{ij}) - p_i & 0 \cdots \\ & \vdots & & \vdots & \end{pmatrix}$$

for  $\lambda_{ij} = \sum_{i=1}^d (m_{ij})_k \lambda_k$ .

**Theorem 2.1.24** (cf. [265, Thm. 4.9]). *A periodic orbit framework  $(\langle G, m \rangle, p)$  is infinitesimally rigid on the fixed torus  $\mathbb{R}^d/\Lambda$  if and only if the rigidity matrix  $R_{\langle G, m \rangle}(p)$  has rank  $d|V|-d$ .*

It is important to realize that this theorem heavily relies on the fact that the torus  $\mathbb{R}^d/\Lambda$  is fixed. By considering two examples, we aim to illustrate the concepts presented in this section.

**Example 2.1.25.** Consider the Archimedean tesselation of the plane consisting of regular triangles and hexagons, which is also called *trihexagonal tiling* or *Kagome weave* as a fabric [121]. We construct the associated 2-periodic orbit framework from the tiling by ignoring its faces and constraining the edge lengths. To describe it, take a graph on three vertices with the following edge orbits:

$$E_m = \{\{1, 2, (0, 0)\}, \{2, 3, (0, 0)\}, \{1, 2, (0, -1)\}, \{3, 1, (0, 1)\}, \{3, 1, (1, 0)\}, \{3, 2, (1, 0)\}\}.$$

This framework can be embedded in  $\mathbb{R}^2$  via  $p(1) = (0, 0)$ ,  $p(2) = (1/2, \sqrt{3}/2)$  and  $p(3) = (3/2, \sqrt{3}/2)$ . The corresponding periodicity lattice is generated by the vectors  $(2, 0)$  and  $(1, \sqrt{3})$ . Note that the periodic unit cell is fixed and we do not allow deformations of the vectors generating the lattice.

This structure is not infinitesimally rigid because the framework's rigidity matrix has a rank-deficiency of 1. Still, it is rigid and cannot flex. Pinning the position of the first vertex makes translations infeasible, effectively factoring out rigid motions. In doing so, the position of the second vertex is fixed, since it appears in two edge orbits with the first vertex. The edge lengths define distinct circles in the framework's configuration space whose center lies in the orbit of the first vertex. These circles touch in the second vertex and consequently fix it. Subsequently, the third vertex lies on a triangle containing the fixed vertices 1 and 2. Hence, it is fixed as well. Figure 2.1.26(l.). portrays the periodic framework together with its infinitesimal motions.

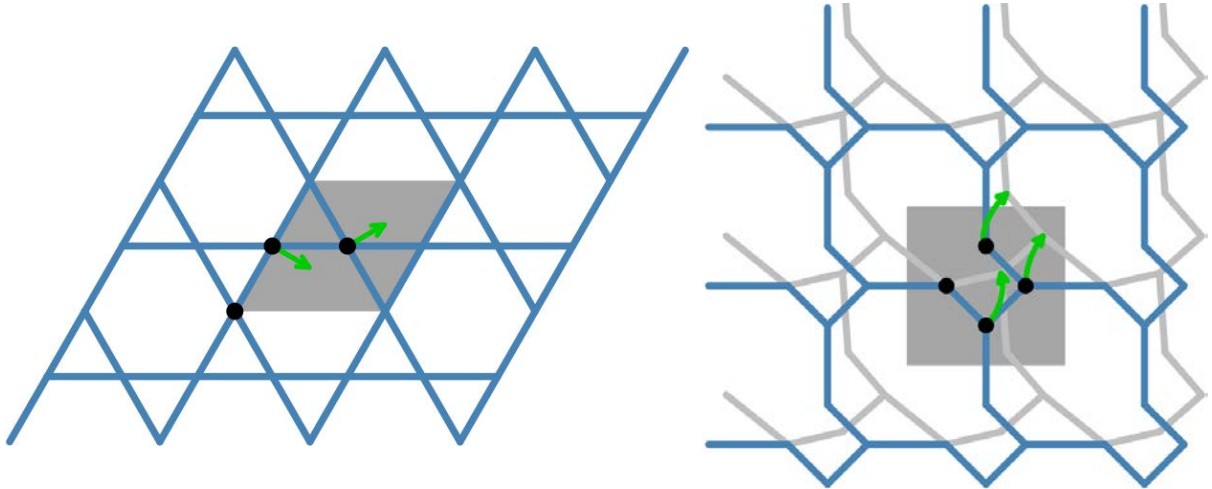


**Figure 2.1.26:** The rigid Kagome framework (l.) and a flexible framework (r.) on a fixed torus.

In both cases, the periodic unit cell is shaded in gray and a flex is depicted in green. In the flexible case the infinitesimal motion extends to a deformation path. A different configuration on this curve is plotted in light gray.

As a second example, we intend to contrast the rigid Kagome framework with a flexible alternative. Consider a periodic graph with four vertex orbits and five edge orbits given by

$$E_m = \{\{1, 2, (0, 0)\}, \{2, 3, (0, 0)\}, \{3, 4, (0, 0)\}, \{3, 1, (1, 0)\}, \{4, 2, (0, 1)\}\}.$$

The edge count suggests that the rigidity matrix is generically rank-deficient with its kernel's dimension given by 1. As a result, we expect that this framework will exhibit flexibility under a suitable embedding. We choose

$$p(1) = (1/4, 1/2), \quad p(2) = (1/2, 1/4), \quad p(3) = (3/4, 1/2) \quad \text{and} \quad p(4) = (1/2, 3/4).$$

The periodicity lattice is then generated by the standard basis of  $\mathbb{R}^2$ . A deformation path corresponding to this initial configuration can be seen in Figure 2.1.26(r.).

### 2.1.2.2 Auxeticity

Auxeticity is known as the dilatant response of a material in lateral directions when expanding it in one direction. Engineers and materials scientists value this unique property because it enables lightweight designs through porosity in its expanded state and allows for compactness when compressed.

Borcea and Streinu provide a geometric perspective on analyzing deformations of more complicated, typically periodic, structures by defining auxeticity mathematically. Recall the definition of a  $d$ -periodic framework from Definition 2.1.20. The rigidity of these types of frameworks is explored in the previous section. However, auxeticity requires deforming the framework. Consequently, we want to understand paths maintaining the framework's periodicity and edge length constraints but possibly deforming the periodicity lattice  $\pi_d(\Gamma)$ . Notice that contrary to the previous chapter, the lattice is not fixed here.

**Definition 2.1.27** (cf. [45]). Given a  $d$ -periodic framework  $\mathcal{F} = (G, \Gamma, p, \pi)$ , a *one-parameter deformation* of  $\mathcal{F}$  is a smooth family of placements  $p_\tau : V \rightarrow \mathbb{R}^d$  parametrized by  $\tau \in (-\varepsilon, \varepsilon)$  for some small  $\varepsilon > 0$  with  $p_0$  defined as the initial placement  $p$ , satisfying two conditions:

- a) The length  $\|p_\tau(i) - p_\tau(j)\|$  of any bar  $ij \in E$  stays unchanged throughout  $\tau \in (-\varepsilon, \varepsilon)$  and
- b) Periodicity under  $\Gamma$  is maintained via a faithful representation  $\pi_\tau : \Gamma \rightarrow \mathcal{T}(\mathbb{R}^d)$ . Note that the periodicity lattice  $\pi_\tau(\Gamma)$  may change with  $\tau$ .

After factoring out Euclidean motions – isometries in  $\mathbb{R}^d$  – the framework's *configuration space* describes the collection of periodic placements in  $\mathbb{R}^d$  that satisfy the bar-length equations in b. The *deformation space* of the framework denotes the connected component of the configuration space containing the initial framework  $p_0$ .

This definition raises the question of how to explicitly derive the configuration space. The group of Euclidean motions consisting of translations, rotations and reflections acts on the set of placements for  $(G, \Gamma, p, \pi)$ . By removing this action to fix some of the vertices [56], two frameworks are considered equivalent if one can be transformed into the other through Euclidean motions. Configuration spaces are algebraic and deformation spaces semi-algebraic

sets, respectively. Therefore, notions from algebraic and differential geometry such as singularity (cf. Def. 2.1.5), tangent space (cf. Def. 2.1.7) and dimension (cf. Def. 2.1.5) apply here as well. The following example clarifies these theoretical notions.

**Example 2.1.28.** Again consider the 2-periodic framework obtained from the trihexagonal tiling in Example 2.1.25. It can be described by six vertices collected in the set  $V = \{1, \dots, 6\}$ . The edges

$$E = \{\{1, 2\}, \{2, 3\}, \{3, 4\}, \{4, 5\}, \{5, 6\}, \{6, 1\}\}$$

describe a hexagon with edge length 1 and a placement  $p : V \rightarrow \mathbb{R}^2$  respecting these constraints. In this example, the periodicity lattice is generated by the directed edges  $(1, 4)$  and  $(6, 3)$ . Contrary to Example 2.1.25, the periodicity lattice is allowed to deform here, so we deliberately omit the lattice's coordinates. This detail alters the rigidity properties of the framework. To calculate the configuration space, we pin the vertex 1 to  $(0, 0)$  and 4 to  $(\tau, 0)$  for some  $\tau > 0$ .

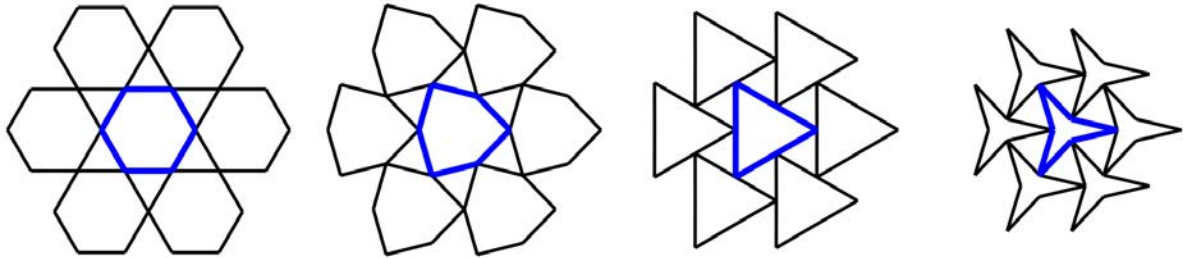


**Figure 2.1.29:** All pictures depict 7 primitive cells of the Kagome framework on a flexible torus.

Their unit cell is highlighted in blue. The left-most vertex is labeled 1 and the other vertices are named clockwise in ascending order. Even though it seems like this unit cell contains no triangles, they are implicitly covered through the translations of the hexagon. We apply a horizontal flex to the framework by controlling the position of vertex 4. At  $\tau = 2$  (l.), the trihexagonal tiling can be observed in all its glory. It deforms over  $\tau = 1.94$  (c.l.) to  $\tau = 1.73$  (c.r.), becoming a tiling with two different types of equilateral triangles. Beyond that configuration, some of the hexagons' vertices move inside the convex hull, making the shape concave, as for  $\tau = 1.37$  (r.).

Figure 2.1.29 depicts a deformation path from  $\tau = 2$  to  $\tau = 1.37$ . The deformation space is fully characterized by  $\tau \in [1, 2]$ , as the configuration becomes complex-valued below 1 and above 2. In addition, the configuration space is 1-dimensional because vertex 5 can be described by a translation of vertex 2. Since the deformation space contains no singularities, no additional components intersect it. All of these arguments combined imply that the complete component of the configuration space can indeed be described by the interval  $[1, 2]$ . The respective limits of the interval are attained by the trihexagonal tiling and the regular triangular tesselation.

Another interesting observation is that the triangles stay the same throughout the deformation. In fact, a triangle is rigid (cf. [87]), meaning that its configuration is realized as the isolated, real solution of the system of polynomial equations derived from the bars' lengths.

Before properly defining auxetic frameworks another theoretical tool is necessary.

**Definition 2.1.30** (cf. [43]). Let  $T : \mathbb{R}^d \rightarrow \mathbb{R}^d$  be a linear operator.  $T$ 's operator norm is defined by

$$\|T\| = \sup_{|x| \leq 1} |Tx| = \sup_{|x|=1} |Tx|.$$

$T$  is called a *contraction*, when  $\|T\| \leq 1$  and a *strict contraction*, if  $\|T\| < 1$ .

Assume now that  $\mathcal{F} = (G, \Gamma, p_\tau, \pi_\tau)$  is a one-parameter deformation with  $\tau \in (-\varepsilon, \varepsilon)$  of a periodic framework in  $\mathbb{R}^d$ , as was introduced in Definition 2.1.27. Given parameters  $\tau_1 < \tau_2$ , the corresponding one-parameter family of periodicity lattices  $\pi_\tau(\Gamma)$  yields a way to compare the framework at  $\tau_1$  with the framework at  $\tau_2$ . Since  $\pi_\tau(\Gamma)$  has rank  $d$  by assumption, the linear operator  $T_{\tau_2\tau_1}$  taking the lattice at  $\tau_2$  to  $\tau_1$  via

$$T_{\tau_2\tau_1} \circ \pi_{\tau_2} = \pi_{\tau_1} \quad (2.1.31)$$

is unique. It appears in the following definition, formalizing auxeticity.

**Definition 2.1.32** (cf. [43]). A differentiable one-parameter deformation  $(G, \Gamma, p_\tau, \pi_\tau)$  with  $\tau \in (-\varepsilon, \varepsilon)$  of a periodic framework in  $\mathbb{R}^d$  is an *auxetic path*, when for any  $\tau_1 < \tau_2$ , the linear operator  $T_{\tau_2\tau_1}$  defined in (2.1.31) is a contraction.

**Example 2.1.33.** To illustrate auxeticity in a periodic structure, we consider a framework based on the honeycomb graph in  $\mathbb{R}^2$ . It can be obtained by the vertices and edges of a tiling by regular hexagons and selected configurations are illustrated in Figure 2.1.34.

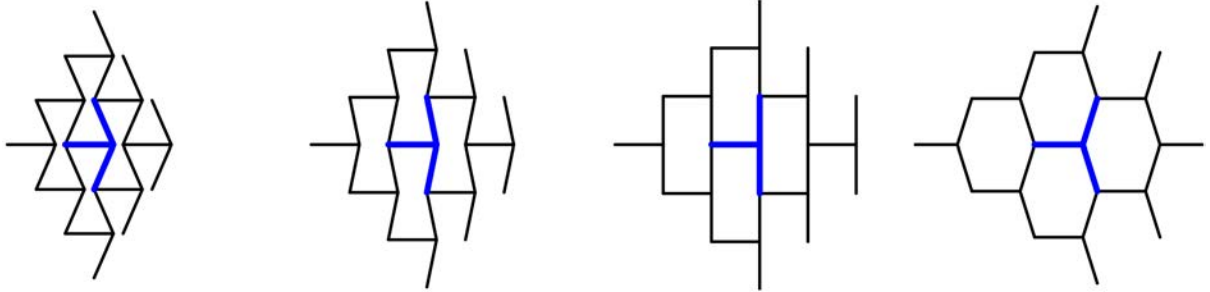


**Figure 2.1.34:** All pictures depict 9 primitive cells of the honeycomb framework, with the unit cell highlighted in blue. The discussed auxetic behavior becomes visible when applying a horizontal flex to the framework. At  $\tau = 0.6$  (l.), the inverted honeycomb is rather compressed and extends over  $\tau = 0.8$  (c.l.) up to its maximally extended configuration at  $\tau = 1.0$  (c.r.). After that threshold, the configuration's lateral extension decreases until  $\tau = 1.3$  (r.) and beyond. In the last picture, the hexagonal honeycomb structure can be observed.

This framework is known to exhibit auxetic behavior. Four vertices  $v_1, v_2, v_3, v_4$  and rigid bars  $(1, 2), (2, 3), (2, 4)$  define the underlying periodic graph. We choose the framework's initial placement as

$$v_1, v_2, v_3, v_4 \mapsto (0, 0), (1, 0), (1, 1), (1, -1).$$

The corresponding periodicity group is generated by  $v_3 - v_1$  and  $v_4 - v_1$ . To factor out Euclidean motions, we fix

$$p(v_1) = (p_{11}, p_{12}) = (0, 0) \text{ and } p(v_2) = (p_{21}, p_{22}) = (p_{21}, 0)$$

for the coordinates  $p_{ij}$  of  $p(v_i)$ . Denoting the edge length of the bar  $(i, j)$  by  $\ell_{ij}$ , the framework's initial placement lets us deduce that  $\ell_{ij} = 1$  for all rigid bars, so  $p_{21} = 1$ . This implies that the configuration space is a 2-dimensional algebraic set, consisting of all points  $(p_{31}, p_{32}, p_{41}, p_{42})$

in  $\mathbb{R}^4$  satisfying

$$\begin{aligned}(p_{31} - p_{21})^2 + (p_{32} - p_{22})^2 &= 1 \quad \text{and} \\ (p_{41} - p_{21})^2 + (p_{42} - p_{22})^2 &= 1.\end{aligned}\tag{2.1.35}$$

There are two degrees of freedom, so we can exploit the framework's symmetry to set  $p_{31} = p_{41}$ . Inserting this into Equation (2.1.35) leads to the equality  $p_{32}^2 = p_{42}^2$ . For the realization  $p$  to be embedded, we choose this equation's negative branch via  $p_{32} = -p_{42}$ . After assuming that the deformation path is parametrized in  $p_{31} = \tau$ , the remaining unknown  $p_{42}$  can be computed. Using the quadratic formula shows that

$$\varphi(\tau) = \left( \tau, \sqrt{2\tau - \tau^2}, \tau, -\sqrt{2\tau - \tau^2} \right) \quad \text{with } \tau \in (0.5, 1.5).$$

This path satisfies Definition 2.1.27 by construction. The periodicity lattice depends on  $\tau$  via

$$\pi_\tau(\Gamma) = (\varphi(\tau)_1, \varphi(\tau)_2) \cdot \mathbb{Z} + (\varphi(\tau)_3, \varphi(\tau)_4) \cdot \mathbb{Z}.$$

According to Equation (2.1.31), this induces a linear operator

$$T_{\tau_2 \tau_1} = \begin{pmatrix} \frac{\tau_1}{\tau_2} & 0 \\ 0 & \sqrt{\frac{2\tau_1 - \tau_1^2}{2\tau_2 - \tau_2^2}} \end{pmatrix}.$$

$T_{\tau_2 \tau_1}$  is well-defined on the interval  $(0.5, 1.5)$ , since for  $\tau_1, \tau_2 \in (0.5, 1.5)$  and  $i \in \{1, 2\}$  it holds that  $2\tau_i - \tau_i^2 > 0$ . Then,  $\|T_{\tau_2 \tau_1}\| < 1$  for  $\tau_1, \tau_2 \in (0.5, 1)$  and  $\|T_{\tau_2 \tau_1}\| > 1$  for  $\tau_1, \tau_2 \in (1, 1.5)$ . Consequently,  $\varphi(\tau)$  is an auxetic deformation path for  $\tau \in (0.5, 1]$  in accordance with Definition 2.1.32.

For an infinitesimal version of auxeticity, again consider an independent set of  $\pi_\tau(\Gamma)$ 's lattice generators  $\Lambda_\tau$ . As  $\pi_\tau(\Gamma)$ 's rank is  $d$  by assumption,  $\Lambda_\tau$  can be represented as a  $d \times d$  matrix, whose column vectors form a generating set of the lattice. The associated *Gram matrix* is described by  $\omega(\tau) = \Lambda_\tau^T \Lambda_\tau$ .

**Theorem 2.1.36** (cf. [43, Thm. 1]). *A deformation path  $(G, \Gamma, p_\tau, \pi_\tau)$  with  $\tau \in (-\varepsilon, \varepsilon)$  is auxetic if and only if the curve of Gram matrices  $\omega(\tau)$  has all its tangents in the cone of positive symmetric semidefinite  $d \times d$  matrices.*

To better understand this result, we want to apply it to a framework that has already been established: The inverted honeycomb. As shown in Example 2.1.33, it has an auxetic deformation path. However, the example does not offer any insights into the region of auxeticity's extent when symmetry is not assumed. While helping to parametrize a deformation path, this additional constraint reduced the configuration space's dimension. Theorem 2.1.36 offers insights into the extent of the entire deformation space, as laid out in the following example.

**Example 2.1.37.** Let us return to the auxetic honeycomb from Example 2.1.33 in a slightly more general setting. Let  $a, b > 0$  and define the corresponding deformation path as

$$\varphi(\tau) = \left( a\tau, \sqrt{2a\tau - a^2\tau^2}, b\tau, -\sqrt{2b\tau - b^2\tau^2} \right)$$

for  $\tau > 0$ . The lattice generators of the periodicity group  $\pi_\tau(\Gamma)$  can then be expressed as

$$\Lambda_\tau = \begin{pmatrix} a\tau & b\tau \\ \sqrt{2a\tau - a^2\tau^2} & -\sqrt{2b\tau - b^2\tau^2} \end{pmatrix},$$

so the corresponding Gram matrix and its derivative with respect to  $\tau$  can be expressed as follows:

$$\omega(\tau) = \begin{pmatrix} 2a\tau & ab\tau^2 - \tau\sqrt{ab}\sqrt{(2-a\tau)(2-b\tau)} \\ ab\tau^2 - \tau\sqrt{ab}\sqrt{(2-a\tau)(2-b\tau)} & 2b\tau \end{pmatrix} \quad \text{and}$$

$$\omega'(\tau) = \begin{pmatrix} 2a & 2ab\tau - \sqrt{ab}\frac{2ab\tau^2 - 3a\tau - 3b\tau + 4}{\sqrt{(2-a\tau)(2-b\tau)}} \\ 2ab\tau - \sqrt{ab}\frac{2ab\tau^2 - 3a\tau - 3b\tau + 4}{\sqrt{(2-a\tau)(2-b\tau)}} & 2b \end{pmatrix}.$$

This symmetric matrix is positive semi-definite, if for any  $x \in \mathbb{R}^2$

$$0 \leq \langle x, w'(\tau) \cdot x \rangle = 2ax_1^2 + 2bx_2^2 + 2x_1x_2 \left( 2ab\tau - \sqrt{ab}\frac{2ab\tau^2 - 3a\tau - 3b\tau + 4}{\sqrt{(2-a\tau)(2-b\tau)}} \right). \quad (2.1.38)$$

Since scaling  $x$  by positive constants does not change the inequality, we can assume without loss of generality that  $x_1 \in \{0, \pm 1\}$ . If  $x_1 = 0$ , Equation (2.1.38) reduces to  $2bx_2^2 \geq 0$ . As  $b > 0$ , this inequality is always true. Conversely, if  $x_1 = \pm 1$ , the above equation becomes

$$0 \leq 2a + 2bx_2^2 \pm 2x_2 \left( 2ab\tau - \sqrt{ab}\frac{2ab\tau^2 - 3a\tau - 3b\tau + 4}{\sqrt{(2-a\tau)(2-b\tau)}} \right).$$

The right-hand side of this expression is a parabola in the variable  $x_2$ . Since the coefficient of  $x_2^2$  is positive, the region where the parabola assumes negative values is between its zeros. Consequently, showing that the parabola's two roots are either confluent or have non-zero imaginary parts is equivalent to proving that  $w'(\tau)$  is positive semi-definite. With the help of the quadratic formula, the quadric from Equation (2.1.37) has no distinct real roots if and only if

$$\left( 2ab\tau - \sqrt{ab}\frac{2ab\tau^2 - 3a\tau - 3b\tau + 4}{\sqrt{(2-a\tau)(2-b\tau)}} \right)^2 \leq 4ab.$$

As the positive constants  $a$  and  $b$  both scale speed, we can without loss of generality assume that  $a = 1$  to make the constants dimensionless. This assumption enables us to plot the region, where the Gram matrix' derivative is positive semi-definite, as depicted in Figure 2.1.39.

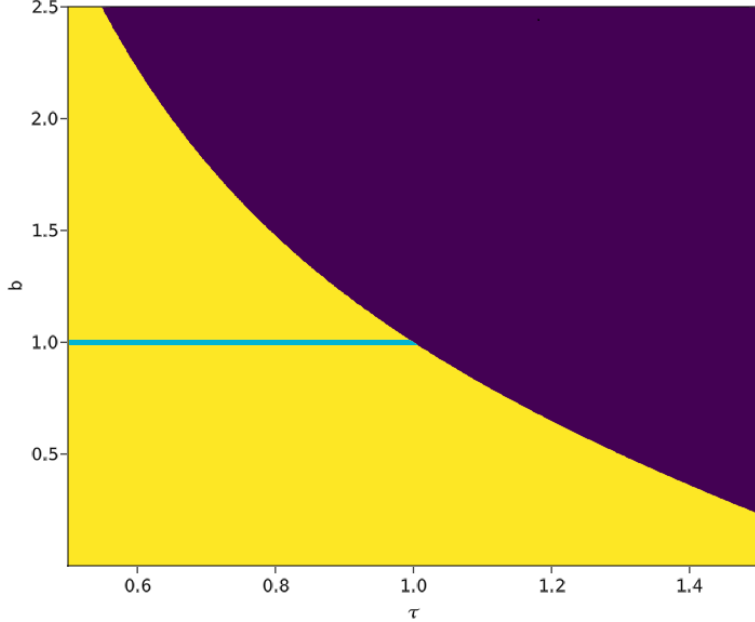


**Figure 2.1.39:** The auxetic region (yellow) and the non-auxetic region (purple) of the honeycomb framework are displayed for  $\tau \in (0.5, 1.5)$ ,  $b \in (0, 2.5)$  and  $a = 1$ . Notably, there is a large neighborhood of auxeticity around the auxetic deformation path that is investigated in Example 2.1.33 (blue).

### 2.1.3 Tensegrity Frameworks

Having explored the main concepts of bar-and-joint frameworks, we are now ready to add an energy component and introduce the concept of a tensegrity framework. This autological portmanteau<sup>1</sup> is derived from the term “tension under integrity” and was coined by the architect Richard Buckminster Fuller [59]. In addition to bars associated with distance constraints that are introduced in Section 2.1.2.2, these structures contain flexible elements under tension, allowing the shapes to be stable. Tensegrities are utilized in architecture and civil engineering [224, 306], robotics [63], art [298], molecular biology [103, 173, 320] and anatomy [200]. Apart from the implementations on earth, their resilience and lightweight design have made tensegrities attractive to aerospace engineers [8, 315, 344]. Due to their flexibility, there is no limit to the structures’ shape and size. Individual frameworks can be deformed significantly.

Given an undirected graph  $G = (V, E; \mathcal{B}, \mathcal{C})$  with labeled vertices  $V$  and edges  $E = \mathcal{B} \sqcup \mathcal{C} \subseteq \binom{V}{2}$  splitting into two disjoint sets. We call the edges  $ij \in \mathcal{B}$  *rigid bars* of length  $\ell_{ij}$  and the edges  $ij \in \mathcal{C}$  *elastic cables* with corresponding natural resting length  $r_{ij}$  and constant of elasticity  $c_{ij}$ . A *tensegrity framework* is such a graph  $G$  together with an embedding  $p : V \rightarrow \mathbb{R}^d$ , assigning a point in  $\mathbb{R}^d$  to each vertex of  $G$  [154, 266]. We call  $p$  a *realization* of  $G$  and denote the coordinates of the  $n$  nodes by  $p_1 = (p_{11}, \dots, p_{1d}), \dots, p_n$ . For every  $ij \in \mathcal{B}$ , we assign the bar constraint polynomial

$$b_{ij} := \sum_{k=1}^d (p_{ik} - p_{jk})^2 - \ell_{ij}^2$$

and denote by  $b$  the polynomial system consisting of the  $b_{ij}$  for  $ij \in \mathcal{B}$ . The cables can be

---

<sup>1</sup>Self-descriptive blend of words.

modeled as one-sided Hookean springs, giving rise to the cables' potential energy with

$$q_{ij} := \frac{c_{ij}}{2} (\max\{0, ||p_i - p_j|| - r_{ij}\})^2, \quad Q = \sum_{ij \in \mathcal{C}} q_{ij}.$$

The variables  $p_{ik}$ ,  $\ell_{ij}$ ,  $r_{ij}$ ,  $c_{ij}$  either lie in the set of externally determined *control parameters*  $Y = \mathbb{R}^{m_1}$ , or in the *internal variables*  $X = \mathbb{R}^{m_2}$ . Some of  $Y$ 's elements are fixed, while others vary in some subset  $\Omega \subset Y$ . We call a configuration  $(x, y) \in X \times Y$  *stable* or an *equilibrium*, if  $x$  is a strict local minimum of the energy function  $Q$  with respect to the algebraic set  $\mathcal{V}(b)$ . Thus, for fixed  $y \in Y$  the search for equilibrium configurations in this tensegrity framework can be modeled as a constraint optimization problem

$$\begin{aligned} & \min_{x \in X} Q(x, y) \\ \text{s.t. } & b_{ij}(x, y) = 0 \quad \forall ij \in \mathcal{B}. \end{aligned} \tag{2.1.40}$$

Naturally, concepts like periodicity and auxeticity that were previously discussed in Section 2.1.2.2 can be transferred to this setting: Periodicity can be extended by considering the two subgraphs  $(V, \mathcal{B})$  and  $(V, \mathcal{C})$  with identical periodicity group  $\Gamma$  (Def. 2.1.20). We expect a deformation path, parametrized by the varying control parameters  $\Omega \subset Y$ , to be in equilibrium at each step (Def. 2.1.27). Similarly, an auxetic deformation path is described by the contraction  $T_{\tau_2 \tau_1}$  (Def. 2.1.32).

**Example 2.1.41.** Let us now consider an example of a tensegrity framework, namely the T3-prism. It has stable configurations [241], finds application as a kids' toy in the real world, and can easily be built using ice cream sticks and rubber bands, as depicted in Figure 2.1.42(r.).

Each of the frameworks' six vertices  $p_i$  have four adjacent edges that divide into 3 elastic cables and 1 rigid bar. We label the vertices such that the first three and the last three vertices respectively form a cable-triangle. Hence, the set of rigid bars connecting both triangles is given by  $\mathcal{B} = \{(1, 5), (2, 6), (3, 4)\}$ . Analogously, the set of elastic cables is

$$\mathcal{C} = \{(1, 2), (2, 3), (1, 3), (4, 5), (5, 6), (4, 6), (1, 4), (2, 5), (3, 6)\}.$$

To be able to meaningfully talk about energy minima, Euclidean motions need to be factored out. Assuming the first vertex lies at the origin, the second vertex lies on the  $x$ -axis, and the third vertex is found in the plane  $z = 0$ . Clearly, the choice of bar and resting length determines the final configuration. A bar length  $\ell = 2$  and cables' resting length of  $r = 0.5$  led to reasonable results in our experiments. Using Lagrange multipliers [234, p.320f.] and Newton's method [60, p.638f.], we numerically solve the constraint optimization problem (2.1.40). The initialization is given by two equilateral triangles lying right above each other in parallel planes, with the rigid bars orthogonal to both planes. Depicting the resulting configuration in Figure 2.1.42(l.), we realize that it can be obtained by a rotation of the upper triangle by  $\frac{5}{6} \cdot \pi$  [61, p.45] and a translation of either of the parallel planes.

While this simple optimization pipeline of using Lagrange multipliers in combination with Newton's method works well in this instance, more complicated structures may warrant a more

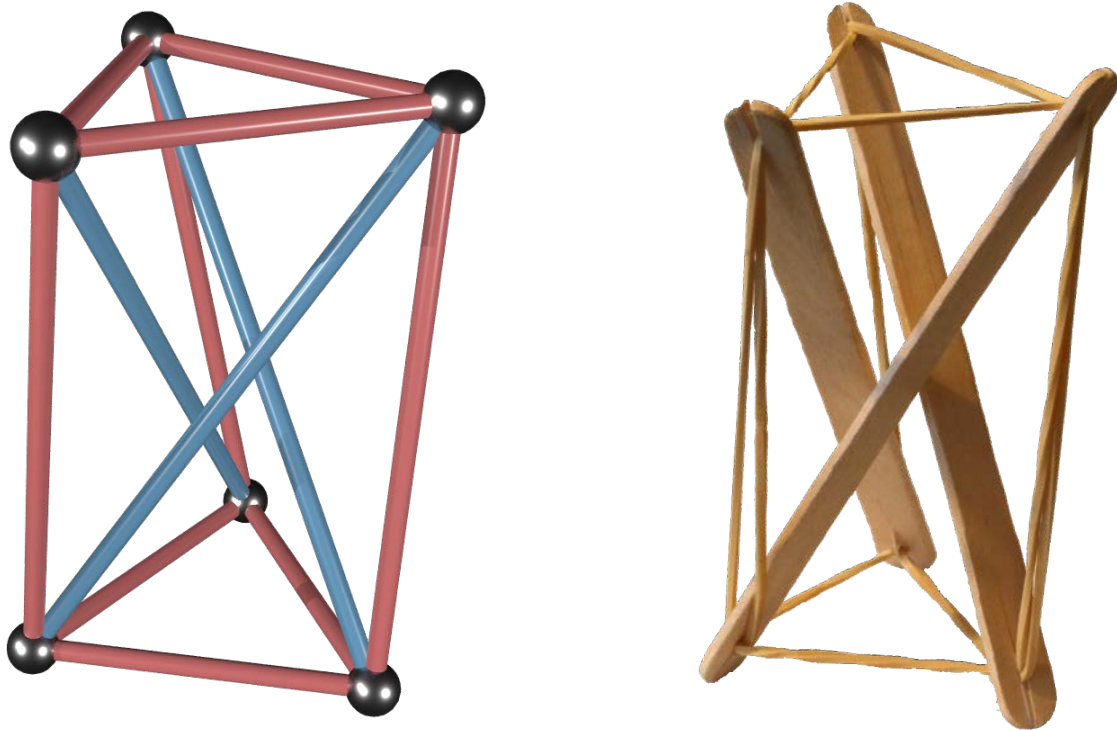


**Figure 2.1.42:** Here, the T3-prism is depicted in two different forms. It can be obtained through optimization with numerical means (l.) and built from ice cream sticks and rubber bands (r.). On the left, red edges symbolize flexible cables and blue edges represent rigid bars.

robust analysis. The tensegrity model for rod packings that will be introduced in Chapter 5 and the tensegrity model for weavings on surfaces from Chapter 6 generates geometric structures that exceed the capabilities of this algorithm. Therefore, in Chapter 3 an iterative predictor-corrector algorithm for solving constraint optimization problems is developed.

### 2.1.3.1 Multistability

Tensegrity frameworks need not only have one stable configuration. Bistability or multi-stability is a desirable property from a materials scientific point of view, as the framework can transition between multiple modes without applying much force. By exploiting this property, a tensegrity can serve multiple purposes that are interchangeable with simple motions [131, 152, 220].

In this section, we follow Heaton and Timme [154] by introducing a way to understand the point where the structure experiences a catastrophic change – i.e. where it “snaps” – in algebro-geometric terms. This set of points is called the catastrophe discriminant, and its importance has long since been known [141, 336], with applications only hindered by its difficulty to compute. However, in recent years the development of efficient tools in numerical nonlinear algebra [31, 54] has made it possible to compute the tensegrities’ tipping points. For this reason, we reformulate

the nonlinear optimization problem (2.1.40) for fixed  $y \in Y$  in purely polynomial terms:

$$\begin{aligned} & \min_{x \in X} \sum_{ij \in \mathcal{C}} c_{ij} \cdot (\delta_{ij} - r_{ij})^2 = \min_{x \in X} \tilde{Q}(x, \delta; y) \\ \text{s.t. } & \sum_{k=1}^d (p_{ik} - p_{jk})^2 = \ell_{ij}^2 \quad \forall ij \in \mathcal{B} \quad \text{and} \\ & \sum_{k=1}^d (p_{ik} - p_{jk})^2 = \delta_{ij}^2 \quad \forall ij \in \mathcal{C}. \end{aligned} \tag{2.1.43}$$

Note that the introduction of the variables  $\delta_{ij}$  makes it possible to express the energy function  $Q$  without using square roots. Clearly, the set of solutions to (2.1.40) is contained in the set of solutions to (2.1.43). If furthermore  $\delta_{ij} \geq 0$ , then the two sets agree. Denote the system of polynomial constraints in (2.1.43) by  $G(x, \delta; y)$  and from now on write  $f_y(z)$  for all functions  $f$  dependent on the parameter  $y$  to represent  $f(z; y)$ . Assume that  $G(x, \delta; y)$  contains no singularities. Otherwise, the following discussion of minimality would not be meaningful [154], restricting the choice of  $y \in \Omega$ .

After introducing the new variables  $\lambda_{ij}$  for  $ij \in \mathcal{B} \sqcup \mathcal{C}$ , we can use the theory of Lagrange multipliers [234, p.320f.] to express the nonlinear optimization problem (2.1.43) as the unconstrained objective function

$$\mathcal{L}_y(x, \delta, \lambda) = \tilde{Q}_y(x, \delta) + \lambda^T \cdot G_y(x, \delta).$$

Critical points  $(x^*, \delta^*, \lambda^*)$  of  $\mathcal{L}_y$  correspond to critical points  $(x^*, \delta^*)$  of  $\tilde{Q}_y$  on  $\mathcal{V}(G_y)$ , which are points in  $\mathcal{V}(G_y)$  where the gradient  $\nabla_{x, \delta} \tilde{Q}_y(x^*, \delta^*)$  is orthogonal to the tangent space  $T_{x^*, \delta^*} \mathcal{V}(G_y)$  (cf. [234, Thm. 12.1]). In unconstrained optimization, criticality is checked by setting the gradient to zero [234, Thm. 2.2], yielding

$$\nabla \mathcal{L}_y(x, \delta, \lambda) = \frac{\partial \mathcal{L}_y}{\partial (x, \delta, \lambda)}(x, \delta, \lambda) = 0$$

and thus simplifying the problem. After allowing the variables  $x, \delta, \lambda$  to take complex values, it can be guaranteed that for general  $y \in \Omega$  the set of solutions  $(\nabla \mathcal{L}_y)^{-1}(0)$  is finite. It contains  $\mathcal{N}$  (complex) points, provided that the cardinalities of  $\Omega$  and  $\bigsqcup_{y \in \Omega} (\nabla \mathcal{L}_y)^{-1}(0)$  agree, while for all  $y \in \Omega$  the number of solutions is at most  $\mathcal{N}$  [299, Thm. 7.1.1]. We are especially interested in parameters  $y \in \Omega$ , where the number of solutions  $|(\nabla \mathcal{L}_y)^{-1}(0)|$  is less than  $\mathcal{N}$ . In these points, the framework may jump from one configuration to another.

Finding these points can be done by employing algorithms for finding isolated solutions of polynomial systems. In Section 3.2.2 a more in-depth discussion of homotopy continuation is provided, though for now, it is sufficient to understand that there are guarantees that *all* isolated solutions of a polynomial system are found with this approach. With the initial terminology in place, we are ready to introduce several definitions appearing in Heaton and Timme [154, Def. 5 and 7].

**Definition 2.1.44.** Given a set of variable control parameters  $\Omega \subset Y$ , define the projection from the collection of the Lagrange multiplier system's solutions to the control parameters as

$$\pi : \bigsqcup_{y \in \Omega} (\nabla \mathcal{L}_y)^{-1}(0) \rightarrow \Omega, \quad z = (x, \delta, \lambda, y) \mapsto y.$$

The *catastrophe discriminant*  $\mathcal{D}_\Omega \subset \Omega$  can then be defined as the Zariski-closure (see Definition 2.1.4) of the map's critical values, i.e.

$$\mathcal{D}_\Omega = \overline{\left\{ \pi(z) \in \Omega : \exists v \in \ker d\pi_z \cap T_z \left( \bigsqcup_{y \in \Omega} (\nabla \mathcal{L}_y)^{-1}(0) \right), v \neq 0 \right\}}.$$

The *catastrophe set*  $\mathcal{CS}_\Omega$  then captures the real values of  $\mathcal{D}_\Omega$  in which the cables have non-negative length. In mathematical terms:

$$\mathcal{CS}_\Omega = \{y \in \mathcal{D}_\Omega \cap \Omega_{\mathbb{R}} : \exists (x, \delta, \lambda, y) \in \pi^{-1}(y) \text{ with } \delta_{ij} \geq 0 \ \forall ij \in \mathcal{C}\}$$

with  $\Omega_{\mathbb{R}}$  denoting the real variable control parameters. For a path in the set of control parameters  $y(t) \in \Omega$ , the hypersurface  $\mathcal{CS}_\Omega$  enables us to locate changes in the number of solutions to the nonlinear optimization problem (2.1.40) [154]. Due to the introduction of inequality constraints,  $\mathcal{CS}_\Omega$  is a semi-algebraic set [154, Prop. 2].

Nevertheless, in Section 2.1.2.2 the stability of a tensegrity framework is defined by strict local minimality. Up until now, we have only considered critical points. In the literature on optimization, a sufficient criterion on strict minimality is given by a positive-definite Hessian [234, Thm. 12.6]. Since tensegrity frameworks are objects in the real world, we are only interested in real solutions; we can therefore assume that  $x \in \mathbb{R}^{|X|}$ . In Heaton and Timme [154, Def. 8] the second-order criterion is formalized for our polynomial setting:

**Definition 2.1.45.** Fix  $y \in \Omega$  and denote by  $g_{\{i,j\}}$  the polynomial in  $G_y$  corresponding to the edge  $\{i,j\} \in \mathcal{B} \sqcup \mathcal{C}$ . We write  $d\tilde{Q}_y$  and  $d^2g_{\{i,j\}}$  for the Hessian matrix of  $\tilde{Q}$  and  $g_{\{i,j\}}$ , respectively. For instance,

$$d\tilde{Q}_y := \frac{\partial \tilde{Q}_y}{\partial (x, \delta)} \quad \text{and} \quad d^2\tilde{Q}_y := \frac{\partial^2 \tilde{Q}_y}{\partial (x, \delta)^2}.$$

For real variables  $(x, \delta)$ , let

$$H_y(x, \delta, \lambda) = d^2\mathcal{L}_y(x, \delta, \lambda) = d^2\tilde{Q}_y(x, \delta) + \sum_{\{i,j\} \in \mathcal{B} \sqcup \mathcal{C}} \lambda_{\{i,j\}} \cdot d^2g_{\{i,j\}}(x, \delta).$$

We say that  $(x, \delta, \lambda, y)$  is *nondegenerate*, if the *projected Hessian*

$$W_y(x, \delta, \lambda) = V(x, \delta)^T \cdot H_y(x, \delta, \lambda) \cdot V(x, \delta)$$

is positive definite. In this case, the columns of  $V(x, \delta)$  are given by an orthonormal basis of the matrix  $(dg_{\{i,j\}}(x, \delta))_{\{i,j\} \in E}$ .

**Remark 2.1.46.** The projected Hessian's positive definiteness is sufficient for the strict minimality of  $(x, \delta)$  in the polynomial optimization problem (2.1.43) [128, p.81]. If a real point  $z \in \bigsqcup_{y \in \Omega} (\nabla \mathcal{L}_y)^{-1}(0)$  has a singular projected Hessian  $W(z)$  and non-negative cable lengths, then  $z \in \mathcal{CS}_\Omega$  [154, Lem. 4]. In contrast, if a real path  $z(t) \in \bigsqcup_{y \in \Omega} (\nabla \mathcal{L}_y)^{-1}(0)$  parametrized by  $[0, 1]$  with non-negative cable lengths does not cross the catastrophe set  $\mathcal{CS}_\Omega$  and has a nondegenerate initial point  $z(0)$ , then the entire path is nondegenerate [154, Thm. 1]. Finally, if we assume that the cables are in tension throughout a smooth path of parameters  $y(t) \in \Omega_{\mathbb{R}} \setminus \mathcal{CS}_\Omega$  parametrized by  $t \in [0, 1]$  – i.e.  $\delta_{ij}(t) > r_{ij} > 0$  for all  $ij \in \mathcal{C}$  – then  $y(t)$  can uniquely be lifted to a smooth path  $z(t) = (x(t), \delta(t), \lambda(t), y(t)) \in \bigsqcup_{y \in \Omega} (\nabla \mathcal{L}_y)^{-1}(0)$  of strict local minima  $(x(t), y(t))$  of the nonlinear optimization problem (2.1.40) such that  $\pi(z(t)) = y(t)$  [154, Thm. 2].

The remark's last part is especially interesting for understanding the behavior of tensegrity frameworks, as it allows us to safely deform the structure without changing modes. To numerically compute the deformation paths, we use path-tracking and homotopy continuation, which will formally be introduced in Section 3.2.2. To better understand these theoretical concepts, we want to consider an example. Zeeman's catastrophe machine [254] is one of the simplest tensegrities, where one can observe discontinuous or catastrophic behavior [336]. A similar example appears in Heaton and Timme [154] and the code that was used to compute the deformation paths is inspired by Sascha Timme's Julia package `Catastrophe.jl`<sup>2</sup>.

**Example 2.1.47.** Let us consider Zeeman's catastrophe machine. This tensegrity framework has four vertices  $p_1, \dots, p_4 \in \mathbb{R}^2$ , two of which are fixed ( $p_1$  and  $p_2$ ),  $p_3$  is a variable control parameter and  $p_4$  is an internal variable. The framework has one rigid bar  $(2, 4)$  with length 0.5 and two elastic cables  $(1, 4)$  and  $(3, 4)$  with resting length 0.25 and constant of elasticity 1.

Its catastrophe set  $\mathcal{CS}_\Omega$  is depicted in Figure 2.1.48 and is symbolically computed in Heaton and Timme [154]. On its interior, there are two stable configurations related by mirror symmetry, while outside of it, there is only one stable configuration. As illustrated in Remark 2.1.46, prescribing a deformation path of  $p_4$  parametrized by a curve of the control parameter  $p_3$  such that  $\Omega = \{p_3(t) : t \in [0, 1]\}$  never meets the catastrophe set guarantees that no sudden changes occur. In particular, a loop satisfying this property will end up at the same position where it started. An example of this behavior is depicted in Figure 2.1.48(l.).

In contrast, it may be more interesting to consider loops that do cross  $\mathcal{CS}_\Omega$ . If it crosses the discriminant on opposite sides of the natural mirror axis the framework indeed exhibits discontinuous behavior: It flips from one mirror configuration to another when crossing the catastrophe set. When deforming the framework in a loop that starts inside of  $\mathcal{CS}_\Omega$ , it can end up in a different configuration than where it started. This is illustrated in Figure 2.1.48(r.): The loop starts in  $p_3(0) = (0.1, -0.23)$ , goes clockwise to reach  $p_3(\frac{3}{10}) = (0.4, -0.3678)$  and  $p_3(\frac{7}{10}) = (0.4, -0.0922)$ . At that point, the loop has crossed the framework's mirror axis and the orientation has changed. The tensegrity framework stays on the deformation path closest to its current mode, when it enters the neighborhood where two stable configurations exist. This results in a different configuration at  $t = 1$  than at  $t = 0$ , even though  $p_3(0) = p_3(1)$ .

---

<sup>2</sup><https://github.com/saschatimme/Catastrophe.jl>

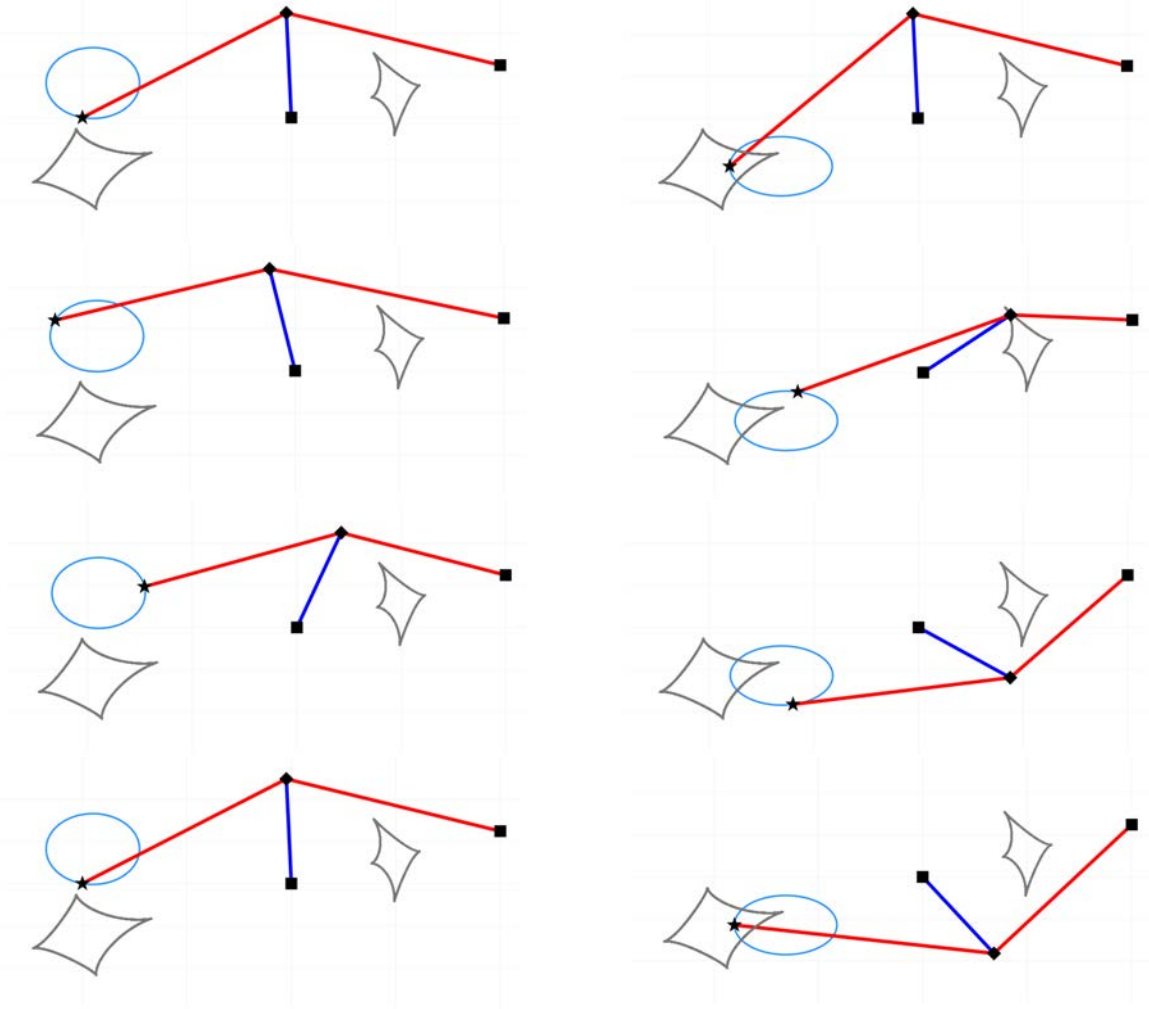


**Figure 2.1.48:** The deformative behavior of Zeeman’s catastrophe machine when the loop of control parameters (light blue) does not intersect the catastrophe set (l.) and when it intersects  $\mathcal{CS}_\Omega$  (r.). Elastic cables (red) and rigid bars (blue) connect the four vertices that are either fixed ( $p_1$  and  $p_2$ , square), an internal variable ( $p_4$ , diamond), or a control parameter ( $p_3$ , star). Inside the compact set that the catastrophe set  $\mathcal{CS}_\Omega$  (gray) bounds, the tensegrity framework has two stable configurations, while outside of that region, the nonlinear optimization problem (2.1.40) only has one solution. This becomes clear when comparing the first and last picture of the left and right series, where the control parameter (star) attains an identical position.

## 2.2 Asymptotic Global Rigidity of Geometric Random Graphs<sup>3</sup>

Having cultivated intuition and equipped ourselves with an array of tools to investigate planar frameworks in the literature review Section 2.1, we are now prepared to answer related questions. As such, the following two sections contain novel contributions to the field of rigidity theory. One might inquire: What if the points of a framework are not strategically placed, but rather selected at random? Such frameworks indeed have applications: Assume there are  $n \in \mathbb{N}$  transmitting devices randomly distributed in a bounded region of  $\mathbb{R}^2$ , each with a broadcasting range  $r > 0$ . Whenever two devices have a distance of at most  $r$ , they can communicate their mutual distance. Can the remaining positions be determined by only knowing the communicated distances, if the

<sup>3</sup>This section is based on joint and ongoing work with Sean Dewar and Katie Clinch.

position of two of these devices is known?

The low-rank matrix completion problem that is described above is related to the underlying framework's rigidity [295] and it can be modeled using geometric random graphs. To make the setup more precise, for  $n \in \mathbb{N}$  denote the square  $[-\sqrt{n}/2, \sqrt{n}/2]^2$  with Lebesgue measure  $n$  in  $\mathbb{R}^2$  by  $\square_n$ . The square's side lengths depend on the number of points  $n$  to normalize the necessary radii. A Poisson point process of density 1 in  $\square_n$  is a random subset  $P_n \subset \square_n$  with the following properties:

1. The number of points in  $P_n$  is Poisson distributed with mean  $n$  and
2. if  $X$  and  $Y$  are disjoint measurable subsets, then the cardinality of  $P_n \cap X$  is independent of the cardinality of  $P_n \cap Y$ .

Assume now that we are given a radius  $r > 0$  and a sample  $P_n = \{x_v : v \in V\} \subset \square_n$  for some finite set  $V$  obtained by such a Poisson point process. Then, the corresponding geometric random graph  $G(P_n, r) = (V, E)$  is constructed by adding an edge between  $v, w \in V$  if and only if  $\|x_v - x_w\| \leq r$ . An example of this construction is depicted in Figure 2.2.1. The [Gilbert framework](#)  $\mathcal{G}_r(n) = (G(P_n, r), p)$  generated by  $(n, r)$  is a framework on the geometric random graph  $G(P_n, r)$ . Its realization  $p : V \rightarrow P_n$  is given by  $p(v) = x_v$  for each  $v \in V$ .

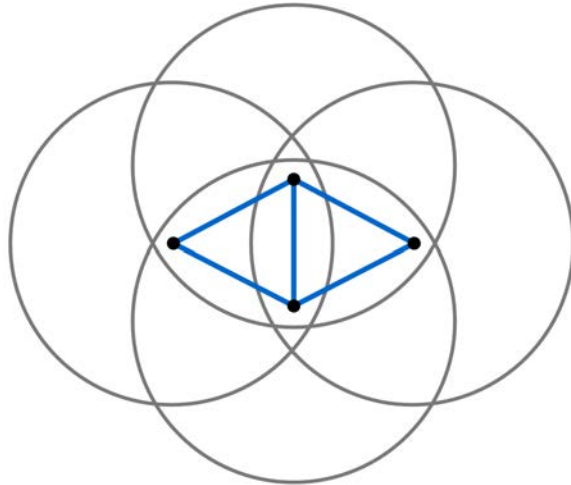


**Figure 2.2.1:** Construction of a rigid geometric random graph on 4 points in  $\mathbb{R}^2$  with a fixed radius.

Contrary to previous chapters, the frameworks that we are now considering are not in special position anymore. Their coordinates are chosen through a random point process, giving rise to the notion of generic configurations. As a gateway to exploring the rigidity of graphs, we will consider a single framework as a representative. The rationale behind this choice will become evident later. Starting off, the preliminary Definitions 2.2.2 – 2.2.3 appear in Jordán and Whiteley [185].

**Definition 2.2.2.** A configuration  $p : V \rightarrow \mathbb{R}^d$  of a graph  $G = (V, E)$  is called [generic](#), if the set of the  $d \cdot |V|$  coordinates of the points is algebraically independent over the rationals  $\mathbb{Q}$ .

**Definition 2.2.3.** A graph  $G = (V, E)$  is called [rigid in  \$\mathbb{R}^d\$](#) , if a generic configuration  $p : V \rightarrow \mathbb{R}^d$  produces a rigid framework in  $d$ -space.

Studying the rigidity of graphs provides deep insights into the infinitesimal rigidity of generic realizations and vice versa. For example, Gluck's theorem shows that almost all realizations of a graph with a single infinitesimally rigid configuration are infinitesimally rigid. Hence, a framework's infinitesimal rigidity is a generic property.

**Theorem 2.2.4** (cf. [158, Thm. 2.1] or [129]). *If a graph  $G$  has a single infinitesimally rigid realization, then all its generic realizations are infinitesimally rigid.*

Another interesting question is how many realizations there are for a given set of edge lengths. Uniquely realizable frameworks in  $\mathbb{R}^d$  are called globally rigid in  $\mathbb{R}^d$ . Drawing upon Definitions 2.2.5–2.2.7 appearing in Jordán and Whiteley [185], the necessary theory for this concept is established.

**Definition 2.2.5.** A graph  $G = (V, E)$  is called *k-connected*, if removing any  $k - 1$  vertices and all incident edges generates a connected graph.

**Definition 2.2.6.** We call a graph  $G = (V, E)$  *redundantly rigid* in  $\mathbb{R}^d$ , if  $G_e = (V, E \setminus \{e\})$  is rigid in  $\mathbb{R}^d$  for all  $e \in E$ .

**Definition 2.2.7.** A framework  $(G, p)$  in  $d$ -space is called *globally rigid*, if every  $d$ -dimensional realization  $(G, q)$  with the same edge lengths as in  $(G, p)$  is congruent to  $(G, p)$ . Moreover, a graph  $G = (V, E)$  is called *globally rigid in  $\mathbb{R}^d$* , if a generic configuration  $p : V \rightarrow \mathbb{R}^d$  produces a globally rigid framework  $(G, p)$ .

In theory, computing a given framework's number of real realizations entails solving a large polynomial system. However, for generic configurations, there is a combinatorial sufficient criterion in terms of Definitions 2.2.5–2.2.6 and the *complete graph*, in which there is an edge between any two vertices.

**Theorem 2.2.8** (cf. [176, Thm. 7.1]). *A graph  $G$  is globally rigid in  $\mathbb{R}^2$  if and only if it is either a complete graph on at most 3 vertices or if it is 3-connected and redundantly rigid in  $\mathbb{R}^2$ .*

Returning to geometric random graphs, an existing result addresses the graph's connectivity. The following theorem establishes an asymptotic threshold on the radius  $r$  that decides whether the corresponding geometric random graph is  $k$ -connected.

**Theorem 2.2.9** (cf. [309, Thm. 7]). *Let  $(r_n)_{n \in \mathbb{N}}$  be a sequence of positive real numbers and let  $P_n$  be drawn from a Poisson point process on  $\square_n = [-\sqrt{n}/2, \sqrt{n}/2]^2$  with density 1. For every integer  $k \geq 2$  and every sequence  $(\omega_n)_{n \in \mathbb{N}}$  where  $\omega_n \rightarrow \infty$  as  $n \rightarrow \infty$ , the following holds:*

1. *If  $\pi r_n^2 > \log n + (2k - 3) \log \log n + \omega_n$  then  $G(P_n, r_n)$  is asymptotically almost surely (a.a.s.)  $k$ -connected.*
2. *If  $\pi r_n^2 < \log n + (2k - 3) \log \log n - \omega_n$  then  $G(P_n, r_n)$  is a.a.s. not  $k$ -connected.*

In combination with Theorem 2.2.8, this result is relevant, as it can help us determine a geometric random graph's global rigidity using  $k = 3$ . For infinitesimal rigidity in  $\mathbb{R}^2$ , the graph must be at least 2-connected. If the graph is only 1-connected, then the two components

resulting from deleting a critical vertex  $v$  can freely rotate around the vertex. By fixing one component and  $v$ , we can demonstrate that this motion is not trivial and thus the framework is not infinitesimally rigid. These two observations let us formulate the following conjecture: Since the Asimow-Roth Theorem [24] states that in generic frameworks local rigidity and infinitesimal rigidity are equivalent, we will from now on conflate both concepts by using the term rigidity.

**Conjecture 2.2.10.** Let  $(r_n)_{n \in \mathbb{N}}$  be a sequence of positive real numbers and let  $P_n$  be drawn from a Poisson point process on  $\square_n$  with density 1. For  $n \in \mathbb{N}$ , fix the Gilbert framework  $\mathcal{G}_r(n)$  with generators  $(n, r_n)$ . If  $(\omega_n)_{n \in \mathbb{N}}$  is a real sequence with  $\omega_n \rightarrow \infty$  as  $n \rightarrow \infty$ , then the following holds:

1. (a) If  $\pi r_n^2 > \log n + \log \log n + \omega_n$  then  $\mathcal{G}_r(n)$  is a.a.s. rigid.  
(b) If  $\pi r_n^2 < \log n + \log \log n - \omega_n$  then  $\mathcal{G}_r(n)$  is a.a.s. not rigid.
2. (a) If  $\pi r_n^2 > \log n + 3 \log \log n + \omega_n$  then  $\mathcal{G}_r(n)$  is a.a.s. globally rigid.  
(b) If  $\pi r_n^2 < \log n + 3 \log \log n - \omega_n$  then  $\mathcal{G}_r(n)$  is a.a.s. not globally rigid.

For testing this conjecture, it seems appropriate to employ a sampling approach. The general strategy is summarized in Algorithm 2.2.11.

---

**Algorithm 2.2.11:** Rigidity of Geometric Random Graphs

---

**Inputs :** A maximum  $N \in \mathbb{N}$  and the amount of point processes  $m$  for each iteration.  
**Output:** A distribution of the radii necessary for rigidity and global rigidity for Gilbert frameworks generated by Poisson point processes  $P_n$  in  $\square_n$  for  $n = 1, \dots, N$ .

```

radii_rigidity, radii_global_rigidity =
{ n : [] for n = 1, ..., N }, { n : [] for n = 1, ..., N }
for n = 1, ..., N do
    for k = 1, ..., m do
        P_n = sample(Poisson(n), □_n)
        push!(radii_rigidity[n], inf{r > 0 : is_rigid(Г_r(n))})
        push!(radii_global_rigidity[n], inf{r > 0 : is_globally_rigid(Г_r(n))})
    end
end

```

---

During the initialization, two dictionaries are set up to collect the minimal radii that produce rigid Gilbert frameworks for each  $n$ . By choosing the maximum number of iterations to be 30 and the number of samples per iteration  $N = 25000$ , the algorithm's runtime is restricted to a reasonable length, while still producing statistically meaningful results.

In each iteration, a Poisson point process  $P_n$  of density 1 on the square  $\square_n$  with side length  $\sqrt{n}$  is generated. It will act as the point set on which the Gilbert framework  $\mathcal{G}_r(n)$  is grown. In the first test rigidity is checked through the routine `is_rigid` by using the combinatorial criterion from Theorem 2.1.14 on the rigidity matrix' rank. For the framework's global rigidity, the characterization Theorem 2.2.8 is employed in the method `is_globally_rigid`, checking for the underlying graph's 3-connectivity and redundant rigidity.

While computing the rank is an operation with efficient implementations, checking if a graph is 3-connected in the worst case requires checking the connectivity of  $\binom{|V|}{3}$  subgraphs. In addition, the criterion for global rigidity requires computing the rigidity matrix' rank for  $|E|$ -many subgraphs to determine redundant rigidity. Potentially, this can correspond to  $\binom{|V|}{2}$  rank-computations. Consequently, verifying global rigidity is considerably more computationally expensive than testing for infinitesimal rigidity.

The results of Algorithm 2.2.11 are depicted in Figure 2.2.12 in the form of box plots. The graphic provides striking empirical evidence for Conjecture 2.2.10. For this data, Algorithm 2.2.11's runtime for  $N = 30$  already exceeds a week, limiting our ability to generate geometric random graphs with more vertices. Nonetheless, this data set lets us infer that the whiskers of the box plots for rigidity lower approach the curve  $\log n + \log \log n$ , while the whiskers corresponding to global rigidity approach  $\log n + 3 \log \log n$ .

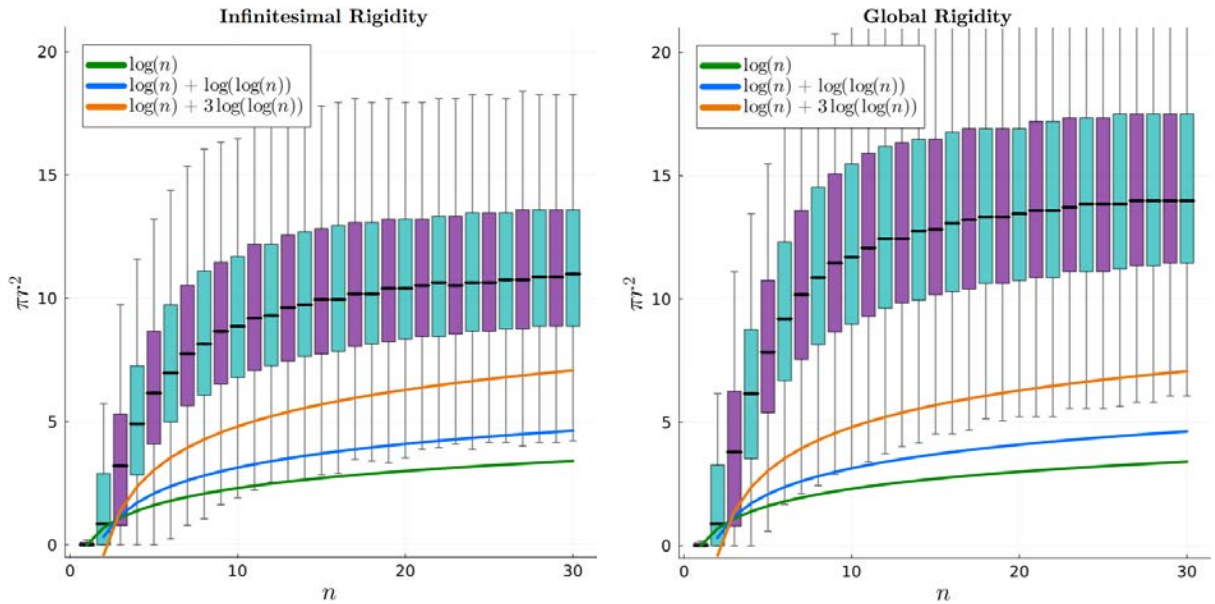


**Figure 2.2.12:** Sampling Gilbert frameworks in  $\square_n$  using Algorithm 2.2.11 produces results for the rigidity of geometric random graphs that are in line with the predictions from Conjecture 2.2.10. Asymptotically, the empirical data lets us deduce that for infinitesimal rigidity (l.) the blue curve is the relevant threshold. For global rigidity (r.) the orange curve is better-suited.

Further consideration of Figure 2.2.12 prompts the question: How close are the rigid Gilbert frameworks produced by Algorithm 2.2.11 to achieving global rigidity? For this purpose, we are interested in generating a maximal subgraph of  $G$  that satisfies a necessary condition for global rigidity. Any vertex  $v$  of degree two can be flipped across the imaginary line spanned by  $v$ 's two neighbors, which generally creates another realization. Therefore, a necessary condition for global rigidity is that each vertex has at least degree 3. In this context, a graph where each vertex has at least degree  $k$  is called *k-coordinated*.

Iteratively removing every vertex of degree at most two from  $G(P_n, r)$  creates the subgraph  $H_3$ . In other words,  $H_3$  is the maximal induced subgraph of the geometric random graph  $G$  in which each vertex has at least degree 3. This subgraph is unique: If there were two distinct vertex-maximal induced subgraphs  $H$  and  $H'$  of  $G$  in which each vertex has at least degree

three, their union  $H \cup H'$  would be strictly larger. In addition, each vertex in  $H \cup H'$  still has at least degree 3 which is a contradiction to the graphs' maximality.

How many vertices need to be removed from  $G(P_n, r)$  to create  $H_3$ , though? In Figure 2.2.13 the ratio of the number of vertices contained in  $H_3$  by the number of vertices in  $G(P_n, r)$  is depicted for  $n = 1, \dots, 30$  with  $N = 25000$  samples drawn for each  $n$ . In this case, the random point process is not generated using the Poisson distribution. We can therefore assume that  $\#P_n = n$ .

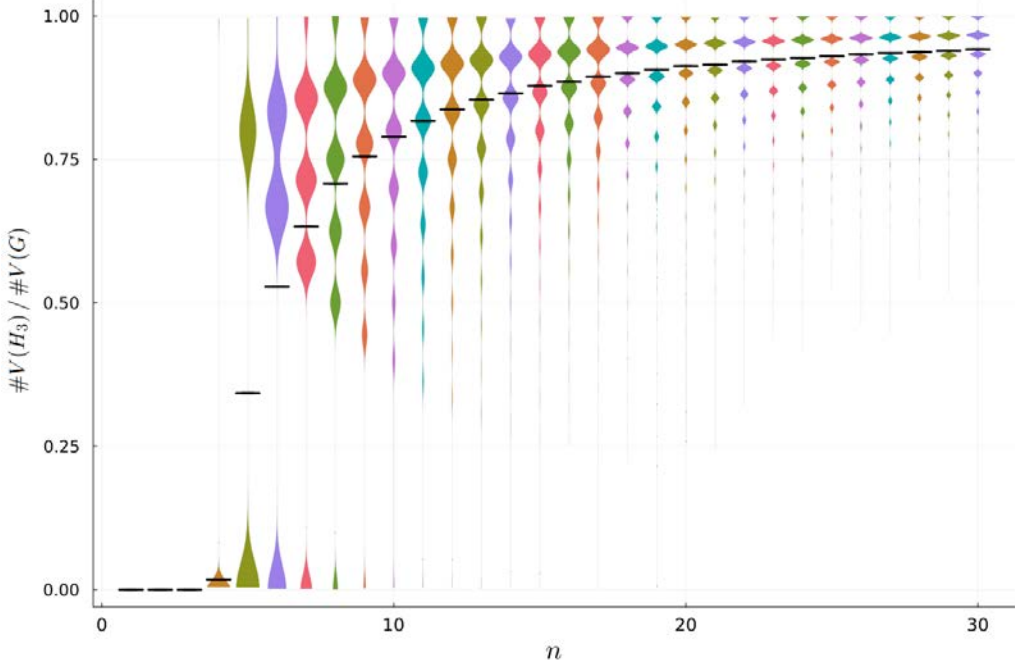


**Figure 2.2.13:** The ratio of the number of vertices in  $H_3$  to the number of vertices in  $G$  is represented as violin plots. Rather than sampling the number of vertices from a Poisson distribution, it is uniformly assigned for each  $n$ . This way, we observe an intricate bifurcation into accumulation points.

The graphic 2.2.13 reveals a mesmerizing pattern. Unsurprisingly, for  $n = 1, 2, 3$  the subgraph  $H_3$  contains no vertices. The complete graph  $K_3$  is a triangle and consequently only contains vertices of degree 2. Beginning from  $n = 4$ , we observe an intricate bifurcation pattern, where the number of accumulation points that the violin plots exhibit grows linearly in  $n$ . Presumably, this occurs because of recurring subgraph patterns and it seems to become more and more likely for vertices in  $G$  to have degree 3 to begin with. The black lines highlighting the ratios' mean, depict that their value monotonously increases and asymptotically approaches 1.

As previously noted, a minimal vertex degree of 3 is a necessary condition for global rigidity. However, it is not always sufficient, implying that we cannot assume every instance of  $H_3$  possesses a single realization. This observation prompts the question: What proportion of subgraphs  $H_3$  are globally rigid, and what factors typically obstruct this property? Revisiting the sufficient criterion outlined in Theorem 2.2.8, we find that redundant rigidity or the graph's 3-connectedness can present obstacles. In Figure 2.2.14(1.), the number of cases where either property prevents the global rigidity of  $H_3$  are graphed.

Most of the time  $H_3$ 's 3-connectedness, or lack thereof, is prohibitive. Expectably, this

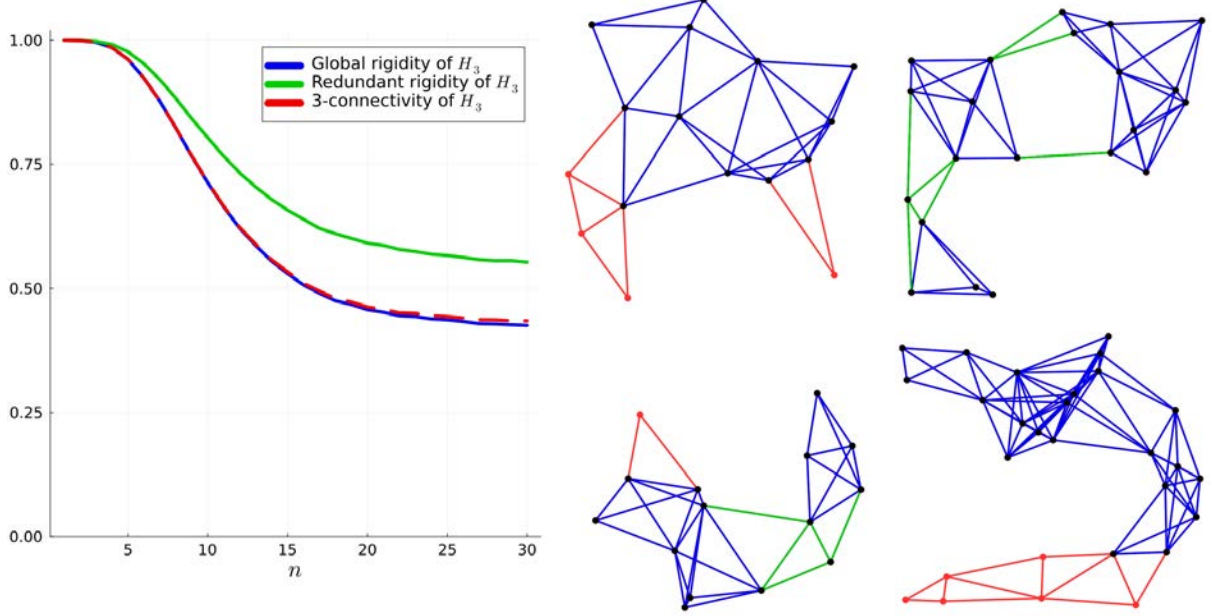


**Figure 2.2.14:** The ratio of globally rigid subgraphs  $H_3$  of  $G(P_n, r)$  with minimum vertex-degree 3 alongside the two sufficient criteria for global rigidity from Theorem 2.2.8 (l.). Here,  $r$  is chosen as the minimal radius such that  $G(P_n, r)$  is rigid. Alongside this graph, four select geometric random graphs are depicted for  $n = 25$  (r.) with  $H_3$  composed of blue and green edges. The redundant edges are displayed in green and the degree 2 vertices and its adjacent edges that are removed from  $G(P_n, r)$  to create  $H_3$  are colored in red.

corresponds to a separation of the vertices into distant clusters inside the framework. While  $H_3$  is not always redundantly rigid, the curves corresponding to global rigidity and 3-connectivity are almost identical. This limited empirical perspective lets us deduce that the ratio of globally rigid  $H_3$  seems to approach a horizontal asymptote situated at around 40%. Even when the graph's vertex degree is at least 3, asymptotically the majority of maximal induced subgraphs with minimal vertex degree 3 of a collection of geometric random graphs are not globally rigid.

Moreover, Figure 2.2.14(r.). depicts four geometric random graphs with  $H_3$  marked in green and blue. The red vertices and edges are removed from  $G(P_n, r)$  to create the maximal induced subgraph with minimal vertex degree 3. Due to limitations of the chosen visualization, the subsets of 2 vertices whose removal creates at least two connected components are left out of the pictures; still, in the chosen examples they are easy to spot and we can deduce that only the induced subgraph in the top left picture is globally rigid.

The two asymptotic observations from Figure 2.2.13 and 2.2.14 provide a compelling conclusion: While we remove a monotonically decreasing ratio of vertices from the geometric random graph to create  $H_3$ , the ratio of these subgraphs that are globally rigid rapidly drops below half. Still, this ratio is bounded below by a positive number around 0.4. Both of these claims combined lead to the anticipation that the size of the maximal globally rigid subgraph of  $G(P_n, r)$  probabilistically increases faster than the size of the graph itself.

### 2.3 Flexing the Regular Dodecahedron<sup>4</sup>

As another example for the applications of rigidity theory, let us consider the deformation space of the five platonic solids. These convex bodies describe regular polyhedra in  $\mathbb{R}^3$  that have been intriguing scientists for millennia and are depicted in Figure 2.3.1.

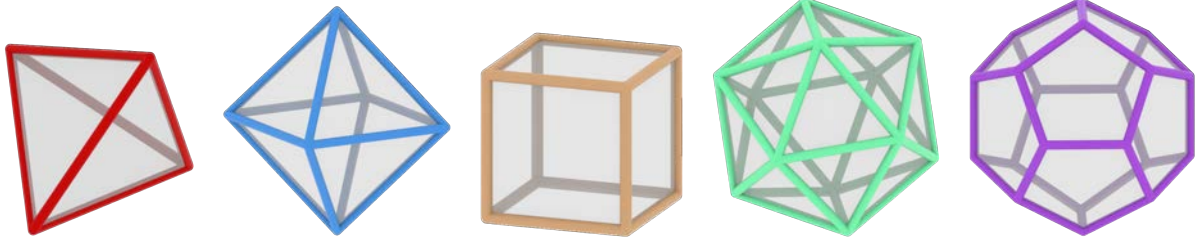


**Figure 2.3.1:** Plato associated the regular solids with the classical elements: The tetrahedron (l.) with fire, the octahedron (l.c.) with water, the cube (c.) with earth and the icosahedron (c.r.) with air. In particular, the dodecahedron fascinated Plato which he expressed by vaguely stating that “...god used it for designing the universe” [269, p.47].

Historically, they have been used as models in astronomy, as fair dice, in mysticism and occultism. Over 2000 years ago, Theaetetus of Athens mathematically described the five platonic solids. He was the first to prove that there are no more of these regular convex bodies than the tetrahedron, cube, octahedron, icosahedron and dodecahedron [16, p.206]. It has been known for over 200 years that the tetrahedron, octahedron and icosahedron are rigid when fixing their edge lengths [14, p.421]. Conversely, the dodecahedron is the only platonic solid whose rigidity with coplanarity and edge length constraints has not yet been determined.

In an ongoing project with Bernd Schulze, Martin Winter and Albert Zhang, we have resolved this question by proving Theorem 2.3.9. Merely, the computation of deformation paths remains an interesting problem and is investigated in Example 2.3.10. Before tackling these tasks, it is essential to introduce several theoretical concepts: First of all, the following definition appearing in Rastanawi, Sinn and Ziegler [257] algebraically describes the realization space of combinatorial polytopes.

**Definition 2.3.2.** A set  $P \subset \mathbb{R}^n$  is a *d-polytope* if it can be written as the convex combination of finitely many points, at least  $(d+1)$  of which are affinely independent. The *centered realization space*  $\mathcal{R}_0(P)$  of a labeled  $d$ -polytope with vertices  $v_1, \dots, v_n$  and facets  $F_1, \dots, F_m$  is

$$\mathcal{R}_0(P) = \left\{ (p_1, \dots, p_n, \mathbf{n}_1, \dots, \mathbf{n}_m) : p_i^T \cdot \mathbf{n}_j \begin{cases} = 1 & \text{if } v_i \in F_j \\ < 1 & \text{if } v_i \notin F_j \end{cases} \right\} \subset \mathbb{R}^{d \times (n+m)}.$$

Given any convex realization  $Q \in \mathcal{R}_0(P)$ , the only active constraints in a neighborhood of  $Q$  are that its facets must remain flat. In other words, all vertices belonging to a facet lie in the same hyperplane. The semialgebraic inequality cuts out an open set in the Euclidean subspace topology from the algebraic variety defined by these facet-constraints. This set gains additional structure by the Legendre–Steinitz theorem about the realization space of convex polytopes.

---

<sup>4</sup>This section contains results from ongoing work with Bernd Schulze, Martin Winter, and Albert Zhang.

**Theorem 2.3.3** (cf. [46, Lem. 2.8]). *Let  $P$  be a 3-polytope. Then  $P$ 's realization space  $\mathcal{R}_0(P)$  is a smooth manifold of dimension  $|E| + 6$ .*

Theorem 2.3.3 implies that there is no hope for the rigidity of convex polytopes whose constraint set is constructed in Definition 2.3.2. Instead, we focus on a subset of  $\mathcal{R}_0(P)$  by fixing the edge lengths and intersecting the realization space with the corresponding Cayley-Menger variety. From now on, all polytopes will come with coplanarity and edge length constraints.

Most concepts from Section 2.1.2 automatically transfer to this setting: Infinitesimal rigidity, prestress stability and second-order rigidity have been defined in terms of the constraint set's Jacobian (cf. Definition 2.1.13), which, in turn, is defined for general algebraic sets. The only aspect requiring attention is the demonstration that all of these forms of rigidity imply local rigidity (cf. Theorem 2.1.17). Nevertheless, the proof is analogous to the proof for bar-and-joint frameworks (cf. [83, Thm. 4.3.1]) and is thus omitted here.

As a first result in the direction of polyhedral rigidity, we state the classical Cauchy-Dehn theorem on the infinitesimal rigidity of polytopes in terms of their facets.

**Theorem 2.3.4** (Cauchy-Dehn [14, p.421]). *A closed convex polyhedron with infinitesimally rigid faces is infinitesimally rigid.*

As a direct consequence, Theorem 2.3.4 proves Dehn's classical theorem about triangulated topological spheres, since nondegenerate triangles are infinitesimally rigid in any dimension (cf. Theorem 2.1.14).

**Corollary 2.3.5.** *Any simplicial, strictly convex 3-polytope in  $\mathbb{R}^3$  is infinitesimally rigid.*

If  $P$  is a simplicial polytope, it is unnecessary to require the facet-constraint from the realization space's definition, making  $\mathcal{R}_0(P)$  an open subset of  $\mathbb{R}^{d \times (n+m)}$ . In particular, Corollary 2.3.5 proves that out of the five platonic solids the tetrahedron, octahedron and icosahedron are infinitesimally rigid. This insight fuels the hope that all platonic solids are rigid. Unfortunately, this is not the case; the cube is flexible.

**Example 2.3.6.** Consider the cube given by the convex combination of the vertices  $V = \{0, 1\}^3$ . Its associated edge lengths are 1 and its facet-normals are given by  $\pm e_i$  for the standard normal basis  $e_1, e_2, e_3$  of  $\mathbb{R}^3$ . By Theorem 2.3.3, its realization space is 18-dimensional. There are 12 constraints on the edges' lengths and 6 constraints on the facets. A naive constraint count could lead us to believe that the cube is rigid. However, it is in special position, necessitating a sense of caution.

As the unit cube's space of nontrivial infinitesimal motions is 3-dimensional. To parametrize a continuous curve passing through this configuration, it is helpful to first factor out the rigid motions of  $\mathbb{R}^3$ . Fixing the first vertex to the origin, the second to the  $x$ -axis, and the third on the  $xy$ -plane leads to constraining the bottom facet entirely to the  $xy$ -plane. We can thus treat it as a planar square and parametrize part of its deformation space:

$$p_1 = (0, 0, 0), \quad p_2 = (1, 0, 0), \quad p_3(t) = (t, \sqrt{2t - t^2}, 0) \quad \text{and} \quad p_4(t) = (t - 1, \sqrt{2t - t^2}, 0)$$

for  $t \in [0, 2]$ . This motion corresponds to a shearing of square and is depicted in Figure 2.3.7 with the initial configuration given by  $p_3(1) = (1, 1, 0)$  and  $p_4(1) = (0, 1, 0)$ .

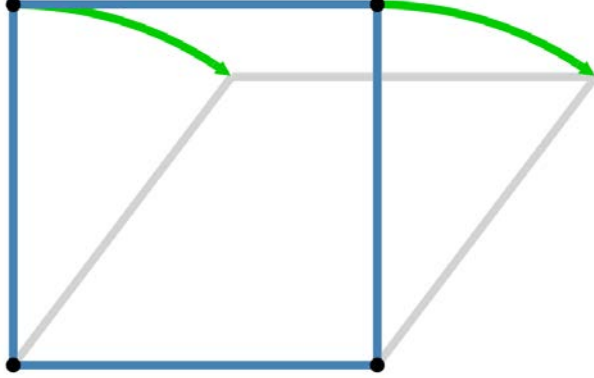


**Figure 2.3.7:** A continuous motion of the square in  $\mathbb{R}^2$ . The green arrows indicate the curves that the vertices  $p_3$  and  $p_4$  describe during this deformation.

We could now continue in this way to parametrize every possible continuous motion of the cube. For the sake of brevity, we are going to pin the bottom square instead. Additionally, we are going to make the top square infinitesimally rigid by incorporating its diagonals as edges, thereby effectively restricting all of its potential non-isometric movements. In this manner, only translations of the hyperplane corresponding to the top square remain feasible. As it turns out, the resulting configuration with additional hyperplane constraints is still flexible. By adding variables to the top vertices as

$$p_5 = (x_1, x_2, x_3), \quad p_6 = (x_1 + 1, x_2, x_3), \quad p_7 = (x_1 + 1, x_2 + 1, x_3) \quad \text{and} \quad p_8 = (x_1, x_2 + 1, x_3),$$

we can verify that all facet constraints are automatically satisfied for arbitrary choices of  $(x_1, x_2, x_3) \in \mathbb{R}^3$ . Therefore, the only remaining constraint that has an impact on the cube's deformation is the bar-length equation  $x_1^2 + x_2^2 + x_3^2 = 1$ . It defines a 2-sphere in  $\mathbb{R}^3$ . To obtain a curve in the deformation space, the constraint set is intersected with the hyperplane  $x_1 = x_2$ , leading to the parametrization

$$p_5(t) = \left( t, t, \sqrt{1 - 2t^2} \right)$$

of the curve associated to the vertex  $p_5$  for  $t \in [-1/\sqrt{2}, 1/\sqrt{2}]$ . The curves corresponding to the other vertices are defined accordingly, giving rise to the deformation's depiction in Figure 2.3.8.

Now you may wonder about the remaining platonic solid, the dodecahedron. It turns out that this polytope is by far the most complicated platonic solid with 60 degrees of freedom coming from the vertex positions, 30 edges, and 12 faces. Each of the dodecahedron's facets is a pentagon, so they come with  $5 - 3 = 2$  coplanarity constraints: 1 for each edge subtracted by the facet normal's degrees of freedom. In total, there are 54 constraints. Since  $\mathbb{R}^3$  has a 6-dimensional space of rigid motions, the naive constraint count works out making us hopeful that the regular dodecahedron is rigid. As we have observed in Example 2.3.6, this is not sufficient, though. All regular polytopes are in special position. Nonetheless, the regular dodecahedron is rigid, as shown in the following theorem.

It is based on a joint work with Albert Zhang during the Focus Program on Geometric

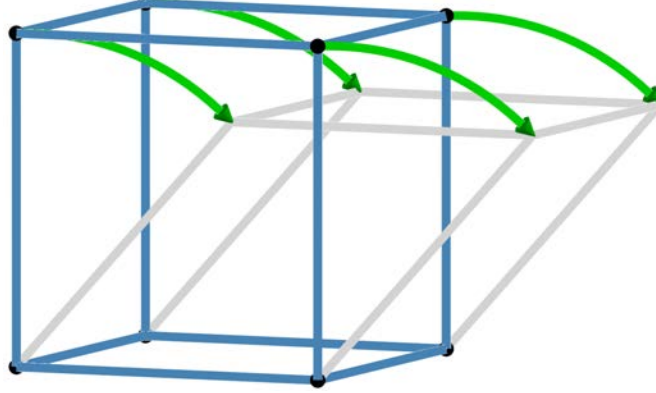


**Figure 2.3.8:** A continuous motion of the cube in  $\mathbb{R}^3$  where the bottom square is pinned and the upper square is constrained to keep its form. The green curves trace the vertices' position  $p_i(t)$  for  $i \in \{5, 6, 7, 8\}$ .

Constraint Systems at the Fields Institute in Toronto, Canada. The exact computations are omitted from the theorem's proof, as they were performed by Albert Zhang in **Wolfram Mathematica** [172] and would span roughly 15 pages. Still, the proof sketch provides a general strategy for proving the second-order rigidity of polytopes, so it is included despite its incompleteness. It uses techniques from algebraic geometry and the hope is to use certificates for the nonnegativity of polynomials (e.g. the SONC decomposition [171]) to generalize the theorem's proof.

**Theorem 2.3.9.** *The regular dodecahedron is second-order rigid.*

*Sketch of Proof.* By denoting  $\phi = 1/2(1 + \sqrt{5})$ , we can list the dodecahedron's symbolic  $20 \cdot 3$  vertex coordinates as

$$(\pm 1, \pm 1, \pm 1), \quad (0, \pm \phi, \pm 1/\phi), \quad (\pm 1/\phi, 0, \pm \phi) \quad \text{and} \quad (\pm \phi, 1/\phi, 0)$$

with its 30 edges chosen appropriately<sup>5</sup>. Denote this centered realization by  $p \in \mathbb{R}^{20 \times 3}$  and the outer normal of facet  $F$  by  $\mathbf{n}_F$ . The 30 edge-length equations and  $5 \cdot 12$  coplanarity constraints are then accumulated in the polynomial system  $g : \mathbb{R}^{96} \rightarrow \mathbb{R}^{90}$  given by fixing  $\|p_i - p_j\|$  for each edge  $ij \in E$  and requiring  $\langle p_i, \mathbf{n}_F \rangle = 1$  for each vertex  $i$  on facet  $F$ . This system's Jacobian  $dg(p)$  at  $p$  will act as the rigidity matrix. All polynomials appearing in  $g$  have degree 2.

When symbolically calculating the kernel of  $dg(p)$ , it becomes evident that there are 5 nontrivial infinitesimal motions  $u_1, \dots, u_5$  and 5 equilibrium stresses  $\omega_1, \dots, \omega_5$  associated to the regular dodecahedron<sup>6</sup>. By Proposition 2.1.16, it suffices to show that for every  $\lambda \in \mathbb{R}^5 \setminus \{0\}$  with  $u = \sum_i \lambda_i u_i$  there exists a  $\mu \in \mathbb{R}^5$  with  $\omega = \sum_i \mu_i \omega_i$  such that

$$\omega \cdot dg(u) \cdot u = \left( \sum_{i=1}^5 \mu_i \omega_i \right) \cdot dg \left( \sum_{i=1}^5 \lambda_i u_i \right) \cdot \left( \sum_{i=1}^5 \lambda_i u_i \right) > 0.$$

Since every entry in the Jacobian matrix  $dg$  is a linear form, we can rewrite this expression as

<sup>5</sup>[https://en.wikipedia.org/wiki/Regular\\_dodecahedron#Cartesian\\_coordinates](https://en.wikipedia.org/wiki/Regular_dodecahedron#Cartesian_coordinates)

<sup>6</sup>The exact computations are performed by Albert Zhang and are omitted here for the sake of brevity.

$\sum_{i=1}^5 \mu_i \cdot Q_i(\lambda_1, \dots, \lambda_5)$  for quadratic polynomials  $Q_i$  only dependent on  $\lambda$ . Computing the Gröbner basis of the ideal  $I = \langle Q_1, \dots, Q_5 \rangle$  and using the Finiteness Theorem [86, Thm. 5.3.6], reveals that  $I$  is zero-dimensional: For each variable  $\lambda_i$  there exists a power  $\lambda_i^{m_i}$  appearing as a leading monomial in  $G$ . Furthermore, the  $Q_i$  are homogeneous polynomials in the variables  $\lambda_i$  by construction, implying that  $\mathcal{V}(I)$  consists only of the origin. If there was  $q \in \mathcal{V}(I) \setminus \{0\}$ , then it would also hold that  $a \cdot q \in \mathcal{V}(I)$  for any  $a \in \mathbb{C}$  because  $Q_i(a \cdot q) = a^2 \cdot Q_i(q) = 0$  for  $i = 1, \dots, 5$  by the polynomials' homogeneity. This is a contradiction to  $I$ 's zero-dimensionality, since  $\mathcal{V}(I)$  would contain the 1-dimensional subvariety  $\{a \cdot q : a \in \mathbb{C}\}$ . As a result, all polynomials  $Q_i$  vanish simultaneously only at the origin, so for any  $\lambda \in \mathbb{R}^5 \setminus \{0\}$  we can choose  $\mu \in \mathbb{R}^5$  such that

$$\sum_{i=1}^5 \mu_i \cdot Q_i(\lambda_1, \dots, \lambda_5) > 0.$$

If this expression is negative, we can simply choose  $-\mu$  instead, reversing the inequality. This proves the claim.  $\square$

Even though the dodecahedron is rigid, this section's title suggests that we intend to deform it. Its realization space is a smooth 36-dimensional manifold by Theorem 2.3.3, containing the 6-dimensional space of rigid motions as a submanifold. Therefore, the regular dodecahedron has 30 degrees of freedom when pinning one of its faces to a hyperplane. Theorem 2.3.9 shows that there is no continuous motion through the regular dodecahedron that maintains its edge lengths. Consequently, the 30 degrees of freedom are concentrated on the edge lengths, suggesting that locally we can freely perturb them.

**Example 2.3.10.** For instance, we can consider how the dodecahedron behaves under the deformation induced by altering a single edge length. By the polytope's regularity, all edges are combinatorially identical. It does not matter which edge is chosen. For this example, we keep all but one edge length constant at  $\ell = 1$  throughout the deformation. Denote the non-constant edge length by  $\ell^*(t) = 1 - t$  with  $t \in (-\delta, +\delta)$  for some  $\delta > 0$ . Sampling from the realization space intersected with the Cayley-Menger variety reveals that there are 6 distinct curves through the regular dodecahedron corresponding to the contraction of a single edge length and 2 corresponding to its expansion. The 6 configurations at  $\ell^*(-0.25)$  are depicted in Figure 2.3.11.

It turns out that there are two types of configurations: Those mitigating the edge contraction by contracting vertically and those that contract horizontally. Both types contain one configuration with two mirror axes and two configurations with one reflection symmetry that are mutual enantiomers. Intriguingly, not all dodecahedra persist until the edge collapses. The configurations in the top left and top right are confluent with the configuration in the top center at  $\approx \ell^*(-0.37194)$ , leaving only 4 configurations beyond this point. All of them persist until  $\ell^*(-1) = 0$ .

Conversely, expanding an edge only produces two configurations that both have 2 distinct reflection axes. They are depicted for the edge length  $\ell^*(0.25)$  in Figure 2.3.12. Despite the dodecahedron's high level of regularity and symmetry, there are more deformation paths for contracting an edge than for expanding it. This behavior is surprising and should be the object

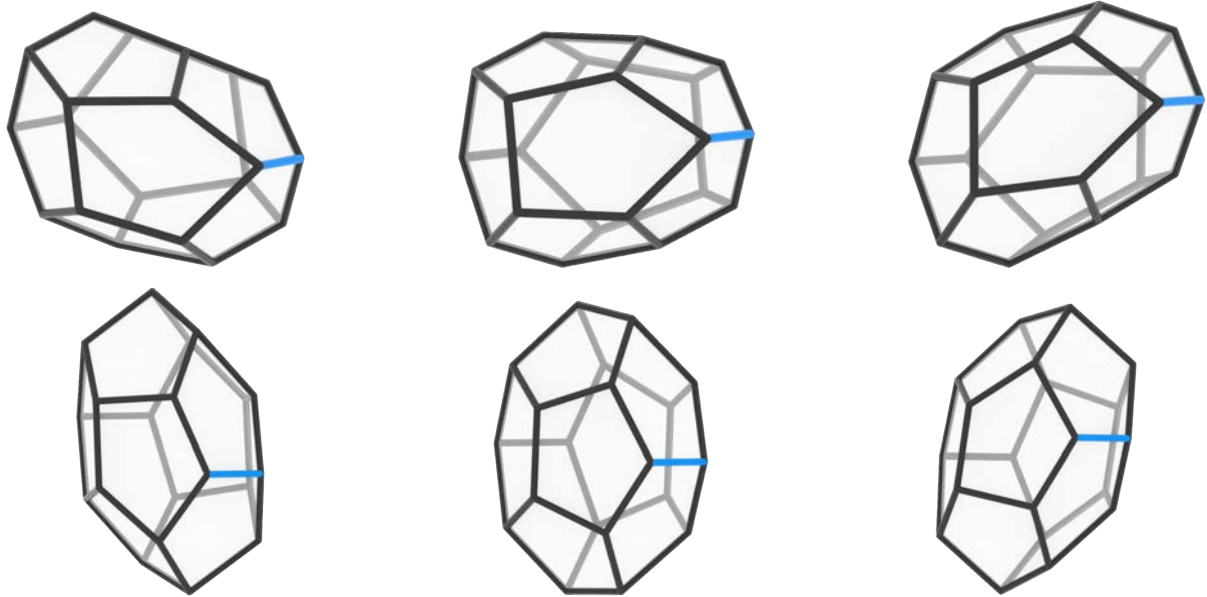


**Figure 2.3.11:** The 6 configurations obtained by contracting the blue edge. They can be split into two types that are organized in the top and bottom row. In the central column, the configurations have 2 reflection axes, while the left and right columns are mutual mirror images with only 1 reflection axis.

of further investigations.

What remains is a qualitative analysis of the eight deformation paths that emerge from contracting any of the dodecahedron's edges. By considering projections of the eight deformation paths onto random 2-dimensional subspaces of  $\mathbb{R}^{54}$  and approximating the curves' derivatives, an understanding of the curves' tangents in the regular dodecahedron can be obtained. Figure 2.3.13 visualizes the curves' behavior.



**Figure 2.3.12:** The 2 configurations are obtained by expanding the blue edge. They both admit to 2 distinct reflection axes.

Remarkably, it appears that the curves can be smoothly matched. As the grey curves correspond to an edge expansion, they seem to have the same tangent in the regular dodecahedron. The two asymmetric green and red deformation paths can be matched as well. Two symmetric deformations remain, which also share the same tangent in the regular dodecahedron. In total, 4 smooth curves are passing through the regular dodecahedron that are parametrized by edge perturbations. Numerically computing the derivative in the regular dodecahedron confirms this observation: Though naturally, we expect that our numerical

calculations are not exact, the respective tangents' sum is sufficiently close to 0.

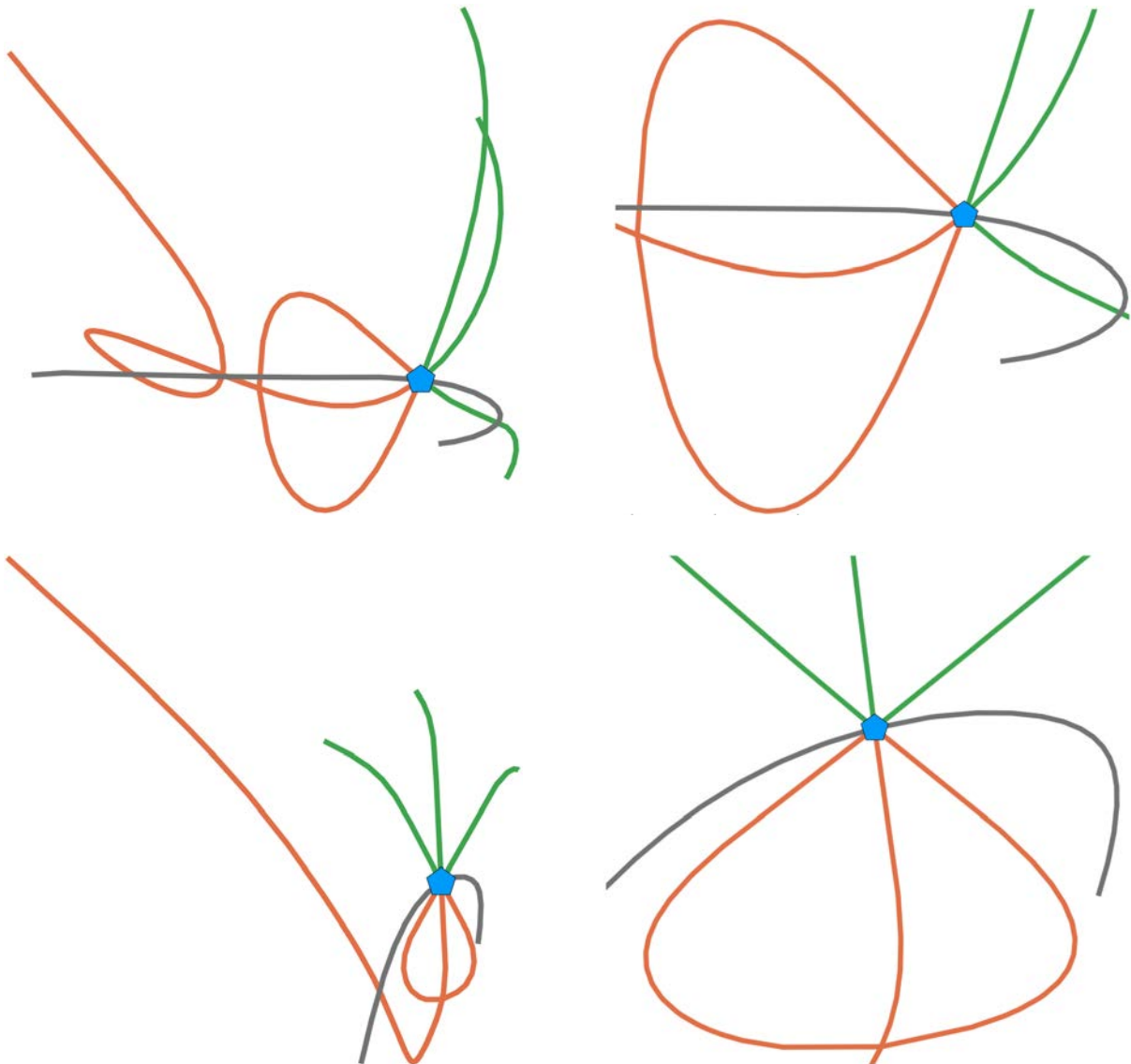


**Figure 2.3.13:** All figures depict projections of the 8 deformation paths parametrized by the expansion (grey) or contraction (green, red) of a single edge in the regular dodecahedron (blue pentagon). The two types of edge contraction paths (cf. Figure 2.3.11) are colored differently. Colored in red, we see the horizontally expansive configurations that are confluent for  $\ell^*(-0.37194)$ , while the other 3 deformations are marked in green. The top and bottom row depict two different random projections and the pictures in the right column are zoomed-in versions of the left plot.

## Riemannian Optimization by Homotopy Continuation<sup>7</sup>

**Chapter Synopsis:** Riemannian optimization uses local methods to solve optimization problems whose constraint sets are given by smooth manifolds. As a linear step along a descent direction typically leaves the constraints, retraction maps are used to approximate the exponential map and return to the manifold. Explicit formulas are available for many common matrix manifolds. For implicitly-defined manifolds, suitable retraction maps are difficult to compute. We therefore develop an algorithm that relies on predictor-corrector-based homotopy continuation to compute the Euclidean distance retraction for any implicitly-defined submanifold of  $\mathbb{R}^n$ .

Furthermore, we consider statistical models as Riemannian submanifolds of the probability simplex, equipped with the Fisher metric. Replacing Euclidean distance with maximum likelihood results in a map which we prove is a retraction. Using the corresponding Levi-Civita connection, this retraction approximates geodesics with second-order accuracy.

Retractions provide a reliable and robust method for traversing the configuration space of geometric constraint systems. The method discussed in this chapter prevents the jumping between connected components. Consequently, retractions can be used to effectively study material deformation. Analyzing the algorithm's performance across multiple examples, Newton's method proves more efficient than the predictor-corrector scheme. However, the theoretical guarantees justify the computational overhead of the predictor step.

Riemannian optimization is a toolbox for solving optimization problems whose constraint sets are smooth manifolds. A linear step along some descent direction usually leaves the constraints. Hence retraction maps are used to approximate the exponential map and return to the manifold. In this chapter, we develop an algorithm that uses homotopy continuation to compute projection-like retractions (cf. [5]) for any implicitly-defined submanifold of  $\mathbb{R}^n$ .

Accordingly, we consider constrained optimization in the case where the constraint set is an implicitly defined manifold or real algebraic variety  $\mathcal{M} \subset \mathbb{R}^n$ . The developed algorithm is local, inspired by examples where local minima offer valuable insights into the system's geometry. The basic idea of Riemannian optimization is simple: To find the minimum, start somewhere on the manifold and move along a descent direction in the tangent space. This usually takes you off the manifold; so you must retract back to the manifold (see Definition 3.2.1), and repeat. Eventually, you hope to find  $p \in \mathcal{M}$  locally minimizing  $f$ . Robust techniques and theoretical results accompany a well-chosen Riemannian metric and retraction map [4, 47, 259]. However, such methods require prior knowledge of a suitable retraction, ideally with an explicit formula. These are available for many common matrix manifolds whose elements have a natural matrix

<sup>7</sup>This chapter contains results and material from the publication in Heaton and Himmelmann [153].

representation, making Riemannian optimization a powerful tool in applications. Nevertheless, for less common, implicitly-defined manifolds or algebraic varieties, there are no readily available formulas for retractions. Therefore, retraction maps applicable to an arbitrary manifold are desirable.

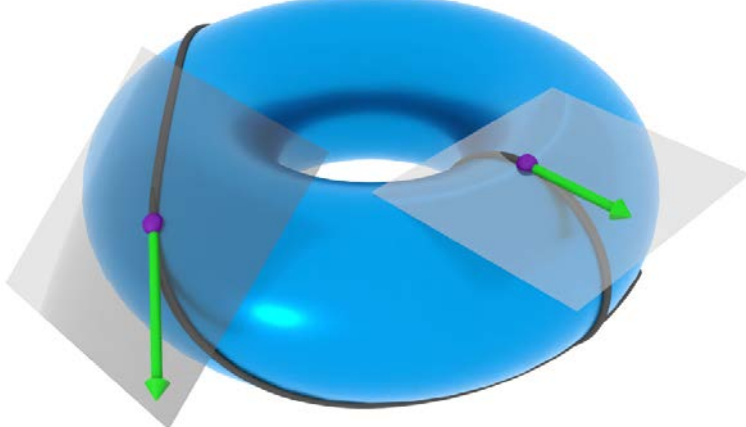


**Figure 3.1.1:** Metric projections make moving on manifolds without explicit knowledge of the exponential map feasible. In this example, from two points on the torus (purple), a linear step (green) is performed in the respective tangent space (grey). The resulting retraction maps (black) are second-order and have been smoothly continued for illustration purposes.

To construct retraction maps on embedded manifolds and algebraic varieties, intuition suggests projecting to the closest point on the manifold. In Boumal [47], such maps are called metric projections [47, p.110f.]. An exemplary metric projection to the torus in  $\mathbb{R}^3$  is depicted in Figure 3.1.1. When stepping linearly off a sphere, this can be achieved by normalizing the resulting point. Similarly, when leaving the manifold of fixed rank matrices, we can apply the singular value decomposition. However, for most implicitly defined manifolds, the closest point retraction does not admit an explicit formula. It is “difficult to compute in general” [47, p.172]. Still, if we can calculate metric projections, it has been shown [5] that they are second-order retractions [47, Def. 5.42], and match geodesics on the manifold up to second-order. This connection makes retractions immensely useful, as they are easier to compute in practice.

Geometric constraint systems are typically given by implicit equations  $\mathcal{M} = g^{-1}(0)$  where  $g : \mathbb{R}^n \rightarrow \mathbb{R}^m$ . We wish to optimize an objective function subject to those constraints. Riemannian optimization is appealing when staying strictly on the constraints is important. For instance, watching a geometric constraint system deform from an initial configuration towards a local minimum of an energy function. We are also wary of multiple connected components and wish to stay on the same connected component throughout the iterations towards a local minimum. Discontinuous jumps between connected components usually signify unphysical behavior. For this reason, homotopy continuation [31, 54, 299] applied to a metric retraction presents itself as a robust way to compute  $R_p(v)$ , the retraction at  $p \in \mathcal{M}$  for a tangent vector  $v \in T_p\mathcal{M}$ . Although continuation methods increase the computational cost, they can still handle the larger examples we consider. They come with the added benefit of reliably computing  $R_p(v)$  without jumping between connected components. For geometric constraint systems, the deformation itself is physically interesting. Note that, in contrast to Séguin and Kressner [307], homotopy continuation is applied locally, rather than globally. In other words, we only use homotopy

continuation to compute the retraction  $R_p(v)$  at each local step.

In Sections 3.1 and 3.2, the theoretical foundation for Riemannian manifolds, homotopy continuation and retraction maps is laid, providing an implicit construction for the Euclidean distance retraction (see Theorem 3.2.2). Section 3.3 describes an algorithm for approximating it (see Algorithm ED2) by using homotopy continuation for any implicitly-defined submanifold of  $\mathbb{R}^n$ . We provide relevant convergence guarantees for this method in Theorem 3.3.7 and Corollary 3.3.13. Besides the choice of descent directions, the algorithm requires suitable step sizes as input. For this reason, Section 3.4 discusses the backtracking line search procedure for discerning intervals of reasonable step choices. The main difference between algebraic varieties and smooth manifolds is that varieties may contain singularities. That is why we investigate a possible way of dealing with such points in Section 3.5. In this way, algebraic constraint sets become admissible as input. In general, it cannot be expected that minima are found with this algorithm. Just consider the minimization problem of  $e^{(x+y)}$  on the line  $x = y$  which is bounded from below by 0. In Section 3.6, we try to find classes of functions in projective space that guarantee the existence of a local minimum. In Section 3.7, statistical models are considered as Riemannian submanifolds of the probability simplex equipped with the Fisher metric. In this setting, Theorem 3.7.6 is proven to show that ideas from maximum-likelihood estimation may be used to create a second-order retraction, applicable to arbitrary statistical models at smooth points. To show second-order, geodesics and covariant derivatives with the Levi-Civita connection on  $\mathcal{M}$  corresponding to the Fisher metric are invaluable tools. Theorem 3.7.6 shows that replacing the linear step  $p + tv$  from Algorithm ED2 by the quadratic curve  $\left(p_i + tv_i + t^2 \frac{v_i^2}{4p_i}\right)_{i=1}^n$  in the usual coordinates on  $\mathbb{R}^n$  allows the resulting retraction  $R_p(tv)$  to follow geodesics on  $\mathcal{M} \subset \Delta_{n-1} \subset \mathbb{R}_{>0}^n$  to second-order accuracy. As another application of the algorithm, Section 3.8 returns to the ideas from Chapter 2 and provides an algorithm for the approximation of deformation paths for framework materials. Section 3.9 describes an easy-to-use software package that implements Algorithm ED2 and briefly demonstrates its usage, while Section 3.10 demonstrates the algorithm's performance on several examples.

### 3.1 Riemannian Manifolds

This section introduces several notions from Riemannian geometry that will be used in the algorithm's development. The basic idea of this area of mathematics is to measure local properties on manifolds known from Euclidean geometry, such as angles, areas, and curvature. A second-countable, Hausdorff topological space  $\mathcal{M}$  is an  $n$ -dimensional *manifold* if it comes with an *atlas* consisting of *charts*  $(U, \varphi)$  such that  $U \subset \mathcal{M}$  is open,  $\varphi : U \rightarrow \mathbb{R}^n$  is a continuous embedding and  $\mathcal{M}$  can be covered by such charts (cf. [198, p.2f.]). If the maps  $\varphi$  are additionally  $C^\infty$ , we call  $\mathcal{M}$  a *smooth manifold*. For the basic Definitions 3.1.2–3.1.6 surrounding smooth manifolds, we follow Lee [197].

**Definition 3.1.2.** If  $\mathcal{M}$  is a smooth manifold, then every coordinate chart  $(U, \varphi)$  in the given maximal atlas is called a *smooth coordinate chart*. For every point  $p \in \mathcal{M}$ , a *tangent vector at  $p$*  is a linear map  $v : C^\infty(\mathcal{M}) \rightarrow \mathbb{R}$  that is a *derivation* at  $p$ , meaning that for all  $f, g \in C^\infty(\mathcal{M})$  it satisfies the product rule

$$v(fg) = f(p) \cdot vg + g(p) \cdot vf.$$

The set of all tangent vectors at  $p$  is called the *tangent space*  $T_p\mathcal{M}$  and is a  $\mathbb{R}$ -vector space. The disjoint union of all tangent spaces on  $\mathcal{M}$  is called the *tangent bundle*  $T\mathcal{M} = \bigsqcup_{p \in \mathcal{M}} T_p\mathcal{M}$ .

A *local frame* for  $T\mathcal{M}$  is an ordered collection of smooth tangent vector fields  $(E_1, \dots, E_n)$  defined on an open set  $U \subset \mathcal{M}$  whose values at each  $p \in U$  constitute a basis for  $T_p\mathcal{M}$ . It is called a *global frame* if  $U = \mathcal{M}$ . Given  $p \in U$  and writing the coordinate functions of a chart  $\varphi$  as  $(x_1, \dots, x_n)$ , the coordinate vectors  $\partial/\partial x_i|_p$  are defined by

$$\frac{\partial}{\partial x_i}|_p f = \frac{\partial}{\partial x_i}|_{\varphi(p)} (f \circ \varphi^{-1})$$

for  $i = 1, \dots, n$  and any  $f \in C^\infty(\mathcal{M})$ . To avoid confusion, we abbreviate  $\partial/\partial x_i|_p$  by the notation  $\partial_i|_p$  and call the corresponding vector field the *induced local frame*.

For  $p \in \mathcal{M}$  the *cotangent space at  $p$* , denoted by  $T_p^*\mathcal{M}$ , is the dual vector space of  $T_p\mathcal{M}$ . This is the space of real-valued linear functionals on  $T_p\mathcal{M}$ , called *tangent covectors at  $p$* . For every  $p \in \mathcal{M}$  and  $f \in C^\infty(\mathcal{M})$  there exists a covector  $df_p \in T_p^*\mathcal{M}$  called the *differential of  $f$  at  $p$*  and defined by  $df_p(v) = vf$  for all  $v \in T_p\mathcal{M}$ .

**Example 3.1.3.** To better grasp the concepts introduced in Definition 3.1.2, consider the  $n$ -unit-sphere  $S^n \subset \mathbb{R}^{n+1}$  as an example. A possible atlas is given by

$$U_i^\pm = \{(x_1, \dots, x_{n+1}) \in S^n : \pm x_i > 0\}$$

with  $\varphi_i^\pm : U_i^\pm \rightarrow \mathbb{R}^n$ ,  $(x_1, \dots, x_{n+1}) \mapsto (x_1, \dots, x_{i-1}, x_{i+1}, \dots, x_{n+1})$

for  $i = 1, \dots, n+1$ . The inverse map sends  $x \in B_1^n(0)$  to  $(x_1, \dots, \pm\sqrt{1-|x|^2}, \dots, x_n)$ . Given  $p \in S^n$ , we want to compute the corresponding induced local frame. Without loss of generality, we can assume that  $p \in U_1^+$ . To distinguish coordinates on  $S^n$  and in  $\mathbb{R}^n$ , we denote the latter manifold's global coordinates by  $(x_1, \dots, x_n)$  and the former's by  $(p_1, \dots, p_{n+1})$ . Choosing the standard basis  $(e_1, \dots, e_{n+1})$  of  $\mathbb{R}^{n+1}$  and applying the multivariate chain rule results in

$$\begin{aligned} \partial_i|_p f &= \left( \frac{\partial}{\partial x_1} f \Big|_p \right) \cdot \frac{-x_i}{\sqrt{1-|x|^2}} \Big|_{\varphi(p)} e_1 + \sum_{j=2}^{n+1} \left( \frac{\partial}{\partial x_j} f \Big|_p \right) \cdot \delta_{i+1,j} e_j \\ &= \left( \frac{\partial}{\partial x_1} f \Big|_p \right) \cdot \frac{-p_{i+1}}{p_1} e_1 + \sum_{j=2}^{n+1} \left( \frac{\partial}{\partial x_j} f \Big|_p \right) \cdot e_{i+1}, \end{aligned}$$

for any  $f \in C^\infty(\mathcal{M})$ , since  $\sum_i p_i^2 = 1$  by definition. Here,  $\delta_{i+1,j}$  denotes the Kronecker delta that is 1 exactly when  $i+1 = j$ . In particular, the partial derivatives of  $f$  at  $p$  are scalars, leading to a basis of  $T_p S^n$  given by  $\mathcal{B} = \{e_{i+1} - p_{i+1}/p_1 e_1 : i = 2, \dots, n+1\}$ .

Recall from linear algebra that the dimension formula  $(T_p S^n)^\perp \oplus T_p S^n \cong \mathbb{R}^{n+1}$  needs to hold. To certify this result, we can take the outer normal field of the sphere  $\mathbf{n}(p) = p$  [198, Ex. 15.22] and multiply an arbitrary tangent vector with it. The result is  $p_{i+1} - p_1 \cdot p_{i+1}/p_1 = 0$ , proving that we found a basis of the sphere's tangent space since  $\mathcal{B}$  is linearly independent by construction.

**Definition 3.1.4.** Let  $\mathcal{M}$  be a smooth manifold. Define an inner product  $g_p : T_p\mathcal{M} \times T_p\mathcal{M}$  for each  $p \in \mathcal{M}$ . Assume that  $g$  is smoothly varying, meaning that for any smooth coordinate chart

$(U, x)$  of  $\mathcal{M}$  the  $(\dim \mathcal{M})^2$  functions  $g_x(\partial_i|_x, \partial_j|_x) : U \rightarrow \mathbb{R}$  are smooth for the induced local frame  $(\partial_i)$ . Then, we call  $g$  a *Riemannian metric* and the pair  $(\mathcal{M}, g)$  is called a *Riemannian manifold*.

In fact, every smooth manifold admits a Riemannian metric [197, Prop. 2.4].

**Example 3.1.5.** The Euclidean inner product  $g_x(v, w) = \sum_{i=1}^n v_i w_i$  defines a Riemannian metric on  $\mathbb{R}^n$ . In the global chart  $(\mathbb{R}^n, \text{id})$  with invariant standard basis  $(e_i)_{i=1}^n$  of  $T_x \mathbb{R}^n \cong \mathbb{R}^n$  for each  $x \in \mathbb{R}^n$ , the maps  $g_x(e_i, e_j) = \delta_{ij}$  are constant and thus smooth.

For Riemann surfaces in  $\mathbb{R}^3$ , the metric tensor  $g$  is also called *first fundamental form*. Often, we use the notation  $\langle \cdot, \cdot \rangle_p$  for the the Riemannian metric  $g_p$  on the tangent space  $T_p \mathcal{M}$ . An important class of examples for Riemannian manifolds comes from submanifolds of Euclidean space. They will be particularly relevant when formulating Riemannian optimization algorithms in later sections, as they automatically become Riemannian submanifolds by inheriting the metric of the ambient manifold through restriction to the tangent space of the submanifold.

**Definition 3.1.6.** Suppose  $(\mathcal{M}, g)$  is a Riemannian manifold and let  $\iota : \mathcal{S} \hookrightarrow \mathcal{M}$  be an embedded submanifold. The pullback metric  $\iota^* g$  makes  $(\mathcal{S}, \iota^* g)$  a Riemannian submanifold. Here, the pullback metric is pointwise defined as the function

$$(\iota^* g)_p(X, Y) = g_p(d\iota_p(X), d\iota_p(Y))$$

for  $X, Y \in T_p \mathcal{S}$  with the differential  $d\iota_p$  at  $p$  mapping  $T_p \mathcal{S} \rightarrow T_p \mathcal{M}$ .

The *normal space* of  $\mathcal{S}$  is given by the vectors orthogonal to  $T_p \mathcal{S}$  in the metric  $\iota^* g$ , namely

$$N_x \mathcal{S} = \{v \in T_x \mathcal{M} : g_x(v, d\iota_x(w)) = 0 \ \forall w \in T_x \mathcal{S}\}.$$

The corresponding *normal bundle* is  $N \mathcal{S} = \bigsqcup_{x \in \mathcal{S}} N_x \mathcal{S}$ .

Having defined a submanifold's normal space, a natural question is if there is an open ball in each normal space that, when joined in the normal bundle, yields a diffeomorphism to a subset of the ambient manifold. In other words: Can we find a tubular neighborhood around the submanifold with a positive minimal diameter that is not self-intersecting? The following theorem answers this question.

**Theorem 3.1.7** (Tubular Neighborhood Theorem [197, Prop. 5.25]). *Let  $\mathcal{S} \hookrightarrow \mathcal{M}$  be a Riemannian submanifold. Then there exists a diffeomorphism from an open neighborhood of  $\mathcal{S}$  in  $N \mathcal{S}$  onto an open neighborhood of  $\mathcal{S}$  in  $\mathcal{M}$ . If  $\mathcal{S}$  is compact, then there exists a uniform tubular neighborhood.*

Having a differentiable structure on Riemannian manifolds, it seems reasonable to provide analogs to directional derivatives. If the Riemannian metric is the same at every point – as it is the case in Euclidean space – we can simply calculate the ordinary gradient and project it onto any submanifold's corresponding tangent space. For general Riemannian metrics, this is not possible anymore, since the local frame generally varies between any two points (cf. Definition 3.1.2). To make up for this variation, the derivative on Riemannian manifolds needs

to carry additional information. The covariant derivative is defined in the following way and appears in Boumal [47, Def. 5.1].

**Definition 3.1.8.** Let  $\mathfrak{X}(\mathcal{M})$  denote the set of all smooth vector fields  $U : \mathcal{M} \rightarrow T\mathcal{M}$  on a smooth manifold  $\mathcal{M}$ . A *connection* on  $\mathcal{M}$  is an operator

$$\nabla : \mathfrak{X}(\mathcal{M}) \times \mathfrak{X}(\mathcal{M}) \rightarrow \mathfrak{X}(\mathcal{M}), \quad (U, V) \mapsto \nabla_U V,$$

which for any  $U, V, W \in \mathfrak{X}(\mathcal{M})$ , smooth  $f, g : \mathcal{M} \rightarrow \mathbb{R}$  and  $a, b \in \mathbb{R}$  has the properties

1.  $\nabla_{fU+gW} V = f\nabla_U V + g\nabla_W V$ ,
2.  $\nabla_U (aV + bW) = a\nabla_U V + b\nabla_U W$  and
3.  $\nabla_U (fV) = (Uf)V + f\nabla_U V$ .

The vector field  $\nabla_U V$  is called the *covariant derivative* of  $V$  along  $U$ .

**Theorem 3.1.9** (cf. [47, Thm. 5.6]). *On a Riemannian manifold  $(\mathcal{M}, \langle \cdot, \cdot \rangle)$  there exists a unique connection  $\nabla$  satisfying the two additional properties for all  $U, V, W \in \mathfrak{X}(\mathcal{M})$ :*

4.  $U(V(f)) - V(U(f)) = (\nabla_U V - \nabla_V U)f$  and
5.  $U\langle V, W \rangle = \langle \nabla_U V, W \rangle + \langle V, \nabla_U W \rangle$

with  $\langle V, W \rangle(x) = \langle V(x), W(x) \rangle_x$  and  $Uf(x) = df(x)[U(x)]$  for the differential  $df(x)[u]$  given by  $\lim_{t \rightarrow 0} (f(x + tu) - f(x)) \cdot t^{-1}$ . We call this connection the *Levi-Civita connection*.

**Theorem 3.1.10** (Covariant Derivative along Curves [47, Thm. 5.29]). *Let  $c : I \rightarrow \mathcal{M}$  be a smooth curve defined on an open interval  $I$  on a manifold  $\mathcal{M}$  equipped with a connection  $\nabla$ . Denote the family of smooth vector fields along  $c$  by  $\mathfrak{X}(c)$ . There is a unique operator*

$$D_t : \mathfrak{X}(c) \rightarrow \mathfrak{X}(c)$$

called the *covariant derivative along  $c$*  which satisfies for all  $Y, Z \in \mathfrak{X}(c)$ ,  $U \in \mathfrak{X}(\mathcal{M})$ , smooth  $g : I \rightarrow \mathbb{R}$  and  $a, b \in \mathbb{R}$ :

1.  $D_t(aY + bZ) = aD_t Y + bD_t Z$ ,
2.  $D_t(gZ) = g'Z + gD_t Z$  and
3.  $(D_t(U \circ c))(t) = \nabla_{c'(t)} U$  for all  $t \in I$ .

Here,  $c'(t) = \lim_{h \rightarrow 0} (c(t + h) - c(t)) \cdot h^{-1}$  denotes the tangent field along  $c$ .  $D_t$  is called the *induced covariant derivative*. If furthermore  $(\mathcal{M}, \langle \cdot, \cdot \rangle)$  is a Riemannian manifold with Levi-Civita connection  $\nabla$ , then the induced covariant derivative  $D_t$  satisfies

$$4. \frac{\partial}{\partial t} \langle Y, Z \rangle_{c(t)} = \langle D_t Y, Z \rangle_{c(t)} + \langle Y, D_t Z \rangle_{c(t)} \text{ for all } t \in I.$$

The covariant derivative is an immensely useful tool for understanding derivatives along curves on manifolds. It takes a particularly nice form when the curve lies on a submanifold embedded in an ambient Riemannian manifold:

**Proposition 3.1.11** (The Gauss Formula [197, Thm. 8.2-8.3]). *Let  $(\mathcal{M}, g)$  be a Riemannian manifold equipped with its Levi-Civita connection  $\tilde{\nabla}$ . Suppose  $\mathcal{S}$  is an embedded submanifold of  $\mathcal{M}$  with induced metric  $\iota^*g$  and Levi-Civita connection  $\nabla$ . If  $U, V \in \mathfrak{X}(\mathcal{S})$  are extended arbitrarily to a neighborhood of  $\mathcal{S}$  in  $\mathcal{M}$ , then we can decompose*

$$\tilde{\nabla}_U V = \nabla_U V + (\tilde{\nabla}_U V)^\perp.$$

into tangent and orthogonal parts. The orthogonal component  $(\tilde{\nabla}_U V)^\perp$  is called the *second fundamental form* of  $\mathcal{S}$ , often denoted by  $\mathbb{II}(U, V)$ . Now, let  $c : I \rightarrow \mathcal{S}$  be a smooth curve defined on an open interval  $I$ . The induced covariant derivatives  $\tilde{D}_t$  and  $D_t$  of  $\mathcal{M}$  and  $\mathcal{S}$ , respectively, satisfy

$$\tilde{D}_t U = D_t U + \mathbb{II}(c', U).$$

The connection coefficients of a Riemannian manifold quantify the change in the local frame that was previously hinted at. Appearing in Lee [197, p.91], Definition 3.1.12 will introduce this concept.

**Definition 3.1.12.** Assume we are given a smooth manifold  $\mathcal{M}$  equipped with a connection  $\nabla$ . Let  $(\partial_i)$  be a smooth local frame for  $T\mathcal{M}$  on an open subset  $U \subset \mathcal{M}$ . For every choice of indices  $i$  and  $j$ , we can expand the vector field  $\nabla_{\partial_i} \partial_j$  in terms of this same frame:

$$\nabla_{\partial_i} \partial_j = \sum_{k=1}^n \Gamma_{ij}^k \partial_k.$$

This defines  $(\dim \mathcal{M})^3$  functions  $\Gamma_{ij}^k : U \rightarrow \mathbb{R}$  called the *connection coefficients* of  $\nabla$ .

**Proposition 3.1.13** (cf. [197, p.102ff.]). *Given a Riemannian manifold  $(\mathcal{M}, g)$  equipped with its Levi-Civita connection  $\nabla$ , the unique corresponding connection coefficients  $\Gamma_{ij}^k$  of  $\nabla$  are called the *Christoffel symbols of second kind* and can be calculated by*

$$\Gamma_{kl}^i = \frac{1}{2} \sum_m g^{im} \left( \frac{\partial g_{mk}}{\partial x_l} + \frac{\partial g_{ml}}{\partial x_k} - \frac{\partial g_{kl}}{\partial x_m} \right)$$

for the local frame  $(\partial_i = \partial/\partial x_i)$  induced by the smooth coordinate chart  $(U, x)$  and the inverse matrix  $(g^{jk})$  of  $(g_{jk})$ . Here,  $g_{ij} = \langle \partial_i, \partial_j \rangle$  denote the corresponding *metric coefficients*. For any vector field  $V \in \mathfrak{X}(c)$  along a curve  $c : I \rightarrow \mathcal{M}$  with ordinary derivative  $\dot{V}$ , the induced covariant derivative can then be expressed as

$$D_t V(t) = \sum_k \left( \dot{V}_k(t) + \sum_i \sum_j \dot{c}_i(t) V_j(t) \Gamma_{ij}^k(c(t)) \right) \partial_k|_{c(t)}.$$

As seen in the previous definition, it is advantageous to distinguish between ordinary derivatives  $\dot{V}$  for a vector field  $V \in \mathfrak{X}(c)$  along a curve  $c : I \rightarrow \mathcal{M}$  and derivatives in terms of the manifold's connection. By slightly abusing notation, we write  $\ddot{c}(t)$  for the ordinary second derivative of a curve.

Let us now shift our view to *geodesics*, which are locally length-minimizing curves on

manifolds [197, Thm. 6.15]. By locally providing the shortest connections on the manifold, these curves are the generalization of straight lines in Euclidean space. Definitions 3.1.14–3.1.15 appear in Boumal [47, p. 101f., 256, 262] and make these ideas rigorous.

**Definition 3.1.14.** Let  $c : I \rightarrow \mathcal{M}$  denote a smooth curve defined on an open interval  $I$ . Its *velocity* is the vector field  $c' \in \mathfrak{X}(c)$ . Its *acceleration* is the smooth vector field  $c'' \in \mathfrak{X}(c)$  defined by  $c'' = D_t c'$ . If  $\mathcal{M}$  is a Riemannian manifold with Levi-Civita connection  $\nabla$  and induced covariant derivative  $D_t$ , a *geodesic* is a smooth curve such that  $c''(t) = 0$  for all  $t \in I$ .  $\mathcal{M}$  is said to be *geodesically complete* if every geodesic can be extended to a geodesic defined on the whole real line.

For each  $(p, v) \in T\mathcal{M}$ , there exists a unique geodesic  $\gamma_v : I \rightarrow \mathcal{M}$  with  $\gamma_v(0) = p$  and  $\gamma'_v(0) = v$ , such that  $I$  is as large as possible [197, Cor. 4.28]. In other words, there are no geodesics  $\tilde{\gamma} : \tilde{I} \rightarrow \mathcal{M}$  defined on an open interval  $\tilde{I} \supsetneq I$  such that  $\tilde{\gamma}|_I = \gamma_v$  and  $\tilde{\gamma}'(0) = v$ . We then call  $\gamma_v$  a *maximal geodesics*. Such maximal geodesics can be used to move on the manifold  $\mathcal{M}$ , as we show in the following.

**Definition 3.1.15.** Construct the set

$$\mathcal{O} = \{(p, v) \in T\mathcal{M} : \text{The maximal geodesic } \gamma_v \text{ is defined on an interval containing } [0, 1]\}.$$

The *exponential map*  $\text{Exp} : \mathcal{O} \rightarrow \mathcal{M}$  is then defined by  $\text{Exp}(p, v) = \text{Exp}_p(v) = \gamma_v(1)$ . The restriction  $\text{Exp}_p$  is defined on  $\mathcal{O}_p = (\{p\} \times T_p\mathcal{M}) \cap \mathcal{O}$ .

**Example 3.1.16.** Consider the unit cylinder  $\mathcal{Z}^2 \subset \mathbb{R}^3$ . This manifold can be described by the implicit equation  $x_1^2 + x_2^2 = 1$  that notably does not contain  $x_3$ . Without loss of generality, we want to find the geodesics through  $p = (1, 0, 0)$ . By the cylinder's rotational symmetry in  $x$ - and  $y$ -direction and its translational symmetry in  $z$ -direction, the geodesics through  $p$  can be extended to the entire cylinder. In other words, every point on the cylinder has the same geodesic properties. Any geodesic  $\gamma : (-\varepsilon, \varepsilon) \rightarrow \mathcal{Z}^2$  for some  $\varepsilon > 0$  with  $\gamma(0) = (1, 0, 0)$  and  $\gamma'(0) = v$  needs to satisfy the following equations:

$$\gamma_1(t)^2 + \gamma_2(t)^2 = 1 \quad \text{and} \quad \gamma''(t) = c(t) \cdot (\gamma_1(t), \gamma_2(t), 0) \quad (3.1.17)$$

for a smooth  $c : (-\varepsilon, \varepsilon) \rightarrow \mathbb{R}$  and all  $t \in (-\varepsilon, \varepsilon)$  by Definition 3.1.14. To satisfy the geodesic differential equation, it would be sufficient for  $\gamma''(t)$  to belong to  $N_{c(t)}\mathcal{Z}^2$ ; however, the curve must also lie on the manifold. Since  $\gamma_3''$  is identical to 0,  $\gamma_3'$  is constant, so  $\gamma_3 = v_3$  by construction. The fact that  $\gamma_3(0) = 0$  implies that  $\gamma_3(t)$  is given by  $t \cdot v_3$ . Moreover, the first equation implicitly defines the unit circle, which is parametrized by cos and sin, so  $\gamma_1(t) = \cos(\theta(t))$  and  $\gamma_2(t) = \sin(\theta(t))$  for a smooth  $\theta : (-\varepsilon, \varepsilon) \rightarrow \mathbb{R}$ .

In order for the differential equation to hold, we determine the second derivative using the principles of the product and chain rule from calculus to obtain

$$\gamma_1''(t) = -\cos(\theta(t)) \cdot \theta'(t) - \sin(\theta(t)) \cdot \theta''(t) \quad \text{and} \quad \gamma_2''(t) = -\sin(\theta(t)) \cdot \theta'(t) + \cos(\theta(t)) \cdot \theta''(t)$$

for all  $t \in (-\varepsilon, \varepsilon)$ . By comparing terms with Equation (3.1.17), this yields  $\theta'' \equiv 0$  and the

scaling factor  $c(t) = -\theta'(t)$ . Since the zero function has a constant antiderivative, we find that  $\theta(t) = d \cdot t + e$  for scalars  $d, e \in \mathbb{R}$ . The geodesics pass through  $p = (1, 0, 0)$  by assumption, implying that  $\cos(\theta(0)) = 1$  and  $\sin(\theta(0)) = 0$ . Hence, it holds that  $e = 0$ . Finally, by differentiating the expressions for  $\gamma_1$  and  $\gamma_2$  we find that  $v_1 = 0$  and  $d = -v_2$ . Alternatively, we could have inferred this result by computing the cylinder's normal space. Therefore, the geodesics through  $p$  can be characterized by

$$\gamma(t) = (\cos(v_2 \cdot t), -\sin(v_2 \cdot t), v_3 \cdot t).$$

Figure 3.1.18 depicts several geodesics on the cylinder  $\mathcal{Z}^2$  passing through  $(1, 0, 0)$ . When investigating the picture, we find several points in which two geodesics intersect. Indeed, between any two points that do not have the same  $z$ -coordinate, there are countably infinitely many geodesics connecting them. They are classified by how often they wind around the cylinder between the two points and whether they turn clockwise or counterclockwise. Nevertheless, between any two points there exists a unique, globally length-minimizing geodesic, which does not complete a full rotation around the cylinder.

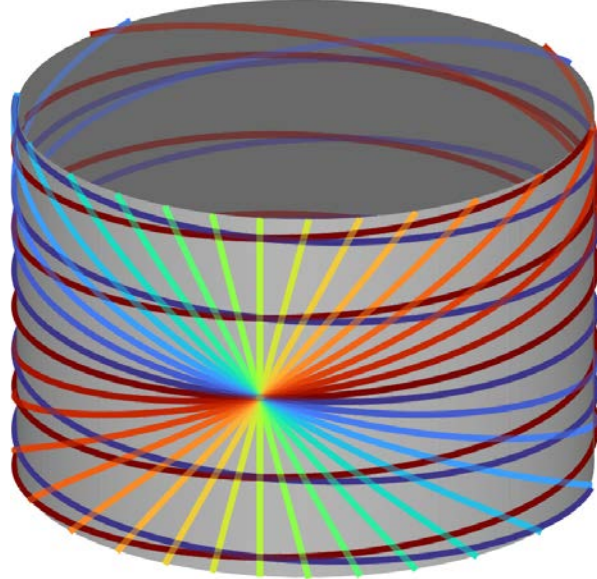


**Figure 3.1.18:** Geodesics on the cylinder  $\mathcal{Z}^2$  passing through  $(1, 0, 0)$ . The curves are color-coded to highlight their pitch. There are several points where two geodesics intersect, hinting at the fact that local curve-length minimization generally does not extend to global minimality.

Conversely, if the points lie on a circle then up to reparametrization there are only two maximal geodesics. They are given by the two directions with which you can traverse the circle. Either way, the cylinder  $\mathcal{Z}^2$  is geodesically complete, since all the geodesics we describe have  $\mathbb{R}$  as their domain.

**Example 3.1.19.** Let us now consider the one-sheeted hyperboloid  $\mathcal{H}_1^2 \subset \mathbb{R}^3$  defined by the implicit equation  $x^2 + y^2 - z^2 = 1$ . We could think of it as a submanifold of Euclidean space and thus, equip it with the corresponding induced metric. However, this is not the only option and this example shows that the choice of metric leads to two different geometric objects. Define

two bilinear forms

$$g^{(e)}(v, w) = v_1 w_1 + v_2 w_2 + v_3 w_3 \quad \text{and} \quad g^{(m)}(v, w) = v_1 w_1 + v_2 w_2 - v_3 w_3$$

on  $\mathbb{R}^3$ . The first is the standard Euclidean scalar product, while the latter is called the *Minkowski metric*, having ramifications in relativity theory when considered in  $\mathbb{R}^4$  [240, p.163f.]. Clearly,  $g^{(m)}$  is not positive definite, so  $(\mathbb{R}^3, g^{(m)})$  is not a Riemannian manifold. Rather, it is called a *pseudo-Riemannian manifold*, solely requiring that the corresponding bilinear form is non-degenerate [197, p.42]. Several properties of Riemannian manifolds persist: There still exists a unique Levi-Civita connection [240, p.61], enabling concepts such as the second fundamental form (cf. Proposition 3.1.11), Christoffel symbols (cf. Definition 3.1.12) and geodesics (cf. Definition 3.1.14).

Both bilinear forms are defined by constant tensors, so all Christoffel symbols associated to  $g^{(e)}$  and  $g^{(m)}$  vanish simultaneously. This fact reduces the problem of finding curves  $\gamma : I \rightarrow \mathcal{H}_1^2$  such that  $\ddot{\gamma}(t) \in N_{\gamma(t)}^{(e)} \mathcal{H}_1^2$  or  $\ddot{\gamma}(t) \in N_{\gamma(t)}^{(m)} \mathcal{H}_1^2$  to the differential equations

$$\ddot{\gamma}^{(e)}(t) = - \underbrace{\frac{g^{(m)}(\dot{\gamma}^{(e)}(t), \dot{\gamma}^{(e)}(t))}{1 + 2(\gamma_3^{(e)}(t))^2}}_{=c(t)} \cdot \begin{pmatrix} \gamma_1^{(e)}(t) \\ \gamma_2^{(e)}(t) \\ -\gamma_3^{(e)}(t) \end{pmatrix} \quad \text{and} \quad \ddot{\gamma}^{(m)}(t) = g^{(m)}(\dot{\gamma}^{(e)}(t), \dot{\gamma}^{(e)}(t)) \cdot \gamma^{(m)}(t)$$

after adequate reparametrization and omission of the trivial cases. Both equations are derived using the property that  $T_p \mathcal{H}_1^2$  is generated by the vectors  $(p_3, p_3, p_1 + p_2)$  and  $(p_2, -p_1, 0)$  for any  $p \in \mathcal{H}_1^2$ . By differentiating the hyperboloid's defining equation  $\gamma_1(t)^2 + \gamma_2(t)^2 - \gamma_3(t)^2 = 1$  twice with respect to  $t$ , inserting the expression for  $\ddot{\gamma}^{(e)}(t)$  and then solving for  $c(t)$ , the geodesics' differential equation in the Euclidean metric can be derived. An analogous computation shows that the differential equation associated with the Minkowski metric can be brought to a similar form. It is possible to solve it analytically when given a unit-speed parametrization, leading to

$$\gamma^{(m)}(t) = \begin{cases} p \cosh(t) + v \sinh(t) & \text{for } \ddot{\gamma}^{(m)}(t) = \gamma^{(m)}(t) \text{ and } g^{(m)}(v, v) = 1 \\ p \cos(t) + v \sin(t) & \text{for } \ddot{\gamma}^{(m)}(t) = -\gamma^{(m)}(t) \text{ and } g^{(m)}(v, v) = -1 \\ p + t v & \text{for } \ddot{\gamma}^{(m)}(t) = 0 \text{ for } v \text{ s.t. } \forall t \in \mathbb{R} : p + t v \in \mathcal{H}_1^2 \end{cases}$$

for the initial values  $\gamma(0) = p$  and  $\dot{\gamma}(0) = v$ . The geodesics of  $(\mathcal{H}_1^2, g^{(m)})$  can alternatively be seen as intersections of  $\mathcal{H}_1^2$  with 2-dimensional linear subspaces of  $\mathbb{R}^3$  [197, Prop. 5.28a]. They are called *great hyperbolae*, analogous to great circles on the sphere. There are two straight lines through  $p$  that separate the hyperboloid's tangent space  $T_p \mathcal{H}_1^2$  into 4 open regions of closed and unbounded geodesics, respectively.

For the former differential equation, we opted for a numerical approach known as *Euler's method* together with a correction step to the manifold  $\mathcal{H}_1^2$ . A thorough discussion of this path-tracking method is included in Sections 3.2–3.3. Finally, Figure 3.1.20 depicts several geodesics in both metrics through the point  $p = (1, 0, 0)$ . In the Euclidean metric, all geodesics but the circle corresponding to  $v = \pm(0, 1, 0)$  are unbounded, reminiscent of the cylinder in

Example 3.1.16.

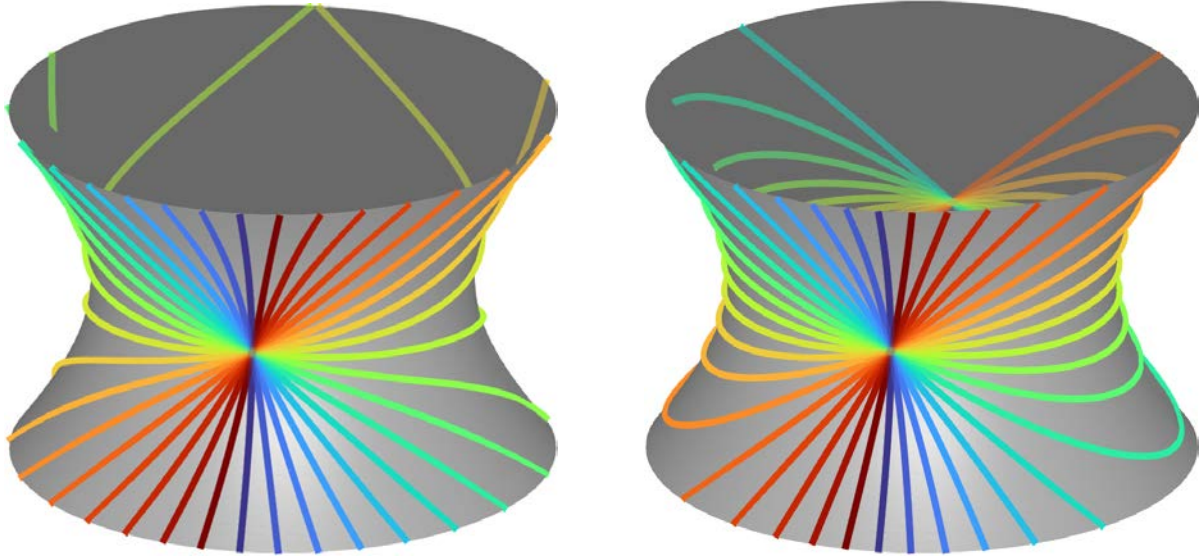


**Figure 3.1.20:** Numerically approximated geodesics through  $(1, 0, 0)$  on  $(\mathcal{H}_1^2, g^{(e)})$  (l.) and analytically calculated geodesics on  $(\mathcal{H}_1^2, g^{(m)})$  (r.) are visualized.

### 3.2 Background: Riemannian Optimization and Homotopy Continuation

In this section, we cite prior results and definitions from the literature to give background information on Riemannian optimization, retraction maps, and homotopy continuation. Our contributions to the problem of computing the Euclidean distance retraction  $R_p(v)$  are discussed in Section 3.3. At a later point, Section 3.7 covers our results concerning the maximum likelihood retraction.

Although we focus on computing the retraction  $R_p(v)$  for use in Riemannian optimization algorithms, many other methods may be used to solve nonlinear constrained optimization problems like those arising in the study of geometric constraint systems. The main advantage of using Riemannian optimization algorithms is that they allow us to move smoothly on manifolds and avoid discontinuous behavior, ensuring that the constraints are consistently satisfied. For geometric constraint systems, this approach hence is particularly suitable. Alternatively, one may use penalty functions or augmented Lagrangians to encode the objective and constraint functions together to solve an unconstrained problem. Another possibility is to use sequential quadratic programming (SQP), which linearizes the constraints and works with a quadratic model for the objective function at each iteration, combined with either line search or trust-region methods. Finally, interior point methods, also called barrier methods, provide another category of algorithms which are effective in tackling nonlinear constrained optimization problems. For a textbook treatment, see Nocedal and Wright [234]. In this chapter, we focus entirely on descent directions, for use in any Riemannian optimization algorithm, such as gradient descent, Newton or quasi-Newton methods, conjugate gradients, or others found in Absil et al. [4] and Boumal [47].

### 3.2.1 Riemannian Optimization

In Section 3.1 we have already seen that even for manifolds that are defined by a single sparse polynomial with integer coefficients, exactly computing geodesics is a nontrivial task. In most cases, the corresponding differential equation cannot be analytically solved. Numerically approximating geodesics is also undesirable since the corresponding second-order differential equation is often stiff, so even sophisticated predictor schemes may diverge. Nevertheless, the ability to compute geodesics is not crucial for us. Consequently, we relax the goal of finding exponential maps to constructing a second-order approximation for geodesics that will ultimately enable Riemannian optimization algorithms. Instead of traversing  $\mathbb{R}^n$  to minimize an objective function, these algorithms' moves stay on an arbitrary constraint manifold. The ability to smoothly move on a manifold is particularly useful in the context of geometric constraint systems, as it allows the approximation of deformation paths. In these cases, if an algorithm exhibits discontinuous behavior and jumps between connected components, it immediately loses its purpose.

Furthermore, one may wonder why a Riemannian optimization algorithm should be considered rather than solvers that do not require that the constraints are constantly satisfied. Specifically, this approach favors local over global minima, and convergence to the closest critical point is highly probable. Often, it is reasonable from a physical perspective to ensure that geometric constraints remain satisfied throughout the entire optimization routine. Otherwise, defects in the structure can be the result. As an example, consider topological changes in a hard sphere packing that occur because a sphere freely passes through another without obstruction. This can potentially happen if a constraint is allowed to be violated.

To introduce the relevant concepts, we begin by considering submanifolds  $\mathcal{M} \subset \mathbb{R}^n$  with the induced Euclidean metric which are implicitly defined. In other words, there exists a smooth function  $g : \mathbb{R}^n \rightarrow \mathbb{R}^m$  defining the manifold via  $\mathcal{M} = g^{-1}(0)$ . Since our proposed methods are local, we also consider real algebraic varieties  $\mathcal{M} \subset \mathbb{R}^n$ . A variety's collection of regular points forms a manifold and the set of singularities again defines an algebraic variety [56, p.26f.]. According to Hartshorne [149, Thm. 5.3], the singular locus is a proper closed subset. Thus, for irreducible varieties  $V$  it holds that  $\dim \text{Sing}(V) < \dim V$  by Definition 2.1.5.

Given any smooth function  $f : \mathbb{R}^n \rightarrow \mathbb{R}$ , the main objective of Riemannian optimization is to solve the constrained optimization problem of minimizing  $f$  restricted to a smooth manifold  $\mathcal{M}$ . For any point  $p \in \mathcal{M}$ , we can evaluate the Euclidean gradient of  $f$  at  $p$ , obtaining a vector  $\nabla f|_p \in \mathbb{R}^n$ . Projecting  $-\nabla f|_p$  onto the tangent space  $T_p \mathcal{M}$  yields a *descent direction*  $\mathbf{v} \in T_p \mathcal{M}$ . Conversely, the projection of  $\nabla f|_p$  onto the tangent space  $T_p \mathcal{M}$  is known as the *Riemannian gradient*  $\text{grad } f(p)$ . There are other ways to produce descent directions: For example, [47, Alg. 6.3 (Riemannian trust-region)] or [4, Alg. 5 (Riemannian Newton method)]. No matter how a descent direction is produced, the idea is to move from  $p \in \mathcal{M}$  to  $p + \mathbf{v} \notin \mathcal{M}$ , and then *retract* back to the manifold in such a way as to approximate the exponential map. In particular, every algorithm in Riemannian optimization requires a retraction map if no explicit exponential map is available. This chapter is focused purely on the computation of the retraction  $R_p(\mathbf{v})$ .

**Definition 3.2.1.** Let  $\mathcal{M} \subset \mathbb{R}^n$  be a manifold and  $p \in \mathcal{M}$  a point. A (*first-order*) *retraction* at  $p$  is a smooth map  $R_p : T_p \mathcal{M} \rightarrow \mathcal{M}$  satisfying

1.  $R_p(0) = p$ , and
2.  $d(R_p)(0) : T_p \mathcal{M} \rightarrow T_p \mathcal{M}$  is the identity map.

Equivalently, for each curve  $c : (-\epsilon, \epsilon) \subset \mathbb{R} \rightarrow \mathcal{M}$  with  $c(t) = R_p(tv)$  for some  $v \in T_p \mathcal{M}$  we have  $c'(0) = v$  and  $c(0) = p$ . A *local retraction at  $p$*  is a retraction defined in some neighborhood of  $0 \in T_p \mathcal{M}$ , while still satisfying the same two properties above.

A retraction is called *second-order* if, in addition, for all  $v \in T_p \mathcal{M}$

$$\frac{d^2}{dt^2} R_p(tv)|_{t=0} \in N_p \mathcal{M}.$$

This implies that the curve  $R_p(tv)$  matches geodesics on  $\mathcal{M}$  up to second order at  $t = 0$ , i.e.  $R_p(tv) = \text{geodesic}(t; p, v) + O(t^3)$  as  $t \rightarrow 0$  [5, Prop. 3].

We note that a retraction map has a different definition in topology, although they are related. Our Definition 3.2.1 is appropriate in the context of *Riemannian optimization*, and matches the definition in the textbooks [4, 47], for instance. Retractions were first defined in Adler et al. [7]. In the more general setting of Section 3.7, we consider Riemannian submanifolds of a Riemannian manifold which is not Euclidean space. In that case, the condition for a second-order retraction must instead be that the covariant derivative of the vector field defined by the velocity of the curve  $R_p(tv)$  lies in the normal space at  $t = 0$  [47, Def. 8.64 and Eqn. 8.27]. The definition of a first-order retraction remains the same, since a manifold's tangent space is independent of the metric. We delay the additional technical details until later.

By a result in Absil and Malick [5], finding the closest point with respect to Euclidean distance defines a local retraction (cf. Definition 3.2.1) on any submanifold of Euclidean space.

**Theorem 3.2.2** (cf. [5]). *Let  $\mathcal{M} \subset \mathbb{R}^n$  be a smooth manifold or real algebraic variety. For any smooth point  $p \in \mathcal{M}$ , define the relation  $R_p \subset T_p \mathcal{M} \times \mathcal{M}$  by*

$$R_p = \{(v, u) \in \mathbb{R}^n \times \mathbb{R}^n : u \in \arg \min_{y \in \mathcal{M}} \|p + v - y\|\}^8.$$

*There exists a neighborhood  $U$  of 0 in  $T_p \mathcal{M}$  such that  $R_p$  defines a local, second-order retraction.*

**Example 3.2.3.** Denote the unit sphere in  $\mathbb{R}^n$  by  $S^{n-1}$ . The expression

$$R_x(v) = \frac{x + v}{\|x + v\|}$$

provides a smooth map  $R : TS^{n-1} \rightarrow S^{n-1}$ .

As can be easily checked, this formula defines a retraction, called the Euclidean distance retraction, which admits an explicit formula in this simple example. Consequently, we can rewrite

$$R_x(v) = \arg \min_{y \in S^{n-1}} \|y - (x + v)\|.$$

---

<sup>8</sup>The *arguments of the minima*  $\arg \min_{x \in S} f(x)$  of a function  $f : S \rightarrow \mathbb{R}$  are given by the collection of points  $x^* \in S$  such that  $f(x^*) \leq f(x)$  for all  $x \in S$ .

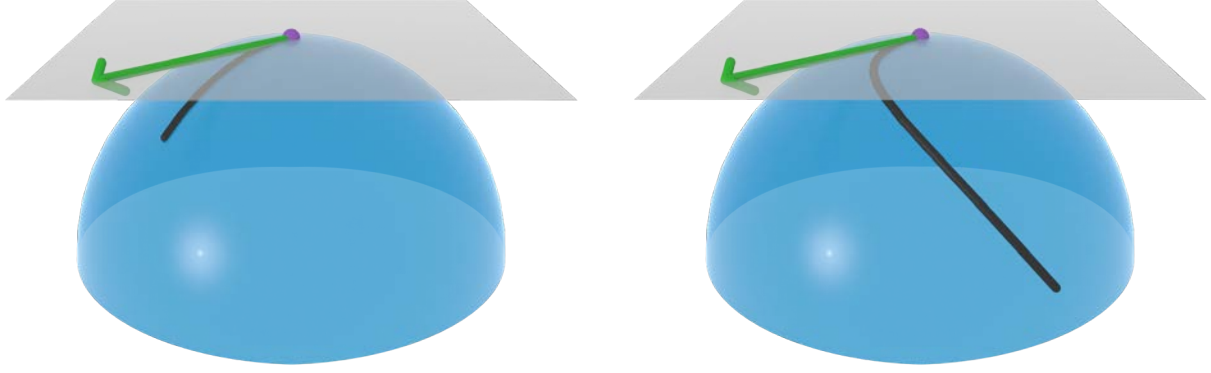


**Figure 3.2.4:** Given the sphere  $S^2$  (blue) and a point  $p = (0, 0, 1) \in S^2$  (purple), consider the tangent space  $T_p S^2$  (gray) and choose a vector  $v = (-1, -1, 0) \in T_p S^2$  (green). The second-order retraction  $R_p(tv)$  from Example 3.2.3 (l.) and the first-order retraction  $t \mapsto R_p(tv + 100 \cdot t^4(1, -1, 0))$  (r.) are depicted in black. Clearly, the projection of  $tv$  is preferable, as its acceleration is controlled locally. This allows us to more reliably maintain the direction dictated by the tangent vector  $v$ .

The arg min is unique in every point except 0 and never equals  $x + v$ . For  $n = 3$ , this retraction is juxtaposed with a first-order retraction on the sphere in Figure 3.2.4.

The construction of a retraction  $R$  that arises from a closest point problem is a constraint optimization problem on the manifold  $\mathcal{M}$  as well. Using the variables  $(x, \lambda) \in \mathbb{R}^n \times \mathbb{R}^m$ , we can formulate it as a Lagrange multiplier problem of the following form:

$$\mathcal{L}(x, \lambda; u) = \frac{1}{2} \sum_{i=1}^n (x_i - u_i)^2 + \lambda^T \cdot g(x)$$

with the parameter  $u = p + v$  in this case.  $\mathcal{L}$ 's zeros encode the critical points of the underlying optimization problem [234, Thm. 12.1]. This leads to the system of equations

$$0 = G(x, \lambda; u) = \nabla_{x, \lambda} \mathcal{L}(x, \lambda; u) = \begin{pmatrix} x - u + \sum_{i=1}^n \lambda_i \cdot \nabla_x g_i(x) \\ g(x) \end{pmatrix} \quad (3.2.5)$$

that we will call the *Lagrange multiplier system* from now on. Notice that  $G$  is a map  $\mathbb{R}^n \times \mathbb{R}^m \rightarrow \mathbb{R}^n \times \mathbb{R}^m$  for any fixed parameter  $u \in \mathbb{R}^n$ , meaning that  $G$  is a square system.

**Example 3.2.6.** Choose  $\mathcal{M} = O_n$  the orthogonal group. Denote by

$$qr : GL_n(\mathbb{R}) \rightarrow O(n) \times S_{upp}^+(n)$$

the QR decomposition of a real, invertible  $n \times n$  matrix into an orthogonal matrix and an upper triangular matrix with strictly positive diagonal entries. Notice that  $GL_n(\mathbb{R})$  is the complement of a hypersurface in  $\mathbb{R}^{n \times n}$ , cut out by  $\{A \in \mathbb{R}^{n \times n} \mid \det(A) \neq 0\}$ . Then, the map

$$R_X(\xi) = \pi_1(qr(X + \xi))$$

is a (local) retraction on the orthogonal group's tangent bundle  $TO(n)$  with  $\pi_1$  the projection onto its first argument from  $O(n)$ . A proof can be found in [4, Ex. 4.1.2].

In general, the Euclidean distance retraction will not admit an explicit formula, except in special cases like those above. In case an explicit formula is not available, it is desirable to develop techniques for computing the Euclidean distance retraction on arbitrary, implicitly defined manifolds. This is accomplished by Algorithm ED2, named after the acronym for “Euclidean Distance”.

For the moment, let us assume that we already know a retraction  $R$ . The corresponding step sizes are treated as given and are later explicitly constructed. Utilizing all these concepts, we formulate the following algorithm for the minimization of an objective function on a Riemannian manifold. It highlights why the Euclidean distance retraction is useful to know. A less specific version can be found in Boumal [47, p.55].

---

**Algorithm 3.2.7:** Riemannian gradient descent

---

**Inputs :** An embedded manifold  $\mathcal{M}$ ,

starting point  $x_0 \in \mathcal{M}$ ,  
 a sequence of step sizes  $(\alpha_k)_{k \in \mathbb{N}_0}$ ,  
 objective function  $f : \mathcal{M} \rightarrow \mathbb{R}$ ,  
 tolerance  $0 < \tau \in \mathbb{R}$  and  
 retraction map  $R$ .

**Output:** Critical point  $x_n \in \mathcal{M}$  with  $|\mathbf{v}_n| \leq \tau$ .

```

k=0
while  $|\mathbf{v}_k| > \tau$  do
     $\mathbf{v}_k = -\text{grad } f(x_k)$ 
     $x_{k+1} = R_{x_k}(\alpha_k \mathbf{v}_k)$ 
     $k = k + 1$ 
end

```

---

### 3.2.2 Homotopy Continuation

In this section, we provide a brief overview of homotopy continuation, a method to compute the retraction  $R_p(v)$ . Given a system of equations  $f(x) = 0$  whose solutions are unknown, homotopy continuation seeks to deform the known solutions of another system  $g(x) = 0$  into the previously unknown solutions of  $f(x) = 0$ . One usually embeds both systems into a parametrized family of systems of equations  $h(x; u) = 0$  such that  $g(x) = h(x; u_0)$ , while  $f(x) = h(x; u_1)$ . Choose a continuous path  $u(t)$  between  $u_0$  and  $u_1$ . Then,  $\frac{d}{dt}h(x(t); u(t)) = 0$  is a system of ordinary differential equations whose solution  $x(t)$  encodes a path between the known solution  $g(x(0)) = h(x(0); u(0)) = 0$  and the unknown solution  $f(x(1)) = h(x(1); u(1)) = 0$ . These ODEs are easy to solve numerically, since at any  $t \in [0, 1]$  we know that the solution  $x(t)$  satisfies the system of equations  $h(x; u(t)) = 0$ . Therefore, we may apply Newton's method to correct any errors arising during numerical path-tracking. This procedure is called homotopy continuation. Already, there exists efficient software specially designed for solving the ODEs arising in this

setup, see for example [31, 54, 76, 201, 319].

For our problem, we view the Lagrange multiplier system  $G(x, \lambda; u) = 0$  (cf. Equation (3.2.5)) as parametrized by  $u$ . Taking  $u = p$  gives us a system with known solution  $(x, \lambda) = (p, 0)$ . Conversely,  $u = p + v$  yields a system of equations, whose solutions include  $(x = R_p(v), \lambda^*)$  for some  $\lambda^*$  we ignore. An issue that can occur while solving the homotopy's associated Davidenko differential equations (cf. [92]) is that for some parameter value  $u(t)$  the Jacobian of the system of equations becomes singular, before reaching  $t = 1$ . Numerical path-tracking may drastically fail if this occurs. For that reason, one usually chooses a path  $u(t)$  through complexified parameter space. The complex parameter values with singular Jacobian form a set of complex codimension one, and real codimension two. Hence, a random path  $u(t)$  in complexified space avoids the bad parameter values with probability one (cf. [299, Lem. 7.1.2]). The associated price of this approach is that a real-valued solution  $x(0)$  may become a complex-valued solution  $x(1)$  by the end of the homotopy. See Figure 3.2.8 for an example. Since we are only interested in one particular real solution  $x = R_p(v)$ , this poses an issue.

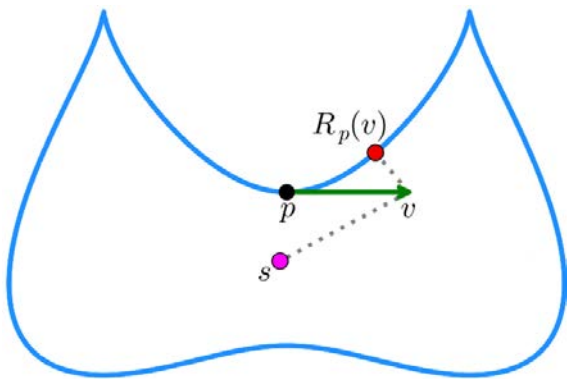


**Figure 3.2.8:** Consider the bicusp-shaped curve  $\mathcal{C}_a = \{(x, y) : (y^2 - a^2) \cdot (y - a)^2 + (x^2 - a^2)^2 = 0\}$  for  $a = 1.5$  with initial point  $p = (0, 0)$  and tangent direction  $v = (1, 0)$  as an example. Using a homotopy in complex parameter space whose starting parameter is too far away from  $p$  in  $\mathcal{C}_a$ 's normal space at  $p$ , results in a complex-valued critical point  $s$  (magenta) the real part of which is depicted here. If instead, we start closer to  $p$ , the intended critical point  $R_p(v)$  (red) is found.  $(p + v)$  lies in the affine linear space  $q + N_q \mathcal{C}_a \subset \mathbb{C}^2$  for both points  $q \in \{s, R_p(v)\}$ .

A solution to this problem is provided by Lemma 3.3.3, which we prove in Section 3.3.2. It is the main theoretical result underlying our method, stating that if we choose a real-valued parameter path  $u(t)$  that stays within a certain distance from  $\mathcal{M}$ , the relevant Jacobian is always invertible. This Lemma only applies to the Lagrange multiplier system of equations specific to our problem. As a result, we may confidently apply homotopy continuation utilizing the complex numbers. By the tubular neighborhood theorem, we can ensure that the final solution is the real-valued  $R_p(v)$ , rather than a different, undesired critical point. All of this works provided that our path  $u(t)$  between  $p$  and  $p + v$  stays sufficiently close to  $\mathcal{M}$ .

**Remark 3.2.9.** While the results we prove in this chapter depend on the fact that we solve the closest-point-problem, the ideas can be generalized to a simple path-tracking algorithm to solve any homotopy in  $\mathbb{C}^n$ , parametrized by a path  $u(t)_{t \in [0,1]} \subset \mathbb{C}^m$  (cf. [32]).

In particular, given two square systems of equations  $g, h : \mathbb{C}^n \rightarrow \mathbb{C}^n$  together with a point  $z_0$  where  $g$  vanishes, we can form a linear homotopy from  $g$  to  $h$  by setting

$$H(z; t) = \gamma t g(z) + (1 - t) h(z)$$

for some random  $\gamma \in \mathbb{C}$ . This is called the *gamma trick* and it is introduced to ensure that  $H(z; t)$  is a nonsingular homotopy [223]. Then, we can track the solution of the system of equations  $H(z; t) = 0$  at  $t \in [0, 1]$  using Algorithm 3.2.10 starting at  $z_0$  to discover a solution  $z_1$  such that  $H(z_1; 1) = h(z_1) = 0$ .

---

**Algorithm 3.2.10:** Path-tracking algorithm (cf. [299, p.22f.])

---

**Inputs :** A homotopy  $H(x; u) : \mathbb{C}^n \times \mathbb{C}^m \rightarrow \mathbb{C}^n$  with  $x(u_1)$  known and

a grid  $0 = t_0 < t_1 < \dots < t_N = 1$ .

**Output:** A solution of  $H(x; u_1) = 0$ .

Set  $w_0 = x(u_0)$ .

**for**  $j \in \{0, \dots, N - 1\}$  **do**

Predict  $w = w_j + \Delta x$ , e.g. by solving  $\frac{\partial H}{\partial x}(w_j, t_j)\Delta x = -\frac{\partial H}{\partial t}(w_j, t_j)h$  (Euler's method).

Correct  $w$  by solving  $H(x, t_{j+1}) = 0$  (Newton's method), yielding  $w_{j+1}$ .

**end**

**return**  $w_N = x(u_0)$

---

In the case of polynomial systems with  $d$  isolated solutions, tracking all solutions simultaneously comes with theoretical guarantees that all solution paths are smooth [299, Thm. 7.1.1]. Furthermore, we can expect that all isolated nonsingular solutions are found this way, provided that the number of nonsingular solutions agrees in both systems [299, Thm. 8.3.1].

### 3.3 Algorithms and Theoretical Results

As the experiments in Section 3.10 will demonstrate, using homotopy continuation allows us to compute the Euclidean distance retraction  $R_p(v)$  more reliably than purely using Newton's method would. Adding novel contributions to the body of literature, we prove theoretical results (Theorem 3.3.7 and Corollary 3.3.13) that partially explain this increased reliability. Starting from this section, we introduce new results that build upon the existing work.

Let  $\mathcal{M} = g^{-1}(0)$ , where  $g : \mathbb{R}^n \rightarrow \mathbb{R}^m$  is a smooth map and  $n - m = \dim(\mathcal{M})$ . In what follows, let  $dg_x$  denote the  $m \times n$  Jacobian matrix of  $g$  in the standard basis, evaluated at the point  $x$ , and let  $dg_x^T$  denote the  $n \times m$  transpose matrix. Given a point  $p \in \mathcal{M}$ , and a descent direction  $v \in T_p\mathcal{M}$ , the idea is to move from  $p \in \mathcal{M}$  to  $p + v \notin \mathcal{M}$ , and then retract back to  $\mathcal{M}$  in such a way as to approximate the exponential map to second-order accuracy. Theorem 3.2.2 of Absil and Malick [5] shows that computing the Euclidean closest point  $R_p(v)$  achieves this goal.

### 3.3.1 Newton's Method

One method to find  $R_p(v)$  is to apply Newton's method to the Lagrange multiplier system in Equation (3.2.5). Set  $u = p + v$ . Recall from Section 3.2.1 that the Lagrange multiplier system for the closest point to  $u$  on  $\mathcal{M}$  is denoted by  $G(x, \lambda; u)$  and is a square system.

We view  $u \in \mathbb{R}^n$  as a parameter, and  $(x, \lambda)$  as variables. Then any solution  $(x_u, \lambda_u)$  of  $G(x, \lambda; u) = 0$  for fixed  $u = p + v$  encodes a point  $x_u \in \mathcal{M}$  which is first-order critical for Euclidean distance from  $u$  to  $\mathcal{M}$ . Among those critical points is the correct solution  $R_p(v)$ .

By applying Newton's method to  $G(x, \lambda; u) = 0$  one hopes to find the correct solution  $x_u = R_p(v)$ . A problem is that Newton's method may diverge, or converge slowly. Consider for example the twisted cubic  $\mathcal{C}$ , parametrized by  $t \mapsto (t, t^2, t^3)$ . Figure 3.3.1 shows part of the normal space at  $(1, 1, 1)$  with points where Newton's method exceeds 10 iterations to converge displayed in red.

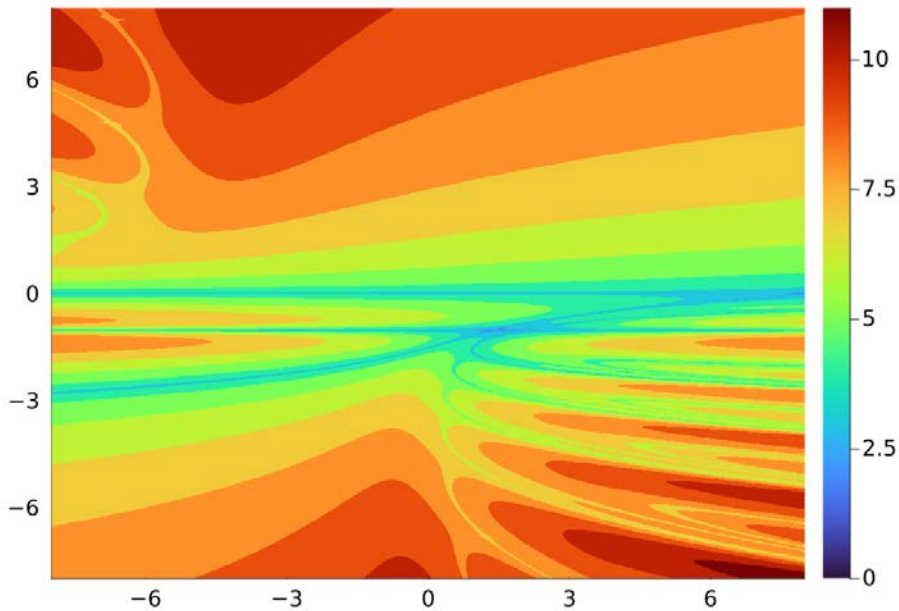


**Figure 3.3.1:** Representation of the twisted cubic's normal space at  $p = (1, 1, 1)$  with the picture's origin corresponding to  $p$ . The colors show how many iterations Newton's method takes to converge.

Even if Newton's method converges, the solution  $x_u$  may not be  $R_p(v)$ , but instead some other critical point. Newton's method is not guaranteed to converge to the closest solution to the starting point. These problems disappear if we find an initial guess  $(x_0, \lambda_0)$  close enough to the desired solution  $G(R_p(v), \lambda_u; u = p + v) = 0$ . This is where homotopy continuation plays a

role. We summarize the discussion from this section in pseudocode below.

---

**Algorithm ED0:** Computing  $R_p(v)$  by Newton's method

---

**Inputs :** A point  $p \in \mathcal{M}$ , vector  $v \in T_p\mathcal{M}$ .

**Output:** The Euclidean distance retraction  $R_p(v)$ .

Apply Newton's method to the system  $G(x, \lambda; p + v) = 0$  with initial point  $(p, 0)$ , obtaining the solution  $R_p(v) = (x^*, \lambda^*)$ .

---

### 3.3.2 Homotopy Continuation by Newton's Method

In order to prove some convergence results (Theorem 3.3.7 and Corollary 3.3.13), we will first analyze a simplified version of homotopy continuation which uses corrector steps, but omits the predictor step. Consider the curve  $u(t) = p + tv$  with  $t \in [0, 1]$ ,  $u(0) = p$  and  $u(1) = p + v$ . Instead of applying Newton's method only to  $G(x, \lambda; u(1)) = 0$ , we partition the interval  $[0, 1]$  as  $0 = t_0 < t_1 < \dots < t_m < t_{m+1} = 1$  with  $m$  intermediate steps and apply Newton's method to each system  $G(x, \lambda; u(t_j)) = 0$ , using the previous solution as the initial guess for the next. This approach is conceptualized in Algorithm ED1. Since most homotopy continuation algorithms consist of predictor steps and corrector steps, the distinguishing feature of Algorithm ED1 is its use only of corrector steps, and no predictor steps.

---

**Algorithm ED1:** Computing  $R_p(v)$  by continuation using only corrector steps

---

**Inputs :** A point  $p \in \mathcal{M}$ , vector  $v \in T_p\mathcal{M}$ , and a partition

$$0 = t_0 < t_1 < \dots < t_m < t_{m+1} = 1.$$

**Output:** The Euclidean distance retraction  $R_p(v)$ .

Set  $x(t_0) = p$  and set  $\lambda(t_0) = 0$ . Let  $u(t) = p + tv$ .

**for**  $j \in \{1, 2, \dots, m + 1\}$  **do**

| Apply Newton's method to the system  $G(x, \lambda; u(t_j)) = 0$  with initial point

|  $(x(t_{j-1}), \lambda(t_{j-1}))$ , obtaining a solution  $(x^*, \lambda^*)$ . Set  $x(t_j) = x^*$  and  $\lambda(t_j) = \lambda^*$ .

**end**

---

Notice that Algorithm ED1 is identical to Algorithm ED0 when  $m = 0$ . For  $m > 0$ , Algorithm ED1 may seem worse than Algorithm ED0, because it requires repeated applications of Newton's Method. However, if each intermediate solution lies in the next solution's region of quadratic convergence, this approach will guarantee convergence to the correct point  $R_p(v)$  and hence avoid jumping connected components. This will be made more precise in Theorem 3.3.7 and Corollary 3.3.13. For now, a qualitative illustration of this method can be found in Figure 3.3.2.

The additional computational cost is a price we are willing to pay within the context of many problems involving geometric constraint systems. For instance, Algorithm ED0 repeatedly failed for Example 6 in Section 3.10, which is given by the tensegrity model for cylinder packings that is more thoroughly discussed in Section 5. This failure provided our initial motivation for investigating homotopy continuation in the first place. First, we prove a technical lemma on

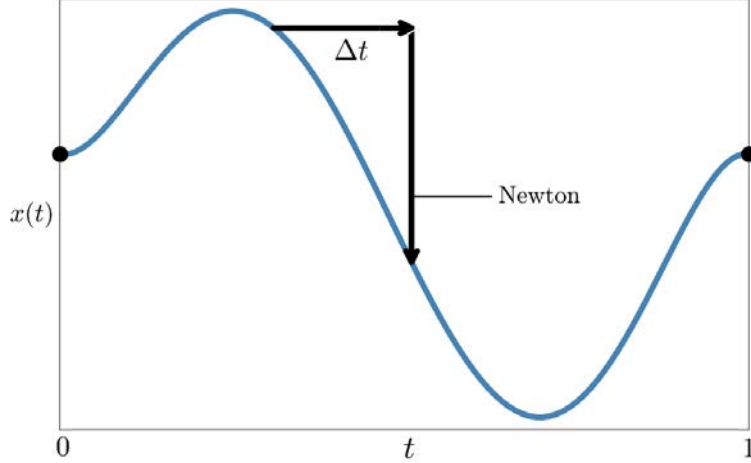


**Figure 3.3.2:** Algorithm ED1 is an intuitive approach to approximate the curve  $x(t) = R_p(tv)$ .

After discretizing the interval  $[0, 1]$ , Newton's method is applied to each subinterval in order to stay on the solution curve.

which our other results depend.

**Lemma 3.3.3.** Let  $\mathcal{M} = g^{-1}(0)$  for some  $C^2$  map  $g : \mathbb{R}^n \rightarrow \mathbb{R}^m$  and let  $u^* \in \mathbb{R}^n$  be given. Let  $x^*$  be the closest point on  $\mathcal{M}$  to  $u^*$  and assume that  $dg(x^*)$  has full rank. If

$$|u^* - x^*| < \frac{1}{|S|} \sum_{i \in S} \frac{|\nabla g_i(x^*)|}{|d^2 g_i(x^*)|} \quad \text{for } S = \{i \in \{1, \dots, m\} : |d^2 g_i(x^*)| \neq 0\}, \quad (3.3.4)$$

then  $\frac{\partial G}{\partial(x, \lambda)}(x^*, \lambda^*)$  is invertible for any Lagrange multiplier  $\lambda^* \in \mathbb{R}^m$  such that  $G(x^*, \lambda^*) = 0$ .

In the formula above  $|u^* - x^*|$  and  $|\nabla g_i(x^*)|$  are the Euclidean norms on  $\mathbb{R}^n$ ,  $d^2 g_i(x^*)$  is the Hessian of  $g_i$  at the point  $x^*$ , and  $|d^2 g_i(x^*)|$  denotes the induced matrix norm. If  $|d^2 g_i(x^*)| = 0$  for all  $i$ , we interpret the right side of (3.3.4) as  $\infty$  and again claim that  $\frac{\partial G}{\partial(x, \lambda)}(x^*, \lambda^*)$  is invertible.

*Proof.* Recall  $G(x, \lambda; u) = (g(x), dg_x^T \lambda - u + x)$  and so  $\partial G/\partial(x, \lambda)$  has a block structure

$$\begin{bmatrix} dg(x)^T & 0 \\ I_n + \sum_{i=1}^m \lambda_i d^2 g_i(x) & dg(x) \end{bmatrix}.$$

To avoid a proliferation of stars we will omit the \* in  $x^*, \lambda^*, u^*$  in the calculations below. Knowing that  $G(x, \lambda, u) = 0$ , then  $dg_x^T \lambda = u - x$  and we obtain after taking norms and applying subadditivity:

$$|u - x| = \left| \sum_{i=1}^m \lambda_i \nabla g_i(x) \right| \leq \sum_{i=1}^m |\lambda_i \nabla g_i(x)| = \sum_{i=1}^m |\lambda_i| |\nabla g_i(x)|. \quad (3.3.5)$$

As  $dg(x)$  has full rank, the matrix  $\partial G/\partial(x, \lambda)$  is invertible if and only if  $I_n + \sum_{i=1}^m \lambda_i d^2 g_i(x)$  is invertible. This is precisely the case when all eigenvalues of the matrix  $A = \sum_{i=1}^m \lambda_i d^2 g_i(x)$  are different from  $-1$  since all involved matrices are symmetric. The spectral radius is the maximum modulus of all eigenvalues. Also, the spectral radius is less than or equal to any matrix norm

induced from a norm on the vector space. Assuming that  $|A| < 1$  thus implies that  $\partial G/\partial(x, \lambda)$  is invertible. If  $|dg_i^2(x)| = 0$  for all  $i$ , it holds that  $|A| = 0$ , implying that  $\partial G/\partial(x, \lambda)$  is invertible.

Otherwise, we can ensure that  $|A| < 1$  because

$$\left| \sum_{i=1}^m \lambda_i d^2 g_i(x) \right| \leq \sum_{i \in S} |\lambda_i| |d^2 g_i(x)| \quad \text{for } S = \{i \in \{1, \dots, m\} : |d^2 g_i(x)| \neq 0\},$$

by assuming for each  $i$  that  $|\lambda_i d^2 g_i(x)| < \frac{1}{|S|}$ . Equivalently,  $|\lambda_i| < \frac{1}{|S| \cdot |d^2 g_i(x)|}$  for all  $i \in S$ . Inserting this into inequality (3.3.5), we see that if

$$|u - x| < \sum_{i \in S} \frac{|\nabla g_i(x)|}{|S| |d^2 g_i(x)|} + \sum_{i \notin S} |\lambda_i \nabla g_i(x)|$$

then the matrix  $\partial G/\partial(x, \lambda)$  is invertible. In particular, the theorem's assumption implies this inequality, proving the claim.  $\square$

To interpret the constant  $S$ , we can consider the lemma's proof. Commonly, the Hessian  $d^2 g_i(x)$  is constantly zero when  $g_i$  is linear. However, it can also happen that a constraint is a homogeneous polynomial of degree at least 3, which would lead to the Hessian vanishing in 0. In the proof, it appears as though we are ignoring these contributions to  $\partial G/\partial(x, \lambda)$ , even though linear constraints are as well-behaved as possible. For the lower-left block of  $\partial G/\partial(x, \lambda)$  to be invertible and using the same approach as in the proof, we would need to bound each  $|\lambda_i d^2 g_i(x)|$  from above by  $1/m$ , which is smaller than  $1/|S|$  by the construction of  $S$ . Therefore, we have already taken these well-behaved cases with vanishing Hessian into account in the lemma's proof. In Section 3.10 we discuss two examples of how the inequality (3.3.7) behaves on plane curves.

Note that for bar-joint frameworks, which are one of the simplest and most common geometric constraint systems, each  $g_i$  records the squared length of the  $i$ -th bar, with variables corresponding to the coordinates of each vertex. In that case, Lemma 3.3.3 admits an especially nice formula in terms of the framework's average bar length.

**Corollary 3.3.6.** *Assume we are given a bar-joint framework  $\mathcal{F} = ((V, E), p : V \rightarrow \mathbb{R}^d)$  that is realized in an arbitrary dimension  $d$  with bar length equations*

$$g_{ij}(p) = |p_i - p_j|^2 - \ell_{ij}^2$$

*for a given set of lengths  $\ell_{ij} > 0$  with  $ij \in E$  and the realization's  $d$  coordinates  $p_i$  at vertex  $i \in V$ . Let  $u^* \in \mathbb{R}^{d|V|}$  be given, let  $x^*$  be the closest point on  $\mathcal{M} = g^{-1}(0) \subset \mathbb{R}^{d|V|}$  to  $u^*$  and assume that  $dg(x^*)$  has full rank. If*

$$|u^* - x^*| < \frac{\sqrt{2}}{2} \cdot \frac{\sum_{ij \in E} \ell_{ij}}{|E|},$$

*then  $\frac{\partial G}{\partial(x, \lambda)}(x^*, \lambda^*)$  is invertible for any Lagrange multiplier  $\lambda^* \in \mathbb{R}^{|E|}$  such that  $G(x^*, \lambda^*) = 0$ . In particular, this expression is independent of the dimension the framework is realized in.*

*Proof.* Differentiating the bar length equations, for any  $ij \in E$  we find that

$$\nabla g_{ij}(x^*) = (0, \dots, 0, \underbrace{2(p_i - p_j)}_{d(i-1)+1, \dots, di}, 0, \dots, 0, \underbrace{2(p_j - p_i)}_{d(j-1)+1, \dots, dj}, 0, \dots, 0)^T.$$

Hence,  $|\nabla g_{ij}(x^*)| = \sqrt{4\ell_{ij}^2 \cdot 2} = 2\sqrt{2} \cdot \ell_{ij}$ . From this expression, we can derive a formula for  $g_{ij}$ 's Hessian. It takes the value 2 in the positions  $(n, n)$  for  $n = d(i-1) + 1, \dots, di, d(j-1) + 1, \dots, dj$  and  $-2$  in the positions  $(n, n+di-dj)$  with  $n = d(i-1) + 1, \dots, di$  and in the positions  $(n, n+di-dj)$  with  $n = d(j-1) + 1, \dots, dj$ . Consequently, each of the Hessian's rows and columns only contains a single 2 and  $-2$  with the positive value on the matrix's diagonal and the negative values at the transposed positions  $(i, j)$  and  $(j, i)$ . By assumption,  $\mathbb{R}^{d|V|}$  is equipped with the Euclidean norm, so the induced matrix norm is the spectral norm. It is given by the largest singular value, i.e., the square root of the largest eigenvalue of the matrix  $A^T A$ . The Hessian matrix  $d^2 g_{ij}(x^*)$  is symmetric, implying that its spectral norm is equal to the spectral radius [15, p.51], the largest absolute value among the matrix' eigenvalues. It can be easily checked that, for example, the matrix has an eigenvalue 4 corresponding to the eigenvector that is 1 in position  $di$ ,  $-1$  in position  $dj$ , and 0 everywhere else.

Since the spectral radius is majorized by any matrix norm [15, p.51], we can without loss of generality compute the induced matrix norm of  $\|\cdot\|_\infty$ , which is given by the absolute row sum norm. For the Hessian  $d^2 g_{ij}(x^*)$  it is 4 by construction; the Hessian's operator norm is 4 as well. Assembling both results, we find that

$$\frac{|\nabla g_{ij}(x^*)|}{|d^2 g_{ij}(x^*)|} = \frac{2\sqrt{2}}{4} \ell_{ij} = \frac{\sqrt{2}}{2} \ell_{ij}.$$

Finally, as we have already shown that all of the Hessians' operator norms are nonzero, it holds that  $|S| = |E|$ . Using Lemma 3.3.3, this proves the claim.  $\square$

For a generic realization, the condition that the Jacobian has full rank is equivalent to the framework's independence in the rigidity matroid [176]. In  $\mathbb{R}^2$ , this is characterized by the underlying graph's  $(2, 3)$ -sparsity, meaning that for every induced subgraph  $G' = (V', E(V'))$  of  $G = (V, E)$ , it holds that  $|E(V')| \leq 2|V'| - 3$ . Geometrically, this means that the framework contains no redundant edges: Deleting any of the graph's edges reduces the rigidity matrix's rank (cf. Definition 2.1.13). For the rigidity matroid in higher dimensions, there currently exists no combinatorial criterion only in terms of the graph.

In general, Newton's method may diverge or converge to the wrong point. However, for the problem of computing the retraction  $R_p(v)$  we can now prove the following

**Theorem 3.3.7.** *Let  $g : \mathbb{R}^n \rightarrow \mathbb{R}^m$  be three times continuously differentiable. Let  $\mathcal{M} = g^{-1}(0) \subset \mathbb{R}^n$  be a smooth manifold with  $dg_x$  having full rank for every  $x \in \mathcal{M}$ , and let  $u(t)$  be a smooth path in  $\mathbb{R}^n$  staying within the tubular neighborhood of  $\mathcal{M}$  for which there is a unique closest point. For each  $t$ , let  $x(t)$  be the closest point to  $u(t)$ . If the path  $u(t)$  satisfies*

$$\text{dist}(u(t), x(t)) < \frac{1}{|S(t)|} \sum_{i \in S(t)} \frac{|\nabla g_i(x(t))|}{|d^2 g_i(x(t))|}$$

for all  $t \in [0, 1]$  where  $S(t) = \{i : |d^2 g_i(x(t))| \neq 0\}$ , then there exists a partition  $0 = t_0 < t_1 < \dots < t_m < t_{m+1} = 1$  such that each of the  $m + 1$  applications of Newton's method in Algorithm ED1 converges quadratically. Hence Algorithm ED1 converges and outputs the correct  $R_p(v)$ .

*Proof.* For each  $u(t)$ , let  $z(t)$  denote the pair  $(x(t), \lambda(t))$  of the closest point on  $\mathcal{M}$  to  $u(t)$  and its associated Lagrange multiplier. We need to show that any partition of  $[0, 1]$  may be refined until  $(x(t_j), \lambda(t_j))$  lies in the region of convergence of Newton's method applied to  $G(x, \lambda; u(t_{j+1})) = 0$ , and so may be used as a starting point for the Newton iteration with guaranteed convergence.

Let  $G'$  denote  $\partial G / \partial (x, \lambda)$ . By Lemma 3.3.3,  $G'(z(t); u(t))$  is invertible and hence by the implicit function theorem we can solve locally for  $z$  in terms of  $u$ . Thus the smooth path  $u(t)$  gives rise to a smooth path  $z(t)$  such that  $G(z(t); u(t)) = 0$  for all  $t$ . The path  $\{(z(t), u(t)) : t \in [0, 1]\}$  is compact and every point has a neighborhood  $U = B_{\delta(t)}(z(t)) \times B_{\delta(t)}(u(t))$  such that if  $(z_0, u_0) \in U$  then  $G'(z_0; u_0)^{-1}$  exists. This is true because by Lemma 3.3.3 we know  $G'(z(t); u(t))^{-1}$  exists and  $G'(z; u)^{-1}$  is continuous in  $z$  and  $u$ . By compactness there exists  $r > 0$  such that for all  $t$ , if  $z_0 \in \overline{B_r(z(t))} =: K_t$  then  $G'(z_0; u(t))^{-1}$  exists.

In preparation for using Taylor's theorem to prove convergence of Newton's method, define

$$M(t) = \sup \frac{1}{2} |G'(w_0; u(t))^{-1}| |G''(w_1; u(t))|,$$

where the supremum is taken over all  $(w_0, w_1) \in K_t \times K_t$ . Then  $M(t)$  is a continuous function of  $t$  and attains its maximum value  $M \geq 0$  over  $t \in [0, 1]$ . By refining any initial partition, we may find a partition  $0 = t_0 < t_1 < \dots < t_s = 1$  such that

$$|z(t_i) - z(t_{i+1})| < \min\{r, 1/M\}.$$

If  $M \equiv 0$ , we interpret  $1/M$  as infinity and the minimum becomes  $r$ . Let  $z_u$  denote the closest point and Lagrange multiplier pair corresponding to  $u$ . By Taylor's theorem, for any  $z_n \in \mathbb{R}^n \times \mathbb{R}^m$  we have

$$0 = G(z_u; u) = G(z_n; u) + G'(z_n; u)(z_u - z_n) + \frac{1}{2} G''(\tilde{z}; u)(z_u - z_n, z_u - z_n), \quad (3.3.8)$$

for some  $\tilde{z}$  lying on the line segment between  $z_n$  and  $z_u$ . Newton's method sets

$$z_{n+1} = z_n - G'(z_n; u)^{-1} G(z_n; u). \quad (3.3.9)$$

Use (3.3.8) to replace  $G(z_n; u)$  in (3.3.9), rearrange, and take norms to obtain

$$\begin{aligned} |z_{n+1} - z_u| &= \frac{1}{2} |G'(z_n; u)^{-1} G''(\tilde{z}; u)(z_u - z_n, z_u - z_n)| \\ &\leq \frac{1}{2} |G'(z_n; u)^{-1}| |G''(\tilde{z}; u)| |z_u - z_n|^2. \end{aligned}$$

Let  $e_n = |z_n - z_u|$ . Then, by induction we have  $e_n \leq \frac{1}{M} (Me_0)^{2^n}$  so that if  $e_0 < 1/M$  we have  $e_n \rightarrow 0$  and Newton's method converges. Since  $|z(t_i) - z(t_{i+1})| < \min\{r, 1/M\}$  we see that  $z(t_i) \in \overline{B_r(z(t_{i+1}))}$ , along with any point on the line segment between, so that using  $z(t_i)$  as the initial point for Newton's method applied to  $G(z; u(t_{i+1})) = 0$  implies that  $|z(t_i) - z(t_{i+1})| =$

$e_0 < 1/M$ , which completes the proof.  $\square$

In practice, rather than applying Newton's method, we use the more general Gauss-Newton method [135] by applying the Jacobian's pseudoinverse rather than its inverse to solve the linear system associated to Newton's method. Given a general linear system of the form  $Ax = b$ , the normal equation is the square linear system  $A^T A x = A^T b$  [15, p.126]. It can be solved using the Moore-Penrose pseudoinverse  $A^\dagger$ , providing a minimum norm least squares solution [15, Prop. 7.2.1]. If the system  $Ax = b$  has a solution, this approach finds it: The least squares solution  $x$  with  $\|Ax - b\|^2 = 0$  is equivalent to  $Ax = b$ . Finally, our matrices are not overly large for numerical linear algebra packages, making this method feasible. In particular, the pseudoinverse also exists for singular matrices and works for rectangular linear systems.

The Gauss-Newton method applies this technique to solve the linear system

$$\frac{\partial G}{\partial z}(z; u) \Delta z = -G(z; u)$$

by applying the pseudoinverse to  $\partial G(z; u)/\partial z$ . It comes with similar convergence guarantees as the classical Newton's method [275], provided that the Jacobian of the target solution has full rank.

### 3.3.3 Predictor-Corrector Approach

Next, we present a predictor-corrector scheme to compute the Euclidean distance retraction. Indeed, most path-tracking algorithms in homotopy continuation use both predictor and corrector steps. While predictor steps require more computations, they also lead to more robust path-tracking. The simplest predictor may be applying Euler's method to numerically solve the ODEs arising in homotopy continuation. However, modern path-tracking algorithms use much more sophisticated methods. For example, in Telen et al. [312] and Timme [316] Padé approximants are used in the predictor step, which additionally gives estimates for the distance to the nearest singularity in the Jacobian, among other benefits. The software `HomotopyContinuation.jl`, which we use in our experiments in Section 3.10, uses a path-tracking algorithm described in Timme [316]. This algorithm chooses the stepsize adaptively, building on a local understanding of the region of convergence of Newton's method, and the distance to the nearest singularity. It rejects stepsizes that are too long by testing if each iterate  $x_k$  is an *approximate zero* in the sense of Smale's  $\alpha$ -theory [296], meaning that Newton's method converges quadratically when applied to  $x_k$ . This statement will be made more precise in Section 3.10. In addition, computational estimates of the region of convergence for Newton's method are maintained.

For now, consider perhaps the simplest predictor, an Euler step [299, p.22f.]. Corollary 3.3.13 below will extend Theorem 3.3.7 to this case. In preparation for the Corollary, we briefly recall the basics of an Euler step. Assume we are in a point  $z = (x, \lambda)$  with parameter  $u$ . We want the subsequent value  $z + \Delta z$  to also solve the polynomial system  $G$  at the parameter  $u + \Delta u$ ; thus, we assume that  $G(z + \Delta z, u + \Delta u) = 0$ . To obtain the corresponding Taylor expansion,

we write

$$G(z + \Delta z, u + \Delta u) = G(z, u) + \frac{\partial G}{\partial z}(z, u) \cdot \Delta z + \frac{\partial G}{\partial u}(z, u) \cdot \Delta u + \mathcal{O}(|\Delta z|^2). \quad (3.3.10)$$

With the additional assumption  $G(z, u) \approx 0$ , and that  $G'$  is invertible at  $z$  (see Lemma 3.3.3), Equation (3.3.10) yields the prediction

$$\Delta z = - \left( \frac{\partial G}{\partial z}(z, u) \right)^{-1} \frac{\partial G}{\partial u}(z, u) \cdot \Delta u. \quad (3.3.11)$$

Having derived a formula for Euler's method, we can now record the main idea of the corresponding predictor-corrector method in the following algorithm.

---

**Algorithm ED2:** Computing  $R_p(v)$  by continuation using predictor-corrector steps

---

**Inputs :** A point  $p \in \mathcal{M}$ , vector  $v \in T_p \mathcal{M}$ , and a partition

$$0 = t_0 < t_1 < \dots < t_m < t_{m+1} = 1.$$

**Output:** The Euclidean distance retraction  $R_p(v)$ .

Set  $x(t_0) = x(0) = p$ , set  $\lambda(t_0) = \lambda(0) = 0$ , and let  $u(t) = p + tv$ . Let  $z = (x, t)$  and

$$\Delta u_j = u_j - u_{j-1}.$$

**for**  $j \in \{0, 1, \dots, m\}$  **do**

Predict  $z = z_j + \Delta z$  by solving  $\frac{\partial G}{\partial z, \lambda}(z_j; u_j) \Delta z = -\frac{\partial G}{\partial u}(z_j; u_j) \Delta u_{j+1}$  (Euler).

Correct  $z$  by solving  $G(z, u_{j+1}) = 0$ , yielding  $z_{j+1}$  (Newton's method).

**end**

---

In Section 3.9 we present an implementation of Algorithm ED2 and show how it performs favorably in comparison with Algorithm ED0 on several examples. A visual representation of a single iteration this algorithm performs is portrayed in Figure 3.3.12.

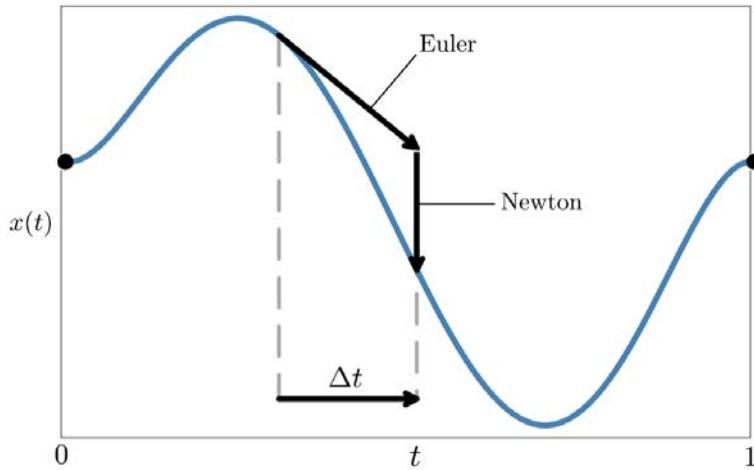


**Figure 3.3.12:** Introducing a linear prediction step for approximating the Euclidean distance retraction curve  $x(t) = R_p(tv)$  has several advantages. By usually staying closer to the constraint set, the amount of Newton iterations is expected to be reduced and larger step sizes become admissible. This makes Algorithm ED2 more efficient in practice.

In our numerical experiments in Section 3.10, we will compare Algorithms ED0, ED1,

and ED2 for reliability, average time, and the number of linear solves required. Note that Algorithm ED2 may be modified to use the adaptive algorithm from Timme [316], which we include in our numerical experiments in Section 3.10 below. However, for this simplified version of Algorithm ED2 with an Euler prediction step, we can easily extend the result from Theorem 3.3.7.

**Corollary 3.3.13.** *Given the same assumptions as in Theorem 3.3.7, let  $0 = t_0 < t_1 < \dots < t_m < t_{m+1} = 1$  be the partition whose existence is guaranteed by Theorem 3.3.7. Then each of the  $m + 1$  applications of Newton's method after the Euler prediction step in Algorithm ED2 converges. Hence Algorithm ED2 converges, and outputs the correct critical point  $R_p(v)$ .*

*Proof.* If we Taylor expand  $G(z_{u+\Delta u}, u + \Delta u)$  in  $z, u$  and assume that  $z_{u+\Delta u}$  is a zero of  $G$  for the parameter  $u + \Delta u$ , we get the equation

$$\begin{aligned} 0 = G(z_{u+\Delta u}, u + \Delta u) &= \underbrace{G(z, u)}_{=0} + \frac{\partial G(z, u)}{\partial z} \cdot (z_{u+\Delta u} - z) + \frac{\partial G(z, u)}{\partial u} \cdot \Delta u \\ &\quad + \frac{1}{2} \frac{\partial^2 G(\xi, \mu)}{\partial z^2} (z_{u+\Delta u} - z, z_{u+\Delta u} - z) \end{aligned}$$

for some  $(\xi, \mu)$  on the line segment between  $(z, u)$  and  $(z_{u+\Delta u}, u + \Delta u)$ . Since  $G(x, \lambda; u) = (g(x), dg_x^T \lambda - u + x)$  then the second derivatives with respect to  $u$  are all zero, explaining their absence in the formula above.  $\partial G/\partial z$  is invertible in the point  $z, u$  by assumption, so we can insert Equation (3.3.11) into the above expression and multiply both sides by the inverse of  $\frac{\partial G}{\partial z}(z, u)$  from the left to obtain

$$z_{u+\Delta u} - z - \Delta z = -\frac{1}{2} \left( \frac{\partial G(z, u)}{\partial z} \right)^{-1} \frac{\partial^2 G(\xi, \mu)}{\partial z^2} (z_{u+\Delta u} - z, z_{u+\Delta u} - z).$$

After taking norms and using the same upper bound  $M$  as appeared in the proof of Theorem 3.3.7 we find

$$\begin{aligned} \|z_{u+\Delta u} - z - \Delta z\| &\leq \frac{1}{2} \left\| \frac{\partial G(z, u)}{\partial z}^{-1} \right\| \cdot \left\| \frac{\partial^2 G(\xi, \mu)}{\partial z^2} \right\| \cdot \|z_{u+\Delta u} - z\|^2 \\ &\leq M \|z_{u+\Delta u} - z\|^2. \end{aligned}$$

This implies that  $z + \Delta z$  lies in the region of quadratic convergence of Newton's method, completing the proof.  $\square$

Therefore, using Euler prediction to get the initialization  $z + \Delta z$  for Newton's method is at least as good as using the original point  $z$  in terms of reliability and convergence. The Euler step is only a first-order predictor, so we do not expect that it improves the convergence speed of Newton's method. This hypothesis will be confirmed in Section 3.10. Only higher-order predictor steps promise a higher accuracy and thus, a faster convergence of Newton's method.

### 3.4 Backtracking Line Search

Having demonstrated that retraction maps are available for arbitrary manifolds, we now want to introduce conditions to determine admissible step sizes. However, additional definitions are necessary. In  $\mathbb{R}^n$ , a vector  $\mathbf{v} \in \mathbb{R}^n$  is a *descent direction* to  $f : \mathbb{R}^n \rightarrow \mathbb{R}$  in  $x \in \mathbb{R}^n$ , if  $\langle \mathbf{v}, \nabla f(x) \rangle < 0$ . Analogously, a tangent vector  $\mathbf{v} \in T_x \mathcal{M}$  is a descent direction to  $f : \mathcal{M} \rightarrow \mathbb{R}$  in  $x \in \mathcal{M}$  if  $\langle \mathbf{v}, \text{grad } f(x) \rangle < 0$ , as the normal component of  $\nabla f(x)$  cancels.

The *parallel transport* along a smooth curve  $c : [0, 1] \rightarrow \mathcal{M}$ , moving  $v \in T_{c(0)} \mathcal{M}$  along  $c$ , is a linear map  $\mathcal{T}_{c(0), c(1)}^c : T_{c(0)} \mathcal{M} \rightarrow T_{c(1)} \mathcal{M}$ . More specifically,  $\mathcal{T}$  is the identity when  $c$  is constant and preserves inner products between tangent vectors (cf. [167]). Having defined these concepts enables us to introduce the Wolfe conditions. These inequalities restrict possible step sizes to an interval, in which both objective function value and slope decrease sufficiently. The following definition appears in [259].

**Definition 3.4.1.** Let  $\mathbf{v} \in T_x \mathcal{M}$  be a descent direction of  $f$  at  $x$ . We deem the stepsize  $\alpha$  to be acceptable if the following conditions are met:

The *Armijo condition* is

$$f(x) - f(R_x(\alpha \mathbf{v})) \geq -r\alpha \langle \mathbf{v}, \text{grad } f(x) \rangle \quad (3.4.2)$$

with a fixed  $r \in (0, 1)$ . Conversely, the *(strong) curvature condition* is given by

$$|\langle \mathcal{T}_{x, R_x(\alpha \mathbf{v})}^{R_x}(\mathbf{v}), \text{grad } f(R_x(\alpha \mathbf{v})) \rangle| \leq s \cdot |\langle \mathbf{v}, \text{grad } f(x) \rangle| \quad (3.4.3)$$

with  $0 < r < s < 1$ . While  $r$  is often taken as  $10^{-4}$ ,  $s$  is usually chosen as 0.9 [234, p.62]. Both conditions together are also called the *(strong) Wolfe conditions*.

After introducing conditions on admissible step sizes, it makes sense to consider the qualitative example in Figure 3.4.4, where the Wolfe conditions are visualized for a specific curve, to better understand how they interact. It becomes clear that while the Armijo condition's job is to ensure a sufficient decrease in the objective function, the (strong) curvature condition is supposed to guarantee that the step size does not become too small by imposing constraints on the objective function's gradient.

There is extensive literature treating the Wolfe conditions, as they have proven to work well in practice. However, this theory only exists for global retractions. We provide minor generalizations for standard results from [4, 25, 167, 259] on step sizes for retraction-based optimization routines. First and foremost, the existence of admissible step sizes is guaranteed.

**Theorem 3.4.5** (Reformulation of [167, Thm. 2.8]). *Assume that  $f : \mathcal{M} \rightarrow \mathbb{R}$  is continuously differentiable. Let  $\mathbf{v}$  be a descent direction of  $f$  in  $x$  and denote by  $R_x : T_x \mathcal{M} \rightarrow \mathcal{M}$  a (global) retraction. Assume that  $f$  is bounded from below on  $\{R_x(t\mathbf{v}) : t \geq 0\}$ . If  $0 < r < s < 1$ , then there exists an open interval of positive step sizes, where the strong Wolfe conditions are satisfied.*

*Proof.* Let us define the following function:

$$g(t) = f(R_x(t\mathbf{v})) - (f(x) + rt \cdot \langle \mathbf{v}, \text{grad } f(x) \rangle).$$

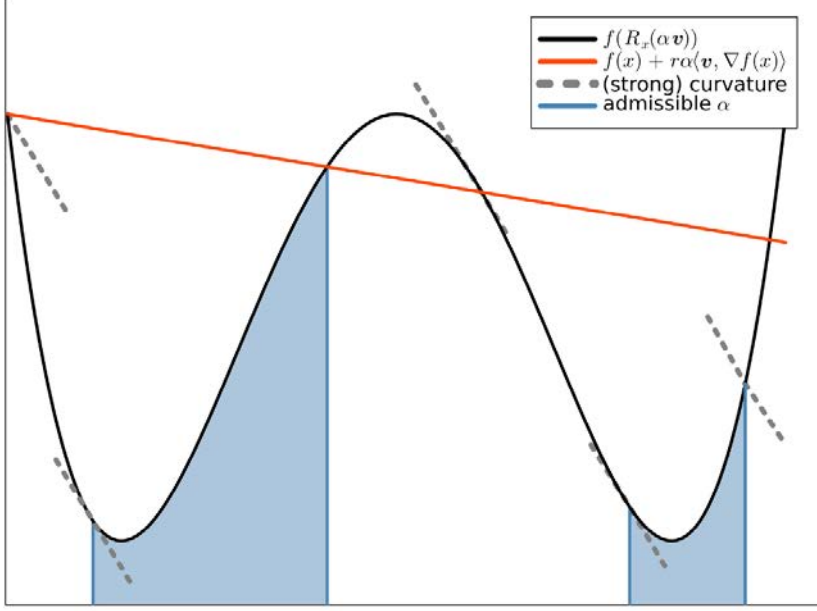


**Figure 3.4.4:** The Armijo condition (red) dictates an upper bound on the objective function (black), such that the accepted step sufficiently decreases its value. The strong Wolfe condition (with  $\mathbf{v}$  depicted in gray) imposes conditions on the objective function's gradient, ensuring that the step size is not too small. Their interplay guarantees that admissible step sizes (blue) are well-behaved.

Notice that  $g(0) = 0$  and  $g'(0) = (1 - r) \langle \mathbf{v}, \text{grad } f(x) \rangle$  by Definition 3.2.1. It holds that  $g'(0) < 0$ , as  $r \in (0, 1)$  and  $\mathbf{v}$  is a descent direction. This implies that there exists  $\hat{t} > 0$  such that each  $t \in (0, \hat{t})$  satisfies  $g(t) < 0$ . Hence, the Armijo condition holds on  $(0, \hat{t})$ .

Since  $\{f(R_x(t\mathbf{v})) : t \geq 0\}$  is bounded from below, we know that  $g(t) \rightarrow \infty$  for  $t \rightarrow \infty$  because  $\mathbf{v}$  is a descent direction. By  $f$ 's continuity, there exists  $\tilde{t} > 0$  such that  $g(\tilde{t}) = 0$ . Let

$$t^* = \inf\{\tilde{t} : \tilde{t} > 0 \text{ and } g(\tilde{t}) = 0\}.$$

As  $g(t) < 0$  on the entire non-empty open interval  $(0, \hat{t})$ , we find  $t^* > 0$  and by continuity  $g(t^*) = 0$ . By the Mean Value Theorem, there exists a  $\xi \in (0, t^*)$  with  $g'(\xi) = 0$ . Thus,

$$\begin{aligned} \langle \text{grad } f(R_x(\xi \mathbf{v})), \mathcal{T}_{x, R_x(\xi \mathbf{v})}^{R_x}(\mathbf{v}) \rangle &= r \cdot \langle \text{grad } f(x), \mathbf{v} \rangle \\ \Rightarrow |\langle \text{grad } f(R_x(\xi \mathbf{v})), \mathcal{T}_{x, R_x(\xi \mathbf{v})}^{R_x}(\mathbf{v}) \rangle| &= r \cdot |\langle \text{grad } f(x), \mathbf{v} \rangle| < s \cdot |\langle \text{grad } f(x), \mathbf{v} \rangle| \end{aligned}$$

because  $0 < r < s < 1$ . Furthermore,  $t^*$  is the smallest nonzero root of  $g$ ,  $g$  is continuous and  $g(t) < 0$  for  $t \in (0, \hat{t})$ . Therefore,  $\xi \in (0, t^*)$  and  $g(\xi) < 0$  holds by construction. By  $g$ 's continuous differentiability, there exists an open neighborhood around  $\xi$  where the Armijo condition (3.4.2) and the curvature condition (3.4.3) hold, proving the claim.  $\square$

**Corollary 3.4.6.** *Under the conditions of Proposition 3.4.5 with a local retraction  $R_x : U \rightarrow \mathcal{M}$ , there exists an open interval of positive step sizes where the Armijo condition (3.4.2) is satisfied.*

*Proof.* By the proof of Proposition 3.4.5, the Armijo condition is satisfied on the open interval

$(0, \hat{t})$ . In contrast to the previously used global retraction, the local retraction may not be defined over the entire interval. Since the set  $U \subset T_x \mathcal{M}$ , where  $R_x$  is defined, is a neighborhood of  $x$ , there exists an open ball  $B_\varepsilon(x) \subset U$  with  $\varepsilon > 0$ . Consequently, the Armijo condition is satisfied on the open interval  $(0, \min(\varepsilon, |\hat{t}\mathbf{v}|))$ .  $\square$

The proof of Corollary 3.4.6 shows that the Armijo condition (3.4.2) is satisfied for sufficiently small positive numbers. This gives rise to an intuitive algorithm: We start with a positive number  $\tau > 0$  and decrease  $\tau$  by a factor  $\beta > 0$  until the Armijo condition is met (cf. [23]). Formally, we choose the smallest possible non-negative integer  $m$  such that the step size  $\alpha = \beta^m \tau$  satisfies inequality (3.4.2). The following proposition is a generalization of [47, Cor. 4.13] to local retractions. It shows that under mild assumptions, step sizes generated by this naïve line search algorithm already imply convergence in the Riemannian gradient descent Algorithm 3.2.7.

**Proposition 3.4.7** (Convergence of Armijo Steepest Descent). *Let  $f : \mathcal{M} \rightarrow \mathbb{R}$  be a smooth function bounded below by  $f_{\text{low}}$ . Choose a local retraction  $R_x$ . Denote by  $x_0, x_1, \dots$  the iterates that the Riemannian Gradient Descent Algorithm 3.2.7 produces with search direction  $\mathbf{v}_k = -\text{grad } f(x_k)$  and step sizes  $\alpha_k > 0$  obtained by consecutively halving an initial guess  $\tau > 0$  until the Armijo condition (3.4.2) is satisfied. Denote the largest interval where the Armijo condition is satisfied at  $x_k$  by  $(0, A_k)$  for some  $A_k > 0$ . Assume  $\liminf_{k \rightarrow \infty} A_k > 0$ . Then,*

$$\|\text{grad } f(x_k)\| \rightarrow 0 \quad \text{as} \quad k \rightarrow \infty.$$

*Proof.* First of all, Corollary 3.4.6 implies the existence of open intervals  $(0, \hat{\alpha}_k)$  where the Armijo condition is satisfied. We calculate

$$\begin{aligned} f(x_0) - f_{\text{low}} &\geq \sum_{k=0}^{N-1} f(x_k) - f(x_{k+1}) \stackrel{(3.4.2)}{\geq} \sum_{k=0}^{N-1} r \alpha_k \cdot \|\text{grad } f(x_k)\|^2 \\ &\geq r \left( \min_{k \in \{0, \dots, N-1\}} \alpha_k \right) \underbrace{\sum_{k=0}^{N-1} \|\text{grad } f(x_k)\|^2}_{=g_{N-1}}. \end{aligned}$$

As  $\liminf_{k \rightarrow \infty} A_k > 0$  and  $r > 0$ , we deduce that  $g_\infty < \infty$ . As a result,  $\|\text{grad } f(x_k)\| \rightarrow 0$ .  $\square$

The Armijo condition can be interpreted as providing an upper bound on the admissible step sizes and Proposition 3.4.7 proves that Algorithm 3.2.7 in combination with the Armijo line search indeed converges. Nevertheless, curvature condition (3.4.3) should not be neglected, as the above proposition requires that the maximal step sizes are bounded away from 0 in each step. Of course, setting  $A_k = c$  for a constant  $c$  would solve this problem. Yet, this approach is anything but dynamic and will lead to a sub-optimal speed of convergence.

The curvature condition (3.4.3) can be interpreted to provide a lower bound on the feasible step sizes. Nonetheless, if step sizes satisfying the Wolfe conditions do exist, Zoutendijk's Theorem is a standard result for comparing the sequence of descent directions to the Riemannian gradient at the corresponding points.

**Theorem 3.4.8** (Zoutendijk's Theorem, [259]). *Given a differentiable  $f : \mathcal{M} \rightarrow \mathbb{R}$  and a (global) retraction  $R_x : T_x \mathcal{M} \rightarrow \mathcal{M}$ , assume the step length sequence  $(\alpha_k)_{k \in \mathbb{N}}$  in Algorithm 3.2.7 satisfies the Wolfe conditions for a given descent direction  $\mathbf{v}_k$ . If the pullbacks  $f \circ R_{x_k}$  are Lipschitz continuously differentiable on the line  $\{t\mathbf{v}_k \mid t \in \mathbb{R}\}$  with uniform Lipschitz constant  $L$ , then*

$$\sum_{k \in \mathbb{N}} \cos^2(\theta_k) \cdot \|\text{grad } f(x_k)\|^2 < \infty$$

where  $\theta_k$  denotes the angle between the Riemannian gradient  $\text{grad } f(x_k)$  and  $\mathbf{v}_k$  in  $T_{x_k} \mathcal{M}$ .

For appropriately chosen descent directions  $\mathbf{v}_k$ , this theorem can be used to prove the convergence of Riemannian optimization algorithms with more general search directions.

**Corollary 3.4.9.** *Assume that the sequence  $(\cos^2(\theta_k))_{k \in \mathbb{N}}$  from Theorem 3.4.8 is bounded away from 0. Then,*

$$\|\text{grad } f(x_k)\| \rightarrow 0 \quad \text{as} \quad k \rightarrow \infty.$$

*Proof.* Zoutendijk's Theorem states that  $\cos^2(\theta_k) \|\text{grad } f(x_k)\|^2 \rightarrow 0$  as  $k \rightarrow \infty$ . By assumption the inequality  $\cos^2(\theta_k) > \varepsilon$  holds for some fixed  $\varepsilon > 0$ , so the Sandwich Theorem for sequences implies that  $\varepsilon^2 \cdot \|\text{grad } f(x_k)\|^2 \rightarrow 0$ .  $\square$

**Remark 3.4.10.** In particular, the direction of steepest descent  $\mathbf{v}_k = -\text{grad } f(x_k)$  meets the assumptions of Corollary 3.4.9, guaranteeing convergence in the Riemannian gradient descent Algorithm 3.2.7. In spite of that, there are other descent directions that work well. For example, Riemannian Newton [7], Riemannian BFGS [256] and conjugate gradient [4, p.180f.] produce reasonable search directions. The latter two procedures do not even depend on explicit knowledge of the Riemannian Hessian [47, p.90f.]. If the eigenvalues of the positive definite matrices these methods use are uniformly bounded away from zero, Corollary 3.4.9 applies again. For the sake of simplicity and as convergence is guaranteed either way, we will stick to the Riemannian gradient descent Algorithm 3.2.7.

With all of these theoretical results in place, we can finally introduce the bisection backtracking line search Algorithm 3.4.11, appearing in a less general form in Nocedal and Wright [234, p.60f.]. Its goal is to increase the step size until either it exceeds a preset maximal step size, satisfies the Wolfe conditions, leads to a non-negative derivative, or does not satisfy the Armijo condition anymore. If the Wolfe condition is not satisfied after this procedure, the interval between the previous and current step sizes is given a closer look by the `zoom` method, which is subsequently introduced.

If only the Armijo condition is satisfied, the zoom Algorithm 3.4.12 bisects the interval that is passed to it until the Wolfe condition is satisfied. For a retraction, Theorem 3.4.5 ensures that an open interval, where the Wolfe condition holds, exists. By avoiding the bisection procedure until a feasible interval of step sizes is identified, we guarantee that the inefficient bisection method is not excessively repeated.

Two questions that have yet to be answered are how to choose the subsequent step length  $\alpha_{i+1}$  from the interval  $(\alpha_i, \alpha_{max})$  and what the maximal step size  $\alpha_{max}$  should be. As argued

---

**Algorithm 3.4.11:** Backtracking Line Search (cf. [234, p.60f.])

---

**input :** An embedded manifold  $\mathcal{M} \subseteq \mathbb{R}^n$ ,  
     a point  $x \in \mathcal{M}$ ,  
     objective function  $f : \mathcal{M} \rightarrow \mathbb{R}$ ,  
     descent direction  $\mathbf{v} \in T_x \mathcal{M}$ ,  
     constants  $0 < r < s < 1$  and  
     maximal step size  $\alpha_{\max} > 0$ .  
**output:** A stepsize  $\alpha_*$ .

```

 $\alpha_0 = 0; i = 1; \alpha_1 \in (0, \alpha_{\max})$ 
while true do
    if Armijo condition (3.4.2) does not hold for  $\alpha_i$  or  $\alpha_{i+1} \geq \alpha_{\max}$  then
         $\alpha_* = \text{zoom}(\alpha_{i-1}, \alpha_i)$  and stop
    else if Strong curvature condition (3.4.3) holds for  $\alpha_i$  then
         $\alpha_* = \alpha_i$  and stop
    else if  $\langle \mathcal{T}_{x, R_x(\alpha_i \mathbf{v})}^{R_x}(\mathbf{v}), \text{grad } f(R_x(\alpha_i \mathbf{v})) \rangle \geq 0$  then
         $\alpha_* = \text{zoom}(\alpha_i, \alpha_{i-1})$  and stop
    end
    Choose  $\alpha_{i+1} > \alpha_i$ 
     $i \leftarrow i + 1$ 
end
return  $\alpha_*$ 
```

---



---

**Algorithm 3.4.12:** zoom( $\alpha_{lo}, \alpha_{hi}; \text{max\_step}=10$ ) (cf. [234, p.60f.])

---

$\alpha_{lo}^{(1)} = \alpha_{lo}$ ,  $\alpha_{hi}^{(1)} = \alpha_{hi}$  and  $j = 1$   
**while**  $j \leq \text{max\_step}$  **do**

```

    Choose  $\alpha_j$  between  $\alpha_{lo}^{(j)}$  and  $\alpha_{hi}^{(j)}$ 
    if Armijo condition (3.4.2) does not hold for  $\alpha_j$  then
         $\alpha_{hi}^{(j+1)} = \alpha_j$ 
    else
        if Strong curvature condition (3.4.3) holds for  $\alpha_j$  then
             $\alpha_* = \alpha_j$  and stop
        else if  $\langle \mathcal{T}_{x, R_x(\alpha_j \mathbf{v})}^{R_x}(\mathbf{v}), \text{grad } f(R_x(\alpha_j \mathbf{v})) \rangle \cdot (\alpha_{hi}^{(j)} - \alpha_{lo}^{(j)}) \geq 0$  then
             $\alpha_{hi}^{(j+1)} = \alpha_{lo}^{(j)}$ 
        end
         $\alpha_{lo}^{(j+1)} = \alpha_j$ 
    end
     $j \leftarrow j + 1$ 
end
return  $\alpha_*$ 
```

---

in Hosseini et al. [167], we can simply set  $\alpha_{i+1} = c \cdot \alpha_i$  for a constant  $c > 1$ . If  $\alpha_{i+1} \geq \alpha_{\max}$ , we zoom into the interval  $(\alpha_i, \alpha_{\max})$ . Furthermore, the inverse function theorem for manifolds guarantees that any local retraction  $R_x$  is a diffeomorphism in some local neighborhood of 0 in  $T_x \mathcal{M}$ , since it is a smooth map and the differential  $d(R_x)$  is invertible by Definition 3.2.1 (cf. [47, p.257]). How large this open neighborhood is, can be quantified by the *injectivity radius*

$\iota_{\mathcal{M}}(x) > 0$ . Choosing  $0 < \alpha_{max} < \iota_{\mathcal{M}} = \inf_{x \in \mathcal{M}} \iota_{\mathcal{M}}(x)$  with

$$\iota_{\mathcal{M}}(x) = \sup\{\varepsilon > 0 \mid R_x : B_\varepsilon(0) \rightarrow \mathcal{M} \text{ is injective}\},$$

the injectivity radius of  $\mathcal{M}$  with respect to the retraction  $R$  provides a reasonable upper bound for  $\alpha_{max}$  (cf. [167]). This definition finds an open ball  $B_\varepsilon(0)$  in the tangent space  $T_x\mathcal{M}$  that the retraction injectively maps to  $\mathcal{M}$ . It makes sense to consider this concept because in the neighborhood  $B_{\iota_{\mathcal{M}}(x)}(0)$ , the geodesic  $\text{Exp}_x(tv)$  is the unique length-minimizing curve connecting  $x$  to any other  $y \in B_{\iota_{\mathcal{M}}(x)}(0)$  (cf. [47, Prop. 10.22]). The same concepts exist for retractions (cf. [47, Def. 10.28]). For this approach to work, the local retraction still needs to be defined for any value of  $\alpha \in (0, \alpha_{max})$  and the maximal step size needs to be finite, placing additional restrictions on  $\alpha_{max}$ .

It is unclear how to compute the injectivity radius in general. Despite that, the retractions we consider are second-order approximations of the exponential map. The Tubular Neighborhood Theorem 3.1.7 can thus locally provide a lower bound – or at least an approximation – for  $\iota_{\mathcal{M}}$ . Di Rocco et al. [104] provide a system of equations for finding the smallest bottleneck; the shortest, bi-orthogonal line segment between two points on  $\mathcal{M}$ . In combination with the largest radius of curvature (cf. [55]), this concept can be utilized as a replacement for the injectivity radius in our setting.

As previously noted, the Wolfe conditions do not need to be satisfied for any step size  $\alpha \in (0, \alpha_{max})$ , making an alternative stopping condition necessary. For instance, this can be achieved by prescribing a maximal amount of iterations in the zoom procedure's while loop. The following generalization of Proposition 2.17 in Hosseini et al. [167] ensures that the Armijo condition is satisfied for the step size that Algorithm 3.4.11 outputs.

**Proposition 3.4.13.** *Assume that  $f : \mathcal{M} \rightarrow \mathbb{R}$  is continuously differentiable, lower-bounded function and assume that  $R_x$  is a local retraction at  $x \in \mathcal{M}$ . Let  $v$  be a descent direction,  $c > 1$  a constant and assume that Algorithm 3.4.11 initializes  $\alpha_{i+1}$  as  $c \cdot \alpha_i$  for  $c > 1$  and Algorithm 3.4.12 initializes  $\alpha_j$  as  $\frac{1}{2}(\alpha_{lo}^{(j)} + \alpha_{hi}^{(j)})$ . Then, either Algorithm 3.4.11 terminates with a step size  $\alpha^*$  satisfying the strong Wolfe conditions after finitely many iterations or Algorithm 3.4.12 generates a sequence of interval bisections, such each of which contains subintervals satisfying the Armijo condition (3.4.2).*

*Proof.* Suppose that the algorithm does not terminate after finitely many iterations. If it did, we would find a step size  $\alpha^*$  satisfying the strong Wolfe conditions. Denote by  $\alpha_{lo}$ ,  $\alpha_{hi}$  the initial values passed to the zoom procedure and denote by  $\alpha_{lo}^{(j)}$ ,  $\alpha_{hi}^{(j)}$  their values after the  $j$ -th step. The equality  $|\alpha_{hi}^{(j)} - \alpha_{lo}^{(j)}| = \frac{|\alpha_{hi} - \alpha_{lo}|}{2^j}$  holds by construction, so  $\alpha_{hi}^{(j)} - \alpha_{lo}^{(j)}$  converges to 0, implying that  $\alpha_{hi}^{(j)}, \alpha_{lo}^{(j)} \rightarrow \alpha^*$  for some  $\alpha^* \geq 0$ .

Next, we prove that after finitely many steps  $\alpha_{lo}^{(j)} > 0$  and by extension  $\alpha^* > 0$ . By construction, the Armijo condition exactly holds at  $\alpha_{lo}$ , while it may not hold at  $\alpha_{hi}$  – even though  $\alpha_{lo} > \alpha_{hi}$  may occur. Now, either one of  $\alpha_{lo}$ ,  $\alpha_{hi}$  is 0, or we are done since the bisection method creates intervals that are arranged in descending chains by inclusion. That can only happen when  $\alpha_{lo} = 0$ . In this case, [167, Prop. 2.17] applies. It states that both,  $\alpha_{lo}$  and  $\alpha_{hi}$ , converge to a positive number. In particular, this proves that  $\alpha_{lo}^{(j)} > 0$  after finitely many steps.

What remains to be shown is that  $\alpha_*$  satisfies the Armijo condition. By construction,  $\alpha_{lo}^{(j)}$  satisfies the Armijo condition in each step. This stems from the fact that  $\alpha_{lo}$  meets the Armijo rule and in the zoom algorithm,  $\alpha_{lo}^{(j)}$  is only ever updated to values satisfying the Armijo condition. Consequently, at least one of the interval's endpoints always meets the Armijo condition. As the infinite intersection of closed intervals is closed,  $\alpha_*$  needs to satisfy the Armijo condition.  $\square$

### 3.5 Algebraic Varieties and Singularities

As observed in the previous sections, the convergence properties of Riemannian gradient descent and backtracking line search extend to the more general setting of a local retraction on a smooth manifold. However, our initial intention was to apply the algorithm to algebraic sets, which are the vanishing locus of arbitrary polynomials and hence, may contain singularities. Singularities usually create problems for optimization algorithms. Consequently, creating a way to deal with them is of interest.

In this context, the resolution of singularities immediately comes to mind as a powerful tool from algebraic geometry. Intuitively, the idea is to repeatedly blow up the singularities and in the process, smooth out the transitions. It is known that varieties over a ground field of characteristic zero admit a resolution of singularities (cf. [162]). By repeatedly blowing up singularities, we can hope to get a smooth variety at some point. However, this procedure is computationally notoriously hard, since a priori knowledge of the singularities is necessary. Even then, the known procedures are relatively inefficient, as they usually involve the computation of Gröbner bases (cf. [3, p.22f.]). Furthermore, the procedure necessitates embedding the variety in even higher-dimensional ambient spaces, significantly increasing the optimization algorithm's run time with each iteration.

For these reasons, we decided to treat singularities with a more practical approach. Intuitively, blowing up a singular point can be viewed as replacing the point with a Riemann sphere. Given a singularity  $z$ , we make use of this idea by introducing a new constraint, namely a sphere of radius  $\varepsilon > 0$  centered in  $z$ . We intersect the newly formed algebraic variety with random hyperplanes having the support vector  $z$ . Iteratively, starting with 0 up to  $d - 1$  random hyperplanes are chosen, where  $d$  denotes the variety  $V$ 's dimension. In each of the steps, with probability 1 we find points on the variety's components of dimension  $1, \dots, d$  that are at most  $\varepsilon$  away from the point  $z$ . To understand this, recall that in singularities the Jacobian's rank behaves inconsistently.

Therefore, we need to check all dimensions up to the variety's actual dimension for finding regular points, where the optimization methods we introduced work again. If any of these points on the sphere intersected with  $V$  has a smaller objective function value than  $z$  itself, the singularity cannot be optimal provided that  $\varepsilon$  is chosen small enough. In this case, we continue the optimization subject to the original variety  $V$  with the new point as initial value. An example of this procedure is depicted in Figure 3.5.1.

Although this approach is undoubtedly heuristic, it performs well in practice. It is an advantage in this setting that the problem is algebraic, as there are robust algorithms for finding all solutions of a zero-dimensional polynomial system computationally [299, Thm. 7.1.1]. Hence,

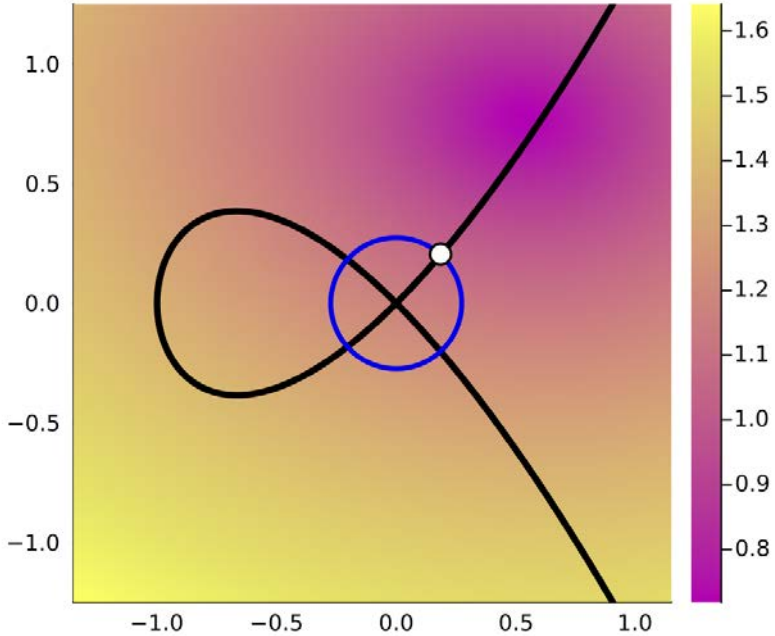


**Figure 3.5.1:** The objective function  $f(x, y) = \sqrt[6]{3(x - 0.7)^2 + 0.3xy + 1.7(y - 0.7)^2}$  (pink to yellow) subject to the nodal cubic  $y^2 - x^2(x + 1) = 0$  (black). The algorithm got stuck in the singularity  $z = (0, 0)$ , so we intersect a sphere centered in  $z$  of radius  $\varepsilon = 0.25$  (blue) with the variety. There are four real intersection points, so we choose the point where the value of  $f$  is smallest to continue the algorithm (white).

the above construction inherits the same theoretical guarantees, provided that the hyperplanes are in relative general position to the variety intersected with a sphere centered at  $z$ .

A question arising from this construction is how to choose the sphere's radius  $\varepsilon$ . Naturally, it should be small enough to capture all components passing through  $z$ . Taking the variety's reach (cf. [104]) as an upper bound to the sphere's radius  $\varepsilon$  does not work in this setting: Arbitrarily close to the singularity, we can find points in the ambient space with at least two closest points on the variety. Thus, the variety's reach is 0. What promises better performance is to decrease the sphere's radius until no new components are found in consecutive iterations. Nevertheless, finding examples where this approach fails is not hard, and computing the sphere's radius based on the optimization problem's properties remains an open problem.

Now,  $\overline{B_\varepsilon(z)} \cap V$  is compact as the intersection of a closed and a compact set in  $\mathbb{R}^n$ . Hence, the continuous objective function  $f$  attains its minimum here. If this happens in this set's interior, it is a local minimum of  $f$  subject to  $V$  as well. Conversely, a minimum on the boundary only has significance relative to the interior of  $B_\varepsilon(z)$ .

Still, finding a smaller objective function value on the boundary than in the singularity suggests that the energy landscape is decreasing somewhere between the singularity and the new point. If additionally,  $\varepsilon$  is sufficiently small,  $z$  is likely not a minimum. Finally, Algorithm 3.5.2 outlines the previously described method for escaping singularities in pseudocode.

---

**Algorithm 3.5.2:** Resolve the Singularity

---

**input :** A set of polynomials  $g \subset \mathbb{R}[x_1, \dots, x_n]$  generating an algebraic set  $V$ ,  
 a point  $z \in V$  deemed singular,  
 the sufficiently small sphere's radius  $\varepsilon > 0$  and  
 an objective function  $f : V \rightarrow \mathbb{R}$ .  
**output:** The new point  $z$  and a boolean indicating whether  $z$  is a local minimum.

```

 $g, \dim \leftarrow \text{set\_equations\_and\_dimension\_at\_point}(g, z)$ 
 $g^\sharp = \text{concat}(g, |x - z|^2 - \varepsilon^2)$ 
for  $i = 0$  to  $\dim - 1$  do
     $L = \text{rand\_affine\_space\_at\_point}(z, \text{codim} = i)$ 
     $solutions = \text{intersect}(L, g^\sharp)$ 
    for  $sol \in solutions$  do
        if  $f(sol) < f(z)$  then
            return  $sol, \text{false}$ 
        end
    end
end

return  $z, \text{true}$ 

```

---

**Remark 3.5.3.** Besides singularities in the constraint set, commonly saddle points of the objective function pose issues for optimization procedures (cf. [91]). Escaping them is notoriously hard, since only a small fraction of tangent directions may decrease the objective function's value. Without information from higher-order derivatives, it is impossible to determine a priori which tangent vectors are required. Consequently, it is necessary to sample the entire tangent space.

Algorithm 3.5.2 makes it surprisingly clear how to solve this problem. Given a regular saddle point  $p \in V$ , we can intersect the constraint variety  $V$  with a sphere centered in the saddle point and sample from this set using random hyperplanes with support vector  $p$ . Conveniently,  $p$  is nonsingular, meaning that the amount of hyperplanes is exactly given by the varieties dimension at  $p$  minus one.

Still, this approach does not solve the problem when only a small ratio of tangent directions correspond to a decrease in the objective function's value. As an alternative approach, we can solve the local Lagrange multiplier system  $L_\varepsilon(x, \mu) = f(x) + \mu^T(g(x), |x - z|^2 - \varepsilon^2)$  encoding the constraints from  $V$  intersected with the sphere  $|x - z|^2 - \varepsilon^2$ . This set is compact in  $\mathbb{R}^n$  and the smooth function  $f$  attains its minimum on it by the generalized Extreme Value Theorem. It can be found by solving the critical point equation  $\nabla_{x, \mu} L_\varepsilon = 0$ , for example by using homotopy continuation. The system's finitely many solutions (cf. [229]) are subsequently filtered for the point  $x^*$  with the smallest objective function value. If  $f(x^*) < f(p)$  and provided that  $\varepsilon$  is sufficiently small,  $p$  cannot be a local minimum and we continue the optimization procedure from  $x^*$ . Otherwise,  $p$  itself is likely to be a minimum.

### 3.6 Guaranteeing the Existence of Minima with Projectivization

It is far from the truth that every smooth function attains a minimum in its domain, let alone subject to a constraint variety. For example, consider  $e^{x+y}$  on the line  $x = y$ . Yet, if we consider a polynomial objective function with polynomial constraints, at least there exists an upper bound on the number of critical points (cf. [229]).

However, our algorithm is supposed to find local minimizers, so we need to be able to provide a positive lower bound on the number of minima. By the generalized Extreme Value Theorem, a real-valued, continuous function  $f : K \rightarrow \mathbb{R}$  is bounded on a compact set  $K$  and attains its infimum and supremum [268, Thm. 4.16]. Hence, there is a minimum and maximum of our objective function  $f$  on each compact real connected component of the constraint variety  $V$ .

If the variety does not contain compact connected components, it is unclear whether  $f$  has extrema. In the example before, the function is bounded below by 0. Its infimum is not attained in  $\mathbb{R}^2$  but only in the line at infinity. Immediately, this insight gives us the idea to consider functions in projective space, rather than affine space.  $\mathbb{P}_{\mathbb{R}}^n$  is a compact, connected  $n$ -dimensional manifold, as  $\mathbb{P}_{\mathbb{R}}^n$  can be obtained via a quotient of  $S^n$  [226, p.373]. Furthermore, the image of a connected and compact set under a continuous map is connected [226, Thm. 23.5] and compact [226, Thm. 26.5] itself. For these reasons, functions on  $\mathbb{P}_{\mathbb{R}}^n$  attain their infimum and supremum.

Functions on  $\mathbb{R}^n$  generally cannot be continued to projective space.  $\mathbb{P}_{\mathbb{R}}^n$  can be represented by lines in  $\mathbb{R}^{n+1}$  [150, p.6], which can be expressed as the quotient

$$\mathbb{R}^{n+1} \setminus \{0\} / x \sim \lambda x \text{ for all } \lambda \in \mathbb{R} \setminus \{0\}.$$

Thus, any well-defined function  $g$  on  $\mathbb{P}_{\mathbb{R}}^n$  needs to satisfy  $g(\lambda x) = g(x)$  for all  $\lambda \in \mathbb{R} \setminus \{0\}$  and  $x \in \mathbb{R}^{n+1}$ . In other words, the function value needs to be constant on the lines in  $\mathbb{R}^{n+1}$ . Only a handful of functions possess this property. Among them are rational functions, whose numerator and denominator are homogeneous polynomials of the same degree. After homogenization, any rational function defined on  $\mathbb{R}^n$  becomes well-defined on all of  $\mathbb{P}_{\mathbb{R}}^n$  if no zeros of the denominator are added. To prove this claim, assume that we are given a rational function  $r(\mathbf{x}) = \frac{p(\mathbf{x})}{q(\mathbf{x})}$  mapping  $r : \mathbb{R}^n \rightarrow \mathbb{R}$ . We know that  $\mathbb{R}^n$  can be embedded in  $\mathbb{P}_{\mathbb{R}}^n$  by choosing an affine patch [86, p. 396], for example

$$\{[1 : z_1 : \dots : z_n] \mid (z_1, \dots, z_n) \in \mathbb{R}^n\} \subseteq \mathbb{P}_{\mathbb{R}}^n.$$

On the function level, this operation corresponds to homogenization by the new coordinate  $x_0$  [218, p.28]. The homogenization of  $r$  can be then written as

$$r^h(x_0, x_1, \dots, x_n) = x_0^{\deg(q) - \deg(p)} \cdot \frac{p^h(x_0, x_1, \dots, x_n)}{q^h(x_0, x_1, \dots, x_n)},$$

with  $p^h(x_0, \dots, x_n) = x_0^{\deg(p)} p(\frac{x_1}{x_0}, \dots, \frac{x_n}{x_0})$  for  $p$ 's total degree  $\deg(p)$  and  $q^h$  defined accordingly [86, p.400f.]. This construction makes  $r$  a well-defined function on  $\mathbb{P}_{\mathbb{R}}^n \setminus \mathcal{V}_{\mathbb{P}}(q^h)$ . Here,  $\mathcal{V}_{\mathbb{P}}(g)$  denotes the projective algebraic variety defined by a homogeneous polynomial  $g$  (cf. [86, p.398f.]).

Therefore, rational objective functions subject to a constraint variety make sense as optimization problems in projective space. The generalized Extreme Value Theorem guarantees that functions on  $\mathbb{P}_{\mathbb{R}}^n$  attain their infimum.

**Example 3.6.1.** Consider the rational function  $r(x) = \frac{1}{x^2+1}$ . This function is globally defined and bounded below by 0, but does not attain its infimum in  $\mathbb{R}$ . The homogenization of  $r$  is  $r^h(x, y) = \frac{y^2}{x^2+y^2}$  and it is well-defined in  $\mathbb{P}_{\mathbb{R}}^1$ . It is always non-negative, so it is bounded from below and attains its infimum in the point  $[1 : 0]$ . Notice that this point does not lie in the affine patch  $\{[a : 1] \mid a \in \mathbb{R}\}$  of  $\mathbb{P}_{\mathbb{R}}^1$  that the real line  $\mathbb{R}$  is embedded in.

However, this construction only works when the homogenized rational function's denominator is globally non-zero in  $\mathbb{P}_{\mathbb{R}}^n$ . Consider for example the polynomial  $x^3$ . With the above homogenization procedure, this becomes  $\frac{x^3}{y^3}$ . In the affine patch  $\{[a : 1] \mid a \in \mathbb{R}\}$ , there is no lower bound on the value of  $\frac{x^3}{y^3}$ . In the remaining part of  $\mathbb{P}_{\mathbb{R}}^1$ , namely  $\{[1 : 0]\}$ , this function has a pole and therefore is not defined. These observations enable us to formulate criteria for admissible rational functions.

**Proposition 3.6.2.** *Let  $p, q \in \mathbb{R}[x_0, x_1, \dots, x_n]$  be homogeneous polynomials of the same degree such that  $q \neq 0$  on  $\mathbb{R}^{n+1} \setminus \{0\}$ . Define*

$$r(x) = \frac{p(x)}{q(x)}.$$

*Then,  $r$  attains its infimum as a function  $r : \mathbb{P}_{\mathbb{R}}^n \rightarrow \mathbb{R}$ . Consequently,  $r$  also attains its infimum as a function on  $\mathbb{R}^{n+1} \setminus \{0\} \rightarrow \mathbb{R}$ .*

*Proof.* By the Extreme Value Theorem, the image of a compact set under a continuous map is compact. Since  $\mathbb{P}_{\mathbb{R}}^n$  is a compact, connected manifold of dimension  $n$ , we only need to show that  $r$  is continuous. However, we know that  $p$  and  $q$  are continuous on  $\mathbb{R}^{n+1}$ , so in particular on the open subset  $\mathbb{R}^{n+1} \setminus \{0\}$ . The denominator  $q$  is non-zero, so the quotient  $r = \frac{p}{q}$  is a continuous function. Given  $\lambda \in \mathbb{R} \setminus \{0\}$  we compute

$$r(\lambda x) = \frac{p(\lambda x)}{q(\lambda x)} = \frac{\lambda^d \cdot p(x)}{\lambda^d \cdot q(x)} = \frac{p(x)}{q(x)} = r(x)$$

for any  $x \in \mathbb{R}^{n+1} \setminus \{0\}$ , since  $p$  and  $q$  are homogeneous polynomials of degree  $d$ . Analogously,  $r$  yields the same value for every representative of points from  $\mathbb{R}^{n+1} \setminus \{0\}$ , implying that  $r$ 's continuity extends to the quotient space  $\mathbb{P}_{\mathbb{R}}^n$ . This proves the first claim.

For the second claim, we realize that  $r$  is well-defined on  $\mathbb{P}_{\mathbb{R}}^n \cong \mathbb{R}^{n+1}/(x \sim \lambda x : \lambda \in \mathbb{R} \setminus \{0\})$ . As a consequence, the function's value is constant on the representatives  $[x] = [\lambda x]$  for  $x \in \mathbb{R}^{n+1}$  and  $\lambda \in \mathbb{R} \setminus \{0\}$ . Then, minimizing  $r$  over  $\mathbb{P}_{\mathbb{R}}^n$  is equivalent to minimizing  $r$  over  $\mathbb{R}^{n+1} \setminus \{0\}$ , finishing the proof.  $\square$

**Proposition 3.6.3.** *Let  $p, q \in \mathbb{R}[x_0, x_1, \dots, x_n]$  be homogeneous polynomials of the same degree and assume that  $q$  is not identically zero. Define*

$$r(x) = \frac{p(x)}{q(x)}.$$

Assume that  $r$  is a reduced fraction and suppose that  $r$  is bounded below on  $\mathbb{R}^{n+1} \setminus \mathcal{V}(q)$ . Then,  $r$  attains its infimum as a function  $\mathbb{P}_{\mathbb{R}}^n \setminus \mathcal{V}_{\mathbb{P}}(q) \rightarrow \mathbb{R}$ . By extension,  $r$  attains its infimum as a function  $\mathbb{R}^{n+1} \setminus \mathcal{V}(q) \rightarrow \mathbb{R}$ .

*Proof.* Denote the quotient map from  $\mathbb{R}^{n+1}$  onto  $\mathbb{P}_{\mathbb{R}}^n$  by  $\pi$ . Notice that  $r$  is meromorphic on  $\mathbb{R}^{n+1}$ . In particular, it is smooth outside its poles. By assumption,  $r$  is bounded below by  $r_{low} \in \mathbb{R}$ , so all of  $r$ 's poles are located at  $+\infty$  and are attained inside of  $\mathcal{V}(q)$ . Consequently,  $r$  defines a smooth function in  $\mathbb{R}^{n+1} \setminus \mathcal{V}(q)$ . This property extends to  $\mathbb{P}_{\mathbb{R}}^n \setminus \mathcal{V}_{\mathbb{P}}(q)$  as the projection map  $\pi$  leaves  $r$ 's fibers untouched. Still,  $\mathbb{P}_{\mathbb{R}}^n \setminus \mathcal{V}_{\mathbb{P}}(q)$  is not necessarily compact, which is why we cannot apply the generalized Extreme Value Theorem as was done in Proposition 3.6.2.

Without loss of generality, assume that  $q$  is not constant. Otherwise,  $p$  is also constant by assumption, making  $r$  a constant function that attains its minimum everywhere. This turns the set of potential poles  $\mathcal{V}_{\mathbb{P}}(q)$  into a hypersurface in  $\mathbb{P}_{\mathbb{R}}^n$ . We distinguish  $r_{\pi} : \mathbb{P}_{\mathbb{R}}^n \setminus \mathcal{V}_{\mathbb{P}}(q) \rightarrow \mathbb{R}$  from the map  $r : \mathbb{R}^{n+1} \rightarrow \mathbb{R} \cup \{\infty\}$  that maps into the extended real line, after identifying poles with  $\infty$ . For some sufficiently small  $\varepsilon > 0$ ,  $r$  maps the open tubular neighborhood

$$U_{\varepsilon}(\mathcal{V}(q)) = \bigcup_{x \in \mathcal{V}(q)} B_{\varepsilon}(x)$$

in  $\mathbb{R}^{n+1}$  to some set with infimum  $C_{\varepsilon} = \inf r(U_{\varepsilon}(\mathcal{V}(q)))$ , such that  $r^{-1}((-\infty, C_{\varepsilon})) \neq \emptyset$ . The reason that this works is that all poles are located at  $+\infty$  by assumption. The rational function  $r$ 's numerator and denominator have the same degree, so it is well-defined on  $\mathbb{P}_{\mathbb{R}}^n$  and attains identical values on all representatives from  $\mathbb{R}^{n+1}$ . By the choice of  $\varepsilon$ ,  $C_{\varepsilon} > \inf r(\mathbb{P}_{\mathbb{R}}^n)$ . so we obtain the proper inclusion

$$[C_{\varepsilon}, +\infty) \subseteq \left( \frac{C_{\varepsilon} + \inf r_{\pi}(\mathbb{P}_{\mathbb{R}}^n)}{2}, +\infty \right) = U$$

with  $r(\mathbb{R}^{n+1} \setminus r^{-1}(U)) \neq \emptyset$  by construction. Since  $r$  is continuous, so is  $r_{\pi}$  as the composition and restriction of continuous maps. Thus,  $r_{\pi}^{-1}(U)$  is open, meaning that  $\mathbb{P}_{\mathbb{R}}^n \setminus r_{\pi}^{-1}(U)$  is closed. As a consequence, the latter set is compact as a closed subset of a compact space. The generalized Extreme Value Theorem dictates that  $r_{\pi}$  attains its infimum there. Finally,  $C_{\varepsilon} > \inf r(\mathbb{P}_{\mathbb{R}}^n)$  and  $\emptyset \neq \mathbb{P}_{\mathbb{R}}^n \setminus r_{\pi}^{-1}(U) \subset \mathbb{P}_{\mathbb{R}}^n \setminus \mathcal{V}_{\mathbb{P}}(q)$ , so the function  $r_{\pi} : \mathbb{P}_{\mathbb{R}}^n \setminus \mathcal{V}_{\mathbb{P}}(q) \rightarrow \mathbb{R}$  also attains its infimum.

Analogous to the proof of Proposition 3.6.2, we realize that  $r$ 's value is constant on the lines  $\lambda x$  with  $x \in \mathbb{R}^{n+1}$  for some  $\lambda \in \mathbb{R} \setminus \{0\}$ . The homogeneity of  $q$  yields that  $x \in \mathcal{V}(q)$  if and only if  $\lambda x \subset \mathcal{V}(q)$  for all  $\lambda \in \mathbb{R} \setminus \{0\}$ . Both of these statements combined imply that if  $x \in \mathbb{P}_{\mathbb{R}}^n \setminus \mathcal{V}_{\mathbb{P}}(q)$  minimizes  $r$ , then  $r$  attains its minimum on the line  $\lambda x \subset \mathbb{R}^{n+1} \setminus \mathcal{V}(q)$  for  $\lambda \neq 0$ .  $\square$

**Remark 3.6.4.** Rational functions are by no means the only functions that are well-defined on  $\mathbb{P}_{\mathbb{R}}^n$ . In fact, any function  $f : \mathbb{R} \rightarrow \mathbb{R}$  is well-defined on  $\mathbb{P}_{\mathbb{R}}^n \setminus \mathcal{V}_{\mathbb{P}}(q)$  after concatenating  $f$  with a rational function  $r = p/q$  with homogeneous numerator and denominator of the same degree  $f \circ r : \mathbb{P}_{\mathbb{R}}^n \setminus \mathcal{V}_{\mathbb{P}}(q) \rightarrow \mathbb{R}$ .

**Remark 3.6.5.** The generalized Extreme Value Theorem holds for both, infima and suprema. Consequently, we expect that the dual optimization problem of maximizing a function

has identical theoretical guarantees. Proposition 3.6.2 holds without alterations, while for Proposition 3.6.3 it needs to be assumed that the function  $r$  is bounded above on  $\mathbb{R}^{n+1} \setminus \mathcal{V}(q)$ .

**Example 3.6.6.** To gain familiarity with the rather abstract concepts from this section, let us consider the rational function  $r(x, y) = (x^2 - y^2)/(y^2 + 1)$  in  $\mathbb{R}^2$ . As a function, it is bounded below by  $-1$  and unbounded above. Nevertheless, this infimum is never attained in  $\mathbb{R}^2$ . In Figure 3.6.7(l.), the function  $r$  is depicted as a heatmap.

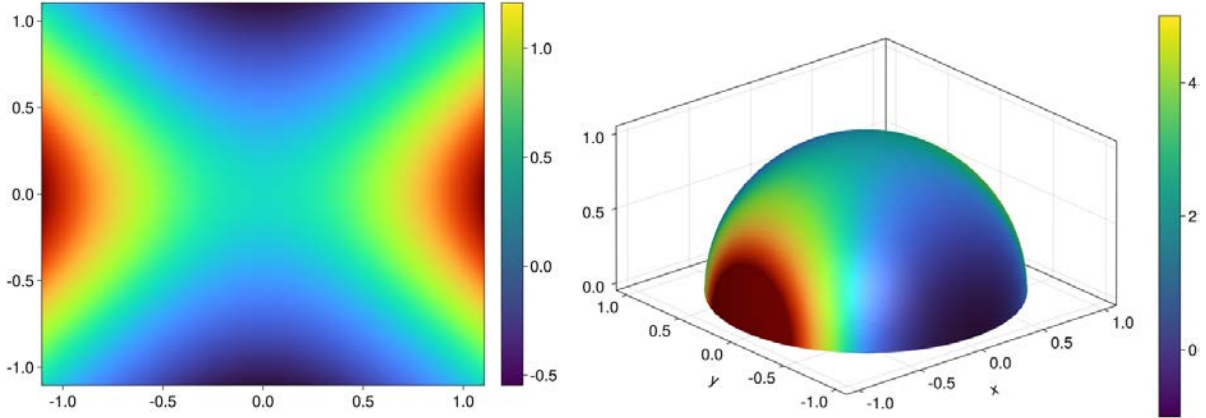


**Figure 3.6.7:** We depict heatmaps of  $r$  as a function on  $\mathbb{R}^2$  (l.) and of  $r^h$  as a function on  $\mathbb{P}_{\mathbb{R}}^2 \setminus \mathcal{V}\{[1 : 0 : 0]\}$  (r.). The red colors are cut off from the legend and represent large, positive values.

Homogenizing  $r$ , we obtain the rational function  $r^h(x, y, z) = (x^2 - y^2)/(y^2 + z^2)$ . By Proposition 3.6.3, this function is well-defined on  $\mathbb{P}_{\mathbb{R}}^2 \setminus \mathcal{V}(y^2 + z^2) = \mathbb{P}_{\mathbb{R}}^2 \setminus \{[1 : 0 : 0]\}$  and attains its infimum there. The sphere  $S^2$  is a twofold covering space of  $\mathbb{P}_{\mathbb{R}}^2$ , meaning that it can be immersed in  $\mathbb{R}^3$  in the form of a half-sphere with boundary (cf. [226, p.372f.]). Correspondingly,  $r^h$  is depicted as a heatmap on  $\mathbb{P}_{\mathbb{R}}^2$  in Figure 3.6.7(r.). As  $r^h$  has a pole at  $+\infty$  in  $[1 : 0 : 0] \in \mathbb{P}_{\mathbb{R}}^2$ , the meromorphic function's value is cut off at 5 for visualization purposes.

From the plots, we can deduce that  $r^h$  attains its infimum  $-1$  in the point  $[0 : 1 : 0]$ . This fact can also be deduced analytically by differentiating  $r^h$  and applying the second-order criterion for optimality (cf. [234, Thm. 2.3]).

While this is an interesting tool to play around with, rational functions put a strong restriction on the family of admissible functions for the optimization problem's objective function. Nevertheless, relative to polynomials, rational functions can be used to model significantly more problems from the physical world. Hence, this topic deserves to be investigated further, as it opens new possibilities. Please see Iori and Ohtsuka [174], and Gustafsson [144] for further references on this topic.

### 3.7 Statistics: Maximum Likelihood Retraction

In this section we leave the setting of submanifolds of Euclidean space and instead consider statistical models as submanifolds of a more general Riemannian manifold whose metric varies from point to point. We will show that replacing the minimization of Euclidean distance with the

maximization of likelihood defines analogous retraction maps to optimize functions on statistical models  $\mathcal{M}$ . Theorem 3.7.6 shows how to make these retractions second-order accurate for the Levi-Civita connection on  $\mathcal{M}$ . Finally, Algorithm 3.7.10 describes how homotopy continuation can be used to compute these retraction maps on arbitrary, implicitly-defined statistical models.

Consider the smooth manifold structure on  $\mathbb{R}_{>0}^n$  induced by viewing the identity map as a global chart. We will denote the coordinates for this global chart by  $(x_i)$  for all of our computations. The chart-induced global frame for the cotangent bundle over  $\mathbb{R}_{>0}^n$  is labeled  $(dx_1, \dots, dx_n)$ , while  $(\partial_1, \dots, \partial_n)$  will denote the chart-induced global frame for the tangent bundle. The individual values at a point  $x \in \mathbb{R}_{>0}^n$  will be called  $\partial_i|_x$ , so that the vectors  $(\partial_1|_x, \dots, \partial_n|_x)$  form a basis for  $T_x \mathbb{R}_{>0}^n$ .

Let  $\Delta_{n-1} \subset \mathbb{R}_{>0}^n \subset \mathbb{R}^n$  be the *open probability simplex* defined by

$$\Delta_{n-1} = \left\{ (x_1, \dots, x_n) \in \mathbb{R}_{>0}^n : \sum_{i=1}^n x_i = 1 \right\}.$$

Given  $u \in \Delta_{n-1}$  we define the *log-likelihood function*  $\ell_u : \mathbb{R}_{>0}^n \rightarrow \mathbb{R}$  by

$$\ell_u : (x_1, \dots, x_n) \mapsto \sum_{i=1}^n u_i \log(x_i) = \log \left( \prod_{i=1}^n x_i^{u_i} \right). \quad (3.7.1)$$

A *smooth statistical model* is a smooth submanifold  $\mathcal{M} \subset \Delta_{n-1}$ . In contrast, an *algebraic statistical model* is a subset  $\mathcal{M} \subset \Delta_{n-1}$  which is a real algebraic variety. Given a point  $u \in \Delta_{n-1}$  coming from the results of an experiment, maximum likelihood estimation seeks to find the point  $p \in \mathcal{M}$  which maximizes the likelihood of observing the results  $u$ . In other words, such a point maximizes  $\ell_u$  restricted to  $\mathcal{M} \subset \Delta_{n-1}$ . For more details, see Hogg et al. [163, §6] or Pachter and Sturmels [244].

Recall that a Riemannian metric is a smooth symmetric covariant 2-tensor field that is positive definite at each point (cf. Definition 3.1.4). In the global chart on  $\mathbb{R}_{>0}^n$ , the *Fisher metric* can be written as

$$g = \sum_{i,j=1}^n g_{ij} dx_i \otimes dx_j$$

in terms of the dual basis  $\{dx_1, \dots, dx_n\}$  where  $g_{ii} = 1/x_i$  and  $g_{ij} = 0$  for any  $i \neq j$ . Therefore, the  $g_{ij}$  are smooth functions written in the global chart coordinates. Indeed, it is a Riemannian metric (cf. [28, p.31]). In statistics and information geometry, the Fisher metric arises naturally as the unique metric invariant under sufficient statistics [28, Thm. 1.2]. In maximum likelihood estimation, one chooses the parameters of a model in order to maximize the likelihood of the observed data. The Fisher metric appears in the Cramér-Rao inequality [28, Thm. 1.3], relating it to the estimator's reliability. The Fisher metric on  $\mathbb{R}_{>0}^n$  induces a metric on the smooth manifold  $\Delta_{n-1}$  and the smooth statistical model  $\mathcal{M}$  in accordance with Definition 3.1.6.

Given a function  $f$  on a manifold, in local coordinates the vector field  $\text{grad } f$  becomes

$$\sum_{j=1}^n \left( \sum_{i=1}^n g^{ij} \partial_i f \right) \partial_j$$

where the  $g^{ij}$  are smooth functions giving the inverse of the matrix  $g_{ij}$  of the metric [197, p.27]. For the Fisher metric,  $g^{ii} = x_i$  and  $g^{ij} = 0$  for  $i \neq j$ . Since  $\partial_j \ell_u = u_j/x_j$  we see that

$$\text{grad } \ell_u = \sum_{j=1}^n \left( x_j \frac{u_j}{x_j} \right) \partial_j = \sum_{j=1}^n u_j \partial_j.$$

Compare this with the Euclidean gradient, which we denote  $\nabla \ell_u$ , given by

$$\nabla \ell_u = \sum_{j=1}^n \frac{u_j}{x_j} \partial_j$$

in the same global frame, but computed with the Euclidean metric  $g_{ij} = \delta_{ij}$ . The metrics themselves will be denoted by  $\langle \cdot, \cdot \rangle_p^{(f)}$  and  $\langle \cdot, \cdot \rangle_p^{(e)}$  when they act as inner products on the tangent space  $T_p \mathbb{R}_{>0}^n$ . Accordingly,  $N_p^{(f)} \mathcal{M}$  and  $N_p^{(e)} \mathcal{M}$  denote the normal spaces inside  $T_p \mathbb{R}_{>0}^n$  with respect to the Fisher and Euclidean metrics. The relation between these two linear spaces can be illustrated by the log-likelihood function (3.7.1), giving rise to an explicit description of the Fisher normal space  $N_p^{(f)} \mathcal{M}$  (cf. [13]):

$$u \in N_p^{(f)} \mathcal{M} \Leftrightarrow \nabla \ell_u(p) \in N_p^{(e)} \mathcal{M}. \quad (3.7.2)$$

To better visualize how these normal spaces differ, let us consider an example that appears in Alexandr and Heaton [13].

**Example 3.7.3.** Flipping a biased coin three times such that the probability of observing heads is given by  $\phi \in [0, 1]$  can be modeled as a curve in the 3-dimensional probability simplex  $\Delta_3 \subset \mathbb{R}_{>0}^4$ . The sample space is given by

$$\{\text{hhh}, \text{thh}, \text{hth}, \text{hht}, \text{htt}, \text{tth}, \text{ttt}\}$$

for heads “h” and tails “t”. This experiment leads to a binomial distribution, so the corresponding probability density can be parametrized by the twisted cubic

$$\phi \mapsto \mathcal{P}(\phi) = (\phi^3, 3\phi^2(1-\phi), 3\phi(1-\phi)^2, (1-\phi)^3).$$

Since it is notoriously hard to visualize 4-space, the simplex  $\Delta_3$  is transformed to  $\mathbb{R}^3$  via the projection  $e_i(\mathbb{R}^4) \mapsto e_i(\mathbb{R}^3)$  for  $i \in \{1, 2, 3\}$  and  $e_4(\mathbb{R}^4) \mapsto e_1(\mathbb{R}^3) + e_2(\mathbb{R}^3) + e_3(\mathbb{R}^3)$ . The twisted cubic and a few Fisher normal spaces along it are depicted in Figure 3.7.4.

The left picture clearly illustrates that the concept of orthogonality significantly differs from the Euclidean case: The normal spaces appear to be parallel, even though the curve bends. Naturally, this phenomenon can be ascribed to a different notion of geodesy, stemming from the Fisher metric on  $\mathbb{R}_{>0}^n$ .

Analogous to Section 3.2.1, we now want to introduce a metric projection (cf. [5]) for the Fisher metric, giving rise to a second-order retraction in the open probability simplex. Viewing  $\mathcal{M}$  as a Riemannian submanifold of  $\mathbb{R}_{>0}^n$ , we will use the Levi-Civita connection (cf. Theorem 3.1.9) corresponding to the Fisher metric in our computations of covariant derivatives

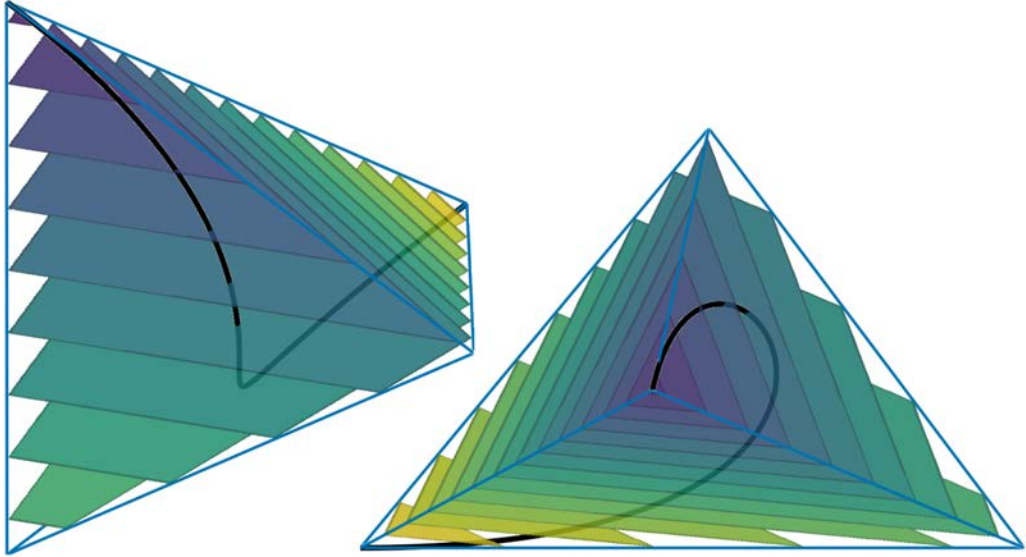


**Figure 3.7.4:** The twisted cubic  $P(\gamma)$  and selected Fisher normal spaces  $N_p^{(f)}\mathcal{P}([0, 1])$  intersected with the 3-dimensional probability simplex  $\Delta_3 \subset \mathbb{R}_{>0}^4$  are depicted here. The last coordinate is projected to  $(1, 1, 1)$  and the projected tetrahedron's edges are depicted in blue. This figure is inspired by Alexandr and Heaton [13].

below to show that our explicitly described function is indeed a retraction. First, we prove a lemma that is akin to the tubular neighborhood theorem (cf. Theorem 3.1.7).

**Lemma 3.7.5.** *Equip  $\mathbb{R}_{>0}^n$  with the Fisher metric. For any smooth statistical model  $\mathcal{M} \subset \Delta_{n-1}$ , there exists a neighborhood of  $p \in \mathcal{M}$  in  $\mathbb{R}_{>0}^n$  for which the maximum likelihood problem has a unique solution.*

*Proof.* Consider the normal bundle  $N^{(f)}\mathcal{M}$  as a submanifold of  $\mathbb{R}_{>0}^n \times \mathbb{R}^n$  and define the addition map  $E : N^{(f)}\mathcal{M} \rightarrow \mathbb{R}^n$  by  $E(y, w) = (y_i + w_i)_{i=1}^n$  in the global coordinates, denoted  $y + w$  for short. As the restriction of the addition map on  $\mathbb{R}^n$ , this is a smooth map. Its differential at  $(p, 0)$  is bijective. To see this, consider  $E$  restricted to the subset  $\mathcal{M}_0 = \{(y, 0) : y \in \mathcal{M}\}$ . Then,  $E|_{\mathcal{M}_0}$  is a diffeomorphism of  $\mathcal{M}_0$  onto  $\mathcal{M}$ . Hence, its differential at  $(p, 0)$  is isomorphic to  $T_p\mathcal{M}$ . Restricting  $E$  to  $N_0 = \{(p, w) : w \in N_p^{(f)}\mathcal{M}\}$  gives a map onto the affine subspace  $p + N_p^{(f)}\mathcal{M} \subset \mathbb{R}^n$  whose differential is also bijective. The dimension formula  $\mathbb{R}^n = T_p\mathbb{R}_{>0}^n = T_p\mathcal{M} \oplus N_p^{(f)}\mathcal{M}$  then shows that  $dE_{(p, 0)}$  is bijective. By the inverse function theorem for manifolds [198, Thm. 4.5],  $E$  is a local diffeomorphism at  $(p, 0)$ . In particular, there is a neighborhood  $W$  of  $(p, 0)$  in the normal bundle  $N^{(f)}\mathcal{M}$  where  $E$  is injective. By the Invariance of Domain Theorem [58], the image of this neighborhood under  $E$  is an open neighborhood of  $p$  in  $\mathbb{R}^n$ .

We claim that the maximum likelihood problem has a unique solution in  $E(W)$ , which we will prove via contradiction. Assume that  $w \in E(W)$  had two points  $y, z \in \mathcal{M}$  which maximized the log-likelihood function  $\ell_w$  restricted to  $\mathcal{M}$ . By the usual first-order criteria for local maxima constrained to a subset of  $\mathbb{R}^n$ , we know that the Euclidean gradients  $\nabla \ell_w|_y$  and  $\nabla \ell_w|_z$  lie in the Euclidean normal spaces  $N_y^{(e)}\mathcal{M}$  and  $N_z^{(e)}\mathcal{M}$ , respectively. We claim that this forces both  $\sum_i (w_i - y_i) \partial_i|_y$  and  $\sum_i (w_i - z_i) \partial_i|_z$  to be in  $N_y^{(f)}\mathcal{M}$  and  $N_z^{(f)}\mathcal{M}$ , respectively. To see this we

calculate with an arbitrary tangent vector  $\nu \in T_y\mathcal{M}$ ,

$$\begin{aligned}\langle \nu, w - y \rangle_y^{(f)} &= \langle \nu, w \rangle_y^{(f)} - \langle \nu, y \rangle_y^{(f)} \\ &= \langle \nu, \nabla \ell_w|_y \rangle_y^{(e)} - \langle \nu, \mathbf{1} \rangle_y^{(e)}.\end{aligned}$$

The first term is zero by first-order criteria for local maxima, and the second term is zero because  $\mathcal{M} \subset \Delta_{n-1}$  is a statistical model.  $\Delta_{n-1}$  describes an open subset of the affine hyperplane whose Euclidean normal vector is the all-ones vector, since probabilities sum to one. In this case, the symbol  $\mathbf{1}$  denotes the all ones vector  $\sum_j \partial_j|_y$ . Therefore,  $\sum_i (w_i - y_i) \partial_i|_y \in N_y^{(f)} \mathcal{M}$  and  $\sum_i (w_i - z_i) \partial_i|_z \in N_z^{(f)} \mathcal{M}$ . However,  $E(y, w-y) = y + w - y = w$  and  $E(z, w-z) = z + w - z = w$  contradict the injectivity of  $E$  on  $W$ . Therefore  $E(W)$  is a neighborhood of  $p \in \mathcal{M}$  in  $\mathbb{R}_{>0}^n$  for which the maximum likelihood problem has a unique solution.  $\square$

With this lemma, we can tackle the problem of constructing a second-order retraction in  $\Delta_{n-1}$  and prove the following:

**Theorem 3.7.6.** *Let  $\mathcal{M} \subset \Delta_{n-1} \subset \mathbb{R}_{>0}^n$  be a smooth statistical model. For  $p \in \mathcal{M}$  and  $v = \sum v_i \partial_i|_p \in T_p \mathcal{M}$ , consider the relation  $R_p \subset T_p \mathcal{M} \times \mathcal{M}$  defined by*

$$\{(v, q^*) : v \in T_p \mathcal{M}, q^* \in \arg \max_{q \in \mathcal{M}} \ell_{u(p,v)}(q)\}$$

where  $u(p, v) \in \mathbb{R}^n$  has components  $u_i = p_i + v_i + \frac{v_i^2}{4p_i}$ . Then there exists a neighborhood  $U \subset T_p \mathcal{M}$  of 0 where the arg max is unique and the relation  $R_p|_U$  defines a function

$$\begin{aligned}R_p|_U : U &\rightarrow \mathcal{M} \\ v &\mapsto \arg \max_{q \in \mathcal{M}} \ell_{u(p,v)}(q),\end{aligned}$$

which is a first-order, local retraction on  $\mathcal{M}$  at  $p$ .

Assume now that  $\mathcal{M}$  is a Riemannian submanifold of  $\mathbb{R}_{>0}^n$  equipped with the Fisher metric and its corresponding Levi-Civita connection. Then,  $R_p|_U$  is a second-order retraction, meaning that the curve  $t \mapsto R_p(tv)$  matches geodesics on  $\mathcal{M}$  up to second-order at  $t = 0$ .

*Proof.* First we check that there exists a neighborhood  $U$  of  $0 \in T_p \mathcal{M}$  such that  $R_p \cap (U \times \mathcal{M})$  actually defines a function  $R_p : U \rightarrow \mathcal{M}$ . Then we will check that this function is a retraction.

By Lemma 3.7.5 there exists a neighborhood  $E(W)$  of  $p$  in  $\mathbb{R}_{>0}^n$  where the maximum likelihood problem has a unique solution. Let  $u(p, \cdot) : T_p \mathcal{M} \rightarrow \mathbb{R}^n$  be the map sending a tangent vector  $v = \sum v_i \partial_i|_p$  to the tuple  $\left(p_i + v_i + \frac{v_i^2}{4p_i}\right)_{i=1}^n$ , where all coordinates are in terms of the global chart. Given  $p \in \Delta_{n-1}$ , recall that  $p_i \neq 0$  for all  $i = 1, \dots, n$ , making  $u$  a continuous function in both of its arguments. Since  $E(W)$  is open, there exists a neighborhood  $U$  of  $0 \in T_p \mathcal{M}$  where  $u(p, v) \in E(W)$  whenever  $v \in U$ , and hence the relation  $R_p$  defines a function on  $U$ . As a result, for  $p \in \mathcal{M}$  and  $v \in U \subset T_p \mathcal{M}$  we can define the function

$$R_p(v) = \arg \max_{q \in \mathcal{M}} \ell_{u(p,v)}(q).$$

First we verify that  $R_p$  is smooth. Let  $\pi : N^{(f)}\mathcal{M} \rightarrow \mathcal{M}$  be the projection onto  $\mathcal{M}$ , sending  $(y, n) \mapsto y$ .  $E$  is a diffeomorphism between  $W$  and  $E(W)$ . so we know that the inverse  $E^{-1}$  exists and is smooth on  $E(W)$ . Since  $R_p = \pi \circ E^{-1} \circ u(p, \cdot)$  is the composition of smooth maps,  $R_p$  is also smooth.

Now we check that  $R_p(0) = p$ . The argmax of the function  $\ell_u$  for any  $u \in \Delta_{n-1}$  over the larger domain  $\Delta_{n-1}$  is unique and equal to  $u$ . This can be verified by noting that  $u$  is the only critical point of  $\ell_u$  on  $\Delta_{n-1}$ , as  $\nabla \ell_u|_u \in N_u^{(e)}\Delta_{n-1}$ . In addition, the Euclidean Hessian of  $\ell_u$  at  $u$  is negative definite because  $\Delta_{n-1} \subset \mathbb{R}_{>0}^n$ , so the second-order criterion on maximality [234, Prop. 2.3] applies, yielding a global maximum in  $\mathbb{R}^n$ . This assertion is stronger than maximality in  $\Delta_{n-1}$ , so the second-order criterion for optimality in constraint optimization (cf. [234, Thm. 12.5]) shows maximality on  $\Delta_{n-1}$ . Therefore, when  $v = 0$  we have a unique argmax at

$$u(p, 0) = p + 0 = p \in \mathcal{M} \subset \Delta_{n-1}$$

Finally, we examine the conditions for a first-order and second-order retraction. The Riemannian structure is not necessary for first-order; still, we are proving second-order as well, so we treat both cases uniformly. Define  $c(t) = R_p(tv)$  for  $t$  in a small enough neighborhood  $\mathcal{I} \subset \mathbb{R}$  of zero, such that  $\mathcal{I} \cdot v \subset U$ . Then  $c(t)$  is the unique point in  $\mathcal{M}$  which maximizes the log-likelihood function  $\ell_{u(p,tv)}$  restricted to  $\mathcal{M}$ . Let  $\dot{c}$  be the vector field on the curve  $c$  given in the global chart by  $\dot{c} = \sum_{j=1}^n \dot{c}_j(t) \partial_j$ , where  $\dot{c}_j(t)$  denotes the derivative of the component function  $c_j(t)$  of the curve  $c : \mathcal{I} \rightarrow \mathcal{M}$ . To prove that  $R_p$  is a first-order retraction we need to show that  $v = \sum_j v_j \partial_j|_p$  is equal to  $\dot{c}|_p = \sum_j \dot{c}_j(0) \partial_j|_p$ . To demonstrate that  $R_p$  is a second-order retraction, it is necessary to show that  $D_t \dot{c}|_p \in N_p^{(f)}\mathcal{M}$  [47, Def. 5.42 and Eqn. 5.23]. Here,  $D_t$  denotes the covariant derivative along the curve  $c$ , using the Levi-Civita connection for the Fisher metric on  $\mathcal{M}$  (see [197, Thm 4.24]).

Let  $A$  be any vector field on the curve  $c$  which is tangent to  $\mathcal{M}$ , so that  $A(t) = A|_{c(t)} \in T_{c(t)}\mathcal{M}$  for all  $t \in \mathcal{I}$ . By the first-order criterion for local maxima we know that  $\langle A(t), \nabla \ell_{u(t)} \rangle_{c(t)}^{(e)} = 0$  for all  $t \in \mathcal{I}$ , since  $A$  is everywhere tangent to  $\mathcal{M}$ . We also know that  $\langle A(t), \mathbf{1} \rangle_{c(t)}^{(e)} = 0$  because  $\mathcal{M} \subset \Delta_{n-1}$ . By  $u(t) = u(p, tv)$  denote the curve in  $E(W)$  with components  $p_i + tv_i + t^2 \frac{v_i^2}{4p_i}$ , and let  $B = B(t)$  be the vector field along the curve  $c$  given by  $\sum_j B_j(t) \partial_j|_{c(t)}$  with the coefficients  $B_j(t) = u_j(t) - c_j(t) = p_j + tv_j + t^2 \frac{(v_j)^2}{4p_j} - c_j(t)$ . This enables us to compute

$$\begin{aligned} 0 &= \langle A(t), \nabla \ell_{u(t)} \rangle_{c(t)}^{(e)} - \langle A(t), \mathbf{1} \rangle_{c(t)}^{(e)} \\ &= \langle A(t), \nabla \ell_{u(t)} - \mathbf{1} \rangle_{c(t)}^{(e)} \\ &= \langle A(t), \sum_{i=1}^n (u_i(t) - c_i(t)) \partial_i|_{c(t)} \rangle_{c(t)}^{(f)} \\ &= \langle A(t), B(t) \rangle_{c(t)}^{(f)}. \end{aligned}$$

Note that  $B(t)$  is the orthogonal projection of  $\text{grad } \ell_{u(p,tv)}$  onto  $T_{c(t)}\Delta_{n-1}$  along the curve  $c$

when using the Fisher metric. Applying  $\frac{d}{dt}$  and  $\frac{d^2}{dt^2}$  using [197, Prop. 5.5] we find

$$0 = \frac{d}{dt} \langle A, B \rangle_{c(t)}^{(f)} = \langle D_t A, B \rangle_{c(t)}^{(f)} + \langle A, D_t B \rangle_{c(t)}^{(f)} \quad (3.7.7)$$

$$0 = \frac{d^2}{dt^2} \langle A, B \rangle_{c(t)}^{(f)} = \langle D_t D_t A, B \rangle_{c(t)}^{(f)} + 2 \langle D_t A, D_t B \rangle_{c(t)}^{(f)} + \langle A, D_t D_t B \rangle_{c(t)}^{(f)}. \quad (3.7.8)$$

Recall (see [197, p.102]) the covariant derivative of a vector field along a curve  $c$  is given by

$$D_t B(t) = \sum_k \left( \dot{B}_k(t) + \sum_i \sum_j \dot{c}_i(t) B_j(t) \Gamma_{ij}^k(c(t)) \right) \partial_k|_{c(t)} \quad (3.7.9)$$

where  $\Gamma_{ij}^k$  are the Christoffel symbols of the metric in the given local frame. For the Fisher metric with the corresponding Levi-Civita connection in the global frame  $\partial_k$  induced by the global chart, every  $\Gamma_{ij}^k = 0$  except  $\Gamma_{jj}^j(c(t)) = \frac{-1}{2c_j(t)}$ , evaluating at the point  $c(t)$  along the curve [197, p.123]. Inserting these Christoffel symbols into Equation (3.7.9) yields

$$D_t B(t) = \sum_k \left( \dot{B}_k(t) - \frac{\dot{c}_k(t) B_k(t)}{2c_k(t)} \right) \partial_k|_{c(t)}.$$

For  $t = 0$ , this expression becomes  $D_t B(0) = \sum_k (v_k - \dot{c}_k(0)) \partial_k|_p$ . Applying the equality  $c(0) = p$  then yields  $B(0) = 0$ . Since both  $v$  and  $\dot{c}|_p$  are in the tangent space at  $p$ , Equation (3.7.7) implies that  $v_k = \dot{c}_k(0)$  and so  $v = \dot{c}|_p$ , which completes the proof that  $R_p$  is a first-order retraction.

Having proved first-order, both  $B(0)$  and  $D_t B(0)$  are zero, and the first two terms of equation (3.7.8) vanish at  $t = 0$ . A somewhat tedious calculation (which we omit) shows that  $D_t D_t B(0) = \sum_k \left( \frac{(v_k)^2}{2p_k} - \ddot{c}_k(0) \right) \partial_k|_p$ . Calculating  $D_t \dot{c}(0)$  using Equation (3.7.9), it is noted that  $D_t D_t B(0) = -D_t \dot{c}(0)$ . Therefore, equation (3.7.8) becomes

$$\langle A(0), -D_t \dot{c}(0) \rangle_p^{(f)} = 0.$$

Since this is true for any vector field  $A$  which is everywhere tangent to  $\mathcal{M}$ , and hence for any tangent vector  $A(0) \in T_p \mathcal{M}$ , we have  $D_t \dot{c}(0) \in N_p^{(f)} \mathcal{M}$ , which completes the proof.  $\square$

Having established Theorem 3.7.6, we now describe how to use homotopy continuation to compute this new retraction map on statistical models  $\mathcal{M}$ . As the basic concepts were already introduced in Section 3.2.2, we omit them here.

Let  $p \in \mathcal{M}$ ,  $v = \sum v_i \partial_i|_p \in T_p \mathcal{M}$ , and a stepsize  $\alpha \in \mathbb{R}_{>0}$  be given, for example by backtracking line search (cf. Section 3.4). Say that  $\mathcal{M} \subset \Delta_{n-1} \subset \mathbb{R}^n$  is equal to the zeros of the smooth map  $g : \mathbb{R}^n \rightarrow \mathbb{R}^m$ . We will also assume that the dimension of  $\mathcal{M}$  is equal to  $n - m$ . If not, standard techniques of randomization in numerical nonlinear algebra [31, p.14f.] can be used to create a new map  $\tilde{g} : \mathbb{R}^n \rightarrow \mathbb{R}^k$  so that  $\mathcal{M} \subset \tilde{g}^{-1}(0)$ ,  $\dim \mathcal{M} = n - k$ , and the additional zeros of  $\tilde{g}$  are well-controlled (see [299, §13.5]). In what follows, let  $dg_x$  denote the  $m \times n$  Jacobian matrix of  $g$  in the standard basis,  $dg_x^T$  denote its  $n \times m$  transpose, and let  $\text{diag}(p_i)$  denote the  $n \times n$  diagonal matrix with entries  $p_i$ . Since  $\mathcal{M} \subset \Delta_{n-1}$ , we may assume that  $g_1 = -1 + \sum x_i$  is the first component function of the map  $g : \mathbb{R}^n \rightarrow \mathbb{R}^m$  implicitly defining

$\mathcal{M}$ . Choose  $\lambda_0 \in \mathbb{R}^m$  so that  $\lambda_0^T dg_p = (1, \dots, 1)$ . Then set  $u_0 = p$ . By construction,  $p \in \mathbb{R}_{>0}^n$  solves the equation  $dg_x^T \lambda_0 = \nabla \ell_{u_0}|_x$  for the variables  $x$ . These equations say that the Euclidean gradient of  $\ell_{u_0}$  at  $p$  is in the Euclidean normal space at  $p$ , which means that  $u_0$  lies in  $N_p^{(f)} \mathcal{M}$  by a previous observation in Equation (3.7.2), making  $p$  a critical point of  $\ell_{u_0}$  restricted to  $\mathcal{M}$ . We will use  $(p, \lambda_0)$  as a starting solution to a homotopy that begins with parameters  $u_0$  and ends with parameters  $u_\alpha = \left(p_i + \alpha v_i + \alpha^2 \frac{v_i^2}{4p_i}\right)_{i=1}^n$ .

Let  $G : \mathbb{R}_{>0}^n \times \mathbb{R}^m \times \mathbb{R}^n \rightarrow \mathbb{R}^{m+n}$  send  $(x, \lambda, u) \mapsto G(x, \lambda, u)$ , where the  $m+n$  component functions of  $G$  are those of  $g$  and the ones given by  $\text{diag}(x_i) dg_x^T \lambda - u$ . We define the homotopy  $H : \mathbb{R}_{>0}^n \times \mathbb{R}^m \times \mathbb{R} \rightarrow \mathbb{C}^{m+n}$  by  $H(x, \lambda; t) = G(x, \lambda, tu_\alpha + (1-t)u_0)$ . By construction,  $H(p, \lambda_0; 0) = 0$  holds at  $t = 0$ . If  $H(q, \lambda_1; 1) = 0$ , then  $q = R_p(\alpha v)$  by Theorem 3.7.6, provided that  $\alpha > 0$  is sufficiently small. We can compute  $(q, \lambda_1)$  by homotopy continuation using the start solution  $(p, \lambda_0)$  at  $u_0$ , though we merely keep  $q = R_p(\alpha v)$ . The auxiliary result  $\lambda_1$  parametrizes the normal space and provides no additional information to the user. We record these ideas in the following algorithm.

---

**Algorithm 3.7.10:** Maximum likelihood retraction by homotopy

---

**Inputs :**  $g, p, v, \alpha$  as described above.

**Output:**  $q = R_p(\alpha v)$  from Theorem 3.7.6.

Set  $u_0 = p$  and  $\lambda_0 = (0, \dots, 0)$

Set  $G(x, \lambda, u) = (g(x), x - u + dg_x^T \lambda)$

Set  $u_\alpha = \left(p_i + \alpha v_i + \alpha^2 \frac{v_i^2}{4p_i}\right)_{i=1}^n$

Set  $H(x, \lambda; t) = G(x, \lambda, tu_\alpha + (1-t)u_0)$ .

Use path-tracking (as described in Section 3.2.2) to discover the solution  $(x(1), \lambda(1))$  at  $t = 1$  from the initial values  $(x(0), \lambda(0)) = (p, \lambda_0)$  at  $t = 0$ . Return  $q = x(1)$ .

---

### 3.8 Rigidity and Flexibility: Approximation of Deformation Paths

Deciding whether a framework is rigid is an important area of research that has ramifications in structural engineering and soft matter. Since a framework is either flexible or rigid, a structure's rigidity can be determined by dually determining its flexibility. In doing so, we consider the linear space of infinitesimal flexes (e.g. [24]). Our aim is to understand which of them extend to finite flexes, meaning actual deformations of the frameworks. Assume that the constraints are given by a polynomial system  $g$  in  $n$  variables and denote the configuration for which we want to decide flexibility by  $p$ . Assume for the moment that we know the infinitesimal flex  $v \in \ker dg(p)$  extends to a finite flex and that  $p$  is a regular point of  $g^{-1}(0)$ . We can then employ the path-tracking Algorithm 3.2.10 to compute the second-order Euclidean distance retraction that was defined in Section 3.2.1.

To decide whether an infinitesimal motion extends to a finite flex, Frohmader and Heaton [120] suggest intersecting with a sphere centered in  $p$  of radius  $\varepsilon > 0$ . All continuous curves through  $p$  will intersect the sphere  $S_\varepsilon(p)$  if  $\varepsilon > 0$  is chosen sufficiently small. Computing witness sets on the algebraic set  $S_\varepsilon(p) \cap g^{-1}(0)$  and forming vectors between  $p$  and the witness points thus provides insights into both, the dimension of the subspace of the infinitesimal motions in  $p$

that extend to finite flexes and their directions.

For generic frameworks, such as Gilbert graphs obtained by random point processes, infinitesimal rigidity, and local rigidity are equivalent concepts [24]. Therefore, computing retractions to the constraint set usually works well. Unfortunately, the interesting configurations of locally rigid frameworks are not generic, but rather singularities of the Cayley-Menger variety  $g^{-1}(0)$ . For these structures, some infinitesimal motions do not extend to finite flexes. Furthermore, in singularities the Jacobian  $dg(p)$  is rank-deficient. For this reason, the linear systems contained in the path-tracking algorithm 3.2.10 do not possess a unique solution, obstructing the convergence of Newton's method.

Singularities as start solutions notoriously pose issues for the path-tracking algorithm because the direction of the continuation is ambiguous and Newton's method has a hard time escaping singularities. We propose an alternative approach. Here, geometric singularities inherent to the vanishing ideal generated by  $g$  and artifacts of algebraic dependencies between the equations in  $g$  are distinguished. To combat the issue of singularities as start solutions, we reverse our approach. Rather than using the singularity as start solution, it is simply used as the target solution instead. While this step may seem redundant, it significantly helps in approximating deformation paths.

To achieve this, we begin by intersecting  $g^{-1}(0)$  with a sphere of radius  $\varepsilon > 0$  centered in the singularity  $p$ . In general, the resulting algebraic set will not be 0-dimensional. Therefore, we need to intersect it with random hyperplanes to generate isolated solutions. The theory of witness sets guarantees that this procedure finds solutions from all connected components in  $\partial B_\varepsilon(p) \cap g^{-1}(0)$  [299, Thm. 13.5.1] and the trace test [202] can be employed to ensure that the witness set is complete. Choosing  $\varepsilon > 0$  small enough will then ensure that we find solutions from all connected components passing through  $p$ .

Commonly, homotopy continuation methods assume that the underlying polynomial system only possesses isolated solutions. While the literature suggests multiplying by a matrix with random entries [32, §9.2] or slicing with random hyperplanes [32, §8.2] to make overdetermined or underdetermined systems admissible, this approach may lead to numerical issues with the corresponding Jacobian's condition number [151]. Rather, there is no reason why the path-tracking procedure should fail in these cases. Since it involves solving linear systems, we can use a least squares approach to approximate a solution. Given the subsequent parameter  $u + \Delta u$ , the Euler predictor step  $\Delta z$  can be calculated via the linear system

$$\frac{\partial}{\partial z} G(z; u) \cdot \Delta z = - \frac{\partial}{\partial u} G(z; u) \cdot \Delta u.$$

This result uses Taylor's Theorem on a general, parametric and real polynomial system  $G$  with  $k$  equations,  $m$  parameters and  $n$  variables and is analogous to the construction from Section 3.3. Similarly, the Newton corrector step can be calculated by

$$G(z; u + \Delta u) = - \frac{\partial}{\partial z} G(z; u + \Delta u) \cdot \Delta z.$$

In both cases, the unknown is the step  $\Delta z$  to reach the subsequent point. Around regular points the Jacobian's rank is constant, so we can without loss of generality assume that the rank of

$\frac{\partial}{\partial z} G(z; u)$  and  $\frac{\partial}{\partial z} G(z; u + \Delta u)$  are identical and maximal for sufficiently small  $\Delta u$ . Analogous to Algorithm 3.2.10, we use a linear homotopy in the parameter  $t$  that will be specified later and set  $H(z; u) = G(z; u)$ .

---

**Algorithm 3.8.1:** Computation of Deformation Paths in Singularities

---

**Inputs :** Sampling radius  $\varepsilon > 0$ , tolerance  $\tau > 0$ , polynomial system  $g : \mathbb{R}^n \rightarrow \mathbb{R}^k$ ,  
point  $p \in \mathbb{R}^n$  such that  $g(p) = 0$ ,  
a discretization  $\varepsilon = t_0 > \dots > t_N = 0$

**Output:** Discretized deformation paths  $\mathcal{D} = \{(x(t_0)^{(i)}, \dots, x(t_N)^{(i)})\}_{i=1}^M$ .

Set  $\mathcal{D}$  to an empty array and set up the polynomial system  $G_\varepsilon(x) = (g(x), \langle x, x \rangle - \varepsilon^2)$ . Sample  $\{q_1, \dots, q_M\}$  from  $\partial B_\varepsilon(p) \cap g^{-1}(0)$  by intersecting with random hyperplanes in all possible dimensions.

```

for  $q \in \{q_1, \dots, q_M\}$  do
    Track the solution to  $G_\varepsilon$  from  $q$  to  $p$  using the path-tracking Algorithm 3.2.10 in
    combination with the provided discretization of the parameter interval  $[0, \varepsilon]$ .
    Append the resulting parameter path to  $\mathcal{D}$ .
end
return  $\mathcal{D}$ 

```

---

What remains is specifying the homotopy system  $G$ . Recall that the initial solutions are samples from  $\partial B_\varepsilon(p) \cap g^{-1}(0)$ . Since we have no additional information about the geometry of the Cayler-Menger variety  $g^{-1}(0)$ , it makes sense to continue with this approach. Namely, we decrease the parameter  $\varepsilon$  until the sphere collapses to a single point. Discretizing the interval  $[0, \varepsilon]$  enables us to path-track the solutions from the boundary of  $B_\varepsilon(p)$  to  $p$ . This algorithm is summarized in pseudocode in Algorithm 3.8.1. The paths corresponding to some of the initial points may not converge, be it because they cross singularities or because the corresponding connected component does not contain the singularity  $p$ . We refer to the homotopy continuation literature on how to approach these issues with all implemented precautions (e.g. Bates et al. [32] or Sommese and Wampler [299]).

**Example 3.8.2.** The Whitney umbrella is given by the implicit equation

$$g(x, y, z) = x^2 - y^2 z = 0.$$

Its singularities lie on the nonnegative  $z$ -axis. For this example, we work with the points  $p_1 = (0, 0, 0)$  and  $p_2 = (0, 0, 1)$ . Setting the sphere's radius to  $\varepsilon = 0.5$  and intersecting  $g^{-1}(0)$  with a random hyperplane, we expect to find 2 samples corresponding to the sphere around  $p_1$ . In contrast, we expect to find 4 samples when working with the sphere around  $p_2$ .

Applying Algorithm 3.8.1, we find deformation paths through  $p_1$  and  $p_2$ . They are depicted in Figure 3.8.3. As it turns out, the Whitney umbrella's symmetry leads to the 4 one-sided deformation paths through  $p_2$  smoothly consolidating into 2 two-sided deformation paths. These curves meet in a nodal singularity. Finding curves that smoothly connect is not generally expected, as the curves' smoothness highly depends on the local geometry around the singularity.

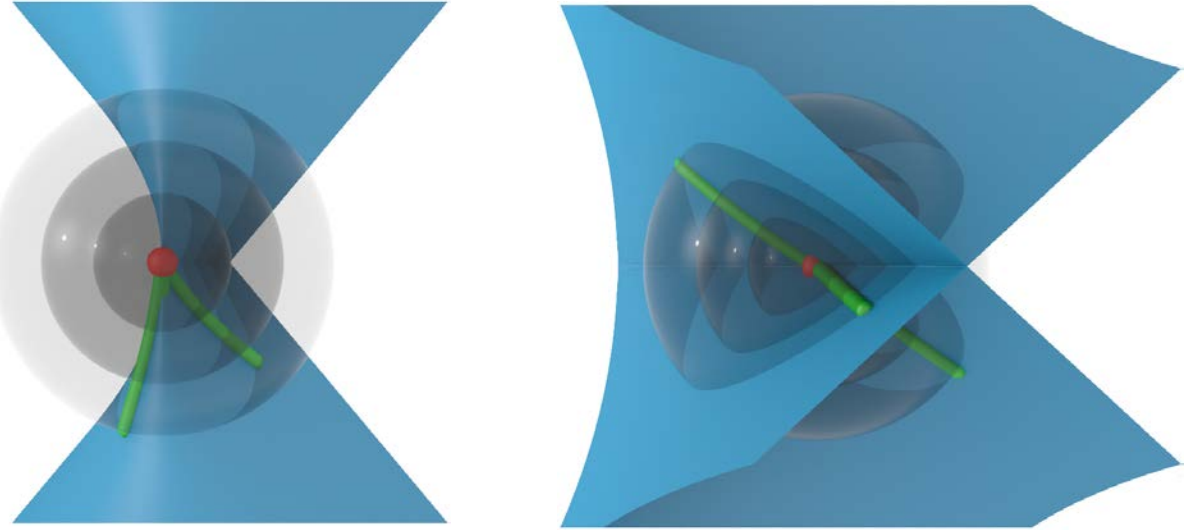


**Figure 3.8.3:** In both pictures, Algorithm 3.8.1 is applied to the Whitney umbrella. The singularities  $p_1 = (0, 0, 0)$  (l.) and  $p_2 = (0, 0, 1)$  (r.) depicted in red are given as input and the sphere's radius is chosen as  $\varepsilon = 0.5$ . The deformation paths obtained when reducing the spheres' radius starting in random samples are displayed in green.

In contrast, we only find two deformation paths corresponding to the two samples around  $p_1$ . They meet in a cuspidal singularity, highlighting that the origin is a special point of the Whitney umbrella.

Regarding the problem of algebraic dependencies between the constraints, the randomization of the polynomial system  $g$  is helpful. Bertini's Theorem [299, Thm. A.8.7] guarantees that with a probability of 1, for  $A \in \mathbb{C}^{n \times k}$  the system  $A \cdot g = 0$  contains all irreducible components of  $g = 0$  with nondecreasing multiplicity. By randomizing, we aim to produce a system that removes the algebraic dependencies between the polynomials in  $g$ . Hence, there is a Zariski open subset in  $g^{-1}(0)$  where the Jacobian  $d(A \cdot g)$  has full rank. By assumption, we know the subspace of the infinitesimal motions extending to finite flexes. This gives us a handle on the real dimension of the variety in a neighborhood of the point  $p$ . Picking  $k = n - \dim_p(g^{-1}(0))$  yields the desired result.

If we instead use this system to initialize the Lagrange multiplier system for the Euclidean distance retraction (cf. Section 3.2.1), we have all necessary tools at our disposal to approximate deformation paths of bar-and-joint frameworks and more general geometric constraint systems.

In Hauenstein et al. [151] it is argued, that this a priori randomization approach can produce ill-conditioned Jacobians and it is suggested to rather use the pseudoinverse of  $g$ 's Jacobian (cf. Section 3.3) in a regular point or regularized preconditioners as matrix  $A$ .

**Example 3.8.4.** The regular octahedron is rigid by the Cauchy-Dehn theorem when equipped with edge-length constraints. Nevertheless, there are nonconvex realizations that can be deformed while maintaining the edge lengths. One such nondegenerate realization is given by Bricard's octahedron [124]. Analogous to the octahedron, for constructing it we start by placing the six vertices in  $(0, 0, \pm 1)$  and  $(\pm 1, \pm 1, 0)$ .

The vertices  $(0, 0, \pm 1)$  are connected by edges to all of the other four vertices. Instead of

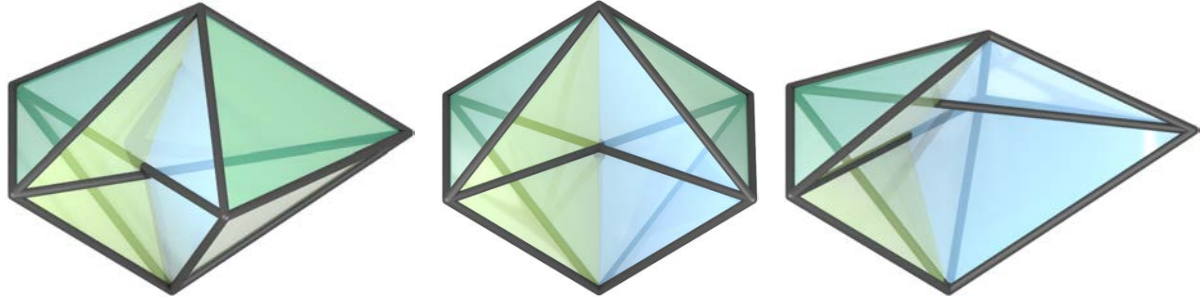


**Figure 3.8.5:** Bricard's octahedron is a flexible polytope in  $\mathbb{R}^3$ . This figure depicts the deformation of one realization of Bricard's octahedron.

then connecting the latter four vertices in a square, as is the case in the convex octahedron, they are connected in a crossed square. After pinning a triangle, this shape has a 1-dimensional space of infinitesimal motions, generated by a unit vector  $v$  corresponding to a shearing of the crossed square. Applying the Euclidean distance retraction from the randomized system  $A \cdot g$  to  $v$  lets us approximate the deformation path depicted in Figure 3.8.5.

### 3.9 HomotopyOpt.jl

The software package `HomotopyOpt.jl`<sup>9</sup> has been written in Julia which is a high-level, dynamic programming language. In particular, this gives us access to `HomotopyContinuation.jl` (cf. [54]), a numerical algebraic geometry package. Note that because we use this package, the map  $g : \mathbb{R}^n \rightarrow \mathbb{R}^m$  defining  $\mathcal{M}$  must have polynomial component functions, while the objective function can be anything smooth. Assume now that we want to optimize the smooth function  $f(x_1, x_2, x_3) = 2^{(x_2-1)^2}$  subject to the constraint set

$$g = \begin{bmatrix} x_1^2 + x_2^2 + x_3^2 - 1 \\ x_3 - x_1^3 \end{bmatrix}.$$

To solve this optimization problem with initial point  $(0, -1, 0) \in \mathcal{M}$  we write:

```

1 using HomotopyOpt # load package
2
3 p = [0, -1., 0]
4 f = x -> 2^((x[2]-1)^2)
5 g = x -> [x[1]^2+x[2]^2+x[3]^2-1, x[3]-x[1]^3]
6 M = ConstraintVariety(g, 3, 1) # M embedded in R^3 with dim 1
7 res = findminima(p, 1e-5, M, f) # Set the tolerance to 10^(-5)
```

Now, we can use Lagrange multipliers to calculate analytically that the minimum of  $f$  on  $\mathcal{V}(g)$  is at  $(0, 1, 0)$ . Indeed, by typing `res.computedpoints[end]` in the command prompt the final point can be examined, revealing the vector

$[-0.0012328615227131664 \ 0.9999992400259441 \ -1.8738848314414474e-9],$

which is an adequate approximation of the true optimum.

---

<sup>9</sup><https://github.com/matthiashimmelmann/HomotopyOpt.jl>

To solve this optimization problem the software takes several local steps (`maxlocalsteps`), running the Riemannian gradient descent Algorithm 3.2.7. First, it calculates a descent direction  $\mathbf{v}$  in  $T_p V$ , given by the negative Riemannian gradient obtained by projecting  $f$ 's gradient onto  $T_p V$ . Afterwards, the algorithm uses backtracking line search with Wolfe conditions to compute a feasible step size corresponding to the previously chosen descent direction (see [167, 259]). These conditions provide a lower and an upper bound on admissible step sizes and come alongside convenient theoretical guarantees, such as the existence of open intervals of step sizes satisfying the Wolfe conditions [167]. When presented with a sequence of step sizes satisfying the Wolfe conditions and well-chosen descent directions such as steepest descent, Zoutendijk's Theorem [259] guarantees convergence for the corresponding Riemannian optimization algorithm. After having chosen a step size  $\alpha$  and a descent direction  $v$ , the linear steps  $p + \alpha v$  are corrected to the variety using the Euclidean distance retraction. By setting the parameter `whichstep="Algorithm 0"` in `findminima`, Algorithm ED0 is used to compute the Euclidean distance retraction. Conversely, setting `whichstep="Algorithm 1"` results in Algorithm ED1 and `whichstep="Algorithm 2"` makes use of Algorithm ED2. It is generally recommended to use one of the latter two algorithms based on homotopy continuation.

Having completed `maxlocalsteps` local steps, we check if the first-order criterion for optimality  $\text{grad}(x_k) \approx 0$  is satisfied, and also whether the algorithm is stuck in a saddle point or singularity. Our method recognizes saddle points by looking for insufficient decrease in the objective function and singularities by comparing the current Jacobian's numerical rank to the previous Jacobian's rank. If it changed, we need to assume that the iteration is currently in or close to a singularity. In either of these cases, we proceed to check whether the current iterate is a minimum by employing the second-order criterion on optimality (see [47, Prop. 6.3]). If it is inconclusive or finds that the current point is not optimal, the algorithm continues. In case of a singularity, we additionally try to resolve the singularity by intersecting the variety with a sphere centered at the current iterate and possibly additional hyperplanes. The intersection point with the smallest objective function value is then chosen to continue the optimization process (cf. Section 3.5). Otherwise, if the second-order criterion has a positive result, the current point is returned to the user as optimal. Finally, if the algorithm is inconclusive and exceeds the prescribed maximal amount of time `maxseconds`, the current point is returned with the additional information `lastpointisminimum=false`.

There are a few additional ways to interact with this package that deserve mentioning. The method `watch` animates the optimization procedure's steps on the manifold; `draw` produces a static picture of both the local steps and a global picture and `setequationsatp!` randomizes the equations at a specific point, such that there are only codimension-many left. For this, the dimension is calculated at the specified point by checking the constraint system's Jacobian rank.

### 3.10 Performance Analysis of the Euclidean Distance Retraction

In this section, we present examples of different  $\mathcal{M}, p, v$  where we compute the Euclidean distance retraction  $R_p(v)$  via the Algorithms ED0, ED1 and ED2. The results are analyzed by comparing the performance of these methods on several examples.

Recall that Algorithm ED0 simply applies Newton's method to the Lagrange multiplier

system  $G(x, \lambda; u) = 0$  (see Equation 3.2.5) with  $u = p+v$ , hoping it converges to the correct point  $R_p(v)$ . Conversely, Algorithms ED1 and ED2 apply versions of homotopy continuation with the aim of more robustly computing  $R_p(v)$ . Algorithm ED1 computes  $R_p(t_j v)$  for a discretization  $0 = t_0 < t_1 < \dots < t_m < t_{m+1} = 1$  of  $[0, 1]$ , applying Newton's method at each step using the solution from the previous step as the initial iterate. We record the number of intermediate steps  $m$  in our tables below and call Newton's method the corrector-step. Similarly, Algorithm ED2 discretizes the interval into  $m$  intermediate steps but uses both a predictor and a corrector step.

To optimally compare Algorithms ED0, ED1 and ED2, identical implementations of Newton's method `newton()` are taken from the `HomotopyContinuation.jl` package. In particular, `newton()` declares a failure to converge if the distance between iterates does not decrease, meaning that for some iterate  $j \geq 1$  the inequality

$$\|x^{(j+1)} - x^{(j)}\| \leq \|x^{(j)} - x^{(j-1)}\|$$

is violated. Notice that this behavior indicates the starting point is far from an approximate zero in the sense of Smale [296]. In the following, such behavior is marked with an “x”. In contrast, convergence to an incorrect point  $q \neq R_p(v)$  is marked with a “w”, an abbreviation for “wrong”.

Since Algorithm ED2 differs from ED0 and ED1 in its use of a predictor step, we compare two different versions. “Alg. ED2 with Euler” refers to our implementation of a basic Euler step, which requires evaluation of the Jacobian and solving the resulting linear system. Our implementation is inferior to the evaluations and linear solves as implemented in `newton()`. Therefore, the “average time” column provides a meaningful comparison among Algorithm ED0, Algorithm ED1, and “Alg. ED2 with HC.jl”. However, it is not meaningful for “Alg. ED2 with Euler” due to the excellent implementation of `newton()` in `HomotopyContinuation.jl`.

To address this issue, we also include the column “linear solves” in our tables, which records the number of linear systems that are solved in computing  $R_p(v)$ . This can be used to compare “Alg. ED2 with Euler” to the other methods. In contrast, “Alg. ED2 with HC.jl” refers to the default path-tracking algorithm implemented in `HomotopyContinuation.jl`. In particular, the predictor step typically uses Padé approximants (cf. [312, 316]), while the corrector step uses `newton()`. We were able to extract the number of intermediate steps for “Alg. ED2 with HC.jl”, but not the total number of linear solves.

In conclusion, the average time column may be used to meaningfully compare Algorithm ED0, Algorithm ED1, and Alg. ED2 with HC.jl, while the column linear solves may be used to meaningfully compare Algorithm ED0, Algorithm ED1, and Alg. ED2 with Euler.

Additionally, we utilize `BenchmarkTools.jl`<sup>10</sup> to repeatedly run the algorithms. This rules out exterior factors independent of the method, such as background processes, precompilation, and startup time, as the cause for performance differences. The three algorithms are then run with the same choice of  $p$  and  $v$ . We compare their results across multiple discretizations of step size  $\Delta t = 1/(m + 1)$  of the interval  $[0, 1]$  and pick the discretization where the algorithm performs best. For that discretization, we record the following benchmarks:

---

<sup>10</sup><https://github.com/JuliaCI/BenchmarkTools.jl>

- The average time it takes to compute  $R_p(v)$ .
- The number  $m$  of intermediate steps in the discretization of  $[0, 1]$ , as in

$$0 = t_0 < t_1 < \cdots < t_m < t_{m+1} = 1.$$

- The number of linear systems solved while computing  $R_p(v)$ .

All numbers are rounded to the same number of digits. The test instances are available in the `HomotopyOpt.jl` repository (cf. Section 3.9) and were run on a Windows 11 64-Bit machine with an Intel i7-10750H @ 2.6GHz processor and 16GB RAM. For reproducibility, a fixed random seed is used, and readers may run the code themselves. It is available by executing the file `testEDRetraction.jl`<sup>11</sup>. The figures are produced with a `GLMakie` backend [90] using the package `ImplicitPlots.jl`<sup>12</sup>.

### 3.10.1 Examples

Our first two examples are simple and low-dimensional. Their purpose is to make it visually clear to the reader that Algorithm ED0 may jump components and return the wrong  $R_p(v)$ . The first two examples clearly illustrate the algorithms' behavior on low-dimensional examples, with a focus on further explaining the open set from the theoretical Lemma 3.3.3. Examples 3 to 6 are larger, with 16, 51, 100, and 147 variables, respectively. Additionally, Examples 3, 4, and 6 are geometric constraint systems.

**Example 1:** As a first test case, consider the planar quartic curve  $\mathcal{V}_1$  given by the implicit equation

$$(y - x^2 - 1) \cdot (y + x^2 + 1) = 0.$$

Over  $\mathbb{R}^2$ , this smooth algebraic set consists of two parabolas that are mirror-symmetric in the  $x$ -axis. The special property of this set is that its medial axis contains the  $x$ -axis. Hence, the closest point to any point in the upper half-plane lies on the upper parabola  $y = x^2 + 1$ , while the closest point to any point in the lower half-plane lies on the lower parabola  $y = -x^2 - 1$ . This poses an issue for any path-tracking scheme: The discretization of the unit interval plays an essential role in ensuring convergence to the Euclidean distance retraction  $R_p(v)$ . To highlight this property, we choose  $p = (-2, 5)$  as initial point and  $v = (2, 8)$  as tangent vector. We find that  $R_p(v) = (0, 1)$ . This retraction is visualized in Figure 3.10.1 alongside the performance analysis corresponding to the different algorithms that are investigated here.

This experiment highlights that Algorithm ED0 converges quickly to the incorrect point by jumping connected components. We can deduce that Algorithm ED1 requires a finer subdivision of the unit interval than the predictor-corrector schemes to converge to  $R_p(v)$ . For coarser discretizations, Algorithm ED1 converges to an incorrect point or even fails to converge. The Euler step's implementation is not optimized. This explains the significant drop in performance relative to only using Newton's method, even though fewer linear systems need to be solved. The robustness that `HomotopyContinuation.jl` offers comes at the cost of a slower runtime.

---

<sup>11</sup><https://github.com/matthias-himmelman/HomotopyOpt.jl/tree/firstbranch/test>

<sup>12</sup><https://github.com/saschatimme/ImplicitPlots.jl>

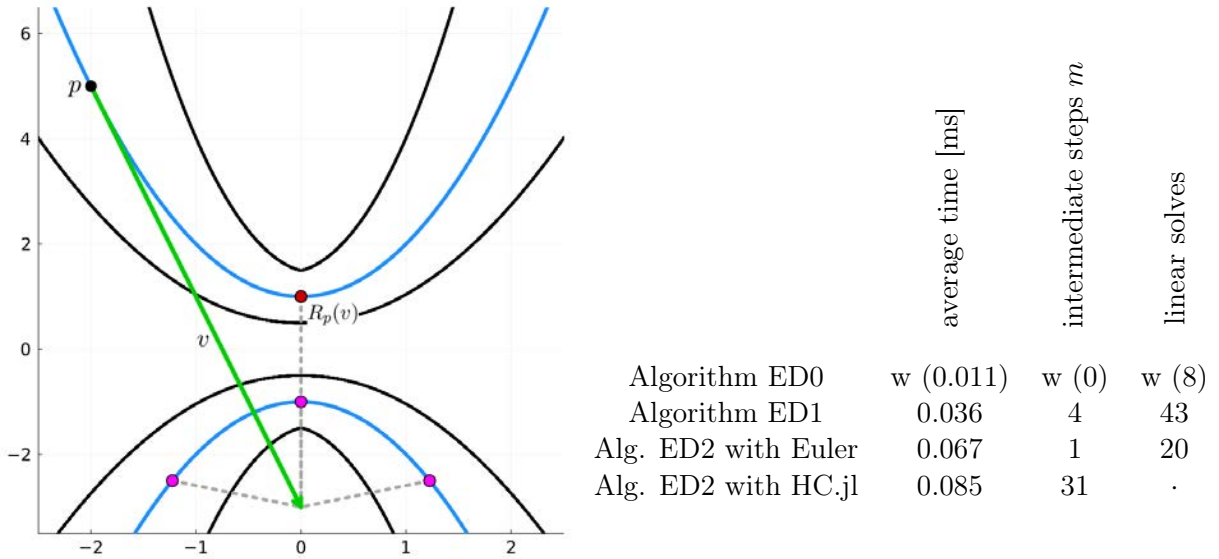


**Figure 3.10.1:** The Euclidean distance retraction is computed on the algebraic curve  $\mathcal{V}_1$  with start point  $p = (-2, 5)$  and tangent vector  $v = (2, -8)$ , yielding  $R_p(v) \in \mathcal{V}_1$  (l.). Adding slight perturbations to  $p + v$ , the points that Algorithm ED0 can converge to are depicted in magenta. The region where Lemma 3.3.3 applies is indicated by black lines. The table displays the benchmarks for each algorithm, where convergence to an incorrect point  $q \neq R_p(v)$  is marked with a “w”.

Furthermore, Lemma 3.3.3 provides a sufficient criterion for the invertibility of the Lagrange multiplier system  $G$ ’s Jacobian. The region around  $\mathcal{V}_1$  this condition produces is visualized in Figure 3.10.1 with a minimum distance to the set  $\mathcal{V}_1$  of  $\frac{1}{2}$ . In this case, it turns out that the inequality is sharp, since for the parameter  $u = (0, 0.5)$  the Jacobian is singular.

**Example 2:** As a second example, consider the sextic planar curve  $\mathcal{V}_2$  given by the implicit equation

$$(x^3 - x \cdot y^2 + y + 1)^2 \cdot (x^2 + y^2 - 1) + y^2 - 5 = 0.$$

We start out from the point  $p \approx (0, -1.833)$  and take the tangent step  $v \approx (2, 2.607)$ . The Euclidean distance retraction is given by  $R_p(v) \approx (1.229, -1.428)$ . All numbers are rounded to three decimal places and were corrected to  $\mathcal{V}_2$  using Newton’s method.

Figure 3.10.2 depicts the results of this experiment. While Newton’s method is really efficient, Algorithm ED0 does not converge to the correct point  $R_p(v)$ . In terms of performance, there does not seem to be a clear-cut advantage to using predictor steps. This suggests that the main focus of predictor-corrector schemes should be stability and robustness, rather than pure runtime optimization. The quadratic convergence of Newton’s method under the right circumstances is hard to match.

Again, we consider the condition from Lemma 3.3.3 about the invertibility of  $G$ ’s Jacobian. In this case, the minimum distance from  $\mathcal{V}_2$  is given by 0.000477 and is attained in the point  $(-2.509, 2.236)$ . Curiously, this value is approximately the curve’s reach (cf. [55]). Considering that Figure 3.10.2 depicts the region where Lemma 3.3.3 applies, the boundary curves look eerily like they are related to the curve’s curvature and medial axis. This correspondence should be the object of further research.

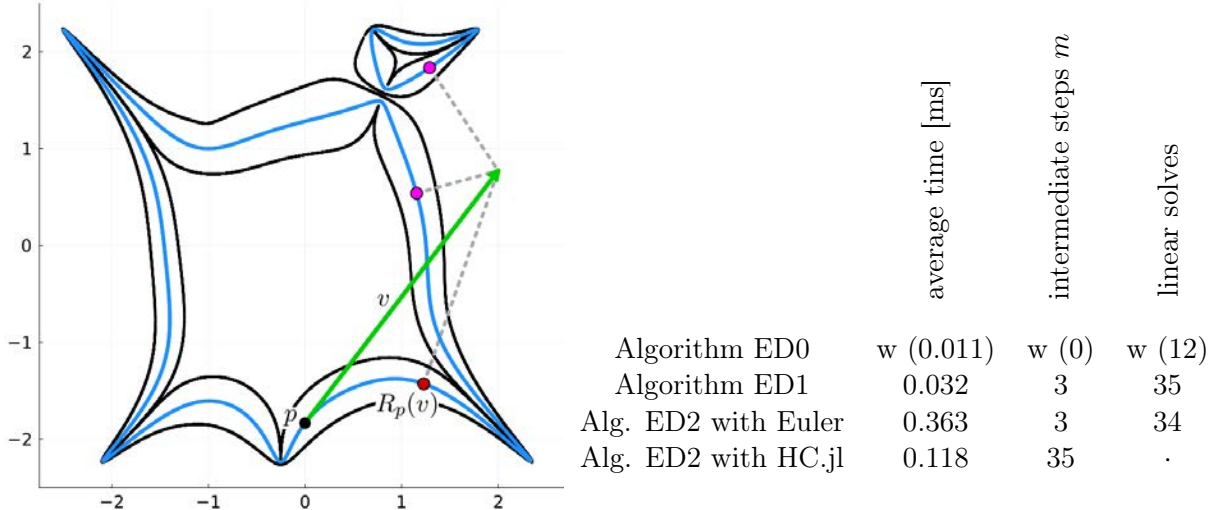


**Figure 3.10.2:** The Euclidean distance retraction  $R_p(v) \in \mathcal{V}_2$  is computed on the algebraic curve  $\mathcal{V}_2$  with start point  $p \approx (0, -1.833)$ , tangent vector  $v \approx (2, 2.607)$  (l.). Adding slight perturbations to  $p + v$ , the points to which Algorithm ED0 converges are depicted in magenta. The table displays the benchmarks for each algorithm, where convergence to an incorrect point  $q \neq R_p(v)$  is marked with a “w”.

Although these two examples may seem artificial, in the geometric applications where we intend to use the Euclidean distance retraction, multiple connected and irreducible components can be expected. Consequently, precautions against component-jumping are necessary. Otherwise, the advantage of our method for moving on manifolds would immediately be voided. In homotopy continuation frameworks, there are heuristics for detecting path-jumping and for adaptively adjusting the step size. Usually, both heuristics take the truncation error estimates of the chosen predictor step into account (cf. Section 3.2.2). These heuristics make the path-tracking algorithm robust, which is why predictors are a necessary part of modern homotopy continuation schemes.

Moreover, if the algorithms jump components in these simple examples, it can be expected that this will happen in more complicated examples with arbitrary step sizes as well. Nevertheless, the step size and the example’s ambient dimension are not mutually independent. One may now argue that results from metric algebraic geometry, such as the reach, smallest bottleneck, and injectivity radius, could potentially be used to bound the step size from above [53]. However, geometric constraint systems and algebraic sets generally contain singularities, meaning that all these numbers are usually 0 in our setting. This makes these global invariants infeasible.

**Example 3:** For the third example, we move to a geometric constraint system. Namely, a bar-and-joint framework with 3 pinned vertices is considered. After choosing appropriate edge lengths, the algebraic set consisting of all configurations satisfying the edge length equations is 1-dimensional. It contains 4 connected components, corresponding to the mirror images of the two triangles (cf. [82]). We randomly sample points from this singular algebraic set by intersecting it with affine hyperplanes.

One such sample is selected. The two corresponding unit tangent vectors are then calculated

and a linear step of length 10 is performed. It should be stressed that this is a large step size relative to the structure. As was argued before, if component jumping occurs in this structure, it will also occur for smaller step sizes in different, potentially more complicated, geometric constraint systems. One such configuration where Newton's method jumps components is depicted in Figure 3.10.3.

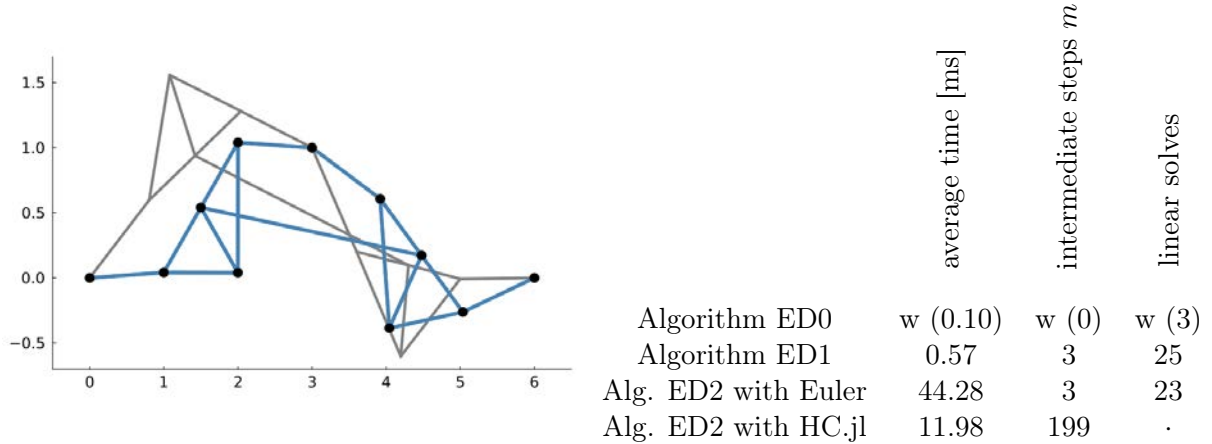


**Figure 3.10.3:** Two flexible configurations of the bar-joint framework from Connelly and Servatius [82] are depicted (l.). The point  $p$  is blue, while the incorrect  $R_p(v)$  computed by Algorithm ED0 is gray. The two configurations lie on two distinct connected components, since the triangles on the left are incorrectly flipped in the gray configuration. The table displays the benchmarks for each algorithm, where convergence to an incorrect point  $q \neq R_p(v)$  is marked with a “w”.

In this instance, the Euler step is even slower than homotopy continuation, even if it takes far fewer steps to converge. This again highlights that our Euler step is not optimally implemented. The comparison to Algorithm ED1 and homotopy continuation also indicates that only a higher-order predictor shows the benefits of predictor-corrector scheme and it is not advisable to use Euler's method in this setting. Nevertheless, the Euler step is useful for proving convergence guarantees that extend to higher-order predictors.

**Example 4:** As a fourth example, let us consider a Gilbert framework, which is constructed by randomly generating  $n$  Poisson-distributed points  $p_1, \dots, p_n$  in the square  $[-\frac{\sqrt{n}}{2}, \frac{\sqrt{n}}{2}]^2$  with area  $n$ . In Section 2.2, this class of examples is examined for their rigidity properties. We construct a geometric random graph on these points as vertices by growing expanding disks of radius  $r > 0$  around the points and adding an edge, whenever two points lie in the same disk (see also Takabe and Wadayama [309]). This process is stopped, when the resulting framework  $\mathcal{G}_r(p)$  is rigid. Since the points are generic by construction, infinitesimal rigidity, and continuous rigidity are equivalent concepts (cf. [24]). Therefore, the combinatorial criterion of computing the rigidity matrix' rank is a sufficient and necessary criterion for any framework's rigidity.

We want to use the geometric random graph as an example of a positive-dimensional constraint set with high ambient dimension. That is why the rigid framework  $\mathcal{G}_r(p)$  cannot be used. By construction, its Cayley-Menger variety is zero-dimensional. For this reason, we first compute its independent edges. Those are exactly the edges of the framework's underlying graph,

whose deletion causes the rigidity matrix to drop rank. Since the framework's realization is generic, the independent edges' removal causes the framework to become flexible. Consequently, by deleting one such edge, we obtain a positive-dimensional constraint set.

In this particular example, we choose  $n = 27$ , resulting in a 51-dimensional ambient space after factoring out the rigid motions of the Euclidean plane. Figure 3.10.4 depicts the resulting continuous motion and the corresponding performance analysis.

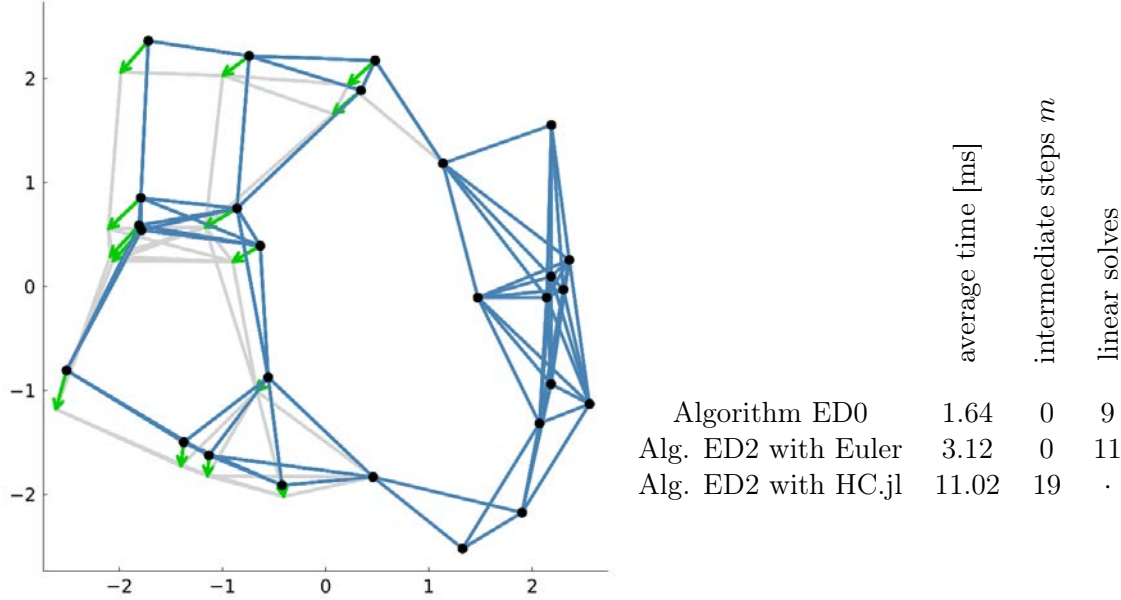


**Figure 3.10.4:** By deleting a single independent edge, the rigid Gilbert framework  $\mathcal{G}_r(p)$  can be made flexible. The resulting continuous motion in the realization  $p$  is depicted in green with the deformation path's endpoint visualized in grey. The table on the right shows the performance of the different algorithms which are compared in this section.

For this example, Algorithm ED0 converges to the correct critical point. There are two main reasons for this. Firstly, the vector  $v$ 's magnitude is relatively small. Since  $v$  comes from the constraint set's linearization in  $p$ , it can be expected that locally  $p + v$  is a good approximation of  $R_p(v)$ . Secondly, deleting a single independent edge does not create a complicated algebraic variety around  $p$ . In fact, there is no other connected component nearby. Still, this example showcases that not only is the Euclidean distance retraction's computation robust, it is also efficient. Not even a 51-dimensional search space poses significant issues for our algorithm.

**Example 5:** As the penultimate example, consider the Stiefel manifold  $V_k(\mathbb{R}^n)$  defined by the implicit equation  $X^T X = I_k$  for matrices  $X \in \mathbb{R}^{n \times k}$ . This system of equations is given by  $k^2$  quadratic equations. Contrary to the simple constraint count, the Stiefel manifold  $V_k(\mathbb{R}^n)$  has dimension  $nk - \frac{1}{2}k(k+1)$ . However, it is sufficient to consider the equations corresponding to this system's upper triangular part. For a matrix manifold, there are explicit formulas for retractions on the Stiefel manifold (cf. [4]). This is the perfect opportunity to compare the implicit Euclidean distance retraction to explicit retractions for special manifolds. The goal is to highlight that our approach is directed at general, implicitly-defined constraint systems, rather than manifolds where a retraction is known. Unsurprisingly, our algorithms cannot compete with these retractions' performance. We consider the Cayley retraction (cf. [341]), a retraction based

on Padé approximators (cf. [342]), the singular-value decomposition-based polar retraction and the QR-decomposition-based QR retraction. While the latter retraction is the most efficient, it only works for square matrices from  $V_n(\mathbb{R}^n)$ . All these algorithms are efficiently implemented in `Manifolds.jl`, a subpackage of `Manopt.jl` [48]. This experiment's results for the Stiefel manifold  $V_{10}(\mathbb{R}^{10})$  are summarized in Table 3.10.5.

|                     | average time [ms] | intermediate steps $m$ | linear solves |                   | average time [ms] | intermediate steps $m$ | linear solves |
|---------------------|-------------------|------------------------|---------------|-------------------|-------------------|------------------------|---------------|
| Algorithm ED0       | 15.20             | 0                      | 9             | Cayley retraction | 0.060             | 0                      | 0             |
| Algorithm ED1       | 15.20             | 0                      | 9             | Padé retraction   | 0.063             | 0                      | 0             |
| Alg. ED2 with Euler | 16.90             | 0                      | 9             | Polar retraction  | 0.016             | 0                      | 0             |
| Alg. ED2 with HC.jl | 1770.91           | 439                    | .             | QR retraction     | 0.014             | 0                      | 0             |

**Table 3.10.5:** This table visualizes the experimental results of the different methods for computing retractions on the Stiefel manifold  $V_{10}(\mathbb{R}^{10})$ .

Clearly, the explicit retractions on the Stiefel manifold perform orders of magnitude better than the continuation-based methods that we develop here. An iterative scheme is often inferior when an explicit formula is available. This does not mean that our methods are inefficient or useless. In fact, homotopy continuation allows us to work in general implicitly defined manifolds, where the explicit computation of a retraction map is hopeless.

**Example 6:** As the final example and the main motivation for this algorithm's development consider the triply periodic cylinder packing  $\Sigma^+$ . Experimental imaging suggests that this curvilinear cylinder packing is the structural component of corneocytes, which could explain the amount of swelling a human's skin exhibits upon soaking in water (cf. [112]). In Chapter 5, triply periodic rod packings are modeled using a tensegrity framework, with the  $\Sigma^+$  packing taking a central role. In that chapter, the Riemannian gradient descent Algorithm 3.2.7 with Euclidean distance retraction is applied to equilibrate the tensegrity model. Subsequently, the path-tracking method is used to traverse the corresponding deformation space.

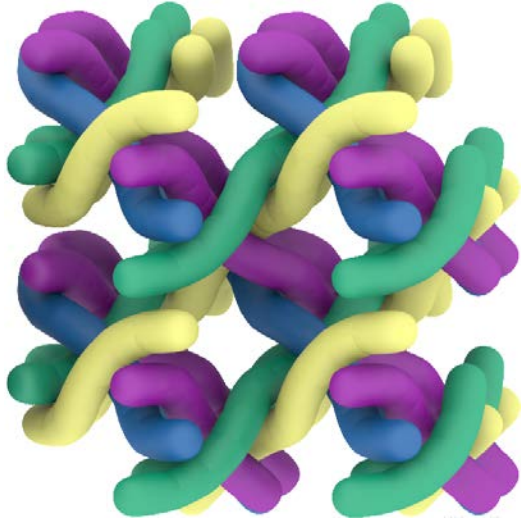
In this experiment, we start from an initial configuration taken from the RCSR database for triply periodic nets<sup>13</sup>. It is then continuously deformed to a feasible point  $p$  before taking a step in a randomly chosen tangent direction  $v$ . We expect that by construction, this structure's constraint set has an overwhelming number of irreducible components, making retraction-based algorithms particularly suitable. These methods make it possible to robustly stay on the same real connected component and compute a continuous deformation to an equilibrium.

The particular geometric constraint system associated with the  $\Sigma^+$  rod packing exists in 147-dimensional ambient space and has dimension 14 as an algebraic variety.

The results of all experiments highlight that Newton's method is fast and if we are in its

---

<sup>13</sup><https://rcsr.anu.edu.au/nets>



|                     | average time [ms] | intermediate steps $m$ | linear solves |
|---------------------|-------------------|------------------------|---------------|
| Algorithm ED0       | x (22.50)         | x (0)                  | x (2)         |
| Algorithm ED1       | 261.99            | 3                      | 28            |
| Alg. ED2 with Euler | 21436.69          | 1                      | 18            |
| Alg. ED2 with HC.jl | 34226.62          | 1885                   | .             |

**Figure 3.10.6:** The  $\Sigma^+$  rod packing (l.) exhibits interesting, dilatant properties called *auxeticity* upon expanding it in one of its cubic unit cell’s orthogonal directions. It can be modeled as a framework-based geometric constraint system. The table displays the benchmarks for each algorithm, where failure to converge is marked with an “x”.

region of quadratic convergence, it can be used as a tool for calculating the Euclidean distance retraction. However, its issue is that a priori it is unknown whether we are in the correct region of quadratic convergence. As was discussed in Section 3.3, divergence is a possibility that cannot be ruled out easily. In Algorithm ED0, we have no control over where Newton’s method converges. Theorem 3.3.7 implies that there exists a discretization of  $[0, 1]$  that allows Algorithm ED1 to find  $R_p(v)$ . In practice, this discretization may be relatively fine compared to the subdivisions that are necessary for predictor-corrector schemes. Without a priori information from the predictor steps, there is no heuristic for determining when connected components are jumped. For Riemannian optimization algorithms it is crucial that connected components are not jumped and that the resulting retraction curves  $t \mapsto R_p(tv)$  for  $t \in [0, 1]$  are smooth. Our homotopy continuation approach achieves both of these goals.

### 3.10.2 Conclusion

It is clear that Algorithm ED0 is faster than Algorithms ED1 and ED2, both in average runtime and the number of linear solves required. However, our examples show that it may return the incorrect point or fail to converge. There is no general way to check whether the point returned by Algorithm ED0 is equal to  $R_p(v)$ . In all our experiments, Algorithms ED1 and ED2 are able to reliably compute the correct  $R_p(v)$ , even in cases where Algorithm ED0 diverged, or failed to compute the correct point. Algorithm ED0 is the fastest, unless there are specialized retractions available. It should be stressed that Algorithm ED0 can compute the correct  $R_p(v)$  in many cases, but our experiments show that it is easy to find examples where it fails. In those examples, some form of homotopy continuation succeeds. In fact, the failure of Algorithm ED0 on an optimization problem over the manifold in Example 6 provides our original motivation for using homotopy continuation.

For applications such as geometric constraint systems, it is thus worth the increased

computational cost to solve  $R_p(v)$  using some form of homotopy continuation as in Algorithms ED1 and ED2. In these cases, the ability to reliably compute  $R_p(v)$  and heuristics for avoiding path-jumping justify the worse runtime.

In our experiments, the simplified homotopy continuation Algorithm ED1 is able to compute the correct point  $R_p(v)$ , even when Algorithm ED0 fails. In the examples with higher-dimensional ambient spaces, the computational cost for Algorithm ED1 is significantly reduced relative to using a more advanced predictor-corrector scheme. This suggests that, should Algorithm ED2 prove too computationally expensive for a certain system, it is worth trying Algorithm ED1, which combines improved reliability over Algorithm ED0 with reasonable performance.

Drawing inspiration from ensemble machine learning [252], a method that adaptively switches between Algorithms ED0, ED1 and ED2 depending on local invariants of the constraint set can potentially combine the best of all three algorithms. The implementation of such a model selection algorithm is left for future work.

Finally, Algorithm ED2 with `HomotopyContinuation.jl` comes with a built-in adaptive step size control and heuristics to detect path-jumping. If the application requires reliability above everything else, this method is preferable.

## Homogeneity of Disordered Minimal Surfaces<sup>14</sup>

**Chapter Synopsis:** Bicontinuous geometries, both ordered and amorphous, are commonly found in many soft matter systems. For ordered phases with crystalline symmetry, periodic minimal surfaces, including Schoen’s Gyroid or Schwarz’s Primitive and Diamond surfaces, provide established models. By contrast, a minimal surface model for amorphous phases does not exist. Using the Surface Evolver with a novel topology-stabilizing minimization scheme, we develop two models for amorphous minimal surfaces: one based on continuous random network models for amorphous Diamond, and another based on random perforated parallel sheets.

As per Hilbert’s embedding theorem, the Gaussian curvature of triply periodic minimal surfaces cannot be constant. Our analysis of Gaussian curvature variances reveals no substantial long-wavelength curvature variations of the amorphous Diamond minimal surfaces. However, their Gaussian curvature variance is substantially larger than that of the cubic Primitive, Diamond and Gyroid minimal surfaces. This analysis highlights the superior curvature uniformity of these three surfaces compared to their entropy-favored amorphous counterparts and to other periodic minimal surfaces. This general geometric result is relevant to bicontinuous structure formation in soft matter and biology across all length scales and is relevant to both ordered and amorphous phases.

The Uniformization Theorem [2] states that the hyperbolic plane  $\mathbb{H}^2$  as depicted in Figure 4.1.1(a) is the unique, simply connected Riemann surface with constant Gaussian curvature  $(-1)$ . Containing an inversion symmetry at every point, it constitutes a non-Euclidean geometry. By Hilbert’s Embedding Theorem (cf. Theorem 4.1.20) there is no embedded surface in  $\mathbb{R}^3$  with constant negative Gaussian curvature and without self-intersections, implying that the hyperbolic plane cannot be isometrically embedded in space. Therefore, any physical system with an infinite interface and without self-intersections striving for constant negative Gaussian curvature is necessarily frustrated, meaning that it has an energy greater than 0. In the absence of an interface without curvature variations, the fundamental question relevant to any such real-world system is which negatively curved surface exhibits the least variations in Gaussian curvature and how small these variations are.

Local constructions for surface patches with constant Gaussian curvature equal to  $(-1)$  exist in  $\mathbb{R}^3$ , as illustrated by crocheted hyperbolic corals [157, 310] (cf. Figure 4.1.1(b)). They can be constructed by gluing crescent-shaped surface patches of constant radius  $\delta > 0$  or through the parametrization of the pseudosphere [239]. However, any such surface intersects itself when extended sufficiently and cannot be a minimal surface with mean curvature 0. In contrast, triply

<sup>14</sup>This chapter contains results and material from an ongoing collaboration with Martin Cramer Pedersen, Myfanwy Evans, Michael Klatt, Philipp Schönhöfer and Gerd Schröder-Turk.

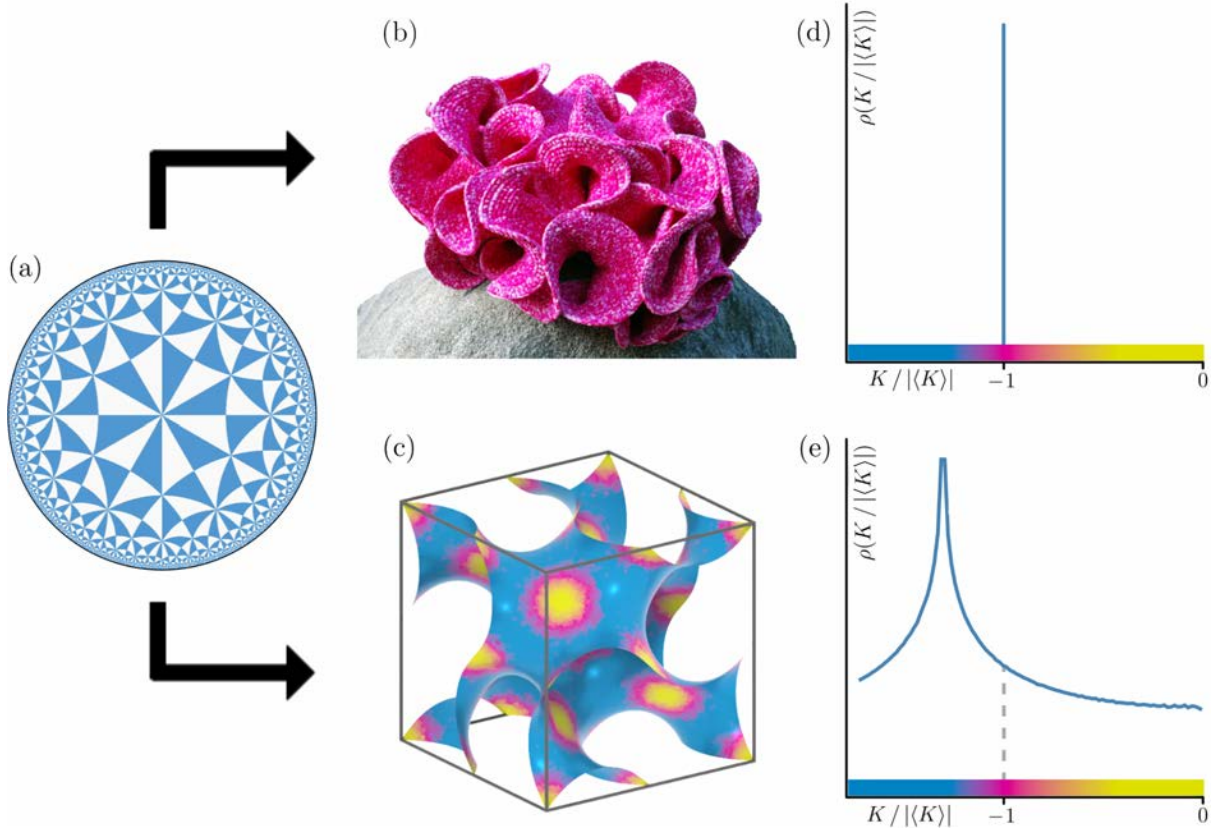


**Figure 4.1.1: Gaussian curvatures of negatively curved surfaces in  $\mathbb{R}^3$ :** (a) As per Hilbert’s embedding theorem, it is not possible to isometrically embed the hyperbolic plane  $\mathbb{H}^2$  in  $\mathbb{R}^3$ . (b,d) The crocheted model for the hyperbolic plane by Daina Tamina [157] has constant Gaussian curvature. Its curvature distribution is a  $\delta$ -function at  $K/|\langle K \rangle| = -1$  for  $\langle K \rangle = \int K dA / \int dA$ . If extended infinitely, it would be self-intersecting (image source: [310]). (c,e) Embedded triply periodic minimal surfaces, here the Gyroid, are smooth intersection-free saddle surfaces. The Gaussian curvature of such surfaces (represented by the surface color) is negative, except at isolated flat points with zero curvature. However, the value varies, leading to a curvature distribution of finite width.

periodic minimal surfaces (TPMS), including Alan Schoen’s Gyroid surface (cf. Figure 4.1.1(c)), are infinite, saddle-shaped surfaces without self-intersection. These surfaces have flat points with zero Gaussian curvature and are on average negatively curved. Consequently, the Gaussian curvature cannot be constant, in line with Hilbert’s Embedding Theorem. The degree to which Gaussian curvature varies is captured by the density function  $\rho$  (cf. Figure 4.1.1(d,e)).

Historically, triply periodic minimal surfaces have been constructed through various approaches. The Weierstrass-Enneper representation provides an analytical tool to parametrize minimal surfaces [105, 322]. Schwarz discovered the Hexagonal, Primitive and Diamond [289] that exist in positive-dimensional deformation families [117, 215] as the first intersection-free triply periodic minimal surfaces. Using the Bonnet transformation, it is possible to generate adjoint minimal surfaces [212]. With this tool, the Gyroid and Lidinoid can be mathematically described [140]. Both surfaces can be continuously deformed while maintaining their minimality [325]. With the introduction of discrete minimal surfaces [251] and an algorithm based on the

conjugate surface method [188], minimal surfaces have become admissible for computers. This led to the development of numerical software packages for optimizing curvature, such as the **Surface Evolver** [50]. By applying conjugate gradient descent to a curvature functional on surface triangulations, this algorithm makes it possible to generate translational unit cells of TPMS.

In 2021, Hao Chen and Matthias Weber discovered the existence of two further deformation families. Inspired by soft matter physics, he proved the existence of the 2-dimensional, orthorhombic deformation family  $\mathbf{oH}$  of Schwarz's Hexagonal surface [74] and the existence of a 2-parameter, orthorhombic deformation family  $\mathbf{o\Delta}$  of the Diamond Surface [73]. By considering reflections in parallel mirrors, an additional family of twin minimal surfaces can be constructed [71].

Bicontinuous minimal surfaces are important structural models for nanometer-scale structures in materials science and biology, particularly in the context of soft matter and biological tissue. The question of curvature uniformity is particularly relevant for self-assembled phases based on minimal surfaces, such as the bicontinuous cubic phases in copolymers [246, 337] or the biological intracellular bicontinuous cubic membranes [17]. In a *bicontinuous* material, two distinct labyrinths are interwoven in a way that each phase forms a continuous network. For these phases, the bilayer, membrane, or majority component mid-surface is given by a TPMS. Curvature considerations are central to investigating their formation's geometric principles. This includes the minimization of Helfrich-type bending functionals [290], especially Canham-Helfrich energy with a Gaussian curvature term [89, p.44f.]. Furthermore, the competition of surface tension with other energy terms [19, 278] and the relationship between the molecular shape and interface curvatures [148] benefit from understanding the role of curvature in organic systems.

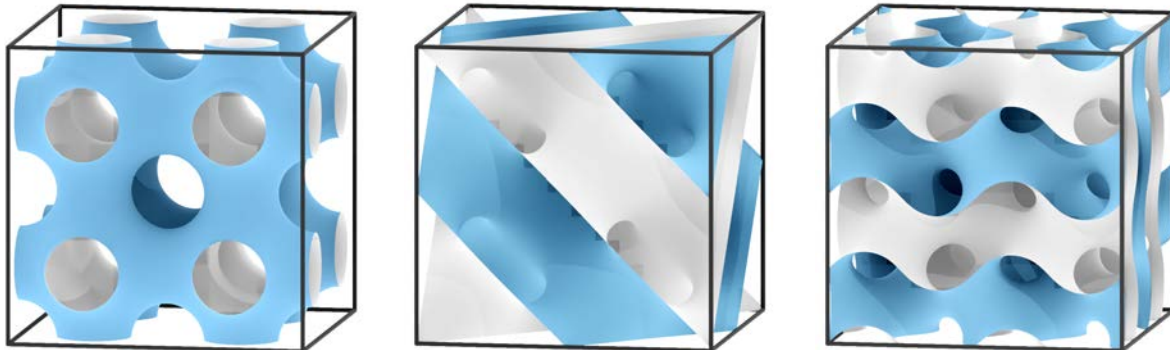


**Figure 4.1.2:** The bincontinuous Primitive (l.), Diamond (c.) and Gyroid (r.) triply periodic minimal surfaces divide space into two congruent labyrinths.

Variations in Gaussian curvature across a surface are typically assessed using the variance of the curvature as a metric. Such analyses have been carried out for cubic minimal surfaces [39, 290] and for one-parameter surface families that contain the cubic Primitive, Diamond and Gyroid surfaces as depicted in Figure 4.1.2. Their deformation families have been suggested as transition geometries between the cubic cases [117, 283]. Given the high symmetry of Primitive, Diamond and Gyroid, it is not surprising that these surfaces have the smallest Gaussian curvature variances among all the surface families studied. This observation raises two key questions:

1. Are Primitive, Diamond and Gyroid minimal surfaces the best interface geometries with regards to curvature variations, or has the best just not been found yet?
2. What aspects of these surfaces' form and shape enable the Primitive, Diamond and Gyroid to achieve their narrow distributions, and consequently low variations, of Gaussian curvature?

In this chapter, we demonstrate that studying the Gaussian curvature properties of amorphous bicontinuous minimal surfaces, which lack periodicity, provides valuable insights into these questions. We add an important structure class to the candidate surfaces to address the first question. For the second question, the qualitative form of the curvature distributions highlights what aspects make the cubic Primitive, Diamond and Gyroid minimal surfaces so homogeneous. In other words, we provide evidence for why the curvature fluctuation of these surfaces is particularly low.

There is an abundance of physical, chemical, and biological systems that form amorphous and, on average, negatively curved interfaces. Their occurrence ranges from porous materials in geology, chemistry, and biology, to phase separation processes such as spinodal decomposition, biological membranes, synthetic bilayer or copolymeric systems, sponge-like carbon phases, and many others. While questions of curvature uniformity are likely relevant to many of these systems, they may be most suitable for systems with interfaces close to minimal surfaces. This includes the L3 sponge phase in ternary lipid systems [214] and the calcium carbonate skeleton of some sea urchin species [178].

Beyond these naturally occurring disordered materials, amorphous meta-materials have attracted significant interest, e.g. for optical [191, 333] and biomaterial applications [194]. This interest is largely due to these materials' high isotropy that crystalline structures cannot achieve. Given the large interest in bicontinuous minimal surface geometries in the context of tissue engineering and bone scaffolds in recent years, it seems likely that amorphous bicontinuous minimal surfaces constitute valuable fully-isotropic candidate structures for such applications. The correlations between curvature and other properties in ordered bicontinuous geometries are documented, for example, in cell adhesion [332]. As the curvature of such structures has already been the target of various analyses [39, 62], this motivates the investigation of similar curvature terms and curvature variances for amorphous structures. However, whether stable minimal surfaces for amorphous network solids exist is largely unknown. This question is addressed here based on curvature optimization using the **Surface Evolver** [50] applied to randomized versions of the Diamond network known as amorphous Diamond or silicon [30].

Even though many differential geometric concepts are discussed throughout this chapter, it is intended as an exploration of physical systems. Complete, mathematical rigor cannot always be brought in line with modeling real-world phenomena. Working on the interface of what is mathematically possible and what is known in physics often provides profound insights and significant scientific progress. It should be stressed that while this chapter contains several, rigorous mathematical concepts and results, there are parts where the arguments are less rigorous because the corresponding mathematical theory has not yet been fully developed.

In that spirit, we begin by introducing the relevant concepts of Gaussian and mean curvature to describe minimal surfaces in Section 4.1. Accordingly, we present the classical Gauss-Bonnet

Theorem 4.1.19 and Hilbert's Embedding Theorem 4.1.20. Moreover, the known triply periodic minimal surfaces of genus three are discussed. Some of the corresponding deformation families have been discovered by Meeks III. [215], Fogden and Hyde [117] and Chen [72]. In Section 4.2, we introduce two measures of homogeneity that are used to compare several surfaces. The curvature fluctuation is a variance term of the Gaussian curvature distribution on the surface, whereas the isotropy index describes the distribution of the surfaces' unit normal vectors. We analyze several ordered bicontinuous phases with respect to both of these invariants.

While the previously mentioned sections are concerned with outlining the mathematical background and state-of-the-art, the following sections contain our results. As a first approach to create disordered minimal surfaces, in Section 4.3.2 the 4-regular amorphous Diamond net is tubified to create an initial configuration for curvature optimization routines. This continuous random network is produced by applying random transpositions to the crystalline Diamond net, significantly limiting the potential topologies. This approach thus seems capable of generating minimal surfaces with low curvature fluctuation. As a second approach, in Section 4.3.3 we consider repulsive point clouds placed on parallel layers in a periodic simulation box. Each point represents a catenoidal neck connecting two non-adjacent voids separated by the parallel planes. This way, the points lie in two disconnected volumes that can be used to create a separating surface by computing generalized Voronoi cells. To obtain a minimal surface from either initial configuration, we implement a robust, topology-stabilizing curvature optimization routine in Section 4.3.1.

Since the homogeneity measures depend on the choice of the simulation box, which is fixed in our experiments, we discuss how to relax the boundary conditions to obtain more isotropic surfaces in Section 4.3.4. Using all previously introduced techniques, we compare the homogeneity measures by using both approaches to generate several disordered minimal surfaces in Section 4.3.5. Finally, the results from the experiments are discussed in Section 4.4 to put our models into perspective.

## 4.1 Curvature and Minimal Surfaces

To understand what a minimal surface is, it is necessary to first take a step back and discuss the concept of curvature. Although our ultimate focus is on surfaces, developing an intuition for plane curves is a helpful intermediate step. A curve's curvature describes changes in direction over small distances. Alternatively, this can be described by the tangent vector's rotation [255, Prop. 2.2.3]. Yet, to formalize this concept we choose a different definition appearing in Presley [255, p.36-44], as it later generalizes to surfaces in  $\mathbb{R}^3$ .

**Definition 4.1.2.** Let a twice differentiable curve  $\gamma : I \rightarrow \mathbb{R}^2$  for an open interval  $I \subset \mathbb{R}$  with nowhere vanishing derivative be given. Then, the *signed curvature*  $k(t)$  in  $\gamma(t)$  is defined by

$$k(t) = \frac{\gamma_1'(t)\gamma_2''(t) - \gamma_1''(t)\gamma_2'(t)}{||\gamma'(t)||^3}$$

and the *radius of curvature* is  $R(t) = 1/|k(t)|$ . The corresponding *center of curvature*  $Q(t)$  is

$$Q(t) = \gamma(t) + \frac{1}{k(t) \cdot \|\gamma'(t)\|} \begin{pmatrix} -\gamma'(t)_2 \\ \gamma'(t)_1 \end{pmatrix}.$$

For  $k(t) \neq 0$ , the circle with center  $Q(t)$  and radius  $R(t)$  is called the *osculating circle* of  $\gamma$  at  $t \in \mathbb{R}$ . When  $k(t) = 0$ , the osculating circle is a line through  $p$  with slope  $\gamma'(t)$ , making it a circle in  $\mathbb{P}_{\mathbb{R}}^2$ . Finally,  $\gamma$ 's *curvature* at  $t \in I$  is  $|k(t)|$  and the *total curvature* is  $H_{2D} = \int_{\gamma(I)} k \, ds$ .

**Theorem 4.1.3** (Steiner's formula for curves). *Let  $\gamma : I \rightarrow \mathbb{R}^2$  be a twice continuously differentiable, injective curve with nowhere vanishing derivative defined on a compact interval  $I \subset \mathbb{R}$ . A unit normal field of  $\gamma$  is given by  $\mathbf{n}(t) = (\gamma_2'(t), -\gamma_1'(t))/\|\gamma'(t)\|$ . We define the  $\varepsilon$ -offset curve of  $\gamma$  by  $\gamma_\varepsilon = \{\gamma(t) + \varepsilon \cdot \mathbf{n}(t) : t \in I\}$  for  $\varepsilon \in \mathbb{R}$ . Then, for sufficiently small  $|\varepsilon|$  the length of  $\gamma_\varepsilon$  is*

$$L(\gamma_\varepsilon) = L(\gamma) + \varepsilon \cdot H_{2D}. \quad (4.1.4)$$

*Proof.* Recall that the arc length of an injective, continuously differentiable curve  $\varphi : I \rightarrow \mathbb{R}^2$  can be calculated using the integral

$$L(\varphi) = \int_I \sqrt{(\varphi_1'(t))^2 + (\varphi_2'(t))^2} \, dt.$$

Assume for the moment that  $\gamma$  is a unit-speed curve, meaning that  $\|\gamma'(t)\| = 1$  for all  $t \in I$ . This assumption will later be justified by reparametrization. Since  $\gamma$  is a smooth curve, so is  $\gamma_\varepsilon$  for a sufficiently small  $|\varepsilon|$ . Consequently, after using the distributive law we can express the length of the  $\varepsilon$ -offset curve by

$$\begin{aligned} L(\gamma_\varepsilon) &= \int_I \sqrt{(\gamma_1'(t) + \varepsilon \cdot \gamma_2''(t))^2 + (\gamma_2'(t) - \varepsilon \cdot \gamma_1''(t))^2} \, dt \\ &= \int_I \sqrt{\|\gamma'(t)\|^2 + \varepsilon^2 \cdot \|\gamma''(t)\|^2 + 2\varepsilon \cdot \langle \gamma'(t), (\gamma_2''(t), -\gamma_1''(t)) \rangle} \, dt. \end{aligned}$$

Now, the geodesic equation reads  $\gamma''(t) = -k(t) \cdot \mathbf{n}(t)$  [255, p.35] for the signed curvature  $k(t)$ . Note that this equation has a “-” sign because by assumption, the unit normal field  $\mathbf{n}(t)$  is obtained by clockwise rotation. A counter-clockwise rotation would produce a “-” in Equation (4.1.4) instead.  $\gamma$  is a unit speed curve by assumption, so Definition 4.1.2 suggests that  $k(t) = \langle \gamma'(t), (\gamma_2''(t), -\gamma_1''(t)) \rangle$ . Therefore,

$$L(\gamma_\varepsilon) = \int_I \sqrt{(\|\gamma'(t)\| + \varepsilon \cdot k(t))^2} \, dt = L(\gamma) + \varepsilon \cdot H_{2D}.$$

What remains is to justify our previous assumption that  $\gamma$  is a unit-speed curve. By assumption,  $\gamma$  contains no singularities and therefore admits a unit-speed reparametrization  $s(t) = \int_a^t \|\gamma'(s)\| \, dt$  starting from  $a = \min(I)$  by Presley [255, Prop. 1.3.6]. This expression is well-defined because  $I$  is compact, implying that  $\gamma$  is bounded by the Extreme Value Theorem. Finally, the arc length is independent of the parametrization. Consequently,  $L(\varphi \circ s) = L(\varphi)$  for any smooth curve  $\varphi : I \rightarrow \mathbb{R}^2$ , which can be shown using integration by substitution. This

concludes the proof.  $\square$

Notice that the size of  $\varepsilon$  is only governed by the property that  $\gamma_\varepsilon$  remains a smooth curve. This relates Steiner's Theorem for curves to the curve's *reach* which describes the largest distance from the curve such that all points within that distance have a unique closest point on the curve. As a consequence, the reach provides a natural upper bound for  $|\varepsilon|$  in Theorem 4.1.3. Moreover, the reach does not only exist for curves but also for embedded Riemannian manifolds.

The following example illustrates the concept of curvature and Steiner's formula for curves.

**Example 4.1.5.** Consider the curve  $\gamma(t) = (t, \sin(t))$  on the interval  $I = [0, 2\pi]$ . We want to understand the previously introduced concepts of the curve's curvature  $k(t)$  and the arc length of its  $\varepsilon$ -offset curves.

The signed curvature  $k(t)$  is a smooth function mapping  $I$  to  $[-1, 1]$  and with maximal signed curvature 1 attained at  $3\pi/2$  and minimal signed curvature  $-1$  attained at  $\pi/2$ . The curvature is 0 whenever  $\sin(t) = 0$ , corresponding to the curve's flat regions. There, the osculating circle describes a line by Definition 4.1.2 and it has a minimal radius in the extrema of  $t \mapsto \sin(t)$ .

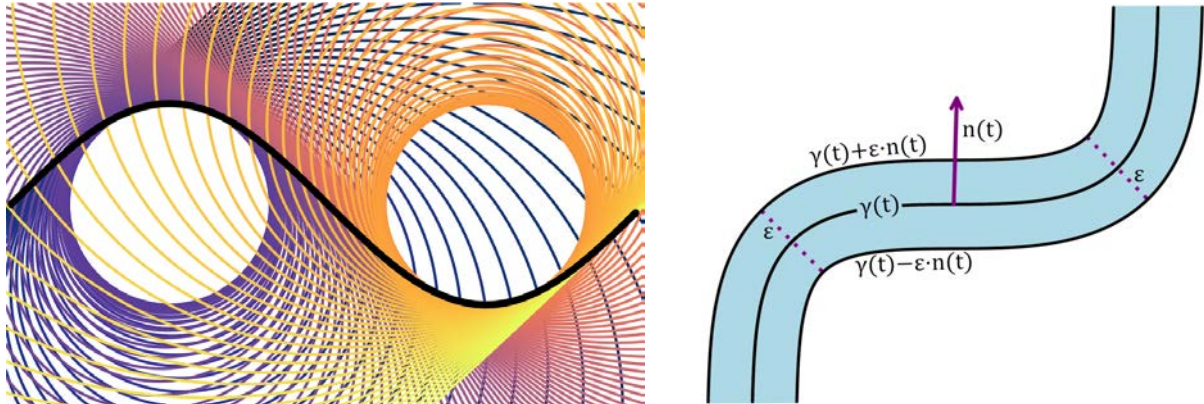


**Figure 4.1.6:** Osculating circles of the curve  $\gamma(t)$  with a color gradient differentiating them (l.) and  $\gamma$  depicted with  $\varepsilon$ -offset curves  $\gamma_\varepsilon$  and  $\gamma_{-\varepsilon}$  for  $\varepsilon = 1/2$  and rotated by  $\pi/4$  (r.).

Figure 4.1.6(l.) visualizes this correspondence: The osculating circles of  $\gamma$  corresponding to the points  $(\pi/2, 1)$  and  $(3\pi/2, -1)$  do not intersect other circles in close proximity. The circles with radius  $r$  and uniform curvature  $1/r$  must increase their radius to accommodate  $\gamma$ 's flat regions. The total curvature  $H_{2D}$  of  $\gamma$  is 0, which can either be seen via the symmetry of  $\sin$  or via integration when realizing the integration bounds match after substitution. Thus, by Theorem 4.1.3 the offset curves  $\gamma_\varepsilon$  have the same length as  $\gamma$ , which is depicted in Figure 4.1.6(r.).

With this theoretical framework at hand, we can move up one dimension to discuss the curvature of smooth 2-dimensional manifolds  $\mathcal{M}$  in  $\mathbb{R}^3$ . These surfaces' unit normal field locally varies smoothly. The locality is an important restriction, since the Möbius strip would otherwise provide a counterexample for a smoothly varying normal field. Therefore, at a given point  $p$  the 1-dimensional normal space  $N_p\mathcal{M}$  lies in a family of planes, called *normal planes*, that is spanned by a non-zero vector  $v$  from the tangent space  $T_p\mathcal{M}$  and a generator  $w$  of  $N_p\mathcal{M}$ . Each such plane transversally intersects  $\mathcal{M}$  and cuts out a curve  $\mathcal{M} \cap \text{span}(v, w)$  [239, p.210]. We now know how to calculate the curvature of a plane curve, so we can calculate the signed curvature

corresponding to each normal plane as well. The following definition appears in [77, p.76].

**Definition 4.1.7.** For a smooth surface  $\mathcal{M}$ , parametrize the normal planes at  $p \in \mathcal{M}$  around  $w \in N_p \mathcal{M}$  by  $v \in S^2 \cap T_p \mathcal{M}$ . These vectors cut out curves  $\gamma_v = \mathcal{M} \cap \text{span}(v, w)$ . Denote the infimum and supremum of the *signed curvature*  $k_v$  of  $\gamma_v$  at  $p$  by  $\kappa_1(p)$  and  $\kappa_2(p)$ , respectively. We call the numbers  $\kappa_1(p)$  and  $\kappa_2(p)$  the *principal curvatures* of  $\mathcal{M}$  at  $p$ .

The surface's *mean curvature*  $H(p)$  and *Gaussian curvature*  $K(p)$  are then defined as

$$H(p) = \frac{\kappa_1(p) + \kappa_2(p)}{2} \quad \text{and} \quad K(p) = \kappa_1(p) \cdot \kappa_2(p).$$

Analogous to Definition 4.1.2, we define the *total mean curvature* as  $H_{\mathcal{M}} = \int_{\mathcal{M}} H(p) dA$  and the *total Gaussian curvature* as  $K_{\mathcal{M}} = \int_{\mathcal{M}} K(p) dA$ . When  $H(p) = 0$  for each  $p \in \mathcal{M}$ , we call  $\mathcal{M}$  a *minimal surface*.

One may wonder why the infimum and supremum of the signed curvatures are even attained. Since the sphere  $S^2$  is compact and  $T_p \mathcal{M}$  is closed, their intersection is compact. Furthermore, the curves  $\gamma_v$  vary smoothly with  $v$ , since the surface  $\mathcal{M}$  is smooth. Given by the composition of continuous functions,  $k_v$  is continuous as well. The Extreme Value Theorem then implies that  $k_v$  attains both its infimum and supremum.

An alternative definition of minimal surfaces locally characterizes them as the area-minimizing surfaces bounded by a simple closed curve [217, Def. 2.5]. This relates minimal surfaces to soap film, as a wireframe dipped in soap solution produces a membrane that minimizes area. By extension, this justifies the naming convention, as the surfaces are indeed locally minimal. To emphasize the concept of a minimal surface, let us consider an example.

**Example 4.1.8.** The *catenoid* is an important example of a surface appearing in nature [305]. It can be parametrized as a surface of revolution from the catenary curve

$$v \mapsto \left( v, c \cosh \left( \frac{v}{c} \right) \right)$$

for  $v \in \mathbb{R}$  and  $c > 0$  and is depicted in Figure 4.1.9.

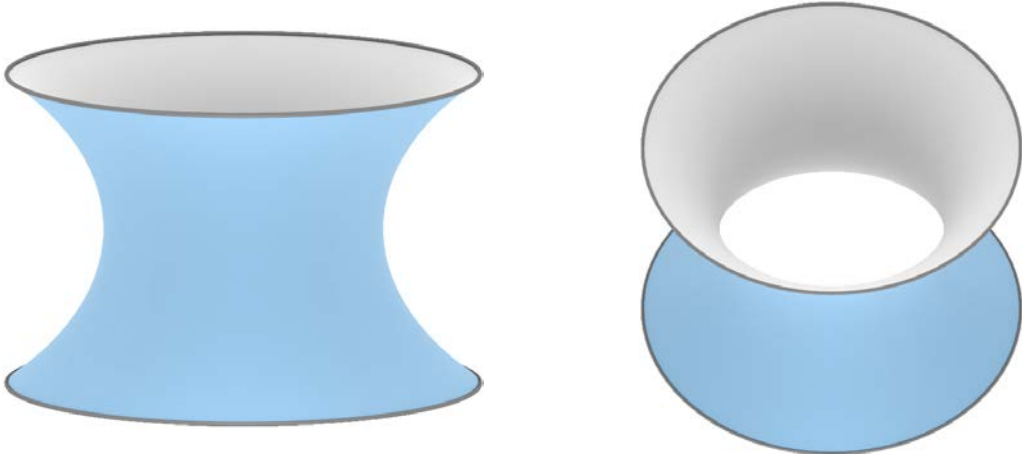


**Figure 4.1.9:** The catenoid with  $c = 0.66$  from two different perspectives with its wireframe depicted in dark gray.

As a surface of revolution, it is apparent on which curves the maximal and minimal signed curvature is attained, namely on meridians and parallels [239, p.253]. By the surface's rotational symmetry, these curves have the parametrizations

$$\gamma_1(t) = \begin{pmatrix} c \cosh(t/c) \\ 0 \\ t \end{pmatrix} \quad \text{and} \quad \gamma_2(t) = \begin{pmatrix} c \cosh(v/c) \cos(t) \\ c \cosh(v/c) \sin(t) \\ v \end{pmatrix}$$

for a fixed  $v \in \mathbb{R}$ . After using the hyperbolic identity  $\cosh(x)^2 - \sinh(x)^2 = 1$ , Definition 4.1.2 implies that the principal curvatures of these plane curves are given by

$$\kappa_{1,2}(u, v) = \mp \frac{1}{c \cosh(v/c)^2}.$$

Consequently, the catenoid's Gaussian curvature is negative and its mean curvature is 0. Definition 4.1.7 then tells us that the catenoid is a minimal surface. Indeed, together with the plane it is the only surface of revolution that is minimal [239, Thm. 7.2].

If the intention is to calculate the mean and Gaussian curvature at every point on the surface, the method for computing the mean and Gaussian curvature from Definition 4.1.7 quickly becomes tedious. For this reason, we introduce an alternative way to calculate these two numbers. The definition can be found in [255, §6-8] and offers a different interpretation to the first and second fundamental form of surfaces presented in Section 3.1.

**Definition 4.1.10.** Let  $\sigma : U \subset \mathbb{R}^2 \rightarrow \mathbb{R}^3$  be a twice continuously differentiable, injective parametrization of a surface with nowhere vanishing partial derivatives and denote these partial derivatives by  $\sigma_z = \partial\sigma/\partial z$ . The *first fundamental form* is the induced Riemannian metric on  $\mathcal{M} = \sigma(U)$  given by

$$I(v, w) = \langle \mathcal{F}_I \cdot v, w \rangle$$

$p \in \mathcal{M}$  and tangent vectors  $v, w \in T_p \mathcal{M}$ . The symmetric matrix  $\mathcal{F}_I$  is given by

$$\mathcal{F}_I = \begin{pmatrix} E & F \\ F & G \end{pmatrix} \quad \text{for} \quad E = \|\sigma_x\|^2, \quad F = \langle \sigma_x, \sigma_y \rangle \quad \text{and} \quad G = \|\sigma_y\|^2$$

for the coordinates  $(x, y)$  of  $\mathbb{R}^2$ . Conversely, for the unit normal  $\mathbf{n} = (\sigma_x \times \sigma_y)/\|\sigma_x \times \sigma_y\|$  the *second fundamental form* can be expressed as

$$\mathbb{II}(v, w) = \langle \mathcal{F}_{II} \cdot v, w \rangle \quad \text{for} \quad \mathcal{F}_{II} = \begin{pmatrix} L & M \\ M & N \end{pmatrix}$$

with functions

$$L = \langle \sigma_{xx}, \mathbf{n} \rangle, \quad M = \langle \sigma_{xy}, \mathbf{n} \rangle \quad \text{and} \quad N = \langle \sigma_{yy}, \mathbf{n} \rangle.$$

All matrices are to be understood with respect to the basis  $\{\sigma_x(u), \sigma_y(u)\}$  of  $T_p \mathcal{M}$  at  $\sigma(u) = p$ .

In case the parametrization  $\sigma$  was not injective, we would create an ambiguity. Furthermore, if one of the partial derivatives vanished somewhere, then the tangent space would not be well-

defined at that point. With these assumptions, the first and second fundamental form let us formulate several statements, one of which is a formula for the surface area:

**Proposition 4.1.11** (cf. [255, Prop. 6.4.2] and [245, (I-78)]). *Let  $\sigma : U \subset \mathbb{R}^2 \rightarrow \mathbb{R}^3$  denote a continuously differentiable and injective parametrization of a surface  $\mathcal{M}$  with nowhere vanishing partial derivatives. The [surface area](#)  $A(\mathcal{M})$  corresponding to the surface patch  $\mathcal{M} = \sigma(U)$  is*

$$A(\mathcal{M}) = \int_U \|\sigma_x \times \sigma_y\| dx dy = \int_U \sqrt{EG - F^2} dx dy.$$

This expression can be used to pass from a surface integral to a planar integral via

$$\int_{\mathcal{M}} f dA = \int_U f(\sigma(u)) \cdot \sqrt{EG - F^2} dx dy$$

for any integrable function  $f : \mathcal{M} \rightarrow \mathbb{R}$  and  $u \in U$ .

**Proposition 4.1.12** (cf. [255, Cor. 8.1.3]). *At a point  $p \in \mathcal{M}$ , the mean curvature  $H(p)$  and the Gaussian curvature  $K(p)$  can be expressed in terms of the first and second fundamental form:*

$$H(p) = \frac{LG - 2MF + NE}{2(EG - F^2)} \Big|_p \quad \text{and} \quad K(p) = \frac{LN - M^2}{EG - F^2} \Big|_p.$$

We can use the previous two Propositions 4.1.11–4.1.12 to prove a result that characterizes the behavior of surface area, mean curvature, and Gaussian curvature under scaling.

**Proposition 4.1.13.** *Let  $\sigma : U \subset \mathbb{R}^2 \rightarrow \mathbb{R}^3$  be a twice continuously differentiable and injective parametrization of a surface with nowhere vanishing partial derivatives. Assume that the surface is uniformly scaled by a constant  $\Gamma > 0$ . In other words, let  $\sigma' : U \rightarrow \mathbb{R}^3$  parametrize the scaled surface  $\mathcal{M}' = \sigma'(U)$  by  $\sigma'(u) = \Gamma \cdot \sigma(u)$  for all  $u \in U$ . Then,*

$$A(\mathcal{M}') = \Gamma^2 \cdot A(\mathcal{M}), \quad H'(\sigma'(u)) = \frac{1}{\Gamma} \cdot H(\sigma(u)) \quad \text{and} \quad K'(\sigma'(u)) = \frac{1}{\Gamma^2} \cdot K(\sigma(u))$$

for all  $p \in \mathcal{M}$ .

*Proof.* Denote by  $E, F, G$  the coefficients of the first fundamental form and by  $L, M, N$  the coefficients of the second fundamental form corresponding to  $\sigma$ . Similarly, we write  $E', F', G', L', M', N'$  for the respective coefficients for  $\sigma'$  (cf. Definition 4.1.10). Firstly, we observe that due to the linearity of the derivative and the bilinearity of both the inner product and the cross product, it follows that

$$\begin{aligned} E' &= \langle \sigma'_x, \sigma'_x \rangle = \langle \Gamma \cdot \sigma_x, \Gamma \cdot \sigma_x \rangle = \Gamma^2 \cdot E, & F' &= \Gamma^2 \cdot F, & G' &= \Gamma^2 \cdot G, \\ L' &= \left\langle \Gamma \cdot \sigma_{xx}, \frac{\Gamma^2 \cdot (\sigma_x \times \sigma_y)}{\Gamma^2 \cdot \|\sigma_x \times \sigma_y\|} \right\rangle = \Gamma \cdot L, & M' &= \Gamma \cdot M & \text{and} & N' &= \Gamma \cdot N. \end{aligned}$$

According to Proposition 4.1.11, this lets us express the surface area of  $\mathcal{M}'$  as follows:

$$A(\mathcal{M}') = \int_U \sqrt{E'G' - (F')^2} dx dy = \int_U \Gamma^2 \cdot \sqrt{EG - F^2} dx dy = \Gamma^2 \cdot A(\mathcal{M}).$$

Analogously, Proposition 4.1.12 provides a formula for the mean and Gaussian curvature in terms of the first and second fundamental form. The claim that the mean curvature scales with  $\Gamma^{-1}$  and that the Gaussian curvature scales with  $\Gamma^{-2}$  follows by inserting the expressions for  $E', F', G'$  and  $L', M', N'$  from above into the formula from Proposition 4.1.12.  $\square$

Propositions 4.1.11–4.1.12 further yield a way to extend Steiner's formula for curves from Theorem 4.1.3 to surfaces. This theorem appears, for example without proof, in Schamberger et al. [277] and due to its versatility finds application in numerous scenarios.

**Theorem 4.1.14** (Steiner's formula for surfaces). *Let  $\sigma : U \subset \mathbb{R}^2 \rightarrow \mathbb{R}^3$  be a twice continuously differentiable and injective parametrization of a surface with nowhere vanishing partial derivatives. Given a compact set  $R \subset U$ , the surface patch  $\sigma(R)$  is called  $\mathcal{M}$ . Denote the unit normal pointing in the opposite direction of the standard unit normal by  $\mathbf{n} = -(\sigma_x \times \sigma_y)/\|\sigma_x \times \sigma_y\|$ . For  $\varepsilon \in \mathbb{R}$  define the  $\varepsilon$ -offset surface  $\mathcal{M}_\varepsilon = \mathcal{M} + \varepsilon \mathbf{n}$ . If  $|\varepsilon|$  is sufficiently small, the area of  $\mathcal{M}_\varepsilon$  is given by*

$$A(\mathcal{M}_\varepsilon) = A(\mathcal{M}) + 2\varepsilon \cdot H_{\mathcal{M}} + \varepsilon^2 \cdot K_{\mathcal{M}}.$$

*Proof.* By Proposition 4.1.11, the surface area can be expressed in terms of the parallelogram area  $\|\sigma_x \times \sigma_y\|$ . Therefore,

$$\begin{aligned} A(\mathcal{M}_\varepsilon) &= \int_R \|(\sigma_x + \varepsilon \mathbf{n}_x) \times (\sigma_y + \varepsilon \mathbf{n}_y)\| dx dy \\ &= \int_R \|(\sigma_x \times \sigma_y) + \varepsilon \cdot (\mathbf{n}_x \times \sigma_y + \sigma_x \times \mathbf{n}_y) + \varepsilon^2 \cdot \mathbf{n}_x \times \mathbf{n}_y\| dx dy. \end{aligned} \quad (4.1.15)$$

To evaluate this expression, the proof of [255, Prop. 7.2.2] implies that  $\mathbf{n}_x = \mathcal{F}_{\text{I}}^{-1} \cdot \mathcal{F}_{\text{II}} \cdot \sigma_x$  and  $\mathbf{n}_y = \mathcal{F}_{\text{I}}^{-1} \cdot \mathcal{F}_{\text{II}} \cdot \sigma_y$  with  $\mathcal{F}_{\text{I}}$  and  $\mathcal{F}_{\text{II}}$  denoting the matrices from the first and second fundamental form, respectively (cf. Definition 4.1.10). Since both matrices share the basis  $\{\sigma_x, \sigma_y\}$ , this expression can be rewritten as  $\mathbf{n}_x = a\sigma_x + c\sigma_y$  and  $\mathbf{n}_y = b\sigma_x + d\sigma_y$  such that  $(a, c)$  is the first column and  $(b, d)$  the second column of  $\mathcal{F}_{\text{I}}^{-1} \cdot \mathcal{F}_{\text{II}}$ . Using standard algebraic properties of the cross product and the multiplicativity of the determinant (see the proof of [255, Thm. 8.1.6.]) shows

$$\begin{aligned} \mathbf{n}_x \times \mathbf{n}_y &= (a\sigma_x + c\sigma_y) \times (b\sigma_x + d\sigma_y) = (ad - bc) \cdot (\sigma_x \times \sigma_y) \\ &= \det(\mathcal{F}_{\text{I}}^{-1} \cdot \mathcal{F}_{\text{II}}) \cdot (\sigma_x \times \sigma_y) = \frac{\det(\mathcal{F}_{\text{II}})}{\det(\mathcal{F}_{\text{I}})} \cdot (\sigma_x \times \sigma_y) \\ &\stackrel{\text{Prop. 4.1.12}}{=} K(\sigma(x, y)) \cdot (\sigma_x \times \sigma_y). \end{aligned}$$

Analogously, we find that

$$\begin{aligned} \mathbf{n}_x \times \sigma_y + \sigma_x \times \mathbf{n}_y &= (a\sigma_x + b\sigma_y) \times \sigma_y + \sigma_x \times (b\sigma_x + d\sigma_y) \\ &= (a + d) \cdot (\sigma_x \times \sigma_y) = \text{tr}(\mathcal{F}_{\text{I}}^{-1} \cdot \mathcal{F}_{\text{II}}) \cdot (\sigma_x \times \sigma_y) \\ &\stackrel{\text{Prop. 4.1.12}}{=} 2 \cdot H(\sigma(x, y)) \cdot (\sigma_x \times \sigma_y). \end{aligned}$$

Inserting these findings into Equation (4.1.15) yields

$$A(\mathcal{M}_\varepsilon) = \int_R \left| \left| (1 + 2\varepsilon \cdot H(\sigma(x, y)) + \varepsilon^2 \cdot K(\sigma(x, y))) \cdot (\sigma_x \times \sigma_y) \right| \right| dx dy.$$

When  $|\varepsilon|$  is chosen sufficiently small so that  $1 + 2\varepsilon \cdot H(\sigma(x, y)) + \varepsilon^2 \cdot K(\sigma(x, y)) > 0$  on all of  $R$ , we can extract this scalar factor from the norm. Finding such an  $\varepsilon$  is possible due to  $H$  and  $K$  being continuous functions, which means that they are bounded on the compact set  $R$  by the Extreme Value Theorem. The compactness of the surface implies that it is orientable (cf. [255, Cor. 5.4.5]). Thus,  $\mathcal{M}$  has a continuously varying normal vector field (cf. [198, p.380f.]). The continuity of  $H$  and  $K$  is then given by the fact that  $\sigma \in C^\infty(U)$ . Hence, we can apply Proposition 4.1.11 and the integral's linearity to conclude that

$$A(\mathcal{M}_\varepsilon) = A(\mathcal{M}) + 2\varepsilon \cdot H_{\mathcal{M}} + \varepsilon^2 \cdot K_{\mathcal{M}},$$

proving the claim.  $\square$

While Steiner's formula is not directly relevant for computing Gaussian curvature fluctuations, it underpins the relation between molecular shape and curvature analysis: A membrane's shape is determined by its constituent molecules. Amphiphilic molecules, i.e. molecules with both hydrophilic and hydrophobic properties, are typically idealized as a truncated cone. This cone has the volume  $V$  and is equipped with a hydrophilic, disk-shaped head group of area  $A$  and a hydrophobic tail of length  $\varepsilon$  attached to it [277]. In a solution, these molecules orient their head groups toward the solvent while aligning their tail groups to form a thin membrane. Consequently, the headgroups of the lipids lie on parallel surfaces, offset by a value of  $\varepsilon$  and  $-\varepsilon$ .

Steiner's Theorem 4.1.14 states that the area change between the mid-surface corresponding to the tail groups and the offset surfaces corresponding to the head groups of the molecules is determined by the membrane's mean and Gaussian curvature. Assuming the parallel membranes are identical on both sides, a shape analysis of the molecules immediately reveals that the mean curvature of the membrane must be zero (cf. [282, p.107f.]). Recall that a zero mean curvature surface is also called a minimal surface. Considering that minimal surfaces are locally area-minimizing, the assumption on the shape of the parallel surfaces is reasonable: Since the head group area is fixed, minimal surfaces locally require the fewest number of molecules. This fact provides a possible explanation of why minimal surfaces appear in the self-assembly process of copolymers.

To gain familiarity with these theoretical concepts, let us consider an example.

**Example 4.1.16.** Let us consider the hyperbolic paraboloid  $\mathcal{M}$  on the set  $U = [-1, 1]^2$ . It can be parametrically represented by the surface patch

$$\sigma(x, y) = (x, y, x^2 - y^2).$$

First, we investigate the curvature behavior in the origin. To calculate the principal curvatures, notice that  $N_0\mathcal{M} = (0, 0, 1) \cdot \mathbb{R}$ . Hence, the corresponding family of normal planes can be

parametrized by the vector  $(\cos(\theta), \sin(\theta), 0)$  with  $\theta \in [0, \pi]$ , resulting in the implicit equation  $\cos(\theta) \cdot x = -\sin(\theta) \cdot y$ . Intersecting that plane with  $\mathcal{M}$  produces the plane curve

$$\gamma(t) = \begin{pmatrix} (\sin(\theta) \tan(\theta) + \cos(\theta)) \cdot t \\ (\tan(\theta)^2 - 1) \cdot t^2 \end{pmatrix}.$$

We can use Definition 4.1.2 to calculate the signed curvature:

$$k_\theta(t) = \frac{2(\sin(\theta) \tan(\theta) + \cos(\theta)) \cdot (\tan(\theta)^2 - 1)}{\sqrt{(\sin(\theta) \tan(\theta) + \cos(\theta))^2 + 4t^2 \cdot (\tan(\theta)^2 - 1)^2}}.$$

At the origin, the signed curvature function  $k_\theta(0)$  stays in the interval  $[-2, 2]$ . This can be seen as follows: Partition  $[0, \pi)$  into  $[0, \pi/2) \sqcup [\pi/2, \pi)$ . Both sine and cosine are positive on  $[0, \pi/2)$ , while only sine is positive on  $[\pi/2, \pi)$ . The bounds follow after squaring the expression for  $k_\theta(0)$  and applying trigonometric identities.

There is a caveat: the plane at  $\theta = \pi$  is equal to the plane at  $\theta = 0$ , only the parametrization is reversed. Consequently,  $k_0(0) = -k_\pi(0)$ . This inconsistency is resolved when considering the corresponding osculating circles since the normal also changes direction. However, this comes at the cost of a discontinuity in the signed curvature at  $\theta = \pi/2$ , where  $\lim_{\theta \nearrow \pi/2} k_\theta(0) = 2$  and  $\lim_{\theta \searrow \pi/2} k_\theta(0) = -2$ . The osculating circles corresponding to the extreme values  $\theta = 0$  and  $\pi/2$  are depicted in Figure 4.1.17(l.).

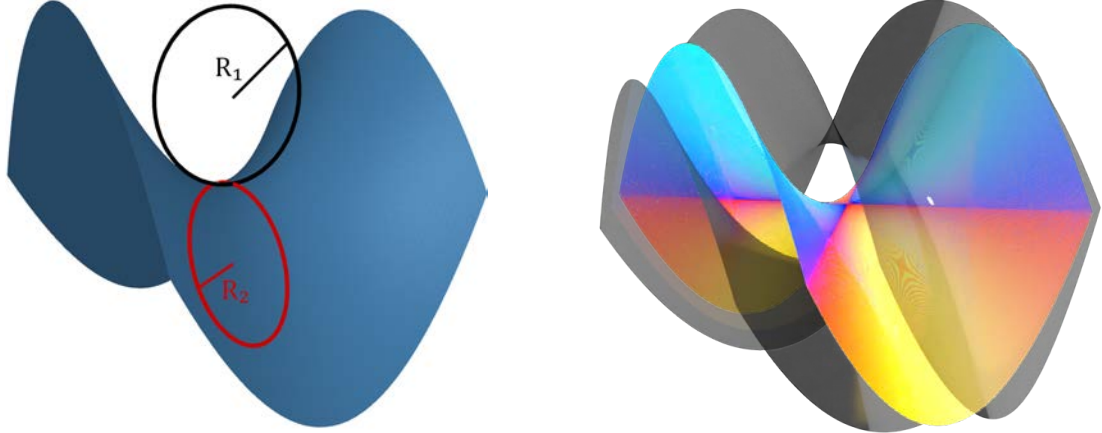


**Figure 4.1.17:** The two osculating circles with radii  $R_1$  and  $R_2$  corresponding to the principal curvatures  $\kappa_1$  and  $\kappa_2$  of the hyperbolic paraboloid in the origin (l.) and two  $\varepsilon$ -offset surfaces of  $\sigma(U)$  with  $\varepsilon = \pm 0.35$  (r.). Furthermore, the mean curvature  $H(p)$  is depicted (r.) with blue regions corresponding to a negative mean curvature and yellow regions corresponding to a positive mean curvature; however, the sign depends on the parametrization. The red lines correspond to the normal planes  $y = \pm x$  and indicate the hyperbolic paraboloid's flat regions where the mean curvature vanishes.

As depicted in Figure 4.1.17(r.), we compute the  $\pm \varepsilon$ -offset surfaces parametrized by

$$\sigma_{\pm \varepsilon}(x, y) = \sigma(x, y) \pm \varepsilon \cdot \frac{(-2x, 2y, 1)}{\sqrt{1 + 4x^2 + 4y^2}}$$

for  $\varepsilon = 0.35$ . The area of the offset surfaces can be calculated with Steiner's formula,

requiring the prior computation of the total mean and Gaussian curvature. The first and second fundamental form from Definition 4.1.10 provide a convenient means to finding these curvatures at every point. We calculate

$$E = \|\sigma_x\|^2 = 1 + 4x^2, \quad F = \langle \sigma_x, \sigma_y \rangle = -4xy, \quad G = \|\sigma_y\|^2 = 1 + 4y^2,$$

$$L = \langle \sigma_{xx}, \mathbf{n} \rangle = \frac{2}{\sqrt{1 + 4x^2 + 4y^2}}, \quad M = \langle \sigma_{xy}, \mathbf{n} \rangle = 0, \quad N = \langle \sigma_{yy}, \mathbf{n} \rangle = \frac{-2}{\sqrt{1 + 4x^2 + 4y^2}}$$

with the surface's unit normal  $\mathbf{n} = (\sigma_x \times \sigma_y) / \|\sigma_x \times \sigma_y\|$ . With these functions at hand, we compute

$$K(x, y) = \frac{-4}{\sqrt{1 + 4x^2 + 4y^2}^3} \quad \text{and} \quad H(x, y) = \frac{4y^2 - 4x^2}{\sqrt{1 + 4x^2 + 4y^2}^3}$$

as prescribed by Proposition 4.1.12. Firstly, the Gaussian curvature is negative everywhere and so is the total Gaussian curvature. Secondly, the mean curvature is symmetric in  $x$  and  $y$ . Since the region  $U$  describes a square and the numerator can be split into equal  $x$ - and  $y$ -parts with opposite signs by the addition laws of integrals, the integral  $\int_M H dA$  evaluates to 0. This fact is also evident from Figure 4.1.17(r.), in which the mean curvature is depicted: The areas of positive and negative mean curvature mutually cancel out. Still, the hyperbolic paraboloid is no minimal surface, because there are points, e.g.  $(1, 0, 1)$ , where the mean curvature does not vanish.

Finally, Theorem 4.1.14 implies that the  $\pm\varepsilon$ -offset surfaces  $M_{\pm\varepsilon}$  both have a strictly smaller area than the surface  $M$  itself. In this case, Steiner's formula becomes  $A(M_{\pm\varepsilon}) = A(M) - c\varepsilon^2$  for a positive constant  $c > 0$  dependent on the surface's Gaussian curvature. Figure 4.1.17(r.) provides an intuition: Both offset surfaces have a longer axis. The area of a rectangle with fixed circumference is maximized by the square, supporting the intuitive understanding that the surface area should be maximized by a balanced shape.

As the final part of this section, we introduce an invariant for 2-dimensional manifolds. In particular, the surface's total Gaussian curvature is independent of scaling and can be computed using the Euler characteristic of a triangulation. The following definition appears in Lee [197, p.276].

**Definition 4.1.18.** Let  $M$  be a compact 2-manifold. A *smooth triangulation* of  $M$  is a homeomorphism from a simplicial complex  $\Sigma$  to  $M$ , whose restriction to each simplex  $s \in \Sigma$  is a smooth embedding. If  $M$  is smoothly triangulated, we define the *Euler characteristic*  $\chi(M)$  of  $M$  as

$$\chi(M) = V - E + F,$$

where  $V$  is the number of vertices in the triangulation,  $E$  denotes the number of edges and  $F$  the number of faces.

This Euler characteristic is independent of the choice of triangulation [199, Cor. 10.25]. Originally, this topological invariant was introduced for polyhedra. Nowadays, it is a much more general tool, arising from homological algebra.

A different topological invariant of a surface is its *genus*. Every orientable 2-manifold is homeomorphic to the connected sum of a sphere with  $g \geq 0$  2-tori  $T^2$  [199, Thm. 6.15].  $M$ 's

genus is then defined as that number  $g$ . These two concepts combined enable us to state the Gauss-Bonnet Theorem that relates a surface's Gaussian curvature to its genus and its Euler characteristic.

**Theorem 4.1.19** (Gauss-Bonnet Theorem (cf. [197, Thm. 9.7])). *If  $(\mathcal{M}, \langle -, - \rangle)$  is a smoothly triangulated, compact, orientable Riemannian 2-manifold of genus  $g$ , then*

$$\frac{1}{2\pi} \int_{\mathcal{M}} K dA = \chi(\mathcal{M}) = 2 - 2g.$$

In particular, this formula applies to triply periodic minimal surfaces. As closed subsets of the compact 3-torus, they are compact. Furthermore, all embedded triply periodic minimal surfaces are orientable since they divide space into two separate labyrinths [71]. This makes Theorem 4.1.19 applicable to TPMS.

#### 4.1.1 Hilbert's Embedding Theorem

In the previous Section 4.1 we demonstrate that for a smooth surface  $\mathcal{M}$ , the principal curvatures  $\kappa_1$  and  $\kappa_2$  at any point  $p \in \mathcal{M}$  are defined by the maximum and minimum curvatures of plane curves obtained from intersecting the surface with planes containing the normal space  $N_p\mathcal{M}$ . By Definition 4.1.7, this allows us to define the Gaussian curvature as  $\kappa_1\kappa_2$  and the mean curvature as  $\frac{\kappa_1 + \kappa_2}{2}$ . The hyperbolic plane is the unique, simply connected Riemann surface with constant Gaussian curvature of  $(-1)$ . One may wonder, whether such surfaces exist in  $\mathbb{R}^3$ . Hilbert's Embedding Theorem provides a negative answer.

**Theorem 4.1.20** (Hilbert's Embedding Theorem [68, p.446]). *There is no geodesically complete, regular surface of constant negative Gaussian curvature in  $\mathbb{R}^3$ .*

As a consequence of Hilbert's Embedding Theorem, the hyperbolic plane cannot be isometrically embedded in  $\mathbb{R}^3$ . Figure 4.1.1 depicts that immersions of the hyperbolic plane  $\mathbb{H}^2$  either contain geometric singularities or curvature fluctuations.

The hyperbolic pseudosphere is a surface in  $\mathbb{R}^3$  with constant negative Gaussian curvature. It can be described as the gyroscope-shaped tractroid, whose equator is a singularity, and which is generated by revolving a tractrix about its asymptote [221]. The pseudosphere is locally isometric to the annular hyperbolic plane, which can be constructed by gluing crescent-shaped annular strips of ring width  $\delta$  and letting  $\delta \rightarrow 0$ . Once sufficiently many such annuli have been glued together, meaning the surface has been extended beyond its equatorial singularity, it starts to “ruffle” and a differentiable embedding becomes impossible [157]. The mathematician William Thurston started making paper models of the annular hyperbolic plane towards the end of the 20th century. Cornell professor Daina Taimina later improved the paper model, by artistically crocheting an immersion of the punctured hyperbolic plane out of yarn (e.g. [310]), an example of which is depicted in Figure 4.1.1(b). Contrary to mathematical intuition, it seems like the crocheted surface does not self-intersect. This is an artifact of the crocheted fabric's flexibility and does not contradict Hilbert's embedding theorem.

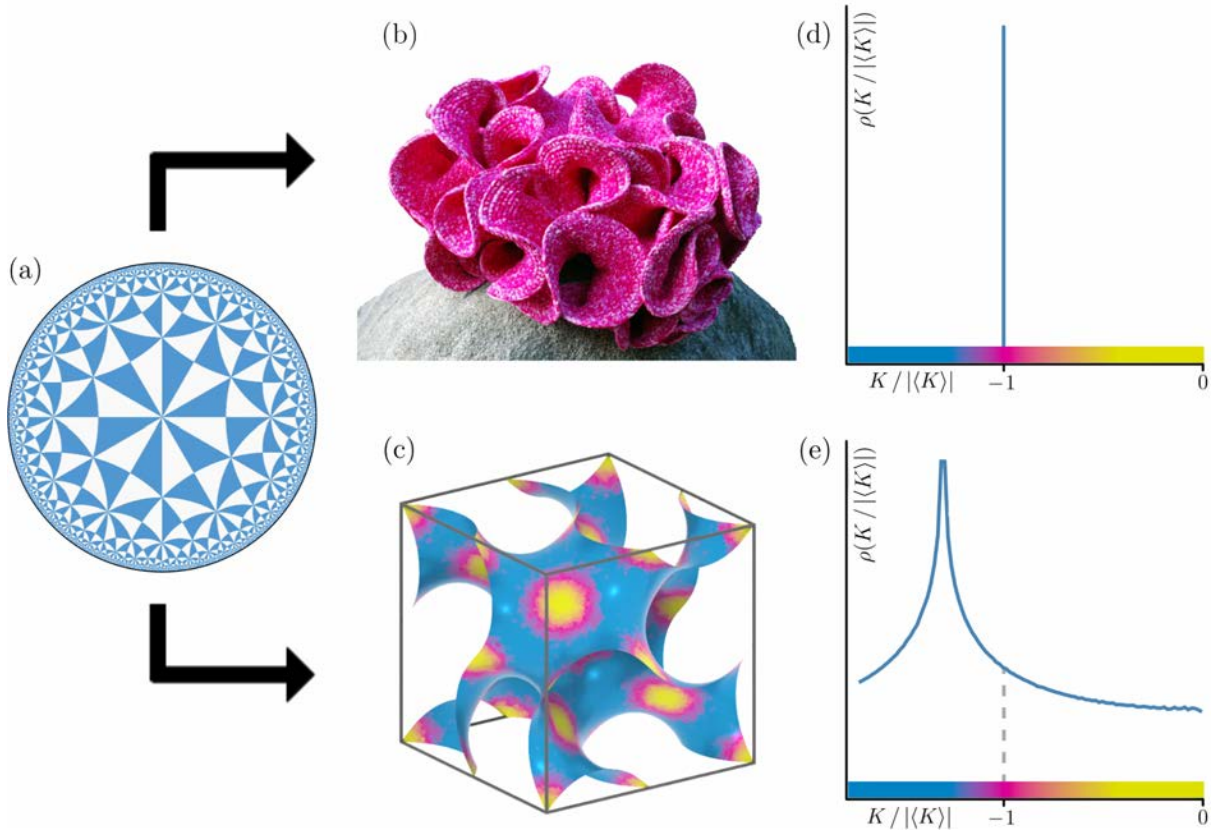


**Figure 4.1.1 (repeated): Gaussian curvatures of negatively curved surfaces in  $\mathbb{R}^3$ :** (a)

As per Hilbert's embedding theorem, it is not possible to isometrically embed the hyperbolic plane  $\mathbb{H}^2$  in  $\mathbb{R}^3$ . (b,d) The crocheted model for the hyperbolic plane by Daina Tamina [157] has constant Gaussian curvature. Its curvature distribution is a  $\delta$ -function at  $K/|\langle K \rangle| = -1$  for  $\langle K \rangle = \int K dA / \int dA$ . If extended infinitely, it would be self-intersecting (image source: [310]). (c,e) Embedded triply periodic minimal surfaces, here the Gyroid, are smooth intersection-free saddle surfaces. The Gaussian curvature of such surfaces (represented by the surface color) is negative, except at isolated flat points with zero curvature. However, the value varies, leading to a curvature distribution of finite width.

#### 4.1.2 Families of Triply Periodic Minimal Surfaces

Aside from self-intersecting immersions, Hilbert's embedding theorem predicts a way to embed the hyperbolic plane by allowing inhomogeneities in the Gaussian curvature. The mean curvature of a minimal surface  $\mathcal{M}$  is 0 by definition, requiring that its principal curvatures  $\kappa_1$  and  $\kappa_2$  are either both 0 at every point or have opposite signs. For triply periodic minimal surfaces, there are only finitely many flat points where both principal curvatures vanish [215, Cor. 3.3]. Therefore, these surfaces have negative Gaussian curvature almost everywhere and are thus a model of hyperbolic geometry. The existence of triply-periodic minimal surfaces in  $\mathbb{R}^3$  with arbitrary periodic boundary conditions and of any genus  $\geq 3$  is known [317]. Since these surfaces are smooth, they provide embeddings of the hyperbolic plane in Euclidean space  $\mathbb{R}^3$ . Nevertheless, they contain finitely many flat points, implying that their Gaussian curvature must fluctuate. Many TPMS are cataloged in Lord-Mackay [206], Fogden-Hyde [117, 119] and in Ken Brakke's **Surface Evolver** [50, 51].

For any genus  $g \geq 3$  there are orientable, embedded minimal surfaces in any flat 3-torus

$\mathbb{R}^3/\Lambda$  for a rank 3 lattice  $\Lambda$  [317]. The assumption  $g \geq 3$  is necessary and sufficient: TPMS of genus 0 cannot exist because they would be topological spheres in  $T^3$  lifting to minimal spheres, which is impossible [262]. Moreover, the only triply periodic minimal surface of genus 1 is given by parallel planes. Since the Gaussian curvature of a minimal surface is nonpositive by Definition 4.1.7 and the total Gaussian curvature is 0 by the Gauss-Bonnet Theorem 4.1.19, the Gaussian curvature's continuity implies that it must be 0 everywhere. Finally, genus 2 minimal surfaces are never triply periodic [216, Cor. 3.1]. Still, this does not imply that no minimal surface can have a genus below 3. In fact, there are 2-periodic minimal surfaces of all genera from 0 to 2 given by Karcher-Scherk surfaces [321].

In summary, connected TPMS can only be obtained when their genus is at least 3. Even the case of genus 3 minimal surfaces is far from fully classified and still brings out new examples to this day. The first such genus 3 minimal surfaces were described by Schwarz and his student Neovius in the nineteenth century [289]. Roughly 100 years later, Schoen named these surfaces and added several more to the collection [280], without providing a proof. Instead, he presented minimal surfaces as separating interfaces between skeletal nets and derived some *Weierstrass-Enneper parametrizations*. Karcher later constructed a proof for the existence of these surfaces and added Weierstrass-Enneper parametrizations for many of Schoen's surfaces [187]. Fogden and Hyde independently discovered these parametrizations and extended them by including various other triply periodic minimal surfaces [116, 118, 119]. To describe the Weierstrass-Enneper parametrization, we first realize that any minimal surface in  $\mathbb{R}^3$  can be parametrized using a non-vanishing analytic *Weierstrass function*  $R : \mathcal{D} \rightarrow \mathbb{C}$  for a simply connected  $\mathcal{D} \subset \mathbb{C} \cup \{\infty\}$  [231, §156], though finding this function for specific TPMS is difficult. By inserting the function  $R$  into the real part of complex integral expressions, we find the Cartesian coordinates of the minimal surface. The Weierstrass-Enneper parametrization completely characterizes the geometry of a surface and can be used to calculate the area, mean, and Gaussian curvature of a minimal surface [282, p.75f.].

Karcher and Große-Brauckmann-Wolgemuth were the first to mathematically prove that Schoen's surfaces are minimal [140, 187]. Notable examples described by Schoen include the cubic *Primitive (P)*, *Diamond (D)* and *Gyroid (G)*. These surfaces have received special attention over the years, as they are frequently observed in nature. They are illustrated in Figure 4.1.21. The Weierstrass-Enneper parametrization of these minimal surfaces is, for example, derived in Fogden-Hyde [119] and Gandy-Klinowski [125]. Alternatively, the Primitive, Diamond and Gyroid can be constructed as the companion surfaces to the skeletal nets **pcu**, **dia**, and **srs** (cf. [243]). They have the crystallographic symmetry groups  $Pm\bar{3}m$ ,  $Fd\bar{3}m$  and  $I4_132$ , respectively [64].

Typically, triply periodic minimal surfaces are not isolated. Rather, there exist curves that allow their deformation into each other. William Meeks III. made progress in this area by constructing a 5-dimensional deformation family of genus 3 minimal surfaces, called the *Meeks-family* [215]. It consists of the **tCLP**, **H**, **tD**, **tP**, and **rPD** deformations. It is remarkable that these families were already known to Schwarz [289]. Notably, Meeks' family neither contains the Gyroid nor the Lidinoid, which is a Bonnet transformation of the Gyroid [204]. They were later added in the form of the **rG** and **tG** surface family by Fogden-Hyde [117], which are not

contained in the Meeks family, though they intersect it [325]. These minimal surface families are included in the deformation diagram in Figure 4.1.21.

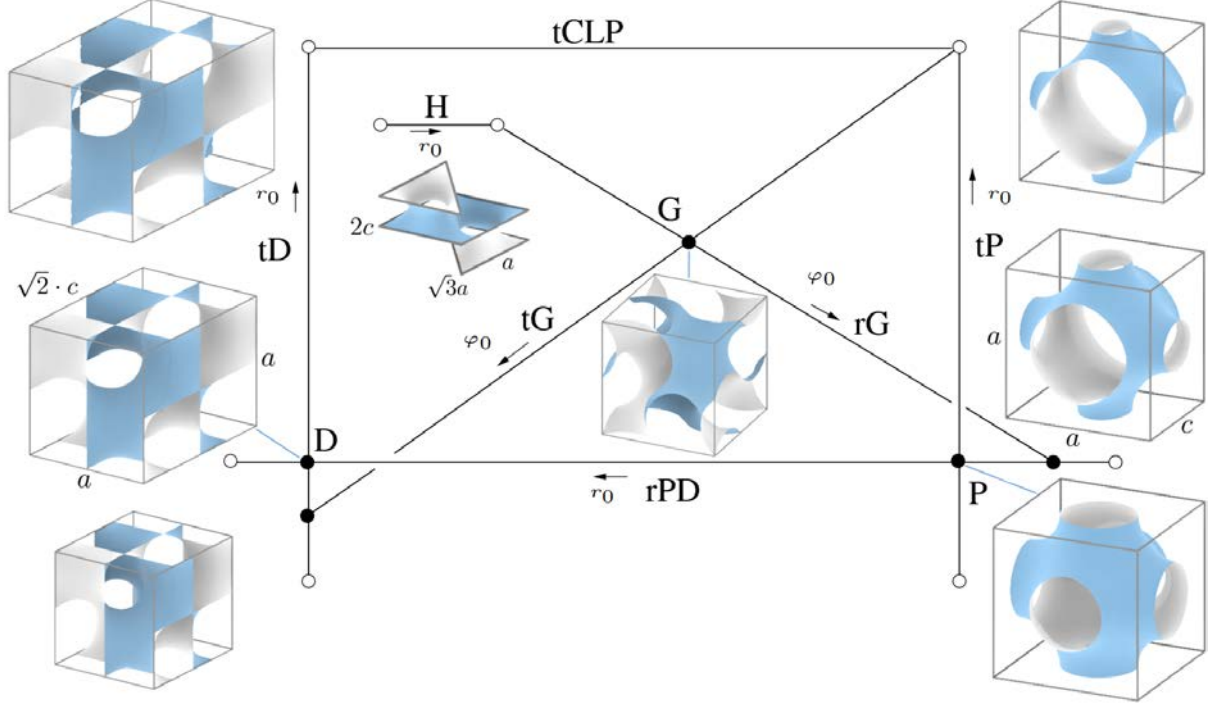


**Figure 4.1.21: Minimal surface families representing tetragonal and rhombohedral deformations of the Gyroid, Diamond and Primitive surfaces:** The depicted translational unit cells of minimal surfaces in the **tD** (l.) and **tP** (r.) family represent tetragonal minimal surface deformations of the cubic Diamond and Primitive minimal surfaces. We also depict a schematic layout of the **tD**, **tG**, **tP**, **rPD**, **rG**, **H** and **tCLP** surface families, indicating the free parameter as per [117, 283]. All surfaces in these families are balanced with the two complementary labyrinth domains of identical shape and related by a symmetry operation. The **tD**, **rPD**, **tP**, **H** and **tCLP** surface families are part of Meeks' five-dimensional surface family [215, Thm. 7.1]. Yet, the Gyroid's (c.) **tG** family and the **rG** family (which contains the Lidinoid) are not [325].

As highlighted in Section 4.1, minimal surfaces arise as the locally area-minimizing membranes bounded by a closed curve. The particular deformation families from Meeks' deformation family can be described by catenoids bounded by two disconnected wireframes. When considering a triangular catenoidal frame with a 60-degree offset and applying a translational symmetry (see Figure 4.1.22(c)), one obtains the classical Schwarz Diamond minimal surface. Allowing the spacing between the two catenoids to vary describes the **rPD** family containing both, the cubic Primitive and Diamond surfaces [117, 281]. Conversely, if the triangular frames are aligned, one obtains Schwarz's Hexagonal surface and the spacing between the frames parametrizes the hexagonal deformation family **H** [117]. Both families lie in Meeks' 5-dimensional family.

The hexagonal Diamond minimal surface, also referred to as Schoen's g-W surface [280], is a combination of both, Hexagonal and Diamond surface. Assume two similar pieces are isolated from the hexagonal Diamond, i.e. within a planar slab perpendicular to the Lonsdaleite net's vertical edges such that the flat points of the surface lie on the boundary (see Fig. 4.1.22(d)).

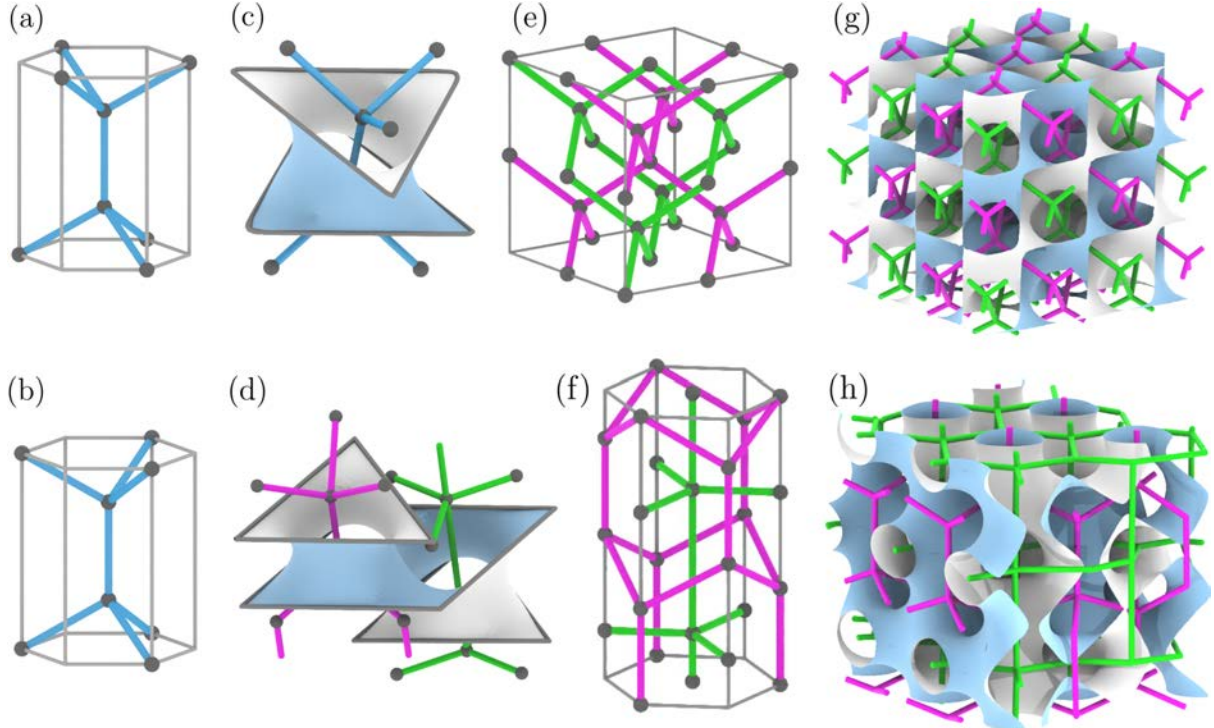


**Figure 4.1.22: The 3-periodic cubic Diamond, the hexagonal Diamond and their dual nets:** The Diamond net **dia** (a) and the Lonsdaleite net **lon** (b), also known as hexagonal Diamond, are generated from the same tetrahedral building block. Associated minimal surfaces are generated from triangular catenoidal frames, aligned with or without a  $60^\circ$  rotation (c,d). The translational unit cells of the Diamond (e) and Lonsdaleite net (f) demonstrate their cubic and hexagonal symmetry, also showing their dual nets. The **dia** net is self-dual, leading to the well-known “balanced” Diamond structure in which the Diamond minimal surface separates two identical nets (g). The dual net of Lonsdaleite is the Graphite net (**gra**, with 3- and 5-connected vertices); therefore the hexagonal Diamond surface is not balanced and rather separates space into two domains of different shape and volume (h).

Then, one obtains a surface patch that resembles but is not the same as, a triangular catenoid that either has aligned wireframes or a 60-degree offset. By Schwarz’s Principle of Symmetry [69, p.75], any holomorphic function whose domain is bounded by a straight line and which takes real values on the line can be holomorphically extended to the complex plane via reflection, which corresponds to complex conjugation. By the Identity Theorem, this extension is unique. The Weierstrass-Enneper parametrization of triply periodic minimal surfaces has the unit disk as its domain. Given a unit patch bounded by straight line segments, we can apply Schwarz’s Principle of Symmetry to each of the three coordinate functions defined on the unit disk, yielding an extension of the minimal surface by a  $180^\circ$  rotation [188]. Although the boundary curves in Figure 4.1.22(d) appear to be straight line segments, they are slightly curved. Likely, this is a consequence of gluing different triangular catenoids together. In addition, the hexagonal Diamond minimal surface is not contained in or connected to Meek’s deformation family since its genus is 5 [280, p.46].

Finally, the space of genus 3 TPMS is far from fully explored. In recent advances, Hao Chen and Matthias Weber discovered the existence of two further deformation families. An octagonal

boundary curve leads to the 2-dimensional orthorhombic deformation family **oH** of Schwarz's Hexagonal surface [74]. Each of this family's elements contains an inversion symmetry in the boundary cuboid's center. Moreover, he proved the existence of a 2-parameter, orthorhombic deformation family **oΔ**, which instead is given by a hexagonal wireframe [73]. Neither of the surface families belongs to Meek's 5-dimensional family.

## 4.2 Homogeneity Measures for Minimal Surfaces

Analogous to frameworks, minimal surfaces can be a-, singly-, doubly- or triply-periodic. In other words, they are invariant under the lattice generated by the infinite surfaces' translational symmetries (cf. Definition 2.1.20). Particularly triply periodic minimal surfaces in  $\mathbb{R}^3$  (TPMS) can be generated by gluing translational copies of a single connected, compact unit cell  $\mathbb{R}^3/\Lambda$  for a 3-dimensional lattice  $\Lambda \subset \mathbb{R}^3$ . The compactness of these surfaces is demonstrated in Corollary 4.2.5.

Since the mean curvature of a minimal surface  $\mathcal{M}$  is 0 by Definition 4.1.7, it is necessary that in each point its principal curvatures  $\kappa_1$  and  $\kappa_2$  are either both 0 or have opposite signs. For TPMS, there are only finitely many flat points where both principal curvatures vanish [216, Cor. 3.3]. Therefore, these surfaces have negative Gaussian curvature almost everywhere and are thus a model of hyperbolic geometry. As triply periodic minimal surfaces are smooth, they provide embeddings of the hyperbolic plane in Euclidean space  $\mathbb{R}^3$ .

Hilbert's Embedding Theorem 4.1.20 states that there is no complete regular surface in  $\mathbb{R}^3$  of constant negative Gaussian curvature. At first glance, this may seem like a contradiction. After all, triply periodic minimal surfaces are complete and regular surfaces. Nonetheless, they contain finitely many flat points. As a result, their Gaussian curvature must vary. Figure 4.1.1 visualizes this connection, depicting that any immersion of the hyperbolic plane  $\mathbb{H}^2$  either contains geometric singularities or curvature fluctuations.

It is therefore expected that TPMS are generally far from having a uniform Gaussian curvature distribution, raising the question of the smallest possible curvature variance among the class of triply periodic minimal surfaces. In the following sections, this question will be thoroughly investigated. As the first step in this direction, we properly define the concepts of curvature fluctuation and isotropy in Sections 4.2.1–4.2.2 as homogeneity measures. Only after defining these invariants are we able to quantify what a homogeneous TPMS represents. We calculate the homogeneity measures for several known instances of TPMS in Section 4.2.3.

### 4.2.1 Curvature Fluctuation

Following Schröder-Turk et al. [283], we define the *curvature fluctuation* in this section. In doing so, we provide several mathematical results for concepts that physicists typically accept without a formal proof. For a surface  $\mathcal{M} \subset \mathbb{R}^3$ , rescaling by a factor  $\Gamma > 0$  can be described on a coordinate level as  $\{x', y', z'\} = \{\Gamma x, \Gamma y, \Gamma z\}$  (cf. Section 4.1), defining a scaled surface  $\mathcal{M}'$ . To ensure the comparability of each sample, we scale the surfaces so that their average Gaussian curvature is constant, leading to the normalization  $\Gamma = \sqrt{\langle -K \rangle}$  with  $\mathcal{M}$ 's average Gaussian curvature given by  $\langle K \rangle = \int_{\mathcal{M}} K dA / \int_{\mathcal{M}} dA$ . This specific normalization gives the average Gaussian curvature and surface area a particularly nice form, as shown in the following.

**Proposition 4.2.1.** *Given a triply periodic minimal surface  $\mathcal{M}$  parametrized by  $\sigma : U \rightarrow \mathbb{R}^3/\Lambda$  for a full-dimensional lattice  $\Lambda$ , we scale its coordinates by  $\Gamma = \sqrt{\langle -K \rangle}$  to obtain  $\mathcal{M}'$  via  $\sigma' : U \rightarrow \mathbb{R}^3/(\Gamma \cdot \Lambda)$ . Then, it holds that  $\langle K' \rangle = -1$  and  $A(\mathcal{M}') = -\frac{1}{2\pi} \cdot \chi(\mathcal{M})$  for  $\mathcal{M}$ 's Euler characteristic  $\chi(\mathcal{M})$ .*

*Proof.* By Proposition 4.1.13 we have an expression for the area, mean curvature, and Gaussian curvature of the scaled surface  $\mathcal{M}'$ . Using the expression  $dA = \sqrt{EG - F^2} dx dy$  to pass from a surface integral to a parametric integral from Proposition 4.1.11, we convince ourselves that

$$\begin{aligned} \int_{\mathcal{M}'} K' dA' &\stackrel{\text{Prop. 4.1.11}}{=} \int_U \sqrt{E'G' - (F')^2} \cdot K' (\sigma'(x, y)) dx dy \\ &= \int_U \Gamma^2 \cdot \sqrt{EG - F^2} \cdot \frac{1}{\Gamma^2} \cdot K (\sigma(x, y)) dx dy \\ &\stackrel{\text{Prop. 4.1.11}}{=} \int_{\mathcal{M}} K dA. \end{aligned}$$

This enables us to prove the first part of the claim by computing

$$\langle K' \rangle = \frac{\int_{\mathcal{M}'} K' dA'}{A(\mathcal{M}')} \stackrel{\text{Prop. 4.1.13}}{=} \frac{\int_{\mathcal{M}} K dA}{\Gamma^2 \cdot A(\mathcal{M})} = -1.$$

since  $\Gamma = \sqrt{-\langle K \rangle}$ . Moreover, the Gauss-Bonnet Theorem 4.1.19 relates the total Gaussian curvature with the Euler characteristic  $\chi(\mathcal{M})$ . The above computation has the auxiliary result that  $\int_{\mathcal{M}'} K' dA' = -A(\mathcal{M}')$ . Combining these two assertions, we find that

$$A(\mathcal{M}') = -\frac{1}{2\pi} \cdot \chi(\mathcal{M}). \quad \square$$

The set of all points with nonnegative Gaussian curvature is a set of measure 0 because not only is the Gaussian curvature of a TPMS nonpositive but also these surfaces contain only finitely many flat points. Accordingly, the total Gaussian curvature has to be negative, justifying the necessity of the minus sign in  $\Gamma$ 's definition and making division by  $\Gamma$  well-defined. Denoting the Gaussian curvature's standard deviation by  $\Delta K = \sqrt{\langle (K - \langle K \rangle)^2 \rangle}$ , we define the *fluctuation of Gaussian curvature* as

$$\left( \frac{\Delta K}{\Gamma^2} \right)^2 = \frac{\langle K^2 \rangle - \langle K \rangle^2}{\langle K \rangle^2} = \frac{\frac{\int_{\mathcal{M}} K^2 dA}{\int_{\mathcal{M}} dA} - 1}{\left( \frac{\int_{\mathcal{M}} K dA}{\int_{\mathcal{M}} dA} \right)^2} - 1 = A(\mathcal{M}) \cdot \frac{\int_{\mathcal{M}} K^2 dA}{\left( \int_{\mathcal{M}} K dA \right)^2} - 1. \quad (4.2.2)$$

By the Gauss-Bonnet Theorem 4.1.19, the total Gaussian curvature is a topological constant independent of scale. For this reason, the term  $(\Delta K/\Gamma^2)^2$  only depends on the total squared Gaussian curvature and the surface area. In fact, the curvature fluctuation is completely independent of scale.

**Proposition 4.2.3.** *The curvature fluctuation is a dimensionless number, meaning that it is invariant under the scaling of any surface in  $\mathbb{R}^3$  that has a twice continuously differentiable and injective parametrization with nowhere vanishing partial derivatives.*

*Proof.* Assume that we uniformly scale the surface  $\mathcal{M}$  parametrized by  $\sigma : U \rightarrow \mathbb{R}^3$  by a constant  $c > 0$  into all directions. According to Proposition 4.1.13, the Gaussian curvature  $K$  then scales with  $1/c^2$  and the area  $A$  scales with  $c^2$ . The scaled versions are denoted by  $\mathcal{M}'$ ,  $\sigma'$ ,  $K'$  and  $A'$ . We label the coefficients of the first fundamental form of  $\mathcal{M}$  by  $E, F, G$  and the corresponding coefficients of the scaled surface  $\mathcal{M}'$  by  $E', F', G'$ . By using the expression  $dA = \sqrt{EG - F^2} dx dy$  to pass from a surface integral to a parametric integral in Proposition 4.1.11, we can calculate:

$$\begin{aligned} \int_{\mathcal{M}'} K'^2 dA' &\stackrel{\text{Prop. 4.1.11}}{=} \int_U \sqrt{E'G' - (F')^2} \cdot K'(\sigma'(x, y))^2 dx dy \\ &= \int_U c^2 \cdot \sqrt{EG - F^2} \cdot \left(\frac{1}{c^2}\right)^2 K(\sigma(x, y))^2 dx dy \\ &\stackrel{\text{Prop. 4.1.11}}{=} \frac{1}{c^2} \int_{\mathcal{M}} K^2 dA. \end{aligned}$$

Based on the proof of Proposition 4.2.1, the curvature fluctuation from Equation (4.2.2) of the scaled surface  $\mathcal{M}'$  evaluates to

$$\frac{\langle K'^2 \rangle - \langle K' \rangle^2}{\langle K' \rangle^2} = A(\mathcal{M}') \cdot \frac{\int_{\mathcal{M}'} K'^2 dA'}{\left(\int_{\mathcal{M}'} K' dA'\right)^2} = c^2 \cdot A(\mathcal{M}) \cdot \frac{\frac{1}{c^2} \int_{\mathcal{M}} K^2 dA}{\left(\int_{\mathcal{M}} K dA\right)^2} = \frac{\langle K^2 \rangle - \langle K \rangle^2}{\langle K \rangle^2}.$$

Consequently, scaling the surface does not affect the curvature fluctuation, proving the claim.  $\square$

Surfaces with low curvature fluctuation are more homogeneous, because deviations from the average Gaussian curvature are punished. After scaling a triply periodic minimal surface so that  $\langle K \rangle = -1$ , the curvature fluctuation can be interpreted as a variance of Gaussian curvature, providing a statistical interpretation of the term. Indeed, for any smooth surface the curvature fluctuation is nonnegative.

**Proposition 4.2.4.** *Given a smooth surface  $\mathcal{M}$  with non-zero Euler characteristic  $\chi(\mathcal{M})$  whose Gaussian curvature is in  $L^2(\mathcal{M})$ , the curvature fluctuation  $(\Delta K/\Gamma^2)^2$  is zero if and only if the Gaussian curvature is constant. Otherwise, it is positive.*

*Proof.* Here,  $L^2(\mathcal{M})$  denotes the normed vector space of measurable functions  $f : \mathcal{M} \rightarrow \mathbb{R}$  such that the integral

$$\|f\|_2 = \sqrt{\int_{\mathcal{M}} f^2 dA} < \infty$$

exists. In particular, the Cauchy-Schwarz inequality is satisfied according to [21, Thm. 10.55]. For  $f, g \in L^2(\mathcal{M})$  it can be expressed as

$$\left(\int_{\mathcal{M}} fg dA\right)^2 \leq \int_{\mathcal{M}} f^2 dA \cdot \int_{\mathcal{M}} g^2 dA,$$

with equality exactly obtained when  $g$  is a scalar multiple of  $f$ . Choosing  $f = K$  and  $g = 1$ , we find that

$$\int_{\mathcal{M}} K^2 dA \cdot \mathcal{A}(\mathcal{M}) - \left(\int_{\mathcal{M}} K dA\right)^2 \geq 0$$

with equality holding if and only if  $K$  is a scalar multiple of 1. Therefore, the Gaussian curvature  $K$  must be a constant function, concluding the proof.  $\square$

In the case of triply periodic minimal surfaces, this proposition can be slightly improved:

**Corollary 4.2.5.** *Triply periodic minimal surfaces  $\mathcal{M}$  are compact. Thus, the curvature fluctuation of  $\mathcal{M}$  is positive.*

*Proof.* Triply periodic surfaces are naturally embedded in a torus  $\mathbb{R}^3/\Lambda$  with a lattice  $\Lambda$  of maximal rank. The 3-torus is compact, since we can consider  $P = \bigoplus_{i=1}^3 \lambda_i \cdot [0, 1]$  for a generating set  $\lambda_1, \lambda_2, \lambda_3$  of  $\Lambda$ . By construction, for each  $x \in \mathbb{R}^3$  we can find  $r \in P$  such that  $x - r \in \Lambda$ , so  $x + \Lambda = r + \Lambda$ . Consequently,  $\mathbb{R}^3/\Lambda = P / (\Lambda \cap P)$ .  $P$  is compact by the Heine-Borel Theorem. As  $\Lambda \cap P$  is closed in the subspace topology,  $P / (\Lambda \cap P)$  is also compact. Finally, the minimal surface  $\mathcal{M}$  is closed in  $\mathbb{R}^3$ . Consequently, it is compact in  $\mathbb{R}^3/\Lambda$  as well. This proves the first claim.

We know that the Gaussian curvature  $K$  is a continuous function, which is why the Extreme Value Theorem yields that  $K$  is bounded on  $\mathcal{M}$ . Hence,  $K \in L^2(\mathcal{M})$ , which makes Proposition 4.2.4 applicable.

Hilbert's Theorem 4.1.20 states that there is no complete regular surface of constant negative Gaussian curvature. Since triply periodic minimal surfaces necessarily have negative curvature at every point except for finitely many flat points [216, Cor. 3.3], Proposition 4.2.4 implies that the curvature fluctuation is positive.  $\square$

### 4.2.2 Isotropy Index

Another measure for homogeneity can be obtained by considering Minkowski tensors. For a surface  $\mathcal{M}$  in  $\mathbb{R}^3$ , the tensor

$$W_1^{0,2}(\mathcal{M}) = \frac{1}{3} \int_{\mathcal{M}} \mathbf{n} \otimes \mathbf{n} \, dA \quad (4.2.6)$$

measures the variation of the normal vectors. Based on this matrix, we define the *isotropy index* of the surface [285]

$$\beta_1^{0,2}(\mathcal{M}) = \left| \frac{\lambda_3(W_1^{0,2}(\mathcal{M}))}{\lambda_1(W_1^{0,2}(\mathcal{M}))} \right| \in [0, 1] \quad (4.2.7)$$

for the eigenvalues' ordered absolute values  $|\lambda_3(W_1^{0,2})| \leq |\lambda_2(W_1^{0,2})| \leq |\lambda_1(W_1^{0,2})|$ . The isotropy index is well-defined since the matrix  $W_1^{0,2}(\mathcal{M})$  is symmetric and non-zero by construction. Its eigenvalues are real numbers and the largest eigenvalue is larger than 0. When  $\beta_1^{0,2} = 1$ , we call the surface *perfectly isotropic*. For instance, any surface with a uniform distribution of its normal vectors on  $S^2$  has an isotropy index of 1. The sphere and cube are perfectly isotropic.

In contrast, a small value of  $\beta_1^{0,2}(\mathcal{M})$  suggests that the normals favor certain directions. For example, an ellipsoid has  $\beta_1^{0,2}(\mathcal{M}) = \ell_{\min}/\ell_{\max}$  for the lengths  $\ell$  of the largest and smallest semi-axes. The normal space of a planar patch does not vary and the resulting matrix  $W_1^{0,2}(\mathcal{M})$

has rank 1, implying that  $\beta_1^{0,2}(\mathcal{M}) = 0$ . The isotropy index can be computed using the software package **karambola**<sup>15</sup> for calculating Minkowski tensors.

**Example 4.2.8.** Consider a cuboid  $\mathcal{Q}$  with rectangular faces identified by the unit facet normals  $\mathbf{n}_x$ ,  $\mathbf{n}_y$ , and  $\mathbf{n}_z$ . This example of Minkowski tensors is illustrated in Figure 4.2.9.

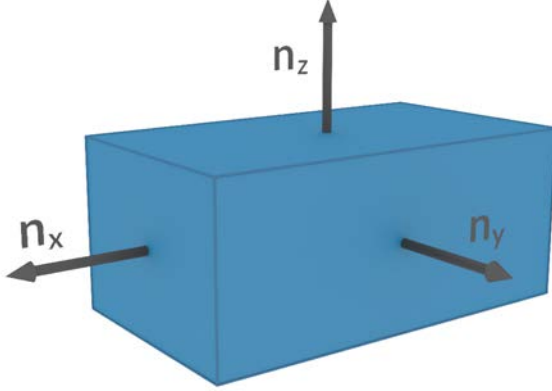


**Figure 4.2.9:** Qualitative image of a cuboid with its facet normals  $\mathbf{n}_x$ ,  $\mathbf{n}_y$ , and  $\mathbf{n}_z$ .

We label the surface area corresponding to one of the facets by  $A_x$ ,  $A_y$ , and  $A_z$ . Notice that each facet appears exactly twice. The facet normals  $\mathbf{n}_x$ ,  $\mathbf{n}_y$  and  $\mathbf{n}_z$  form an orthonormal basis of  $\mathbb{R}^3$ . After potentially reorienting  $\mathcal{Q}$ , we can assume that the normal vectors are given by the standard unit basis. Using Equation (4.2.6) we calculate the Minkowski tensor  $W_1^{0,2}$ :

$$\begin{aligned} W_1^{0,2}(\mathcal{Q}) &= \frac{1}{3} \int_{\mathcal{Q}} \mathbf{n} \otimes \mathbf{n} \, dA = \frac{2}{3} A_x \cdot (\mathbf{n}_x \otimes \mathbf{n}_x) + \frac{2}{3} A_y \cdot (\mathbf{n}_y \otimes \mathbf{n}_y) + \frac{2}{3} A_z \cdot (\mathbf{n}_z \otimes \mathbf{n}_z) \\ &= \frac{2}{3} \begin{pmatrix} A_x & 0 & 0 \\ 0 & A_y & 0 \\ 0 & 0 & A_z \end{pmatrix}. \end{aligned}$$

Since the matrix  $W_1^{0,2}(\mathcal{Q})$  is diagonal, computing the isotropy index (4.2.7) is simple and we obtain

$$\beta_1^{0,2}(\mathcal{Q}) = \frac{\min_{\omega \in \{x,y,z\}} A_\omega}{\max_{\omega \in \{x,y,z\}} A_\omega}$$

for the surface area  $A_\omega$  associated to the facet normal  $n_\omega$ . As a consequence, the cuboid is isotropic if and only if it is a cube.

Similar to Section 4.2.1, we can show that the isotropy index is independent of scale:

**Proposition 4.2.10.** *The isotropy index  $\beta_1^{0,2}$  is a dimensionless number. It is invariant under the scaling of any smooth, oriented surface.*

*Proof.* The matrix  $W_1^{0,2}$  is defined by the integral over the surface's unit normal field  $\mathbf{n}$  tensored with itself. Assume that the surface  $\mathcal{M}$  is parametrized by  $\sigma : U \rightarrow \mathbb{R}^3$  and scaled by  $c > 0$ , yielding the scaled parametrization  $\sigma' : U \rightarrow \mathbb{R}^3$  for  $\mathcal{M}'$ . The two corresponding unit normal

<sup>15</sup><https://morphometry.org/software/karambola/>

fields are given by  $\mathbf{n}' = \sigma'_x \times \sigma'_y / ||\sigma'_x \times \sigma'_y||$  and  $\mathbf{n} = \sigma_x \times \sigma_y / ||\sigma_x \times \sigma_y||$ . Using the formula to pass from a surface integral to a parametric integral and back from Proposition 4.1.11, we calculate

$$W_1^{0,2}(\mathcal{M}') = \int_{\mathcal{M}'} \mathbf{n}' \otimes \mathbf{n}' dA' = c^2 \cdot \int_{\mathcal{M}} \mathbf{n} \otimes \mathbf{n} dA = c^2 \cdot W_1^{0,2}(\mathcal{M}).$$

The eigenvalues of a matrix scale exactly like the matrix itself, which is why we find that  $\lambda_i(W_1^{0,2}(\mathcal{M}')) = c^2 \cdot \lambda_i(W_1^{0,2}(\mathcal{M}))$  for  $i = 1, 2, 3$ . The isotropy index  $\beta_1^{0,2}$  is a ratio of two eigenvalues, proving that it is independent under scaling.  $\square$

#### 4.2.3 Examples of Triply Periodic Minimal Surfaces

Having established two measures for the homogeneity of minimal surfaces, one may wonder which TPMS is the most homogeneous. In this work, we call a minimal surface *homogeneous*, if it has a curvature fluctuation of below 0.4 and an isotropy index above 0.95. This choice is not arbitrary but it is inspired by the Primitive, Diamond and Gyroid minimal surfaces with the currently known least amount of curvature variance. These surfaces are discussed in greater detail in this chapter.

In recent times, there have been new developments in minimal surface research, driven by the emergence of increasingly powerful computational tools. One such numerical program motivating the discovery of new minimal surfaces is Ken Brakke's **Surface Evolver**<sup>16</sup>. His curvature toolbox allows the application of various numerical optimization techniques to an initial surface to find a surface with zero mean curvature.

The Primitive, Diamond and Gyroid are among the most well-studied triply-periodic minimal surfaces and appear in a significant number of natural organisms. All of them are embedded, orientable, and have genus 3. The Gyroid is not contained in Meeks' 5-dimensional family. Instead, it lies in its own deformation space (cf. Figure 4.1.21). However, these families intersect, implying that there is a continuous transformation between all three surfaces. For a more detailed discussion about this topic, we refer to Section 4.1.2.

A combination of sin and cos terms describes explicit nodal approximations of many TPMS [126]. Alternatively, these surfaces can be parametrized using the implicit Weierstrass-Enneper representation (cf. Section 4.1.2). For our intents and purposes, a different approach is suited even better: A numerical approximation through simple, polyhedral initial configurations, combined with the **Surface Evolver** software. The initial surface is constructed by placing parallel planes in space and connecting the space between alternating planes with tubes, forming two separate labyrinths [71]. The three minimal surfaces and the corresponding polyhedral initial cell can be observed in Figure 4.2.11. Note that the Gyroid and Diamond structures are obtained in a similar manner. The key difference is that the initial configuration of the Gyroid consists of four rhombic cells arranged in four planes oriented in a helical tower, while the Diamond features four square cells per plane.

A previous study on the homogeneity of known deformation families revealed that the Primitive, Diamond and Gyroid exhibit the lowest curvature fluctuations (4.2.2) and the highest isotropy indices (4.2.7) within their respective deformation families (cf. [277]). For reference, the

---

<sup>16</sup><http://facstaff.susqu.edu/brakke/evolver/evolver.html>

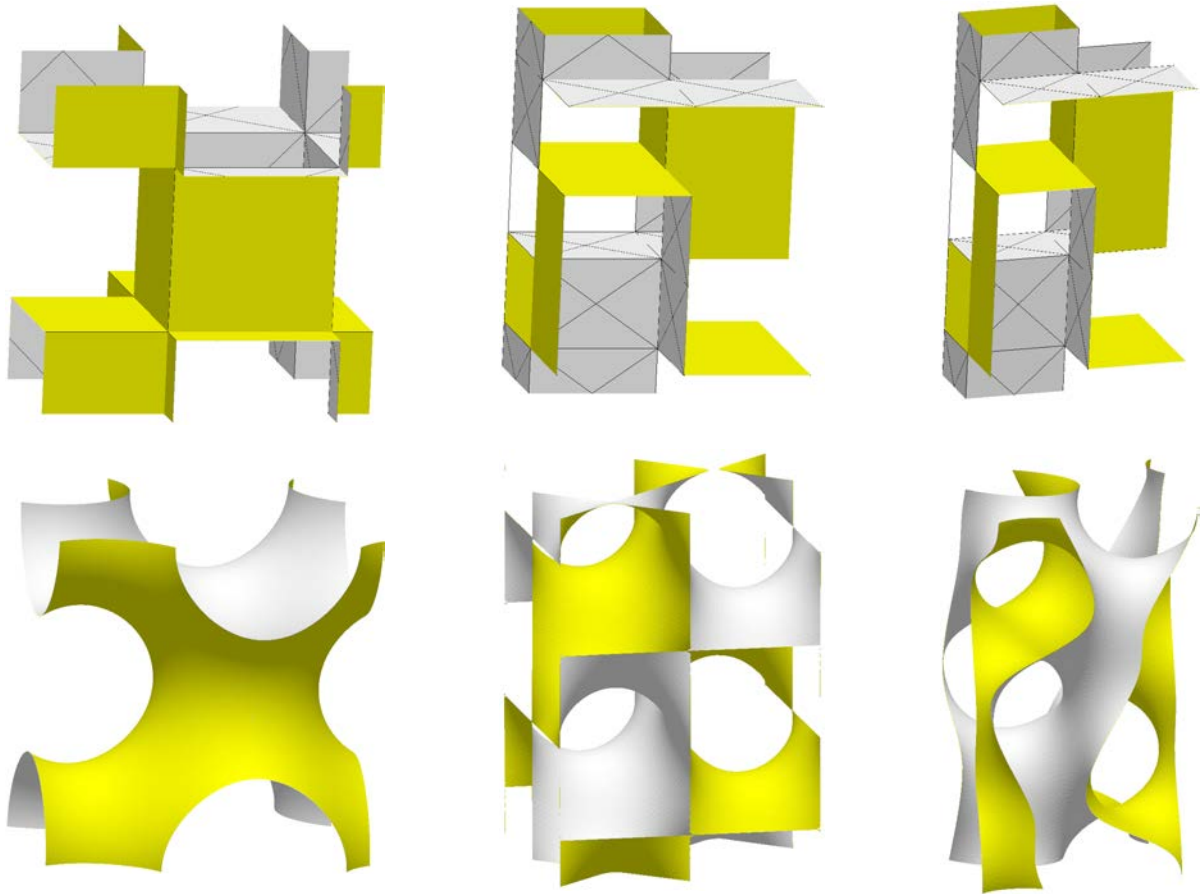


**Figure 4.2.11:** We depict polyhedral initial configurations (t.) and the corresponding minimal surface generated by the **Surface Evolver** based on these initializations (b.). The Primitive (l.), Diamond (c.) and Gyroid (r.) minimal surfaces are considered.

value of their respective curvature fluctuation is approximately 0.2188 and they are maximally isotropic. In other words, their normals are uniformly distributed on the unit sphere. We hypothesize that the curvature fluctuation of the Primitive, Diamond and Gyroid is optimal among the class of triply periodic minimal surfaces.

**Conjecture 4.2.12.** Among the bicontinuous triply periodic minimal surfaces we suspect that the Primitive, Diamond and Gyroid minimal surfaces have the smallest curvature fluctuation. They share the value 0.2188... [283].

Naturally, not all bicontinuous minimal surfaces have congruent labyrinths on both sides. To get an idea of nonoptimal curvature fluctuations, we want to consider five other surfaces. Specifically, the hexagonal Diamond, I-WP, Schwarz's Hexagonal surface and the Fisher-Koch S and C(Y) surfaces are further examined.

Schoen's I-WP<sup>17</sup> surface does not have topologically similar labyrinths – they even differ in volume. While the skeletal graph of the first labyrinth contains vertices of degree 8, the second one only has vertices with a valency of 4.

Schwarz's Hexagonal surface family **H** can be generated by a catenoid with a triangular boundary. We parametrize a part of the family by the ratio of the catenoid's height and the

---

<sup>17</sup>Innenzentriert - Wrapped Parcel. This surface is generated from the BCC sphere packing.

triangular boundaries' side length. In this case, the triangles have the same orientation, allowing them to tile space.

The crystal Lonsdaleite is also called hexagonal Diamond (cf. Section 4.1.2). Its name is inspired by the Diamond surface as the Lonsdaleite net **lon** is topologically similar to the **dia** net. The corresponding hexagonal Diamond minimal surface combines the triangular catenoid for the Diamond and Hexagonal minimal surfaces of the same edge length and height. The ratio between the catenoids' height edge lengths parametrizes the hexagonal Diamond's deformation family **L**. All of the mentioned surfaces are depicted in Figure 4.2.13.

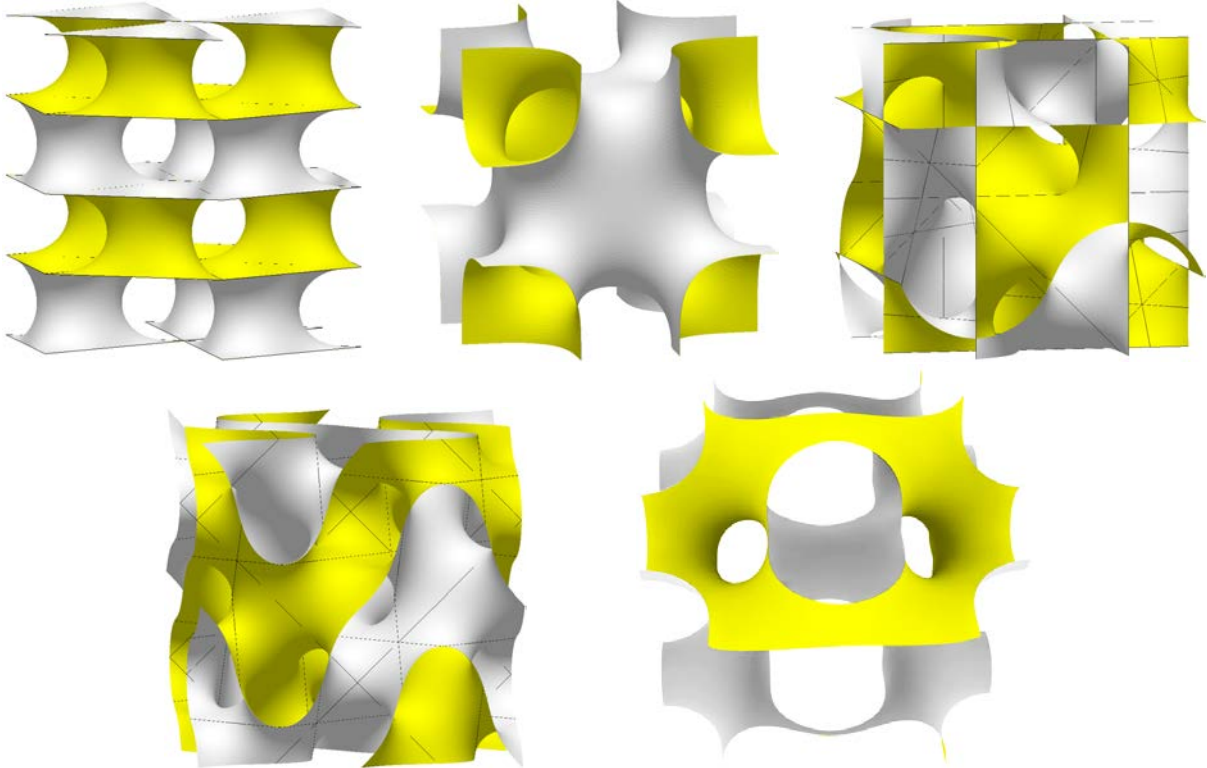


**Figure 4.2.13:** These pictures depict the H-surface (t.l.), the I-WP surface (t.c.) and the Fisher-Koch C(Y) surface (t.r.). Furthermore, we see the Fisher-Koch S surface (b.l.) and the hexagonal Diamond (b.r.).

For all of these surfaces, we compute the corresponding homogeneity measures via numerical means and provide additional data for the quality of the surfaces' discretizations. The results are laid out in Table 4.2.14. After normalizing all surfaces so that  $\langle K \rangle = -1$ , we calculate their curvature fluctuation  $(\Delta K / \Gamma^2)^2$ , their isotropy index  $\beta_1^{0,2}$  and volume fraction  $\phi$ . Since TPMS divide space into two disconnected labyrinths, the corresponding *volume fraction* represents the ratio of the smaller labyrinth's volume to the total volume. In particular, the value for the volume fraction of the I-WP surface is consistent with previously published results [284].

| Name  | $\phi$ | $-\chi$ | $(\Delta K/\Gamma^2)^2$ | $\beta_1^{0,2}$ | $l_e$             | $N_t/(-\chi)$ | $W/(-\chi)$ |
|---|--------|---------|-------------------------|-----------------|-------------------|---------------|-------------|
| P,D,G   | 0.5    | 4       | 0.2188                  | 1               | .                 | .             | 0           |
| C(Y)  | 0.5    | 24      | 0.5379                  | 1               | 0.0335 ... 0.2803 | 6432          | $10^{-4}$   |
| S   | 0.5    | 20      | 0.3878                  | 1               | 0.0489 ... 0.1736 | 7691          | $10^{-4}$   |
| IW-P  | 0.4635 | 12      | 0.4831                  | 1               | 0.0019 ... 0.1018 | 3125          | $10^{-4}$   |
| Most uniform member of surface families with hexagonal symmetry   |        |         |                         |                 |                   |               |             |
| L(1.684)  | 0.4830 | 8       | 0.2795                  | 0.9075          | 0.0147 ... 0.0718 | 10632         | $10^{-5}$   |
| H(0.431)  | 0.5    | 4       | 0.3284                  | 0.8213          | 0.0119 ... 0.1216 | 12013         | $10^{-5}$   |
| Most isotropic member of surface families with hexagonal symmetry |        |         |                         |                 |                   |               |             |
| L(1.647)  | 0.4894 | 8       | 0.3133                  | 0.9948          | 0.0168 ... 0.0782 | 10644         | $10^{-5}$   |
| H(0.416)  | 0.5    | 4       | 0.3561                  | 1               | 0.0096 ... 0.1192 | 12288         | $10^{-5}$   |

**Table 4.2.14:** Invariants of several TPMS are displayed here. The surfaces under consideration range from the cubic Primitive, Diamond, Gyroid, the Fisher-Koch C(Y) and S, the IW-P, the hexagonal Diamond **L** and the hexagonal **H** family. All surfaces are normalized so that  $\langle K \rangle = -1$ . We compute their curvature fluctuation  $(\Delta K/\Gamma^2)^2$ , their isotropy index  $\beta_1^{0,2}$  and volume fraction  $\phi$ . The value  $l_e$  is the average edge length of the triangles used in the discretization of the surface.  $N_t$  is the total number of triangles. The value  $W$  is the Willmore energy of the surface mesh in its final converged state.

### 4.3 Results: Construction Methods for Disordered Minimal Surfaces

Having thoroughly introduced the concept of curvature for surfaces in the previous sections, we are now equipped to shift our attention to new problems. The curvature fluctuation has relevance in molecular self-assembly and varies significantly between different TPMS. In contrast to the many known examples of ordered phases, examples of amorphous minimal surfaces are scarce. We call a minimal surface  $\mathcal{M}$  *amorphous* or *disordered* if it satisfies the following properties:

1. The surface is aperiodic and does not contain symmetries.
2. There exists a tesselation of  $\mathbb{R}^3$  into compact tiles of positive volume such that the total Gaussian curvature of  $\mathcal{C} \cap \mathcal{M}$  in each tile  $\mathcal{C}$  is equal to  $(-2\pi)$ . The diameter<sup>18</sup> of these tiles is bounded from above.

As a direct consequence of the second property, there is a  $\delta > 0$  such that for any translation  $\lambda \in \mathbb{R}^3$  the intersection  $(\lambda + \delta \cdot [0, 1]^3) \cap \mathcal{M}$  is non-empty. In fact, choosing  $\delta$  as the supremum over all diameters of the compact tiles suffices. This captures the idea that an aperiodic surface has surface pieces everywhere in  $\mathbb{R}^3$ . In a way, the tiles are aperiodic cells that emulate the behavior of translational unit cells in TPMS. Furthermore, the total Gaussian curvature of amorphous minimal surfaces is  $(-\infty)$  and the average Gaussian curvature is smaller than 0.

It should be stressed that this definition is the attempt to make a phenomenon that is observed in various organic systems mathematically tangible. However, finding an accurate definition is a subtle problem. It is not uncommon for a material to be well-understood from a

<sup>18</sup>The *diameter* of a set  $\mathcal{S}$  in a metric space is the supremum over all distances between points  $x, y \in \mathcal{S}$ .

physical perspective, yet remain elusive and difficult to describe in precise mathematical terms. Quasicrystals are an example of this. With the discovery of aperiodic tilings, the crystallography community had to redefine what a crystal is. Evidently, breaching the boundary between physical and experimental observation to formulate an accurate geometric model is generally a difficult task.

In this section, methods for constructing disordered minimal surfaces by numerical means are investigated. Because amorphous minimal surfaces often exhibit significant variations in channel thickness, the careless application of optimization schemes can lead to topological changes. For that reason, we devise a robust optimization scheme for generating minimal surfaces in Section 4.3.1. To produce initial configurations for this algorithm, we construct two models in Sections 4.3.2–4.3.3. As these models both use a cubic simulation box, the resulting surfaces are likely frustrated, intuitively meaning that they would prefer a different simulation box. In Section 4.3.4, we implement an algorithm to relax the simulation box for an improved isotropy index. This setup allows us to sample many amorphous minimal surface models. We examine the homogeneity of these surfaces in Section 4.3.5 and compare the results to the previously investigated ordered phases.

Note that the constructions we present in the following are merely models for amorphous structures in a periodic simulation box. Simulating an infinite asymmetric and disordered structure is computationally infeasible. Although our models have inherent long-range symmetry, they locally mimic the behavior of amorphous minimal surfaces. The increasing size of the simulation box and the high genus of these surfaces ensure that boundary effects are minimized.

### 4.3.1 Topology-Stabilized Generation of Minimal Surfaces

For generating numerical minimal surfaces, a routine to evolve non-minimal surfaces or meshes to approximations of minimal surfaces is necessary. Minimizing the *Willmore functional*  $\int_{\mathcal{M}} H^2 dA$ , a special case of the *Helfrich energy* for zero mean curvature, is a common strategy. Often, this approach is accompanied by the application of a gradient descent algorithm, referred to as *Willmore flow*. The *Surface Evolver* [50], an interactive program for modeling surfaces as simplicial complexes, contains implementations of the Willmore energy among various other curvature terms.

Given an initial surface that is reasonably close to being minimal, applying an iterative optimization scheme to minimize the Willmore functional works well. Nevertheless, neither of the methods used to generate initial configurations in Sections 4.3.2 and 4.3.3 guarantees proximity to minimal surfaces. As a result, we observe slow convergence, get trapped in local minima, and encounter the *pinch-off effect*. The latter phenomenon describes a topological change in the surface that occurs when catenoidal necks become overly narrow and collapse. It is depicted in Figure 4.3.1(a-b).

The annulus of a catenoid-like surface patch collapses to a line when the bounding circles' radius drops below the critical radius  $R_c \approx 1.50888$ . This number  $R_c$  is given by the reciprocal of Laplace's limit constant. For radii below  $R_c$ , the pinch-off occurs because the catenoid is not a solution to the variational problem anymore and only the Goldschmidt solution, consisting of two parallel disks, persists. Yet, the topology of the surface triangulation prevents it

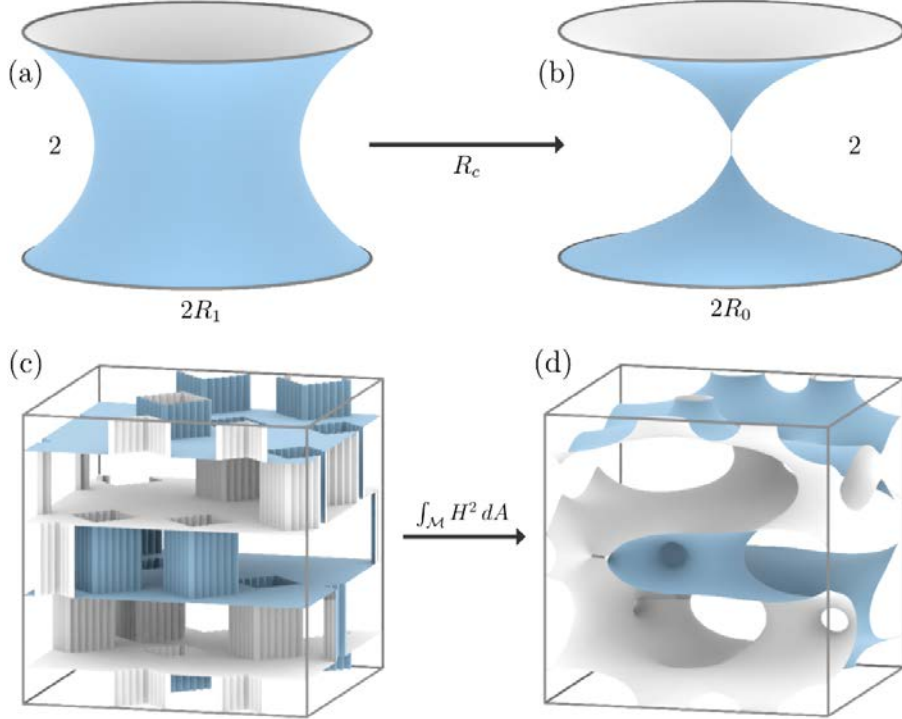


**Figure 4.3.1: The pinch-off effect in the catenoid:** (a) From the soap film model’s application to two parallel circular frames, the catenoid minimal surface can be constructed. It comes with a 1-dimensional deformation family that is parametrized by the circle’s radius, when fixing the catenoid’s height to 2. (b) There exists a critical radius  $R_c \approx 1.50888$  where the catenoid collapses and “pinches off” [130]. For radii  $R_0 < R_c$ , the only minimal surface inscribed in the two circles is the Goldschmidt solution consisting of two parallel disks. (c-d) This behavior can be observed in the disordered surface models from Sections 4.3.2–4.3.3 as well.

from attaining the Goldschmidt solution, causing the surface to collapse into a line instead of discontinuously separating. Solely minimizing the Willmore energy thus produces the pinch-off effect. This outcome transfers to a more general setting and the pinch-off can be observed in the configurations that we generate later in this chapter, as can be observed in Figure 4.3.1(c-d).

To prevent channel collapse in the minimal surface and avoid local minima, we propose incorporating an additional curvature term into the objective function. The squared Gaussian curvature has the property that it increases the catenoidal necks’ diameter. Therefore, the squared Gaussian curvature is an antithesis to the Willmore energy and balances out the occasional catenoid contraction. In addition, it aids in minimizing the curvature fluctuation. Particularly in the early stages of the algorithm, a squared Gaussian curvature term helps to avoid local minima. However, there is no guarantee for convergence to a minimal surface using this objective function, so it is necessary to steadily reduce the squared Gaussian curvature’s influence on the total energy. All of these considerations are summarized in the curvature energy term

$$E_\alpha(\mathcal{M}) = \int_{\mathcal{M}} H^2 dA + \alpha \cdot \int_{\mathcal{M}} K^2 dA \quad (4.3.2)$$

associated with the surface  $\mathcal{M}$  for some  $\alpha \geq 0$ . The choice of the elastic modulus  $\alpha$  plays an

important role in enhancing the method's convergence. The value of  $\alpha$  should depend on the ratio of  $\int_{\mathcal{M}} K^2 dA$  and  $\int_{\mathcal{M}} H^2 dA$ . Moreover, when the energy function  $E_\alpha(\mathcal{M})$  stagnates,  $\alpha$  should slowly decrease to guarantee convergence. In our experiments, we find that

$$\alpha = \min \left\{ \alpha', w \cdot \alpha' \cdot \frac{\int_{\mathcal{M}} H^2 dA}{\int_{\mathcal{M}} K^2 dA} \right\} \quad (4.3.3)$$

provides a reasonable choice, satisfying our requirements. Here,  $\alpha'$  denotes the previous elastic modulus  $\alpha$  and  $w > 0$  represents a damping factor. This way, the curvature energy term  $E_\alpha(\mathcal{M})$  weighs the Gaussian curvature roughly  $w$  times more than the mean curvature. In practice, the squared mean curvature contributes significantly less to the objective function than the squared Gaussian curvature and converges quickly to zero. To allow the surface to be impacted by the Gaussian curvature at all, a relatively large weighting  $w$  is necessary. The initialization of  $\alpha$  is chosen so that  $\alpha \cdot \int_{\mathcal{M}} K^2 dA$  is roughly  $w$  times as large as the integrated squared mean curvature. In our experiments, the value of  $\alpha$  is adjusted every few iterations, specifically every 10 iterations. Additionally,  $w$  is reset roughly every 300 steps to a smaller value. In our experiments, this is done by setting  $w \leftarrow 0.85 w$ . In this way, the influence of the squared Gaussian curvature term is guaranteed to go to 0.

To implement this method, we need to be able to calculate curvatures. Starting from a triangular surface mesh  $\Sigma$ , we approximate discrete analogs of the mean and Gaussian curvature. Given a vertex  $v$ , it is surrounded by a star of facets with area  $A(v)$ . Since in a triangulation each facet has exactly 3 incident vertices, the total surface area is  $\frac{A(v)}{3}$ . The discrete Gaussian curvature at  $v$  is given by the angle defect  $K(v) = 2\pi - \sum_i \alpha_i$ , where  $\sum_i \alpha_i$  is the sum of the simplices' interior angles  $\alpha_i$  at  $v$ . The discrete mean curvature is calculated for each edge  $e$ , by computing the oriented angle  $\theta(e)$  between the normals of facets incident to  $e$  and setting  $H(e) = \frac{1}{2}l(e)\theta(e)$  for the edge's length  $l(e)$ . At a vertex  $v$ , we take the average over the mean curvatures in all incident edges. For computing the Willmore energy and squared Gaussian curvature at  $v$ , we square  $H(v)$  and  $K(v)$  and divide by the area contribution  $\frac{A(v)}{3}$  of  $v$ . In the **Surface Evolver** [50], more robust, but equivalent, formulations are used for the squared terms.

Curvature calculations are carried out on triangulated meshes. Details about the discretization are later provided in Table 4.3.8. The finest meshes used in this chapter have average normalized edge lengths of approximately 0.1 and consist of approximately 300 – 12300 triangles per Euler characteristic  $\chi$ . Additionally, it is generally recommendable to use a volume constraint in the early stages of the optimization to avoid local minima by setting the volume of one labyrinth to 50% of the total volume. For the triply periodic minimal surface's first labyrinth, this constraint is added via `set body[1] target 0.5` at half the total volume – provided that the surface exists in the unit cube with periodic boundary conditions. This enables us to run an optimization routine with the objective function  $E_\alpha(\mathcal{M})$ .

Figure 4.3.4 depicts the application of the optimization routine to an amorphous Diamond structure, generated by a tubular configuration created from a disordered, 4-regular amorphous Diamond net. This amorphous Diamond net and the associated minimal surfaces are discussed in detail in Section 4.3.2. The optimization routine is split into three phases: First, the volume

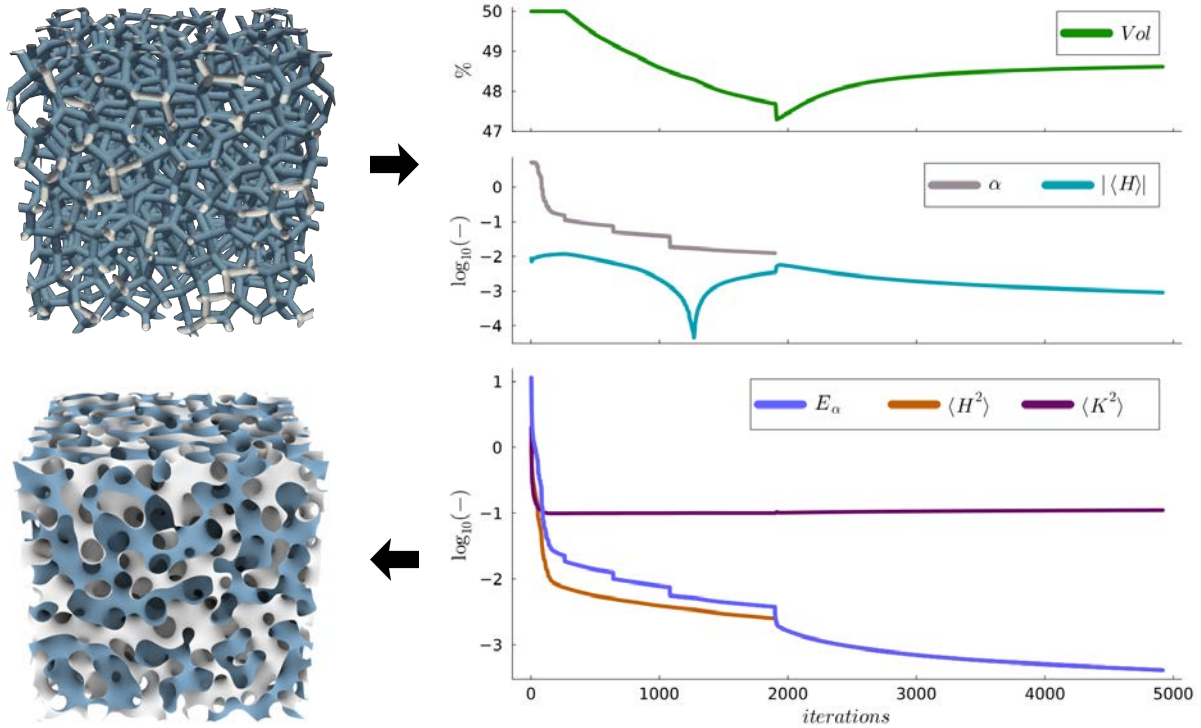


**Figure 4.3.4: Evolution from a tubular initial configuration to a minimal surface under a topology-stabilized version of the Willmore functional:** A surface mesh approximating an amorphous Diamond minimal surface (b.l.) is obtained from an initial tubular representation of the amorphous Diamond network (top left) by minimising the functional  $E_\alpha(\mathcal{M})$ , Eq. 4.3.2, using the **Surface Evolver** software [50]. In the initial stages, a term  $\alpha(n) \int K^2 dA$  penalizing high absolute values of Gaussian curvature is included with a modulus  $\alpha(n)$  that decays as the evolution progresses. This term prevents “pinch off” effects, thereby stabilizing the topology and a smooth negatively curved surface.

is fixed and  $\alpha$  is active. Second, the volume constraint is relaxed, while  $\alpha$  remains active. In the first two phases, a coarser discretization is used to converge quickly. Finally,  $\alpha$  is set to 0 and the discretization is improved, leading to a *numerical minimal surface* with average Willmore energy below  $10^{-3}$ . These optimization routines are summarized in Algorithm 4.3.5.

The optimization routine is subdivided into two methods. The function `loop` displays the current curvature values and updates the value of  $\alpha$  before applying five optimization steps with the function `g`. Whenever an integer `n` follows a function call `fun` in **Surface Evolver** code (i.e. `fun n`), that function is executed `n` times. Using the subroutine `loop`, the main function `curvature_optimization` initializes `w = 5`, sets the facet tension to 0, and activates the square Gaussian curvature `sqg` and Willmore energy `willmore` as targets. In addition, we record the total mean curvature `meancurv`, the current volume of the first labyrinth `body[1].volume` and the elastic modulus  $\alpha$ . During the initialization, the surface mesh is regularized by equiangulations `u` and vertex averaging `V`.

We set the volume of both labyrinths to 50% of the total volume each. After taking a few gradient descent steps to avoid divergence, the conjugate gradient direction of descent is activated instead. The rest of the routine is divided into three parts: While the average Willmore energy is above  $10^{-2}$ , the prefactor `w` is reduced to 85% after `loop` is computed. Afterward, the channel

---

**Algorithm 4.3.5:** Topology-stabilized curvature optimization

---

**Data:** Triangulated surface mesh  $\Sigma$ .  
**Result:** Numerically minimal surface mesh with  $\mathcal{W}(\Sigma)/A(\Sigma) < 5 \cdot 10^{-4}$ .

**Function** loop():

```
printf "%f %f %f %f %f %f \n",
    total_area, willmore.value, meancurv.value, body[1].volume,
    sqg.value/sqg.modulus, sqg.modulus;
    sqg.modulus := w · sqg.modulus · willmore.value/sqg.value;
    g 5;
```

**Function** curvature\_optimization():

```
quiet ON; w := 5;
set facets density (0); printf "area willmore mean body[1]  $K^2 \alpha$  \n";
set willmore energy; set sqg energy;
willmore.modulus := 1; sqg.modulus := 1; meancurv.modulus := 1;
u; V 10; u; V 10; u;
g 5; conj_grad ON;
while willmore.value > 0.01 · total_area do
    u; V 3; u;
    loop 10;
    w := w · 0.85;
unset body[1] target; unset body[2] target;
while willmore.value > 0.0025 · total_area do
    u; V 3; u;
    loop 10;
    w := w · 0.85;
set sqg info_only; sqg.modulus := 1; refine facets;
while willmore.value > 0.0005 · total_area do
    u; V 3; u;
    loop 15; u; loop 15;
```

---

```
curvature_optimization();
```

target volumes are removed and the same routine is performed until the average Willmore energy is below  $2.5 \cdot 10^{-3}$ . Lastly, we set the term  $\alpha$  to 0 and refine the discretization for the final steps so that we can be confident in the result. The algorithm stops when the average Willmore energy drops below  $5 \cdot 10^{-4}$ . Before `Loop` is applied in all of the while-loops, the surface mesh is improved through equiangulations and vertex averaging.

### 4.3.2 Construction of Amorphous Diamond Minimal Surfaces

The surfaces discussed in Section 4.2.3 are ordered structures, with high symmetry on a small length scale. Among the class of triply periodic minimal surfaces, the Primitive, Diamond and Gyroid minimal surfaces are portrayed as minimally fluctuant. Several deformation families are associated with these surfaces, including the tetragonal and rhombohedral families: **rG**, **rPD**, **tD**, **tG** and **tP** (cf. Figure 4.1.21). These families enable continuous transformations between the Primitive, Diamond and Gyroid surfaces. The deformations can, for example, be described in terms of their skeletal graphs [36].

As one of our key results, this section describes the analysis of Gaussian curvature variations of the amorphous Diamond minimal surfaces. While we find these surfaces to be more homogeneous than other amorphous minimal surfaces, their curvature variances are significantly greater than those of the cubic Primitive, Diamond and Gyroid surfaces.

#### 4.3.2.1 Skeletal Graphs of Bicontinuous Minimal Surfaces

The connection between 3-periodic nets and triply periodic minimal surfaces has already been established by Schoen [280]. In his article, the Primitive, Diamond and Gyroid Surfaces are expressed in terms of their skeletal nets, existing inside the medial axes of the surfaces.

When a net's *cyclomatic number*  $g = 1 + |V| - |E|$  is equal to the net's periodicity, we call it a *minimal net*. In this case, the periodicity is 3. As it turns out, the 15 triply periodic minimal nets are completely classified, with some corresponding to the skeletal nets in the Primitive, Diamond and Gyroid surfaces [64]. Having the minimum possible number of vertices and edges in their periodic unit cell, minimal nets are as simple as possible [41]. Alongside ordered networks, in the natural world disordered or amorphous phases are sometimes favored, representing local energy minima. As an example, amorphous silicon forms in nature [155]. These amorphous networks provide an interesting class of examples.

Locally, amorphous networks can look similar to the networks associated with the Primitive, Diamond and Gyroid surfaces [30, 293], while their global structure deviates significantly. This leads to the question of whether these amorphous networks can be used to generate minimal surfaces. If so, we want to know whether the corresponding surfaces perform well in terms of the homogeneity measures that are introduced in Sections 4.2.1–4.2.2.

One might expect the amorphous Diamond to exhibit low curvature fluctuations for the following reasons: The continuous random network algorithm of Markema and Mousseau [30] starts with a Diamond structure (see Figure 4.1.22(a)) which is then randomized by adding random transpositions through a flip of the central edge from a vertical to a horizontal position. Figure 4.3.6 depicts this process.

The Wootton-Winer-Weaire Algorithm only displaces two of the 8 vertices from the Diamond

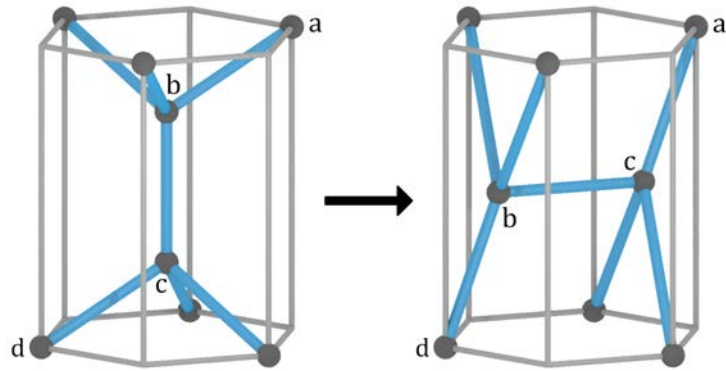


**Figure 4.3.6:** The Wooton-Winer-Weaire Algorithm [330] starts from the Diamond net (l.). By flipping the edge  $bc$  and reorganizing the connecting edges,  $ab$  becomes  $ac$  and  $cd$  becomes  $bd$  (r.). The resulting structure is then relaxed so that the angles between edges are again  $109.5^\circ$ . A possible relaxation is the minimization of the Keating potential (cf. [30]).

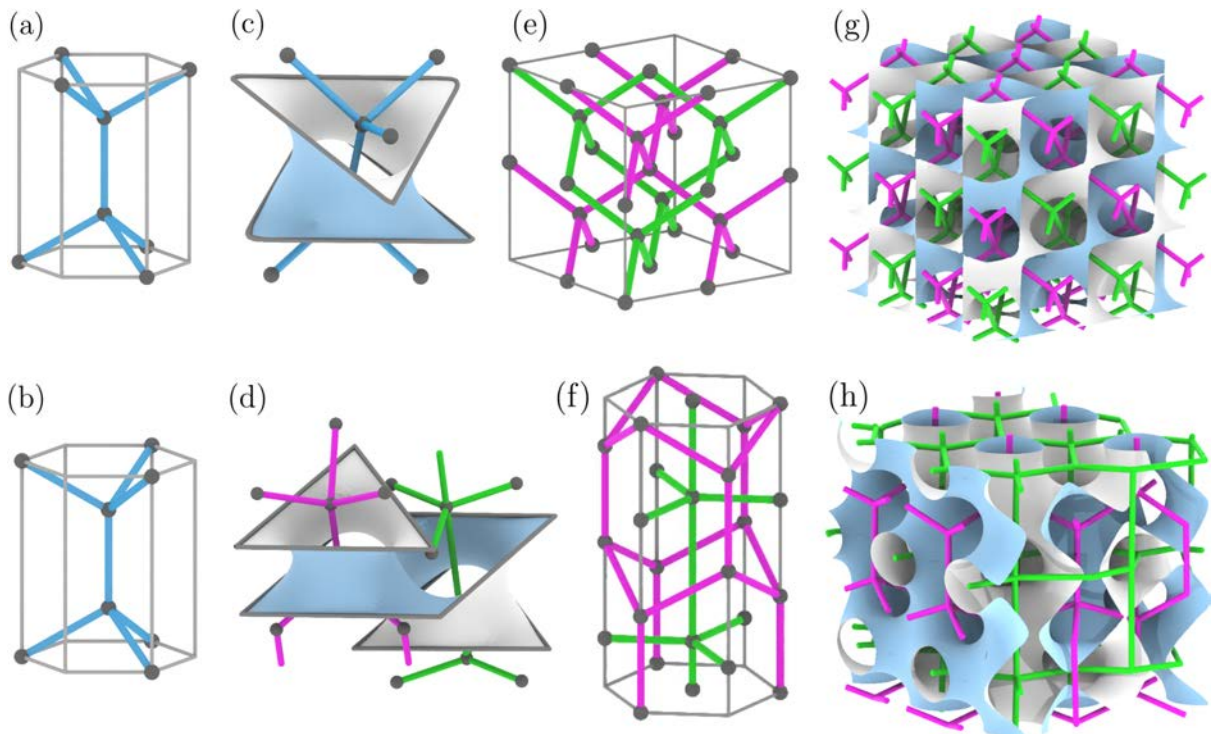


**Figure 4.1.22 (repeated): The 3-periodic cubic Diamond, the hexagonal Diamond and their dual nets:** The Diamond net dia (a) and the Lonsdaleite net lon (b), also known as hexagonal Diamond, are generated from the same tetrahedral building block. Associated minimal surfaces are generated from triangular catenoidal frames, aligned with or without a  $60^\circ$  rotation (c,d). The translational unit cells of the Diamond (e) and Lonsdaleite net (f) demonstrate their cubic and hexagonal symmetry, also showing their dual nets. The dia net is self-dual, leading to the well-known “balanced” Diamond structure in which the Diamond minimal surface separates two identical nets (g). The dual net of Lonsdaleite is the Graphite net (gra, with 3- and 5-connected vertices); therefore the hexagonal Diamond surface is not balanced and rather separates space into two domains of different shape and volume (h).

net's unit cell. Therefore, it is unclear whether the periodicity of the embedded net is maintained in a larger unit cell. While two edges change incident vertices during this procedure, the vertex

degree remains unchanged. The resulting structure is then relaxed through a sequence of Monte-Carlo moves, as described by Markema and Mousseau [30]. Intuitively, the network generated by this algorithm consists exclusively of vertices with a degree of 4. However, it cannot be guaranteed that the angle between the two 4-regular top and bottom building blocks is given by  $\pi/3$ , as is the case in the cubic **dia** network. Rather, the angle lies somewhere between 0 (**lon**: Figure 4.1.22(b)) and  $\pi/3$  (**dia**: Figure 4.1.22(a)). On a side note, many of the discussed nets are classified in the RCSR database [243].

Recent advances make it possible to create large continuous random networks [30, 191] with comparable properties as observed in experiments. In order to consider these networks as the labyrinth graph of a minimal surface, it is necessary to create a second labyrinth. Still, it is unclear how this can be achieved consistently and without self-intersections. Alternatively, we can replace the edges with cylinders of radius  $r$ , determined by the value when the cylinders' union contains exactly half of the unit cell's volume. In the literature, the process of incrementally growing a volume from an embedded graph is known as “tubification” [37, p.243f.]. This surface of this volume is then triangulated for the software **Surface Evolver** and subsequently optimized, resulting in a minimal surface, as is done in previous examples. For the ordered Diamond network, tubification reproduces the crystalline Diamond surface.

Since an amorphous Diamond net is built using intermediate pieces between the Diamond and Lonsdaleite nets, we expect the tubified surface to be an amalgamation of the Diamond (cf. Figure 4.1.22(c)) and hexagonal Diamond (cf. Figure 4.1.22(d)) surface patches. Contrary to the cubic Diamond net (cf. Figure 4.1.22(e)), the Lonsdaleite net has hexagonal symmetry (cf. Figure 4.1.22(f)). Because the generated amorphous Diamond samples stay within a cubic simulation box, the Diamond net is likely favored over the Lonsdaleite net.

### 4.3.2.2 Homogeneity of the Amorphous Diamond Minimal Surface

In Section 4.2, with the isotropy index and the curvature fluctuation two homogeneity measures for minimal surfaces are introduced. Figure 4.3.7 on the following page presents data on how the amorphous Diamond surfaces perform in terms of these measures. The triply periodic minimal surfaces discussed in Section 4.2.3 are added to the picture for reference.

The amorphous Diamond surfaces investigated here are generated by considering simulation boxes of different sizes. Since the homogeneity measures from Section 4.2 are invariant under the scaling of the unit cell, we label the surfaces by their Euler characteristic. Out of the 5 available samples, we have one sample with  $\chi = -432$ , two with  $\chi = -2000$ , and two with  $\chi = -8192$ , with their genera changing accordingly. Yet, considering these surfaces directly is not meaningful: Intuitively, a higher genus allows the surfaces to distribute their normals more evenly, leading to a lower isotropy index (cf. Equation (4.2.7)). In fact, the isotropy index averages the unit normals over the entire surface, so dominant normal directions average out over large simulation boxes. Conversely, the curvature fluctuation (cf. Equation (4.2.2)) is a variance measure for the Gaussian curvature and not an average. In our experiments, we observed a positive correlation between Gaussian curvature fluctuation and the simulation box size. However, this observation is potentially a finite-size artifact of the simulation box.

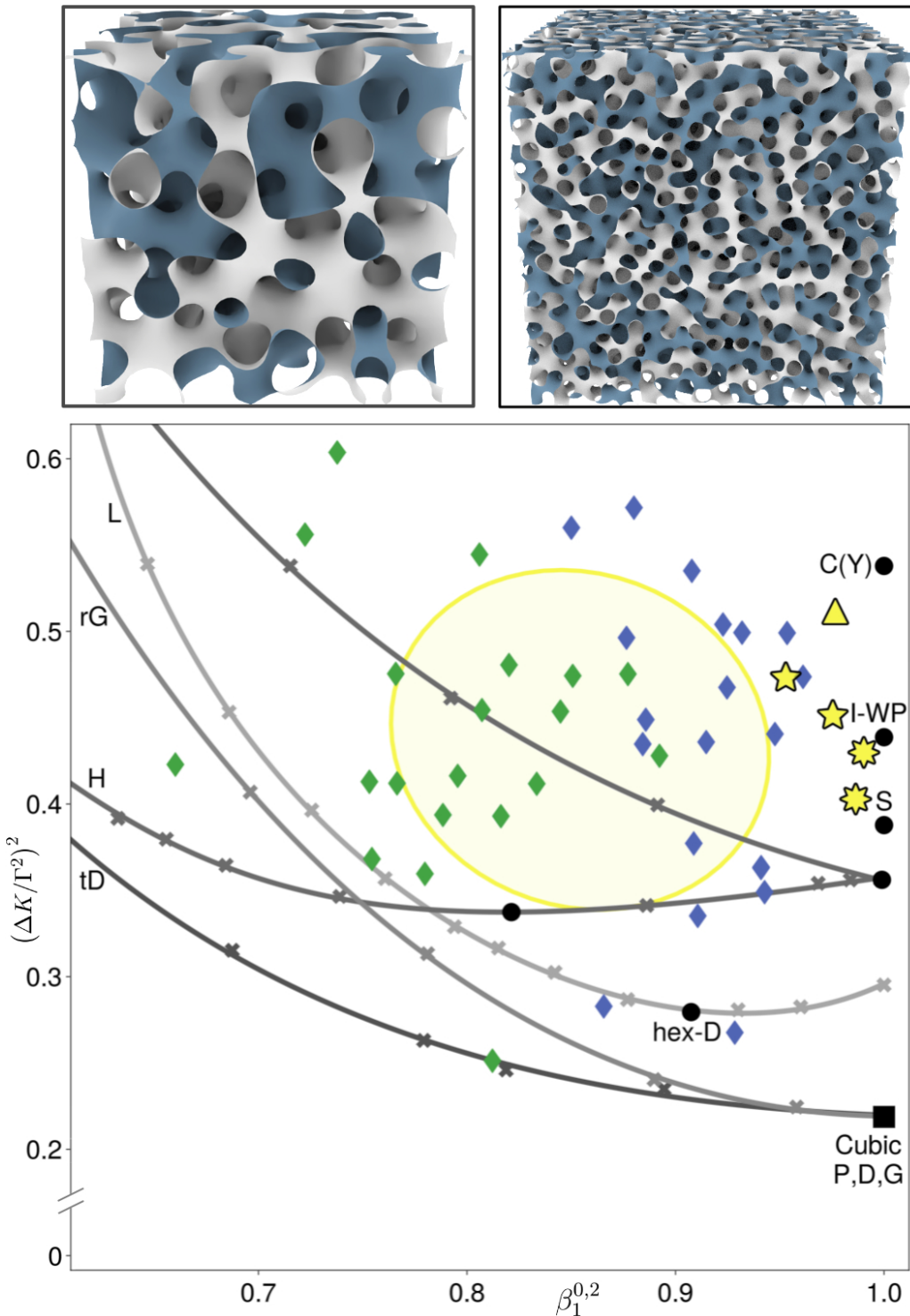


**Figure 4.3.7: Curvature and isotropy of the amorphous Diamond surfaces:** For assessing the quality of amorphous Diamond surfaces, the isotropy index  $\beta_1^{0,2}$  and the curvature fluctuation  $(\Delta K/\Gamma^2)^2$  are depicted. We compare this data to TPMS (solid disks and square) and one-parameter TPMS families (solid lines). We sample 5 amorphous Diamond surfaces in the sizes  $\chi = -432$  (triangle),  $\chi = -2000$  (5-star) and  $\chi = -8192$  (8-star). From these surfaces, we cut out random cubical subsamples with Euler characteristic  $\chi = -16$  (green) and  $\chi = 2^3 \cdot (-16)$  (blue). The principal component ellipse (yellow) provides a statistical interpretation of the data. Two amorphous Diamond surfaces with  $\chi = -432$  (t.l.) and  $\chi = -8192$  (t.r.) are included.

Indeed, the amorphous Diamond minimal surfaces have curvature fluctuations of  $(\Delta K/\Gamma^2)^2 > 0.4$ , about twice as large as the cubic Primitive, Diamond and Gyroid surfaces. The surface samples are highly isotropic, with  $\beta_1^{0,2} > 0.95$ . While the curvature fluctuation  $(\Delta K/\Gamma^2)^2$  decreases with increasing topological complexity (i.e.  $\chi$ ), the isotropy index may not be affected as significantly as we anticipated.

To make the data independent of the surfaces' genus, we perform a subset analysis. This is done by cutting out random cubical subsets so that their average Euler characteristic is  $\chi = -16$  and  $\chi = 2^3 \cdot (-16)$ , respectively. These numbers are chosen in a way that doubling the cubical boxes' side lengths yields the other. The resulting surfaces are depicted as blue and green diamonds in Figure 4.3.7. We perform a principal component analysis on the cubical subsamples to find that their isotropy varies significantly, whereas their Gaussian curvature fluctuation is comparable to the 5 initial samples. In particular, the Gaussian curvature fluctuation remains above and mostly well above the value of the cubic Primitive, Diamond and Gyroid surfaces.

Figure 4.3.7 also shows data for some one-parameter families of TPMS, including data for **tD**, **rG**, **H** [117, 283, 286] and for the hexagonal Diamond family (**L**). These families can be understood as deformations of particular members with higher symmetry, such as the cubic Primitive, Diamond and Gyroid surface, or with particularly high spatial isotropy. This includes the members of **H** and **L** with  $\beta_1^{0,2} \approx 1$ . These families highlight that deformations exist that have only small continuous changes of  $(\Delta K/\Gamma^2)^2$  at the expense of a rapidly changing isotropy index. Similar to the **H** surface family [286], the member of the hexagonal Diamond family with the lowest curvature fluctuation is not the most isotropic one (cf. Table 4.3.8). The relevant data used to generate Figure 4.3.7 is presented in Table 4.3.8.

We find that the model amorphous Diamond surfaces and their subsamples exhibit a similar curvature fluctuation to the cubic minimal surfaces such as the I-WP and the Fisher-Koch S and C(Y) surfaces. Still, the amorphous Diamond surface samples do not reach the curvature homogeneity of the cubic Primitive, Diamond and Gyroid. Nevertheless, they are perfectly competitive with the depicted deformation families. All produced complete amorphous Diamond surfaces are nearly isotropic, putting them in the same class of surfaces as the bicontinuous phases.

To better understand the global behavior and why the Gyroid minimal surface exhibits significantly lower curvature fluctuation compared to the amorphous Diamond surface, let us consider Figure 4.3.9. In this picture, the curvature distribution of the Gyroid is compared to an amorphous Diamond minimal surface sample with  $\chi = -2000$ . For this purpose, the normalized curvatures on the  $x$ -axis are split into ‘‘buckets’’. For each triangle, the normalized Gaussian curvature is then calculated and the normalized surface area is added to said bucket. We choose the normalization in such a way that the average Gaussian curvature  $\langle K \rangle$ , i.e. the sum over all products of  $x$ - and  $y$ -values divided by the total surface area, is  $(-1)$ . The Gaussian curvature density function is  $\rho(K) = \int_{\mathcal{M}} \delta(K - K(p)) dA$  with  $\delta$  the delta distribution;  $\rho(K) dK$  is the total surface area of the patches in the surface with Gaussian curvature between  $K$  and  $(K+dK)$ . The density function for a surface whose length scale is normalized to  $\langle K \rangle = -1$  is given by  $|\langle K \rangle| \cdot \rho(K/|\langle K \rangle|)$ .

We demonstrate that the discretizations of the surfaces are sufficient for obtaining accurate

| Name  | $\phi$ | $-\chi$ | $(\Delta K/\Gamma^2)^2$ | $\beta_1^{0,2}$ | $l_e$             | $N_t/(-\chi)$ | $W/(-\chi)$       |
|---|--------|---------|-------------------------|-----------------|-------------------|---------------|-------------------|
| Amorphous Diamond Surfaces  |        |         |                         |                 |                   |               |                   |
| aD(30)  | 0.4880 | 432     | 0.5093                  | 0.9766          | 0.0511 ... 0.1911 | 1147          | $5 \cdot 10^{-4}$ |
| aD(50) <sub>a</sub>   | 0.4818 | 2000    | 0.4730                  | 0.9529          | 0.0932 ... 0.3546 | 536           | $5 \cdot 10^{-4}$ |
| aD(50) <sub>b</sub>   | 0.4865 | 2000    | 0.4512                  | 0.9754          | 0.0993 ... 0.2988 | 754           | $5 \cdot 10^{-4}$ |
| aD(80) <sub>a</sub>   | 0.4766 | 8142    | 0.4298                  | 0.9903          | 0.1032 ... 0.4711 | 356           | $5 \cdot 10^{-4}$ |
| aD(80) <sub>b</sub>   | 0.4855 | 8142    | 0.4029                  | 0.9864          | 0.1270 ... 0.4591 | 315           | $5 \cdot 10^{-4}$ |
| Surfaces with cubic symmetry                                      |        |         |                         |                 |                   |               |                   |
| P,D,G   | 0.5    | 4       | 0.2188                  | 1               | .                 | .             | 0                 |
| C(Y)  | 0.5    | 24      | 0.5379                  | 1               | 0.0335 ... 0.2803 | 6432          | $10^{-4}$         |
| S   | 0.5    | 20      | 0.3878                  | 1               | 0.0489 ... 0.1736 | 7691          | $10^{-4}$         |
| IW-P  | 0.4635 | 12      | 0.4831                  | 1               | 0.0019 ... 0.1018 | 3125          | $10^{-4}$         |
| Most uniform member of surface families with hexagonal symmetry   |        |         |                         |                 |                   |               |                   |
| L(1.684)  | 0.4830 | 8       | 0.2795                  | 0.9075          | 0.0147 ... 0.0718 | 10632         | $10^{-5}$         |
| H(0.431)  | 0.5    | 4       | 0.3284                  | 0.8213          | 0.0119 ... 0.1216 | 12013         | $10^{-5}$         |
| Most isotropic member of surface families with hexagonal symmetry |        |         |                         |                 |                   |               |                   |
| L(1.647)  | 0.4894 | 8       | 0.3133                  | 0.9948          | 0.0168 ... 0.0782 | 10644         | $10^{-5}$         |
| H(0.416)  | 0.5    | 4       | 0.3561                  | 1               | 0.0096 ... 0.1192 | 12288         | $10^{-5}$         |

**Table 4.3.8:** We lay out invariants corresponding to several minimal surfaces ranging from the amorphous Diamond samples to the cubic Primitive, Diamond, Gyroid, the Fisher-Koch C(Y) and S, the IW-P, the hexagonal Diamond **L** and the hexagonal **H** family. After normalizing all surfaces so that  $\langle K \rangle = -1$ , we compute their curvature fluctuation  $(\Delta K/\Gamma^2)^2$ , their isotropy index  $\beta_1^{0,2}$  and volume fraction  $\phi$ . The value  $l_e$  is the average edge length of the triangles used in the discretization of the surface.  $N_t$  denotes the total number of triangles. The value  $W$  is the Willmore energy of the surface mesh in its final converged state.

curvature results by visualizing the curvature distributions for both, the analytic Weierstrass-Enneper parametrization of TPMS (cf. Section 4.1.2) and the corresponding numerical approximation. Recall that the Weierstrass formalism parametrizes minimal surfaces as maps from the complex Riemann plane to  $\mathbb{R}^3$ . The explicit formulae for Gauss curvature

$$K = -4(1 + |w|^2)^{-4} \cdot |R(w; w_n)|^2$$

and area element

$$dA = (1 + |w|^2)^2 \cdot |R(w; w_n)|^2 dx dy$$

for  $w \in \mathcal{D} \subset \mathbb{C} \cup \{\infty\}$  and a fixed flat point  $w_n \in \mathcal{D}$  enable the calculation of means, variances, and distributions for the surface families **tD**, **tP**, **tG**, **rG**, **rPD** and **H**. The corresponding Weierstrass functions  $R$  and asymmetric domain patches are given in Fogden and Hyde [117].

For the cubic Gyroid, the distribution is finite between 0 (corresponding to symmetry point \*6) and  $K/|\langle K \rangle| = -1.72$  (corresponding to symmetry point \*4) where the distribution sharply

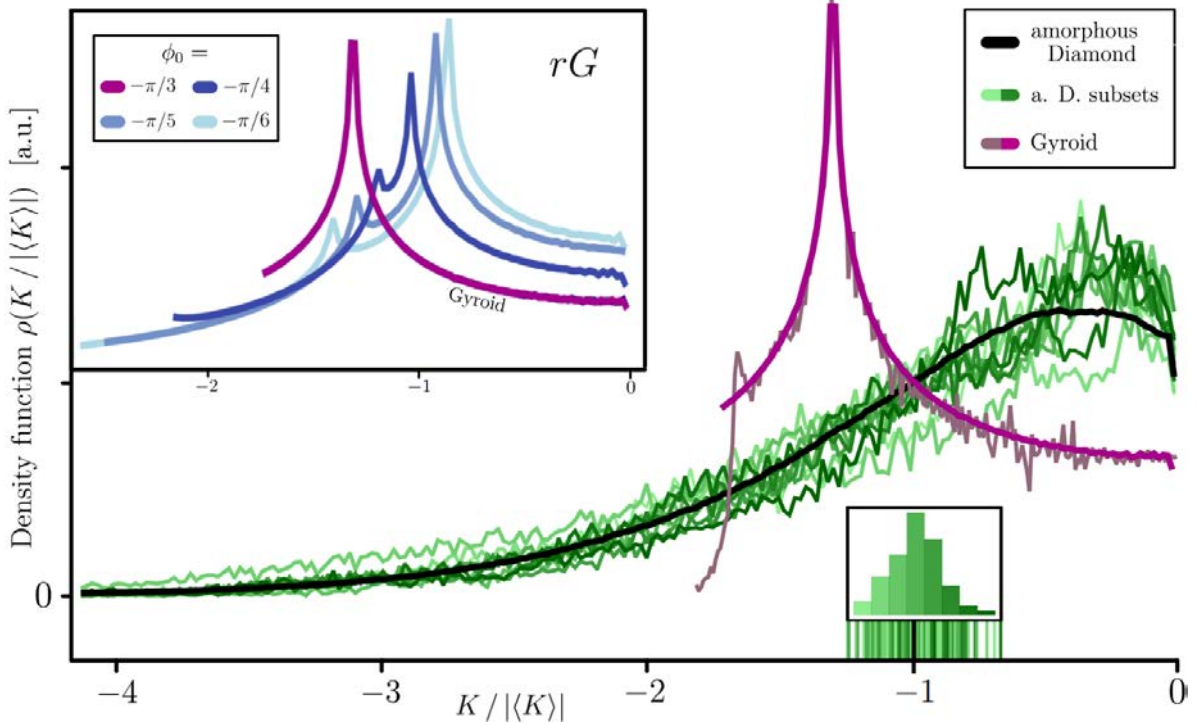


**Figure 4.3.9: Curvature distributions of an amorphous Diamond surface next to Gyroid deformation families:** Slicing an amorphous Diamond surface into cubes that on average contain the same genus as the cubic Gyroid enables us to compare their respective curvature distributions. After normalizing their Gaussian curvature with respect to the entire amorphous Diamond, 10 representative distributions (green) are depicted alongside a scatter and histogram plot of their mean (l.). It is compared to curvature distribution inferred from the Gyroid's Weierstrass representation (purple) and numerically optimized Gyroid (light purple). To assess these results, we analytically calculate the curvature distributions of several samples from the rhombohedral Gyroid family **rG** (l.).

drops to 0. The maximum at  $K/|\langle K \rangle| = -1.30$  corresponds to the symmetry point \*2. These symbols arise from the Conway orbifold notation [85] for the tiling \*246 of the hyperbolic plane  $\mathbb{H}^2$ . This tiling generates a minimal surface patch of the Gyroid using a particular crystallographic space group. It is later depicted in Figure 5.1.2. For additional details, we refer to Section 5.1.

Notably, the Bonnet transformation provides an isometry between the cubic Primitive, Diamond and Gyroid minimal surfaces [212], so it suffices to only consider one of these surfaces here. The other surfaces have the same local geometric properties. We also depict an insert in Figure 4.3.9 that shows how the curvature distributions change when members of the **rG** surface with rhombohedral symmetry are considered. This deformation family contains the cubic Gyroid as the member with  $\phi_0 = -\pi/3$ . For all members of the **rG** family, the distribution ranges from 0 to a minimum of  $K/|\langle K \rangle| = -2.58$ , corresponding to symmetry point \*4, where the value sharply drops to zero.

The Gaussian curvature distribution of the amorphous Diamond surface analyzed over the  $\chi = -2000$  sample approximates a smooth function with a tail that has largely decayed to zero

for  $K/|\langle K \rangle| = -4$ . In comparison with the Gyroid's sharp peak, the curve corresponding to the amorphous Diamond surface has a relatively broad and smooth maximum. The maximal value of the distribution at  $K/|\langle K \rangle| \approx -0.45$  is greater than the mean Gaussian curvature value of  $-1$ , different from the cubic Gyroid surface. The ratio  $\theta = \int_{-1}^0 \rho(K/|\langle K \rangle|) dK$  of the area of surface patches with  $K/|\langle K \rangle| \in [-1, 0]$  divided by the total surface area is lower for the cubic Gyroid ( $\theta = 43.2\%$ ) than for all other surfaces, including the amorphous Diamond ( $\theta = 60.1\%$ ).

To discern inherent local curvature fluctuations and variations on larger scales, an amorphous Diamond surface is subdivided into a grid of equal-sized cubical domains such that the average Euler characteristic of each subsample is  $\chi = -8$ . Gaussian curvature distribution functions evaluated for individual domains fluctuate around the distribution for the whole surface and show no indications of sharp peaks. For instance, this leads to the subdivision of the  $\chi = -2000$  amorphous Diamond into 216 cubes. Analogous to the Gyroid, the entire surface is scaled so that  $\langle K \rangle = -1$ . This ensures the comparability of all structures. Since this procedure scales the subsamples with respect to the entire amorphous Diamond, their mean Gaussian curvature is generally not  $(-1)$ . All average Gaussian curvatures and the corresponding histogram of these subsamples are depicted in the picture's bottom right.

A one-way analysis of variances (ANOVA) of this particular amorphous Diamond surface confirms the absence of substantial large-scale curvature variations. With  $\langle K \rangle_i$  the average of Gaussian curvature within the cubical cell  $i$ , the *within-cell* variance for cell  $i$  is given by  $\sigma_w = \langle (K - \langle K \rangle_i)^2 \rangle_i = 0.3834$ . The distribution of  $\langle K \rangle_i$  is shown in the lower insert in Figure 4.3.9. With  $\langle K \rangle$ , which is equal to  $\sum_i \frac{A_i}{A} \cdot \langle K \rangle_i$  where  $A_i$  the area within the cubical cell labeled  $i$ , the *between-cells* variance is  $\sigma_b = \sum_i \frac{A_i}{A} \cdot (\langle K \rangle_i - \langle K \rangle)^2 = 0.0116$ . The fact that  $F = \sigma_b/\sigma_w = 0.0303 \ll 1$  demonstrates that the inherent Gaussian curvature variations within each cell are far greater than the larger-scale variations of Gaussian curvature averages between cells.

All of these observations explain why the Gyroid has such a low curvature fluctuation. Most of the surface patches have a Gaussian curvature close to the mean value of  $(-1)$ . In addition, the Gyroid combines a narrow curvature distribution that sharply drops to zero with a small percentage of the surface area associated with flat points. In this way, the Gyroid minimal surface manages to minimize its in-cell variance. Due to its high symmetry, the between-cell variance is additionally zero. Since curvature heterogeneity corresponds to a frustration of the surface [156, 168], the investigation from this chapter provides insights into why the Gyroid appears in so many organic systems: This minimal surface manages to avoid high curvatures and manages to accumulate most of the necessary curvature around a single value.

### 4.3.3 Construction of Minimal Surfaces by Repulsive Catenoidal Necks

The previous section demonstrated that by fixing the topology of a regular net and locally deforming it to create disorder, we can generate amorphous minimal surfaces. For our second method of generating disordered minimal surfaces, we relax the strong assumptions on the surfaces' topology to sample a larger portion of the space of TPMS. The first part of Section 4.2.3 discusses an approach for finding suitable initial configurations for the Primitive, Diamond and Gyroid minimal surface, on which to run a curvature optimization routine (e.g. Section 4.3.1). In

the article underlying that example, Chen [71] suggests placing  $2k$  parallel planes into the 3-torus  $T^3 = \mathbb{R}^3/\Lambda$  for some full-dimensional lattice  $\Lambda$  and connecting alternating layers by discretized, square, catenoidal necks (cf. Section 4.2.3). To obtain a minimal surface, these necks need to be balanced [317]. Hence, this problem can be viewed in terms of minimally energetic point configurations on the parallel planes, where each point represents one of the catenoids' centers. Since a triply periodic minimal surface separates the 3-torus into two disconnected labyrinths, the points are separated into two sets of the same size. To find minimally fluctuant minimal surfaces (see Section 4.2), it is assumed that the catenoidal necks are evenly spaced out, corresponding to applying a purely repulsive potential to the points and subsequently minimizing energy.

Afterward, we place catenoidal necks attached to parallel planes with the previously generated repulsive point cloud located in the center. These catenoids connect points of the same color. With this procedure, we generate an initial configuration that a curvature optimization software as in Section 4.3.1 can be applied to obtain a minimal surface from the polyhedral initial configuration. The three steps of generating such a minimal surface are depicted in Figure 4.3.10.

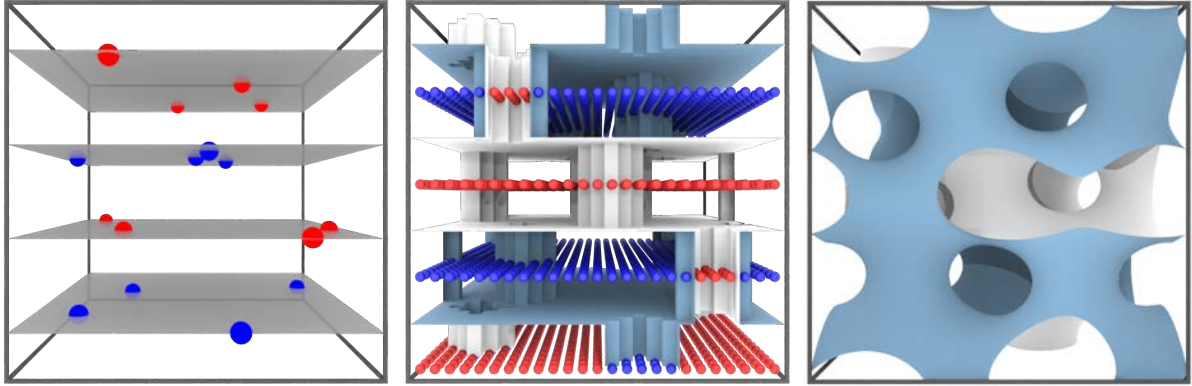


**Figure 4.3.10: Generating triply periodic minimal surfaces from repulsive point potentials:**

By placing points on alternately-colored parallel planes in the 3-torus equipped with a repulsive point potential (l.), the catenoidal necks connecting the two labyrinths in bicontinuous minimal surfaces can be modeled (c.). Using **Pomelo**, a tool for computing Voronoi set diagrams, the bilayer separating the two differently-colored labyrinths are computed. This polyhedral surface can in turn be used as initialization for the **Surface Evolver**, which in tandem with minimizing the energy functional  $E_\alpha(\mathcal{M})$  leads to a minimal surface (r.).

To formalize this concept, assume  $\ell \in 2\mathbb{N}$  denotes the number of layers and  $N$  denotes the number of points per layer. Therefore, we are given  $\ell N$  points in the 3-torus  $T^3 = \mathbb{R}^3/\Lambda$  for a cuboidal lattice  $\Lambda = \langle e_1, e_2, e_3 \rangle$ . An exemplary configuration is depicted in Figure 4.3.10(l.). Chen [71] argues that a cubical lattice is not ideal for the Diamond and Gyroid. Nevertheless, both surfaces have cubic symmetry. Restricting  $\Lambda$  to the lattice given by the standard unit basis simplifies our initial computations. The search space is not prohibitively restricted by this assumption.

#### 4.3.3.1 Distance Functions on the Flat Torus

In this section, we mathematically describe distance functions in a flat torus  $T^3 = \mathbb{R}^3/\Lambda$ . That is, we consider conventional distance functions between two points in  $\mathbb{R}^3$  while taking into account the periodic boundary conditions dictated by the lattice  $\Lambda$ .

Any distance function  $d : T^3 \times T^3 \rightarrow \mathbb{R}$  needs to be compatible with the group action of  $\Lambda$ , implying that

$$d(x, y) = d(x + \lambda_1, y + \lambda_2) \quad \text{for any } \lambda_1, \lambda_2 \in \Lambda \text{ and } x, y \in T^3.$$

This property is not satisfied for common, nontrivial distance functions in  $\mathbb{R}^n$ , such as the Euclidean distance. Nonetheless, there is a natural way to restrict distance functions in  $\mathbb{R}^n$  to the  $n$ -torus, respecting the group action of  $\Lambda$ : Given any translation-invariant distance function  $d_{\mathbb{R}^n}$  on  $\mathbb{R}^n$ , meaning that  $d_{\mathbb{R}^n}(x + \lambda, y + \lambda) = d_{\mathbb{R}^n}(x, y)$  for all  $x, y, \lambda \in \mathbb{R}^n$ , we define

$$d_{T^n}(x, y) = \inf_{\lambda \in \Lambda} d_{\mathbb{R}^n}(x, y + \lambda). \quad (4.3.11)$$

**Lemma 4.3.12.**  *$d_{T^n} : T^n \times T^n \rightarrow \mathbb{R}$  defines a distance function on the  $n$ -torus  $T^n = \mathbb{R}^n / \Lambda$  for a full-dimensional lattice  $\Lambda \subset \mathbb{R}^n$  generated by mutually orthogonal vectors.*

*Proof.* To see that Equation (4.3.11) indeed defines a distance on  $T^n$  requires checking if all axioms are satisfied. While positive definiteness follows immediately from the fact that  $d_{\mathbb{R}^n}$  is a distance function, proving symmetry and the triangle inequality requires more consideration.

To show that the function is symmetric, take any  $x, y \in T^n$ . By the symmetry and translation-invariance of  $d_{\mathbb{R}^n}$ , the invariant group action of  $\Lambda$  on  $T^n$  and the fact that the lattice  $\Lambda$  is a group, we find that

$$\begin{aligned} d_{T^n}(x, y) &= \inf_{\lambda \in \Lambda} d_{\mathbb{R}^n}(x, y + \lambda) = \inf_{\lambda \in \Lambda} d_{\mathbb{R}^n}(x - \lambda, y) \\ &= \inf_{\lambda \in \Lambda} d_{\mathbb{R}^n}(y, x - \lambda) = \inf_{\lambda \in \Lambda} d_{\mathbb{R}^n}(y, x + \lambda) \\ &= d_{T^n}(y, x), \end{aligned}$$

proving the symmetry axiom.

Take any  $x, y, z \in T^n$ . After applying rigid motion transformations, the lattice  $\Lambda$  can be expressed as  $\Lambda = \langle \lambda_1 \cdot e_1, \dots, \lambda_n \cdot e_n \rangle$  for  $\lambda_i \in \mathbb{R} \setminus \{0\}$  and the unit normal basis  $(e_i)_{i=1}^n$  of  $\mathbb{R}^n$ . Since the metric is translation-invariant by assumption, we can without loss of generality assume that  $x = (\lambda_1/2, \dots, \lambda_n/2)$ , the midpoint of the translational unit cuboid  $\text{Conv}(0, \lambda_1 \cdot e_1, \dots, \lambda_n \cdot e_n)$ . This simplifies the computations significantly because then  $\inf_{\lambda \in \Lambda} d_{\mathbb{R}^n}(x, y + \lambda)$  is always attained in  $\lambda = 0$  for any  $y \in T^n$ . Therefore,

$$\begin{aligned} d_{T^n}(y, z) &= \inf_{\lambda \in \Lambda} d_{\mathbb{R}^n}(y, z + \lambda) \leq \inf_{\lambda \in \Lambda} d_{\mathbb{R}^n}((\lambda_1/2, \dots, \lambda_n/2), y) + d_{\mathbb{R}^n}((\lambda_1/2, \dots, \lambda_n/2), z + \lambda) \\ &= d_{\mathbb{R}^n}((\lambda_1/2, \dots, \lambda_n/2), y) + \inf_{\lambda \in \Lambda} d_{\mathbb{R}^n}((\lambda_1/2, \dots, \lambda_n/2), z + \lambda) \\ &= \inf_{\lambda \in \Lambda} d_{\mathbb{R}^n}((\lambda_1/2, \dots, \lambda_n/2), y + \lambda) + \inf_{\lambda \in \Lambda} d_{\mathbb{R}^n}((\lambda_1/2, \dots, \lambda_n/2), z + \lambda) \\ &= d_{T^n}(x, y) + d_{T^n}(x, z) \end{aligned}$$

because the infimum is a monotonic function and  $d_{\mathbb{R}^n}$  satisfies the triangle inequality. This proves that  $d_{T^n}$  also satisfies the triangle inequality, completing the proof.  $\square$

It is computationally infeasible to calculate the distance in  $\mathbb{R}^n$  for every grid point  $\lambda \in \Lambda$ ,

as there are infinitely many. Conveniently, this is not necessary, since the smallest distance is always attained in the vicinity of  $T^n$ .

**Lemma 4.3.13.** *Suppose we are given a distance function  $d$  on  $\mathbb{R}^n$  induced by an  $L^p$ -norm with  $p \geq 1$ . It induces a distance function  $d_{T^n}$  on the cubic  $n$ -torus  $T^n = \mathbb{R}^n / \mathbb{Z}^n$ . Denote the family of translations in  $\Lambda$  corresponding to the torus  $T^n$  by*

$$\mathcal{A}(T^n) = \left\{ \sum_{i=1}^n \delta_i e_i : \delta_i \in \left[ -C \cdot n^{1/p}, C \cdot n^{1/p} \right] \cap \mathbb{Z} \right\} \subset \Lambda \quad \text{with } C = \frac{1}{2} + \frac{1}{n^{1/p}}.$$

Then, we can restrict the distance function to  $\mathcal{A}(T^n)$ :

$$d_{T^n}(x, y) = \min_{\lambda \in \mathcal{A}(T^n)} d(x, y + \lambda).$$

*Proof.* Clearly, the distance  $d(x, y) = \|x - y\|_p$  induced by the  $L^p$  norm  $\|x\|_p = (\sum_{i=1}^n |x_i|^p)^{1/p}$  for  $x \in \mathbb{R}^n$  is translation-invariant for any  $p \geq 1$ , making it a well-defined distance function on  $T^n$  by Lemma 4.3.12. By the translation-invariance of  $d_{T^n}$ , we can pick  $x^* = (1/2, \dots, 1/2)$  as one of the two points passed to the distance function. Any point  $y$  in  $T^n$  is at most  $\|x^*\|_p$  away from  $x^*$ , implying that  $d_{T^n}(x, y) \leq \|x^*\|_p = \frac{n^{1/p}}{2}$  for all  $x, y \in T^n$ . In particular, the floor function has the property that

$$\lfloor C \cdot n^{1/p} \rfloor - \frac{n^{1/p}}{2} > C \cdot n^{1/p} - 1 - \frac{n^{1/p}}{2} = 0.$$

When applying this observation to the distance from  $[0, 1]^n$  to the boundary of  $\mathcal{A}(T^n)$  and the torus-distance from the mid-point  $x^*$  to any point  $y \in T^n$ , we find that  $\max_{x, y \in T^n} d_{T^n}(x, y) < \min_{z \in \partial(\mathcal{A}(T^n))} d(z, [0, 1]^n)$ . Moreover, the  $L^p$  distances  $d(x, x + tv)$  are monotonously increasing along the rays  $tv$  for  $t \geq 0$  and  $v \in \mathbb{R}^n \setminus \{0\}$ , implying that the distance minimum is attained in the interior of  $\mathcal{A}(T^n)$ .  $\square$

#### 4.3.3.2 Minimally Energetic Point Clouds on the Torus

Having identified a class of suitable distance functions on the  $n$ -torus enables us to properly set up the problem that we intend to solve. Namely, our goal is to evenly distribute point clouds on parallel layers in  $T^3$ . As measures for the uniformity, consider the Euclidean distance  $d^{(e)}$  and the Manhattan distance  $d^{(m)}$  on  $\mathbb{R}^3$ . By Equation (4.3.11), both give rise to distance functions  $(d^{(e)})_{T^3}$  and  $(d^{(m)})_{T^3}$  on the flat 3-torus  $T^3 = \mathbb{R}^3 / \mathbb{Z}^3$ . Taking the reciprocal of these distance functions yields the purely repulsive *Riesz energy* [52]. We can combine the Manhattan and Euclidean distance into a single energy functional by summing two Riesz energy terms:

$$q_c(x, y) = \frac{1}{(d^{(e)})_{T^3}(x, y)} + \frac{c}{(d^{(m)})_{T^3}(x, y)}$$

for a penalty term  $c \geq 0$ . Even though the potential  $q_c$  is purely repulsive,  $T^3$  is compact. The Extreme Value Theorem guarantees that the energy functional attains its infimum since  $q_c$  is bounded below. It is a natural question to ask, whether all distances between points in the 3-torus should be simultaneously considered, or if only subsets of the points should be taken

into account. This consideration results in three distinct potentials, which we refer to as 3D, 2D, and 2D-3.

**Energy model 3D:** While the points are fixed to parallel planes in  $T^3$ , the model 3D assumes that every single point interaction contributes to the energy functional. This yields the objective function

$$Q_{3D} = \sum_{i \neq j} q_c(p_i, p_j).$$

An exemplary configuration obtained by the potential  $Q_{3D}$  is depicted in Figure 4.3.14(l.) as a projection to the plane  $z = 0$ .

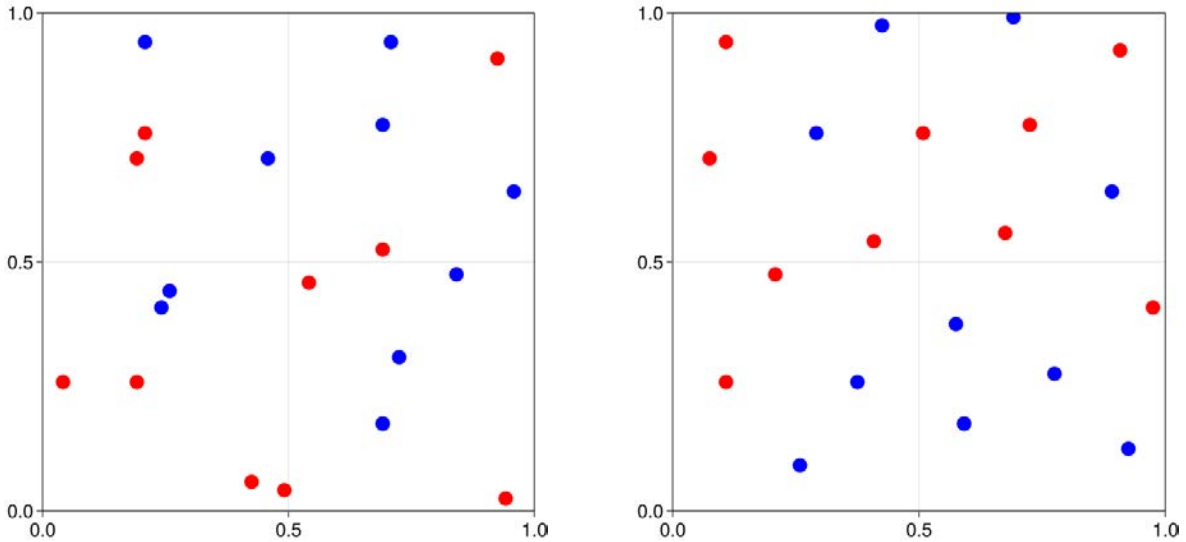


**Figure 4.3.14:** An energy minimum of the objective functions  $Q_{3D}$  (l.) and  $Q_{2D}$  (r.) for  $N = 5$  and  $\ell = 4$ . The points are colored with respect to their layers and are projected via  $\pi : T^3 \rightarrow T^2$  to the plane with  $z = 0$ . On the one hand,  $Q_{3D}$  offers little structure to the configuration, making it unsuitable. On the other hand,  $Q_{2D}$  produces a regular and structured picture in  $T^2$ , though it is too restrictive when lifted to  $T^3$ . An intermediate energy function unifies both approaches.

**Energy model 2D:** This model builds on the belief that since the points are restricted to planes, only planar interactions should be taken into account. Therefore, we project all points to the same plane via  $\pi : T^3 \rightarrow T^2$ , where the relevant distances are calculated. We can express the corresponding energy functional as

$$Q_{2D} = \sum_{i \neq j} q_c(\pi(p_i), \pi(p_j)).$$

An exemplary configuration obtained by this potential is depicted in Figure 4.3.14(r.) as a projection to the plane  $z = 0$ .

**Energy model 2D-3:** The catenoidal necks are placed between adjacent layers, so any given catenoid can only interact with catenoids from the layer below and above it. Translated to the language we use here, each point only interacts with points from adjacent layers. The interactions are then, analogous to the previous model, only considered in a single plane. To simplify the notation, we relabel the points as  $p_{i,j}$  for the point  $i$  in layer  $j$ , leading to

$$Q_{2D-3} = \sum_{j=1}^{\ell} \sum_{m=j-1}^{j+1} \sum_{i=1}^N \sum_{k=i+1}^N q_c(\pi(p_{i,j}), \pi(p_{k,m}))$$

with  $p_{i,0} = p_{i,\ell}$  and  $p_{i,\ell+1} = p_{i,1}$  by the translational group action on  $T^3$ . Again,  $\pi : T^3 \rightarrow T^2$  denotes the projection onto the same plane by removing the last coordinate. A configuration obtained by this repulsive potential is depicted in Figure 4.3.15.

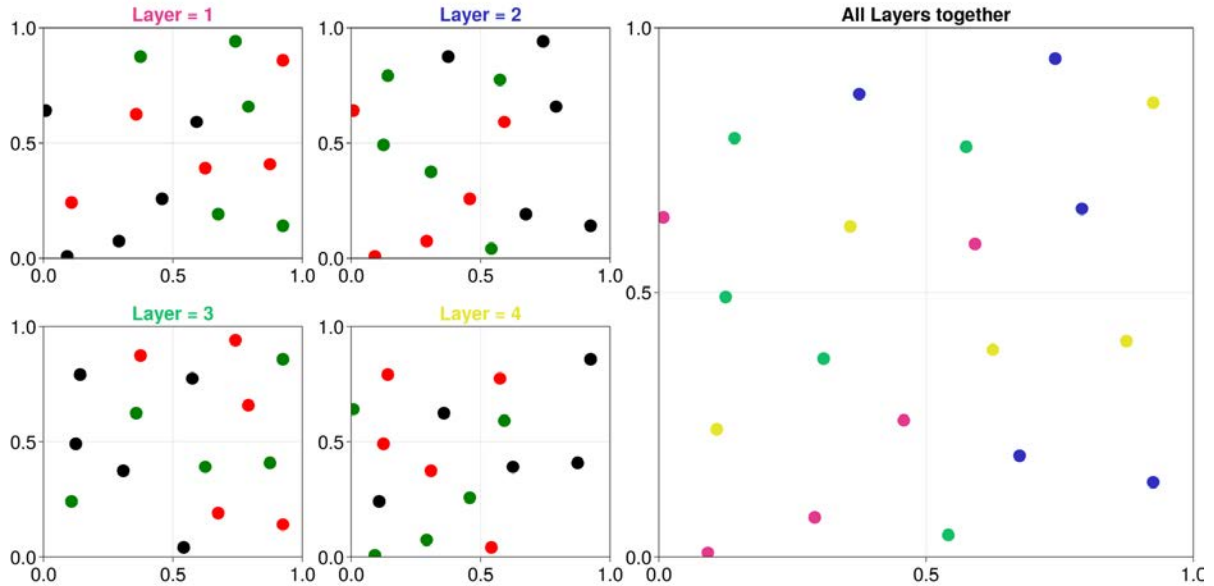


**Figure 4.3.15:** An energy minimum of the objective function  $Q_{2D-3}$  with  $N = 5$  and  $\ell = 4$ . On the left side of the figure, the individual layers with corresponding adjacent layers are depicted, with points in the layer colored black, points above the layer colored green, and points below the layer colored red. On the picture's right side, the points from all layers are combined, using the projection  $\pi : T^3 \rightarrow T^2$ .

To guarantee convergence, for most iterations the binary point potential  $q_c$  only uses the Euclidean distance ( $c = 0$ ). However, for the last 10% of iterations, the truncated Manhattan distance is activated ( $c \gg 0$ ), heavily penalizing when two points become closer than twice the catenoids' preimposed radius. This last step is supposed to guarantee that the catenoids do not intersect. Subsequently, a Monte Carlo approach is used to minimize the energy  $Q_{2D-3}$ . The complete procedure for generating disordered point clouds on parallel layers in  $T^3$  is summarized in pseudocode in Algorithm 4.3.16 and is implemented by the Julia package `DisorderedPointClusters.jl`<sup>19</sup>. To ensure degenerate local minima are avoided, it is recommended to run the code several times for obtaining a single configuration.

---

<sup>19</sup><https://github.com/matthiashimmelmann/DisorderedPointClusters.jl>

---

**Algorithm 4.3.16:** Disordered Point Clusters

---

**Inputs :** The number of necks per layer  $N \in \mathbb{N}$ , the amount of layers  $\ell \in 2\mathbb{N}$ , the radius of the catenoidal necks  $r > 0$  and the fineness of the grid  $\delta$ , amount of iterations  $m$ .

**Output:** A local minimum of the energy functional  $Q_{2D-3}$  on the grid, labeled by color.

Set up  $\ell$  parallel layers  $1/\ell$  apart in  $T^3$ . For each layer, place  $1/\delta^2$  equidistant grid points. Randomly place  $N$  points per layer, marked by opposite colors. If a point agrees with a point in an adjacent layer, reject the sample. Save the points and their labels inside  $p$ .

```
for  $j \in \{1, \dots, m\}$  do
    Select  $d \in \{0, \pm 1\}^{2 \cdot \#p}$  randomly.
    if  $Q_{2D-3}(p + d) < Q_{2D-3}(p)$  then
        |  $p \leftarrow p + d$ 
    end
end
```

$\forall i \in \{1, \dots, \ell N\}$  : Label points  $z$  in the same layer as  $p_i$  with  $d_m(p_i, z) < r$  identically to  $p_i$ .

---

For determining the radius  $r > 0$  required as input for Algorithm 4.3.16, we take inspiration from the tetragonal **tP** surface family that can be described via square catenoids [72]. This deformation family is parametrized by the ratio of the square catenoid's side length and its height. The minimal curvature fluctuation in the **tP** family is attained at the Primitive surface [283]. A priori, the number of layers Algorithm 4.3.16 uses is fixed and the only free parameter is the radius of the catenoids. Choosing it to match the radius of the Primitive's square catenoid promises to aid in the curvature minimization routine. In particular, the ratio between catenoid height and width is 1 for the Schwarz Primitive surface, indicating that we should choose  $r = \frac{1}{2\ell}$ .

#### 4.3.3.3 Voronoi-Based Polyhedral Interface Between Two Networks

The previous section presents ways to induce an energy functional on point clusters in order to find minimally energetic point configurations. What remains is to partition these points into two labyrinths, so that the separating surface acts as an input for **Surface Evolver**.

The points have already been marked with two colors, dependent on which labyrinth they belong to, and are organized in lattices covering each plane in the 3-torus. Consequently, there is a natural way to assign the points to labyrinths: Whenever two points are neighbors of different colors, they should be separated by the surface, while neighbors of the same color should lie in the same labyrinth. The following definition of a Voronoi diagram from Cifuentes et al. [78] formalizes this notion.

**Definition 4.3.17.** Let  $X$  denote a metric space, let  $\mathcal{S} \subset X$  be a set and let  $d : X \times X \rightarrow \mathbb{R}$  denote a distance function on  $X$ . The *Voronoi cell* of  $x \in \mathcal{S}$  is defined as

$$\text{Vor}_x(\mathcal{S}) = \{y \in X : d(x, y) \leq d(x', y) \text{ for all } x' \in \mathcal{S}\}.$$

The *Voronoi diagram* is then simply the collection of all Voronoi cells, namely

$$\text{Vor}(\mathcal{S}) = \{\text{Vor}_x(\mathcal{S}) : x \in \mathcal{S}\}.$$

Voronoi diagrams classically arise from discrete sets (e.g. Figure 4.3.18(l.)) but they can also be considered on continuous sets, such as smooth manifolds or algebraic varieties. In the latter case, they give rise to the *medial axis*, which is a tool for examining the geometric properties of a surface. It comprises the points in the ambient space that have at least 2 closest points on  $\mathcal{S}$ . If  $X$  carries a differentiable structure and  $\mathcal{S}$  is a submanifold of  $X$ , then the medial axis arises as the intersection of different normal spaces of  $\mathcal{S}$  [165]. Alternatively, it can be approximated by a subset of the Voronoi diagram of finitely many densely sampled points [95].

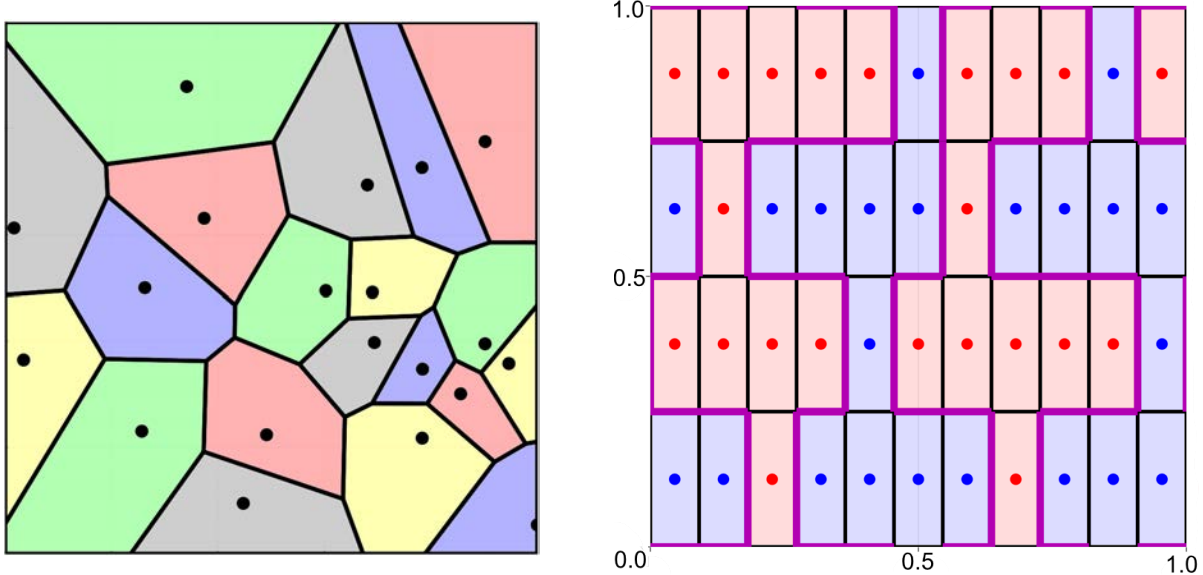


**Figure 4.3.18:** Voronoi diagram of 20 random points confined to the unit square using the Euclidean distance (l.) and segmentation of  $4 \cdot 11$  blue and red points in the 2-torus into two unicolored labyrinths, separated by a purple membrane (r.). By labeling the points, the Voronoi tesselation gains additional information that we use to generate a separating hypersurface.

There is a multitude of algorithms available that are capable of computing Voronoi diagrams. Here, we use the package `Pomelo`<sup>20</sup> (cf. [323]), which implements the algorithm from Schaller et al. [276] for set Voronoi diagrams. It computes generalized Voronoi diagrams that take collections of sets instead of points as the objects around which polyhedra are built.

Recall that our ultimate goal is to separate points of opposite colors into unicolored labyrinths. After having computed the Voronoi diagram, this task becomes rather simple. The Voronoi cells inherit the color of their seeds. Whenever two cells of opposite colors share a facet, that facet is added to the membrane. A 2D sketch of this procedure is depicted in Figure 4.3.18(r.).

Formally, we label each point  $p_1, \dots, p_m \in \mathbb{R}^n$  with  $\ell(p_i) \in \{0, 1\}$ . These labels can be understood as a height function partitioning the points. The collection of labeled Voronoi cells  $\text{Vor}_{p_i}(\{p_1, \dots, p_m\}) \times \{\ell(p_i)\} \subset \mathbb{R}^n \times \{0, 1\}$  that emerges as a disjoint union from the points

<sup>20</sup><https://github.com/spatialfruitsalad/pomelo>

$p_1, \dots, p_m$  is then intersected in the following way to obtain the polyhedral membrane  $\mathcal{M}$ :

$$\mathcal{M} = \pi_{n+1} \left( \bigcup_{i=1}^m \bigcup_{j=i+1}^m (\text{Vor}_{p_i}(\{p_1, \dots, p_m\}) \times \{\ell(p_i)\}) \cap (\text{Vor}_{p_j}(\{p_1, \dots, p_m\}) \times \{1 - \ell(p_j)\}) \right).$$

Here,  $\pi_{n+1}$  is the projection of the first  $n$  coordinates to  $\mathbb{R}^n$  by setting the last coordinate to 0. In other words, the expression inside the unions is nonempty if and only if the Voronoi cells are adjacent and the corresponding labels are different from each other.

This procedure is implemented within **Pomelo**, so no further programming is necessary. Figure 4.3.19 depicts the surface resulting from feeding points generated from the construction procedure for minimally energetic point clouds from Section 4.3.3.2 into the algorithm that is described in this section.

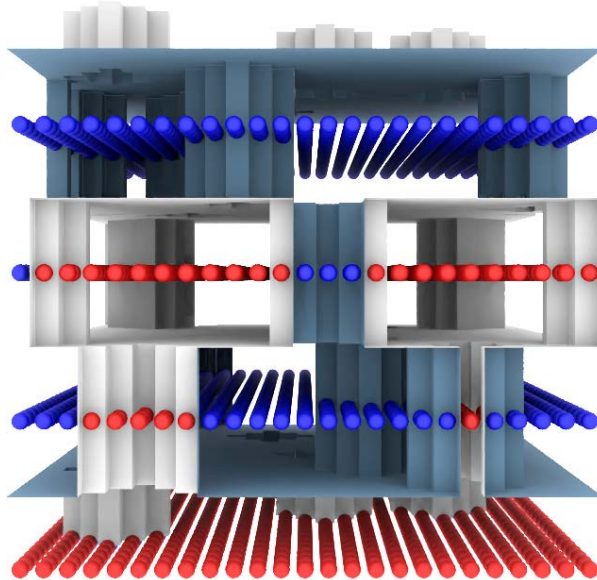


**Figure 4.3.19:** The points generated by Algorithm 4.3.16 are color-coded in blue and red according to the labyrinth they belong to. **Pomelo** separates the points with a polyhedral surface.

#### 4.3.4 Relaxation Algorithm to Enhance Isotropy

The imposed cubic simulation box does not need to be the optimal choice for every minimal surface. In particular, in the tetragonal and rhombohedral deformation families of the Primitive, Diamond and Gyroid surface [72], the unit cell is deformed alongside the surface. The Diamond and the Gyroid minimal surfaces additionally have a rhombohedral minimal translational unit cell, since their symmetry admits an elongated axis. For some surfaces, the isotropy index (cf. Section 4.2.2) deviates from the value 1, which homogeneous minimal surfaces would attain. We call a surface *frustrated*, if their preferred embedding is in a different flat torus, meaning that the curvature fluctuation is not minimized in a cubic simulation box. The majority of the cubic triply periodic minimal surfaces are likely frustrated.

Therefore, we develop an iterative method to transform a frustrated minimal surface into its isotropic variant by deforming the periodic unit cell. In Evans, Schröder-Turk, and Kraynick

[113], the authors consider random monodisperse soap froth in periodic boundary conditions and exposed the unit cell to recurring compression and extension cycles in the hope of finding a structure with improved geometric properties. Inspired by this article, we compute the Minkowski tensor  $W_1^{0,2}$  (cf. Section 4.2.2) and use it to inform the desired unit cell deformation, aiming at minimizing the disparity between the eigenvalues. The corresponding procedure when applied to a frustrated diamond surface from the **tD** family is depicted in Figure 4.3.20.

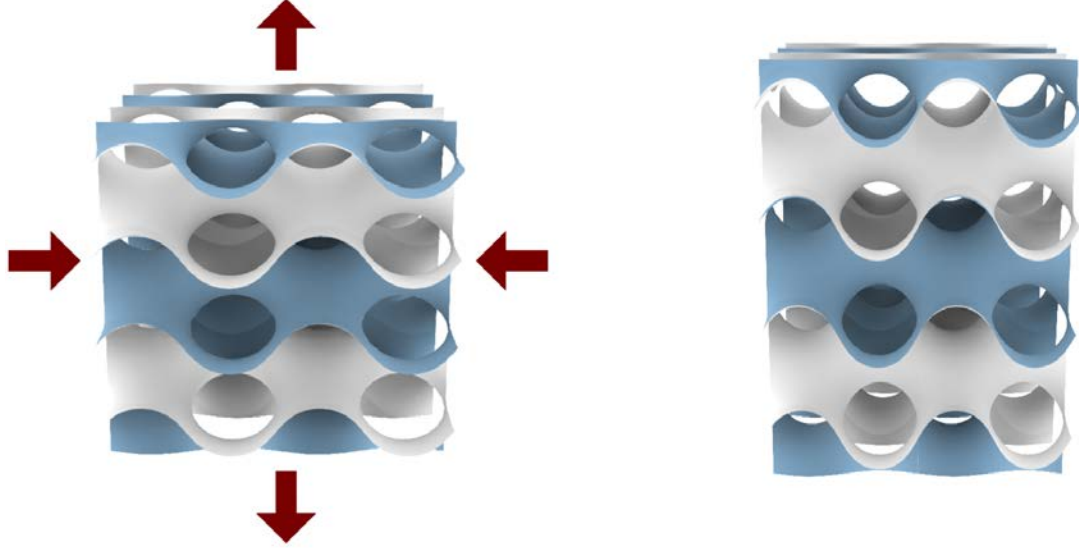


**Figure 4.3.20:** Known as Householder's method, we recursively qr-decompose the Minkowski tensor  $W_1^{0,2}$  into the product of orthogonal matrices  $U$  and a diagonal matrix  $D$ . Afterwards, the unit cell is rotated according to  $U$  and then scaled by  $D^{-1}$ . Finally, the surface is rotated back by multiplying with  $U^{-1}$ .

The symmetric matrix  $W_1^{0,2}$  admits an orthogonal basis of eigenvectors forming a matrix  $O$  with real eigenvalues accumulated in the diagonal matrix  $D$ . Intuitively, our goal is to rotate the periodic unit cell according to the eigenvectors  $O$ , then multiply it by the matrix of eigenvalues  $D$  and rotate the unit cell back to its original position via  $O^{-1}$ . This procedure encompasses stretching and shearing alike and should, in practice, produce a more isotropic surface. However, the surface may not be minimal anymore.

One may wonder, how to robustly compute eigenvectors and eigenvalues. The QR-decomposition [60, §9.5] is a matrix reduction technique that factorizes a real matrix  $A$  into an orthogonal matrix  $Q$  and an upper-triangular matrix  $R$ . If the original matrix is invertible, then this decomposition is unique. When successively applying this decomposition to the upper-triangular matrices  $R$ , we can compute the eigenvalues and eigenvectors via recurrence. If we set  $A_{k+1} = R_k Q_k$  for  $A_k = Q_k R_k$ , then

$$A_{k+1} = R_k Q_k = Q_k^{-1} Q_k R_k Q_k = Q_k^{-1} A_k Q_k = Q_k^T A_k Q_k.$$

As a consequence, all matrices  $A_k$  have the same eigenvalues. Inductively applying the above equation yields

$$A_{k+1} = Q_1^T \dots Q_k^T A Q_k \dots Q_1.$$

After applying Householder's method [60, §9.4], which is a similarity transformation, we can assume that  $A$  is in Hessenberg form. In other words, the matrix is mostly upper-triangular, with additional nonzero entries on the subdiagonal. Crucially, the QR-decomposition produces a sequence of Hessenberg matrices when applied to a Hessenberg matrix [247]. Since a surface is isotropic if and only if all eigenvalues are identical, we can assume, without loss of generality, that at most two eigenvalues are distinct. Otherwise, this procedure converges after a single step. Furthermore,  $A$  is diagonalizable, implying that  $A_k$  converges to the matrix of eigenvalues  $D$  [247]. Therefore, the composite of similarity transforms  $Q_k \dots Q_1$  converges to the matrix of orthogonal eigenvectors  $O$ .

We use the results of the QR-decomposition to make the surface  $\mathcal{M}$  isotropic according to a previous construction. Since  $D$  does not need to have a determinant of 1, we weigh it by  $1/\sqrt[3]{\det(D)}$ , so that the unit cell's volume is preserved. Algorithm 4.3.21 summarizes these ideas.

---

**Algorithm 4.3.21:** Relaxation Algorithm for Enhanced Isotropy

---

**Inputs :** A triply periodic minimal surface  $\mathcal{M}$  in a unit cell  $\mathbb{R}^3/\Lambda$ , tolerance  $\tau > 0$ .

**Output:** An isotropic triply periodic surface  $\mathcal{M}'$  in a unit cell  $\mathcal{R}^3/\Lambda'$ .

```

 $i \leftarrow 0; O \leftarrow \text{id}_3$ 
 $A_i \leftarrow W_1^{0,2}(\mathcal{M}) = 1/3 \int_{\mathcal{M}} \mathbf{n} \otimes \mathbf{n} dA$ 
while  $\sum_{j \neq k} |(A_i)_{jk}| > \tau$  do
     $Q_i, R_i \leftarrow \text{qr}(A_i)$ 
     $A_{i+1} \leftarrow R_i \cdot Q_i$ 
     $i \leftarrow i + 1$ 
     $O \leftarrow Q_i \cdot O$ 
end
 $D \leftarrow A_i / \sqrt[3]{\det(A_i)}$ 
return  $\mathcal{M}' = O^{-1} D O \mathcal{M}$  and  $\Lambda' = O^{-1} D O \Lambda$ 

```

---

### 4.3.5 Superior Uniformity of Bicontinuous Cubic Phases

We have now provided all the necessary ingredients to reliably generate disordered minimal surfaces. We use these results to sample the space of TPMS. The goal is to see if it is possible to improve the curvature fluctuation of the Primitive, Diamond and Gyroid surfaces that are hypothesized to be optimal by Conjecture 4.2.12.

In Section 4.3.1, we propose incorporating a squared Gaussian curvature term into the Willmore functional to prevent topological changes in the surface mesh during the optimization process. This algorithm lets us produce and evaluate five amorphous Diamond minimal surface samples in Section 4.3.2. Although the curvature of these surfaces is lower than some bicontinuous cubic phases, we find that it remains significantly above that of the Primitive, Diamond and Gyroid.

A second model for the construction of disordered minimal surfaces based on repulsive point clouds on parallel planes is introduced in Section 4.3.3. When combined with the relaxation

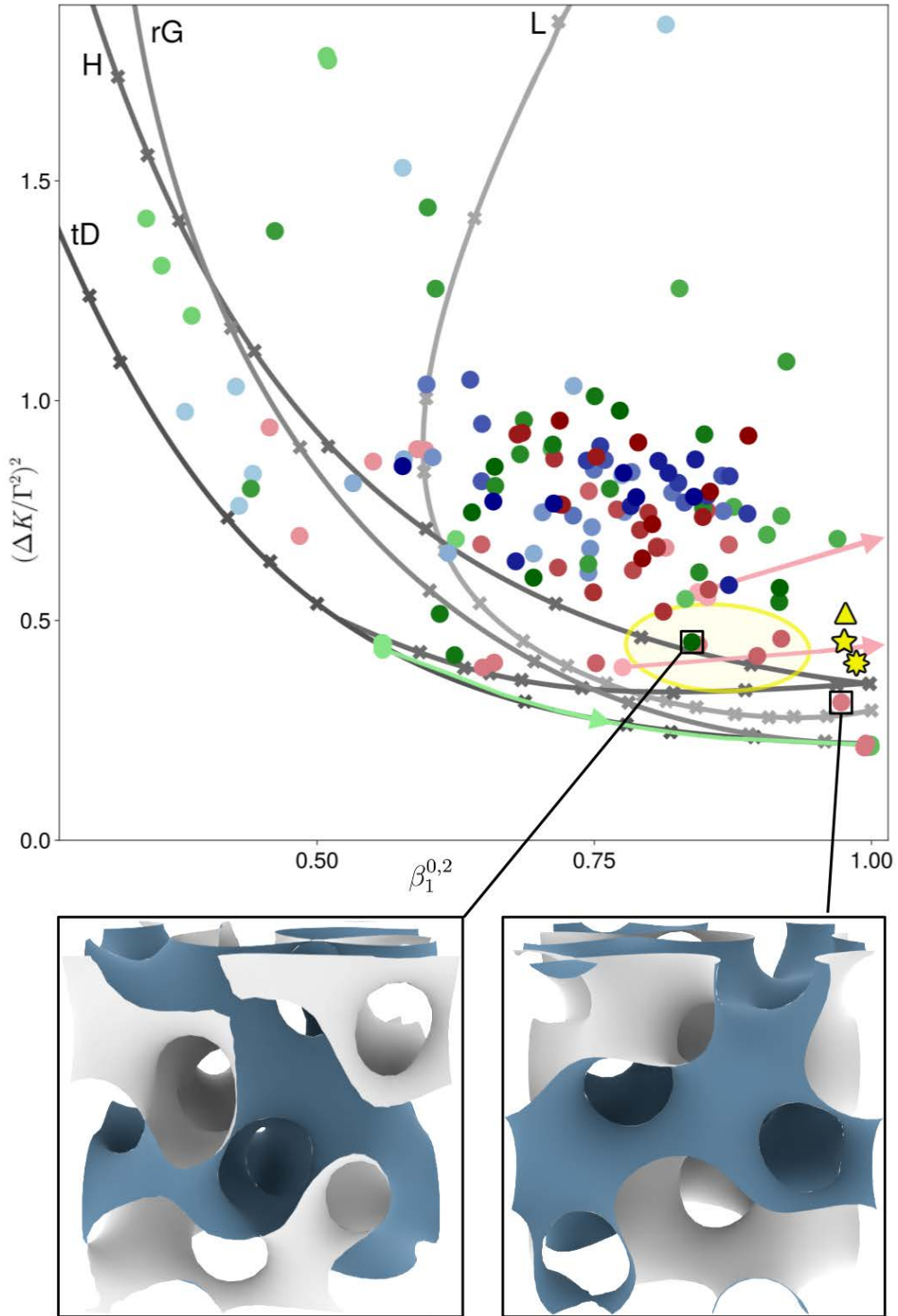


**Figure 4.3.22: Curvature and isotropy of disordered minimal surfaces:** The isotropy index  $\beta_1^{0,2}$  and the curvature fluctuation  $(\Delta K / \Gamma^2)^2$  are depicted for the surfaces generated by a repulsive point potential (cf. Section 4.3.3.2). The data for surfaces with  $\ell = 2$  (shades of green),  $\ell = 4$  (shades of red), and  $\ell = 6$  layers (shades of blue) of parallel planes with catenoidal necks per layer ranging from  $N = 2$  (light color) to  $N = 9$  (dark color) is scattered. In addition, the result of the relaxation algorithm for enhanced isotropy (cf. Algorithm 4.3.21) is graphed for 3 selected minimal surfaces (arrow). The principal component analysis ellipse of the amorphous Diamond surface with three samples (cf. Figure 4.3.9) is included as well.

algorithm for the unit cell described in Section 4.3.4, which enhances the isotropy of the surfaces isotropy, we can add new examples to the comparison.

The algorithm for generating disordered minimal surfaces based on repulsive point clouds in the cubic 3-torus from Section 4.3.3 lets us produce surfaces of various genera. Here, the algorithm is applied to initial configurations with 2, 4, 6 parallel layers and between 2 and 9 necks per layer. As a consequence, we obtain minimal surfaces with an Euler characteristic  $\chi$  between  $-8$  and  $-108$ , given by  $-2 \cdot N \cdot \ell$ , which is  $(-2)$  times the product of the number of layers  $\ell$  and necks per layer  $N$ . This construction generally does not produce symmetric surfaces. Nevertheless, due to the uncontrolled randomness of the process, symmetric structures can and occasionally do occur.

These surfaces accompany the amorphous Diamond minimal surfaces that have already been analyzed in Section 4.3.2. For now, we find that the surfaces generated by the parallel layers approach from Section 4.3.3 are significantly less homogeneous than the amorphous Diamond surfaces, as highlighted in Figure 4.3.22. While some surfaces even outperform the amorphous Diamond minimal surfaces, most samples have an isotropy index  $\beta_1^{0,2}$  below 0.85 and curvature fluctuation  $(\Delta/\Gamma^2)^2$  above 0.6. These numbers are more inhomogeneous than all amorphous Diamond samples included in Figure 4.3.9. Surprisingly, the number of layers does display a significant relevance for the surfaces' homogeneity. This result is promising for the model for minimal surfaces based on parallel layers in the 3-torus.

As we want to obtain isotropic minimal surfaces, we alternate between using the optimization routine from Section 4.3.1 and the relaxation algorithm for enhanced isotropy from Section 4.3.4. Not all of the surfaces that are produced by the minimization of the Willmore energy have the ability to be deformed into an isotropic minimal surface. While the tetragonal and rhombohedral deformation families of the Primitive, Diamond and Gyroid surfaces include an isotropic member, it remains unclear whether more general or disordered surfaces belong to deformation families that contain any isotropic surfaces. For all we know, isotropy might be a special property, connected to surfaces satisfying further assumptions. To illustrate, it seems necessary but not sufficient that the triply periodic minimal surface's labyrinths divide the 3-torus into two equal parts, as is the case in some of the bicontinuous minimal surface examples.

Upon further contemplation of Figure 4.3.22, we realize that the algorithm from Section 4.3.3 for constructing initial configurations based on repulsive point clouds produces some outliers that have comparable and even superior homogeneity to the amorphous Diamond samples. This realization makes us hopeful that tweaking the algorithm for generating disordered point clouds in the 3-torus from Section 4.3.3.2 by adding additional constraints has the potential to generate highly homogeneous amorphous minimal surfaces. This observation is reserved for future work.

#### 4.4 Concluding Remarks

In this chapter, we investigate the occurrence of amorphous minimal surfaces by examining the behavior of their curvature fluctuation and isotropy. This provides novel answers as to both, why amorphous surfaces form in organic settings and why the Primitive, Diamond and Gyroid minimal surfaces are favored in self-assembly processes.

After we introduce the concepts of mean and Gaussian curvature in Section 4.1, we

define minimal surfaces. These provide a meaningful model for lipid membranes in solution by locally minimizing surface area. Hilbert's Embedding Theorem 4.1.20 states that in physically meaningful interfaces without self-intersections, variations in the Gaussian curvature are expected. Investigating various construction methods for minimal surfaces in Section 4.1.2 highlights that triply periodic minimal surfaces typically exist in deformation families.

For self-assembly processes, the surfaces' homogeneity is a relevant factor. Exploring two surface invariants in Section 4.2 enables us to quantify how uniform minimal surfaces can become. First, the curvature fluctuation is a variance measure of the surfaces' Gaussian curvature. We prove that it is a dimensionless number that attains positive values for TPMS. By normalizing the surface so that the average Gaussian curvature is equal to  $(-1)$ , we provide a way to bring different triply periodic minimal surfaces to the same length scale. Second, as a dimensionless number the isotropy index measures how the surface normals are distributed on the unit sphere. Considering Hao Chen's model to generate polyhedral initial configurations and following the application of a minimization scheme for the Willmore energy in **Surface Evolver**, we generate numerical minimal surfaces. It is a common assumption that the Primitive, Diamond and Gyroid are the most homogeneous TPMS.

Even though ordered phases are prevalent, disordered or amorphous phases can form as well. Accordingly, Section 4.3 is concerned with implementing a scheme for the construction of disordered minimal surfaces. To avoid the pinch-off effect that leads to collapsing channels, we present a topology-stabilized optimization algorithm in Section 4.3.1. The objective function in this algorithm generalizes the Willmore energy with the addition of a squared Gaussian curvature term. This enables us to robustly generate numerical minimal surfaces from coarse polyhedral surface meshes. To obtain the initial configurations, we propose two construction methods.

First, the amorphous Diamond network is considered in Section 4.3.2. Tubifying it, leads to an initial configuration that is sufficiently close to minimality. Applying the previously introduced algorithm for robustly generating minimal surfaces thus produces amorphous Diamond minimal surfaces. This represents the first successful construction of these structures. Even though the resulting minimal surfaces are relatively homogeneous, they do not reach as low curvature fluctuations as the Primitive, Diamond and Gyroid. By cutting cubical subsamples from the amorphous Diamond minimal surfaces, we demonstrate that the Gyroid concentrates the necessary curvature variation around a single point. In contrast, the amorphous Diamond minimal surfaces have larger surface patches with both, low and high Gaussian curvature. Even when considering the tetragonal and rhombohedral deformation families of the bicontinuous TPMS, the curvature distributions behave differently. This investigation further reveals that the within-cell variance is larger than the between-cell variance, meaning that the average Gaussian curvature does not significantly vary between the cubical subsamples.

Second, we revisit the method Hao Chen proposes for constructing polyhedral initial meshes for the **Surface Evolver** in Section 4.3.3. After proving the existence of a class of distance functions on the flat torus, we consider repulsive distance-based energies. The use of Monte-Carlo simulations generates minimally energetic point clouds on parallel layers in the 3-torus. Labeling these points depending on the layer and relying on an approach based on Voronoi diagrams, we separate the points into two labyrinths disconnected by a polyhedral interface. This polyhedral

interface functions as an initial configuration that we can run the topology-stabilized Willmore energy minimization algorithm from.

While these approaches are capable of creating meaningful disordered minimal surface models, the resulting surfaces are often not isotropic because they are constrained to a cubic simulation box. In Section 4.3.4, we thus develop a relaxation algorithm for frustrated minimal surfaces to enhance their isotropy. To explore the extent of homogeneity that disordered minimal surfaces can achieve, in Section 4.3.5 we make use of all the previously introduced concepts. Leaving aside that some subsamples of the amorphous Diamond minimal surfaces and samples from the parallel layers construction algorithm have a comparatively low curvature fluctuation and isotropy index, the Primitive, Diamond and Gyroid minimal surfaces are still significantly more homogeneous. The impact of curvature fluctuations on self-assembly processes helps explain why the Gyroid is frequently observed in many organic settings.

#### 4.4.1 Future Experiments and Mathematical Analyses

In the future, we hope to gain a better understanding of the space of disordered triply periodic minimal surfaces with the goal of defining additional constraints in the construction laid out in Section 4.3.3. In doing so, the generation of homogeneous minimal surfaces becomes more reliable and the resulting surfaces are more homogeneous. To an extent, we compare the highly restrictive and uniform amorphous Diamond surfaces to disordered minimal surfaces of arbitrary topology and geometry. Choosing a method of construction that has the potential to generate surfaces of many different genera in combination with appropriate constraints is a promising approach. The existence of surfaces without obvious symmetries generated by the parallel planes algorithm whose curvature fluctuation falls in the interval  $[0.3, 0.45]$  motivates the continuation of this line of research. For the moment, our amorphous Diamond minimal surface model from Section 4.3.2 provides the most homogeneous samples.

Furthermore, our numerical results and their relevance to self-assembly give a strong impetus to a rigorous mathematical treatment of two optimality questions: Which regular, embedded, and infinite minimal surface  $\mathcal{M}$  in  $\mathbb{R}^3$  with  $\langle K \rangle = -1$  has the lowest fluctuation of Gaussian curvature? Are estimates of the total squared Gaussian curvature available? Considering the local behavior of the Gaussian curvature around flat points might provide lower bounds for the squared Gaussian curvature and, by extension, for the curvature fluctuation.

A specific hypothesis to be tested is that the Gyroid minimal surface has the lowest curvature fluctuation, as claimed in Conjecture 4.2.12. Similar to other spatial optimization problems, such as the famous Kepler conjecture on the densest packing of spheres [146], it is likely that proving optimality among all crystalline or periodic candidates is easier and precedes proving the general case without spatial periodicity. It is conceivable that results about minimal nets (cf. Section 4.3.2) and a Thompson-like problem [106] on the distribution of the surfaces' flat points via the Gauss map will play a fundamental role in a formal proof.

Research into bicontinuous minimal surfaces has seen a wide array of approaches. The strategies range from architectural soap film models and physical free energy modeling to structure enumeration, experimental and numerical mathematics, and rigorous mathematical proofs, e.g.

of embeddedness or uniqueness. Our findings of Chapter 4 open up the diverse family of amorphous surfaces. This new class of minimal surfaces is likely to contribute to answering various related research questions.

The specific question of which minimal surfaces minimize the curvature fluctuation  $(\Delta K/\Gamma^2)^2$  needs further mathematical analysis, conceivably reinforced through our results. For now, the hypothesis stands that the cubic Gyroid, Diamond, and Primitive represent the minimally fluctuant triply periodic minimal surfaces. These surfaces may well be nature's best, albeit imperfect, attempt at embedding the hyperbolic plane in Euclidean space.

## Robust Modeling of Curved Cylinder Packings<sup>21</sup>

**Chapter Synopsis:** Cylinder packings are discussed extensively in the context of structural chemistry and metal-organic frameworks. These structures generalize sphere packings by consisting of infinitely long cylinders with finite cross-sections. Tensegrity frameworks, comprised of rigid bars and elastic cables, provide a reliable model for curvilinear cylinder packings. Physical distance constraints within a framework transform into quadratic polynomial constraints via the Euclidean distance between two points, enabling associated numerical strategies for finding feasible configurations and deformation pathways.

In this chapter, we study the configuration space of two cylinders in tight contact to build the necessary geometric formulations to robustly transform cylinder packings to tensegrity frameworks. This construction leads to a nonlinear optimization problem with polynomial constraints. Since the constraints are smooth almost everywhere, techniques from Riemannian optimization become admissible, allowing us to provide numerical strategies for exploring the deformative behavior of two exemplary triply periodic cylinder packings. As a result, we show that the structures are auxetic by multiple definitions, intuitively meaning that when expanded in a fixed direction, these materials also expand in their lateral directions.

Framework materials – known as trusses in the engineering world [34, p.287f.] – are structures composed of many rigid bars (or edges), pinned together at vertices where the bars can freely rotate relative to each other. These structures can be rigid or deformable, depending on the combinatorics of how the bars are joined together. For example, take three bars of equal length connected to form a triangle, or four bars connected into a square; the triangle is rigid, whereas the square can be deformed into a family of parallelograms. With increasing complexity, in particular periodicity, frameworks can be used as a simplified model of various materials, such as zeolites and metal-organic frameworks [264]. Due to their high porosity, mechanics and other properties, which stem from the underlying geometric structure, framework materials are engineered for various applications. The precise understanding of geometric structure in framework materials is thus a valuable contribution to enhanced material design.

Possible deformation pathways of a framework structure can be described algebraically. Each rigid rod can be represented by a polynomial constraint on its endpoints. They are always separated by a distance equal to the length of the rod, meaning that one end of the rod is constrained to a sphere centered in the other end of the rod. The solution set of the polynomial system arising when accumulating all such constraints provides possible configurations of the framework, be it isolated real solutions for a rigid structure, or one- or higher-dimensional configuration spaces for flexible structures.

<sup>21</sup>This chapter contains results and material from the publication in Himmelmann and Evans [161].

Auxetic frameworks, or auxetic materials more generally, can be characterized as those structures that exhibit a perpendicular expansion upon stretching the material in a chosen direction, a somewhat counterintuitive property. This is quantified by a negative Poisson's ratio [195]. These materials occur in various forms, such as polyurethane foam [203], skin cells [112], arteries, and tendons [263]. They are also a prime target in the geometric design of metamaterials with prescribed microstructures and targeted functionality, such as impact protection and filtration. In a mathematical context, Section 2.1.2.2 introduces a geometric description of auxetic deformations that we use extensively in parts of this chapter.

Our target in this chapter is the analysis of a set of slightly more complicated structures than a simple framework, namely tensegrity structures derived from cylinder packings. We start with a particular family of three-periodic curved cylinder packings, discussed extensively in the structural chemistry literature in relation to metal-organic frameworks [264]. The basic geometry consists of cubic cylinder packings, where rods lie along the invariant axes of the cubic crystallographic symmetry groups [236]. These cylinder packings have been explored in a geometric setting, where their curved counterparts induced an interesting dilatant property in the material [107, 111]. The curved, mostly helical cylinders that we are considering in this chapter have a cooperative unwinding mechanism that expands the material isotropically, reminiscent of an auxetic deformation. In a biological context, this expansive mechanism has been proposed as the strategy by which human skin cells expand and imbibe water like a sponge, driven purely by geometry [112]. The keratin intermediate filaments of the cell microstructure form one of the cubic rod packings well-known in structural chemistry [236]. It has already been considered as a geometric constraint system in Section 3. Figure 5.1.1 shows two such rod packings, called the  $\Pi^+$  packing and the  $\Sigma^+$  packing, with the latter being the packing seen in the skin structure.

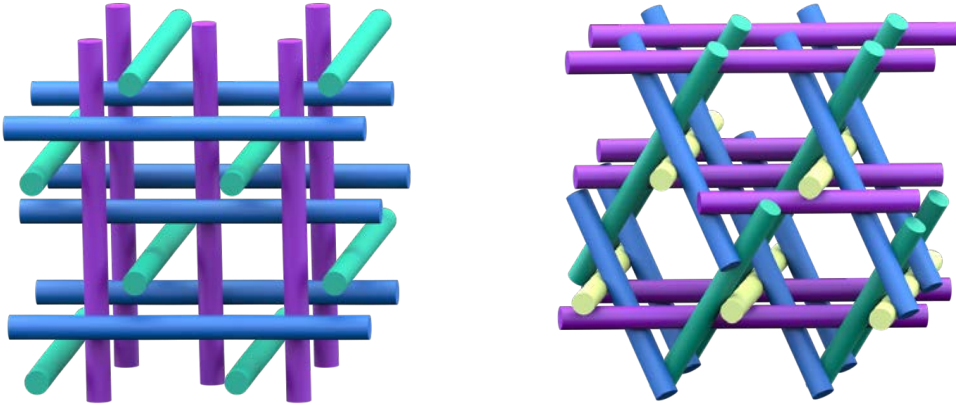


**Figure 5.1.1:** The chiral rod packings  $\Pi^+$  (l.) and  $\Sigma^+$  (r.) are depicted here. They have rods aligned along 3 or 4 axes respectively, each colored differently.

In a previous study, the dilatant property of the  $\Pi^+$  filament packing was considered through a 3-periodic tensegrity structure [242], designed to represent the packing constraints of the original curvilinear cylinders. Tensegrity structures are like framework materials, except some of the rigid bars are replaced by elastic elements under tension. Deformation of the tensegrity structure corresponding to the  $\Pi^+$  rod packing, which is dilatant, demonstrated auxetic behavior, albeit with somewhat unstable numerics. Given this foundation, we perform an enhanced

investigation of these tensegrity structures, where the strategy for designing the tensegrity is improved for stability in Section 5.4, as well as analyzing the dilatant rod packing  $\Sigma^+$  which is the filament packing in mammalian skin described above. These results have been published in Himmelmann and Evans [161].

In addition to these geometric considerations, a robust algorithm plays a crucial role in modeling the behavior of filament packings. Considering the framework's elastic elements as one-sided Hookean springs, its equilibration becomes a nonlinear optimization problem. As all of the proposed constraints can locally be expressed as polynomials, the constraint set can be interpreted as an algebraic variety. In Section 5.5, we describe how to apply the Riemannian optimization algorithm that is developed in Chapter 3 to our problem. Given the cylinder packing's previous tensegrity model [242] as initialization, the Euclidean distance retraction [153] enables Riemannian gradient descent [47] to yield a static energy minimum for a given initial lattice extension. Afterward, parametrizing a path in the deformation space by one fixed lattice direction gives rise to a linear homotopy describing the system's quasi-static configurations. By varying this parameter, stress is induced on the framework and we track the resulting behavior using homotopy continuation [32, 54, 76].

## 5.1 Cylinder Packings on the Gyroid Minimal Surface

The intuitive way to view cylinder packings is as tight arrangements of curvilinear cylinders in space. Alternatively, there is a strong geometric relation between cylinder packings and triply periodic minimal surfaces (cf. [279]): Through hyperbolic line arrangements on the cubic Primitive, Diamond, and Gyroid minimal surfaces [110]. In Chapter 4, the Gyroid is painted as the most homogeneous TPMS. It is further unique among the other bicontinuous cubic structures due to its chirality [98], meaning that the surface cannot be transformed into its mirror image through Euclidean motions alone. A material's chirality has been linked with auxeticity [181], making the Gyroid a prime candidate in the context of the current chapter.

The Gyroid can be generated using the  $I4_132$  space group on an oriented triangular fundamental region or by applying  $Ia\bar{3}d$  to an unoriented fundamental piece [125]. The Gyroid's unoriented, smallest generating triangle has the interior angles  $\pi/2$ ,  $\pi/4$ , and  $\pi/6$ , summing to  $\frac{11}{12}\pi$  and reflecting its hyperbolicity. Figure 5.1.2(l.) depicts the tiling generated by this particular triangle in the hyperbolic plane  $\mathbb{H}^2$ . As a next step, we introduce the Conway orbifold notation to enhance clarity. It provides a way to classify tilings and thus simplifies our discussion moving forward.

Orbifolds are a mathematical tool for understanding surface symmetries. They generalize manifolds by locally being homeomorphic to  $\mathbb{R}^n/G$  for a finite group  $G$  acting on  $\mathbb{R}^n$  [314, §13.2]. A 2-dimensional orbifold can be obtained from the sphere  $S^2$  by adding cone points, pinching holes and adding boundary curves (“\*”), adjoining handles (“o”), or cross-caps (“x”) [84]. Here, we only focus on cone and corner points represented by the symbol “\*”, as they allow the generation of polygonal shapes. The enumeration of such orbifolds reveals that all of them are uniquely characterized by symbols  $AB\dots C*ab\dots c$ , with the letters representing the shapes' interior angles. We assume that  $A, B, \dots, C, a, b, \dots, c \in \mathbb{N} \cup \{+\infty\}$  such that  $A \leq B \leq \dots \leq C$  and  $a \leq b \leq \dots \leq c$ . Each capital letter  $L$  represents a gyration point corresponding to a

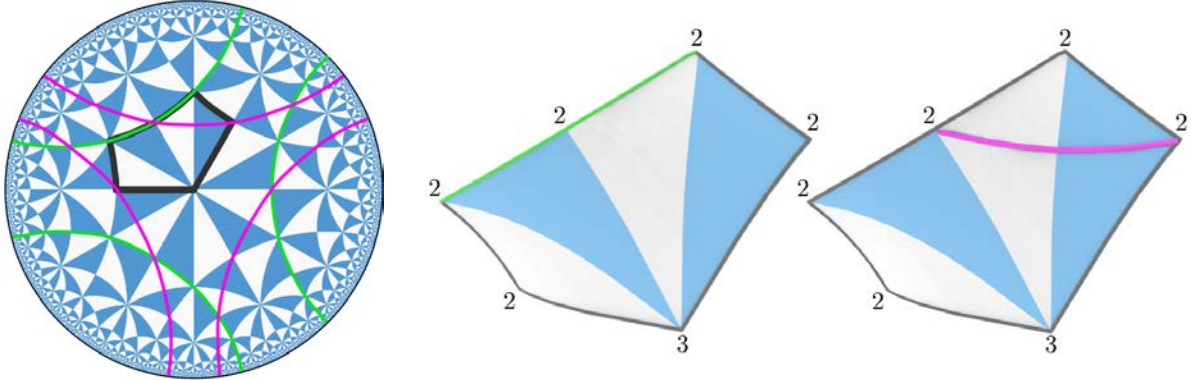


**Figure 5.1.2:** The space group  $Ia\bar{3}d$  allows the generation of the Gyroid minimal surface from a polygonal surface patch. For example, it can be obtained by embedding the triangular  $*246$  tiling of the hyperbolic plane  $\mathbb{H}^2$  (l.) in Euclidean space [119]. The first layer of the 124RL and 129RL (cf. [110]) line arrangements in  $\mathbb{H}^2$  are depicted in green and magenta, respectively. Lifting them to the Gyroid's pentagonal surface patch (c., r.) with symmetry 2223 (framed in black, l.) lets us construct the  $\Pi^+$  (c.) and  $\Sigma^+$  (r.) rod packing.

rotation of  $2\pi/L$  and each lower-case letter  $\ell$  represents a set of  $\ell$  mirror lines meeting at an angle  $\pi/\ell$  [85]. In hyperbolic polygons, a vertex can asymptotically lie on the Poincaré disk model's boundary, necessitating the vanishing of the corresponding internal angle. This is the only time  $C, c = \infty$  is admissible.

In this notation, the torus is given by the symbol “ $\circ$ ”, the Möbius strip has the symbol “ $*\times$ ” and the Klein bottle has the symbol “ $\times\times$ ” [85]. The triangular tiling of the Euclidean plane where each edge constitutes a mirror has the orbifold symbol “ $*333$ ”, whereas a hemisphere with a reflection symmetry across its equator has the symbol “ $*11$ ”.

Any orbifold  $\mathcal{O}$  gives rise to a decoration of either the sphere  $S^2$ , the Euclidean plane  $\mathbb{R}^2$ , or the hyperbolic plane  $\mathbb{H}^2$ . These cases can be distinguished by computing  $\mathcal{O}$ 's Euler characteristic  $\chi(\mathcal{O})$ : a positive  $\chi(\mathcal{O})$  corresponds to tilings of  $S^2$ , 0 corresponds to tilings of  $\mathbb{R}^2$  and a negative Euler characteristic to tilings of  $\mathbb{H}^2$  [170]. For  $\mathcal{O}$  given by the notation  $AB\dots C * ab\dots c$ , the corresponding Euler characteristic can be computed with the corresponding formula from Conway and Huson [85]:

$$\chi(\mathcal{O}) = 2 - \left( \frac{A-1}{A} + \frac{B-1}{B} + \dots + \frac{C-1}{C} \right) - \left( 1 + \frac{a-1}{2a} + \frac{b-1}{2b} + \dots + \frac{c-1}{2c} \right).$$

In this context, the Gyroid arises from the tiling  $*246$  of hyperbolic space [170]. Using the unoriented Gyroid's symmetry group  $Ia\bar{3}d$ , it tiles the cubic 3-torus, creating the well-known triply periodic minimal surface. Four such fundamental regions, combined to form the pentagonal 2223 orbifold, are shown in Figure 5.1.2.

Embedding packings of non-intersecting geodesics in  $\mathbb{H}^2$  into  $\mathbb{R}^3$ , provide novel ways of describing curvilinear rod packings [110]. In Evans et al. [109], the regular line array characteristic of the branched ribbon tilings 124RL and 129RL is derived. These line arrangements correspond to the  $\pi^+$  and  $\Sigma^+$  rod packings (cf. Figure 5.1.1). While they are naturally embedded in different fundamental regions, they both live in the hyperbolic pentagonal

tiling 2223, which naturally contains the triangle \*246. Consequently, they can be embedded on the Gyroid minimal surface, as can be seen in Figure 5.1.2(r.).

We now inflate the geodesics on the Gyroid and color-code them so that non-adjacent, translational copies of the curvilinear rods have the same color. An appropriate inflation reveals the  $\Pi^+$  and  $\Sigma^+$  rod packings. They are shown as line arrangements on the Gyroid in Figure 5.1.3.

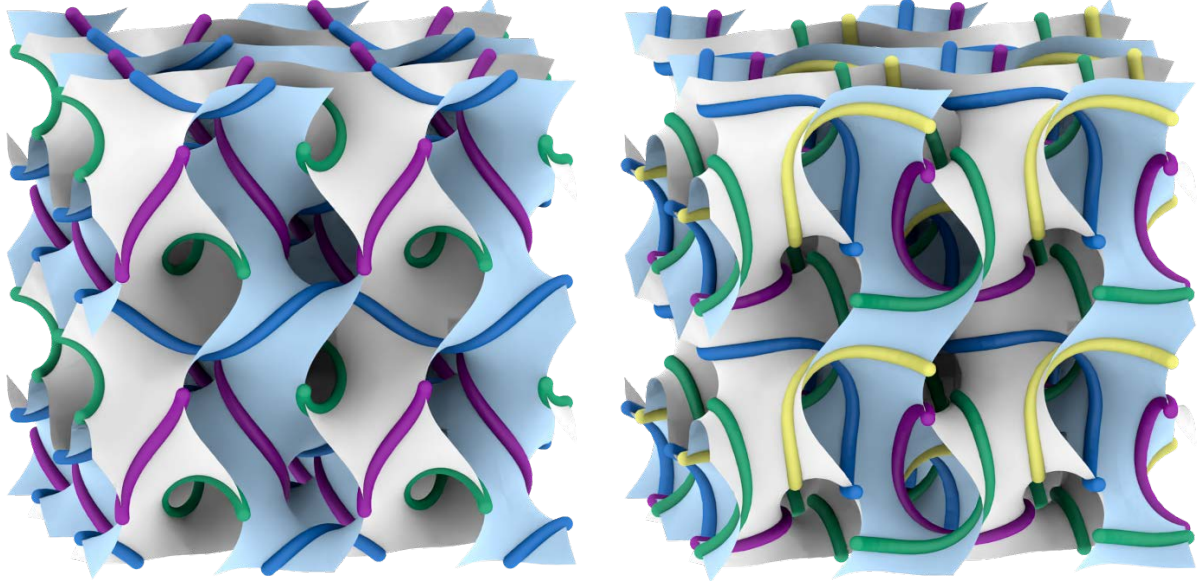


**Figure 5.1.3:** The  $\Pi^+$  (l.) and the  $\Sigma^+$  rod packing (r.) depicted as line arrangements on the gyroid. The colors represent different filament orbits of the packings.

Experimental imaging suggests that the curvilinear cylinder packing  $\Sigma^+$  is the structural component of corneocytes (cf. [235]), which are cells in the outer layer of the skin. When soaking skin in water, the expansive response is beyond what is expected from the swelling of the single filaments' [107], implying that the packing's geometry has an impact. The cooperative unwinding of the curved cylinders produces a dilatant response, as they "lever off each other and cause an expansion of the material beyond an isotropic stretching" [112]. This expansive mechanism is reminiscent of auxeticity (cf. Section 2.1.2.2), a material's property that is characterized by a negative Poisson's ratio. For that reason, the following section investigates the connection between the geometric Definition 2.1.32 for auxeticity and the materials-scientific definition.

## 5.2 Negative Poisson's Ratio

From a materials science perspective, the Poisson's ratio is a mechanical property that describes a material's deformation behavior under loading. It is defined as the ratio of the lateral strain (change in width or thickness) to the axial strain (change in length) of a material when subjected to an applied load. It is an infinitesimal quantity of a linear elastic material.

The tensegrity structures that we analyze here have non-linear behavior exhibited over large deformations. We refer then to the *instantaneous Poisson's ratio*, which allows us to consider behavior over a larger range of deformations. For a given set of timesteps  $t_0 < t_1 < \dots < t_N$ ,

this quantity is defined in terms of the *instantaneous true strain* [297, Eqn. (3)]:

$$\nu_{xy} = -\frac{e_y}{e_x} \quad (5.2.1)$$

with  $e_x = \frac{(L_x)_{t_j} - (L_x)_{t_{j-1}}}{(L_x)_{t_{j-1}}}$  and  $e_y = \frac{(L_y)_{t_j} - (L_y)_{t_{j-1}}}{(L_y)_{t_{j-1}}}.$

Here,  $x$  is the direction of applied strain and  $y$  is an orthogonal direction.  $(L_x)_t$  and  $(L_y)_t$  are the lattice extensions in the  $x$ - and  $y$ -directions taken at timestep  $t$ . Materials with negative Poisson's ratio are called *auxetic*.

Notice that we have now introduced two different concepts of auxeticity – the geometric Definition 2.1.32 and the instantaneous Poisson's ratio over large deformations in Equation (5.2.1) – which we wish to compare. The geometric definition of auxeticity considers shearing as well as orthogonal extensions of the unit cell, in contrast to the instantaneous Poisson's ratio shown above, whose increase in all orthogonal directions is not sufficient for a deformation path to be auxetic geometrically [43]. Nevertheless, the instantaneous Poisson's ratio is easier to compute in certain experimental and numerical contexts, so often it is preferred in practice. The following proposition relates these two concepts.

**Proposition 5.2.2.** *Assume that  $G = (V, E, p, \pi)$  is a  $d$ -periodic tensegrity framework. If the deformation path  $(p_\tau, \pi_\tau)$  induced by stretching the framework in a fixed direction is auxetic in the sense of Definition 2.1.32, then the Poisson's ratio is non-positive for any discretizations  $-\varepsilon < t_0 < \dots < t_N < \varepsilon$ . Conversely, if the unit cell of the lattice  $\pi_\tau$  is generated by mutually orthogonal vectors for all  $\tau$  and the Poisson's ratio is non-positive for all discretizations of  $(-\varepsilon, \varepsilon)$ , then the deformation path is auxetic.*

*Proof.* Let  $\Lambda_\tau \in \mathbb{R}^{d \times d}$  denote the matrix of generators for the full-dimensional periodicity lattice  $\pi_\tau(\Gamma)$  corresponding to the framework's deformation path. After factoring out Euclidean motions, applying the assumption that the framework is stretched in a fixed direction and potentially reordering, the matrix of generators becomes

$$\Lambda_\tau = \begin{pmatrix} \tau + \ell_0 & 0 & \dots & 0 \\ c_{12}(\tau) & c_{22}(\tau) & & \vdots \\ \vdots & & \ddots & 0 \\ c_{1d}(\tau) & \dots & c_{(d-1)d}(\tau) & c_{dd}(\tau) \end{pmatrix} \quad (5.2.3)$$

for continuous functions  $c_{ij}$  – a topological path is continuous – and the initial extension  $\ell_0 \neq 0$ . Since  $\Lambda_\tau$  is lower-triangular, for any  $-\ell_0 < \tau_1 < \tau_2$ , the linear operator  $T_{\tau_2 \tau_1}$  defined in (2.1.31) taking the lattice  $\pi_\tau$  from time  $\tau_2$  to  $\tau_1$  has a lower-triangular matrix representation. Therefore, its eigenvalues are on the diagonal [27, p.152] and are precisely given by

$$\lambda(T_{\tau_2 \tau_1}) = \left( \frac{\tau_1 + \ell_0}{\tau_2 + \ell_0}, \frac{c_{22}(\tau_1)}{c_{22}(\tau_2)}, \dots, \frac{c_{dd}(\tau_1)}{c_{dd}(\tau_2)} \right).$$

By the Spectral Radius Theorem [164, p.347], the eigenvalues' absolute values are bounded above by any matrix norm. As a consequence, the deformation path's auxeticity immediately proves

that  $|c_{ii}(\tau_2)| \geq |c_{ii}(\tau_1)|$  for  $\tau_2 > \tau_1$ . By the framework's  $d$ -periodicity,  $\Lambda_\tau$  has full rank for any  $\tau$ , implying that  $c_{ii}(\tau) \neq 0$ . Denoting the instantaneous true strain in the  $i$ -th orthogonal direction by  $e_i$  (cf. Equation (5.2.1), so  $e_i \geq 0$  for each  $i$ , implying that the instantaneous Poisson's ratio is non-positive for any discretization of the interval  $(-\varepsilon, \varepsilon)$ .

Conversely, assume that the Poisson's ratio is non-positive. This lets us deduce that  $\ell_0 > \varepsilon$ , by choosing a positive branch and by the framework's  $d$ -periodicity. Therefore, for  $\tau_2 > \tau_1$

$$\begin{aligned} 0 &\geq \nu_{1i} = -\frac{e_i}{e_1} = -\frac{\tau_1 + \ell_0}{|c_{ii}(\tau_1)|} \cdot \frac{|c_{ii}(\tau_2)| - |c_{ii}(\tau_1)|}{\tau_2 - \tau_1} \quad \forall i > 1, \quad \text{so} \\ 0 &\leq \frac{|c_{ii}(\tau_2)| - |c_{ii}(\tau_1)|}{|c_{ii}(\tau_1)|} \quad \forall i > 1. \end{aligned}$$

In particular,  $|c_{ii}(\tau_2)| \geq |c_{ii}(\tau_1)|$ . By assumption, the unit cell is orthogonal, so after potentially reordering, the lattice  $\Lambda_\tau$  can be chosen as a diagonal matrix at each step. Because the framework is  $d$ -periodic, its periodicity lattice has rank  $d$ , implying that  $c_{ii}(\tau) \neq 0$  for each  $\tau$ . By the deformation path's continuity, we find that  $c_{ii}(\tau_1)$  and  $c_{ii}(\tau_2)$  have the same sign. Consequently,  $c_{ii}(\tau_1)/c_{ii}(\tau_2) \leq 1$ . Therefore, all eigenvalues of  $T_{\tau_2\tau_1}$  are smaller than 1, yet still positive. Previous observations then imply that the linear operator  $T_{\tau_2\tau_1}$  is also diagonal. As a diagonal matrix is normal, the absolute values of its eigenvalues and singular values agree. Thus, the operator norm induced by the Euclidean norm is equal to the largest eigenvalue of  $T_{\tau_2\tau_1}$ , which is at most 1, making the linear operator a contraction. As a result, the deformation path is auxetic by Definition 2.1.32.  $\square$

However, Proposition 5.2.2 is not practical in determining, whether an arbitrary framework is auxetic. The assumption that the lattice stays orthogonal at every time step often is too much to ask for. For this reason, it seems beneficial to give another sufficient criterion for auxeticity in terms of the lattice generators' coordinates – at least on a given discretization. Basically, we formulate a bound on the size of the lattice's off-diagonal entries relative to the diagonal entries, dependent on the step size with which the deformation path is discretized. As our setting is motivated by real-world examples, we only prove the result for 3-periodic frameworks, though the proposition can be analogously proven for 2-periodic structures.

**Proposition 5.2.4.** *Assume that  $G = (V, E, p, \pi)$  is a 3-periodic tensegrity framework. Let the deformation path  $(p_\tau, \pi_\tau)$  with  $\tau \in (-\varepsilon, \varepsilon)$  be induced by stretching the framework in a fixed direction along a given discretization  $-\varepsilon < t_0 < \dots < t_N < \varepsilon$ . Further assume that the absolute values of  $\Lambda_\tau$ 's (cf. (5.2.3)) off-diagonal entries  $|c_{jk}(\tau)|$  are bounded above by  $\alpha|c_{ii}(\tau)|$  for some  $\alpha > 0$ , all grid points  $\tau$  and  $i \in \{1, 2, 3\}$ . Finally, assume that*

$$\begin{aligned} \left( \frac{c_{11}(\tau_1)}{c_{11}(\tau_2)} \right)^2 &\leq \frac{1 - 3\alpha - 11\alpha^2 - 12\alpha^3 - 4\alpha^4}{1 + 2\alpha^2}, \\ \left( \frac{c_{22}(\tau_1)}{c_{22}(\tau_2)} \right)^2 &\leq \frac{1 - 3\alpha - 7\alpha^2 - 3\alpha^3}{1 + \alpha + \alpha^2 + \alpha^3} \quad \text{and} \\ \left( \frac{c_{33}(\tau_1)}{c_{33}(\tau_2)} \right)^2 &\leq \frac{1 - 2\alpha - \alpha^2}{1 + 2\alpha + \alpha^2} \end{aligned}$$

for grid points  $\tau_2 > \tau_1$ . Then, the linear operator  $T_{\tau_2\tau_1}$  defined in Equation (2.1.31) is a contraction for all grid points  $\tau_2 > \tau_1$ .

*Proof.* Analogous to Proposition 5.2.2's proof (cf. Equation (5.2.3)), after removing Euclidean motions the linear operator taking the lattice  $\pi_\tau$  from time  $\tau_2$  to  $\tau_1$  can be represented as the lower-triangular matrix

$$T_{\tau_2\tau_1} = \begin{pmatrix} a_1 & 0 & 0 \\ a_2 & a_4 & 0 \\ a_3 & a_5 & a_6 \end{pmatrix},$$

with

$$\begin{aligned} a_i &= \frac{c_{ii}(\tau_1)}{c_{ii}(\tau_2)} \quad \text{for } i \in \{1, 4, 6\}, \\ a_{3i-1} &= \frac{c_{i,i+1}(\tau_1)c_{i+1,i+1}(\tau_2) - c_{i,i+1}(\tau_2)c_{i+1,i+1}(\tau_1)}{c_{i,i}(\tau_2)c_{i+1,i+1}(\tau_2)} \quad \text{for } i \in \{1, 2\} \quad \text{and} \\ a_3 &= \frac{c_{13}(\tau_1)c_{33}(\tau_2) - a_5c_{12}(\tau_2)c_{33}(\tau_2) - c_{13}(\tau_2)c_{33}(\tau_1)}{c_{11}(\tau_2)c_{33}(\tau_2)}. \end{aligned}$$

To show that  $T_{\tau_2\tau_1}$  is a contraction, we need to show that the largest eigenvalue of  $T_{\tau_2\tau_1}^T T_{\tau_2\tau_1}$  is at most 1. To calculate the matrix' eigenvalues, we want to utilize the Greshgorin Circle Theorem [127, Satz II]. It states that the eigenvalues of  $T_{\tau_2\tau_1}^T T_{\tau_2\tau_1}$  lie in (complex) circles whose centers are the matrix's diagonal entries and whose radii are given by the sum of the off-diagonal row entries' absolute values. With the claim's assumptions and the triangle inequality, we can now compute the following:

$$\begin{aligned} |a_{3i-1}| &\stackrel{\Delta}{\leq} \left| \frac{c_{i,i+1}(\tau_1)}{c_{i,i}(\tau_2)} \right| + \left| \frac{c_{i,i+1}(\tau_2) \cdot c_{i+1,i+1}(\tau_1)}{c_{i,i}(\tau_2) \cdot c_{i+1,i+1}(\tau_2)} \right| \\ &\leq \alpha \cdot (|a_{3i-2}| + |a_{2i+2}|) \quad \text{for } i \in \{1, 2\} \quad \text{and} \\ |a_3| &\stackrel{\Delta}{\leq} \left| \frac{c_{13}(\tau_1)}{c_{11}(\tau_2)} \right| + |a_5| \cdot \left| \frac{c_{12}(\tau_2)}{c_{11}(\tau_2)} \right| + |a_6| \cdot \left| \frac{c_{12}(\tau_2)}{c_{11}(\tau_2)} \right| \\ &\leq \alpha \cdot (|a_1| + |a_6| + \alpha \cdot (|a_4| + |a_6|)). \end{aligned}$$

These results finally enable us to calculate the row sums in absolute values:

$$\begin{aligned} \text{I : } &(a_1^2 + a_2^2 + a_3^2) + |a_2a_4 + a_3a_5| + |a_3a_6| \\ &\leq |a_4|^2 \cdot (\alpha + \alpha^2 + \alpha^3 + \alpha^4) + |a_1|^2 \cdot (1 + 2\alpha^2) + |a_4a_6| \cdot (2\alpha^2 + 4\alpha^3 + 2\alpha^4) \\ &\quad + |a_1a_4| \cdot (\alpha + 3\alpha^2 + 2\alpha^3) + |a_1a_6| \cdot (\alpha + 3\alpha^2 + 2\alpha^3) + |a_6|^2 \cdot (2\alpha^2 + 3\alpha^3 + \alpha^4) \\ \text{II : } &(a_4^2 + a_5^2) + |a_2a_4 + a_3a_5| + |a_5a_6| \leq |a_4|^2 \cdot (1 + \alpha + \alpha^2 + \alpha^3) \\ &\quad + |a_1a_4| \cdot (\alpha + \alpha^2) + |a_1a_6| \cdot \alpha^2 + |a_4a_6| \cdot (\alpha + 3\alpha^2 + 2\alpha^3) + |a_6|^2 \cdot \alpha \cdot (1 + \alpha)^2 \\ \text{III : } &(a_6^2) + |a_3a_6| + |a_5a_6| \leq |a_6| \cdot (\alpha |a_1| + (\alpha + \alpha^2) |a_4| + (1 + 2\alpha + \alpha^2) |a_6|) \end{aligned}$$

By the assumptions on  $(a_1)^2$ ,  $(a_4)^2$  and  $(a_6)^2$ , the values of I – III are bounded above by 1. Accordingly, Greshgorin's Circle Theorem implies that the eigenvalues of  $T_{\tau_2\tau_1}^T T_{\tau_2\tau_1}$  are also

bounded above by 1. By Definition 2.1.30, the linear operator  $T_{\tau_2 \tau_1}$  then is a contraction.  $\square$

**Remark 5.2.5.** Naturally, Proposition 5.2.4 begs the question whether the assumptions on the quotients  $c_{ii}(\tau_1)/c_{ii}(\tau_2)$  are reasonable. Indeed, for  $0 \leq \alpha < 0.183$ , the expressions on the right of the inequalities are positive. Nevertheless, having  $\alpha$  close to 0.183 would mean that  $c_{ii}(\tau_2)$  is extremely large relative to  $c_{ii}(\tau_1)$ . More sensibly, by choosing a constant step length of  $10^{-2}$ , maximum extension  $c_{ii}(0) = 1$  for  $i \in \{1, 2, 3\}$  and constant Poisson's ratio  $-1$ , we can deduce that  $\alpha \leq 4 \cdot 10^{-3}$ . In particular, the smaller the step size, the smaller  $\alpha$  will be.

### 5.3 The Configuration Space of Two Filaments in Tight Contact

For the stability of any model for a cylinder packing's global structure the local geometry of two cylinders in contact is likely the driving factor. In a previous study, the contact of two filaments in tight contact has been approximated by a tensegrity model with a rigid bar where two cylinders touch [242], corresponding to a single point of contact. However, numerical experiments suggest that this model leads to instabilities.

For an enhanced model, we therefore use the configuration space of two filaments in tight contact. Notably, it is well-understood in the limit cases of the orthogonal clasp, where the filaments meet at an angle of  $\pi/2$ , and the double helix, where the filaments wind around each other. Even though the theory for intermediate configurations has not yet been fully developed, we intend to use associated theoretical and experimental results to inform our model.

First, let us consider the orthogonal clasp that arises when one rope is pulled tightly over another [301]. It can be parametrized by two curves  $\gamma$  and  $\tilde{\gamma}$  in the filaments' centers lying in perpendicular planes. In this case, we choose the  $xz$ - and  $yz$ -plane. This pins the end points of  $\gamma$  and  $\tilde{\gamma}$  to  $z = \pm C$ . Then, their symmetry is given by fourfold rotation around the  $z$ -axis together with a reflection across the  $xy$ -plane [65, 301], with orbifold notation  $2 * 2$ . As it is isomorphic to the dihedral group of the square  $D_4$ , we know that

$$\begin{aligned}\gamma(\pm u) &= (\pm x(u), 0, z(u)) && \text{and} \\ \tilde{\gamma}(\pm u) &= (0, \pm x(u), -z(u))\end{aligned}$$

for  $u \in [0, 1]$ . Given  $0 \leq \tau \leq 1$ , we follow Cantarella et al. [65] to define the  $\tau$ -clasp by the arc  $\gamma$  starting in  $u = -\tau$ , then turning  $2 \arcsin \tau$  to reach  $u = \tau$ . This curve meets the line  $z = z(\tau)$  in the  $xz$ -plane with an angle of  $\arcsin \tau$ . Hence,  $\tau$  parametrizes the opening angle of the two filaments. The following theorem gives an explicit description for the  $\tau$ -clasp's critical configuration with central curve  $\gamma$ , meaning that the curvature forces of  $\gamma$  must balance with those of  $\tilde{\gamma}$ .

**Theorem 5.3.1** (cf. Cantarella et al. [65, Thm. 9.5]). Let  $\tau \in [0, 1]$ , and let  $\gamma = \gamma_\tau$  be the curve in the  $xz$ -plane given parametrically for  $u \in [-\tau, \tau]$  by

$$\begin{aligned} x_\tau(u) &= \frac{u\sqrt{1-(\tau-|u|)^2}}{\sqrt{1-u^2(\tau-u^2(\tau-|u|)^2)}}, \\ z_\tau(u) &= \int \frac{u}{\sqrt{1-u^2}} \frac{du}{\kappa_\tau(u)}, \\ \text{where } \kappa_\tau(u) &= \frac{\sqrt{(1-u^2(\tau-|u|)^2)^3(1-(\tau-|u|)^2)}}{1-(\tau-|u|)^2+(\tau-|u|)|u|(1-u^2)} \end{aligned}$$

and the constant of integration for  $z_\tau$  is chosen so that

$$z(0) + z(\tau) = -\sqrt{1-\tau^2}.$$

Then the union of  $\gamma$  with its image  $\tilde{\gamma}$  under the symmetry group  $2*2$  described above is a  $\tau$ -clasp that is strongly critical for link-rope length.

After placing two filaments of fixed radius  $r$  determined by the curve  $\gamma$  around both arcs  $\gamma$  and  $\tilde{\gamma}$ , we receive a critical configuration for two filaments in tight, orthogonal contact. In the idealized mathematical model, the two cylinders meet in a diamond-shaped loop with four cusps bounding a gap chamber [65]. If the filaments are elastic, allowing them to deform, physical experiments suggest that the contact line becomes a contact surface [132]. The experiments also found that the surface patch usually contains 4 regions of maximal pressure, roughly located in the idealized curve's cusps. One configuration of the  $\tau$ -clasp with its corresponding contact surface is depicted in Figure 5.3.2(l.).

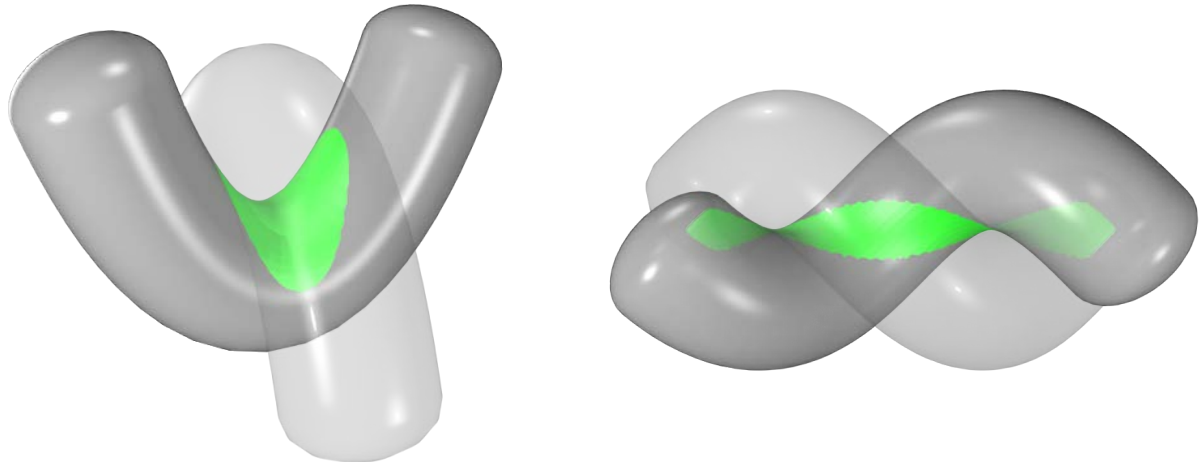


**Figure 5.3.2:** A critical  $\tau$ -clasp configuration with  $\tau \approx 0.88$  (l.) and the critical helix configuration with pitch angle  $\pi/4$  (r.). Assuming elastic filaments, in both cases the corresponding contact surface is depicted in green.

As a second step, let us consider the double helix. Generally, the double helix can be described by two periodic curves  $\varphi_1$  and  $\varphi_2$  with pitch  $h$  on a cylinder with radius  $r$  that are

offset by half a period [237]. In formulas,

$$\begin{aligned}\varphi_1(t) &= (r \cos(t), r \sin(t), ht) \\ \varphi_2(t) &= (r \cos(t - \pi), r \sin(t - \pi), ht)\end{aligned}\quad \text{and}$$

for  $t \in [0, 2\pi]$ . If the ratio  $h/r \geq 1$ , the contact line is straight, while it becomes helical when  $h/r < 1$  [250, 302]. When  $h = r$ , the configuration is tightly packed, corresponding to a pitch angle of  $\pi/4$  [237]. This configuration is critical in the sense that the helix transitions from one contact cord to two. Similar to the physical trefoil knot [183], it is likely that in the configurations with  $h/r \leq 1$  the contact lines connect to form a contact surface. This is further evidenced by the behavior of a helix wound around a torus, which forms a bridge between the trefoil torus knot and the straight double helix [238]. The critical double helix with an approximation of its corresponding contact patch is depicted in Figure 5.3.2(r.).

While little is known about the intermediate configurations, intuition quickly leads to a continuous deformation between the family of orthogonal  $\tau$ -clasps and the collection of single-period helices. Starting with the clasp, we pull the ends of one filament in opposite directions until the tips of both filaments lie in the same plane. In other words, the filaments are intertwined or wound around each other. We expect that the contact surface is well-behaved under this deformation.

## 5.4 Constructing a Stable Periodic Tensegrity

In a previous study, the  $\Pi^+$  rod packing [107] (Figure 5.1.1(l.)) was transformed into a tensegrity by adding balancing equations [242]. In that model, each contact between filaments is described by an incompressible bar of length  $2r$ , where  $r > 0$  denotes the cylinders' radius. The bar is assumed to stay normal to the contact, connecting the central axes of the cylinders. As depicted in Figure 5.4.1(l.), flexible elastic cables are placed along the cylinders' central axes to model the filaments' elasticity. The tensegrity structure was shown to exhibit auxetic behavior, albeit with very unstable numerics for the initial phase of the deformation parametrized by stretching the corresponding framework along the  $x$ -axis. We suspect that the unstable behavior is induced by the instability of the contact bar between two filaments.

As described in Section 5.3, theoretical studies and recent experiments of the contact set of two orthogonal tubes in a clasp configuration show that the system balances through a more complicated intersection than just a single point: Two compressible filaments in tight contact meet in a contact surface, on which the pressure varies. There are 4 points of maximum pressure on this contact surface. This idea suggests that the contact between two filaments could be better modeled as a tetrahedron of constraints, encapsulating the four points of highest pressure. We describe this model in the following.

To build the new model for two filaments in contact, let  $p_{11}, p_{12}, p_{21}, p_{22} \in \mathbb{R}^3$  denote four points in space. If these four points  $p_{ij}$  are in general position, they form a tetrahedron with 12-dimensional configuration space. Now assume that  $p_{i1}$  and  $p_{i2}$  lie in the center of the same filament. We place cables  $c_{ij}$  along the cylinders' central axes, following the same notation as the point they are attached to, so  $c_{12}$  would be attached to  $p_{12}$ . We do not place cables between

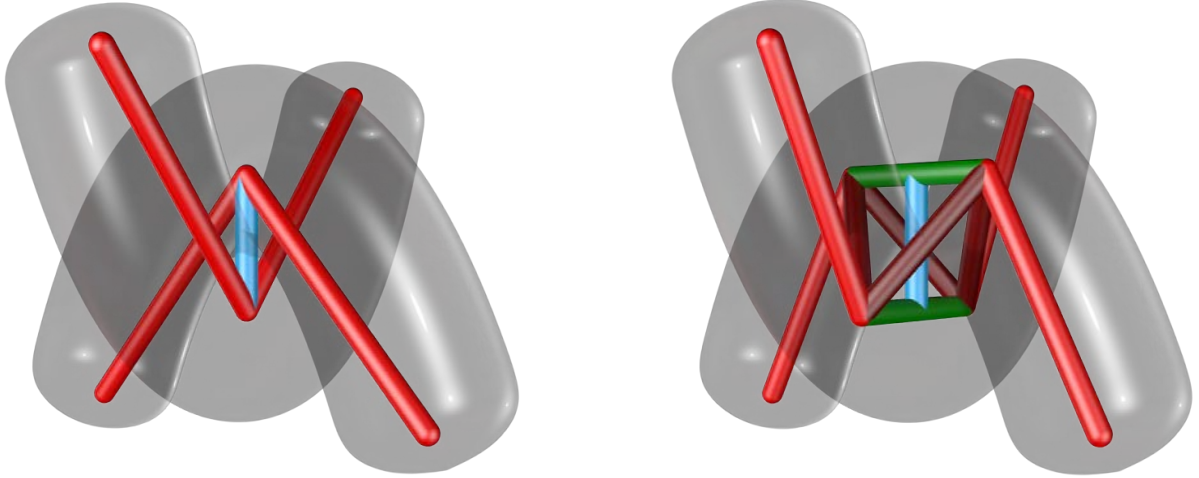


**Figure 5.4.1:** The original tensegrity model (l.) and the tetrahedral tensegrity model (r.) for two filaments in tight, orthogonal contact. Red edges correspond to flexible cables, blue edges correspond to a rigid bar maintaining the filaments' distance and green edges are rigid bars with variable length dependent on the clasp's opening angles. The translucent filaments have been added as visual reference for what is being modeled; they are not explicitly part of the optimization pipeline.

$p_{i1}$  and  $p_{i2}$  for reasons that will become clear later. Denote the cylinders' radius by  $r > 0$ . Analogous to the previous model, we want the cylinders' centers to be  $2r$  apart, meaning that we place a bar of length  $2r$  in the tetrahedron's center, depicted in blue in Figure 5.4.1(r.). This gives rise to the first constraint,

$$\left| \frac{p_{11} + p_{12}}{2} - \frac{p_{21} + p_{22}}{2} \right| = 2r. \quad (5.4.2)$$

Furthermore, this constraint should not only keep the cylinders apart at one position, but rather throughout the entire contact. Because of this and for symmetry reasons, we require the center bar (blue) to be orthogonal to both of the tetrahedron's sides (green) by setting

$$\left\langle \frac{p_{11} + p_{12}}{2} - \frac{p_{21} + p_{22}}{2}, p_{i1} - p_{i2} \right\rangle = 0 \quad \text{for } i \in \{1, 2\}. \quad (5.4.3)$$

To maintain its symmetry, we assume that the angles between the incoming cables  $c_{i1}, c_{i2}$  and the tetrahedron's sides  $p_{i2} - p_{i1}$  (green) are consistent. To make this equation more robust, we consider the dual angle with the rigid bar (blue). Its length has been fixed and it is orthogonal to the tetrahedron's sides (green) by previous equations. This translates to the constraint

$$\frac{\left\langle \frac{p_{11} + p_{12}}{2} - \frac{p_{21} + p_{22}}{2}, c_{i1} \right\rangle}{|c_{i1}|} = \frac{\left\langle \frac{p_{11} + p_{12}}{2} - \frac{p_{21} + p_{22}}{2}, c_{i2} \right\rangle}{|c_{i2}|} \quad \text{for } i \in \{1, 2\}. \quad (5.4.4)$$

Additionally, we require that the tetrahedron does not twist in unforeseen ways by assuming that the incoming cables  $c_{i1}$  and  $c_{i2}$  lie in the same plane as the tetrahedron's sides (green).

This can be expressed by the equation

$$\langle c_{i1} \times c_{i2}, p_{i1} - p_{i2} \rangle = 0 \quad \text{for } i \in \{1, 2\}. \quad (5.4.5)$$

Lastly, the tetrahedron can open. For that reason, the tetrahedron's sides (green) are not fixed, but should rather depend on the attached cables. Denote the angle between the cables  $c_{i1}$  and  $c_{i2}$  by  $\theta_i \in (0, \pi)$ . We can express the variable bar's length (green) as  $d_i = 2 \sin(\theta_i/2)$  (cf. [65, Thm. 9.5]). By applying trigonometric identities, we then calculate

$$d_i = 2 \cdot \sin\left(\frac{\theta_i}{2}\right) = 2 \cdot \operatorname{sgn}\left(\sin\left(\frac{\theta_i}{2}\right)\right) \cdot \sqrt{\frac{1 - \cos(\theta_i)}{2}} = 2 \cdot \operatorname{sgn}\left(\sin\left(\frac{\theta_i}{2}\right)\right) \cdot \sqrt{\frac{1 - \frac{\langle c_{i1}, c_{i2} \rangle}{|c_{i1}| \cdot |c_{i2}|}}{2}}.$$

To be meaningful, this expression needs to be scaled with respect to the tetrahedron's size. We multiply the right-hand side of the above equation by  $r$ . As  $\theta_i \in (0, \pi)$ , it holds that  $\sin(\theta_i/2) \geq 0$ , enabling us to rewrite the expression in point coordinates, i.e.  $d_i = |p_{i1} - p_{i2}|$ :

$$\langle c_{i1}, c_{i2} \rangle = |c_{i1}| \cdot |c_{i2}| \cdot \left(1 - \frac{|p_{i1} - p_{i2}|^2}{2 \cdot r^2}\right). \quad (5.4.6)$$

Besides the four incoming cables  $c_{ij}$  (red), we also place four internal cables (dark red) on the remaining edges of the tetrahedron to penalize twisting. This energy term enforces proximity to the orthogonal clasp, where the tetrahedron's deformations model the behavior of two filaments in tight contact well (cf. Section 5.3). In total, for generic placements  $p$ , there are  $4 \cdot 3 - 9 = 3$  degrees of freedom per tetrahedron. They can be parametrized by the lengths of the two variable bars (green) and the relative orientation of these two bars. The constraints are smooth almost everywhere, except when the external cables or variable bars have zero length, making Riemannian optimization algorithms (cf. Chapter 3) feasible.

To formalize the tetrahedra and relate them to the geometric theory for auxeticity introduced in Section 2.1.2.2, we now consider an embedded hypergraph  $G_{\mathcal{T}} = (V \sqcup V, \mathcal{T}, p, \pi)$  with the set of ordered hyperedges defined by the tetrahedron's edges. We write  $i_1$  for an element of the first  $V$  in the disjoint union,  $i_2$  for an element of the second  $V$  in the disjoint union and  $i$  for an element of the original set of vertices  $V$ . Recall that in the original model, each vertex has two cables attached and one bar.

$$\mathcal{T} = \{\{(h_2, i_1, i_2, k_1), (m_2, j_1, j_2, n_1)\} : \text{for } ij \in \mathcal{B} \text{ with } hi, ik, mj, jn \in \mathcal{C}\}$$

For a tetrahedron  $T \in \mathcal{T}$ , we denote the  $j$ -th element in the  $i$ -th entry of  $T$  by  $T_{i,j}$  for  $i \in \{1, 2\}$ ,  $j \in \{1, 2, 3, 4\}$ . We replace  $p(T_{i,j})$  by  $p_{ij}$  for the sake of brevity. With the notation in place, the objective function derived from the cables envisioned as one-sided Hookean springs combined with the constraints (5.4.2) – (5.4.6) can be expressed as a nonlinear optimization problem of

the form

$$\begin{aligned}
\text{local min}_{p:V \rightarrow \mathbb{R}} \quad & \sum_{T \in \mathcal{T}} \left( \sum_{\substack{i \in \{1,2\}, \\ j \in \{1,3\}}} \frac{c_{ij}}{2} (\max\{0, \|p_{ij} - p_{ij+1}\| - r_{ij}\})^2 + \right. \\
& \left. \sum_{i,j \in \{2,3\}} \frac{c_{ij}}{2} (\max\{0, \|p_{1i} - p_{2j}\| - r_{ij}\})^2 \right) \tag{5.4.7} \\
\text{s.t.} \quad & \left| \frac{p_{12} + p_{13}}{2} - \frac{p_{22} + p_{23}}{2} \right| = 2r, \\
& \left\langle \frac{p_{12} + p_{13}}{2} - \frac{p_{22} + p_{23}}{2}, p_{i2} - p_{i3} \right\rangle = 0, \\
& \frac{\left\langle \frac{p_{12} + p_{13}}{2} - \frac{p_{22} + p_{23}}{2}, p_{i2} - p_{i1} \right\rangle}{|p_{i2} - p_{i1}|} = \frac{\left\langle \frac{p_{12} + p_{13}}{2} - \frac{p_{22} + p_{23}}{2}, p_{i4} - p_{i3} \right\rangle}{|p_{i4} - p_{i3}|}, \\
& \langle (p_{i2} - p_{i1}) \times (p_{i4} - p_{i3}), p_{i3} - p_{i2} \rangle = 0 \quad \text{and} \\
& \langle p_{i2} - p_{i1}, p_{i4} - p_{i3} \rangle = |p_{i2} - p_{i1}| \cdot |p_{i4} - p_{i3}| \cdot \left( 1 - \frac{|p_{i3} - p_{i2}|^2}{2 \cdot r^2} \right)
\end{aligned}$$

with constraints taken for each  $T \in \mathcal{T}$  and  $i \in \{1, 2\}$ . For the incoming cables, we choose the resting length  $r_{ij} = 0.1$  and for the cables inside the tetrahedron  $r_{ij} = 2r$ . Analogously, the cables' constant of elasticity is  $c_{ij} = 1$  for incoming cables and  $c_{ij} = 30$  for the interior cables to strongly penalize deviations from the orthogonal case. While the left sum in the objective function corresponds to the incoming cables  $c_{ij}$ , the right part corresponds to the cables on the tetrahedron's sides. The constraints are obtained by inserting the representation from  $\mathcal{T}$  into Equations (5.4.2) – (5.4.6).

This outlines the setup of a tetrahedron of constraints, providing a stable tensegrity structure. The challenge with this model is to generate a set of constraints that make the tetrahedron robust with respect to perturbations, while at the same time remaining flexible enough to adjust depending on the incoming cables to accommodate for the different ways two filaments can be in contact. Our use of the orthogonal clasp's contact set in the tensegrity structure's design means that our model best approximates those structures with orthogonal cylinders. Some twisting of the tetrahedron extending beyond these constraints is allowed, yet penalized. Still, a more comprehensive study of non-orthogonal cylinders is left for future research.

While these geometric constraints appear to form a reasonable and physically motivated model for two filaments in tight contact, it is still unclear, whether a configuration satisfying the constraints even exists. Since intersections of algebraic hypersurfaces in  $\mathbb{R}^n$  do not necessarily follow the conditions imposed by Bézout's theorem [86, Thm. 5.5], we have no a priori information about the set of feasible points' degree and dimension. In this specific case though, we can impose conditions on the single *contact bar* of the previous tensegrity model, enabling us to explicitly construct a feasible point of the optimization problem (5.4.7).

**Proposition 5.4.8.** *Let a single contact bar with 4 attached cables from the original tensegrity model for cylinder packings (Figure 5.4.1(l.)) be given. Assume it satisfies the following:*

- *The four distinct points not attached to the rigid bar are fixed in space.*
- *The contact bar lies in both planes spanned by the incoming cables.*
- *In these planes, the angles between the bar and both cables are identical.*
- *The incoming cables have the same length.*

*Then, we can explicitly construct a feasible point of optimization problem (5.4.7) by introducing two new edges.*

*Proof.* Denote the four fixed points attached to the bars' endpoints  $q_i$  through a cable by  $p_{ij}$  for  $i, j \in \{1, 2\}$ . First, replace the rod's endpoints  $q_i$  by two points  $q_{ij}$  in the same position so that  $p_{ij}$  now is attached to  $q_{ij}$ . For  $i \in \{1, 2\}$ , we add variable-length bars (green) between  $q_{i1}$  and  $q_{i2}$ . Currently, their length is 0. For  $i \in \{1, 2\}$ , we will call the incoming cables defined by  $q_{i1} - p_{i1}$  and  $p_{i2} - q_{i2}$   $c_{i1}$  and  $c_{i2}$ , and denote the plane these two vectors span by  $\mathcal{C}_i$ . This construction immediately satisfies Equations (5.4.2), (5.4.4) and (5.4.5) by assumption and Equation (5.4.3), since the variable bar's length is 0. In order to construct a feasible point of the optimization problem (5.4.7), the variable length Equation (5.4.6) also needs to be satisfied.

If we symmetrically move the points  $q_{i1}$  and  $q_{i2}$  in the plane  $\mathcal{C}_i$  in opposite directions, so that  $q_{i1} - q_{i2}$  remains orthogonal to the center bar, we can guarantee that the angle between the center bar and incoming cables stays the same, since all cables have the same length and share the same angle with  $q_1 - q_2$  by assumption. The Side-Angle-Side Theorem for Triangles then implies that the points  $p_{i1}$  and  $p_{i2}$  have the same distance from the contact bar, so symmetrically changing the distance between  $q_{i1}$  and  $q_{i2}$  will produce symmetric angles. To summarize, this procedure always satisfies Equations (5.4.2) – (5.4.5), since it does not change the contact bar's length, the points  $q_{ij}$  stay in the plane  $\mathcal{C}_i$  and orthogonality with the contact bar is maintained by assumption. A visual representation of this construction can be found in Figure 5.4.9.

Now, the left hand side of Equation (5.4.6) attains its extrema, when the cables  $c_{i1}$  and  $c_{i2}$  are either parallel or pointing in opposite directions. The scalar product's value then becomes  $-|c_{i1}| |c_{i2}|$  or  $|c_{i1}| |c_{i2}|$ , leading to the two equations

$$\begin{aligned} 2r &= |q_{i1} - q_{i2}| \quad \text{or} \\ 0 &= |q_{i1} - q_{i2}|, \end{aligned}$$

after several equivalent transformations. Therefore, the expression  $|q_{i1} - q_{i2}|$  can attain any value in  $[0, 2r]$ . Since  $\langle c_{i1}, c_{i2} \rangle / |c_{i1}| |c_{i2}|$  is a continuous function for increasing  $|q_{i2} - q_{i1}| \in [0, 2r]$  bounded by  $\pm 1$ , and  $1 - |q_{i2} - q_{i1}|^2 / 2r^2$  can take any value in  $[-1, 1]$ , the two values must be equal for some configuration. This concludes the proof, since we established the existence of a configuration satisfying Equation (5.4.6), while maintaining all other equations.  $\square$

Proposition 5.4.8 provides a constructive procedure to deform a clasp's original tensegrity model into the tetrahedral model characterized by optimization problem (5.4.7). Nevertheless,

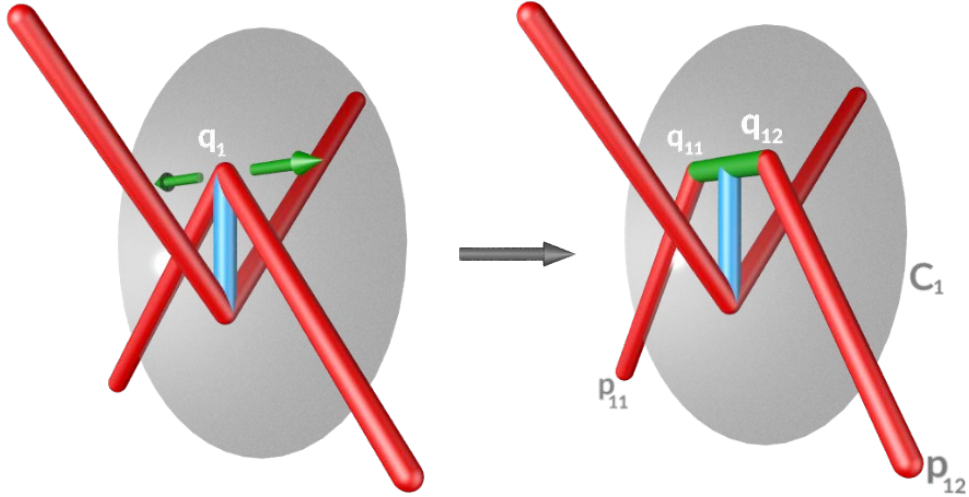


**Figure 5.4.9:** When symmetrically splitting the point  $q_1$  into two (l.), we can stay on the plane  $C_1$ , while  $q_{11} - q_{12}$  remains orthogonal to the contact bar (blue). If this is done on both sides of the tetrahedron (green), we create a feasible tetrahedral model.

the goal of this chapter is to not only consider a single clasp, but rather a series of contact bars. Together, they represent a 3-periodic helical cylinder packing.

One may then wonder, whether this construction generalizes to triply periodic cylinder packings. Restricting the class of rod packings in consideration to the chiral packings  $\Pi^+$  and  $\Sigma^+$  (see Figure 5.1.1), that are investigated in much more detail in Section 5.6, we find that all of the corresponding contact bars are identical up to Euclidean motions. These contact bars can be obtained from the RCSR database for triply-periodic nets [243], by considering the midpoints of the cross-bar edges and using the packings' symmetry. In particular, we consider maximally symmetric embeddings of the **bmn** and **sgn** graphs, which are naturally associated with the  $\Pi^+$  and  $\Sigma^+$  cylinder packings. In their case, there is a 1-dimensional deformation family, parametrized by the contact bar's length. As it turns out, the original tensegrity model's initialization (cf. Figure 5.4.1(l.)) is identical to an embedding of the mentioned nets after reasonably distributing the edges into bars and cables, so we can use it as initialization.

**Corollary 5.4.10.** *The tensegrity model associated with the nets **bmn** and **sgn** can be transformed into a feasible point of optimization problem (5.4.7) by applying the construction described in Proposition 5.4.8's proof to each contact bar.*

*Proof.* First of all, we need to check that the nets **bmn** and **sgn** satisfy the assumptions of Proposition 5.4.8. Since in both nets, their symmetry guarantees that all contact bars are identical up to rigid motions [264], we can without loss of generality investigate any such structure. For example, a typical contact bar in **bmn** can be described using the RCSR database, leading to a configuration of the form

$$\begin{aligned} p_{11} &= (1.0, 0.5, 0.8), \quad q_1 = (0.75, 0.65, 0.65), \quad p_{12} = (0.5, 0.5, 0.5), \\ p_{21} &= (0.9, 0.25, 0.9), \quad q_2 = (0.75, 0.1, 0.65), \quad p_{22} = (0.6, 0.25, 0.4). \end{aligned}$$

We can then easily verify that all points  $p_{ij}$  are mutually different and that the bar  $q_1 - q_2$

lies in both planes  $C_1$  and  $C_2$ . Moreover, all cables  $q_i - p_{ij}$  have the same length and the angle between cables and contact bar. Therefore, Proposition 5.4.8 is applicable. Since in the **bmn** net, along a chain of cables in the periodic unit cell, there appear four contact bars with respective rotations of  $90^\circ$ , we can perform the procedure from Proposition 5.4.8's proof on two non-adjacent tetrahedra along this chain and the other two automatically follow by symmetry. This construction is then inductively extended to all of **bmn**.

For **sgn**, the RCSR database lets us describe a typical contact bar by the coordinates

$$\begin{aligned} p_{11} &= (-0.125, 0.375, -0.125), \quad q_1 = (-0.125, 0.125, 0.125), \quad p_{12} = (0.125, 0.125, 0.375), \\ p_{21} &= (0.125, 0.125, 0.375), \quad q_2 = (0.125, 0.375, 0.125), \quad p_{22} = (-0.125, 0.375, -0.125). \end{aligned}$$

This configuration satisfies all assumptions of Proposition 5.4.8. In the case of **sgn**, along a chain of cables in the periodic unit cell there are three contact bars with relative rotations of  $120^\circ$ , so we need to consider three distinct contact bars. After one tetrahedron is changed, the remaining two have two different angles between the contact bar and the unique cable not adjacent to the previously altered tetrahedron. This issue can be resolved by using a trick.

Pick one of the remaining contact bars along the chain of cables, in which a tetrahedron has been altered. Instead of expanding  $q_{11}$  and  $q_{12}$  symmetrically away from  $q_1$ , only  $q_{12}$  – the point not adjacent to the altered contact tetrahedron – is moved. Since all contact bars of **sgn** are identical up to Euclidean motions, for some distance  $|q_1 - q_{12}|$  the angles at the third and remaining contact bar will match again. This is the case because this procedure does not change Equations (5.4.2) – (5.4.3), yet strictly decreases the corresponding angle in the contact. This is a direct consequence of Proposition 5.4.8's proof, so its assumptions are again satisfied for the third contact bar. This lets us deform it into a tetrahedron satisfying optimization problem (5.4.7)'s constraints.

What remains is to transform the last contact bar, which now has an edge sticking out only on one side. Analogously, by growing the opposite distance  $|q_{11} - q_1|$ , there exists a point where the angles between  $q_1 - q_2$  and the cables  $c_{11}$  and  $c_{12}$  will match again. Once that point is reached, we can again apply the construction from the proposition's proof. Therefore, this process can be generalized to all of **sgn**, concluding the proof.  $\square$

## 5.5 Computing Deformation Paths Algorithmically

With the well-defined nonlinear optimization problem (5.4.7) for our tensegrity in place, we utilize a robust optimization algorithm to solve it. A natural approach to finding an equilibrium is using Lagrange multipliers [234, p.320ff.], as we are exclusively dealing with equality constraints. This leads to a square polynomial system that can be solved using classical methods from numerical algebraic geometry, such as Homotopy Continuation (cf. Section 3.2.2). This method can be used to find *all* isolated solutions of a polynomial system with theoretical guarantees. However, Bernstein's Theorem predicts that the number of solutions can grow exponentially in the amount of variables [86]. Since the system involved in these tensegrity structures exceeds 100 equations in roughly 150 variables, the global approach is infeasible.

For that reason, instead of trying to find all solutions, we only intend to find one solution.

Indeed, finding one configuration in equilibrium sufficiently close to the initial configuration suffices to model the tensegrity's behavior. There is a myriad of algorithms to find a local optimum, e.g. conjugate gradient or quasi-Newton [234, p.101ff.], interior point [234, p.392f.] and augmented Lagrangian [234, p.497f.]. However, such methods usually require a good initialization, which we were not able to provide in our experiments. Consequently, we could not get them to converge to a critical point. Discussing this property further, Section 3.10 contains examples of geometric constraint systems for which Newton's method did not converge.

These methods' second drawback for our setting is that they try to balance the constraints with the objective function, while we really want the constraints to be satisfied at every iteration to prevent catastrophic behavior in the framework (cf. Section 2.1.3.1). As mentioned in Section 5.4, the constraints are smooth almost everywhere, so Riemannian optimization techniques become feasible. Consequently, we intend to use the Euclidean distance retraction introduced in Section 3.2.1 in combination with the Riemannian gradient descent Algorithm 3.2.7 to equilibrate the initial placement. As the problem of finding the closest point on an algebraic variety can be expressed as a square polynomial system with finitely many solutions [101], we can even use the previously mentioned homotopy continuation methods to solve it. In particular, this procedure yields a critical point of the Lagrange multiplier function corresponding to (5.4.7) and equivalently, a zero of the Lagrange multiplier system [234, p.321].

One may wonder how Riemannian optimization solves the previous issue of finding a sufficiently good initialization. As it turns out, while a cylinder packing's contact graph is too far away from a solution of optimization problem (5.4.7) to use local methods directly, it indeed is close enough to a feasible point to be analytically deformed into it by considering a single contact in space that is in balance (cf. [242, p.3]) and continuously deforming it. An algorithmic description of this procedure is included in Corollary 5.4.10's proof. Given a point on the constraint set, the theoretical convergence guarantees for the Riemannian gradient descent algorithm from Sections 3.3–3.4 apply.

Subsequently, we want to investigate the framework's displacement that occurs when expanding it in a fixed direction. As this extension can be realized as a one-parameter deformation path (cf. Definition 2.1.27), we can view it as a homotopy of polynomial systems. To solve it, we can employ the path-tracking Algorithm 3.2.10. The Riemannian optimization routine for equilibration followed by the path-tracking algorithm for computing deformation

paths of tensegrities are described in pseudocode by Algorithm 5.5.1.

---

**Algorithm 5.5.1:** Tensegrity deformation

---

**Inputs :** The rod packing's original tensegrity model (cf. Section 5.4), amount of steps  $N$  and a maximum extension  $T > 0$ .

**Output:** An animation of the one-parameter deformation of the tensegrity framework induced by stretching the rod packing in  $x$ -direction.

Replace each rod with a tetrahedron in accordance with the nonlinear optimization problem (5.4.7), yielding an objective function  $Q$  and a set of constraints  $g$ .

Apply the Riemannian gradient descent Algorithm 3.2.7 to find an energy minimum at  $x_0$ .

Formulate the Lagrange multiplier function  $\mathcal{L}(x, \lambda; \tau) = Q(x; \tau) + \lambda^T g(x; \tau)$ , yielding a deformation path parametrized by  $\tau \in [0, T]$  with  $\nabla_{x, \lambda} \mathcal{L}(x_0, \lambda_0; 0) = 0$ .

Apply Algorithm 3.2.10 to track  $\nabla_{x, \lambda} \mathcal{L}$ 's solution from  $(x_0, \lambda_0, 0)$  to  $(x_\tau, \lambda_\tau, \tau)$ , recording  $x(t)$ 's value at each step  $0 = t_0 < t_1 < \dots < t_N = T$  with  $t_i = t_{i-1} + T/N$ .

**return** the discretized curve  $x(t)$ .

---

## 5.6 Deformation Results for the Tensegrity Structures

We now have a system of constraints for our tensegrity framework and a robust optimization algorithm at hand. This enables us to tackle the problem of modeling the mechanical behavior of the tensegrity structures related to the  $\Pi^+$  and  $\Sigma^+$  rod packings from [107], which both display dilatant behavior. To set up the experiments, we first factor out rigid motions and consider the first coordinate as a parameter  $\tau$  that will induce the frameworks' extension. This leaves us with the lattice

$$\Lambda_\tau = \begin{pmatrix} \tau & 0 & 0 \\ c_{12}(\tau) & c_{22}(\tau) & 0 \\ c_{13}(\tau) & c_{23}(\tau) & c_{33}(\tau) \end{pmatrix}.$$

In the case of the  $\Pi^+$  tensegrity depicted in Figure 5.6.1, we record the framework's behavior for  $\tau \in [0.93, 1.52]$ , which amounts to an extension of roughly 63%. Beyond that, the structure is unstable. Having access to the lattice  $\Lambda_\tau$ , we can discretize the interval  $\mathcal{I}_{\Pi^+} = [0.93, 1.52]$  with step size  $10^{-3}$  and perform the path-tracking Algorithm 3.2.10 to learn the lattice generators' value at each step. For the Poisson's ratio, just the orthogonal directions are relevant, so only  $\Lambda_\tau$ 's diagonal entries are involved in the calculation.

In Figure 5.6.2, the orthogonal lattice extensions  $L_y$  and  $L_z$  in  $y$ - and  $z$ -direction respectively are depicted, along with the corresponding Poisson's ratios  $\nu_{xy}$  and  $\nu_{xz}$ . It allows us to conclude that the  $\Pi^+$  tensegrity is auxetic in terms of the definition from materials science (cf. Section 5.2), since the Poisson's ratio remains negative throughout the entire deformation path. The curves corresponding to the  $y$ - and  $z$ -direction are nearly identical, suggesting that the framework stays symmetric in these directions. Figure 5.6.1 depicts the tensegrity structures corresponding to two selected parameters from the chosen interval. We can use the pictures to qualitatively deduce that the  $\Pi^+$  packing extends in both  $y$ - and  $z$ -direction when stretched in

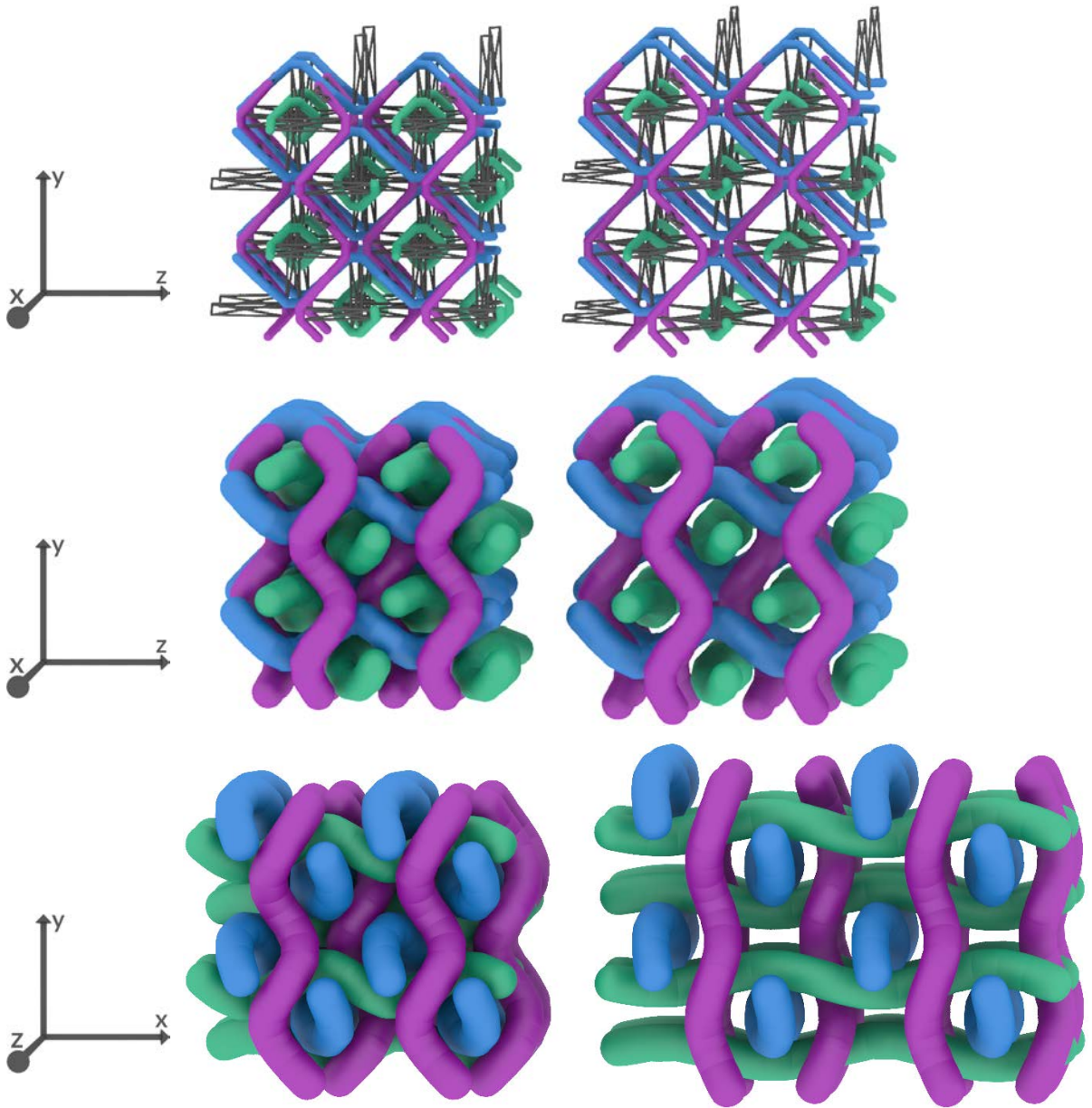


**Figure 5.6.1:** Eight unit cells of the  $\Pi^+$  tensegrity (t.) and its related cylinder packing (c., b.) at parameter values  $\tau = 1.0$  (l.) and  $\tau = 1.5$  (r.). The filaments' radii are displayed significantly smaller, without contacts, to better show how the structure deforms. The first projection is onto the  $yz$ -plane (t., c.), so the deformation's direction comes out of the page. In contrast, the second projection is onto the  $xy$ -plane (b.), showcasing the deformative behavior in  $x$ -direction.

$x$ -direction.

Moreover, we analyze the  $\Sigma^+$  tensegrity which is related to the structure found in skin cells. Two selected configurations of this material are depicted in Figure 5.6.3. Similar to  $\Pi^+$ , we stretch the framework in the  $x$ -direction, recording the framework's behavior for  $\tau \in [0.81, 1.52] = \mathcal{I}_{\Sigma^+}$ . Again, the structure is unstable outside of that region. Discretizing the interval  $\mathcal{I}_{\Sigma^+}$  with step size  $10^{-3}$  and performing the path-tracking Algorithm 3.2.10 allows us to calculate the Poisson's ratio. In Figure 5.6.4, the (orthogonal) lattice extensions  $L_y$  and  $L_z$  along with the corresponding Poisson's ratios  $\nu_{xy}$  and  $\nu_{xz}$  are displayed.

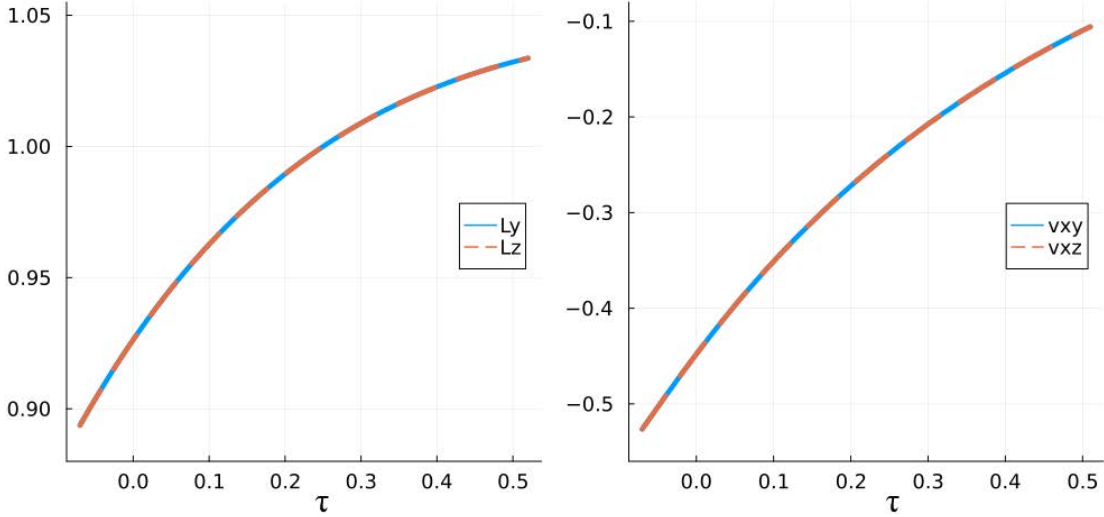


**Figure 5.6.2:** The lattice extensions  $L_y$  and  $L_z$  (l.) and the Poisson's ratios  $\nu_{xy}$  and  $\nu_{xz}$  (r.) corresponding to the homotopy of the  $\Pi^+$  tensegrity, taking the model framework from  $\tau = 0.93$  to  $\tau = 1.52$ . For each step with length  $10^{-3}$ , a data point is recorded. It can be observed that the lattice continuously grows from an extension of 0.89 to 1.04 in both  $y$ - and  $z$ -direction, amounting to a relative extension of 17%, compared to 63% in  $x$ -direction. The Poisson's ratio ranges from  $-0.52$  to  $-0.11$ , so the deformation path is auxetic. Contrary to the model introduced in Oster et al. [242], this model leads to an isotropic extension, signified by  $L_y$  and  $L_z$  behaving identically.

The Poisson's ratio's curve is smooth and both curves are almost identical, ensuring the rod packing's symmetry in  $y$ - and  $z$ -direction. Still, the Poisson's ratio does not assume the value of  $-1$  everywhere. We deduce that the packing cannot extend perfectly symmetrically. Furthermore, the Poisson's ratio is negative throughout the entire deformation path. As a result, auxeticity in terms of the definition from materials science is guaranteed.

It remains to investigate, whether the tensegrity structures are also auxetic by the geometric interpretation given in Definition 2.1.32. As was already proven in Proposition 5.2.2, the geometric definition of auxeticity is stronger than considering the Poisson's ratio. While the lattice  $\Lambda_\tau$  is not exactly diagonal, throughout the deformation paths the off-diagonal entries are orders of magnitude smaller than the lattice's diagonal entries for the tetrahedral models associated to both  $\Pi^+$  and  $\Sigma^+$ , giving us hope that the deformation path is geometrically auxetic after all.

Indeed, we can apply Proposition 5.2.4 to suggest that both tensegrity structures are auxetic. To do so, let us start with the  $\Pi^+$  tensegrity with corresponding deformation path parametrized by the interval  $\mathcal{I}_{\Pi^+}$ . First, we choose the step size  $3 \cdot 10^{-3}$ . Taking a look at the results our deformation path Algorithm 5.5.1 produced, we find that  $c_{ii}(\tau_1)/c_{ii}(\tau_2)$  is bounded above by 0.99975. Consequently, we can show that all three inequalities from Proposition 5.2.4 are satisfied for  $\alpha = 10^{-4}$ . We can then easily check that the off-diagonal entries' norms are bounded above by  $10^{-5}$  throughout the deformation path, implying that the operator defined in Equation (2.1.31) is a contraction.

By continuity, we can expect that this property persists for arbitrary discretizations and that the deformation path is actually auxetic as per Definition 2.1.32. This result is documented by Figure 5.6.5, which shows that the linear operator's norm is indeed bounded above by 1.

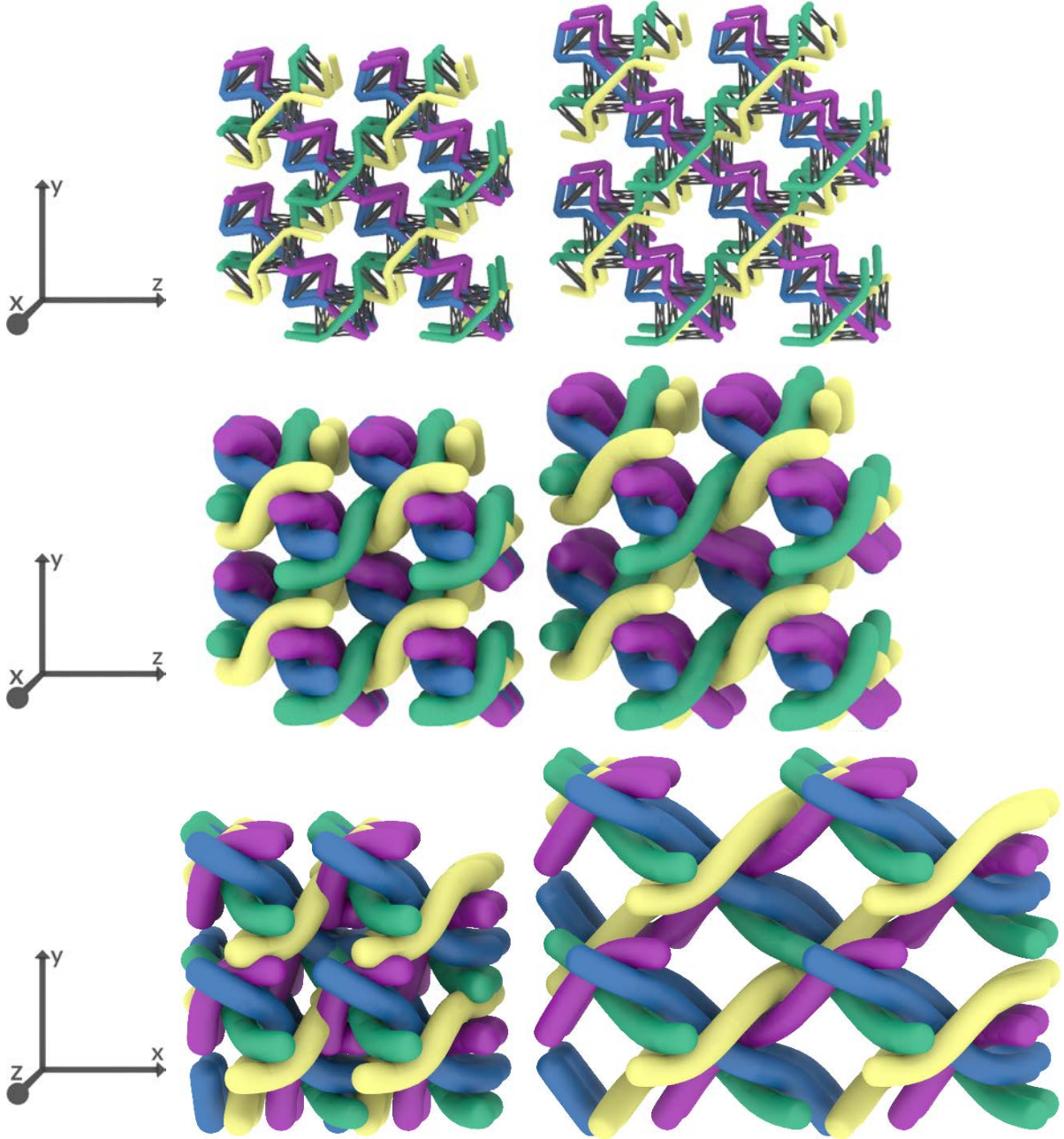


**Figure 5.6.3:** Eight unit cells of the  $\Sigma^+$  tensegrity (t.) and its related cylinder packing (c., b.) at parameter values  $\tau = 1.0$  (l.) and  $\tau = 1.5$  (r.). The filaments' radii are displayed significantly smaller, without contacts, to show how the structure deforms. The first projection is onto the  $yz$ -plane (t., c.), so the deformation's direction comes out of the page. The second projection is onto the  $xy$ -plane (b.), showcasing the deformative behavior in  $x$ -direction.

For the  $\Sigma^+$  tensegrity, the deformation path is parametrized by the interval  $\mathcal{I}_{\Sigma^+}$  with step size  $3 \cdot 10^{-3}$ . The numerical path-tracking Algorithm 3.2.10 returns  $c_{ii}(\tau_1)/c_{ii}(\tau_2) \leq 0.999962$  and that the off-diagonal entries' norms are bounded above by  $2 \cdot 10^{-6}$ . As Proposition 5.2.4 suggests,  $\alpha = 1.5 \cdot 10^{-5}$  suffices. Hence, the operator defined in Equation (2.1.31) is a contraction. Again, continuity suggests that arbitrary discretizations will have this property, so the deformation path is likely auxetic in the geometric sense, too. Figure 5.6.5 verifies this result. Close to  $\tau = 1.55$ , the Poisson's ratio is close to zero, which is consistent with the operator norms approaching 1.

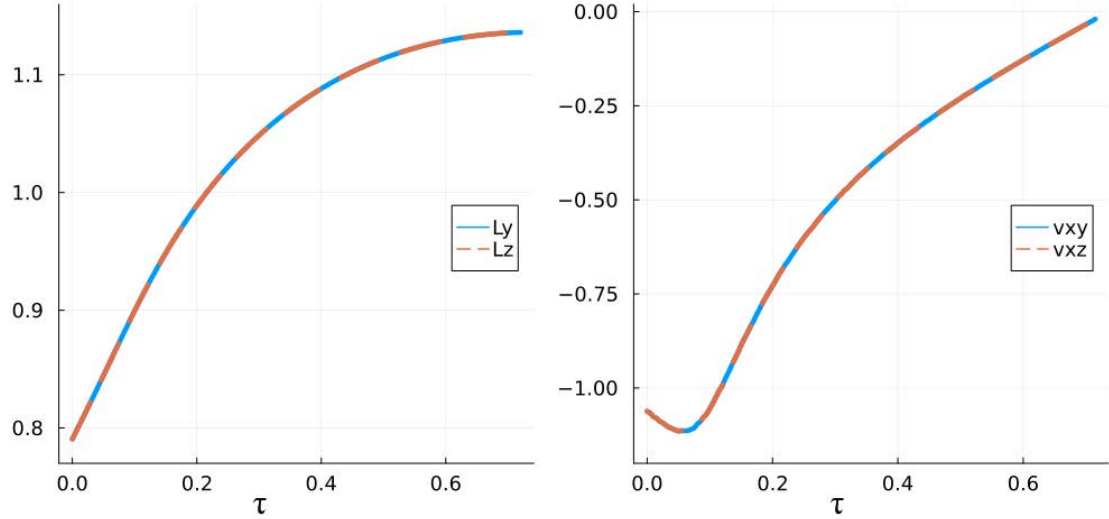


**Figure 5.6.4:** The lattice extensions  $L_y$  and  $L_z$  (l.) and the Poisson's ratios  $\nu_{xy}$  and  $\nu_{xz}$  (r.) corresponding to the homotopy of the  $\Sigma^+$  rod packing, taking the model framework from  $\tau = 0.81$  to  $\tau = 1.52$ . For each step with length  $10^{-3}$ , a data point is recorded. It can be observed that the lattice continuously grows from an extension of 0.79 to 1.14 in both  $y$ - and  $z$ -direction, amounting to a relative extension of 44%, compared to 88% in  $x$ -direction. The Poisson's ratio grows from  $-1.1$  over  $-1.3$  until  $-0.02$ , so the deformation path is auxetic in the engineer's sense. Contrary to the model introduced in Oster et al. [242], this model leads to an isotropic extension, signified by  $L_y$  and  $L_z$  behaving identically.

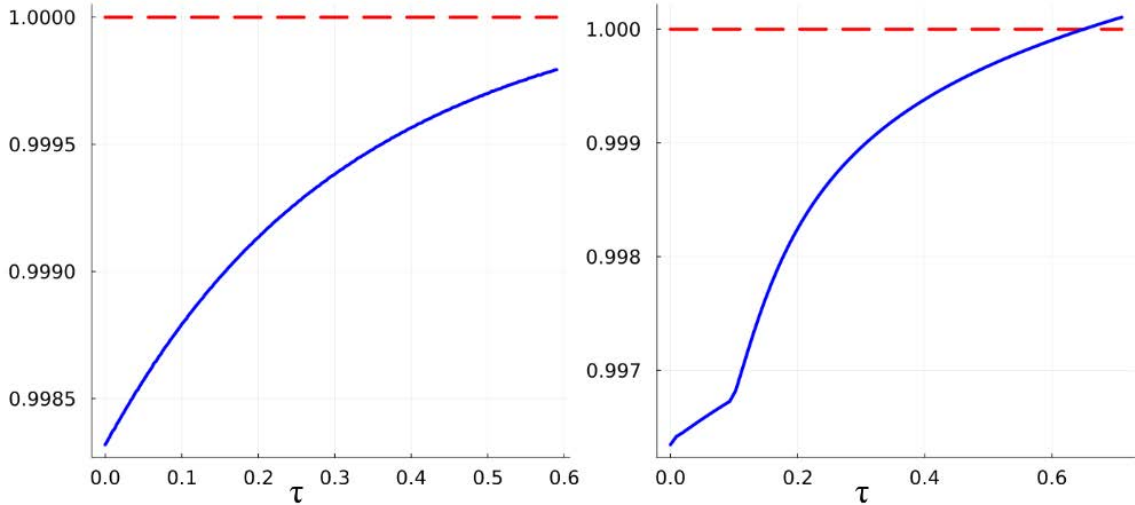


**Figure 5.6.5:** These diagrams depict the operator norms of the linear operator  $T_{\tau_2, \tau_1}$  taking the lattice  $\pi_\tau$  corresponding to  $\Pi^+$  tensegrity (l.) and the  $\Sigma^+$  tensegrity (r.) from time  $\tau_2$  to  $\tau_1$  (see Section 2.1.2.2) for fixed step length  $\tau_2 - \tau_1 = 3 \cdot 10^{-3}$ . Throughout most of the paths, the operator norm remains smaller than 1, suggesting that the deformation paths are auxetic by Definition 2.1.32, as expected. Intriguingly,  $\Sigma^+$  already becomes non-auxetic geometrically before the Poisson's ratio becomes positive.

As a final invariant of the frameworks' deformations corresponding to the rod packings  $\Pi^+$  and  $\Sigma^+$ , we consider the progression of the elastic cables' energy. As summarized in optimization problem (5.4.7), there are two different kinds of cables, that we call tetrahedral cables, if they are

located in the tetrahedron, or incoming cables, if they lie on the cylinders' central axes. These cables are different by their respective resting lengths  $r_{ij}$  and their elastic modulus  $c_{ij}$ . For this experiment, we choose  $r_{ij} = 0.15$  and  $c_{ij} = 1$  for the internal cables and  $r_{ij} = 2r$  and  $c_{ij} = 50$  for the tetrahedral cables for both  $\Pi^+$  and  $\Sigma^+$ . After scaling the energies of the respective initial configurations in order to make them comparable, the resulting energy diagrams are depicted in Figure 5.6.6.

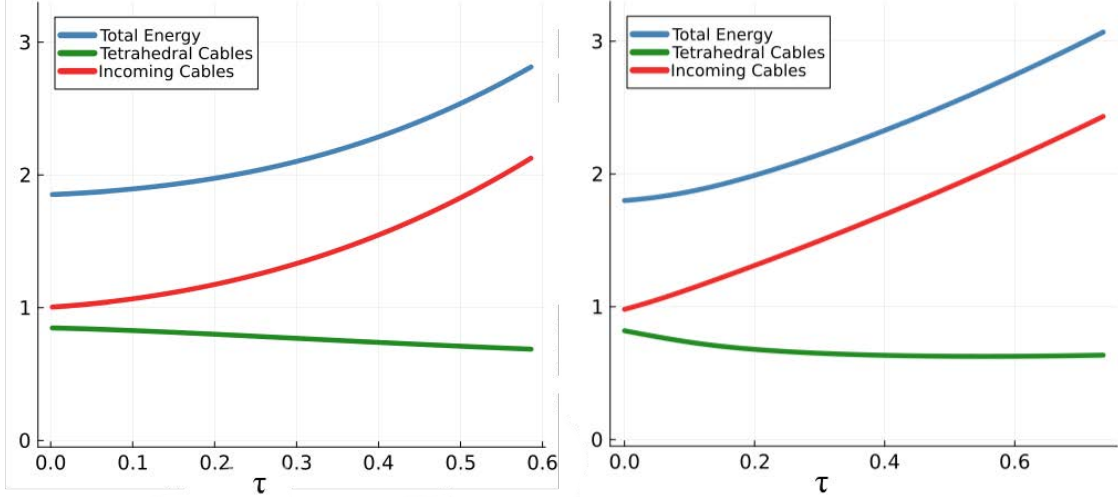


**Figure 5.6.6:** In these graphs, for the cylinder packings  $\Pi^+$  (l.) and  $\Sigma^+$  (r.) we depict the objective function (blue) of optimization problem (5.4.7) together with the energy terms corresponding to elastic cables inside the tetrahedron (green) and cables outside of it (red). Before applying Algorithm 3.2.10, the elasticity coefficients  $c_{ij}$  of the internal cables and the tetrahedral cables in optimization problem (5.4.7) have been chosen so that all three initial energies are comparable across both rod packings.

From this figure, it becomes clear that the energy distributions behave quite similarly. While in the  $\Pi^+$  rod packing, the tetrahedra seem to rotate with constant speed, for  $\Sigma^+$  there is an initial period where the cylinders rotate faster, though the energy stagnates at the end of the optimization. Conversely, the incoming cables' energy of  $\Pi^+$  behaves nonlinearly, while the corresponding energy of  $\Sigma^+$  seems to become linear at the end of the optimization. All in all, both graphs behave similarly, though.

## 5.7 Conclusion

In this chapter, the deformations of two examples of 3-periodic tensegrity structures are explored, showing that they are auxetic. We analyze the frameworks from a numerical optimization perspective, using the Euclidean distance retraction constructed in Chapter 3.2.1, as well as through existing techniques on geometric auxeticity. The result is a robust measurement of the Poisson's ratio of the tensegrity structures, which are clearly auxetic with well-behaved numerics. These results have a meaningful impact on theoretical materials science, where these structures are potential targets for auxetic material design. The tensegrity models also demonstrate the usefulness of numerical geometric techniques on complicated 3-periodic framework materials, where a more systematic study of material properties is necessary.

Our tensegrity structure is designed to mimic the mechanics of filament packings and shows

a dilatant property related to auxeticity. The parallel between the filament packing mechanics and the tensegrity is still a work in progress, but we believe that this study contributes to an understanding of the general problem. One complication is that the contacts of the filament packing are approximated by a constraint system designed for a perpendicular clasp. Yet, in a material this is not always the case. Generally, we should get a good approximation in a material where the filaments contact each other roughly perpendicularly and stay so throughout the deformation. More problematic results are expected, when this is not the case. This is indeed what we see in further examples. Refining this model, and more accurately modeling the mechanics of filamentous materials, is the subject of future research. In Section 6, we take a step in this direction by investigating weavings on surfaces.

In summary, we demonstrate the use of these mathematical techniques in obtaining meaningful results in materials science, where the high complexity of the structure is challenging for existing approaches. For the analysis of complicated material microstructures, we believe these techniques, which require research from both the materials science and mathematical perspective, are fruitful.

---

## Weaving Models on Manifolds

---

**Chapter Synopsis:** The spontaneous creation of curvature in woven materials is a fascinating topic with ramifications in intelligent fabrics, the inverse design of membranes and metal-organic frameworks. In this chapter, we extend the theory of weavings to surfaces in order to investigate the role of curvature. By considering the existing theory about frameworks on surfaces, we construct a robust tensegrity model to study weavings in curved space. This tensegrity model is suitable for analyzing tangled weaves and complex contact geometries. Taking the corresponding augmented edge function into account, this construction yields a nonlinear optimization problem that can be solved by applying the previously introduced Riemannian optimization techniques. We test our tensegrity model on various surface types and weavings. It is most robust on the sphere and the flat torus because there all points are geometrically identical. To find the weaving that energetically favors the sphere the most, the underlying surface is deformed into a spheroid using homotopy continuation. The energy landscape resulting from this deformation reveals that the more regular the weaving, the more it prefers the sphere.

Weaving is a technique of creating textiles by interlacing two distinct sets of threads or filaments. Examples include denim and linen, but also cotton fabric. Along with knitted and chemically-bonded fabrics, weavings constitute one of the most popular forms of textile. Weavings and entanglements are part of the same structure family as knots and polycatenanes and can be described using straight edges and corners [205]. This concept is reminiscent of bar-and-joint frameworks that are introduced in Section 2.1. When applying this construction to model weavings, we can study their topological features and their behavior under deformation.

Historically, weaving was considered to be “woman’s work” and many early “computers” were women [138]. Ada Lovelace was the first to see a connection between programming and the production of textiles [186]. Accordingly, textile production played an important role in technological advances and “the Jacquard loom is often [considered] as [...] a predecessor of the modern [...] computer” [114]. Instead of using binary to store information, the relevant instructions in weavings are encoded as “over” and “under”. In fact, it is likely that some terminology in modern programming such as “loops”, “spooling” and “threading” is derived from the production of textiles [175].

Nonetheless, weaving holds far greater cultural significance than merely representing a crafting technique. Women’s contributions to the foundations of Western society and culture have mostly remained unrecorded [260, p.12]. Anthropologists believe that textiles were used as a platform for women to tell and record stories and beliefs important to their culture, as women were often not allowed to read and write [193]. This claim is underpinned by the Latin origin “textus” of textiles, which translates to the past participle of “to weave”. When writing a text,

you are metaphorically weaving words.

The cultural significance of weavings is further highlighted by the diverse material properties that a woven material can assume [248]. Recent materials research has increasingly focused on the inverse design of curved surfaces and intelligent fabrics [9, 142, 258, 291]. Controlling heat transfer in fabrics could enable clothing to adapt its properties to changing weather conditions [271]. By selectively heating and cooling parts of a material, it is possible to create arbitrary shapes through the manipulation of curvature [9, 139]. The challenge of explicitly describing the necessary moves to construct a target surface from an initial material is known as the *inverse problem* for surfaces. Although “morphing a shape from 2D to 3D has been demonstrated in various ways,” the inverse problem is much harder to solve [9]. For a woven fabric, the problem translates to the task of specifying positions requiring actuation. Accordingly, an optimization-based design algorithm has been proposed for weaving the Kagome lattice with topological defects into an arbitrary shape [258]. This algorithm can produce any smooth surface out of curved ribbons and outputs an energy-minimized structure that is robust against deformations.

Indeed, the spontaneous creation of curvature is not limited to woven fabrics and elastic sheets. Membranes of interlocking rings are a generalization of both concepts. In chemistry, linked rings are called polycatenanes and are investigated for the construction of metal-organic frameworks [123] and covalent organic frameworks [97]. By considering chainmail-like arrangements of rings, it is possible to generate both positively- and negatively-curved surfaces [207]. Similarly, the threading of metal-peptide rings has led to the construction of various nanostructures, such as polyhedral links and torus knots [273]. Such entanglements of polymer rings can induce a topological phase transition from a liquid or gas to a gel, triggered by altering the stiffness of the polymers [40]. The spontaneous creation of curvature in entangled systems through geometric considerations is thus a scientifically relevant problem.

We begin this chapter by introducing the theory of bar-and-joint frameworks on surfaces in Section 6.1 to investigate how infinitesimal rigidity can be defined in Euclidean, elliptic, and hyperbolic geometries. By defining the augmented edge function, a geometric constraint system describing both the surface and the distance constraints is constructed. As it turns out, the frameworks’ rigidity properties depend on the dimension of the surfaces’ group of isometries. Using the coning operation for the sphere and the hyperboloid, any bar-and-joint framework constrained to these surfaces can be transformed into a classical bar-and-joint framework.

Based on the theory of frameworks on surfaces, we construct a discrete tensegrity model for weavings on surfaces in Section 6.2 to capture the weavings’ idealized behavior. For that reason, we generalize the definition of a weave in the Euclidean plane established by Fukuda et al. [121] to smooth, orientable surfaces  $\mathcal{M}$  with positive reach. On these surfaces, we consider the collection of  $N$  sets of colored geodesics such that two geodesics belong to the same color group if they do not intersect. An untwisted weave is then defined as the lift of the geodesics to the thickened surface  $\mathbb{X}^3(\mathcal{M})$  in such a way that no two geodesics intersect anymore. Given a crossing diagram that describes whether a geodesic passes over or under another curve in intersection points, the geodesics are either deformed into the positive or negative unit normal direction.

To construct a tensegrity model for weavings, each strand is described by a curvilinear

cylinder with a constant radius  $r > 0$ , seeking to minimize its length. Hence, elastic cables discretize the rods. At each intersection of two geodesics on  $\mathcal{M}$  two vertices are placed and constrained to the  $\pm\epsilon$ -offset surfaces of  $\mathcal{M}$ . A rigid bar is then inserted between these vertices to keep the two strands at a radius of  $2r$ . The rods mutually repulse each other, balancing the forces.

This construction resembles the tetrahedral tensegrity framework used in Chapter 5 to robustly model cylinder packings. Analogously, the geometric constraint system resulting from weavings on surfaces corresponds to a nonlinear optimization problem. To solve it via the Riemannian optimization techniques described in Chapter 3, we need a sufficiently good initial configuration. Such an initial configuration can be obtained by an analytic construction that we call the vertex split operation.

Having defined this tensegrity model for weavings on surfaces, we consider several examples of 4-regular nets on surfaces as a construction tool to explore the behavior and shortcomings of the model. With a few tricks, this construction can be augmented to allow vertices with a degree of 3. This adjustment produces entanglements where the strands twist around each other. In Hyde and Evans [169], such tangles are investigated on platonic solids and the authors provide a descriptive symbol in terms of the number of strands per edge and the associated twist. Some of the weavings considered in that article exist as metal-organic nanostructures [273], justifying our interest in studying them.

Finally, in Section 6.3 we investigate what happens to a spherical weaving, when the sphere is deformed into a spheroid, while fixing the volume. We use the robust path-tracking routine outlined in Chapter 3 to compute the resulting deformation of the weave. The goal of this section is to test our model against perturbations to determine which weave energetically favors a perfect sphere and which weave might prefer existing on a deformed sphere.

## 6.1 Frameworks on Surfaces

In the previous chapters, our analysis is limited to frameworks within  $\mathbb{R}^d$  and  $d$ -dimensional flat tori. In both instances, straight lines are the shortest connections between two points. Nevertheless, there is a natural extension of frameworks to curved space using metric geometry.

Since the most well-studied space in rigidity theory is the plane, considering weavings on surfaces is a natural generalization. More specifically, let  $\mathcal{M} \subset \mathbb{R}^3$  denote a smooth surface. According to Definition 3.1.6, the metric on the submanifold  $\mathcal{M}$  is automatically induced by the ambient metric on  $\mathbb{R}^3$ . In this section, we investigate the Euclidean metric  $ds$  and the Minkowski pseudo-metric  $ds_m$ , defined by

$$ds^2 = dx^2 + dy^2 + dz^2 \quad \text{and} \quad ds_m^2 = dx^2 + dy^2 - dz^2.$$

In addition, we can consider the degenerate metric that does not take the  $z$ -coordinate into account at all. It should be stressed that  $ds_m$  is not a metric on all of  $\mathbb{R}^3$ . In particular, on the cone  $x^2 + y^2 = z^2$  in  $\mathbb{R}^3$  (cf. Figure 2.1.10(r.)) the definiteness property is violated. Instead, it is called a *pseudo-Riemannian metric* [197, p.40f.]. Nevertheless, it makes sense to restrict the Minkowski metric to subsets of  $\mathbb{R}^3$ , as several models for the hyperbolic plane can be constructed

in this way [197, Thm. 3.7]. All these metrics are induced by bilinear forms

$$\langle x, y \rangle_a = x_1y_1 + x_2y_2 + a \cdot x_3y_3$$

for  $x, y \in \mathbb{R}^3$  and  $a \in \{-1, 0, 1\}$ . We have already encountered  $\langle \cdot, \cdot \rangle_1$  and  $\langle \cdot, \cdot \rangle_{-1}$  in Example 3.1.19. Some spherical, Euclidean and hyperbolic surfaces can be described in terms of these bilinear forms:

|                              |  |
|------------------------------|--|
| The 2-sphere:                | $S^2 = \{x \in \mathbb{R}^3 : \langle x, x \rangle_1 = 1\},$                   |
| The cylinder:                | $\mathcal{Z}^2 = \{x \in \mathbb{R}^3 : \langle x, x \rangle_0 = 1\},$         |
| The double cone:             | $\mathcal{C}^2 = \{x \in \mathbb{R}^3 : \langle x, x \rangle_{-1} = 0\},$      |
| The one-sheeted hyperboloid: | $\mathcal{H}_1^2 = \{x \in \mathbb{R}^3 : \langle x, x \rangle_{-1} = 1\}$ and |
| The two-sheeted hyperboloid: | $\mathcal{H}_2^2 = \{x \in \mathbb{R}^3 : \langle x, x \rangle_{-1} = -1\}.$   |

Analogous to Section 2.1.2, a *bar-and-joint framework*  $(G, p)$  on  $\mathcal{M}$  is a graph  $G = (V, E)$  together with an embedding  $p : V \rightarrow \mathcal{M}$ . Following Saliola and Whiteley [270], this construction lets us define first-order rigidity on surfaces.

**Definition 6.1.1.** Suppose  $(G, p)$  is a framework with a graph  $G = (V, E)$  and a realization  $p : V \rightarrow \mathcal{M}$  on the surface  $\mathcal{M}$  with ambient (pseudo-)Riemannian metric  $g : \mathbb{R}^3 \times \mathbb{R}^3 \rightarrow \mathbb{R}$ . An *infinitesimal motion* of the framework is an assignment  $(p, u) : V \rightarrow T\mathcal{M}$  of the vertices in the surface's tangent bundle with  $u(v) \in T_{p(v)}\mathcal{M}$  for all  $v \in V$  such that

$$g(p_i, u_j) + g(p_j, u_i) - g(p_i, u_i) - g(p_j, u_j) = 0 \quad (6.1.2)$$

for each  $ij \in E$ . A *trivial infinitesimal motion* is a map  $(-, u) : \mathcal{M} \rightarrow T\mathcal{M}$  that satisfies

$$g(x, u(y)) + g(y, u(x)) - g(x, u(x)) - g(y, u(y)) = 0$$

for all  $x, y \in \mathcal{M}$ . We call  $(G, p)$  *infinitesimally rigid* if all infinitesimal motions arise as the restrictions of trivial infinitesimal motions to the image  $p(V)$ . If  $(G, p)$  is not infinitesimally rigid, we call it *infinitesimally flexible*. Furthermore,  $(G, p)$  is called *minimally infinitesimally rigid* if  $(G, p)$  is rigid and the removal of any edge from  $G$  makes the framework infinitesimally flexible.

This definition subtly distinguishes trivial motions from nontrivial framework flexes in the following way: The trivial motions arise from isometries of the surface, while the infinitesimal motions are purely defined on the framework's coordinates. Inherently, this makes nontrivial motions a local property, while trivial motions constitute a global property of the surface. With this distinction in mind, we can show that Definition 6.1.1 generalizes planar rigidity as introduced in Section 2.1.2.

**Remark 6.1.3.** Planar rigidity in the Riemannian manifold  $(\mathbb{R}^2, \langle \cdot, \cdot \rangle)$  equipped with the Euclidean scalar product is a special case of framework rigidity on surfaces from Definition 6.1.1. When embedding  $\mathbb{R}^2 \hookrightarrow \mathbb{R}^3$  via  $(x, y) \mapsto (x, y, 0)$ , we can specify this relation by expanding the

linear equation for infinitesimal motions  $(p_i - p_j)^T \cdot (u_i - u_j) = 0$  (cf. Definition 2.1.13 or [287]). After comparing terms for the realization  $p$  and the infinitesimal motion  $u$  with Equation (6.1.2), we realize that both conditions are equal.

The following Definitions 6.1.4–6.1.5 appear in Nixon et al. [233]. They generalize the concept of genericity that is first introduced in Definition 2.2.2 and the rigidity matrix from Definition 2.1.13.

**Definition 6.1.4.** Suppose the surface  $\mathcal{M} \subset \mathbb{R}^3$  is given by the vanishing locus of an irreducible polynomial  $m \in \mathbb{Z}[x, y, z]$ . Then, a framework  $(G, p)$  is called *generic* on  $\mathcal{M}$  if the algebraic dependence  $h(\{x_i\}, \{y_i\}, \{z_i\}) = 0$  holds between the coordinates  $(x_i, y_i, z_i)$  of all points  $p_i$  only if  $h$  lies in the ideal  $\langle m(x_i, y_i, z_i) : i = 1, \dots, |V| \rangle$ .

In other words, any rational polynomial  $h$  vanishing on the generic realization  $p \in \mathcal{M}^{|V|}$  vanishes on all of  $\mathcal{M}^{|V|}$ . Analogous to the planar case in Definition 2.1.13, we can formulate the rigidity matrix for surfaces.

**Definition 6.1.5.** The *rigidity matrix*  $R_{\mathcal{M}}(G, p)$  of a framework  $(G, p)$  on a surface  $\mathcal{M} \subset \mathbb{R}^3$  given by the vanishing locus of some smooth function  $m : \mathbb{R}^3 \rightarrow \mathbb{R}$  is given by  ${}^{1/2} \cdot (df_G)(p)$ . This expression is half the Jacobian of the augmented edge-function  $\tilde{f}_G : \mathbb{R}^{|V|} \rightarrow \mathbb{R}^{|E|+|V|}$  which includes the surface constraints, namely

$$\tilde{f}_G(q) = \begin{pmatrix} \|q_i - q_j\|^2 & \text{for } ij \in E \\ m(q_i) & \text{for } i = 1, \dots, |V| \end{pmatrix}$$

for the Euclidean norm  $\|\cdot\|$ . A surface  $\mathcal{M}$  has *type k* if  $\dim(\ker(R_{\mathcal{M}}(K_n, p))) \geq k$  for all complete graph frameworks  $(K_n, p)$  with  $n \geq 1$  on  $\mathcal{M}$  and  $k$  is the largest such number.

The infinitesimal motions of  $(G, p)$  span the kernel of  $R_{\mathcal{M}}(G, p)$  (cf. Definition 6.1.1). As a consequence, the type of a surface  $\mathcal{M}$  characterizes the dimension of the isometry Lie group of  $\mathcal{M}$ . For computing the trivial infinitesimal motions corresponding to a framework  $(G, p)$ , it suffices to compute all infinitesimal motions of the complete framework  $(K_n, p)$  on  $n = |V|$  vertices, provided that  $n \geq 6 - k$  where  $k$  is the type of the surface [233, p.11].

| Surfaces   | Type | cf. Source |
|--|------|------------|
| Plane $\mathbb{R}^2$ , sphere $S^2$ , hyperboloids $\mathcal{H}_1^2$ and $\mathcal{H}_2^2$ | 3    | [232, 270] |
| Cylinder $\mathcal{Z}^2$ , flat torus $\mathbb{R}^2/\mathbb{Z}^2$                          | 2    | [232, 265] |
| Double cone $\mathcal{C}^2$ , torus of revolution, spheroid                                | 1    | [233]      |
| Ellipsoid, general surfaces  | 0    | [233]      |

**Table 6.1.6:** Surfaces defined by the metric  $\langle \cdot, \cdot \rangle_a$  for  $a \in \{\pm 1, 0\}$  and their corresponding types, i.e. the dimension of their isometry group.

Having encountered the surface type  $k$  multiple times, we want to understand what values  $k$  can attain. For algebraic surfaces of type  $0 \leq k \leq 3$  there exists a classification of the corresponding surfaces. The corresponding results are collected in Table 6.1.6. We can formulate the following theorem about the infinitesimal rigidity of frameworks constrained to surfaces.

**Theorem 6.1.7** (cf. [232]). *Let  $(G, p)$  be a minimally infinitesimally rigid, generic framework on the algebraic surface  $\mathcal{M}$  of type  $k$ , with  $G$  not equal to the complete graph  $K_1, K_2, K_3$  or  $K_4$ . Then,  $|E| = 2|V| - k$  and for every subgraph  $H$  of  $G$  with at least one edge it holds that  $|E(H)| \leq 2|V(H)| - k$ .*

### 6.1.1 Coning

A popular tool in rigidity theory to transfer results about a framework's rigidity from  $\mathbb{R}^d$  to  $\mathbb{R}^{d+1}$  is *coning* [326]. To define this operation, assume that  $G = (V, E)$  denotes a graph. By adding a vertex  $v$  to  $G$  alongside an edge to all previously present vertices  $V$ , we obtain the *cone graph*  $G * \{v\}$ . Given  $v \notin V$ , coning a graph therefore corresponds to the construction

$$G * \{v\} = \left( V \cup \{v\}, E \cup \bigcup_{w \in V} \{vw\} \right).$$

On framework level, denote a realization of the graph  $G$  by  $p : V \rightarrow \mathbb{R}^d$ . We embed  $\mathcal{F} = (G, p)$  in the hyperplane  $\{x \in \mathbb{R}^{d+1} : x_{d+1} = 1\}$  via  $p_i \mapsto (p_{i1}, \dots, p_{id}, 1) \in \mathbb{R}^{d+1}$  for each  $i = 1, \dots, d$ . Subsequently,  $G$  is coned with the vertex  $v \notin V$  that is placed in the origin, yielding the *cone framework*

$$\mathcal{F} * \{v\} = \left( G * \{v\}, p^* : V \cup \{v\} \rightarrow \mathbb{R}^{d+1} \right)$$

with  $p^*(w) = (p_{i1}, \dots, p_{id}, 1)$  for  $w \neq v$  and  $p^*(v) = 0$  [288]. The *cone rigidity matrix* (cf. Definition 2.1.13) is then constructed by adding  $|V|$  rows and columns to the original rigidity matrix  $R_G(p)$ , reflecting the  $|V|$  new edges and  $|V|$  new coordinates for each  $w \in V$ . Note that the cone vertex  $v$  is omitted from the columns of the rigidity matrix. Adding  $v$  would increase the kernel's dimension by  $d + 1$  and its omission restricts the potential infinitesimal motions to those that keep the origin unchanged [288]. Coning is a useful operation, as the space of infinitesimal motions of  $(G * \{v\}, p^*)$  is isomorphic to the space of infinitesimal motions of  $(G, p)$ . The same holds for the equilibrium stresses, and coning preserves infinitesimal rigidity (cf. [288, Thm. 3.1]).

Since infinitesimal rigidity in the plane has the same combinatorial characterization as the infinitesimal rigidity of frameworks on the sphere and the hyperboloid (cf. Theorem 6.1.7), it can be expected that coning is feasible in these contexts as well. Indeed, a framework coned in the origin is identical to a framework constrained to the sphere [288]. For other surfaces such as the hyperboloid, the approach is not as direct. A suitable projection must be chosen, making the combinatorial classification of infinitesimal rigidity on the sphere and the one- and two-sheeted hyperboloid identical [270]. Allowing a different measurement function on the framework's edges than Euclidean distance, the hyperboloid is a sphere in Minkowski space. An analogous argument to the one used for the sphere makes coning in the origin identical to constraining frameworks to the hyperboloid. Therefore, studying frameworks constrained to the hyperboloid and the sphere is equivalent to using the established rigidity theory of unconstrained bar-and-joint frameworks.

### 6.1.2 Concentric Spheres

Up until now, the considered surfaces have all been connected. However, to untwist a weave it needs to be lifted to the thickened plane, meaning that the underlying framework's vertices need to be transformed to the associated  $\pm\varepsilon$ -offset surfaces. The two offset surfaces associated with an oriented 2-dimensional manifold are discussed in the context of Steiner's Theorem 4.1.14 that relates the surface area of the  $\pm\varepsilon$ -offset surfaces with the mean and Gaussian curvature. Given an oriented surface  $\mathcal{M}$ , the  $\pm\varepsilon$ -offset surface  $\mathcal{M}_{\pm\varepsilon}$  can be defined as

$$\mathcal{M}_{\pm\varepsilon} = \bigcup_{p \in \mathcal{M}} \{p \pm \varepsilon \cdot n_{\mathcal{M}}(p)\}$$

for a continuous unit normal field  $n_{\mathcal{M}}(p)$ . Until now,  $\pm\varepsilon$ -offset surfaces are not covered by the previously introduced theory of frameworks. Still, for concentric spheres, planes, and cylinders, minimal infinitesimal rigidity can be characterized as follows:

**Theorem 6.1.8** (cf. [233]). *Assume  $G = (V, E)$  is a graph and let  $\mathcal{M}$  be a union of parallel planes or a union of concentric spheres and let  $p$  be generic on  $\mathcal{M}$ . Then  $(G, p)$  is minimally infinitesimally rigid on  $\mathcal{M}$  if and only if  $G$  is the complete graph  $K_1$ ,  $K_2$  or  $|E| = 2|V| - 3$  and for every subgraph  $H$  of  $G$  with at least one edge:  $|E(H)| \leq 2|V(H)| - 3$ .*

**Theorem 6.1.9** (cf. [233]). *Assume  $G = (V, E)$  is a graph and let  $\mathcal{M}$  be a union of parallel cylinders and let  $p$  be generic on  $\mathcal{M}$ . Then  $(G, p)$  is minimally infinitesimally rigid on  $\mathcal{M}$  if and only if  $G$  is the complete graph  $K_1$ ,  $K_2$ ,  $K_3$  or  $|E| = 2|V| - 2$  and for every subgraph  $H$  of  $G$  with at least one edge:  $|E(H)| \leq 2|V(H)| - 2$ .*

By Table 6.1.6, the sphere and plane have type 3, while the cylinder has type 2. Therefore, the combinatorial characterization of rigidity is preserved in the cases specified by these theorems. Moreover, there is a simple description of the  $\varepsilon$ -offset surfaces. For the Euclidean plane given in Hesse normal form  $n_1x + n_2y + n_3z = \mathbf{n}^T \mathbf{a}$  with unit normal  $\mathbf{n} = (n_1, n_2, n_3)$  and support vector  $\mathbf{a}$ , the  $\pm\varepsilon$ -offset surfaces are characterized by a translation of the support vector by  $\pm\varepsilon \mathbf{n}$ . On the cylinder of radius  $r > 0$  defined by the implicit equation  $x^2 + y^2 = r^2$ , as well as on the sphere of radius  $r > 0$  given by the equation  $x^2 + y^2 + z^2 = r^2$ , the  $\pm\varepsilon$ -offset surfaces can be generated by substituting the radius  $r$  with  $(1 \pm \varepsilon)r$ .

## 6.2 Weavings on Surfaces

Following Fukuda et al. [121], a weave in the Euclidean plane can be described by geodesics (cf. Definition 3.1.14) in  $\mathbb{R}^2$  belonging to  $N \geq 2$  disjoint families or *color groups* that are at most countably infinite. Denote this set by  $\mathcal{F} = F_1 \sqcup \dots \sqcup F_N$ . Assume that two geodesics from the same family  $F_i$  do not intersect, have a distance of at least  $\epsilon$  for some  $\epsilon > 0$ , and that no three geodesics intersect in the same point. Each intersection between curves from different color groups is then given an additional over- or under-information. In knot theory, this is called a *crossing*  $\chi : \mathbb{R}^2 \times \mathcal{F}^2 \rightarrow \{-1, 0, 1\}$  [88, p.6]. The map  $\chi$  assigns 0 if the geodesics do not intersect in  $p \in \mathbb{R}^2$  and  $\chi_p(\gamma, \mu) = 1$  if geodesic  $\gamma \in \mathcal{F}$  passes over geodesic  $\mu \in \mathcal{F}$  in  $p \in \mathbb{R}^2$ . In case that  $\gamma$  passes under  $\mu$  in  $p$ , this map attains the value  $\chi_p(\gamma, \mu) = -1$ .

It becomes apparent that the value of the crossing depends on the order of the curves. As a consequence, we assume antisymmetry: For each  $p \in \mathbb{R}^2$  and geodesics  $\gamma \in \mathcal{F}$  and  $\mu \in \mathcal{F}$  it holds that  $\chi_p(\gamma, \mu) = -\chi_p(\mu, \gamma)$ . Following a specific geodesic  $\gamma$  thus gives rise to a sequence in  $\{-1, 1\}$  with an entry whenever another curve intersects  $\gamma$ . This is called the *crossing sequence* of the weave. Finally, the *untwisted weave* is the lift of  $\bigcup_{\gamma \in \mathcal{F}} \text{im}(\gamma)$  to the thickened Euclidean plane  $\mathbb{X}^3 = \mathbb{R}^2 \times [-1, 1]$  which respects the crossing information and which satisfies that the lifted geodesics, called *threads*, do not intersect in  $\mathbb{X}^3$  [121]. The procedure of lifting the weave in  $\mathbb{R}^2$  to  $\mathbb{X}^3$  is depicted in Figure 6.2.1 for a single-vertex weave with  $N = 2$ .

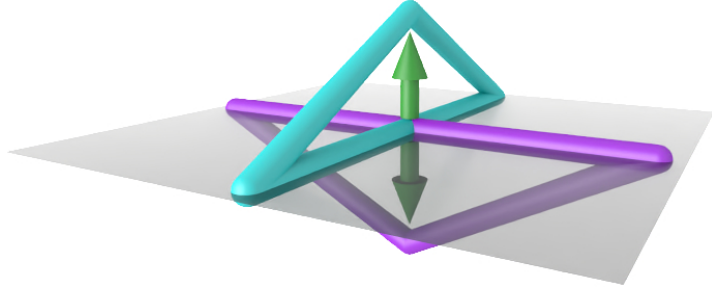


**Figure 6.2.1:** Intuitively, lifting a weave to the thickened Euclidean plane can be understood as separating a vertex of degree 4 into two vertices of degree 2.

The relevant information can be recorded in a graph that has a node for every occurring intersection between two geodesics. Each vertex in this graph is of degree 4. Its edges between vertices  $p$  and  $q$  correspond to open geodesic segments  $\gamma(I)$  for  $I = (a, b)$  such that  $\gamma(a) = p$ ,  $\gamma(b) = q$  and

$$\gamma(I) \cap \bigcup_{\mu \in \mathcal{F} \setminus \{\gamma\}} \text{im}(\mu) = \emptyset.$$

By construction, no three geodesics intersect in the same point, justifying that the graph is 4-regular. There are only finitely many families of geodesics, each of which contains countably many curves. The line segment  $\gamma(I)$  is non-empty, since  $d(\gamma(a), \gamma(b)) \geq \epsilon$  by assumption. These two arguments conclude that there are countably many crossings inside  $\mathcal{F}$ .

Now, geodesics in  $\mathbb{R}^2$  are simply lines. Even when considering periodic weavings defined in a flat torus, the corresponding geodesics are lines again. One may wonder why we choose to define the weavings in such a general way. As it turns out, we can generalize the definition of weaves on the plane to orientable Riemannian surfaces  $\mathcal{M}$  in  $\mathbb{R}^3$ . In this setting, the term “geodesic” becomes more intricate.

The Tubular Neighborhood Theorem 3.1.7 guarantees that every embedded submanifold of  $\mathbb{R}^3$  has a tubular neighborhood. In other words, there exists a continuous function  $\delta : \mathcal{M} \rightarrow \mathbb{R}_{>0}$  with the property that the subset of the normal bundle given by

$$V_\delta = \{(p, v) \in N\mathcal{M} : |v| < \delta(p)\}$$

is diffeomorphically mapped to an open subset of  $\mathbb{R}^n$  under the addition map  $E(p, v) = p + v$ . We call the image  $E(V_\delta)$  a *tubular neighborhood*, carrying a useful intuition of the appearance of this set. A related property is the *local reach*  $\tau_{\mathcal{M}}(p)$  of  $\mathcal{M}$ . It can be defined as the maximum

distance  $r \geq 0$  such that any point  $q \in p + N_p\mathcal{M}$  at a distance less than  $r$  from  $p$  has a unique closest point on  $\mathcal{M}$  [53, Eq. (15.1)]. The surface's *reach*  $\tau_{\mathcal{M}}$  is then given by the infimum  $\inf_{p \in \mathcal{M}} \tau_{\mathcal{M}}(p)$  [53, p.195]. This result lets us define weavings on surfaces.

**Definition 6.2.2.** Let  $(\mathcal{M}, g)$  denote a 2-dimensional Riemannian manifold in  $\mathbb{R}^3$  with positive reach  $\tau_{\mathcal{M}} > 0$ . Given  $N \in \mathbb{N}$  color groups  $\mathcal{F} = F_1 \sqcup \dots \sqcup F_N$  consisting of geodesics on  $\mathcal{M}$ , the *crossing diagram* is defined via  $\chi : \mathcal{M} \times \mathcal{F}^2 \rightarrow \{-1, 0, 1\}$ . This map assigns 0 if the geodesics  $\gamma, \mu \in \mathcal{F}$  do not intersect in  $p \in \mathcal{M}$  or  $\gamma = \mu$ . This function evaluates to  $\chi_p(\gamma, \mu) = 1$  if the geodesic  $\gamma$  passes over the geodesic  $\mu$  in  $p \in \mathcal{M}$ . In addition,  $\chi$  is antisymmetric, meaning that  $\chi_p(\gamma, \mu) = -\chi_p(\mu, \gamma)$ . We define the corresponding *untwisted weave* as the lift of  $\mathcal{F}$  to the tubular neighborhood  $\mathbb{X}^3(\mathcal{M})$ , given by the image of the set

$$\bigcup_{p \in \mathcal{M}} \{p\} \times \left( N_p\mathcal{M} \cap \overline{B_\varepsilon(0)} \right) \subset N\mathcal{M}$$

under the addition map  $E(p, v) = p + v$  for some  $\varepsilon \in (0, \tau_{\mathcal{M}})$ . The lift of  $\mathcal{F}$  is chosen in such a way that no two curves intersect.

A positive local reach does not necessarily extend to the entire manifold, as one can easily imagine the sequence  $(\frac{1}{n})_{n \in \mathbb{N}}$  that is always positive but converges to 0. Nevertheless, compact manifolds have a positive reach that can be chosen as a global constant [197, Lemma 6.16]. For the approach of this chapter to work it is reasonable to assume that the surfaces in consideration are compact. In case a surface is not compact, we can intersect it with a compact set, such as the hypercube. Since the 2-dimensional algebraic sets introduced in Section 6.1 are all closed, the set resulting from this operation is compact again.

**Remark 6.2.3.** In the case of the Euclidean plane embedded in  $\mathbb{R}^3$  via  $(x, y) \mapsto (x, y, 0)$ , the surface's normal space at any point is given by the line  $t \mapsto (0, 0, t)$  for  $t \in \mathbb{R}$ . Intersecting the normal space with the closed ball  $\overline{B_1(0)}$  recovers the interval  $[-1, 1]$  that was used in the construction of the thickened Euclidean plane  $\mathbb{X}^3$ . Therefore, Definition 6.2.2 is a true generalization of the definition of weaves from Fukuda et al. [121] to Riemannian manifolds.

Rather than using the entirety of the tubular neighborhood  $\mathbb{X}^3(\mathcal{M})$ , we only want to consider the boundary  $\partial\mathbb{X}^3(\mathcal{M})$ . This approach is motivated by Section 6.1.2. If  $\mathcal{M}$  is orientable, we can smoothly choose a unit normal field  $n_{\mathcal{M}}(p)$  (cf. [198, p.380f.]), leading to the equality

$$\partial\mathbb{X}^3(\mathcal{M}) = \bigcup_{p \in \mathcal{M}} p \pm \varepsilon \cdot n_{\mathcal{M}}(p).$$

Provided that  $\varepsilon < \tau_{\mathcal{M}}$ , the boundary of  $\mathbb{X}^3(\mathcal{M})$  splits into two disconnected branches. By Theorem 6.1.8, the rigidity on concentric spheres is combinatorially identical to that on the sphere. Hence, this approach seems promising.

**Example 6.2.4.** To understand the procedure of how to transform a crossing diagram into an untwisted weave, consider the octahedron. As a polytope, it constitutes a tesselation of the unit sphere. As a visual aid, the octahedron's edges are first orthogonally projected onto the sphere. The resulting crossing diagram with 3 color groups is depicted in Figure 6.2.5(l.).

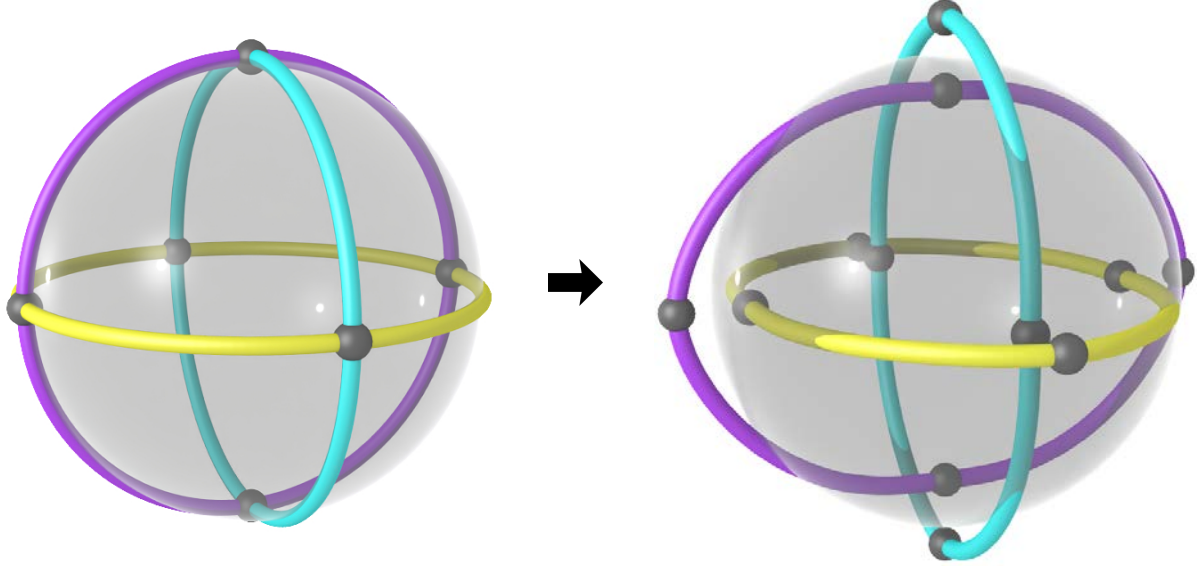


**Figure 6.2.5:** The octahedron gives rise to a weaving diagram on the unit sphere with  $N = 3$  color groups (l.). Using appropriate crossing information, the weave can be lifted to  $\mathbb{X}^3(S^2)$ , where it avoids intersections (r.). This structure is also known as the polyhedral winding  $[\frac{1}{2}]_{\text{tet}}$  on the tetrahedron (cf. [169]) and is equal to the 3-component Borromean rings.

Since the unit sphere's injectivity radius is 1, the  $\varepsilon$  that we intend to deform the vertices to can be chosen rather liberally. By the Cauchy-Dehn Theorem 2.3.4, the octahedron is infinitesimally rigid. If we choose  $\varepsilon > 0$  sufficiently small, the untwisted weave that has an additional bar between the vertices that have been generated from the same vertex, is rigid as well.

### 6.2.1 A Tensegrity Model for Weavings

In this section, we build a discrete, geometric model based on a nonlinear optimization problem for weavings on surfaces. As introduced in Section 2.1.3, a tensegrity framework is as an embedded graph with rigid bars and flexible cables under tension, modeled after one-sided Hookean springs. However, this definition is a special case of the classical definition for tensegrity frameworks, which contains a third element. The following complete definition appears in Roth and Whiteley [266].

**Definition 6.2.6.** Suppose we are given a graph  $G = (V, E)$  where the edge set is partitioned as  $E = \mathcal{B} \sqcup \mathcal{C} \sqcup \mathcal{S}$  into bars  $\mathcal{B}$ , cables  $\mathcal{C}$  and struts  $\mathcal{S}$ . A *d-dimensional tensegrity framework* is the pairing of such a graph  $G$  with a realization  $\varphi : V \rightarrow \mathbb{R}^d$ . The bars  $\mathcal{B}$  come with polynomial equations fixing their length; the cables are under tension and the struts are under compression.

Analogous to Section 2.1.3, the equilibration of a tensegrity framework can be modeled as a nonlinear optimization problem. In this model, cables and struts are represented by one-sided Hookean springs, while bars are treated as Euclidean distance constraints.

As described in Chapter 5, curvilinear cylinder packings can be modeled by a tensegrity framework by placing cables along the threads' central axes and bars between touching threads to maintain their appropriate distance. Weavings generalize cylinder packings when thinking of the yarn as compressible cylinders, making associated solution strategies applicable. In this

chapter, the balancing equations (cf. Equation 5.4.3–5.4.6) are replaced by constraining the points to  $\varepsilon$ -offset surfaces. By placing struts between vertices that are adjacent in the crossing diagram and are on the same side of the surface, e.g. in  $\bigcup_{p \in \mathcal{M}} p + \varepsilon \cdot n_{\mathcal{M}}(p)$  for a unit normal field  $n_{\mathcal{M}}(p)$ , the weave is regularized. The choice of unit normal does not matter here, only that we can choose a unit normal field consistently. This is possible by  $\mathcal{M}$ 's orientability. In this scenario, the struts model that two adjacent threads repulse themselves: The closer they are, the more the thread between them needs to bend.

Starting from a 4-connected, embedded graph  $(G = (V, E), \varphi : V \rightarrow \mathcal{M})$ , we first introduce the discrete analogue of a crossing sequence  $\chi : E^2 \rightarrow \{-1, 0, 1\}$  that was previously introduced for color groups of geodesics in Section 6.2.

**Definition 6.2.7.** Given a 4-regular graph  $G = (V, E)$ , a *crossing sequence* is an antisymmetric map  $\chi : E^2 \rightarrow \{\pm 1, 0\}$  with the following property: Given any vertex  $v \in V$  with adjacent edges  $e_1, \dots, e_4$ , the function  $\chi$  attains the value  $+1$  on exactly four pairs of distinct edges  $(e_1, e_3)$ ,  $(e_1, e_4)$ ,  $(e_2, e_3)$ , and  $(e_2, e_4)$ , in such a way that the same two edges only appear in the first position and the other two edges only appear in the last position.  $\chi$  has the value  $(-1)$  on the reversed pairs by its antisymmetry and is 0 everywhere else.

In other words, the indicator function  $\chi$  is 0 if  $e_1$  and  $e_2$  belong to the same thread, when the edges  $e_1$  and  $e_2$  are not adjacent, or when  $e_1 = e_2$ . The crossing sequence  $\chi$  describes whether one thread passes above or below the other thread. Using this information, we perform the vertex split operation visualized in Figure 6.2.1. In rigidity theory, this construction involves removing an edge  $uv$  and a vertex  $v$  and adding a complete graph  $K_3$  on the vertices  $u, v_1, v_2$ , while the original edges  $xv$  are either assigned to  $xv_1$  or  $xv_2$  (cf. [233]). However, it is necessary to transform the graph on the surface to the coned framework first (cf. Section 6.1.1) and choose the coned vertex 0 as base point  $u$ . In that case, the vertex split preserves the framework's rigidity [184, Lem. 4.1]. As previously observed, coning does not apply to arbitrary surfaces, making a new definition necessary.

Given a framework supported on a surface  $\mathcal{M}$ , the *vertex splitting move* in this chapter's context removes an edge  $uv$  and a vertex  $v$  and adds the vertices  $v_1, v_2$  and edges  $v_1v_2$  and either  $uv_1$  or  $uv_2$ , creating a new framework. The new vertices are initially realized in the same position but are later transformed to the  $\pm\varepsilon$ -offset surfaces. The original edges  $xv$  are either assigned to  $xv_1$  or  $xv_2$ , making the operation consistent. Hence, the vertex splitting move transforms the embedded graph to a framework in the thickened surface  $\mathbb{X}^3(\mathcal{M})$ . It corresponds to the augmented embedding

$$\begin{aligned} \overline{\varphi}_\varepsilon : V_+ \sqcup V_- &\rightarrow \partial \mathbb{X}^3(\mathcal{M}), & v_+ &\mapsto \varphi(\pi(v_+)) + \varepsilon \cdot n_{\mathcal{M}}(\varphi(\pi(v_+))) \\ && v_- &\mapsto \varphi(\pi(v_-)) - \varepsilon \cdot n_{\mathcal{M}}(\varphi(\pi(v_-))) \end{aligned} \tag{6.2.8}$$

for the over vertices  $V_+ \cong V$  and the under vertices  $V_- \cong V$  with the canonical isomorphisms  $\iota_+ : v \mapsto v_+$  and  $\iota_- : v \mapsto v_-$ . It is also necessary to define the projection  $\pi : V_+ \sqcup V_- \rightarrow V$  mapping the split vertices to the original vertex:  $\pi(v_+) = \pi(v_-) = v$  for all  $v_+ \in V_+$  and  $v_- \in V_-$ . This framework's set of cables  $\mathcal{C}$  is then given by an embedding of the original, 4-regular graph's edge set  $\iota_\chi : E \rightarrow \binom{V_+ \sqcup V_-}{2}$  such that  $\{v, w\}$  maps to one of the four edges

$\{v_{\pm}, w_{\pm}\}$ . The specific edge is found by the crossing information: If  $\chi(\{v, w\}, e) \geq 0$  for all  $e \in E$  incident to  $v$ , then the target edge's first entry is  $v_+$ , else  $v_-$ . By Definition 6.2.7, it is impossible for the crossing sequence  $\chi(\{v, w\}, e)$  to attain both positive and negative values for  $e \in E$  that are adjacent to  $v$ . An analogous argument constructs the image of the edge's endpoint  $w$  from the crossing diagram. Another operation that becomes useful later on is *edge-doubling*, where a single edge between two vertices is replaced with a double edge. This allows us to make more general networks than 4-regular graphs admissible. The following proposition demonstrates that all the aforementioned operations are rigidity-preserving.

**Proposition 6.2.9.** *Edge-doubling preserves the local rigidity of any framework  $\mathcal{F}$  in  $\mathbb{R}^3$ . If every vertex of  $\mathcal{F}$  has degree 4, then vertex-splitting is rigidity-preserving. The lift  $\bar{\varphi}_\varepsilon$  preserves the infinitesimal rigidity of any framework on the sphere, in the plane, or on the cylinder if  $\varepsilon > 0$  is sufficiently small.*

*Proof.* Let  $\mathcal{F} = (G = (V, E), p : V \rightarrow \mathbb{R}^3)$  denote a bar-and-joint framework. Adding edges preserves rigidity, as it corresponds to adding constraints. Consequently, the edge-doubling operation preserves rigidity. Assuming that every vertex in  $\mathcal{F}$  has degree 4, the vertex-split operation doubles each  $v \in V$  into  $v_+$  and  $v_-$ . We place these vertices in the same position and connect them by a bar of length 0, fixing  $v_+$  and  $v_-$  to identical positions. The four incident edges to  $v$  are transformed into two incident edges to  $v_+$  and two incident edges to  $v_-$ . Hence, any continuous motion deforming the split vertex  $\bar{\varphi}_0(v_+) = \bar{\varphi}_0(v_-) = p(v)$  projects to a deformation of the original framework, implying that the vertex-split operation preserves rigidity. Under both of these operations, the framework remains realizable since the new points remain in the same position and the new edges do not add any additional information.

Assume now that  $\mathcal{F}$  is infinitesimally rigid and additionally is constrained to the unit sphere, the unit cylinder, or the Euclidean plane. Then, the Jacobian  $d\tilde{f}|_p$  of the augmented distance measurement map  $\tilde{f} : \mathbb{R}^V \rightarrow \mathbb{R}^{|E|+|V|}$  in the realization  $p : V \rightarrow \mathbb{R}^3$  has full rank. The rank of the Jacobian is stable under sufficiently small perturbations since the regular locus of algebraic sets is a smooth manifold. In addition, Theorems 6.1.8 and 6.1.9 guarantee that the isometry group's dimension does not change. Therefore, the infinitesimal rigidity of  $\mathcal{F}$  is preserved under the curve  $t \mapsto \bar{\varphi}_t$  for  $t \in [0, \varepsilon]$  if  $\varepsilon > 0$  is chosen sufficiently small.  $\square$

If there exists an edge between  $V_+$  and  $V_-$ , we call the split graph *entangled* and otherwise *untangled* (cf. [192]). The cables are modeled by a contractive, one-sided Hookean spring (cf. [154]) with resting length 0. All this information allows us to generalize the concept of color groups that have previously been introduced for periodic weaves.

**Definition 6.2.10.** Given a 4-regular graph  $G = (V, E)$ , a crossing sequence  $\chi : E^2 \rightarrow \{\pm 1, 0\}$  and the set of cables  $\mathcal{C} = \iota_\chi(E) \subset \binom{V_+ \sqcup V_-}{2}$ , we partition  $\mathcal{C}$  into families of  $N \geq 2$  *color groups*  $F_1, \dots, F_N$  with the property that whenever two cables  $e_1, e_2 \in \mathcal{C}$  are incident, they belong to the same color group  $F_i$ .

Next, we define the set of struts  $\mathcal{S}$ . The struts' purpose is to balance the framework and repulse vertices that are not connected by a cable. Physically, this can be interpreted as the inability of any material to be squashed beyond a certain point. In our model, the struts help to organize

the points in a regular and symmetric way on the surface. Otherwise, the structure may fail to converge to a physically meaningful energy minimum. The struts are only placed between vertices with the same over-under information to reduce the computational complexity, which means that

$$\mathcal{S} = \{\{v_+, w_+\} \text{ for } v_+ \neq w_+ \in V_+\} \cup \{\{v_-, w_-\} \text{ for } v_- \neq w_- \in V_-\}.$$

We model the struts as a repulsive point potential, heavily penalizing the proximity of points. In other words, we utilize the so-called Riesz energy (cf. [52]), which is the objective function in the Thompson problem. It models the configurations of electrons constrained to the sphere by determining an electrostatic minimum of the Coulomb energy [106]. The Riesz energy is also used to produce ideal embeddings of weaves in Kotani et al. [192], albeit in a different context. In this article, it is claimed that a 0-dimensional energy on the points instead of a 1-dimensional graph-based energy given by edges is advantageous for understanding and modeling the interactions between atoms. For applications in chemistry and materials science, finding stable configurations of this energy would then become more physically meaningful.

As the next step, we describe the set of bars  $\mathcal{B}$ . By construction, the weaving's color groups merely intersect in the vertices, meaning the only bars of length  $2\varepsilon$  are given by the edges  $\{\iota_+(v), \iota_-(v)\} = \{v_+, v_-\}$  between split vertices. Summarizing this explanation in formulas leads to the nonlinear optimization problem

$$\begin{aligned} \text{local } \min_{\overline{\varphi}_\varepsilon: V_+ \sqcup V_- \rightarrow \mathbb{R}^3} \quad & \sum_{ij \in \mathcal{C}} \frac{c_{ij}}{2} \cdot \|\overline{\varphi}_\varepsilon(i) - \overline{\varphi}_\varepsilon(j)\|^2 + \sum_{ij \in \mathcal{S}} \frac{d_{ij}}{\|\overline{\varphi}_\varepsilon(i) - \overline{\varphi}_\varepsilon(j)\|} \\ \text{s.t.} \quad & \overline{\varphi}_\varepsilon(v_+) \in \bigcup_{p \in \mathcal{M}} p + \varepsilon \cdot n_{\mathcal{M}}(p) \quad \text{for } v_+ \in V_+, \\ & \overline{\varphi}_\varepsilon(v_-) \in \bigcup_{p \in \mathcal{M}} p - \varepsilon \cdot n_{\mathcal{M}}(p) \quad \text{for } v_- \in V_- \quad \text{and} \\ & \|\overline{\varphi}_\varepsilon(v_+) - \overline{\varphi}_\varepsilon(v_-)\| = 2\varepsilon \end{aligned} \tag{6.2.11}$$

for spring constants  $c_{ij} > 0$  and elastic moduli  $d_{ij} > 0$  dependent on the number of vertices. For our experiments, we choose  $c_{ij} = 1$  and  $d_{ij} = 8/\#\mathcal{V}$ . Two exemplary solutions to this optimization problem are depicted in Figure 6.2.12. We are interested in local energy minima that are sufficiently close to the initial configuration, i.e. points found by local, iterative schemes. While there might be a global minimizer that has lower energy, it may be degenerate and topologically different from the initial configuration. From now on, we will denote the  $\pm\varepsilon$ -offset surface by  $\mathcal{M}_{\pm\varepsilon}$ .

Due to the explicit formulation of the constraints, the Riemannian optimization algorithm constructed in Chapter 3 is not yet applicable to the optimization problem (6.2.12). Assume that the smooth surface  $\mathcal{M}$  is given by an implicit equation  $g: \mathbb{R}^3 \rightarrow \mathbb{R}$  with  $\mathcal{M} = g^{-1}(0)$ . This assumption enables us to express a unit normal field  $n_{\mathcal{M}}(p)$  as

$$n_{\mathcal{M}}(p) = \frac{\nabla g(p)}{\|\nabla g(p)\|}.$$

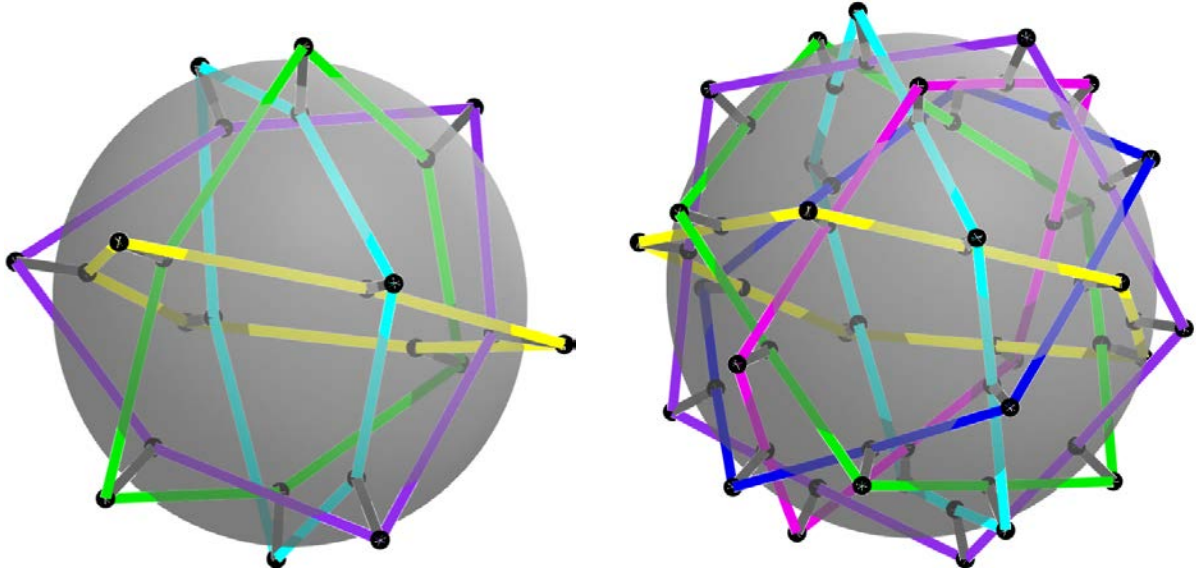


**Figure 6.2.12:** Polytopes provide tessellations of the sphere. When applying the lift  $\bar{\varphi}_{0,15}$  into the thickened sphere's boundary to the 1-skeleton underlying the cuboctahedron (l.) and icosidodecahedron (r.), we obtain tensegrity models with 4 and 6 color groups, respectively. The bars are depicted in dark gray. Compare this to the untwisted weaves depicted in Figure 6.2.18, which are a result of optimization problem (6.2.11)'s application.

Any curve  $c : [0, 1] \rightarrow \mathcal{M}$  satisfies  $g(c(t)) = 0$ . By the chain rule from multivariate calculus, differentiating this expression results in the equation

$$0 = \frac{\partial g(c(t))}{\partial t} = \nabla g(c(t))^T \cdot c'(t).$$

In particular, any smooth smooth curve  $c$  on  $\mathcal{M}$  with  $c(0) = p$  has a tangent at  $t = 0$  that is normal to  $g$ 's gradient at  $p$ . By Definition 3.1.2,  $\nabla g$  then is orthogonal to the tangent space of  $\mathcal{M}$  at every point. In other words, the gradient field of an implicitly-defined surface provides a normal vector at each point. Moreover, the normal spaces  $N_{p+\varepsilon \cdot n_{\mathcal{M}}(p)}\mathcal{M}_{\varepsilon}$  and  $N_p\mathcal{M}$  are identical for all  $p \in \mathcal{M}$  if  $\varepsilon$  is sufficiently small. This is a consequence of Theorem 4.1.14's proof, which states that the normal field of the offset surface is parallel to the original surface's normal field if  $\mathcal{M}$  is parametrized. As a smooth manifold,  $\mathcal{M}$  is covered by a smooth atlas, so  $\mathcal{M}$  is locally parametrized. Therefore, the normal spaces are identical on each of the open domains of the atlas. Consequently, the  $\pm\varepsilon$ -offset surfaces are locally characterized by the implicit equations

$$g \left( p \mp \varepsilon \cdot \frac{\nabla g(p)}{\|\nabla g(p)\|} \right) = 0. \quad (6.2.13)$$

Since the defining maps glue smoothly, the  $\pm\varepsilon$ -offset surfaces of an implicitly-defined manifold can also be described by implicit equations.

Hence, the Riemannian optimization techniques from Chapter 3 can be applied to the nonlinear optimization problem described above. Assuming that  $g$  consists of polynomials, analogous to Section 5.4 we can turn all constraints of the nonlinear optimization problem (6.2.11) into polynomials. As a consequence, we can apply the robust path-tracking routines from the package `HomotopyContinuation.jl` for computing deformation paths (cf. Sections

3.2.2 and 5.5).

As a next step, we construct a feasible point of the optimization problem (6.2.11) from the original framework on  $\mathcal{M}$ .

**Proposition 6.2.14.** *Let  $G = (V, E)$  be a 4-regular graph that is realized on a smooth, orientable surface  $\mathcal{M} \subset \mathbb{R}^3$  via  $\varphi : V \rightarrow \mathcal{M}$  with crossing sequence  $\chi : E^2 \rightarrow \{\pm 1, 0\}$ . Then, we can explicitly construct a feasible point of the nonlinear optimization problem (6.2.11) by continuously deforming the initial structure after a vertex-split operation and the introduction of a new bar.*

*Proof.* To construct the vertex-split, first consider a single vertex  $v \in V$ . By construction, it has 4 adjacent edges  $e'_{1+}, e'_{2+}, e'_{1-}$  and  $e'_{2-}$  such that  $\chi(e'_{i+}, e'_{j-}) = 1$  for all  $i, j \in \{1, 2\}$ . Subsequently, we split vertex  $v$ , obtaining  $v_+$  and  $v_-$  using the isomorphisms  $\iota_+$  and  $\iota_-$ . We denote the edges' image under the map  $\iota_\chi$  as  $e_{i\pm} = \iota_\chi(e'_{i\pm}) \in \binom{V_+ \sqcup V_-}{2}$ . As a consequence,  $v_+$  is now incident to  $e_{1+}$  and  $e_{2+}$ , while  $v_-$  is incident to  $e_{1-}$  and  $e_{2-}$ .

On a coordinate level, the vertex-splitting to obtain  $V_+ \sqcup V_-$  can be realized via  $\varphi_0 : V_+ \sqcup V_- \rightarrow \mathcal{M}$  (cf. Equation (6.2.8)). To satisfy the constraints in the optimization problem (6.2.11), we add a bar  $\{v_+, v_-\}$  of length 0. Currently, all constraints are satisfied with  $\varepsilon = 0$ . However, to obtain an untwisted weave,  $\varepsilon > 0$  is necessary. When expanding the  $\pm t$ -offset surfaces for  $t \in [0, \varepsilon]$  along the homotopy  $\bar{\varphi}_t$ , the distance between  $\bar{\varphi}_t(v_+)$  and  $\bar{\varphi}_t(v_-)$  is given by

$$\begin{aligned} \|\bar{\varphi}_t(v_+) - \bar{\varphi}_t(v_-)\| &= \|(\varphi(v) + t \cdot n_{\mathcal{M}}(\varphi(v))) - (\varphi(v) - t \cdot n_{\mathcal{M}}(\varphi(v)))\| \\ &= \|2t \cdot n_{\mathcal{M}}(\varphi(v))\| = 2t. \end{aligned}$$

In these equations,  $n_{\mathcal{M}}$  denotes a unit normal field that can be consistently chosen because  $\mathcal{M}$  is orientable. Since  $\bar{\varphi}_t$  is continuous in  $t$  by construction, in the limit  $t \rightarrow \varepsilon$  this distance becomes  $2\varepsilon$ . This concludes the proof, as we constructed a feasible point of the optimization problem (6.2.11).  $\square$

After the optimization problem (6.2.11) is solved for a local minimizer, the next step is to visualize the weave on the surface. While the discretized tensegrity framework may be useful in modeling increasingly complicated geometric constraint systems, it is not visually appealing. This issue is combatted by interpolating splines in the edges. To obtain a differentiable curve, a tangent condition in the vertices is added, meaning that the interpolating polynomial has degree 3. The following remark formalizes this construction.

**Remark 6.2.15.** To turn a discretized tensegrity model on a surface  $\mathcal{M} \subset \mathbb{R}^3$  into a smooth, untwisted weave in  $\mathbb{X}^3(\mathcal{M})$ , we use polynomial interpolation. Assume that we have already optimized the tensegrity framework to obtain a realized  $p : V \rightarrow \partial \mathbb{X}^3(\mathcal{M})$ . For a sequence  $hi, ij, jk \in \mathcal{C}$  of three cables, we interpolate a smooth curve

$$\varphi : [0, 1] \rightarrow \mathbb{X}^3(\mathcal{M}), \quad t \mapsto A \cdot \begin{pmatrix} t^3 \\ t^2 \\ t \\ 1 \end{pmatrix}$$

for a matrix  $A \in \mathbb{R}^{3 \times 4}$  that is yet to be determined. To ensure that  $\varphi$  is smooth, we impose the following boundary conditions:

$$\begin{aligned}\varphi(0) &= p_i, \quad \varphi(1) = p_j, \quad \varphi'(0) = \pi_{T_{p_i}(\mathcal{M})}(p_j - p_h) \\ \text{and } \varphi'(1) &= \pi_{T_{p_j}(\mathcal{M})}(p_k - p_i)\end{aligned}$$

for the projection  $\pi_L$  onto a linear subspace  $L$  of  $\mathbb{R}^3$ . This construction results in a linear system with 12 equations and 12 indeterminates. Generically, it has a unique solution, allowing us to smoothly interpolate between  $p_i$  and  $p_j$ .

This construction is then repeated for every cable in  $\mathcal{C}$ . For this to work, the only assumption that we make on the weave is that every cable has a predecessor and successor. Since every vertex in the crossing diagram has degree 4 before the split after potentially doubling some edges (cf. Figure 6.2.1), each vertex has exactly two incident cables in the crossing sequence that contains over and under information. Each of these cables has two incident vertices, ultimately proving that every cable has a predecessor and a successor. Therefore, this interpolation is applicable to construct smooth untwisted diagrams from arbitrary crossing sequences. By design of the boundary conditions, the resulting curve will be continuously differentiable in the realization's vertices and analytic everywhere else.

All untwisted weaves depicted in this chapter are obtained by applying Riemannian optimization to the optimization problem (6.2.11). The initialization is chosen reasonably close to the expected structure. For instance, the initial configurations on the sphere are obtained via semi-regular, convex polytopes, which provide tessellations of the sphere. Subsequently, the smooth interpolation described in Remark 6.2.15 yields an untwisted weave in the thickened surface  $\mathbb{X}^3(\mathcal{M})$ . The examples from this section are set up as nonlinear optimization problems in the Julia package `WeavingsOnManifolds.jl`<sup>22</sup>.

### 6.2.2 Examples of Entangled Weavings

Polytopes provide a plethora of examples, as they are tilings of the sphere. Among the Archimedean solids, whose faces are regular polygons and whose vertices are all alike, there are several 4-regular polytopes. Including the Platonic solids, there are exactly five: the octahedron (cf. Figure 6.2.5), the cuboctahedron, the icosidodecahedron, the rhombicuboctahedron, and the rhombicosidodecahedron. Through the construction from Section 6.2.1, all of them can easily be transformed into untwisted weaves on the sphere.

However, they are far from the only weavings on the sphere, even when considering all possible 4-regular polytopes. In Hyde and Evans [169] tangled platonic polyhedra are discussed, generalizing the notion of polytopes by winding helices with varying numbers of strands around the polytope's tubification. The authors require curvilinear edges since the resulting vertices remain in the same position as the polytopes' vertices. It immediately becomes clear that this approach is suitable for our setting as well, as it allows untwisting the weave using the lift  $\bar{\varphi}_\varepsilon$ . Later in this chapter, ways to achieve this construction in the discretized tensegrity model will be discussed.

---

<sup>22</sup><https://github.com/matthiashimmelmann/WeavingsOnManifolds>

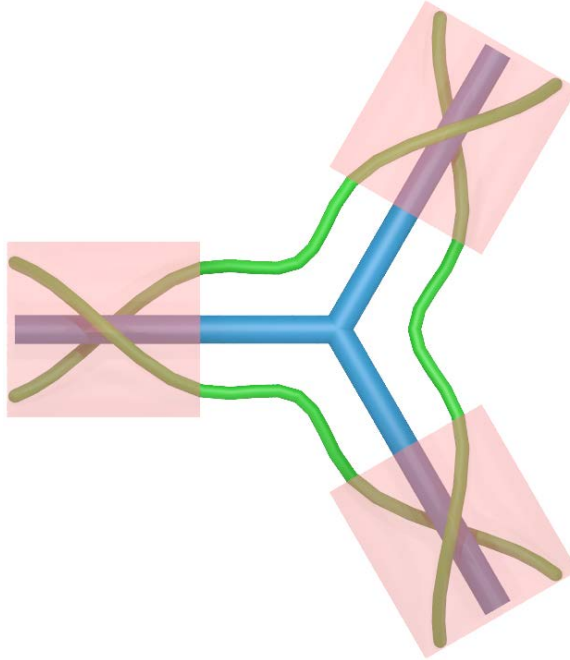


**Figure 6.2.16:** Symmetric tangles on a net  $G$  can be enumerated using the symbol  $[\frac{t}{m}]_G$ . In this label,  $m$  denotes the strands per edge and  $t$  describes the amount of  $\pi$ -twists per edge. In this example,  $G$  (blue) is given by a vertex with three incident edges. Inside the red boxes, the strands (green) are allowed to twist, though the strands' entering and exiting points to the box are fixed. Here, the strands perform a  $\pi$ -twist, resulting in the symbol  $[\frac{1}{2}]_G$ .

For constructing entangled polyhedra, we follow Evans and Hyde [108], who describe a label for enumerating entangled polytopes. It simplifies referring to the weaves that are investigated in this chapter. Given any net  $G$ , symmetric polyhedral tangles are constructed by first tubifying the embedded graph  $G$ . This process inflates the graph's edges and vertices, resulting in a smooth surface. The entanglement consists of a decoration of non-intersecting curves on this surface. On each of the graph's edges, it is recorded how many strands lie on the edge. These helical curves can then twist around the edge, with a  $2\pi$  twist constituting a full rotation. As only symmetric polytopes are considered in this section, it is assumed that the number of strands per edge is 2 and that each strand has the same twist per edge, given by an integer multiple of  $\pi$ . Two strands per edge is a reasonable assumption by Section 6.2 of weaving diagrams, where it is assumed that no three geodesics meet at the same point. We denote the number of  $\pi$  twists of each strand around an edge by  $m$ . If  $m = 0$ , the decoration of the tubified surface is untangled. A qualitative pictogram is shown in 6.2.16.

This construction leads to the symbol  $[\frac{m}{2}]_P$  for the polytope  $P$ . For instance, the untwisted weave corresponding to the octahedron's lift to the thickened sphere (cf. Figure 6.2.5) lives on the tetrahedron and has  $m = 1$ , leading to the symbol  $[\frac{1}{2}]_{tet}$ . When further increasing  $m$ , the becomes increasingly more entangled. Later in this chapter, we will see how the construction from Section 6.2.1 behaves in this case.

In the following, we apply the tensegrity model for weavings (cf. Section 6.2.1) to several entangled polytopes described by symbols  $[\frac{m}{2}]_P$  for platonic polyhedra  $P$  and  $m \in \{1, 2\}$ . We start by considering the previously mentioned cuboctahedron and icosidodecahedron.

**Example 6.2.17.** Leaving aside the octahedron that appeared in Example 6.2.4, two other Archimedean solids are natural to consider due to their high regularity: the cuboctahedron and the icosidodecahedron that are depicted as untwisted weaves in Figure 6.2.18. These polytopes' rings lift to great circles and each of their vertices has degree 4. Hyde and Evans [169] call them the tangled polytopes  $[\frac{1}{2}]_{oct}$  and  $[\frac{1}{2}]_{dodec}$ , that are equivalent to  $[\frac{1}{2}]_{cub}$  and  $[\frac{1}{2}]_{icos}$ , respectively.

To study their rigidity, the cuboctahedron has a single Flex along the great circle that is not adjacent to the triangle which is pinned by fixing the rigid motions. We can show that this polytope is prestress stable by checking condition Definition 2.1.15 for a random stress. Conversely, the icosidodecahedron has an 8-dimensional space of stresses and a 5-dimensional space of infinitesimal motions. Analogous to the proof of Theorem 2.3.9, we can show the second-order rigidity of that polytope. For the sake of brevity, the proof is omitted.

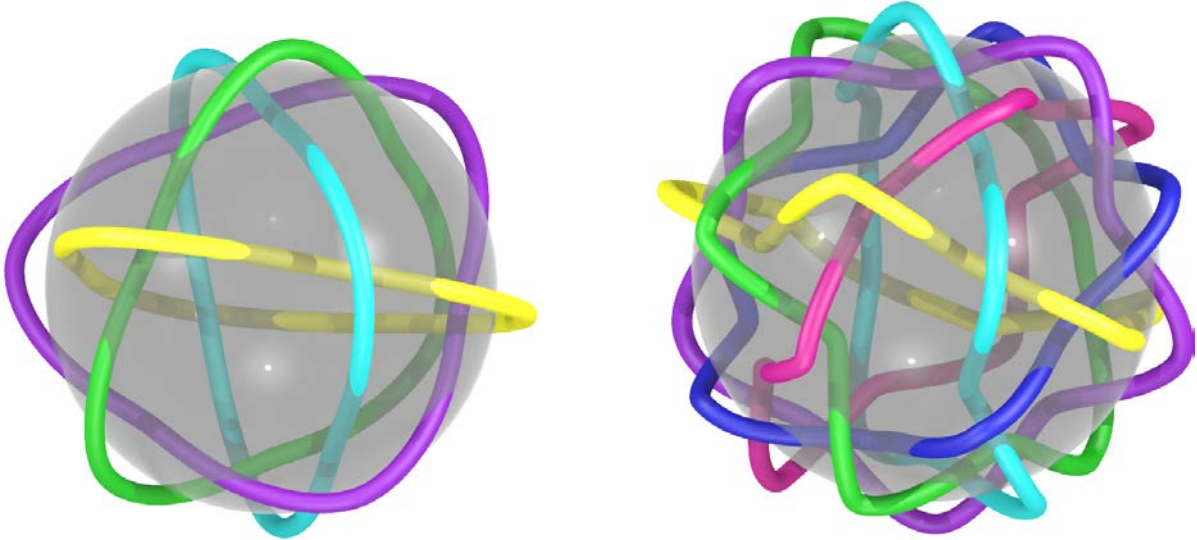


**Figure 6.2.18:** The cuboctahedron with  $N = 4$  color groups (l.) and the icosidodecahedron with  $N = 5$  color groups (r.) are visualized after lifting them to untwisted weaves on the sphere. These structures are known as the polyhedral windings  $[\frac{1}{2}]_{oct} = [\frac{1}{2}]_{cub}$  on the octahedron or cube (l.) and  $[\frac{1}{2}]_{icos} = [\frac{1}{2}]_{dodec}$  on the icosahedron or dodecahedron (cf. [169]).

Neither type of rigidity is sufficient for Proposition 6.2.9 to apply. This is a recurring theme when working with polytopes and is a hint that in highly symmetric settings, infinitesimal rigidity is rare. Therefore, we need to rely on optimizing the tensegrity model from Section 6.2.1.

Nonetheless, a rigid framework is rigid almost everywhere (cf. Theorem 2.2.4). If the aim is to obtain a rigid structure, we can slightly perturb the realization  $p$ . Then, there exists a  $\varepsilon > 0$  such that the untwisted weave with added bars between the separated vertices (cf. optimization problem 6.2.11) is rigid.

Definition 6.2.2 puts rather strong assumptions on the types of weaves that we can consider, so we relax the assumptions in the following. First of all, the fact that the curves are geodesics is a strong restriction. Instead, we want to consider smooth curves on the surfaces that are put in the same color group if they do not intersect. A first generalization of geodesics is given by *geodesic circles*, describing the curve at a constant geodesic distance to a fixed point. Fukuda et al. [122] call this operation the *crossed curve with an untwisted double line covering*. On the sphere, geodesic circles can be obtained by intersecting the sphere with an affine hyperplane

rather than a linear subspace. Contrary to the previous examples, now each color group can contain multiple curves. Figure 6.2.19 demonstrates, how to go from a generalized crossing diagram on the sphere to an untwisted weave for the rhombicuboctahedron.

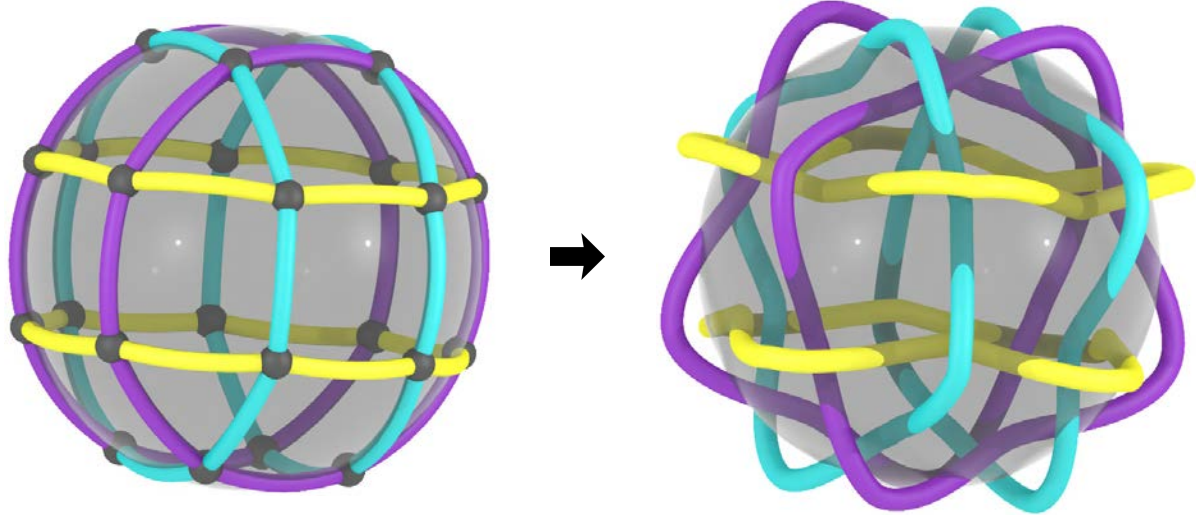


**Figure 6.2.19:** The rhombicuboctahedron gives rise to a weaving diagram on the unit sphere with  $N = 3$  color groups (l.). Using appropriate crossing information, the weave can be lifted to  $\mathbb{X}^3(S^2)$ , where it avoids intersections (r.). Notably, the cuboctahedron is generated by a nonlinear, affine hyperplane arrangement. Orthogonally projecting it to the sphere does not create smooth transitions between adjacent edges. This map lifts edges to geodesic arcs on the sphere and since geodesics are precisely given by intersections of  $S^2$  with linear hyperplanes, the edges necessarily create creases in the vertices.

The rhombicuboctahedron is the first structure that cannot be described by symbols of the form  $[\frac{1}{2}]_P$  for a platonic polyhedron  $P$  because the weave's rings are reminiscent of parallels of great circles. Nevertheless, the tensegrity model can be applied.

Further examples can be generated using the *Euler transformation* [143]. This construction provides the means to create an arbitrary amount of graphs where each vertex has degree 4, starting from any polytope. However, this construction adds complexity, so it is only mentioned here as a tool, but not applied.

Finally, relax the assumption that each of the underlying graph's vertices needs to have degree 4. If there are two adjacent vertices that both have degree 3, we can replace the edge connecting them with a double bond. When lifting the crossing diagram to  $\mathbb{X}^3(\mathcal{M})$ , this operation produces two edges organized in a crossed square. In the weaving, the two threads tangle helically around each other with a  $180^\circ$  rotation. Fukuda et al. [122] describe this edge-operation as a *branched curve with a 1-twisted double line covering*. This case is described by the symbol  $[\frac{2}{2}]_P$ . For an example of this construction, consider Figure 6.2.20 and Figure 6.2.21.

Subdividing the double edge through the introduction of  $m$  new vertices, we can produce helical tangles with  $m$   $180^\circ$  twists for  $m \in \mathbb{N}_0$ . Fukuda et al. [122] call the resulting structure a *branched curve with  $m$ -twisted double line covering*, producing the symbol  $[\frac{m}{2}]_P$ . Lifting the resulting crossing diagram to  $\mathbb{X}^3(\mathcal{M})$  generates a sequence of  $m$  crossed squares.

Beyond the  $[\frac{2}{2}]_{\text{tet}}$  and  $[\frac{2}{2}]_{\text{cub}}$  weave, Figure 6.2.20 contains the weave obtained by applying

---

<sup>23</sup><https://knotinfo.math.indiana.edu/homelinks/knotfinder.php>

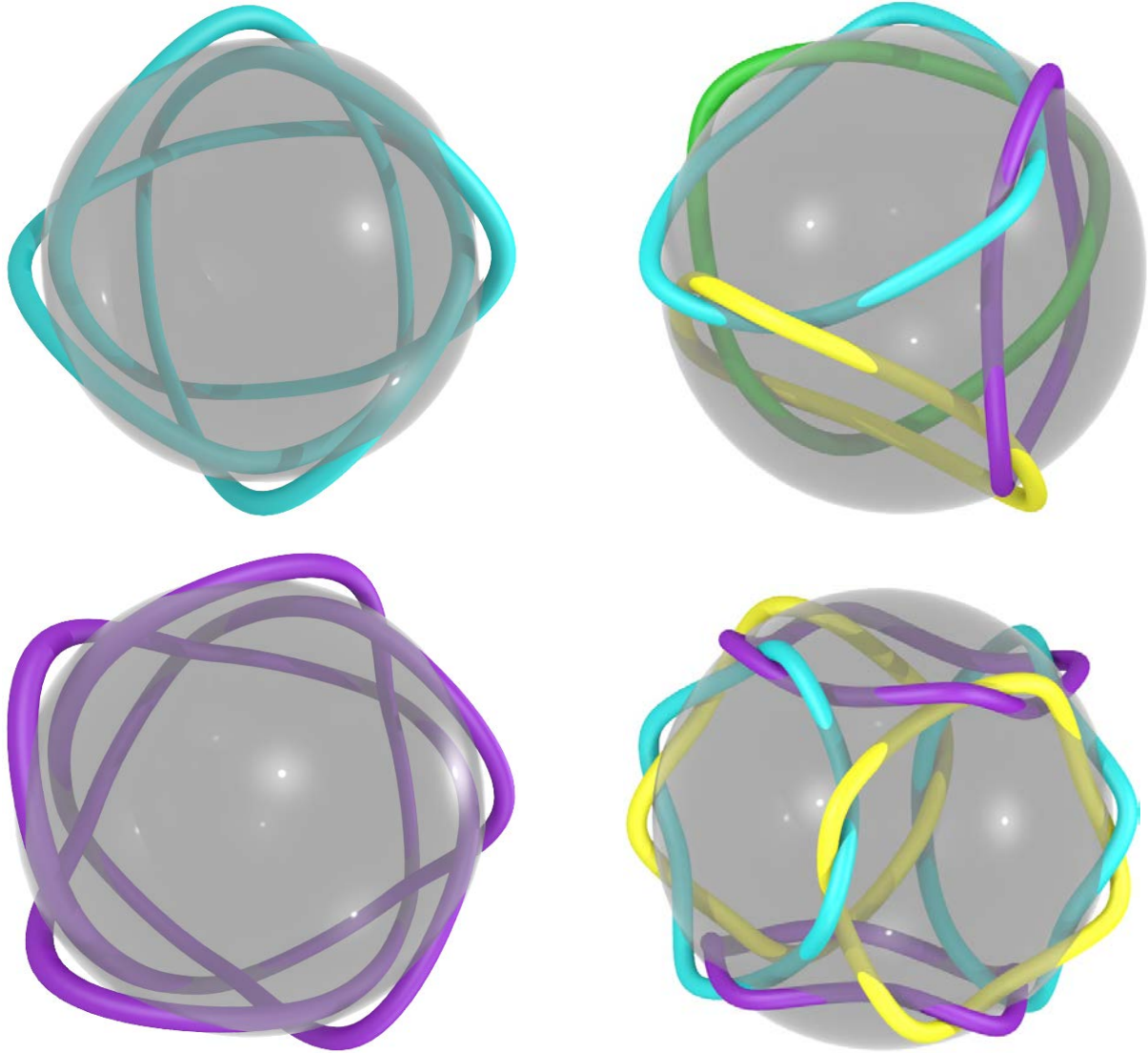


**Figure 6.2.20:** The square antiprism (t.l.) and the pentagonal antiprism (b.l.) only require a single thread. The knot identification software KnotFinder<sup>23</sup> tells us that neither weaving corresponding to the antiprism is a prime knot. An entangled truncated tetrahedron (t.r.) and truncated cube (b.r.) can be obtained by doubling some edges. They are known as the  $[2]_{2,tet}$  and  $[2]_{2,cub}$  polyhedral windings (cf. [169]).

the lift  $\overline{\varphi}_\varepsilon$  to the square and pentagonal antiprism after doubling some of the edges. Consisting of a single strand, these tangles constitute knots.

In Figure 6.2.21, the  $[2]_P$  tangles for the remaining polytopes octahedron, icosahedron and dodecahedron are depicted. For these structures, an algorithm has been devised for constructing tensegrity models for  $(m + 1)$ -twisted weaves for arbitrary  $m > 0$  from configurations of the platonic solids.

Up until now, only weavings on the sphere have been considered, which stands in stark contrast to the title of the current chapter. Except for the flat torus that is used as a basis for the definition of weaving diagrams by Fukuda et al. (see Section 6.2), it becomes increasingly hard to describe weaves on surfaces other than the sphere. The complete rotational symmetry of the sphere makes it irrelevant where we place the first point, mimicking the Euclidean plane.

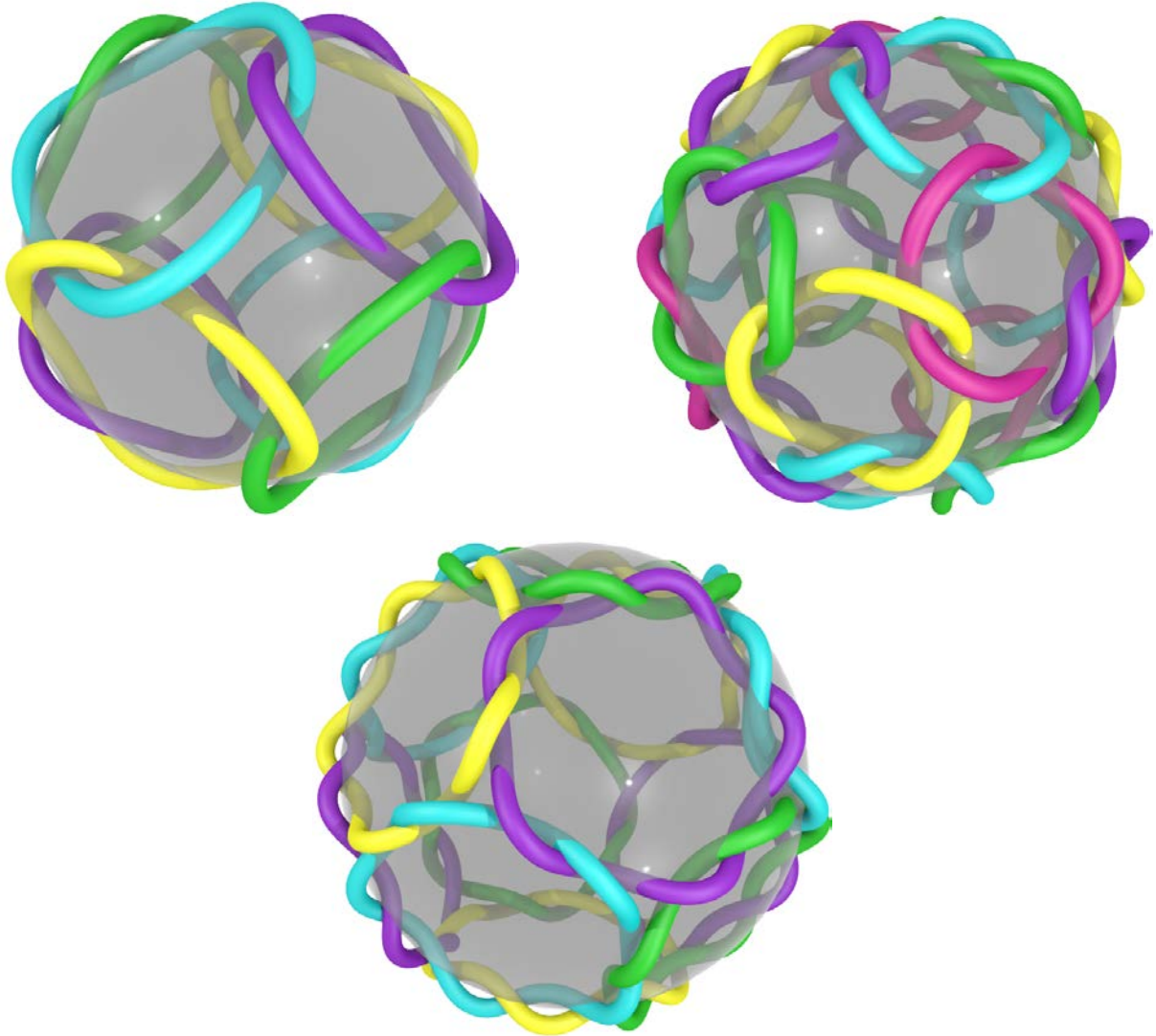


**Figure 6.2.21:** The entangled truncated octahedron (l.), icosahedron (r.) and dodecahedron (b.) are known as the  $[2]_{oct}$ ,  $[2]_{icos}$  and  $[2]_{dodec}$  polyhedral windings (cf. [169]).

For other surfaces, such as the curved torus or the hyperboloid, the local geometry differs from point to point. Therefore, it seems most likely that a contractive weave will cluster along the surface's narrowest parts, defeating the purpose of studying weaves that use the geometry of the entire surface to equilibrate. For the hyperboloid and the torus of rotation, we need to use a significant amount of tools, such as Dirichlet boundary conditions and additional energy terms, to ensure the weaves converge to a non-degenerate configuration. That holds true, even though the hyperboloid's isometry group has the same rank as the sphere's (see Table 6.1.6) and the hyperboloid admits a similar coning construction as the sphere (see Section 6.1.1). Using a different metric can potentially help with some of these problems. Still, the hyperboloid's unboundedness together with its non-periodicity makes it hard to understand how to describe weaves on it.

In contrast, the cylinder satisfies that its local geometry is identical at every point. The only problem is its unboundedness in  $z$ -direction. Motivated by the flat torus, we consider a compact, singly periodic cylinder here that has periodic boundary conditions. The choice of the distance

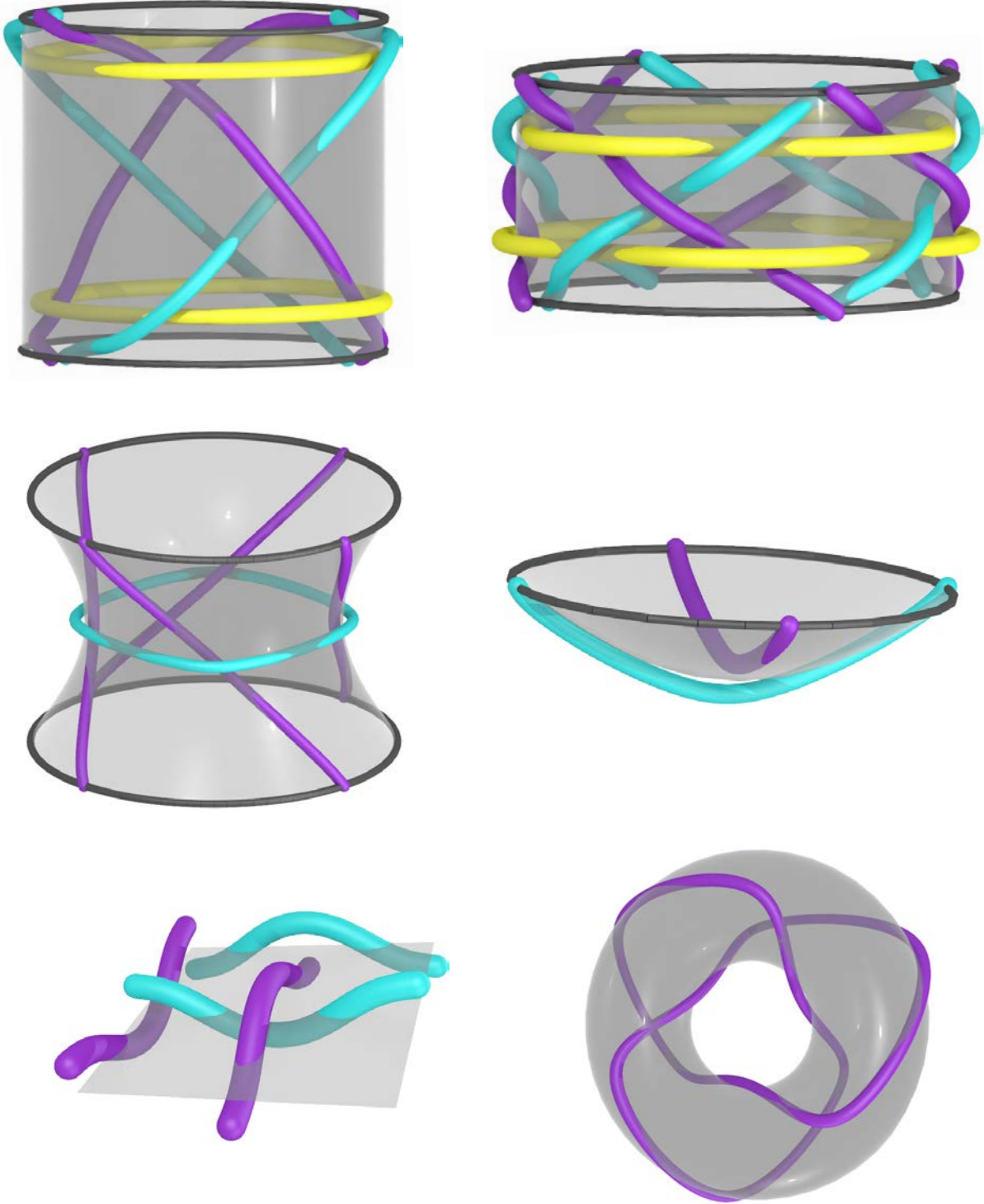


**Figure 6.2.22:** We investigate Kagome weaves with 2 (t.l.) and 4 (t.r.) hexagons wrapping around the cylinder with periodic boundary conditions (black curve). Weaves on the one-sheeted hyperboloid (c.l.) and a connected component of the two-sheeted hyperboloid (c.r.) with Dirichlet boundary conditions (black curve) are considered as well. Finally, we depict the plain weave on the doubly periodic, flat torus (b.l.), and Trefoil torus knot (b.r.).

between the boundary conditions matters and affects the outcome. In the experiments depicted in Figure 6.2.22, the distance between the boundaries is a variable. This has an interesting result: The denser Kagome weave on the right reduces the distance, whereas the coarse Kagome

weave expands it. Both weaves aim at attaining a similar regular configuration.

To summarize, the tensegrity model described in Section 6.2.1 has proven to reliably work on both, the sphere and the flat torus. It enables us to model weavings using comparatively few variables. While we manage to extend this model to more general manifolds, it quickly shows shortcomings when the surface is unbounded or when it is not completely symmetric. How to address these shortcomings and find a way to adjust the optimization problem (6.2.11) to work on these surfaces is the object of future research.

### 6.3 Weavings on Deforming Spheres

Up until now we have only considered weaves on the unit sphere and other fixed surfaces. Nevertheless, the tensegrity model introduced in Section 6.2.1 can be used to describe the weaves' behavior on deforming surfaces as well. Related questions involve: What happens to the weave if the sphere becomes a spheroid or an ellipsoid, reminiscent of a football's deformation upon bouncing off a wall? Does the weave return to its original shape when we relax the surface back to the sphere? In this section, we conduct several numerical experiments on deforming spheres.

By starting from a stable equilibrium, we hope that the deformation maintains the minimality in a small neighborhood. Even though in the previous section we have observed that the tensegrity model for weavings does not immediately apply to arbitrary surfaces, a homotopy-based approach allows us to find stable equilibria on spheroids sufficiently close to the sphere. By fixing the spheroid's volume, an exemplary deformation becomes reminiscent of a ball that is squashed into a wall before bouncing back. Applying the path-tracking Algorithm 3.2.10, we can robustly compute the resulting deformation path. Although the tensegrity model from Section 6.2.1 is to be understood as a toy model rather than an actual physical system, we can investigate its behavior to see how it can be turned into a physical model on the sphere. Going forward, experimental data could be harnessed to further refine the model, leading to more precise simulations of physical woven materials. The hypothesis underlying this chapter is that some weavings are inherently more "bouncy" than others. In other words, the energy landscape corresponding to the optimization problem (6.2.11) may depend significantly on the selected weave.

Before diving into the experiments, an *ellipsoid* can be described by the implicit equation  $a_1x^2 + a_2y^2 + a_3z^2 = 1$  for the principal axis lengths  $a_1, a_2, a_3 > 0$ . Its volume is given by  $\frac{4\pi}{3}a_1a_2a_3$ . A *spheroid* is an ellipsoid in which two principal axes have equal lengths. Without loss of generality, we assume that  $a_1 = a_2$ . If  $a_1 < a_3$ , then the spheroid is *prolate*. If  $a_1 > a_3$ , the spheroid is *oblate*. Prolate spheroids are often associated with favorable aerodynamical properties [11]. For instance, predatory birds roughly resemble this shape at high velocities<sup>24</sup> and several sports balls are modeled with the prolate spheroid in mind. In contrast, oblate spheroids are associated with forces coming from rotations or applied pressure. Prime examples are a ball that is thrown against a wall and a deformable mass rotating around a fixed axis.

The spheroid's volume can be computed via  $\frac{4\pi}{3}a_1^2a_3$ . We fix the volume to  $\frac{4\pi}{3}$ , implying that the product of the principal axis lengths is 1. For appropriate choices of elastic moduli  $c_{ij}$  and  $d_{ij}$ , we do not expect a qualitative difference in the weavings' behavior that depends on the

---

<sup>24</sup>The peregrine falcon's airfoil more closely resembles the shape of a teardrop [334].

volume of the spheroid, justifying this choice. This lets us express one of the spheroid's principal axis lengths in terms of the other:  $a_3 = \sqrt{\frac{1}{a_1}}$ . Setting  $t = a_1$ , the defining equation associated to the spheroid's deformation becomes

$$\sqrt{\frac{1}{t}}x^2 + \sqrt{\frac{1}{t}}y^2 + t z^2 = 1. \quad (6.3.1)$$

According to Equation (6.2.13), the corresponding  $\pm\varepsilon$ -offset surfaces are given by the implicit equation

$$\sqrt{\frac{1}{t}} \cdot \left( x \mp \varepsilon \sqrt{\frac{1}{t}} \cdot x \right)^2 + \sqrt{\frac{1}{t}} \cdot \left( y \mp \varepsilon \sqrt{\frac{1}{t}} \cdot y \right)^2 + t \cdot (z \mp \varepsilon z)^2 = 1.$$

The parameter  $t$  then defines the homotopy from the sphere ( $t = 1$ ) to oblate spheroids with one smaller principal axis ( $t > 1$ ) and prolate spheroids with two smaller principal axes ( $t < 1$ ). This homotopy is used to investigate the weavings' energetic response. An exemplary deformation of the dodecahedron weave with symbol  $[\frac{1}{2}]_{dodec}$  is depicted in Figure 6.3.2.

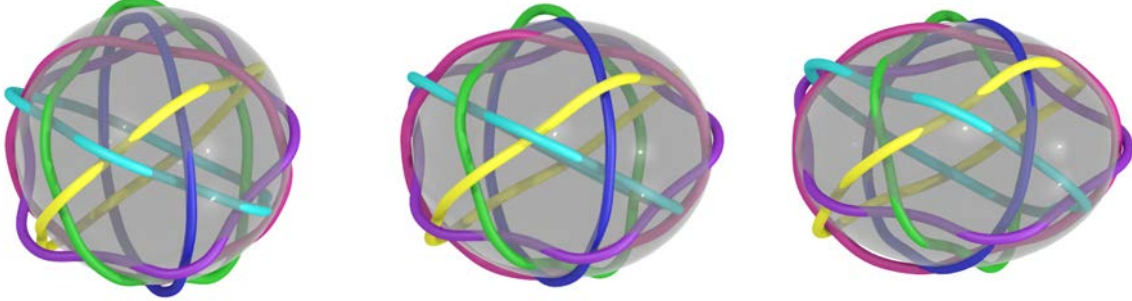


**Figure 6.3.2:** The dodecahedron weave  $[\frac{1}{2}]_{dodec}$  is deformed from the sphere  $t = 1$  (l.) via  $t = 0.8$  (c.) to a prolate spheroid at  $t = 0.6$  (r.).

We denote the spheroid deformation by  $D_{\tau_1\tau_2}$  for  $\tau_1, \tau_2 > 0$ . This continuous deformation transforms the spheroid with  $t = \tau_1$  into the spheroid at  $t = \tau_2$  via the solution path  $x(t)$  that can be obtained by solving the homotopy (6.3.1). If the weave is appropriately parametrized in terms of the resulting deformation path, we can study the underlying framework's rigidity. This can be done by altering the  $\pm\varepsilon$ -offset surface equations in the optimization problem (6.2.11) to fit the spheroid.

It is far from obvious that the weaving returns to its original shape when the deformation  $D_{\tau_1\tau_2}$  and its inverse homotopy  $D_{\tau_2\tau_1}$  are applied. To investigate the question of which weavings return to their original configurations, a so-called *hysteresis loop* is considered. Typically, this phenomenon describes a dependency of a physical system on preceding states and is often associated with irreversible changes such as phase transitions.

**Example 1:** As a first experiment, we consider the oblate spheroid. Here, the sphere is deformed until  $t = 2$  and then the inverse homotopy is applied to return to the sphere at  $t = 1$ . We observe which deformation the weaves undergo when constrained to the sphere.

Analogous to Section 5.5, the hysteresis loop can be modeled by first applying the Riemannian optimization Algorithm 3.2.7 to find an equilibrium on the sphere. Second, the path-tracking Algorithm 3.2.10 is applied to the Lagrange multiplier system associated with the optimization

problem (6.2.11) to track the local minimizer over the entire parameter range. The cables of the tensegrity model are physically motivated, distance-induced energy contributions. Conversely, the Riesz energy on the struts is mainly used to stabilize the structure, so we record the system's total energy and cable energy in each step. The interval is discretized with the constant step size  $\Delta t = 0.01$ .

To make the results comparable to each other and to reduce the effect of the weave's initial placement on the sphere, we multiply the initial configuration with a random rotation matrix  $Q \in \mathbb{R}^{3 \times 3}$ . It should be stressed that on the sphere, all configurations are equivalent because rotations in  $\mathbb{R}^3$  fix the sphere and further describe its isometries. This is not the case with spheroids. Therefore, the point coordinates of all weaves discussed in this section are multiplied by the same orthogonal matrix

$$Q = \begin{pmatrix} -0.9188824523658923 & -0.3509183022611896 & 0.18030913418950417 \\ 0.23167305673407199 & -0.11000208491682795 & 0.9665542592619633 \\ -0.3193471990131362 & 0.9299225163700875 & 0.18237730130251661 \end{pmatrix}.$$

Otherwise, some of the tensegrity model's edges could be parallel to the spheroid's equator or a vertex could lie exactly in one of the poles. This particular placement may behave differently under deformation than a generic configuration. We construct the random rotation matrix  $Q$  by first drawing its entries from a normal distribution before applying the QR-decomposition to project to the Stiefel manifold (cf. Example 3.2.6). Since the special orthogonal group  $SO(n)$  represents rotations as linear transformations,  $\det(A) = 1$  for matrices  $A \in \mathbb{R}^{n \times n}$  completely classifies all rotations in  $\mathbb{R}^n$ .

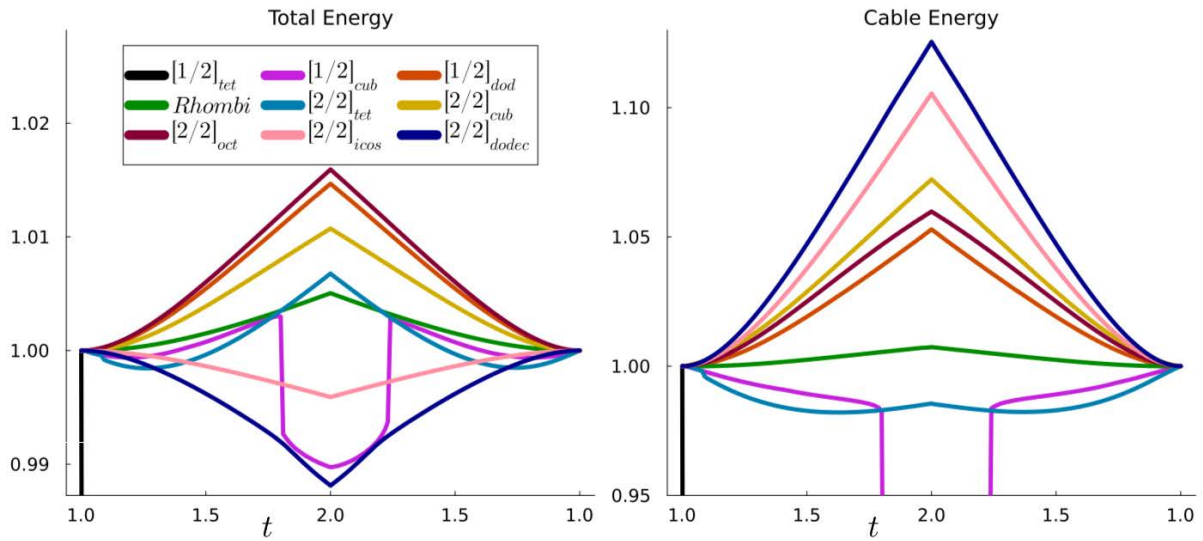


**Figure 6.3.3:** The hysteresis loops start from the sphere at  $t = 1$  and lead to an oblate spheroid at  $t = 2$  for some of the weavings introduced in Section 6.2.2. In each step, the total energy (l.) and energy associated with the cables  $\mathcal{C}$  (r.) is recorded. Both values are normalized so they are 1 at  $t = 1$ . The legend (l.) applies to both subfigures. Here, the rhombicuboctahedron weave is denoted by “Rhombi”.

Among other things, the objective function value in the nonlinear optimization problem (6.2.11) depends on the tensegrity's combinatorial complexity: The struts scale nonlinearly in

the number of vertices. To be able to meaningfully compare the weaves, we normalize every energy landscape resulting from the hysteresis loop by the corresponding initial energy. In other words, the curves for both, total energy and cable energy, start at an energy of 1. Applying the aforementioned hysteresis loop to several of the weavings from Section 6.2.2 results in the curves depicted in Figure 6.3.3.

As a first observation, most weaves return to their original configuration. Only the octahedron weave  $[\frac{1}{2}]_{tet}$  which possesses the fewest vertices is highly unstable. After a few deformation steps, this structure becomes degenerate, clustering on a hemisphere. It should be noted that the surface type changes from 3 at  $t = 1$  to 1 at  $t \neq 1$  (cf. Table 6.1.6), so chaotic behavior right when the sphere becomes a spheroid is possible. As it turns out, the geometric model is sufficiently robust and stabilizes most weavings anyway. After a long range of deformations, the cuboctahedron weave  $[\frac{1}{2}]_{cub}$  attains a degenerate configuration by slipping off the sphere. The corresponding deformation is depicted in Figure 6.3.4.

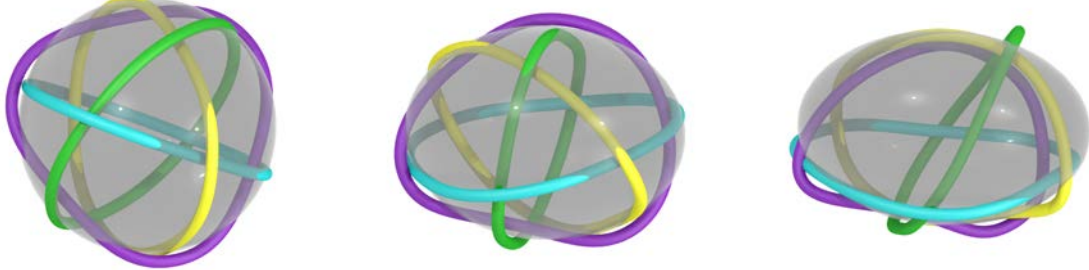


**Figure 6.3.4:** The cuboctahedron weave  $[\frac{1}{2}]_{cub}$  is deformed from  $t = 1$  (l.) via  $t = 1.5$  (c.) to the oblate spheroid at  $t = 1.85$  (r.). At the end of the deformation, the weave becomes degenerate.

**Example 2:** As a second example we consider deformations into the prolate spheroid. In this case, the hysteresis loop is modeled via a homotopy from  $t = 1$  to  $t = 0.5$  with a constant step size of  $\Delta_t = 0.005$ . The corresponding hysteresis loop is depicted in Figure 6.3.5.

Again, most weaves return to their original configuration except for  $[\frac{1}{2}]_{tet}$ . This particular weave clusters on a hemisphere after a few steps. A similar, yet better-stabilized phenomenon occurs in the  $[\frac{1}{2}]_{cub}$  and  $[\frac{2}{2}]_{tet}$  tangles, where the weave steadily slips off the spheroid. This procedure is depicted in Figure 6.3.6.

As a general trend, a structure's complexity seems to be correlated with its preference for the sphere. The semi-regular polytopes that are considered here for the construction of weavings only have two differently-shaped regular polygons as faces. The experiments suggest that these weaves tend to orient themselves in a way that allows as many of the larger polygons to lie on the spheroid's equator as possible. Potential triangles are moved to the poles.

Further contemplation of Figures 6.3.3 and 6.3.5 reveals that most structures prefer the sphere over any spheroid in terms of the cable energy. Two of them particularly protrude: The truncated icosahedron  $[\frac{2}{2}]_{icos}$  and truncated dodecahedron  $[\frac{2}{2}]_{dodec}$  have a sharp increase in their cable energy and robustly deform in both hysteresis loops. For either of these structures, the repulsive Riesz energy even decreases. It can be argued that the spheroid's variable eccentricity enables the distribution of vertices along the elongated axes, reducing the Riesz energy. Our initial intuition was that the surface area of the spheroid positively influences the energetic behavior. Yet, the area decreases when the spheroid deforms from the sphere.

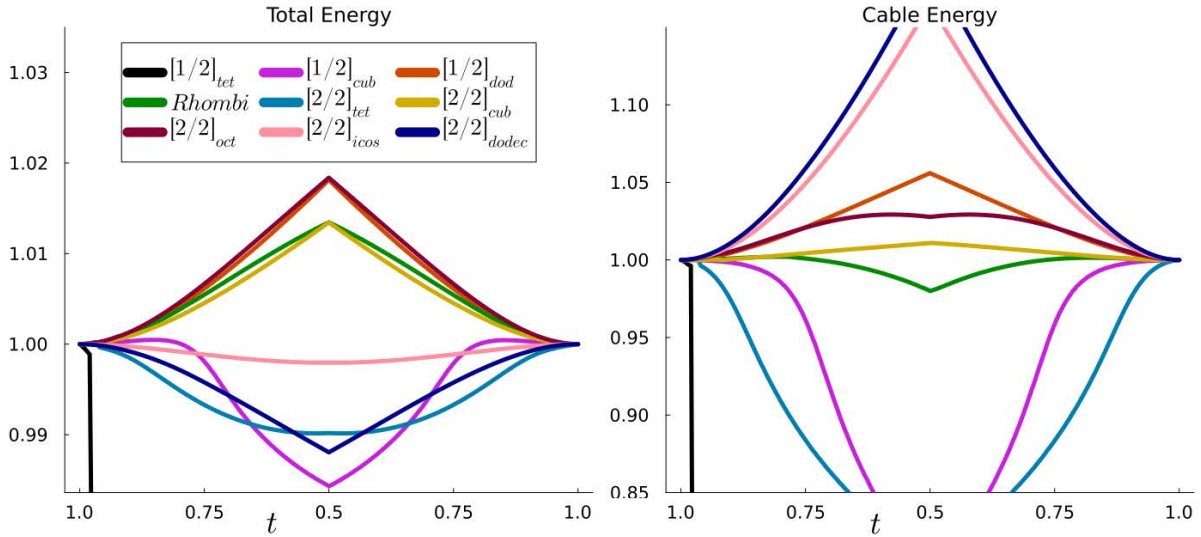


**Figure 6.3.5:** The hysteresis loops start from the sphere at  $t = 1$  and lead to a prolate spheroid at  $t = 0.5$  for some of the weavings introduced in Section 6.2.2. In each step, the total energy (l.) and energy associated with the cables  $\mathcal{C}$  (r.) is recorded. Both values are normalized so they are 1 at  $t = 1$ . The legend (l.) is representative for both subfigures. Here, the rhombicuboctahedron weave is denoted by ‘‘Rhombi’’.

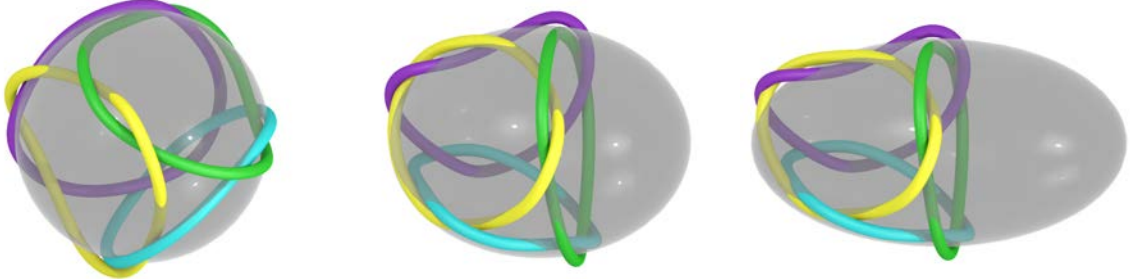


**Figure 6.3.6:** The truncated tetrahedron weave  $[\frac{2}{2}]_{tet}$  is deformed from  $t = 1$  (l.) via  $t = 0.75$  (c.) to the prolate spheroid at  $t = 0.5$  (r.). It can be observed that the weave slowly slips off the prolate spheroid and is barely kept together at the end of this deformation.

Beyond these two weavings, the truncated cube  $[\frac{2}{2}]_{cub}$ , the truncated octahedron  $[\frac{2}{2}]_{oct}$  and the icosidodecahedron  $[\frac{1}{2}]_{icos}$  are considered on both, the prolate and oblate spheroid in the hysteresis loops. Their energy does not change as drastically. A possible interpretation of this observation is that the weavings’ complexity and high level of regularity are correlated with their preference for more regular surfaces. The deformation of the truncated octahedron weave is depicted in Figure 6.3.7.

It is striking how in Figure 6.3.7 the weave quickly equilibrates by placing its rings on the equator. This phenomenon occurs in all entangled weavings except for the degenerate truncated tetrahedron. We can observe that the seams of the tangle – i.e. where strands twist around each other – orient orthogonally instead of parallel to the equator line. This provides the weaving with additional stability, as Figures 6.3.3 and 6.3.5 suggest.

Lastly, the rhombicuboctahedron is a curious case and motivates considering less regular weaves in the future. Throughout both hysteresis loops, this structure stays stable. The

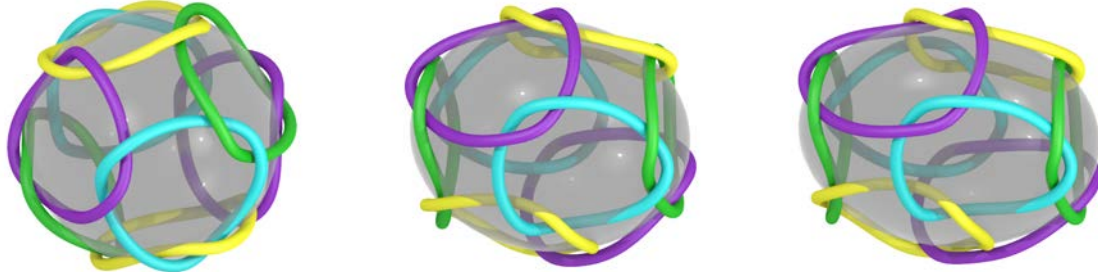


**Figure 6.3.7:** The truncated octahedron weave  $[2]_{oct}$  is deformed from the sphere  $t = 1$  (l.) via  $t = 1.5$  (c.) to an oblate spheroid at  $t = 2$  (r.).

rhombicuboctahedron weaving increases its cable energy in the oblate case and decreases its energy in the prolate case when applying the deformation  $D_{1t}$ . Investigating similar weaves that are not defined by great circles can help in designing weaves that prefer a particular surface shape.

In conclusion, we construct a tensegrity model for weavings on two-dimensional manifolds by considering the corresponding  $\pm\varepsilon$ -offset surfaces. Through the combination of attractive and repulsive forces, this tensegrity model approximates the physical behavior of curved weavings. The equilibration and deformation of these models are achieved through the combination of a Riemannian optimization scheme with a path-tracking algorithm. This approach not only enables the exploration of weavings in curved spaces but also provides insights into the behavior of these structures when the underlying surface is deformed. Although not all examples of weaves on the sphere remain stable under perturbation, many regular weavings energetically favor the sphere.

This chapter highlights the power of combining geometric principles with robust optimization techniques to investigate a wide range of geometric constraint systems. Applying this methodology to physical systems has the potential to yield interesting insights. In particular, this chapter brings us one step closer to spontaneously creating curvature in woven materials. In the future, experimental data could be used to refine the tensegrity model, enabling more accurate simulations of physical woven materials.

## Conclusion

---

In this thesis, we set out to answer the research question of whether we can combine smooth optimization techniques with robust geometric modeling to analyze and design materials. The answer is a resounding yes: We demonstrate that geometric materials and optimization go hand in hand. As polynomials appear in various real-world scenarios, a particular focus is put on algebro-geometric techniques. This makes the investigation of several geometric materials and their deformations possible.

The three stages of geometric design introduced in Section 1.1 guide this work. Beginning with an understanding of physical structures as the initial inspiration, geometric constraint systems are used for modeling. To these systems, smooth optimization schemes are applied for equilibration. The application of this process allows the construction of new geometric materials with targeted functionality.

This thesis explores a variety of problems concerning geometric materials. In this chapter, we recapitulate the investigated problems and highlight the progress made in addressing them. We recount the story behind the development of this thesis and reflect on the research process that shaped it in Section 7.1. Given the breadth of the covered topics, it is unsurprising that some questions remain unanswered. Therefore, in Section 7.2 we identify several open problems for future research.

### 7.1 Reflection on the Research Process of this Thesis

Interdisciplinary research has a distinctly different flavor from pure mathematical research. In this thesis, I start with concrete problems inspired by physical systems and use a broad spectrum of mathematics to solve them. The combination of geometry and optimization opens up interesting and unusual solution methods. Because of this, I provide a chronological reflection and documentation of how this thesis unfolded, highlighting how the various topics influence and relate to each other.

The project underlying this dissertation began with the question of how to accurately simulate the **bmn** and **sgn** nets associated with the cylinder packings  $\Pi^+$  and  $\Sigma^+$ . These two chiral cylinder packings come from a special class of packings that describe the structure of  $\beta$ -Manganese and the packing of skin cells [112, 242], respectively. After applying multiple different constraint optimization algorithms to the tensegrity model that was originally introduced by Oster et al. [242], I concluded that the optimization methods at my disposal were not suitable to model the complicated geometry of these packings. On the one hand, it was not possible to obtain a sufficiently good initial configuration for iterative optimization algorithms to converge. On the other hand, the previous geometric model exhibited chaotic behavior in the initial phase of equilibration, breaking its symmetry. This realization quickly led to the development of the Riemannian optimization algorithm in Chapter 3. Independently of the initialization, the

convergence to a critical point of the Riemannian gradient descent algorithm with suitable step sizes is guaranteed by Zoutendijk’s Theorem.

While Riemannian optimization fixed the initial problem of divergence, the geometric model was still insufficiently robust to accurately represent the symmetry of the cylinder packings’ deformations. Inspired by the configuration space of two filaments in tight orthogonal contact, I devised a tetrahedral tensegrity model in Section 5 that takes into account the geometry of the respective contact surface. The combined runtime of the equilibration and deformation took multiple days for either structure, which increased to several weeks when taking into account bug fixing. Nevertheless, this approach allowed me to quickly generate interesting results for a complicated geometric system. This demonstrates that combining robust optimization techniques with physically inspired geometric models holds great potential for studying the behavior of large and complex structures.

The ideas concerning the modeling of cylinder packings extend to more general settings, as demonstrated in Chapter 6. Even though at first glance, the model for weavings on surfaces is different from the model for cylinder packings, it follows the same design principles. The idea for this approach was inspired by the inverse design problem for surfaces and led to the question of how to induce curvature in weavings. Considering the  $\pm\epsilon$ -offset surfaces was a natural extension of the “over” and “under” information that appears in the crossing sequence of a planar weave.

The methods from Chapter 4 did not produce results as quickly. When the underlying collaboration started at the 2022 summer school “Geometry and Topology in Contemporary Materials Science” in Copenhagen, I was able to learn a vast array of facts about minimal surfaces in physical systems and developed many new skills. Still, the results were not immediately statistically robust. I took this challenge as an opportunity to deepen my knowledge in differential geometry and data analysis. This required a relatively long research period before I could achieve meaningful results. By generating a large data set of disordered minimal surfaces, it became possible to compare surface invariants across various minimal surface classes. This meant simultaneously handling four different pieces of software and many repetitions of similar tasks. By working on the interface of mathematics and physics, this project was pushing the boundaries of what is mathematically possible and was consequently a difficult task. The project constantly required coming up with new solution approaches to computational problems and due to its interdisciplinarity, this research has immediate implications for real-world systems. Both of these facts make this direction of research fascinating.

## 7.2 Contributions to the Field and Future Research

In this section, we highlight the most significant results of this dissertation and identify open problems that offer promising new research directions.

### Geometric Theory of Framework Materials

In Chapter 2, we begin by investigating bar-and-joint frameworks as one of the simplest geometric constraint systems. Frameworks are defined as embedded graphs with edge length constraints. Such embedded graphs can either be flexible or rigid. We call a framework rigid when the edge length constraints do not allow them to move beyond the ambient Euclidean isometries.

Otherwise, they are flexible, signifying the existence of a continuous motion deforming the structure. The dual concepts of rigidity and flexibility are two sides of the same coin.

As an initial application of the theoretical foundation on framework materials, we consider geometric random graphs  $G$  generated from a Poisson point process in the plane. It is experimentally verified that these graphs satisfy asymptotic lower bounds concerning their local and global rigidity. Moreover, we show that a 3-coordinated graph is not necessarily globally rigid in  $\mathbb{R}^3$ , not even for generic realizations. As the rigid graph  $G$  is typically not 3-connected, its largest 3-coordinated subgraph cannot be globally rigid.

In a second case study, the rigidity of polytopes with coplanarity and edge length constraints is considered. These constraints allow us to prove the regular dodecahedron's rigidity and investigate what happens when some of the edge lengths change. We find that altering the length of a single edge results in 3 curves through the regular dodecahedron that can be obtained by smoothly gluing the deformation paths corresponding to 8 unique configurations nearby. One of these deformation paths loops back to the regular dodecahedron, forming a nodal singularity.

### Riemannian Optimization by Homotopy Continuation

To make it possible to traverse manifolds and equilibrate geometric constraint systems, we develop a robust Riemannian optimization algorithm in Chapter 3. Constituting a second-order approximation of the exponential map, the Euclidean distance retraction based on the metric projection is introduced. We show that the closest point problem is a second-order retraction in the statistical probability simplex as well. Using homotopy continuation, it is possible to solve the corresponding constraint optimization problem for arbitrary implicitly defined submanifolds of Euclidean space. This allows us to prove relevant convergence guarantees. By implementing a heuristic for escaping singularities, we extend the Riemannian optimization scheme to algebraic varieties. Combining the Euclidean distance retraction with a choice of step sizes informed by the Wolfe conditions and a suitable descent direction, the Riemannian optimization package `HomotopyOpt.jl` is created.

In numerical experiments, the homotopy continuation algorithm demonstrates its increased robustness. Conversely, it is not difficult to find examples where Newton's method diverges or converges to the wrong point. In case a manifold carries an explicit retraction map, it is significantly slower to use our method. Nevertheless, our algorithm makes it possible to use Riemannian optimization on general, implicitly defined manifolds. In particular, geometric constraint systems fall into this category and we show that retractions can be used for computing deformation paths. For applications, computing the Euclidean distance retraction using homotopy continuation methods is thus worth the increased computational cost.

Even though the Riemannian optimization package `HomotopyOpt.jl` has proven to work well in practice, it can be generalized in two key directions. Firstly, we restrict the constraints to algebraic sets defined by polynomial equations. This enables the usage of Lagrange multipliers, turning the Euclidean closest point problem into a square polynomial system. As a generalization, Kahn-Karush-Tucker constraints are an analogous construction to Lagrange multipliers for semialgebraic sets and come with similar theoretical results. It is thus possible

to incorporate these more general constraints in a Riemannian optimization algorithm. In particular, this makes the algorithm applicable to constraint polynomial optimization problems, where the nonnegativity of polynomials is investigated.

Secondly, we show that statistical manifolds equipped with the Fisher metric have a second-order retraction arising from the metric projection. We conjecture that this approach generalizes to arbitrary Riemannian manifolds with algebraic metrics, though the proof likely requires careful index treatment of the corresponding Christoffel symbols.

### Homogeneity of Disordered Minimal Surfaces

Riemannian geometry is not only a useful concept in optimization. It also gives rise to the principles of curvature and describes how a surface changes locally. A particular class of curved membranes is given by minimal surfaces and is investigated in Chapter 4. These structures appear in many organic systems through the minimization of surface tension. As the crystalline behavior of periodic structures allows the tiling of large volumes, periodic minimal surfaces can be observed in various organic settings. The Gyroid is among the most prevalent triply periodic minimal surfaces in nature and is conjectured to have the lowest curvature variance.

The development of two distinct models for generating disordered minimal surfaces, along with a topology-stabilized curvature optimization routine, enables the sampling of the configuration space of triply periodic minimal surfaces. By evaluating two homogeneity measures on all of these samples, we provide novel evidence for why the Gyroid is favored in nature: It is exceptionally good at distributing its curvature variation around a single point. While some of our disordered minimal surface models are highly isotropic, their curvature fluctuation is above the value of the Primitive, Diamond and Gyroid surfaces. When comparing the homogeneity measures to other classical bicontinuous interfaces that have been observed in nature, we find that this discrepancy becomes relatively small. Some disordered samples even perform better in the curvature fluctuation. This observation is evidence for why disordered phases appear in nature.

While we provide statistical evidence that the Gyroid is the most homogeneous triply periodic minimal surface, we are still far from a rigorous mathematical proof. The first step to a formal mathematical proof would be to obtain an understanding of the local Gaussian curvature behavior around flat points. With that information, it becomes possible to establish a lower bound for the integral of the average squared Gaussian curvature. By extension, this result would provide a lower bound on the Gaussian curvature variance.

Additionally, the algorithm for the generation of initial configurations based on parallel layers discussed in Section 4.3.3 is not yet fully explored. Potential constraints to enhance the homogeneity produced by this algorithm should be investigated more thoroughly.

### Deformations of Curved Cylinder Packings

Framework materials are used as a model for a multitude of real-world structures. In particular, they can be applied to describe packing problems by maintaining the minimal distance between the packed objects. In Chapter 5, we explore two examples of triply periodic cylinder packings and their deformations. This is achieved by constructing a robust tensegrity model based on

the configuration space of two filaments in tight orthogonal contact. This model comes with a corresponding nonlinear optimization problem, for which we explicitly construct a feasible initial configuration. Combined with a robust path-tracking algorithm, we compute deformation paths associated with the cylinder packings. The result is a robust measurement of the Poisson’s ratio for the tensegrity structures, capturing the extent of a material’s lateral response when stretched in a fixed direction. We demonstrate that the  $\Pi^+$  and  $\Sigma^+$  cylinder packings are auxetic by multiple definitions with well-behaved numerics. These results have a meaningful impact on theoretical materials science, where such structures are promising candidates for auxetic material design. Moreover, the Poisson’s ratio drops below  $(-1)$  in a small parameter range corresponding to the  $\Sigma^+$  packing. The value  $(-1)$  constitutes a lower bound for stable isotropic materials, making this result particularly significant.

As a next step, additional chiral cylinder packings should be considered with similar methods and checked for auxeticity. Potentially, this requires adjusting the corresponding tensegrity model to accurately represent the configuration space of two filaments in tight contact to understand the intermediate configurations in between the orthogonal clasp and the double helix. An enhanced understanding of the complete deformation space of two filaments in tight contact could open up the design space for materials based on cylinder packings even further, allowing for an array of different deformative behaviors. Furthermore, the “hyper-auxetic” parameter region observed in the  $\Sigma^+$  cylinder packing is intriguing and has already been verified by molecular dynamics simulations in the unpublished Master’s thesis of Anna Pini. The recent interest in such structures from the materials science community motivates us to investigate this intriguing behavior further.

## Weaving Models on Manifolds

Another application of framework materials is highlighted when constrained to curved surfaces. Starting from a 4-regular graph which is realized on a surface, we model weavings on manifolds in Chapter 6. When transforming these frameworks’ vertices to the  $\pm\varepsilon$ -offset surfaces, we can model the crossing information of weavings. Generalizing the existing theory for planar weaves to surfaces lets us create a tensegrity model to study the associated energy. By relaxing the initial assumption that the underlying framework is 4-regular, this model works for helical contacts and tangled weaves as well. This fact contrasts the previously discussed tensegrity model for cylinder packings. It is then possible to explicitly construct a feasible point of the nonlinear optimization problem corresponding to the tensegrity model. Polytopes provide many of our examples since they are tilings of the sphere. For surfaces other than the flat torus, the cylinder, and the sphere, we show that it is nontrivial how to properly model weavings.

By examining the quasistatic behavior of weavings on deforming spheres, we demonstrate that not all considered examples of weaves are stable under perturbations. This causes some weaves to deform into degenerate configurations. Our work illustrates how topologically more complex weaves energetically favor the sphere over deformed spheroids.

With this approach, we produce robust results for weavings constrained to the sphere and flat torus. Additional work is necessary to properly define weavings in that context for more general – in particular unbounded – manifolds. Further research should also investigate irregular

polytopes and their preferred types of ellipsoids to establish a general framework for spherical weavings.

In conclusion, this thesis explores the relationship between geometric materials and optimization. We demonstrate that many physical systems benefit from a joint approach that combines geometric modeling with smooth optimization. This allows us to propose a three-stage program for geometric design, emphasizing how various geometric techniques can be used to study materials and their deformations.

---

## References

---

- [1] Timothy G. Abbott. “Generalizations of Kempe’s Universality Theorem”. Master’s Thesis. Massachusetts Institute of Technology (2008).
- [2] William Abikoff. “The Uniformization Theorem”. In: *The American Mathematical Monthly* 88.8 (1981).
- [3] Dan Abramovich, Anne Frühbis-Krüger, Michael Temkin, and Jarosław Włodarczyk. *New Techniques in Resolution of Singularities*. 1st ed. Oberwolfach Seminars Vol. 50. Birkhäuser Verlag (2023).
- [4] Pierre-Antoine Absil, Robert Mahony, and Rodolphe Sepulchre. *Optimization Algorithms on Matrix Manifolds*. Princeton University Press (2008).
- [5] Pierre-Antoine Absil and Jérôme Malick. “Projection-like Retractions on Matrix Manifolds”. In: *SIAM Journal on Optimization* 22.1 (2012).
- [6] Daniel Acuna, Francisco Gutiérrez, Rodrigo Silva, Humberto Palza, Alvaro S. Nunez, and Gustavo Düring. “A three step recipe for designing auxetic materials on demand”. In: *Communications Physics* 5.1 (2022).
- [7] Roy L. Adler, Jean-Pierre Dedieu, Joseph Y. Margulies, Marco Martens, and Mike Shub. “Newton’s method on Riemannian manifolds and a geometric model for the human spine”. In: *IMA Journal of Numerical Analysis* 22.3 (2002).
- [8] Adrian Agogino, David Atkinson, and Vytas SunSpiral. *Super Ball Bot – Structures for Planetary Landing and Exploration*. Tech. rep. Intelligent Systems Division, National Aeronautics and Space Administration (2013).
- [9] Hillel Aharoni, Yu Xia, Xinyue Zhang, Randall Kamien, and Shu Yang. “Making Faces: Universal Inverse Design of Surfaces with Thin Nematic Elastomer Sheets”. In: *Proceedings of the National Academy of Sciences* 115 (2017).
- [10] Selman Akbulut and Henry C. King. “On Approximating Submanifolds by Algebraic Sets and a Solution to the Nash Conjecture”. In: *Inventiones Mathematicae* 107 (1992).
- [11] Firoz Alam, Aleksandar Subic, Simon Watkins, and Alexander John Smits. “Aerodynamics of an Australian Rules Foot Ball and Rugby Ball”. In: *Computational Fluid Dynamics for Sport Simulation*. Springer Berlin Heidelberg (2009).
- [12] Kim Alderson, Andrew Alderson, Subhash Anand, Virginia Simkins, Shonali Nazare, and Naveen Ravirala. “Auxetic warp knit textile structures”. In: *Physica Status Solidi (b)* 249.7 (2012).
- [13] Yulia Alexandr and Alexander Heaton. “Logarithmic Voronoi Cells”. In: *Algebraic Statistics* 12 (2021).

- [14] Aleksandr D. Alexandrov. *Convex Polyhedra*. 1st ed. Springer Monographs in Mathematics. Springer Science & Business Media (2005).
- [15] Grégoire Allaire and Sidi Mahmoud Kaber. *Numerical Linear Algebra*. Texts in Applied Mathematics Vol. 55. Springer Science & Business Media (2008).
- [16] George J. Allman. *Greek Geometry from Thales to Euclid*. Hodges, Figgis & Co., Dublin (1889).
- [17] Zakaria A. Almsherqi, Tomas Landh, Sepp D. Kohlwein, and Yuru Deng. “Cubic Membranes the Missing Dimension of Cell Membrane Organization”. In: *International Review of Cell and Molecular Biology* 274 (2009).
- [18] Martine Ben Amar, Martin Michael Müller, and Miguel Trejo. “Petal shapes of sympetalous flowers: the interplay between growth, geometry and elasticity”. In: *New Journal of Physics* 14.8 (2012).
- [19] David M. Anderson, Sol M. Gruner, and Stanislas Leibler. “Geometrical Aspects of the Frustration in the Cubic Phases of Lyotropic Liquid Crystals”. In: *Proceedings of the National Academy of Sciences* 85.15 (1988).
- [20] Sten Andersson and Michael O’Keefe. “Body-centred cubic cylinder packing and the garnet structure”. In: *Nature* 267.5612 (1977).
- [21] Tom M. Apostol. *Mathematical Analysis*. 2nd ed. Addison Wesley Publishing Company (1981).
- [22] Donu Arapura. *Algebraic Geometry over the Complex Numbers*. 1st ed. Universitext. Springer Science & Business Media (2012).
- [23] Larry Armijo. “Minimization of Functions having Lipschitz Continuous first partial Derivative”. In: *Pacific Journal of Mathematics* 16.1 (1966).
- [24] Leonard Asimow and Ben Roth. “The Rigidity of Graphs II”. In: *Journal of Mathematical Analysis and Applications* 68.1 (1979).
- [25] Azam Asl and Michael L. Overton. “Analysis of the Gradient Method with an Armijo–Wolfe Line Search on a Class of non-smooth convex Functions”. In: *Optimization Methods and Software* 35.2 (2020).
- [26] Daphne Attard, Aaron R. Casha, and Joseph N. Grima. “Filtration Properties of Auxetics with Rotating Rigid Units”. In: *Materials* 11.5 (2018).
- [27] Sheldon Axler. *Linear Algebra Done Right*. 3rd ed. Undergraduate Texts in Mathematics. Springer Cham (2015).
- [28] Nihat Ay, Jürgen Jost, Hông Vân Lê, and Lorenz Schwachhöfer. *Information Geometry*. 1st ed. A Series of Modern Surveys in Mathematics Vol. 64. Springer Science & Business Media (2017).
- [29] Maria-Florina Balcan, Travis Dick, Tuomas Sandholm, and Ellen Vitercik. “Learning to Branch”. In: *Proceedings of the 35th International Conference on Machine Learning*. Vol. 80. Proceedings of Machine Learning Research. (2018).

- [30] Gerard Barkema and Normand Mousseau. “High-Quality Continuous Random Networks”. In: *Physical Review B* 62 (1999).
- [31] Daniel J. Bates, Jonathan D. Hauenstein, Andrew J. Sommese, and Charles W. Wampler. *Bertini: Software for Numerical Algebraic Geometry*. (2013). Available online: [bertini.nd.edu](http://bertini.nd.edu) (visited on 04/16/2024).
- [32] Daniel J. Bates, Andrew J. Sommese, Jonathan D. Hauenstein, and Charles W. Wampler. *Numerically Solving Polynomial Systems with Bertini*. Society for Industrial and Applied Mathematics (2013).
- [33] Gary Becigneul and Octavian-Eugen Ganea. “Riemannian Adaptive Optimization Methods”. In: *International Conference on Learning Representations*. Ernest N. Morial Convention Center, New Orleans (2019). Available online: <https://openreview.net/forum?id=r1eiqi09K7>.
- [34] Ferdinand P. Beer, Russell Johnston, Jr., David F. Masurek, Phillip J. Cornwell, and Elliot R. Eisenberg. *Vector Mechanics for Engineers: Statics and Dynamics*. 9th ed. McGraw-Hill Professional (2010).
- [35] Mara Belotti, Michael Joswig, Chiara Meroni, Victoria Schleis, and Johannes Schmitt. “Algebraic and Geometric Computations in OSCAR”. In: *SIAM news* 56.7 (2023).
- [36] Alto D. Benedicto and David F. O’Brien. “Bicontinuous Cubic Morphologies in Block Copolymers and Amphiphile/Water Systems: Mathematical Description through the Minimal Surfaces”. In: *Macromolecules* 30.11 (1997).
- [37] Janine Bennett, Fabien Vivodtzev, and Valerio Pascucci. *Topological and Statistical Methods for Complex Data*. 1st ed. Mathematics and Visualization. Springer-Verlag Berlin Heidelberg (2015), (2015).
- [38] Daniel I. Bernstein and Robert Krone. “The Tropical Cayley–Menger Variety”. In: *SIAM Journal on Discrete Mathematics* 33.3 (2019).
- [39] Sébastien B. G. Blanquer, Maike Werner, Markus Hannula, Shahriar Sharifi, Guillaume P. R. Lajoinie, David Eglin, Jari Hyttinen, André A. Poot, and Dirk W Grijpma. “Surface curvature in triply-periodic minimal surface architectures as a distinct design parameter in preparing advanced tissue engineering scaffolds”. In: *Biofabrication* 9.2 (2017).
- [40] Andrea Bonato, Davide Marenduzzo, Davide Michieletto, and Enzo Orlandini. “Topological gelation of reconnecting polymers”. In: *Proceedings of the National Academy of Sciences of the United States of America* 119.44 (2022).
- [41] Charlotte Bonneau, Olaf Delgado-Friedrichs, Michael O’Keeffe, and Omar M. Yaghi. “Three-periodic nets and tilings: minimal nets”. In: *Acta Crystallographica Section A* 60.6 (2004).
- [42] Ciprian S. Borcea and Ileana Streinu. “Periodic Frameworks and Rigidity”. In: *Proceedings of the Royal Society A* 466 (2010).
- [43] Ciprian S. Borcea and Ileana Streinu. “Geometric Auxetics”. In: *Proceedings of the Royal Society A: Mathematical, Physical and Engineering Science* 471 (2015).

- [44] Ciprian S. Borcea and Ileana Streinu. “New principles for auxetic periodic design”. In: *SIAM Journal on Applied Algebra and Geometry* 1.1 (2017).
- [45] Ciprian S. Borcea and Ileana Streinu. “Auxetic Regions in Large Deformations of Periodic Frameworks”. In: *Interdisciplinary Applications of Kinematics* 71 (2019).
- [46] Alexander Borisov, Mark Dickinson, and Stuart Hastings. “A Congruence Problem for Polyhedra”. In: *The American Mathematical Monthly* 117.3 (2010).
- [47] Nicolas Boumal. *An Introduction to Optimization on Smooth Manifolds*. Cambridge University Press (2023).
- [48] Nicolas Boumal, Bamdev Mishra, Pierre-Antoine Absil, and Rodolphe Sepulchre. “Manopt, a Matlab Toolbox for Optimization on Manifolds”. In: *Journal of Machine Learning Research* 15.42 (2014). Available online: [manopt.org](http://manopt.org).
- [49] Stephen Boyd and Lieven Vandenberghe. *Convex Optimization*. Cambridge University Press, (2004).
- [50] Kenneth A. Brakke. “The surface evolver”. In: *Experimental Mathematics* 1.2 (1992).
- [51] Kenneth A. Brakke. *Triply Periodic Minimal Surfaces*. (2000). Available online: <http://kenbrakke.com/evolver/examples/periodic/periodic.html> (visited on 08/15/2024).
- [52] Johann Brauchart, Douglas P. Hardin, and Edward B. Saff. “Riesz Energy and Sets of Revolution in  $\mathbb{R}^3$ ”. In: *Proceedings of the Conference on Functional Analysis and Complex Analysis* 481 (2009).
- [53] Paul Breiding, Kathlén Kohn, and Bernd Sturmfels. *Metric Algebraic Geometry*. 1st ed. Oberwolfach Seminars Vol. 53. Birkhäuser Cham (2024).
- [54] Paul Breiding and Sascha Timme. “HomotopyContinuation.jl: A Package for Homotopy Continuation in Julia”. In: *Mathematical Software – ICMS 2018*. Springer International Publishing (2018).
- [55] Paul Breiding and Sascha Timme. *The reach of a plane curve*. (2019). Available online: <https://www.JuliaHomotopyContinuation.org/examples/reach-curve/> (visited on 06/24/2024).
- [56] Paul Breiding, Türkü Çelik, Timothy Duff, Alexander Heaton, Aida Maraj, Anna-Laura Sattelberger, Lorenzo Venturello, and Oğuzhan Yürük. “Nonlinear Algebra and Applications”. In: *Numerical Algebra, Control & Optimization* 13 (2021).
- [57] Raoul Bricard. “Mémoire sur la Théorie de l’Octaèdre Articulé”. In: *Journal de Mathématiques Pures et Appliquées* 5.3 (1897).
- [58] Luitzen E.J. Brouwer. “Beweis der Invarianz des  $n$ -dimensionalen Gebiets”. In: *Mathematische Annalen* 71 (1912).
- [59] Richard Buckminster Fuller. “Tensile-Integrity Structures”. Pat. United States, patent no. 3063521. (1962). Available online: <https://www.freepatentsonline.com/3063521.html>.
- [60] Richard L. Burden and J. Douglas Faires. *Numerical Analysis*. 9th ed. Cengage Learning (2011).

- [61] Robert William Burkhardt, Jr. *A Practical Guide to Tensegrity Design*. 2nd ed. (2008). Available online: <https://www.bobwb.tripod.com/tenseg/book/cover.html>.
- [62] Sébastien Callens, Christoph Arns, Alina Kuliesh, and Amir Zadpoor. “Decoupling Minimal Surface Metamaterial Properties Through Multi-Material Hyperbolic Tilings”. In: *Advanced Functional Materials* 31 (2021).
- [63] Ken Caluwaerts, Jérémie Despraz, Atil İşçen, Andrew P. Sabelhaus, Jonathan Bruce, Benjamin Schrauwen, and Vytas SunSpiral. “Design and Control of Compliant Tensegrity Robots Through Simulation and Hardware Validation”. In: *Journal of The Royal Society Interface* 11.98 (2014).
- [64] Liliana de Campo, Olaf Delgado-Friedrichs, Stephen T. Hyde, and Michael O’Keeffe. “Minimal nets and minimal minimal surfaces”. In: *Acta Crystallographica Section A* 69.5 (2013).
- [65] Jason Cantarella, Joseph Fu, Rob Kusner, John Sullivan, and Nancy Wrinkle. “Criticality for the Gehring Link Problem”. In: *Geometry & Topology* 10 (2006).
- [66] Ke Cao, Shizhe Feng, Ying Han, Libo Gao, Thuc Hue Ly, Zhiping Xu, and Yang Lu. “Elastic Straining of Free-Standing Monolayer Graphene”. In: *Nature Communications* 11.1 (2020).
- [67] Jose Capco, Matteo Gallet, Georg Grasegger, Christoph Koutschan, Niels Lubbes, and Josef Schicho. “The Number of Realizations of a Laman Graph”. In: *SIAM Journal on Applied Algebra and Geometry* 2.1 (2018).
- [68] Manfredo P. do Carmo. *Differential Geometry on Curves and Surfaces*. Prentice-Hall (1976).
- [69] Henri Cartan. *Elementary Theory of Analytic Functions of one or several complex variables*. Dover Publications, Inc., (1963).
- [70] Augustin-Louis Cauchy. “Recherche sur les Polyèdres – Premier Mémoire”. In: *Journal de l’École Polytechnique* 9 (1813).
- [71] Hao Chen. “Minimal Twin Surfaces”. In: *Experimental Mathematics* 28.4 (2019).
- [72] Hao Chen. “Existence of the Tetragonal and Rhombohedral Deformation Families of the Gyroid”. In: *Indiana University Mathematics Journal* 70.4 (2021).
- [73] Hao Chen and Matthias Weber. “A new deformation family of Schwarz’ D surface”. In: *Transactions of the American Mathematical Society* 374 (2021).
- [74] Hao Chen and Matthias Weber. “An Orthorhombic Deformation Family of Schwarz’ H Surfaces”. In: *Transactions of the American Mathematical Society* 374 (2021).
- [75] Jia-Ji Chen, Hui Xie, Ling-Zhi Liu, Huai Guan, Zesheng You, Lijie Zou, and Hai-Jun Jin. “Strengthening gold with dispersed nanovoids”. In: *Science* 385.6709 (2024).
- [76] Tianran Chen, Tsung-Lin Lee, and Tien-Yien Li. “Hom4PS-3: A Parallel Numerical Solver for Systems of Polynomial Equations Based on Polyhedral Homotopy Continuation Methods”. In: *Mathematical Software – ICMS 2014*. Springer (2014).

- [77] Albert Chern. *Discrete Differential Geometry*. Lecture Notes. Department of Computer Science and Engineering, UC San Diego, (2020). Available online: <https://cseweb.ucsd.edu/~alchern/teaching/DDG.pdf> (visited on 06/27/2024).
- [78] Diego Cifuentes, Kristian Ranestad, Bernd Sturmfels, and Madeleine Weinstein. “Voronoi Cells of Varieties”. In: *Journal of Symbolic Computation* 109 (2022).
- [79] Robert Connelly. “The Rigidity of Certain Cabled Frameworks and the Second-Order Rigidity of Arbitrarily Triangulated Convex Surfaces”. In: *Advances in Mathematics* 37 (1980).
- [80] Robert Connelly. “Generic Global Rigidity”. In: *Discrete & Computational Geometry* 33.4 (2005).
- [81] Robert Connelly and Steven J. Gortler. “Prestress Stability of Triangulated Convex Polytopes and Universal Second-Order Rigidity”. In: *SIAM Journal on Discrete Mathematics* 31.4 (2017).
- [82] Robert Connelly and Herman Servatius. “Higher-Order Rigidity – What Is the Proper Definition?” In: *Discrete & Computational Geometry* 11 (1994).
- [83] Robert Connelly and Walter Whiteley. “Second-Order Rigidity and Prestress Stability for Tensegrity Frameworks”. In: *SIAM Journal on Discrete Mathematics* 9.3 (1996).
- [84] J.H. Conway. “The Orbifold Notation for Surface Groups”. In: *Groups, Combinatorics and Geometry*. London Mathematical Society Lecture Note Series. Cambridge University Press (1992).
- [85] John H. Conway and Daniel H. Huson. “The Orbifold Notation for Two-Dimensional Groups”. In: *Structural Chemistry* 13.3/4 (2002).
- [86] David Cox, John Little, and Donal O’Shea. *Ideals, Varieties, and Algorithms. An Introduction to Computational Algebraic Geometry and Commutative Algebra*. 2nd ed. Springer Science & Business Media (2015).
- [87] Henry Crapo. “Structural Rigidity”. In: *Structural Topology* 1 (1979).
- [88] Richard H. Crowell and Ralph H. Fox. *Introduction to Knot Theory*. 1st ed. Graduate Texts in Mathematics Vol. 57. Springer New York (1963).
- [89] Jeremy Dalphin. “Study of Geometric Functionals Depending on Curvature by Shape Optimization Methods. Applications to the Functionals of Willmore and Canham-Helfrich”. Doctoral Thesis. Institut Élie Cartan de Lorraine (2014). Available online: <https://theses.hal.science/tel-01097663/> (visited on 06/15/2024).
- [90] Simon Danisch and Julius Krumbiegel. “Makie.jl: Flexible High-Performance Data Visualization for Julia”. In: *Journal of Open Source Software* 6 (2021).
- [91] Yann Dauphin, Razvan Pascanu, Caglar Gulcehre, Kyunghyun Cho, Surya Ganguli, and Yoshua Bengio. “Identifying and Attacking the Saddle Point Problem in High-Dimensional Non-Convex Optimization”. In: *Advances in Neural Information Processing Systems* 4 (2014).

- [92] Dmytro F. Davidenko. “On a New Method of Numerical Solution of Systems of Nonlinear Equations”. In: *Doklady Akademii Nauk SSSR* 88.4 (1953).
- [93] Wolfram Decker, Gert-Martin Greuel, Gerhard Pfister, and Hans Schönemann. SINGULAR 4-4-0 — *A computer algebra system for polynomial computations.* (2024). Available online: <http://www.singular.uni-kl.de>.
- [94] Max Dehn. “Über die Starrheit konvexer Polyeder”. In: *Mathematische Annalen* 77 (1916).
- [95] Tamal K. Dey and Wulue Zhao. “Approximate Medial Axis as a Voronoi Subcomplex”. In: *Computer-Aided Design* 36.2 (2004).
- [96] Alicia Dickenstein. “Algebraic Geometry Tools in Systems Biology”. In: *Notices of the American Mathematical Society* 67 (2020).
- [97] Christian S. Diercks and Omar M. Yaghi. “The atom, the molecule, and the covalent organic framework”. In: *Science* 355.6328 (2017).
- [98] James A. Dolan, Bodo D. Wilts, Silvia Vignolini, Jeremy J. Baumberg, Ullrich Steiner, and Timothy D. Wilkinson. “Optical Properties of Gyroid Structured Materials: From Photonic Crystals to Metamaterials”. In: *Advanced Optical Materials* 3.1 (2015).
- [99] Aleksandar Donev, Salvatore Torquato, Frank Stillinger, and Robert Connelly. “Jamming in Hard Sphere and Disk Packings”. In: *Journal of Applied Physics* 95 (2004).
- [100] Michael Dorff. “Soap Films, Differential Geometry, and Minimal Surfaces”. In: *Explorations in Complex Analysis*. American Mathematical Society, (2012).
- [101] Jan Draisma, Emil Horobet, Giorgio Ottaviani, Bernd Sturmfels, and Rekha Thomas. “The Euclidean Distance Degree”. In: *Proceedings of the 2014 Symposium on Symbolic-Numeric Computation.* (2014).
- [102] Mareike Dressler, Sadik Iliman, and Timo de Wolff. “An approach to constrained polynomial optimization via nonnegative circuit polynomials and geometric programming”. In: *Journal of Symbolic Computation* 91 (2019).
- [103] Scott A. Edwards, Johannes Wagner, and Frauke Gräter. “Dynamic Prestress in a Globular Protein”. In: *PLOS Computational Biology* 8.5 (2012).
- [104] David Eklund, Madeleine Weinstein, and Sandra Di Rocco. “The Bottleneck Degree of Algebraic Varieties”. In: *SIAM Journal on Applied Algebra and Geometry* 4.1 (2019).
- [105] Alfred Enneper. “Analytisch-geometrische Untersuchungen.” ger. In: *Nachrichten von der Königlichen Gesellschaft der Wissenschaften und der Georg-Augusts-Universität zu Göttingen* 1868 (1868).
- [106] Thomas Erber and George M. Hockney. “Complex Systems: Equilibrium Configurations of  $N$  Equal Charges on a Sphere ( $2 \leq N \leq 112$ )”. In: *Advances in Chemical Physics*. John Wiley & Sons (1997).
- [107] Myfanwy E. Evans and Stephen T. Hyde. “From Three-Dimensional Weavings to Swollen Corneocytes”. In: *Journal of the Royal Society Interface* 8.62 (2011).
- [108] Myfanwy E. Evans and Stephen T. Hyde. “Symmetric Tangling of Honeycomb Networks”. In: *Symmetry* 14.9 (2022).

- [109] Myfanwy E. Evans, Vanessa Robins, and Stephen T. Hyde. “Periodic Entanglement I: Networks From Hyperbolic Reticulations”. In: *Acta Crystallographica Section A* 69 (2013).
- [110] Myfanwy E. Evans, Vanessa Robins, and Stephen T. Hyde. “Periodic Entanglement II: Weavings from Hyperbolic Line Patterns”. In: *Acta Crystallographica Section A* 69 (2013).
- [111] Myfanwy E. Evans, Vanessa Robins, and Stephen T. Hyde. “Ideal Geometry of Periodic Entanglements”. In: *Proceedings of the Royal Society A: Mathematical, Physical and Engineering Science* 471.2181 (2015).
- [112] Myfanwy E. Evans and Roland Roth. “Shaping the Skin: the Interplay of Mesoscale Geometry and Corneocyte Swelling”. In: *Physical Review Letters* 112.3 (2014).
- [113] Myfanwy E. Evans, Gerd E. Schröder-Turk, and Andrew M. Kraynik. “A Geometric Exploration of Stress in Deformed Liquid Foams”. In: *Journal of Physics: Condensed Matter* 29.12 (2017).
- [114] Ylva Fernaeus, Martin Jonsson, and Jakob Tholander. “Revisiting the jacquard loom: threads of history and current patterns in HCI”. In: *Proceedings of the SIGCHI Conference on Human Factors in Computing Systems*. CHI ’12. Austin, Texas, USA: Association for Computing Machinery, (2012).
- [115] Johann Fischer and Martin Wendland. “On the History of Key Empirical Intermolecular Potentials”. In: *Fluid Phase Equilibria* 573 (2023).
- [116] Andrew Fogden. “Parametrization of Triply Periodic Minimal Surfaces. III. General Algorithm and Specific Examples for the Irregular Class”. In: *Acta Crystallographica Section A* 49 (1993).
- [117] Andrew Fogden and Stephan T. Hyde. “Continuous Transformations of Cubic Minimal Surfaces”. In: *The European Physical Journal B* 7.1 (1999).
- [118] Andrew Fogden and Stephen T. Hyde. “Parametrization of Triply Periodic Minimal Surfaces. I. Mathematical Basis of the Construction Algorithm for the Regular Class”. In: *Acta Crystallographica Section A* 48 (1992).
- [119] Andrew Fogden and Stephen T. Hyde. “Parametrization of Triply Periodic Minimal Surfaces. II. Regular Class Solutions”. In: *Acta Crystallographica Section A* 48 (1992).
- [120] Andrew Frohmader and Alexander Heaton. “Epsilon local rigidity and numerical algebraic geometry”. In: *Journal of Algebra and Its Applications* 21.01 (2022).
- [121] Mizuki Fukuda, Motoko Kotani, and Sonia Mahmoudi. “Classification of Doubly-Periodic untwisted  $(p, q)$ -Weaves by their Crossing Number and Matrices”. In: *Journal of Knot Theory and its Ramifications* (2023).
- [122] Mizuki Fukuda, Motoko Kotani, and Sonia Mahmoudi. *Construction of weaving and polycatenane motifs from periodic tilings of the plane*. (2023). arXiv: 2206 . 12168 [math.GT].
- [123] Hiroyasu Furukawa, Kyle Cordova, Michael O’Keeffe, and Omar Yaghi. “ChemInform Abstract: The Chemistry and Applications of Metal-Organic Frameworks”. In: *Science (New York, N.Y.)* 341 (2013).

- [124] Matteo Gallet, Georg Grasegger, Jan Legerský, and Josef Schicho. “Combinatorics of Bricard’s Octahedra”. In: *Comptes Rendus Mathématique* 359.1 (2021).
- [125] Paul Gandy and Jacek Klinowski. “Exact computation of the triply periodic G (‘Gyroid’) minimal surface”. In: *Chemical Physics Letters* 321 (2000).
- [126] Paul J.F. Gandy, Sonny Bardhan, Alan L. Mackay, and Jacek Klinowski. “Nodal Surface Approximations to the P, G, D and I-WP Triply Periodic Minimal Surfaces”. In: *Chemical Physics Letters* 336.3 (2001).
- [127] Semyon A. Gershgorin. “Über die Abgrenzung der Eigenwerte einer Matrix”. In: *Bulletin de l’Académie des Sciences de l’URSS* 6 (1931).
- [128] Philip E. Gill, Walter Murray, and Margaret H. Wright. *Practical Optimization*. 11th ed. Academic Press (1997).
- [129] Herman Gluck. “Almost All Simply Connected Closed Surfaces are Rigid”. In: *Chapter 17. Geometric Topology*. Lecture Notes in Mathematics Vol. 438. Springer Berlin Heidelberg (1975).
- [130] Raymond Goldstein, Adriana Pesci, Christophe Raufaste, and James Shemilt. “Geometry of Catenoidal Soap Film Collapse Induced by Boundary Deformation”. In: *Physical Review E* 104 (2021).
- [131] Andres Gonzalez, A. Luo, and Dongyan Shi. “Multi-Stable Deployment of Unitary Tensegrity Structures”. In: *IOP Conference Series: Materials Science and Engineering* 649 (2019).
- [132] Paul Grandgeorge, Changyeob Baek, Harmeet Singh, Paul Johanns, Tomohiko G. Sano, Alastair Flynn, John H. Maddocks, and Pedro M. Reis. “Mechanics of Two Filaments in Tight Orthogonal Contact”. In: *Proceedings of the National Academy of Sciences* 118.15 (2021).
- [133] Georg Grasegger, Christoph Koutschan, and Elias Tsigaridas. “Lower Bounds on the Number of Realizations of Rigid Graphs”. In: *Experimental Mathematics* 29.2 (2020).
- [134] Georg Grasegger and Jan Legerský. “Flexibility and rigidity of frameworks consisting of triangles and parallelograms”. In: *Computational Geometry* 120 (2024).
- [135] S. Gratton, A. S. Lawless, and N. K. Nichols. “Approximate Gauss–Newton Methods for Nonlinear Least Squares Problems”. In: *SIAM Journal on Optimization* 18.1 (2007).
- [136] Jack E. Graver. *Counting on Frameworks: Mathematics to Aid the Design of Rigid Structures*. Dolciani Mathematical Expositions Vol. 25. Mathematical Association of America, (2001).
- [137] George N. Greaves, Alan L. Greer, Roderic Lakes, and Tanguy Rouxel. “Poisson’s Ratio and Modern Materials”. In: *Nature Materials* 10 (2011).
- [138] David A. Grier. *When computers were human*. 3rd ed. Princeton University Press, (2007).
- [139] Itay Griniasty, Hillel Aharoni, and Efi Efrati. “Curved Geometries from Planar Director Fields: Solving the Two-Dimensional Inverse Problem”. In: *Physical Review Letters* 123.12 (2019).

- [140] Karsten Große-Brauckmann and Meinhard Wohlgemuth. “The gyroid is embedded and has constant mean curvature companions”. In: *Calculus of Variations and Partial Differential Equations* 4.6 (1996).
- [141] John Guckenheimer. “The Catastrophe Controversy”. In: *The Mathematical Intelligencer* 1 (1978).
- [142] Yaqi Guo, Saurav Sharma, and Siddhant Kumar. “Inverse Designing Surface Curvatures by Deep Learning”. In: *Advanced Intelligent Systems* 6.6 (2024).
- [143] Prashant Gupta and Bala Krishnamoorthy. “Euler Transformation of Polyhedral Complexes”. In: *International Journal of Computational Geometry & Applications* 30.03n04 (2020).
- [144] Lukas Gustafsson. “Topics in Projective Algebraic Optimization”. Doctoral Thesis. Kungliga Tekniska Högskolan Stockholm (2023).
- [145] Merse E. Gáspár and Peter Csermely. “Rigidity and Flexibility of Biological Networks”. In: *Briefings in Functional Genomics* 11.6 (2012).
- [146] Thomas Hales et al. “A Formal Proof of the Kepler Conjecture”. In: *Forum of Mathematics, Pi* 5 (2017).
- [147] Thomas C. Hales. “The Honeycomb Conjecture”. In: *Discrete & Computational Geometry* 25.1 (2001).
- [148] Hendrik Hansen-Goos, Roland Roth, Klaus Mecke, and Dietrich Stoyan. “Solvation of proteins: Linking thermodynamics to geometry”. In: *Physical Review Letters* 99.12 (2007).
- [149] Robin Hartshorne. *Algebraic Geometry*. 1st ed. Springer Graduate Texts in Mathematics Vol. 52. Springer Science & Business Media (1977).
- [150] Allen Hatcher. *Algebraic Topology*. Cambridge University Press (2002).
- [151] Jonathan D. Hauenstein and Margaret H. Regan. “Adaptive Strategies for Solving Parameterized Systems Using Homotopy Continuation”. In: *Applied Mathematics and Computation* 332 (2018).
- [152] Shan-Shan He, Xu Yin, Li-Yuan Zhang, Zhi-Ying Gao, and Guang-Kui Xu. “Directional Snapping Instability in a Bistable Tensegrity under Uniaxial Loads”. In: *Composite Structures* 283 (2022).
- [153] Alexander Heaton and Matthias Himmelmann. “Computing Euclidean distance and maximum likelihood retraction maps for constrained optimization”. In: *Computational Geometry* 126 (2025).
- [154] Alexander Heaton and Sascha Timme. “Catastrophe in Elastic Tensegrity Frameworks”. In: *Arnold Mathematical Journal* 8.3 (2022).
- [155] Miroslav Hejna, Paul J. Steinhardt, and Salvatore Torquato. “Nearly hyperuniform network models of amorphous silicon”. In: *Physical Review B* 87.24 (2013).
- [156] Wolfgang Helfrich and Helmut Rennschuh. “Landau Theory of the Lamellar-to-Cubic Phase Transition”. In: *Journal de Physique Colloques* 51.C7 (1990).

- [157] David W. Henderson and Daina Taimina. “Crocheting the Hyperbolic Plane”. In: *The Mathematical Intelligencer* 23 (2009).
- [158] Bruce Hendrickson. “The Molecule Problem: Exploiting Structure in Global Optimization”. In: *SIAM Journal on Optimization* 5.4 (1995).
- [159] Susanne M.A. Hermans, Christopher Pfleger, Christina Nutschel, Christian A. Hanke, and Holger Gohlke. “Rigidity theory for biomolecules: concepts, software, and applications”. In: *WIREs Computational Molecular Science* 7.4 (2017).
- [160] David Hilbert. “Über die Darstellung definiter Formen als Summe von Formenquadraten”. In: *Mathematische Annalen* 32.3 (1888).
- [161] Matthias Himmelmann and Myfanwy E. Evans. “Robust Geometric Modeling of 3-Periodic Tensegrity Frameworks Using Riemannian Optimization”. In: *SIAM Journal on Applied Algebra and Geometry* 8.2 (2024).
- [162] Heisuke Hironaka. “Resolution of Singularities of an Algebraic Variety over a Field of Characteristic Zero: I”. In: *Annals of Mathematics* 79.1 (1964).
- [163] Robert V. Hogg, Joseph W. McKean, and Allen T. Craig. *Introduction to Mathematical Statistics*. 8th ed. Pearson (2019).
- [164] Roger A. Horn and Charles R. Johnson. *Matrix Analysis*. 2nd ed. Cambridge University Press (2012).
- [165] Emil Horobet and Madeleine Weinstein. “Offset Hypersurfaces and Persistent Homology of Algebraic Varieties”. In: *Computer Aided Geometric Design* 74 (2019).
- [166] Reshad Hosseini and Suvrit Sra. “An alternative to EM for Gaussian mixture models: batch and stochastic Riemannian optimization”. In: *Mathematical Programming* 181.1 (2020).
- [167] Seyedehsomayeh Hosseini, Wen Huang, and Rohollah Yousefpour. “Line Search Algorithms for locally Lipschitz Functions on Riemannian Manifolds”. In: *SIAM Journal on Optimization* 28.1 (2018).
- [168] Stephen T. Hyde. “Curvature and the Global Structure of Interfaces in Surfactant-Water Systems”. In: *Le Journal de Physique Colloques* 51.C7 (1990).
- [169] Stephen T. Hyde and Myfanwy E. Evans. “Symmetric Tangled Platonic Polyhedra”. In: *Proceedings of the National Academy of Sciences* 119.1 (2022).
- [170] Stephen T. Hyde, Stuart J. Ramsden, and Vanessa Robins. “Unification and Classification of Two-Dimensional Crystalline Patterns Using Orbifolds”. In: *Acta Crystallographica Section A* 70 (2014).
- [171] Sadik Iliman and Timo de Wolff. “Amoebas, Nonnegative Polynomials and Sums of Squares Supported on Circuits”. In: *Research in the Mathematical Sciences* 3.1 (2016).
- [172] Wolfram Research, Inc. *Mathematica, Version 14.0*. Champaign, IL (2024). Available online: <https://www.wolfram.com/mathematica>.
- [173] Donald E. Ingber. “The Architecture of Life”. In: *Scientific American* 278.1 (1998).

- [174] Tomoyuki Iori and Toshiyuki Ohtsuka. “Limit Operation in Projective Space for Constructing Necessary Optimality Condition of Polynomial Optimization Problem”. In: *Journal of the Operations Research Society of Japan* 63.4 (2020).
- [175] Francis R. L. Israel. *How weavers helped invent computers and put them on the moon.* (2019). Available online: <https://medium.com/@reil/how-the-weaving-helped-invent-computers-and-put-them-on-the-moon-9af1c85a09e6> (visited on 08/17/2024).
- [176] Bill Jackson and Tibor Jordán. “Connected Rigidity Matroids and Unique Realizations of Graphs”. In: *Journal of Combinatorial Theory, Series B* 94.1 (2005).
- [177] Bill Jackson, Tibor Jordán, and Shin ichi Tanigawa. “Unique low rank completable of partially filled matrices”. In: *Journal of Combinatorial Theory, Series B* 121 (2016).
- [178] Anna-Lee Jessop, Allan Millsteed, Jacob Kirkensgaard, Jeremy Shaw, Peta Clode, and Gerd Schröder-Turk. “Composite Material in the Sea Urchin Cidaris Rugosa: Ordered and Disordered Micrometre-Scale Bicontinuous Geometries”. In: *Journal of the Royal Society, Interface* 21 (2024).
- [179] Tianjian Ji. “Concepts for Designing Stiffer Structures”. In: *Structural Engineer* 81 (2003).
- [180] Caigui Jiang, Florian Rist, Hui Wang, Johannes Wallner, and Helmut Pottmann. “Shape-morphing mechanical metamaterials”. In: *Computer-Aided Design* 143 (2022).
- [181] Yunyao Jiang and Yaning Li. “3D Printed Chiral Cellular Solids with Amplified Auxetic Effects Due to Elevated Internal Rotation”. In: *Advanced Engineering Materials* 19.2 (2017).
- [182] Jose Beltrán Jiménez, Lavinia Heisenberg, and Tomi S. Koivisto. “The Geometrical Trinity of Gravity”. In: *Universe* 5.7 (2019).
- [183] Paul Johanns, Paul Grandgeorge, Changyeob Baek, Tomohiko G. Sano, John H. Maddocks, and Pedro M. Reis. “The Shapes of Physical Trefoil Knots”. In: *Extreme Mechanics Letters* 43 (2021).
- [184] Tibor Jordán and Zoltán Szabadka. “Operations preserving the global rigidity of graphs and frameworks in the plane”. In: *Computational Geometry* 42.6 (2009).
- [185] Tibor Jordán and Walter Whiteley. “Global Rigidity”. In: *Handbook of Discrete and Computational Geometry*. 3rd ed. Chapter 63. CRC Press LLC (2017).
- [186] Yasmin Kafai. “Celebrating Ada Lovelace”. In: *The MIT Press* (2016). Available online: <https://mitpress.mit.edu/celebrating-ada-lovelace/> (visited on 08/16/2024).
- [187] Hermann Karcher. “The Triply Periodic Minimal Surfaces of Alan Schoen and their Constant Mean Curvature Companions”. In: *Manuscripta Mathematica* 64 (1989).
- [188] Hermann Karcher and Konrad Polthier. “Construction of triply periodic minimal surfaces”. In: *Philosophical Transactions of the Royal Society of London. Series A: Mathematical, Physical and Engineering Sciences* 354.1715 (1996).

- [189] Muhammad Imran Khan, Muhammad Umair, and Yasir Nawab. “8 - Use of auxetic material for impact/ballistic applications”. In: *Composite Solutions for Ballistics*. Woodhead Publishing Series in Composites Science and Engineering. Woodhead Publishing, (2021).
- [190] Derek Kitson and Stephen C. Power. “Infinitesimal rigidity for non-Euclidean bar-joint frameworks”. In: *Bulletin of the London Mathematical Society* 46.4 (2014).
- [191] Michael A. Klatt, Paul J. Steinhardt, and Salvatore Torquato. “Gap Sensitivity Reveals Universal Behaviors in Optimized Photonic Crystal and Disordered Networks”. In: *Physical Review Letters* 127.3 (2021).
- [192] Motoko Kotani, Hisashi Naito, and Eriko Shinkawa. *Stable Configurations of Entangled Graphs and Weaves with Repulsive Interactions*. (2023). arXiv: 2309.01613 [math.DG].
- [193] Kathryn Sullivan Kruger. “Weaving the word: The metaphorics of weaving and female textual production”. PhD thesis. University of Miami, (1994).
- [194] Siddhant Kumar, Stephanie Tan, Li Zheng, and Dennis M. Kochmann. “Inverse-designed spinodoid metamaterials”. In: *npj Computational Materials* 6.1 (2020).
- [195] Rod S. Lakes. “Response: Negative Poisson’s Ratio Materials”. In: *Science* 238 (1987).
- [196] Gerard Laman. “On Graphs and Rigidity of Plane Skeletal Structures”. In: *Journal of Engineering Mathematics* 4.4 (1970).
- [197] John M. Lee. *Introduction to Riemannian Manifolds*. 2nd ed. Graduate Texts in Mathematics Vol. 176. Springer Science & Business Media (2018).
- [198] John M. Lee. *Introduction to Smooth Manifolds*. 2nd ed. Graduate Texts in Mathematics Vol. 218. Springer New York (2012).
- [199] John M. Lee. *Introduction to Topological Manifolds*. 2nd ed. Graduate Texts in Mathematics Vol. 202. Springer Science & Business Media (2011).
- [200] Stephen Levin. “The Tensegrity-Truss as a Model for Spine Mechanics: Biotensegrity”. In: *Journal of Mechanics in Medicine and Biology* 2 (2002).
- [201] Anton Leykin. “Numerical Algebraic Geometry for Macaulay2”. In: *Journal for Software of Algebra and Geometry* 3 (2011).
- [202] Anton Leykin, Jose Israel Rodriguez, and Frank Sottile. “Trace Test”. In: *Arnold Mathematical Journal* 4.1 (2018).
- [203] Yan Li and Changchun Zeng. “On the successful fabrication of auxetic polyurethane foams: Materials requirement, processing strategy and conversion mechanism”. In: *Polymer* 87 (2016).
- [204] Sven Lidin. “Some Results of the Bonnet Transformation”. In: *Journal de Physique Colloques* 51.C7 (1990).
- [205] Yuzhong Liu, Michael O’Keeffe, Michael M. J. Treacy, and Omar M. Yaghi. “The Geometry of Periodic Knots, Polycatenanes and Weaving from a Chemical Perspective: a Library for Reticular Chemistry.” In: *Chemical Society Reviews* 47 12 (2018).

- [206] Eric Lord and Alan Mackay. “Periodic Minimal Surfaces of Cubic Symmetry”. In: *Current Science* 85 (2003).
- [207] Juan Luengo-Márquez, Salvatore Assenza, and Cristian Micheletti. “Shape and size tunability of sheets of interlocked ring copolymers”. In: *Soft Matter* (2024).
- [208] Nathaniel A. Lynd, Adam J. Meuler, and Marc A. Hillmyer. “Polydispersity and block copolymer self-assembly”. In: *Progress in Polymer Science* 33.9 (2008).
- [209] Luigi Malomo, Jesus Perez, Emmanuel Iarussi, Nico Pietroni, Eder Miguel, Paolo Cignoni, and Bernd Bickel. “FlexMaps: Computational design of flat flexible shells for shaping 3D objects”. In: *ACM Transactions on Graphics* (2018).
- [210] Luigi Malomo, Jesús Pérez, Emmanuel Iarussi, Nico Pietroni, Eder Miguel, Paolo Cignoni, and Bernd Bickel. “FlexMaps: computational design of flat flexible shells for shaping 3D objects”. In: *ACM Transactions on Graphics* 37.6 (2018).
- [211] Weining Man, Aleksandar Donev, Frank H. Stillinger, Matthew T. Sullivan, William B. Russel, David Heeger, Souheil Inati, Salvatore Torquato, and Paul M. Chaikin. “Experiments on Random Packings of Ellipsoids”. In: *Physical Review Letters* 94.19 (2005).
- [212] Shashank Markande, Matthias Saba, Gerd Schröder-Turk, and Elisabetta Matsumoto. “A chiral family of triply-periodic minimal surfaces derived from the quartz network”. In: (2018).
- [213] James C. Maxwell. “On Reciprocal Figures and Diagrams of Forces”. In: *Philosophical Magazine* 27.4 (1864).
- [214] Kathryn M. McGrath, Daniel M. Dabbs, Nan Yao, Karen J. Edler, Ilhan A. Aksay, and Sol M. Gruner. “Silica Gels with Tunable Nanopores through Templating of the L3 Phase”. In: *Langmuir* 16.2 (2000).
- [215] William H. Meeks III. “The Conformal Structure and Geometry of Triply Periodic Minimal Surfaces in  $\mathbb{R}^3$ ”. In: *Bulletin of the American Mathematical Society* 83.1 (1977).
- [216] William H. Meeks III. “The Theory of Triply Periodic Minimal Surfaces”. In: *Indiana University Mathematics Journal* 39.3 (1990).
- [217] William H. Meeks III. and Joaquín Pérez. “The classical Theory of Minimal Surfaces”. In: 48.3 (2011).
- [218] Mateusz Michałek and Bernd Sturmfels. *Invitation to Nonlinear Algebra*. Graduate Studies in Mathematics. American Mathematical Society (2021).
- [219] Alessandra Micheletti and Vincenzo Capasso. “The Stochastic Geometry of the Crystallization Process of Polymers”. In: *International Series of Numerical Mathematics* 147 (2003).
- [220] Andrea Micheletti. “Bistable Regimes in an Elastic Tensegrity System”. In: *Royal Society of London Proceedings Series A* 469 (2013).

- [221] Ferdinand Minding. “Wie sich entscheiden lässt, ob zwei gegebene krumme Flächen auf einander abwickelbar sind oder nicht; nebst Bemerkungen über die Flächen von unveränderlichem Krümmungsmaße.” In: *Journal für die Reine und Angewandte Mathematik* 19 (1839).
- [222] Nina Miolane et al. “Geomstats: A Python Package for Riemannian Geometry in Machine Learning”. In: *Journal of Machine Learning Research* 21.223 (2020).
- [223] Alexander P. Morgan and Andrew J. Sommese. “A Homotopy for Solving General Polynomial Systems that Respects  $m$ -Homogeneous Structures”. In: *Applied Mathematics and Computation* 24 (1987).
- [224] René Motro. “Tensegrity: From Art to Structural Engineering”. In: *IASS-APCS Symposium.* (2012).
- [225] David Mumford. *The Red Book of Varieties and Schemes*. 2nd ed. Lecture Notes in Mathematics. Springer Science & Business Media (1999).
- [226] James Munkres. *Topology*. 2nd ed. Pearson Education (2014).
- [227] Riley Murray, Venkat Chandrasekaran, and Adam Wierman. “Newton Polytopes and Relative Entropy Optimization”. In: *Foundations of Computational Mathematics* 21.6 (2021).
- [228] Stefan Müller, Elisenda Feliu, Georg Regensburger, Carsten Conradi, Anne Shiu, and Alicia Dickenstein. “Sign Conditions for Injectivity of Generalized Polynomial Maps with Applications to Chemical Reaction Networks and Real Algebraic Geometry”. In: *Foundations of Computational Mathematics* 16.1 (2016).
- [229] Jiawang Nie and Kristian Ranestad. “Algebraic Degree of Polynomial Optimization”. In: *SIAM Journal on Optimization* 20.1 (2009).
- [230] Andrea Ninarello, José Ruiz-Franco, and Emanuela Zaccarelli. “Onset of Criticality in Hyper-Auxetic Polymer Networks”. In: *Nature Communications* 13.1 (2022).
- [231] Johannes C. C. Nitsche. *Vorlesungen über Minimalflächen*. Die Grundlagen der mathematischen Wissenschaften in Einzeldarstellungen Vol. 199. Springer-Verlag, (1975).
- [232] Anthony Nixon, John Owen, and Stephen Power. “Rigidity of Frameworks Supported on Surfaces”. In: *SIAM Journal on Discrete Mathematics* 26 (2010).
- [233] Anthony Nixon, John Owen, and Stephen Power. “A Characterization of Generically Rigid Frameworks on Surfaces of Revolution”. In: *SIAM Journal on Discrete Mathematics* 28 (2014).
- [234] Jorge Nocedal and Stephen Wright. *Numerical Optimization*. 2nd ed. Springer Series in Operations Research and Financial Engineering. Springer New York (2006).
- [235] Lars Norlén and Ashraf Al-Amoudi. “Stratum Corneum Keratin Structure, Function, and Formation: The Cubic Rod-Packing and Membrane Templating Model”. In: *Journal of Investigative Dermatology* 123.4 (2004).

- [236] Michael O’Keeffe, Jacques Plevert, Yoshinori Teshima, Yoshinori Watanabe, and Toru Ogawa. “The Invariant cubic rod (cylinder) packings: symmetries and coordinates”. In: *Acta Crystallographica Section A* 57 (2001).
- [237] Kasper Olsen and Jakob Bohr. “The Generic Geometry of Helices and their Close-Packed Structures”. In: *Theoretical Chemistry Accounts* 125.3 (2010).
- [238] Kasper Olsen and Jakob Bohr. “Geometry of the Toroidal  $n$ -Helix: Optimal-Packing and Zero-Twist”. In: *New Journal of Physics* 14 (2012).
- [239] Barrett O’Neill. *Elementary Differential Geometry*. 2nd ed. Academic Press (2006).
- [240] Barrett O’Neill. *Semi-Riemannian Geometry With Applications to Relativity*. 1st ed. Pure and Applied Mathematics Vol. 103. Academic Press (1983).
- [241] Irving J. Oppenheim and William O. Williams. “Geometric Effects in an Elastic Tensegrity Structure”. In: *Journal of Elasticity* 59 (2000).
- [242] Mathias Oster, Marcelo A. Dias, Timo de Wolff, and Myfanwy E. Evans. “Reentrant Tensegrity: A three-periodic, chiral, Tensegrity Structure that is auxetic”. In: *Science Advances* 7.50 (2021).
- [243] Michael O’Keeffe, Maxim A. Peskov, Stuart J. Ramsden, and Omar M. Yaghi. “The Reticular Chemistry Structure Resource (RCSR) Database of, and Symbols for, Crystal Nets”. In: *Accounts of Chemical Research* 41.12 (2008).
- [244] Lior Pachter and Bernd Sturmfels. *Algebraic Statistics for Computational Biology*. Cambridge University Press (2005).
- [245] Lothar Papula. “Oberflächenintegrale”. In: *Mathematik für Ingenieure und Naturwissenschaftler: Vektoranalysis, Wahrscheinlichkeitsrechnung, Mathematische Statistik, Fehler- und Ausgleichsrechnung*. Vieweg & Teubner Verlag, (1997).
- [246] So Jung Park, Frank S. Bates, and Kevin D. Dorfman. “Single Gyroid in H-Shaped Block Copolymers”. In: *Physical Review Materials* 7.10 (2023).
- [247] Beresford Parlett. “Global Convergence of the Basic QR Algorithm On Hessenberg Matrices”. In: *Mathematics of Computation* 22.104 (1968).
- [248] Antonella Patti and Domenico Acierno. “Materials, Weaving Parameters, and Tensile Responses of Woven Textiles”. In: *Macromol* 3.3 (2023).
- [249] Jason D. Perlmutter and Michael F. Hagan. “Mechanisms of Virus Assembly”. In: *Annual Review of Physical Chemistry* 66 (2015).
- [250] Piotr Pieranski. “In Search of Ideal Knots”. In: *Ideal Knots*. Series on Knots and Everything. World Scientific, 1998.
- [251] Ulrich Pinkall and Konrad Polthier. “Computing discrete minimal surfaces and their conjugates”. In: *Experimental Mathematics* 2.1 (1993).
- [252] Robi Polikar. “Ensemble Based Systems in Decision Making”. In: *IEEE Circuits and Systems Magazine* 6.3 (2006).

- [253] Hilda Pollaczek-Geiringer. “Über die Gliederung ebener Fachwerke”. In: *Zeitschrift für Angewandte Mathematik und Mechanik* 7.1 (1927).
- [254] Tim Poston and Alexander Woodcock. “Zeeman’s Catastrophe Machine”. In: *Mathematical Proceedings of the Cambridge Philosophical Society* 74 (1973).
- [255] Andrew Presley. *Elementary Differential Geometry*. 2nd ed. Undergraduate Texts in Mathematics. Springer London (2010).
- [256] Chunhong Qi, Kyle Gallivan, and Pierre-Antoine Absil. “Riemannian BFGS Algorithm with Applications”. In: *Recent Advances in Optimization and its Applications in Engineering* (2010).
- [257] Laith Rastanawi, Rainer Sinn, and Günter M. Ziegler. “On the Dimensions of the Realization Spaces of Polytopes”. In: *Mathematika* 67.2 (2021).
- [258] Yingying Ren, Julian Panetta, Tian Chen, Florin Isvoranu, Samuel Poincloux, Christopher Brandt, Alison Martin, and Mark Pauly. “3D Weaving with Curved Ribbons”. In: *ACM Transactions on Graphics* 40.4 (2021).
- [259] Wolfgang Ring and Benedikt Wirth. “Optimization Methods on Riemannian Manifolds and their Application to Shape Space”. In: *SIAM Journal on Optimization* 22.2 (2012).
- [260] Elizabeth Roberts. “Women’s Work 1840–1940”. In: *British Trade Union and Labour History A Compendium*. 1st ed. Macmillan Education UK, (1990).
- [261] Emmanuel Rodriguez, Georges-Pierre Bonneau, Stefanie Hahmann, and Mélina Skouras. “Computational Design of Laser-Cut Bending-Active Structures”. In: *Computer-Aided Design* 151 (2022).
- [262] M. Magdalena Rodríguez. “Minimal surfaces with genus zero”. In: *Publicaciones de la Real Sociedad Matemática Española* 11 (2007).
- [263] Sean Rose, Dexter Siu, J. Zhu, and Reem Roufail. “Auxetics in Biomedical Applications: A Review”. In: *Journal of Minerals and Materials Characterization and Engineering* 11 (2023).
- [264] Nathania L. Rosi, Jaheon Kim, Mohamed Eddaoudi, Banglin Chen, Michael O’Keeffe, and Omar M. Yaghi. “Rod packings and metal-organic frameworks constructed from rod-shaped secondary building units”. In: *Journal of the American Chemical Society* 127.5 (2005).
- [265] Elissa Ross. “The Rigidity of Periodic Frameworks as Graphs on a Fixed Torus”. In: *Contributions to Discrete Mathematics* 9 (2012).
- [266] Ben Roth and Walter Whiteley. “Tensegrity Frameworks”. In: *Transactions of The American Mathematical Society* 265 (1981).
- [267] Didier Roux. “Sponge phases: An Example of Random Surfaces”. In: *Physica A: Statistical Mechanics and its Applications* 213.1 (1995).
- [268] Walter Rudin. *Principles of Mathematical Analysis*. 3rd ed. International Series in pure and applied Mathematics. McGraw-Hill Education (1976).

- [269] Eva Sachs. *Die Fünf Platonischen Körper*. Weidmannsche Buchhandlung Berlin (1917).
- [270] Franco V. Saliola and Walter Whiteley. *Some Notes on the Equivalence of First-Order Rigidity in Various Geometries*. (2007). arXiv: 0709.3354 [math.MG].
- [271] Vanessa Sanchez et al. “Smart Thermally Actuating Textiles”. In: *Advanced Materials Technologies* 5.8 (2020).
- [272] Vijayaventaraman Sanjairaj, Lei Zhang, Shuo Zhang, J. Fuh, and Wen-Feng Lu. “Triply Periodic Minimal Surfaces Sheet Scaffolds for Tissue Engineering Applications: An Optimization Approach toward Biomimetic Scaffold Design”. In: *ACS Applied Bio Materials* 1 (2018).
- [273] Tomohisa Sawada and Makoto Fujita. “Orderly Entangled Nanostructures of Metal–Peptide Strands”. In: *Bulletin of the Chemical Society of Japan* 94.10 (2021).
- [274] Anupam Saxena. “Kempe’s Linkages and the Universality Theorem”. In: *Resonance* 16.3 (2011).
- [275] Robert Schaback. “Convergence Analysis of the General Gauss-Newton Algorithm”. In: *Numerische Mathematik* 46 (1985).
- [276] Fabian M. Schaller, Sebastian C. Kapfer, Myfanwy E. Evans, Matthias J.F. Hoffmann, Tomaso Aste, Mohammad Saadatfar, Klaus Mecke, Gary W. Delaney, and Gerd E. Schröder-Turk. “Set Voronoi Diagrams of 3D Assemblies of Aspherical Particles”. In: *Philosophical Magazine* 93.31-33 (2013).
- [277] Barbara Schamberger et al. “Curvature in Biological Systems: Its Quantification, Emergence, and Implications across the Scales”. In: *Advanced Materials* 35.13 (2023).
- [278] Michael Schick. “Avatars of the Gyroid”. In: *Physica A: Statistical Mechanics and its Applications* 251.1 (1998).
- [279] Hans G. von Schnerring and Reinhard Nesper. “How Nature Adapts Chemical Structures to Curved Surfaces”. In: *Angewandte Chemie International Edition in English* 26.11 (1987).
- [280] Alan H. Schoen. *Infinite Periodic Minimal Surfaces without Self-Intersections*. Tech. rep. TN D-5541. NASA, (1970).
- [281] Gerd E. Schröder, Stuart J. Ramsden, Andrew Fogden, and Stephen T. Hyde. “A Rhombohedral Family of Minimal Surfaces as a Pathway Between the P and D Cubic Mesophases”. In: *Physica A* 339 (2004).
- [282] Gerd E. Schröder-Turk. “Skeletons in the labyrinth: Medial Representations and packing properties of bicontinuous space partitions”. PhD thesis. Australian National University, (2005).
- [283] Gerd E. Schröder-Turk, Andrew Fogden, and Stephen T. Hyde. “Bicontinuous Geometries and Molecular Self-Assembly: Comparison of Local Curvature and Global Packing Variations in Genus-Three Cubic, Tetragonal and Rhombohedral Surfaces”. In: *The European Physical Journal B* 54 (2006).

- [284] Gerd E. Schröder-Turk, Andrew Fogden, and Stephen T. Hyde. “Local v/a variations as a measure of structural packing frustration in bicontinuous mesophases, and geometric arguments for an alternating  $\text{Im}\bar{3}\text{m}$  (I-WP) phase in block-copolymers with polydispersity”. In: *The European Physical Journal B* 59.1 (2007).
- [285] Gerd E. Schröder-Turk, Walter Mickel, Sebastian C. Kapfer, Fabian M. Schaller, Boris Breidenbach, Daniel Hug, and Klaus Mecke. “Minkowski Tensors of Anisotropic Spatial Structure”. In: *New Journal of Physics* 15.8 (2013).
- [286] Gerd E. Schröder-Turk, Trond Varslot, Liliana de Campo, Sebastian C. Kapfer, and Walter Mickel. “A Bicontinuous Mesophase Geometry with Hexagonal Symmetry”. In: *Langmuir* 27.17 (2011).
- [287] Bernd Schulze and Walter Whiteley. “Rigidity and Scene Analysis”. In: *Handbook of Discrete and Computational Geometry*. 3rd ed. Chapter 61. CRC Press LLC (2017).
- [288] Bernd Schulze and Walter Whiteley. “Coning, Symmetry and Spherical Frameworks”. In: *Discrete and Computational Geometry* 48 (2011).
- [289] Hermann A. Schwarz. *Gesammelte Mathematische Abhandlungen*. 1st ed. Vol. 1. Springer-Verlag Berlin (1890).
- [290] Ulrich S. Schwarz and Gerhard Gompper. “Bending Frustration of Lipid-Water Mesophases Based on Cubic Minimal Surfaces1”. In: *Langmuir* 17.7 (2001).
- [291] Bettina Schülke. “New Materialism - the Transformation of intelligent Fabrics towards an interactive Youser generated Interface”. In: *European Scientific Journal* 10.10 (2014).
- [292] Class for Physics of the Royal Swedish Academy of Sciences. *Scientific Background on the Nobel Prize in Physics 2010: Graphene*. (2010). Available online: [https://web.archive.org/web/20180701222510/https://www.nobelprize.org/nobel\\_prizes/physics/laureates/2010/advanced-physicsprize2010.pdf](https://web.archive.org/web/20180701222510/https://www.nobelprize.org/nobel_prizes/physics/laureates/2010/advanced-physicsprize2010.pdf) (visited on 08/01/2024).
- [293] Steven R. Sellers, Weining Man, Shervin Sahba, and Marian Florescu. “Local self-uniformity in photonic networks”. In: *Nature Communications* 8.1 (2017).
- [294] Naum Z. Shor. “Class of global minimum bounds of polynomial functions”. In: *Cybernetics* 23.6 (1987).
- [295] Amit Singer and Mihai Cucuringu. “Uniqueness of Low-Rank Matrix Completion by Rigidity Theory”. In: *SIAM Journal on Matrix Analysis and Applications* 31 (2010).
- [296] Steve Smale. “Newton’s Method Estimates from Data at One Point”. In: *The Merging of Disciplines: New Directions in Pure, Applied, and Computational Mathematics*. Springer New York (1986).
- [297] Christopher W. Smith, Robin J. Wootton, and Kenneth E. Evans. “Interpretation of Experimental Data for Poisson’s Ratio of Highly Nonlinear Materials”. In: *Experimental Mechanics* 39 (1999).
- [298] Kenneth Snelson. “The Art of Tensegrity”. In: *International Journal of Space Structures* 27 (2012).

- [299] Andrew Sommese and Charles Wampler. *The Numerical Solution of Systems of Polynomials Arising in Engineering and Science*. World Scientific (2005).
- [300] Georg Sperl, Rahul Narain, and Chris Wojtan. “Homogenized Yarn-Level Cloth”. In: *ACM Transactions on Graphics (TOG)* 39.4 (2020).
- [301] Eugene L. Starostin. “A Constructive Approach to Modelling the Tight Shapes of Some Linked Structures”. In: *Forma* 18.4 (2003).
- [302] Andrzej Stasiak and John H. Maddocks. “Best Packing in Proteins and DNA”. In: *Nature* 406 (2000).
- [303] Ileana Streinu. “Pseudo-Triangulations, Rigidity and Motion Planning”. In: *Computer Science: Faculty Publications, Smith College* 34.4 (2005).
- [304] Bernd Sturmfels. *Solving Systems of Polynomial Equations*. Vol. 97. CBMS Regional Conference Series in Mathematics. American Mathematical Society, 2002.
- [305] Rui Su, Shuyuan Wang, Zachary McDargh, and Ben O’Shaughnessy. “Three membrane fusion pore families determine the pathway to pore dilation”. In: *Biophysical Journal* 122.19 (2023).
- [306] Ann C. Sychterz and Ian F. C. Smith. “Deployment and Shape Change of a Tensegrity Structure Using Path-Planning and Feedback Control”. In: *Frontiers in Built Environment* 4 (2018).
- [307] Alex Séguin and Daniel Kressner. “Continuation Methods for Riemannian Optimization”. In: *SIAM Journal on Optimization* 32.2 (2022).
- [308] Tomohiro Tachi. “Designing Rigidly Foldable Horns Using Bricard’s Octahedron”. In: *Journal of Mechanisms and Robotics* 8.3 (2016).
- [309] Satoshi Takabe and Tadashi Wadayama. “ $k$ -connectivity of Random Graphs and Random Geometric Graphs in Node Fault Model”. In: *2018 International Symposium on Information Theory and Its Applications (ISITA)*. Institute of Electrical and Electronics Engineers (2018).
- [310] Daina Taimina. *Global Warm( $n$ )ing*. (2009). Available online: <https://dainataimina.blogspot.com> (visited on 06/30/2024).
- [311] Michael E. Taylor. *Introduction to Analysis in Several Variables: Advanced Calculus*. Pure and Applied Undergraduate Texts Vol. 46. American Mathematical Society (2020).
- [312] Simon Telen, Marc Van Barel, and Jan Verschelde. “A Robust Numerical Path Tracking Algorithm for Polynomial Homotopy Continuation”. In: *SIAM Journal on Scientific Computing* 6 (2020).
- [313] D’Arcy Wentworth Thompson. *On Growth and Form*. Dover Publications, (1942).
- [314] William P. Thurston. *The Geometry and Topology of 3-Manifolds*. Princeton Lecture Notes (1980).
- [315] Gunnar Tibert. “Deployable Tensegrity Structures for Space Applications”. Doctoral Thesis. Kungliga Tekniska Högskolan Stockholm (2002).

- [316] Sascha Timme. "Mixed Precision Path Tracking for Polynomial Homotopy Continuation". In: *Advances in Computational Mathematics* 47 (2019).
- [317] Martin Traizet. "On the Genus of Triply Periodic Minimal Surfaces". In: *Journal of Differential Geometry* 79 (2008).
- [318] Ljubica S. Velimirović, Grozdana Radivojević, Miomir S. Stankovic, and Dragan Kostic. "Minimal Surfaces for Architectural Constructions". In: *Facta Universitatis - Series: Architecture and Civil Engineering* 6 (2008).
- [319] Jan Verschelde. "Algorithm 795: PHCpack: A General-Purpose Solver for Polynomial Systems by Homotopy Continuation". In: *ACM Transactions on Mathematical Software* 25.2 (1999).
- [320] Konstantin Y. Volokh, Oren Vilnay, and Michael Belsky. "Tensegrity Architecture Explains Linear Stiffening and Predicts Softening of Living Cells". In: *Journal of Biomechanics* 33.12 (2000).
- [321] Fusheng Wei. "Some existence and uniqueness theorems for doubly periodic minimal surfaces". In: *Inventiones mathematicae* 109.1 (1992).
- [322] Karl Weierstrass. *Mathematische Werke*. Vol. 3. Mayer & Müller Berlin, (1903).
- [323] Simon Weis, Philipp Schönhöfer, Fabian Schaller, Matthias Schröter, and Gerd E. Schröder-Turk. "Pomelo, a Tool for Computing Generic Set Voronoi Diagrams of Aspherical Particles of Arbitrary Shape". In: *EPJ Web of Conferences* 140 (2017).
- [324] Ture Wester. "The Structural Morphology of Penrose and Quasicrystal Patterns Part I". In: *International Conference On Adaptable Building Structures*. TU Eindhoven (2006).
- [325] Adam G. Weyhaupt. "Deformations of the Gyroid and Lidinoid Minimal Surfaces Using Flat Structures". In: *Pacific Journal of Mathematics* 235.1 (2008).
- [326] Walter Whiteley. "Cones, infinity and one-story buildings". In: *Topologie Structurale* 8 (1983).
- [327] Walter Whiteley. "Counting out to the Flexibility of Molecules". In: *Physical Niology* 2 (2005).
- [328] Thomas J. Willmore. "A survey on Willmore immersions". In: *Geometry and topology of submanifolds, IV*. World Scientific Publishing Co., (1992).
- [329] Bodo D. Wilts, Benjamin Apeleo Zubiri, Michael A. Klatt, Benjamin Butz, Michael G. Fischer, Stephen T. Kelly, Erdmann Spiecker, Ullrich Steiner, and Gerd E. Schröder-Turk. "Butterfly Gyroid Nanostructures as a Time-Frozen Glimpse of Intracellular Membrane Development". In: *Science Advances* 3.4 (2017).
- [330] Frederick Wooten, Kris Winer, and Denis L. Weaire. "Computer Generation of Structural Models of Amorphous Si and Ge". In: *Physical Review Letters* 54 (1985).
- [331] Nachuan Xiao, Xiaoyin Hu, Xin Liu, and Kim-Chuan Toh. *CDOpt: A Python Package for a Class of Riemannian Optimization*. 2022. arXiv: 2212.02698 [math.OC].

- [332] Yuhe Yang et al. “Gaussian curvature–driven direction of cell fate toward osteogenesis with triply periodic minimal surface scaffolds”. In: *Proceedings of the National Academy of Sciences* 119.41 (2022).
- [333] Sunkyu Yu, Cheng-Wei Qiu, Yidong Chong, Salvatore Torquato, and Namkyoo Park. “Engineered Disorder in Photonics”. In: *Nature Reviews Materials* 6.3 (2021).
- [334] S. Yuvaraj, A. Adithya, G. Banu, and S. Srithar. “Numerical and Experimental Investigation of Airfoil Derived from Peregrine Falcon”. In: *Measurement: Sensors* 31 (2024).
- [335] Isiah Zaplana, Hugo Hadfield, and Joan Lasenby. “Closed-Form Solutions for the Inverse Kinematics of Serial Robots Using Conformal Geometric Algebra”. In: *Mechanism and Machine Theory* 173 (2022).
- [336] Erik C. Zeeman. “Catastrophe Theory”. In: *Scientific American* 234.4 (1976).
- [337] Xiangbing Zeng, Silvio Poppe, Anne Lehmann, Marko Prehm, Changlong Chen, Feng Liu, Huanjun Lu, Goran Ungar, and Carsten Tschierske. “A Self-Assembled Bicontinuous Cubic Phase with a Single-Diamond Network”. In: *Angewandte Chemie International Edition* 58.22 (2019).
- [338] Tingting Zhang, Shuang Wu, Rong Yang, and Guangyu Zhang. “Graphene: Nanostructure engineering and applications”. In: *Frontiers of Physics* 12 (2017).
- [339] Di Zhou, Leyou Zhang, and Xiaoming Mao. “Topological Boundary Floppy Modes in Quasicrystals”. In: *Physical Review X* 9.2 (2019).
- [340] Hong-Cai Zhou, Jeffrey R. Long, and Omar M. Yaghi. “Introduction to Metal–Organic Frameworks”. In: *Chemical Reviews* 112.2 (2012).
- [341] Xiaojing Zhu. “A Riemannian Conjugate Gradient Method for Optimization on the Stiefel Manifold”. In: *Computational Optimization and Applications* 67.1 (2017).
- [342] Xiaojing Zhu and Chunyan Duan. “On Matrix Exponentials and their Approximations Related to Optimization on the Stiefel Manifold”. In: *Optimization Letters* 13.5 (2019).
- [343] Xiaoqin Wang Zhuming Bi. *Computer Aided Design and Manufacturing*. John Wiley & Sons Ltd and ASME Press, (2020).
- [344] Valfredo Zolesi, Pier Ganga, Lucio Scolamiero, Andrea Micheletti, Paolo Podio-Guidugli, Gunnar Tibert, Alessandro Donati, and Michele Ghiozzi. “On an Innovative Deployment Concept for Large Space Structures”. In: *42nd International Conference on Environmental Systems*. Curran Associates, Inc. (2012).